Multi-Spurious Harmonic Suppression in Miniaturized Planar Bandpass Filters

Thesis submitted

by

Tarun Kumar Das

Doctor of Philosophy (Engineering)

Department of Electronics and Telecommunication Engineering

Faculty Council of Engineering & Technology

Jadavpur University

Kolkata, India

2022

JADAVPUR UNIVERSITY

KOLKATA - 700032, INDIA

INDEX NO. 43/16/E

1. **Title of the Thesis**: Multi-Spurious Harmonic Suppression in Miniaturized Planar Bandpass Filters
2. **Name, Designation & Institution of the Supervisor**:

   Dr. Sayan Chatterjee

   Professor, Dept. of Electronics and Telecommunication Engineering

   Jadavpur University, Kolkata - 700032, West Bengal, India
3. **List of Publication**: Refer to Appendix-I
4. **List of Patents**: Nil
5. **List of Presentations in National/ International/Conferences/Workshops**:

[1] **Tarun Kumar Das** and Sayan Chatterjee, "Design of a finite attenuation pole miniaturized S-band lowpass filter using elliptic function," *Proceedings of International Conference on Microwave, Optical and Communication Engineering (ICMOCE 2015)*, Bhubaneswar, India, pp. 404-407, 18-20 December, 2015, doi: 10.1109/ICMOCE.2015.7489778.

[2] **Tarun Kumar Das** and Sayan Chatterjee, "Design of a compact symmetrical C-Band Micro Strip Band Pass Filter with periodic Saw tooth Grooves," *Proceedings of 2nd International Conference on Innovative Advancements in Engineering & Technology (IAET 2016)*, Jaipur, India, vol. 5, no. 1, pp. 254-259, 1-2 April, 2016.

[3] **Tarun Kumar Das** and Sayan Chatterjee, "Performance of periodic grooves on harmonic rejection in C band folded edge coupled microstrip band pass filters," *Proceedings of International Conference on Computational Science and Engineering (ICCSE 2016)*, Kolkata, India, pp. 205-209, 4-6 October, 2016, doi: 10.1201/9781315375021-40.

[4] **Tarun Kumar Das** and Sayan Chatterjee, "2^{nd} Harmonic Suppression in Parallel-Coupled Microstrip Bandpass Filter by using Koch Fractals," *Proceedings of IEEE Annual India Conference (INDICON 2016)*, Bengaluru, India, pp. 1-6, 16-18 December, 2016, doi: 10.1109/INDICON.2016.7838919.

[5] **Tarun Kumar Das** and Sayan Chatterjee, "Spurious Harmonic Suppression in a Folded Parallel-Coupled Microstrip Bandpass Filter by using Triangular Corrugations," *Proceedings of Devices for Integrated Circuit (DevIC 2017)*, Kalyani, India, pp. 391–395, 23-24 March, 2017, doi: 10.1109/DEVIC.2017.8073977.

[6] Sayan Chatterjee, **Tarun Kumar Das**, and Bhaskar Gupta, "Harmonic Suppression in In-line Parallel-Coupled Microstrip Bandpass Filter by Minkowski Fractals," *Proceedings of 17th Mediterranean Microwave Symposium (MMS 2017)*, Marseille, France, pp. 1-4, 28-30 November, 2017, doi: 10.1109/MMS.2017.8497142.

[7] **Tarun Kumar Das** and Sayan Chatterjee, "Harmonic Suppression in an In-line Chebyshev Bandpass Filter by Asymmetrical Perturbations," *Proceedings of IEEE MTT-S International Microwave and RF Conference (IMaRC 2017)*, Ahmedabad, India, pp. 1-5, 11-13 December, 2017, doi: 10.1109/IMaRC.2017.8449689.

[8] **Tarun Kumar Das** and Sayan Chatterjee, "Phase Velocity Compensation in Compact Coupled-Line Bandpass Filter with Square Corrugations," *Chapter of Social Transformation – Digital Way, Communications in Computer and Information Science Book Series (CCIS) Springer, Singapore, Annual Convention of the Computer Society of India, (CSI 2018)*, Kolkata, India, vol. 836, pp. 29–41, 19-21 January, 2018, doi:10.1007/978-981-13-1343-1_4.

[9] Sayan Chatterjee and **Tarun Kumar Das**, "Multispurious Harmonic Suppression in Compact Coupled-Line Bandpass Filters by Trapezoidal Corrugations," *Proceedings of IEEE 18th Mediterranean Microwave Symposium (MMS 2018)*, Istanbul, Turkey, 31 October-2 November, 2018, pp. 149-152, doi: 10.1109/MMS.2018.8611809.

[10] Sayan Chatterjee and **Tarun Kumar Das**, "Compact Hairpin-Line Bandpass Filter with Harmonic Suppression by Periodic Grooves," *Proceedings of IEEE 19th Mediterranean Microwave Symposium (MMS 2019)*, Hammamet, Tunisia, pp. 1-4, 31 October-2 November, 2019, doi: 10.1109/MMS48040.2019.9157328.

[11] **Tarun Kumar Das** and Sayan Chatterjee, "Compact coupled-line microstrip bandpass filter with spurious passband suppression using Minkowski fractal," *Proceedings of URSI Regional Conference on Radio Science (URSI-RCRS 2020)*, Varanasi, India, pp. 1-4, 12-14 February, 2020, doi: 10.23919/URSIRCRS49211.2020.9113422.

[12] **Tarun Kumar Das** and Sayan Chatterjee, "Improved Stopband Rejection in Compact Microstrip Filters by Transmission Zero Reallocation," *Proceedings of IEEE Calcutta Conference (CALCON2020)*, Kolkata, India, pp. 10-14, 28-29 February, 2020, doi: 10.1109/CALCON49167.2020.9106476.

[13] **Tarun Kumar Das** and Sayan Chatterjee, "Harmonic Suppression in a Folded Hairpin-Line Cross-Coupled Bandpass Filter by using Spur-Line," *Proceedings of IEEE Devices for Integrated Circuit (DevIC 2021),* Kalyani, India, pp. 474-478, 19-20 May, 2021**,** doi: 10.1109/DevIC50843.2021.9455915

[14] **Tarun Kumar Das**, Pritam Paul, Suprava Das, and Sayan Chatterjee, "Multi-Folded Bandpass Filter with Harmonic Suppression by Meander Spurline," *Proceedings of IEEE INDICON 2022,* Guwahati, India, pp. 1-6, 19-21 December, 2021, doi: 10.1109/INDICON52576.2021.9691654.

[15] **Tarun Kumar Das** and Sayan Chatterjee, "Wide Stopband Centrally Corrugated Folded Bandpass Filter with Trapezoidal Spurline," *Proceedings of IEEE WAMS 2022*, 5-8 June, 2022, Rourkela, India. pp. 1-5, doi: 10.1109/WAMS54719.2022.9848230.

[16] **Tarun Kumar Das**, Ayona Chakraborty, Sayan Chatterjee, and Bhaskar Gupta, "Centrally Corrugated Cross-Coupled Wide Stopband Folded Bandpass Filter with Spurline," *Proceedings of 2022 Microwave Mediterranean Symposium (MMS)*, pp. 1-6, May 2022, Itally, doi: 10.1109/MMS55062.2022.9825567.

Dedicated to My Beloved Mother

STATEMENT OF ORIGINALITY

I, Tarun Kumar Das, registered on 18th October, 2016 do hereby declare that this thesis entitled **"Multi-Spurious Harmonic Suppression in Miniaturized Planar Bandpass Filters"** contains literature survey and original research work done by the undersigned candidate as part of Doctoral studies.

All information in this thesis have been obtained and presented in accordance with existing academic rules and ethical conduct. I declare that, as required by these rules and conduct, I have fully cited and referred all materials and results that are not original to this work.

I also declare that I have checked this thesis as per the "Policy on Anti Plagiarism, Jadavpur University, 2019", and the level of similarity as checked by iThenticate software is 8 %.

Signature of the candidate:

Tarun Kumar Das.

(Tarun Kumar Das)

Date: 03.11.22

Certified by Supervisor:
(Signature with date, seal)

Sayan Chatterjee 03/11/22

Prof. Sayan Chatterjee
Professor
Dept. of Electronics and Communication Engineering
Jadavpur University
Kolkata-700032, India

Dr. Sayan Chatterjee
Professor
Electronics & Telecomm. Engg. Dept.,
Jadavpur University, Kolkata - 700032.

CERTIFICATE FROM THE SUPERVISOR

*This is to certify that the thesis entitled "**Multi-Spurious Harmonic Suppression in Miniaturized Planar Bandpass Filters**" submitted by **Shri Tarun Kumar Das** who got his name registered on **18th October 2016** for the award of Ph. D. (Engg.) degree of Jadavpur University is absolutely based on his own work under the supervision of **Prof. Sayan Chatterjee** of Electronics and Telecommunication Engineering Department of Jadavpur University, Kolkata, West Bengal and that neither his thesis nor any part of the thesis has been submitted for any degree/diploma or any other academic award anywhere before.*

Sayan Chatterjee 03/11/22

(Signature of the Supervisor and Date with Office Seal)

Dr. Sayan Chatterjee
Professor
Electronics & Telecomm. Engg. Dept.,
Jadavpur University, Kolkata - 700032.

Acknowledgements

I would like to take this opportunity to express my deep and sincere gratitude to my supervisor Professor Sayan Chatterjee, Electronics and Telecommunication Engineering Department of Jadavpur University. I thank Professor Chatterjee for his immensely helpful suggestions regarding the technological aspects of compact microstrip filter design and different methodologies for their harmonics suppression performances.

I would like to thank Prof. Dipak Ranjan Poddar, Ex-Professor, Electronics and Telecommunication Engineering Department of Jadavpur University for his valuable suggestions and mental support throughout my journey of research work. I also would like to thank Dr. Arijit Majumder, Officer in Charge, SAMEER, Kolkata for his constant support, suggestions in performing my proposed work and allowing me for some of the experimental measurements of the fabricated filters. At this outset, I would also like to thank Dr. Amartya Banerjee, Dr. Ayona Chakraborty, and Mr. Joydeep Pal, my fellow friends of research in PC Lab, Jadavpur University for their support during measurement works. I recollect the helpful comments and encouragement provided by my beloved teacher, Prof. Bhaskar Gupta, Dept. of Electronics and Telecommunication Engineering, Jadavpur University. I sincerely pay my gratitude to Dr. K. Srinivas Reddy, Director, Atlantic Circuits, Hyderabad for fabricating all the prototypes of my proposed filters.

I must also mention the encouragement and active cooperation from my mother, Smt. Rekha Das, my wife, Mrs. Jhumpa Das, my elder son, Swarnadeep Das and younger son, Shankhadeep Das for their love and cooperation during my studies and research work.

Tarun Kumar Das

Date: 03.11.22 (Tarun Kumar Das)

Table of Contents

List of Figures

List of Tables

INTRODUCTION

1.1. Brief Discussions

In the modern-day of communication systems, Information and Communications Technology (ICT) enables users to access, store, transmit, understand, and manipulate information wirelessly with enhanced security and in less time [1]. It encompasses all the technologies and services involved in computing, data management, and telecommunications by using cyber-physical systems. In ICT, the communication network and media are of the utmost importance to distribute information at a very high speed, irrespective of channel conditions. With the evolution and advancements of the internet, telephone, mobile phone, TV, and office automation systems, wireless networks play an important role in ICT. Thus, different compact-sized functional blocks of the communication network are required primarily to be integrated on a common platform in the transmitter and receiver module. Likewise, at present, the platform for large data transfer and communication between people and things worldwide over the internet has been provided by the Internet-of-things (IoT) [1]. However, various functionalities are to be included in the transmitter and receiver modules due to the continuous advancements in the modern IoT-based wireless communications systems, especially compactness of modules, which is the major concern. Moreover, with the requirement of larger bandwidth in allocated spectrum, 5G and IoT jointly explore a new generation of wireless technology that provides a powerful combination of extraordinary speed, expanded bandwidth, low latency, and increased power efficiency [2]. In this context, wireless local area networks (WLAN) serve the key role in interconnecting devices for IoT in 5G [3]. The WLAN is specified by the IEEE 802.11/a/b/g/n/ac standard, which uses 2.4 GHz (2.401-2.483 GHz) in the ISM band and 5 GHz (5.15-5.35 GHz) in the C-band as the centre frequency with a data rate of 2-700 Mbps. However, new functionalities are continuously being embedded into the WLAN architecture to cope with the world-wide popularity of IoT-based 5G systems. This obviously demands very compact sizes of different blocks in the WLAN communication system.

In a complete transceiver chip with a compact floor plan and low power application, subsystem design specifications are becoming more stringent. Therefore, researchers are moving towards digital-based control and communication systems where signal processing at

baseband level can provide better solutions. However, there are situations where multiple fabrication platforms are not acceptable due to signal integrity problems. Accordingly, RF sub blocks, designed on a single tape out platform, are still very attractive. Among several RF blocks, filters play a very crucial role in the rejection of unwanted signal frequencies while permitting good transmission of the required passband. Moreover, filters are also used as the building blocks for duplexers and diplexers to combine or separate multiple frequency bands. Thus, with the advancements of today's wireless communication systems, high quality filters are the utmost necessary components for the efficient transmission and reception of the baseband signal. Moreover, emerging applications of wireless communication systems (WLANs, cellphones, Wi-Fi, etc.) continue to challenge RF/microwave filters with even more stringent requirements like smaller size, lighter weight, lower cost, and sharper skirt characteristics [4]. In general, filters are broadly categorized into low-pass, high-pass, bandpass, and band reject based upon the transmission characteristics. However, narrowband bandpass filters are playing an important role in the transmitter and receiver modules of ICT systems for their efficient performance.

Several major developments have been carried out in the last three decades for the filters' technology, such as performance improvement, development of CAD tools, full-wave EM analysis, designing of new compact structures and topologies, employment of advanced materials and associated fabrication technologies such as monolithic microwave integrated circuit (MMIC) [5], microelectromechanic systems (MEMS) and micromachining [6], high-temperature superconductor (HTS) [7], and low-temperature cofired ceramics (LTCC) [8] etc. With the requirements of an integration platform, coaxial cables, waveguides, strip lines, microstrip lines, and co-planar waveguide (CPW) based filter designs are employed for high frequency applications. Among different planar transmission lines, microstrip transmission lines are more advantageous due to their planar and compact structures, being easy to integrate, light weight, and easy to fabricate using most standard PCB processes. The most attractive feature of the microstrip lines is that very compact filters can be designed by employing different types of folding mechanisms. Thus, the sizes of the microstrip line filters are smaller than those of waveguide, CPW, and stripline filters. Although planar filters have several limitations, such as low power handling capacity, higher losses, poor isolation among

adjacent lines, and unwanted radiation in uncovered microstrip-based configurations when compared to waveguide filters, their applications are limited in some specific areas.

Various topologies have been employed by the designers for the last three decades to design very compact microstrip bandpass filters, such as end-coupled line, parallel-coupled line, hairpin-line, interdigital, combline, open-loop cross-coupled resonators, dual-mode filters, etc. However, at the initial stage of the evolution of filter design, the parallel-coupled microstrip line bandpass filter (PCMLBF) has been extensively used in wireless communication systems due to its ease of design and integration with other components [9]. However, asymmetrical modal phase velocities imbalances have occurred for parallel-coupled line filters due to the inhomogeneous nature of the microstrip structure. This results in asymmetry in the passband and generates multiple spurious harmonics in the stopband. Moreover, depending upon the design constraints, the coupled-line filter requires a relatively higher amount of floor plan, making it not suitable for miniaturized subsystems. Therefore, the design of compact and miniaturized filters with improved out-of-band performance has become a major challenge. In this context, some researchers have made efforts to achieve compactness in coupled-line filters by following different folding mechanisms [10-13]. However, the effects of the folding mechanisms on the harmonics' attenuation levels have not been investigated in such work. Accordingly, different nonuniform perturbations have been employed by the researchers in the conventional parallel-coupled line bandpass filters to suppress the spurious harmonics [14-15]. However, the size of those filters is pretty large due to their conventional structure. In this context, very few works have focused on the compactness and harmonic suppression of parallel-coupled line filters.

Accordingly, researchers have started to design hairpin-line bandpass filters, which are modifications of the parallel-coupled-line filters. In hairpin-line filters, the half-wavelength lines are folded into a U-shape and such cells are placed alternately in hybrid-mode of coupling [16-17]. Such filters occupy much less area than parallel-coupled line filters, along with the advantages of improved skirt selectivity and low insertion loss. However, the spurious harmonics are still present due to the modal phase velocity imbalance between the coupled lines. Accordingly, some of the research has been focused only on the folding of hairpin-line filters to achieve more compactness and improvement of the passband [18-19]. Other research has concentrated on the suppression of spurious harmonics using various

reactive structures [20-21]. However, very few studies have been carried out based on both the size reduction and harmonics suppression for hairpin-line filters.

Moreover, hairpin-line filters are also suffering from some limitations, such as the sizes of the filters are still pretty large and not suitable for modern wireless communication systems. Besides, the skirt selectivity is generally governed by the improvement at the upper passband edge due to the hybrid configuration, and thus, an asymmetrical passband response still occurs. In this context, researchers have started work to integrate electric, magnetic, and hybrid couplings in cross-coupled open-loop resonator filters [22-23]. Such filters are based on quasi-elliptic transfer functions, generating finite transmission zeros at the passband edges, greatly improving the skirt selectivity over the other filter topologies. In addition, the cross-coupled structure exhibits a very compact size suitable for modern wireless systems. Several methods for suppressing spurious harmonics in conventional open-loop cross-coupled filters have been proposed by researchers [24-25]. Very little research has been carried out to combine both the folding and harmonics-free performance of the cross-coupled filters [26]. Thus, the design of the compact bandpass filter with enhanced skirt characteristics, symmetrical passband response, wide stopband and improved rejection level is still a major challenge for researchers for the effective use of filters in modern wireless systems where the sizes of the filters are truly a major concern.

1.2. Motivations of the Proposed Design

In the present thesis, a miniaturized bandpass filter with improved skirt characteristics, extended stopband and enhanced rejection level has been investigated in line with the requirements of modern ICT. From the literature survey, it has been revealed that microstrip bandpass filters have been studied by researchers for the last three decades for various advantages. In the present thesis, work has mainly focused on designing filters in the microstrip domain, either on the passband improvement or on the harmonics suppression performance. As a result, the goals of this thesis are as follows: (1) design a folded parallel-coupled line bandpass filter, folded hairpin-line bandpass filter, and folded cross-coupled bandpass filter; and (2) investigate different reactive perturbations for harmonics suppression for all such folded filters. As an optimum result, a compactness of 68% along with a stopband bandwidth of $4f_0$ (where f_0 is the center frequency of the filter) with a rejection level of 40 dB has been obtained by meander spurline.

1.3. Outline of the Chapters

From the reviews of the harmonics suppression performances for the compact microstrip bandpass filters, the contribution of this thesis will cover the following topics:

a. Designing of compact bandpass filters by folding the conventional microstrip filter structures.
b. A detailed study of the issues raised after folding the couple lines
c. A detailed circuit analysis of the folded filter
d. Detailed comparison of different reactive structures based on their harmonic suppression performances.
e. Justification of the circuit analysis results with the EM simulation results
f. Validation of the proposed designs by fabrication and testing
g. A detailed comparison between the performances of the parallel-coupled line filter, hairpin-line filter, and cross-coupled-line filter based on their figure-of-merit

Investigations reported in the thesis are mainly divided into the following chapters:

Chapter 2:

In this chapter, historical appraisal has been reported through different compact structures of the bandpass filters and their harmonic suppression performances by different reactive structures. Following the review, motivations for the present design are addressed using the already developed concept of folding and harmonic suppression. At this outset, multi-spurious harmonics suppression for compact filters is also highlighted.

Chapter 3:

A design of compact parallel-coupled line filters is proposed. By rearranging the parallel-coupled lines in a folded and inline manner, a size reduction of more than 60% has been achieved. The equivalent lumped elements circuit diagram is derived and a detailed synthesis procedure is described for all the filters. Subsequently, different nonuniform structures have been employed to suppress the harmonics for coupled-line filters. Prototypes are fabricated and tested experimentally. As an optimum result, size reduction of 60% with a wide stopband of $4.72f_0$ and a rejection level of 33 dB has been obtained for a folded parallel-coupled-line filter with trapezoidal corrugations..

Chapter 4:

Compact hairpin-line bandpass filters are proposed by folding the open-end of the lines. As a result, more compactness has been achieved. Different reactive structures have been investigated for the compact hairpin-line filters. The details of the synthesis procedure and equivalent lumped element circuit are analyzed. Spurline has been employed and studied in detail. All the filters are fabricated and tested experimentally. Subsequently, the folded arms of the hairpin-line cells have been modified with corrugated folded arms to achieve more compactness. An optimum filter size reduction of 72% and an extended stopband upto $4.68f_0$ with a rejection level better than 37 dB has been recorded by an L-shaped spurline.

Chapter 5:

Cross-coupled filters have been investigated as an extension of Chapter 4. The folded hairpin-line cells are arranged in a cross-coupled configuration to generate sharp transmission zeros at the passband edges. Thus, the skirt selectivity has been improved. Subsequently, spurline has been employed to achieve a wide stopband with enhanced rejection level. Subsequently, corrugated folded hairpin-line cells have been studied for the cross-coupled filters for better improvement of the skirt selectivity further. As an optimum result, a compactness of 68% along with a stopband bandwidth of $4f_0$ with a rejection level of 40 dB has been obtained by meander spurline.

Chapter 6:

A summary of all the chapters that have been analyzed. The novelties of the proposed filters have been highlighted. The application areas of the proposed filters have been mentioned. Along with the design, new possibilities are briefly mentioned on which future research can be carried out.

References:

[1] A. Rejeb, K. Rejeb, S. Simske, H. Treiblmaier, S. Zailani, "The big picture on the internet of things and the smart city: a review of what we know and what we need to know," *Internet of Things*, vol. 19, no. 100565, August 2022.

[2] K. F. Muteba, K. Djouani, T. Olwal, "5G NB-IoT: Design, Considerations, Solutions and Challenges, *Procedia Computer Science*, vol. 198, pp. 86-93, January 2022.

[3] Q. V. Khanh, N. V. Hoai, L. D. Manh, A. N. Le, G. Jeon, "Wireless communication technologies for IoT in 5G: vision, applications, and challenges," *Wireless Communications and Mobile Computing*, vol. 2022, no. 3229294, pp. 1-12, February 2022.

[4] G. Mattaei, L. Young and E. M. T. Jones, "Microwave Filters, Impedance-matching Networks and Coupling Structures," *Artech House*, Norwood, MA, vol. 1, ch. 4, pp. 84-94, 1980.

[5] L. Pantoli, G. Leuzzi, F. Deborgies, P. Jankovic, F. Vitulli, "A Survey of MMIC Active Filters," *Electronics*, vol. 10, no. 14, pp. 1680, July 2021.

[6] S. K. Koul, S. Dey, "Micromachined Tunable Filters Using MEMS Switches," *Micromachined Circuits and Devices*, pp. 195-223, Springer, Singapore, 2022.

[7] C. Zhang, W. Xie, C. Li, J. Dai, Y. Yuan, R. Jiang, X. Wang, J. Wang, Y. Wu, L. Sun, and Y. He, "Recent progress on high-temperature superconducting filters," *Superconductivity*, vol. 2, pp. 100012, May 2022.

[8] W. Zhao, Y. Wu, Y. Yang, W. Wang, "LTCC Bandpass Filter Chips With Controllable Transmission Zeros and Bandwidths Using Stepped-Impedance Stubs," *IEEE Transactions on Circuits and Systems II: Express Briefs*, vol. 69, no. 4, pp. 2071-2075, January 2022.

[9] J. S. Hong and M. J. Lancaster, "Microstrip Filters for RF/Microwave Applications," *John Willey & Sons, Inc*., New York, NY, 2001, ISBN 0-471-22161-9, Ch. 3, pp. 29-30, 2001.

[10] K. S. Chin, L. Y. Lin and J. T. Kuo, "New formulas for synthesizing microstrip bandpass filters with relatively wide bandwidths," *IEEE Microwave and Wireless Components Letters*, vol. 14, no. 5, pp. 231-233, May 2004.

[11] K. S. Chin and J. T. Kuo, "Insertion loss function synthesis of maximally flat parallel-coupled line bandpass filters," *IEEE Transactions on Microwave Theory and Techniques*, vol. 53, no. 10, pp. 3161-3168, October 2005.

[12] K. C. Yoon and J. C. Lee, "Design of a Compact Wide-Bandwidth Bandpass Filter using a Parallel-Coupled Structure," *Microwave and Optical technology Letters*, vol. 54, no. 11, pp. 2581-2584, November 2012.

[13] X. H. Wang, and H. Zhang, "Novel Balanced Wideband Filters Using Microstrip Coupled Lines," *Microwave and Optical Technology Letters*, vol. 56, no. 5, 1139-1141, May 2014.

[14] T. Lopetegi, M. A. G. Laso, J. Hernández, M. Bacaicoa, D. Benito, M. J. Garde, M. Sorolla, and M. Guglielmi, "New microstrip 'wiggly-Line' filters with spurious passband suppression," *IEEE Trans. Microwave Theory Tech.*, vol. 49, no. 9, pp. 1593-1598, September 2001.

[15] B. S. Kim, J. W. Lee, and M. S. Song, "An Implementation of Harmonic-Suppression Microstrip Filters with Periodic Grooves," *IEEE Microwave and Wireless Components Letters*, vol. 14, no.9, pp. 413-415, September 2004.

[16] E. G. Cristal and S. Frankel, "Hairpin-Line and Hybrid Hairpin-Line/ Half-Wave Parallel-Coupled-Line Filters," *IEEE Transactions on Microwave Theory and Techniques*, vol. MTT-20, no. 11, pp. 719-728, November 1972.

[17] M. Sagawa, K. Takahashi, M. Makimoto, "Miniaturized hairpin resonator filters and their application to receiver front-end MICs," *IEEE Transactions on Microwave Theory and Techniques*,; vol. 37, no. 12, pp. 1991-1997, December 1989.

[18] X. M. Qing, Y. W. Chia, J. Sun, "A novel miniaturized microstrip bandpass filter using a meander-line resonator," *Microwave and Optical Technology Letters*. vol. 32, no. 4, pp. 319-321, February 2002.

[19] C. L. Huang, C. H. Hsu, C. M. Tsai, "Miniaturization of hairpin bandpass filters using high-permittivity substrate," *Microwave and Optical Technology Letters*, vol. 45, no. 3, pp. 222-225, May 2005.

[20] M. L. Her, M. W. Hsu, Y. D. Wu, W. Ko, C. J. Hsu, "A wide rejection bandwidth bandpass filter with stepped-impedance hairpin resonator and interlaced coupled-line," *Microwave and Optical Technology Letters*, vol. 49, no. 3, pp. 542-545, March 2007.

[21] M. Naser-Moghadasi, M. Alamolhoda, B. Rahmati, "Harmonics blocking in hairpin filter using Defected Microstrip Structure," *IEICE Electronics Express*, vol. 8, no. 9, pp. 629-635, April 2011.

[22] J. S. Hong and M. J. Lancaster, "Design of highly selective microstrip bandpass filters with a single pair of attenuation poles at finite frequencies," *IEEE Transactions on Microwave theory and Techniques*, vol. 48, no. 7, pp. 1098-1107, July 2000.

[23] C. S. Ahn, J. Lee and Y. S. Kim, "Design flexibility of an open-loop resonator filter using similarity transformation of coupling matrix," *IEEE microwave and wireless components letters*, vol. 15, no. 4, pp. 262-264, April 2005.

[24] N. Kumar and Y. K. Singh, "Compact stub-loaded open-loop BPF with enhanced stopband by introducing extra transmission zeros," *Electronics Letters*, vol. 51, no. 2, pp. 164–166, January 2015.

[25] C. Han, Y. Rao, H. J. Qian, and X. Luo, "High-selectivity bandpass filter with wide upper stopband using harmonic suppression structure," *Proceedings of IEEE International Symposium on Radio-Frequency Integration Technology (RFIT)*, pp. 1-3, August 2019.

[26] S. Lu, K-D Xu, Y. Guo, Y. Ren, and Q. Chen, "Bandpass filter using coupled-line-stub cascaded structure with high stopband rejection," *Microw Opt Technol Lett*., vol. 63, no. 1, pp. 69-74. January 2021.

LITERATURE REVIEW

2.1. Introduction

The filter is a two-port network that provides low-loss transmission and linear phase response in the passband and high attenuation in the stopband. Radio transmitters and receivers require RF filters to suppress unwanted frequencies from being transmitted or received [1]. Moreover, filters are also used as the building blocks for duplexers and diplexers to combine or separate multiple frequency bands. The transfer function of a filter network is a mathematical description of its response characteristics. Accordingly, different types of distribution functions like Butterworth, Chebyshev, elliptic, Gaussian responses, etc. have been employed depending on applications [1-3].

2.2. History of Microwave Filters

Work on microwave filters started before World War-II. In 1937, filters at high radio frequencies in the range of 80 MHz–120 MHz with coaxial and balanced transmission lines were designed by Mason and Sykes [4], in which, the image impedance, image phase, and attenuation functions were derived by using the ABCD parameters for the filter sections. Subsequently, Darlington [5] explained the numerical synthesis of filters by using cascaded network theory. Although major advances and applications, primarily using image parameters, were commenced at M.I.T. Radiation Laboratory, Harvard Radio Research Laboratory, Bell Laboratories, NRL, etc. from 1941 to 1945 [6]. The main focus was given to waveguide cavity filters at the Radiation Laboratory, while broad-band low-pass, bandpass, and high-pass coaxial filters applicable for Engine Control Module (ECM) applications were studied at the Radio Research Laboratory. At the same time, narrow-band tunable coaxial resonator filters were also carried out for search receivers. Much of this work has also been described in the M.I.T. Radiation Laboratory Series by Fano and Lawson [7]. However, the coaxial transmission line filters and waveguide cavity filters were very bulky in size, costly, and difficult to install, especially at low frequencies. Furthermore, the presence of harmonics in these types of design mediums limited their applications in miniaturized communication systems.

With the advent of distributed circuit analysis, described by Paul I. Richards [8], a comprehensive relationship between the lumped and distributed circuits has enabled the transformation of the lumped network by using Richards' transformation. Subsequently, various filters with distributed components have been designed and, among them, planar filters have exhibited the most promising broadband response and ease of design in terms of size and performance compared to coaxial line, transmission line, and waveguide based filters. Besides compact dimensions, ease of integration in a modular environment, as well as well-developed and automated manufacturing procedures, have attracted filter designers and researchers to pay more attention to planar filters. Accordingly, planar transmission line structures become effective as they support either pure TEM mode (stripline) or hybrid or quasi TEM mode (microstrip and coplanar waveguide). Planar filters have been manufactured by creating flat 2D resonators with patterns of strip elements on a dielectric substrate. The width of the strip element, the dielectric constant of the substrate, and its thickness determine the characteristic impedance.

In general, the planar filter supports various EM modes propagating simultaneously, and further steps have been taken to suppress all modes except the desired one for achieving a wide stopband. Moreover, the transmission of more than one mode has been considered for the design of a dual-mode filter. Accordingly, various planar filters have been designed in the past decades, such as stripline filters [9-10] and suspended stripline filters [11]. Stripline was invented by Robert M. Barrett at the Air Force Cambridge Research Center in 1950. It is a conductor sandwiched by a dielectric between two ground planes. Stripline filters have supported pure TEM mode and are non-dispersive. They have exhibited improved bandwidth and symmetrical roll-off. However, such filters have suffered from the limitations of narrower bandwidths for given impedance and laminate thickness, being difficult to fabricate, more costly, and complicated to incorporate discrete, lumped, and active elements between the two ground planes.

Subsequently, microstrip lines were invented by D. D. Grieg and H. F. Engelmann of the Federal Telecommunications Laboratories of ITT in 1952 as a counterpart to striplines. The Microstrip line structure is made by sandwiching two conductor strips on both sides of a dielectric layer, forming the top surface and the ground plane, respectively [12-13]. It supports the quasi-TEM mode due to the inhomogeneous dielectric structure. However, it

suffers from radiation problems and accordingly exhibits more losses. Moreover, as an alternative to the planar microstrip structure for filter design, the coplanar waveguide was invented by Cheng P. Wen at RCA's Sarnoff Laboratories in New Jersey in 1969. A coplanar waveguide is created by putting a conductor strip in the centre and surrounding it with two ground planes on either side in the same plane [14-15]. They have the advantages of low dispersion, simple realization due to etching on one side. Besides, they exhibit broadband performance as there is no need for via holes for shunt and series elements. However, it suffers from the limitations of high fabrication costs due to the requirement of gold ribbons to suppress higher-order modes at every quarter wavelength and the necessity of relatively thick substrates.

Subsequently, slotline filters [16-17] have been employed in which balanced lines are used and are easy to integrate with active components into the line. Moreover, high impedance lines are easier to achieve for slotlines. However, the characteristic impedance and the group velocity suffer from strong variation with frequency, resulting in a more dispersive nature than the microstrip line. Alternately, substrate integrated waveguide (SIW) has been incorporated recently to design planar filters [18-19]. A SIW is a waveguide formed in the substrate dielectric by constraining the wave between two rows of posts or plated through holes and ground planes. SIW has the greatest benefit in that, as an effectively enclosed waveguide, it has considerably less radiation loss than the microstrip line with a moderate Q value.

With the rapid advancement of radar, satellite, and mobile wireless communication systems, there has been a requirement for miniaturization in filters. Moreover, with the advent of additive manufacturing technology, flexible and thin substrate-based transmission lines, and complex printed geometries in metal counterparts, miniaturized and high-degree of specification-based planar filter design is an attractive new-age research domain. In the following sections, the reviews of stepped-impedance line lowpass filters, parallel-coupled line bandpass filters, hairpin-line bandpass filters, and cross-coupled open-loop resonator filters will be discussed.

2.3. Review of Parallel-Coupled Line Bandpass Filters

The stepped-impedance microstrip lines are suitable for designing low-pass filters at low microwave frequencies such as for the L band. Furthermore, very high values of characteristic impedances for series inductors and very low values of characteristic impedances for shunt capacitors are difficult to realize by a stepped-impedance impedance line. Accordingly, the study of parallel-coupled lines has been started by the researcher to overcome such limitations of filter design. The key advantages of coupled-line filters are that the coupling between the parallel resonators can be controlled efficiently to achieve very high (30-70%), medium (10-30%), or low (5-10%) bandwidths.

The study of the shielded coupled-strip transmission line was first carried out by S. B. Cohn in 1955 [20] by analyzing the odd and even TEM modes. The characteristic impedance and the phase velocities of these two modes carried the necessary information for the design of coupled-line filters. Subsequently, the knowledge and analysis methodology of coupled-line theory in [20] have been extended to the study of direct-coupled resonator filters [21] and parallel-coupled transmission-line resonator filters [22]. In [22], Cohn described the synthesis of the parallel-coupled stripline bandpass filter in which accurate design for Chebyshev, Butterworth, or any other physically realizable response has been investigated. The successive striplines are coupled at a distance of a quarter-wavelength. Several important advantages were reported for this arrangement, such as (1) the length of the filter is approximately half that of the end-coupled type, (2) the coupling gaps are larger and therefore less critical, and (3) the insertion-loss curve is symmetrical on a frequency scale, with the first spurious response occurring at three times the center frequency of the passband. Subsequently, Zysman and Johnson [23] investigated a two-port network composed of symmetrically coupled transmission lines embedded in an inhomogeneous dielectric (e.g., suspended substrate, microstrip). In this study, the ABCD parameters of the circuit configurations were obtained by considering the lateral electromagnetic coupling between the parallel lines using finite difference time domain techniques (FDTD).

Accordingly, Akhtarzad et al. [24] have proposed a design procedure for parallel-coupled line filters with comprehensive design formulas in support of even and odd-mode field variation. The geometry of the coupled lines could be obtained directly from the required even- and odd-mode impedances by applying such a technique. However, uniform coupled

lines exhibit a relatively narrow-band coupling response restricting their applications for wideband filters. Thus, nonuniform line techniques have started in design to improve the performance. These consist of cascaded or stepped parallel-coupled microstrip lines with continuously varying coupling coefficients imposing a high degree of freedom to control the modal characteristic impedances and phase velocities.

In this context, Adair et al. [25] have derived the transmission-line equations describing field propagation along non-uniform coupled transmission lines, and accordingly, different coupling coefficients and the impedance variation have been obtained directly. However, in [25], the study considered the pure TEM mode of propagation based on coupled-mode theory. In continuation, Tripathy [26] has derived the expressions of terminal characteristic parameters for asymmetric couplers in an inhomogeneous system in terms of even-and odd-modes, propagating in two nonuniformly coupled lines based on quasi-TEM coupled-mode theory.

However, because microstrip structures suffer from fringing effects at the open ends of the resonators and the coupling gap between them, the observation of reflections at the open ends and scattering parameter variations due to different amounts of coupling in the gaps between the coupled resonators becomes more critical. Accordingly, a solution for the characteristics of microstrip open-end and gap discontinuities has been reported in [27] by Jackson et al., in which the Green's function of the grounded dielectric slab was developed by the method of moment technique, so that surface waves, as well as space-wave radiation, were considered. The electric currents on the coupled edges of the lines are expanded in terms of longitudinal piecewise sinusoidal modes near the discontinuity. In addition, the power loss due to surface and space waves has been calculated for a representative gap discontinuity. This study became very useful for designing parallel-coupled microstrip line filters for the researchers as fringing fields' effects at the open-ends have been considered.

With the advancement of communication systems, the necessity of compact wideband filters has become important as narrowband filters have imposed restrictions on communication systems demanding a fast data rate and a wide range of signals to be transmitted. Wideband filters offer fast data communication with linear frequency response and the ability to notch out narrow noise sources in the frequency spectrum. In this context, the design of a wideband parallel-coupled microstrip bandpass filter has been extended in

[28] by Chin et al., in which the dimensions of each coupled stage of the filter have been determined by incorporating the modified formula for fractional bandwidth. Accordingly, a significant improvement has been achieved in predicting the filter bandwidth without deterioration in the passband response. Subsequently, the parallel-coupled line bandpass filters having maximally flat responses have been synthesized by deriving the expression of insertion loss functions in [29]. In this study, the derivation has been performed by successively multiplying the ABCD matrices of all the coupled stages. Accordingly, the line width and line spacing of the coupled stages have been determined by the overall quality factor of the filter and by the comparison of the insertion loss function with the canonical form. The study of [29] has been further extended by Chin et al. in [30], where the insertion-loss functions were derived for Chebyshev type parallel-coupled line filters by converting the composite ABCD matrices of all the coupled stages. Accordingly, the EM simulation and measurement results have shown an accurate passband response.

The research so far has been concentrated mostly on the performance of conventional parallel-coupled line filters. However, the size of the conventional half-wavelength parallel-coupled resonator filters is unsuitable for modern-day satellite and mobile communications, where limitations in size are a critical parameter. Moreover, the even-and odd-modes of the TEM wave are propagating with unequal phase velocities in the inhomogeneous microstrip structures [31]. In general, the odd-mode propagates with high phase velocity compared to the even-mode due to its lower phase constant due to the inhomogeneous dielectric medium for microstrip line structure [32]. Accordingly, the passband of the parallel-coupled line filter has become asymmetrical and the skirt characteristics have also degraded. The frequency response symmetry is also an important issue in applications involving pulsed signals.

Accordingly, the design of a compact and miniaturized coupled-line filter with improved passband performance has become a recent trend. In this respect, a miniaturized parallel-coupled line filter was designed with improved upper stopband rejection and symmetrical response by Chang and Itoh [33]. In this article, the conventional microstrip bandpass filter was modified to a compact parallel-coupled structure by considering the open-end length correction of the coupled lines due to fringing field effects. Accordingly, instead of the microstrip open ends; there are microstrip gaps in the modified structure. By carefully choosing the gap dimension, the stopband rejection and the passband response symmetry

have been optimized by placing transmission zeros at the edges of the passband. The size of the modified filter has been reduced by more than 50% compared to the conventional filter, and it has become easier to layout owing to the in-line structure. However, the effect of such folding on the attenuation level of harmonics was not investigated by the authors.

The study of the miniaturization of parallel-coupled filters has been further extended in [34] by Prigent et al. In this report, various modifications have been made to classical coupled-line narrow bandpass filters to achieve a small filter size with improved frequency response. For both the filters, the resonator's strip width has been broadened to improve the lines' unloaded Q factor. In extension, the in/out coupled-line sections have been replaced by tapped-line type feeding. Besides a transmission zero, a geometrical modification favourable for the coupling between the nonadjacent resonators has been incorporated. Although the modified structures improve the passband response, their attenuation level at the spurious passbands has been degraded due to the mutual coupling between the non-adjacent resonators.

Subsequently, a novel compact microstrip bandpass filter was proposed by Jianxin et al. in [35] using a half-wavelength microstrip line resonator and an end-coupling resonator. The proposed compact design has two transmission zeros at both low and high rejection bands, with a rejection level of more than 40 dB, as well as a low insertion loss of 0.46 dB. Later, in [36], a compact bandpass filter using folded quarter-wavelength coupled-line resonators was designed by Wang et al. Equations for the extraction of the equivalent parallel-coupled-line structure representing the folded-line section have also been developed in this report. The said folded coupled-line filter has exhibited a 36% reduction in footprint as compared to the conventional design.

Afterward, Liao et al. [37] proposed a modified microstrip parallel-coupled filter with two independently controlled transmission zeros in the upper stopband. In this study, shielding lines have been incorporated at the ends of vertically flipped input and output feed lines over a conventional Chebyshev type parallel-coupled line filter. Accordingly, two independent transmission zeros have been implemented in the upper stopband by adjusting the positions and trimming the lengths of lines. In this respect, J. Z. Gu and X. W. Sun [38] have proposed a compact microstrip bandpass filter with folded parallel-coupled lines in a spiral shape. It has been observed that low insertion loss in the passband and sharp and high rejection in the

upper stopband have been achieved with a size reduction of 70% compared to the conventional coupled-line filters. The study has been continued by Zhang in [39], where a novel microstrip millimeter-wave band-pass filter with a slow-wave resonator was proposed in which a slow-wave structure has been suggested to improve both the selectivity and the stopband rejection by introducing cross-coupling capacitance between the input and output ports of the filter.

The folding mechanism of the conventional parallel-coupled line filter was further investigated in [40] by Kung et al. This article, a triple-band parallel-coupled line bandpass filter with a center frequency of 1.8 GHz, 3.5 GHz, and 5.2 GHz applicable for DCS, WIMAX, and WLAN. The filter structure has been designed by folding the filter structure symmetrically subject to the center of the structure by cascading over-coupled and insufficient-coupled lines. Accordingly, low insertion losses, wide bandwidths, and high stopband rejection levels have been reported. In general, a bandpass filter with a parallel-coupled line structure has a wide and limited fractional bandwidth of 20-40%. Moreover, the frequency response related to a very narrow coupling gap between the resonators prevents the generation of a wideband parallel-coupled line filter. In this context, Kuo and Shih [41] proposed a wideband parallel-coupled three-line microstrip filter having fractional bandwidths of 40%-70%. Accordingly, the stopband rejections have been improved by relaxing the tight line spacing of the end stages compared to the conventional parallel-coupled line filters.

These three-line structures are further studied in [42] to design compact wideband bandpass filters. In [42], Zhang et al. proposed a three-line microstrip unit cell which is cascaded to design millimeter-wave bandpass filters in the Ka-band. Compared to the conventional design with parallel-coupled line microstrip structures, it has been observed that a minimum insertion loss of 1.48 dB in the passband has been achieved, and stopband rejections are improved by more than 25 dB. Furthermore, the compact structure has saved 50% of the circuit area. However, for all the studies [38-42], the effects of harmonics have not been addressed, putting some limitations on their uses for modern day receivers.

Parallel-coupled lines are also very effective building blocks to design highly selective, miniaturized wide and ultra-wideband filters applicable for modern wireless communications systems where a large range of frequencies is to be transmitted with minimum attenuation

loss, high data rate, and low power consumption. In this context, Yoon and Lee [43] have designed a compact, small-sized wide-band bandpass filter based on a three-line theory with 70% wide bandwidth. The filter structure consists of two long coupling sections and an extra capacitive coupling gap between the quarter-wavelength non-adjacent lines to achieve wide bandwidth. Consequently, an ultra-wideband (UWB) compact parallel-coupled line bandpass filter with a fractional bandwidth of 110% has been designed by Shaman and Hong [44]. In this work, the filter has been designed by combining only one section of the quarter-guided wavelengths long, parallel-coupled three-line structure with one short-circuited stub. As a result, two transmission zeros have been generated around the passband edges. This has increased the sharpness of both edges of the UWB passband. A balanced wideband filter with a fractional bandwidth of 88% has been proposed by Wang et al. [45] in which four quarter-wavelength coupled lines have been cascaded to achieve wideband response and small size along with the suppression of the common-mode signal larger than 18.7 dB. Subsequently, in [46], Chen et al. proposed a novel synthesis scheme for wideband filters composed of parallel-coupled three-lines by considering the cross-coupling of nonadjacent lines, which had not been considered in early works [43-45].

Accordingly, better accuracy and low insertion loss have been achieved, along with a fractional bandwidth of 60%. Afterward, a wideband high selectivity filter centered at 2.5 GHz exhibiting a fractional bandwidth of 54.4% with finite transmission zeros at the passband edges with attenuation of more than 65 dB has been proposed by Huang et al. [47]. In this study, the conventional parallel-coupled lines have been folded into a U-shape by means of mirroring the output feeding line. As a result, the effective overall size has been reduced to less than $0.35\lambda_g \times 0.35\lambda_g$. However, all the filters proposed in [43-47] have been focused on constant fractional bandwidth. As an alternative, Cheng et al. [48] have proposed a reconfigurable wideband filter centered at 5.7 GHz based on cross-shaped coupled resonators and PIN diodes. As a result, an absolute BW tuning range of 1.22 GHz has been obtained while the fractional BW has been varied from 34.8% to 56.5%. This work has been extended in [49] to design a wideband BPF centered at 2 GHz with reconfigurable FBW from 85.3 to 94.2% with a tuning range of 8.9% and two fixed notch bands by incorporating four PIN diodes and a capacitor at the ends of the cross-shaped resonator cascaded with three parallel coupled-lines. By controlling the states of the PIN diodes and the value of the

capacitor, wide bandwidth tuning has been achieved. Very recently, a broadband bandpass filter centered at 4.3 GHz with a cross-coupled line structure has been proposed in [50] by combining parallel-coupled lines and an open stub. As a result, a very compact size of $0.12\lambda_g \times 0.14\lambda_g$ and improved skirt characteristics with an attenuation level of 40 dB at the passband edges have been obtained.

From the literature study, it has been revealed that lots of research has been performed for the parallel-coupled line bandpass filters, essentially focusing on their passband response concerning low insertion loss, high return loss, high selectivity, wide fractional bandwidth tuning, and linear passband phase response. Moreover, the researchers have put their efforts into reducing the size of the filters by following different miniaturization techniques. However, the effects of such compactness on the harmonics' attenuation levels and their suppression have not been focused on. Hence, the literature survey on the harmonics suppression performance of parallel-coupled line filters has been covered in the next section.

2.4. Review of Parallel-Coupled Line Bandpass Filters with Harmonic Suppression

The historical development of parallel-coupled line planar bandpass filters has been highlighted by several authors due to the miniaturization of the filter size, improvement in passband symmetry, skirt characteristics, and stopband rejection levels as mentioned in earlier sections. However, the even-and odd-modes have the same length for each coupled section in a parallel-coupled filter, and as a result, their corresponding half-wavelength frequencies become different due to the unequal phase velocities. As a result, spurious passbands with low insertion loss are generated at multiples of the center frequency. Thus, the performance of the planar filters degrades owing to the presence of these harmonics, especially for applications involving two-tone signals. Accordingly, by providing different electrical lengths for these modes, phase velocity compensation between the modes has been achieved in the recent past.

The study of harmonic suppression in parallel-coupled stripline filters was initiated in 1980 by Makimoto et al. [51]. In this report, nonuniform stepped impedance resonators (SIR) have been employed, and the spurious response has been suppressed by controlling the impedance ratio of the resonators. Inverted microstrip and suspended substrate stripline can

offer reduced loss and are of interest for the higher frequency ranges, but these media exhibit a considerably greater difference in mode velocities, and thus, the filter design problem is more severe. Accordingly, Easter and Mirza proposed a parallel-coupled-resonator filter in inhomogeneous media such as inverted microstrip and suspended stripline [52] in which a modified filter section had been used. The structure was comprised of a parallel-coupled section cascading with short un-coupled line sections. Improved characteristics, both in the passband and in the stopband, have been achieved by tuning the lengths of the un-coupled line section.

Subsequently, phase velocity compensation in parallel-coupled microstrip couplers has been achieved by S. L. March [53] by incorporating a pair of lumped capacitors at the ends of the coupled section. In the even-mode, the capacitors become open circuits, while the odd-mode phase length has been increased effectively. A. Ridley [54] later extended the study of phase velocity compensation for a parallel-coupled filter by using over-coupled resonators. The odd-mode phase length has been extended by overlapping the coupled edges of the lines, while the even-mode length was unaltered. As the coupling between the resonators has been increased due to overlapping, the bandwidth enhancement has also occurred. Accordingly, more than 30 dB of suppressed level has been obtained. Afterward, I. J. Bahl in [55] continued the work of parallel-coupled line filter design and harmonic suppression of more than 40 dB up to 2.5 times the center frequency has been reported. However, the exact values of the capacitors and additional soldering steps for connecting them have created difficulties for the application of such capacitive compensation techniques in filter design.

Subsequently, the forbidden bands for electromagnetic transmission have been generated in the microstrip lines by etching the ground plane with a PBG structure like periodic elements as proposed by Radisic et al. [56]. In this study, the ground plane of microstrip lines has been etched by a periodic 2D pattern consisting of circles without any drilling through the substrate. Accordingly, three PBG circuits with different circle radii have been designed to estimate the optimum dimensions, along with an additional compensated right-angle microstrip bend-based PBG circuit. Such PBG structures have been investigated further in a parallel-coupled-line microstrip filter by Yang et al. [57] in which a uniplanar compact photonic-bandgap (UC-PBG) structure has been employed as a machined ground plane.

Accordingly, a periodic disturbance has been introduced which rejects the spurious passbands of the microstrip filter and, at the same time, acts as a slow-wave structure that reduces the total physical size of the parallel-coupled line microstrip filter itself, exhibiting a reduction of 20%. However, this slow-wave effect is achieved strongly in the even-mode of the coupled lines but shows weak coupling in the odd-mode. It has substantially increased the difference between the phase constant of the even-and odd-modes, which were also highlighted in [58] by Yang et al. In this report, microstrip coupled-lines with a periodically patterned ground plane have been analyzed using the FDTD method to compute the effect of strip width and gap spacing on the effective dielectric constant and the characteristic impedance of even-and odd-modes. Measured data shows good passband response with an insertion loss of 1.6 dB, fractional bandwidth of 9%, and 25 dB of spurious suppression. The filter length has been reduced by 20% due to the slow-wave effect.

Afterward, the coupled wiggly microstrip lines have been studied by Lopetegi et al. [59] to suppress the spurious passbands. In this article, the wave impedance has been modulated by using a continuous sinusoidal perturbation of the width of the coupled lines. Accordingly, the harmonic passband of the filter has been rejected by more than 40 dB with a 47.5% width modulation factor. With such strip-width perturbation, the classical design methodology for coupled-line microstrip filters has been used without recalculating the filter parameters. However, the etching of sinusoidal perturbations on the transmission line is not an easy task, and the fabrication difficulty remains. Subsequently, corrugated coupled microstrip lines were proposed by Kuo et al. [60] to form the building blocks for planar microstrip filters with suppression of the spurious passband at the second harmonic. The coupled edges of the parallel lines had been modified with the rectangular corrugations to reduce the phase velocity of the odd-mode, keeping the even-mode unaltered. Accordingly, the response symmetry of the filter has been greatly improved, along with a harmonic suppression of more than 30 dB and a 10% shortening of the filter size.

As an alternative approach, defected ground structures (DGS) are also considered for harmonic suppression in microstrip filters. The DGS with periodic or random arrays provides a rejection band in some frequency ranges due to the increase in the effective inductance of the transmission line. In this respect, Park et al. [61] proposed a novel three-pole coupled-line bandpass filter with defected ground structure (DGS) sections to simultaneously realize a

resonator and an inverter. The proposed coupled-line filter exhibited attenuation poles for a wide upper stopband due to the self-resonance characteristic of DGS, compact size, and an improved insertion-loss characteristic compared to a conventional coupled-line bandpass filter. However, like PBGs, these structures are also suffering from fabrication difficulties as ground planes are to be perturbed separately with precise alignment.

Later, the study of [60] was extended further by Kuo in 2003 to design a parallel-coupled line microstrip filter with improved harmonic suppression [62]. In this article, tapped couplings have been applied to the first and last resonators to control the transmission zeros. By this method, the image frequencies have been rejected significantly for the practical receivers, and the rejection level in the stopband has been enhanced. Subsequently, Weng [63] modified the over-coupled resonators with stepped impedance sections in a parallel-coupled line filter for the improvement of passband and insertion loss along with the suppression of the spurious response. In addition, the input and output feed lines with tapping have been used to create the extra transmission zeros for the improvement of stopband rejection. Subsequently, a microstrip bandpass filter with multi-order spurious-mode suppression has been designed by Chen et al. in [64]. With a combination of different SIR structures, the spurious passbands of the filter centered at 1.51 GHz have been rejected with more than 30 dB of rejection up to $5.4f_0$. In this context, the effectiveness of the over-coupled resonators has been investigated further by Kuo [65], in which the harmonic suppression characteristic of the coupled-line filter has been improved by more than 50 dB by applying over-coupling to the end stages only. In addition, by increasing the image impedance of the coupled stages and thus, by reducing the difference between the effective dielectric constant of even-and odd-mode, the suppression of the spurious harmonic has been enhanced by more than 15 dB. Following that, the research on compensating phase velocities between even and odd modes in a parallel-coupled line filter using substrate suspension was expanded [66].

Complementary split-ring resonators (CSRRs) are also widely used in harmonic suppression for coupled-line bandpass filter design as proposed by Falcone et al. [67]. The property of negative effective permittivity in CSRRs has been utilized in [67], and accordingly, more than 40 dB of harmonic suppression level has been achieved. However, the proposed perturbations in the ground plane have increased the fabrication complexity. Subsequently, as an alternative approach, periodic square grooves have been introduced to the

coupled edges of the parallel-coupled lines of the microstrip filter [68] to achieve phase velocity compensation. More than 30 dB of harmonic suppression has been obtained in this design, by choosing an appropriate number of grooves with proper dimensions. Afterward, wiggly lines with sinusoidal perturbations of different periods have been employed in [69] to achieve a wide stopband with a rejection level of more than 30 dB up to $4f_0$.

Subsequently, the even-and odd-mode guided-wave characteristics of periodically nonuniform coupled microstrip lines (PNCML) proposed earlier in [68] have been investigated by S. Sun and L. Zhu [70] in terms of transmission parameters such as characteristic impedance and phase constant. The authors have extended their work in [71] in which the derived synthesis model of [70] has been applied to design a coupled-line filter with harmonic suppression. As a result, the first spurious harmonic passband of the filter has been suppressed by more than 40 dB. Jiang et al. investigated the over-coupled resonators proposed in [63] further in [72] for multi-spurious suppression in parallel-coupled line filters. In [72], it was shown that the inherent transmission zero of a microstrip coupled stage near twice the design frequency ($2f_0$) is tunable by varying its coupling length. This transmission zero has been reallocated in the stopband of the filter to suppress the unwanted spurious harmonics by using over-coupled end stages. The above idea has been extended in [63] to design over-coupled middle stages for suppressing the spurious peaks at $3f_0$ and $4f_0$ of the filter, and accordingly, the upper stopband has been enhanced up to $5f_0$ with a rejection level of more than 30 dB.

The incorporation of fractal geometry into planar filters has been started by Kim et al. [73] as an alternative approach to suppress harmonics for parallel-coupled line filters. The advantages of fractal geometries have been utilized in designing a microstrip line bandpass filter in which the coupled lines are modified with fractals at the edges. Accordingly, a Ku-band filter has been designed on a liquid crystal polymer (LCP) substrate with Koch rectangular fractals, and the maximum harmonic suppression of 42 dB has been obtained. Later, in [74], Koch triangular fractals were used in a parallel-coupled line filter centered at 2.0 GHz to achieve a stopband up to $2.25f_0$, with a rejection level of 60 dB and a size reduction of 31%, demonstrating an improvement over [73].

Subsequently, the study of corrugated coupled lines has been extended further in [75-76] by Kuo et al. for multispurious harmonic suppression in a parallel-coupled line filter. In [75],

quarter-wavelength corrugated stages have been tuned to allocate inherent transmission zeros at $2f_0$ and $4f_0$ where f_0 is the center frequency. Intermediate coupled stages with proper coupling lengths have been arranged to cancel spurious harmonics at $3f_0$, $6f_0$, and $7f_0$ along with a tapped input/output scheme to tackle the harmonic peak at $5f_0$. Accordingly, the upper stopband has been extended up to $7.8f_0$ with a rejection level better than 30 dB. However, in [76], corrugated coupled stages have been employed in a folded parallel-coupled line filter centered at 1.0 GHz and spurious harmonics have been suppressed up to $10f_0$ with a rejection level of more than 30 dB by properly tuning the number of corrugations.

As an alternative approach, the application of the grooved substrate to suppress the first spurious response of microstrip parallel coupled-line filters has been employed in [77] by Moradian. In this design, the grooves were oriented parallel to the coupled lines. It has been reported that the spurious response has been suppressed by more than 35 dB. Later, Yamaguchi et al. [78] employed floating conductors loaded into periodic slots on the inner edges of each coupled section to compensate for the modal phase velocities in a parallel-coupled line filter. As a result, a suppression level of 40 dB has been obtained. Following that, [79] extends the study of periodic grooves in harmonic suppression by using a right-angle triangle groove instead of square and rectangle grooves [71]. Moreover, it has been investigated that the use of one right-angle triangle groove at the middle of the coupled sections is sufficient for the cancellation of the spurious frequencies.

Subsequently, a parallel-coupled microstrip bandpass filter (BPF) with folded stepped impedance resonator (SIR) cells on the intermediate layer has been proposed in [80] for spurious suppression, where a wide stopband with suppression levels of over 50 dB and 30 dB for the second and third harmonics has been obtained. Additionally, by selecting the impedance ratio and physical length ratio of the folded SIRs properly, the parallel-coupled BPF with a wide stopband has been implemented without causing the packaging problem. As a modification, Ardakani et al. [81] have presented a technique for equalization of phase velocities in coupled microstrip lines using the dispersive characteristics Ω-shaped particles. Accordingly, a harmonic suppression level of more than 60 dB has been achieved for a Chebyshev type parallel-coupled line filter.

Afterward, a wide stopband with a rejection level of 25 dB up to $5.5f_0$ for a filter centered at 2.0 GHz has been reported in [82] by precisely controlling the amount of coupling between

the parallel-coupled lines. In this study, closed-form expressions of the coupling coefficients as a function of the coupling section lengths at resonant frequencies have been derived. Subsequently, different harmonics suppression techniques have been combined effectively in [83] by Huang for a bandpass filter centered at 1.0 GHz. In this work, stagger tuning using additional stubs has been employed for quarter-wavelength lines. The resonators have been overlapped suitably to provide transmission zeroes to suppress the spurious peaks. Besides, coupling capacitor pads have been incorporated, which are used to act as shorting stubs, and accordingly, a wide stopband with a harmonics suppression level better than 33 dB up to $6.3f_0$ has been obtained. In this context, Chen et al. [84] have presented a novel approach to designing a bandpass filter centered at 1.0 GHz with a very wide stopband ($14.9f_0$) having a rejection level of 28 dB by combining open-circuited stubs and uniform impedance parallel-coupled resonators. However, due to the conventional parallel-coupled line structures, the proposed filters in [82-84] are quite large, restricting their applications in modern communication systems. As an alternative approach, step-impedance resonators and step-impedance capacitor coupling pads have been employed by Huang in [85] to suppress the spurious harmonics for the bandpass filter centered at 1.0 GHz up to $8.8f_0$ with a rejection level of 67 dB. However, the overall size of the filter is quite large ($0.85\lambda_g \times 0.18\lambda_g$).

From the review of harmonics suppression in parallel-coupled line bandpass filters, it has been summarized that most of the studies have been performed on conventional parallel-coupled line filters, which limits their applications in modern miniaturized wireless communication systems. Moreover, second harmonic suppression has been investigated mostly by researchers on conventional filters. Also, very few researchers have investigated the multispurious harmonic suppression in parallel-coupled line filters. Thus, the effect of compactness on harmonic suppression has been a challenging research idea till now. Moreover, another serious issue related to parallel coupled lines is that of passband fractional bandwidth. Accordingly, as an alternative topology, hairpin-line bandpass filters have been investigated by the researchers for their narrower fractional bandwidth and compact size.

2.5. Review of Hairpin-Line Bandpass Filters

With modern wireless and satellite communication systems, the demands for narrowband, miniaturized, high selectivity filters are welcome solutions compared to the conventional

parallel-coupled line filters occupying a large circuit area. Moreover, the fractional bandwidths of such filters are restricted to 10% as it is very difficult to design narrowband filters (less than 10%) by parallel-coupled line topology due to the increased coupling gap, resulting in large circuit size. In this context, the conventional half-wavelength parallel-coupled lines have been folded symmetrically into U-shaped hairpin lines and placed alternately in hybrid mode configuration [1-3]. As a result, not only the size of the filter has been greatly reduced, but also the skirt characteristics have been significantly improved.

The hairpin-line filters have also been designed based on the concept of the parallel-coupled, half-wavelength resonator lines. However, some design constraints are to be considered, such as the decrease in the coupled-line lengths due to the folding mechanism and the reduction in coupling between the resonators. Cristal and Frankel proposed a class of hairpin-line and hybrid-hairpin-line filters in the L-band for the first time in 1972 [86] using these design constraints. In this study, the size of the filters had been reduced by more than 50%, with the controllable fractional bandwidths ranging from 5% to 25%. The detailed analysis of the equivalent lumped element circuits and the derivation of the design equations based on the synthesis of different parameters have been reported. However, the radiation effects of such filters have not been addressed in [86], as such effects are not so important for filters in the *L*-band. However, for filters operating in the *S*, *C*, and *X* bands, the radiation effects are considered critical design criteria. Accordingly, such issues have been studied by Easter in [87] for the hairpin-line filter centered at 11 GHz (*X*-band). The abrupt bends of the hairpin-line had been modified by smooth curvature bends to reduce the radiation effects, and accordingly, significant improvements in the skirt characteristics and bandwidth had been obtained over [86].

The design theories presented in [86-87] were based on the assumption of a sparse inductance matrix for the array of coupled lines, which is much harder to satisfy for practical filters. Besides, the bandwidth contraction factors depending on the hairpin resonator coupling were determined empirically in [86-87]. These two restrictions have been corrected by Gysel [88] by assuming a sparse capacitance matrix for the hairpin-line filters. Moreover, explicit design equations have been established for the bandwidth contraction factor. Accordingly, the design of practical hairpin-line filters with controllable bandwidths became

easy and rapid, with a significant improvement in the passband frequency response over [86-87].

For all the hairpin-line and hybrid-hairpin-line filters proposed in [86-88], the input/output feed lines have been parallel-coupled to the first and last resonators, increasing the overall circuit area of the fabricated filters. Moreover, the physical realization of the filters became impractical where the parallel coupling at the end sections had compact floor planning restrictions. Accordingly, a microstrip tapped-line filter has been proposed in [89], where the input/output feed lines have been tapped to the appropriate locations of the end resonators of the filter. However, till then, the filters [86-89] have occupied quite a large circuit area due to their conventional-hairpin line structures, especially operating in the L-band. In this context, the conventional hairpin lines have been modified to folded hairpin-shaped split-ring resonators with a pair of parallel coupled lines in place of the loaded lumped element capacitor between the folded arms [90]. As a result, the filter size has been reduced by 50%, along with the improvement of the skirt characteristics of the passband. However, the incorporation of extra parallel-coupled lines has resulted in extra discontinuities and a low *Q*-factor due to radiation loss, large-quality factor Q = 350 and very narrow bandwidth (5.08%).

Afterward, the conductor loss and the radiation loss of the hairpin-line filters have been greatly reduced (less than 0.5 dB) by designing the hairpin-line filter centered at 0.905 GHz [91] on a high dielectric substrate material (solid solution of barium titanate and barium zirconate, dielectric constant ε_r = 80). The proposed filter has exhibited high-temperature stability. Later, Hsieh et al. [92] proposed a new class of slow-wave bandpass filters using periodically loaded stepped-impedance hairpin resonators by utilizing their parallel and series resonance characteristics. As a result, a low insertion loss of 1.82 dB, a high unloaded Q-factor of 146, and two stopbands exhibiting a rejection level greater than 60 dB have been reported. However, the overall size of the filter ($0.9\lambda_g \times 0.11\lambda_g$) was pretty large, restricting its applications.

Subsequently, the size of the hairpin-line filter centered at 2.445 GHz was reduced by Qing et al. in [93] by meandering the lines along the coupling regions to obtain a size of $\lambda_g/8 \times \lambda_g/8$. The attenuation level at the upper passband edge frequency has been documented as 50 dB. However, the lower passband edge response has not improved by this method of

folding. A multiple-coupled hairpin-line filter has been demonstrated in [94] where two sharp attenuation poles have been incorporated at the passband edges with attenuation levels of more than 40 dB. This has improved the skirt characteristics of the filter at both ends of the passband response. To further reduce the size of the hairpin-line filter, Huang et al. used stepped-impedance hairpin resonators over high-permittivity ceramic substrates in [95]. Accordingly, a size reduction of 43% has been obtained with a passband return loss of 34 dB and an insertion loss of 5.44 dB. In this context, by controlling the degree of coupling between the hairpin-lines along two separate electric and magnetic coupling paths, the size of the bandpass filter has been reduced to as small as $0.06\lambda_g \times 0.0545\lambda_g$ by Ma et al. [96].

The study of [96] has been extended in [97] to achieve a size reduction of 21% over the conventional hairpin-line filter by combining the stepped-impedance hairpin resonator with an interdigital capacitor. Shen and Huang [98] achieved a size reduction of more than 43% by using hairpin-shaped split-ring resonators fabricated on high dielectric constant ceramic substrates. Later, by utilizing the interaction of mixed electric and magnetic coupling between the hairpin resonators with the tapped feeding position, and the source-load coupling configuration in a single filter structure, a compact bandpass filter has been designed by Wang et al. [99]. The skirt characteristics of the filter have been improved significantly by introducing two transmission zeros with attenuation levels of more than 35 dB at the passband edges. Further, the improvement in the attenuation levels of the transmission zeros to 55 dB along with their controllability of placement at the passband edges has been achieved by Ouyang and Chu in [100] by adjusting the coupling lengths and the distances between the hairpin resonators. The proposed filter with a compact size of $0.21\lambda_g \times 0.27\lambda_g$ has excellent skirt characteristics improvement over [99]. Afterward, as an alternative approach, by using multilayered stripline folded quarter-wavelength resonators, a compact filter centered at 1.10 GHz and a size reduction of more than 50% to the equivalent single-layer hairpin-line filter [98-100] has been proposed in [101].

Later, two approaches have been investigated by Basti et al. [102] to design lossy bandpass filters applicable for receivers in satellite transponders: (1) nonuniform quality factor resonators in a transversal network; and (2) using an inline network with resistive cross-couplings. However, the size of the proposed filter is pretty large, not suitable for modern wireless systems. Subsequently, as an improvement in the size, window hairpin-

based bandpass filters with symmetrical T-shaped feeder coupling line resonators have been designed in [103]. Two compact filters centered at 5.13 GHz and 4.93 GHz with sizes of $0.16\lambda_g \times 0.25\lambda_g$ and $0.19\lambda_g \times 0.21\lambda_g$ have been proposed. In this context, a two-layer microstrip structure along with two aperture-coupled hairpin resonators etched on the ground plane has been utilized in [104] to obtain a size reduction of 40% compared to a conventional filter. Very recently, the improvement in the insertion loss and selectivity of the folded hairpin-line filter has been investigated in detail in [105] by applying the port-tuning method. Passband insertion loss of less than 0.5 dB and return loss of better than 20 dB has been documented.

From the literature surveys [86-105] it can be concluded that a lot of research has been carried out to design compact bandpass filters based on hairpin lines. Different efficient methods and structures have been incorporated into the filters to improve the selectivity, reduce the insertion loss and increase the return loss in the passband along with the size reduction. However, these studies have not focused on the effects of such compactness on harmonics.

2.6. Review of Hairpin-Line Bandpass Filters with Harmonic Suppression Performance

The presence of spurious harmonics has a significant impact on hairpin-line filters, which must be suppressed for improved out-of-band performance. The primary reason for the generation of spurious harmonics for the hairpin-line bandpass filters is the even-and odd-mode phase velocities imbalance, much like the parallel-coupled line filters. In this context, Hong et al. [106] investigated asymmetrical strip width modulation, i.e., wiggly lines, as the first work to suppress harmonics for the conventional hairpin-line filter. In this work, however, the attenuation level of the 2^{nd} harmonic frequency has been suppressed to 15 dB. A wide rejection bandwidth up to $3.13f_0$ with a rejection level of 30 dB has been achieved for a bandpass filter centered at 2.4 GHz with a stepped-impedance hairpin (SIH) resonator and interlaced coupled line in [107]. Subsequently, a three-pole hairpin-line filter with embedded open-stub has been proposed in [108] to obtain a stopband rejection level of 15 dB with a rejection bandwidth of $2.6f_0$. In 2007, Mondal et al. [109] proposed a T-shaped microstrip feed line for a hairpin-line filter centered at 0.904 GHz to produce frequency-dependent

external coupling, leading to upper stopband extension of $6.6f_0$ with a rejection level of 29 dB. Later, as an alternative approach, Baral and Signal [110] incorporated Koch rectangular fractals into the coupled arms of the hairpin-line filter to achieve a rejection bandwidth of $2.5f_0$ with an attenuation level of 17 dB.

Following that, Chen et al. achieved a rejection bandwidth of $12.2f_0$ with a rejection level of 30 dB for a hairpin-line bandpass filter using open-circuited stubs in [111]. However, the required compactness has not been achieved. Subsequently, a hairpin-line trisection bandpass filter has been proposed in [112] and a rejection level of 25 dB up to $3.3f_0$ has been achieved by changing the nature and degree of direct couplings of the inter-digital coupling structure and defected ground structure (DGS). The study of wiggly-lines [69] has been extended further in [113] by Partal for a cross-coupled hairpin-line filter to obtain the rejection bandwidth of $3f_0$ with an attenuation level of 30 dB. Later, [114] reported a rejection bandwidth of $8.3f_0$ with an attenuation level of 20 dB for a bandpass filter centered at 2.4 GHz by utilizing split-mode excitations in the resonating structure. In this context, an alternative defected microstrip structure (DMS) [115] has been employed for a fifth-order hairpin-line filter to obtain the spurious harmonic suppression up to $3.48f_0$ with a rejection level of 35 dB. However, the size of the proposed filter is quite large due to its conventional structure.

In order to decrease the size of the filter, Ghalibafan et al. [116] proposed the meandering of the coupled arms of the hairpin lines, and accordingly, a size reduction of 50% has been achieved. Besides, a stopband bandwidth of $2.5f_0$ with a rejection level of 35 dB has been reported. Afterward, the self-similarity and space-filling properties of quasi-Minkowski fractals have been utilized in [117] to obtain a size reduction of 11% and a stopband rejection bandwidth of $2.7f_0$ with a rejection level of 30 dB for a third-order hairpin-line filter. In this work, different iteration orders of the fractals have been compared to investigate their effects on harmonic suppression. As an alternative approach, stub-loaded hairpin lines have been embedded with lumped resistors in [118] to achieve spurious harmonics suppression up to $4f_0$ with a rejection level of 30 dB.

Subsequently, a size reduction of more than 80% has been obtained in [119] by Hsu and Chiang by incorporating a single lumped capacitor between the folded arms in each hairpin line cell. With the reactive nature of lumped capacitors compared to the dissipative nature of

the resistor [120], a degree of shifting of the resonant frequency has occurred, and accordingly, the overall size of the filter has been reduced greatly. Besides, an extended stopband bandwidth up to $6f_0$ with an attenuation level better than 30 dB has been reported. Afterward, open-circuited stubs with appropriate dimensions have been employed in the hairpin-line cells to make the resonators in stagger tuned mode. Accordingly, the coupling coefficients have been perturbed by voltage redistributions, and a wide stopband bandwidth of $3.2f_0$ with a rejection level of 37 dB has been reported. A moderately compact-sized bandpass filter (9.6 mm × 19.8 mm) has been proposed by Marimuthu et al. in [121] with a miniaturized coupled structure loaded with stepped-impedance stubs. Multiple transmission zeros have been generated and thus, stopband rejection bandwidth has been extended up to $5f_0$ with an attenuation level of 16 dB. However, the attenuation level of the stopband demands more suppression. In this context, to achieve the size reduction, good selectivity, and wide stopband with an improved rejection level, a novel compact filter structure (size: $0.09\lambda_g \times 0.12\lambda_g$) has been proposed by Killamsetty and Mukherjee in [122]. In this work, tri-section half-wavelength stepped impedance resonators (SIR) have been combined with the stub-loaded shorted ring resonator to achieve the miniaturized size. Spur-lines and tapped feeding techniques have been embedded to suppress the harmonics for a wide stopband up to $8.7f_0$ with an attenuation level of 25 dB. Cross-coupling has been introduced to achieve good selectivity at the passband edges with attenuation levels of more than 55 dB.

From the literature survey of hairpin type filters, it has been revealed that the researchers have incorporated different topologies to suppress the spurious harmonics along with the extension of the stopband bandwidth. However, most of the work has been performed for the conventional hairpin-line structure, restricting its use in compact transceivers. Also, the effects of compactness, whatever achieved, are not extended to study the effects on harmonic suppression. Moreover, the skirt characteristics of the passband have been improved, mostly at the upper passband edge. Very little work has been focused on the improvement of skirt characteristics at the lower passband edge. Accordingly, a different kind of filter design topology has been proposed by another group of researchers, popularly known as the cross-coupled bandpass filter, as discussed in the next section.

2.7. Review of Cross-Coupled Bandpass Filters

In general, cross-coupled bandpass filters are constructed using four open-loop quarter-wavelength resonators placed in hybrid electric and magnetic coupling configurations to generate a pair of transmission zeros at the finite passband edge frequencies. Such a result is an improvement over the skirt selectivity of the filter to large extents, along with a compact structure and narrower passband. The design steps of open-loop cross-coupled filters are quite simple as they mainly focus on the determination of coupling coefficients between open-loop resonators and external quality factors for the first and last resonator. The study of such filters was initiated first by Hong and Lancaster [123] in 1996. Later, in [124], the size of the filter was reduced by 50% by meandering the open-loop resonators.

Afterward, the accurate design formulas and complete synthesis of the cross-coupled filters were performed in [125] by the authors of [123-124]. By following those design formulas, more than 60 dB of attenuation level in the transmission zeros had been obtained and were located very close to the passband edges. As a result, in [126], the open-end arms of the cross-coupled resonators were folded inward symmetrically to create a compact (size reduction of 13% compared to [123]), narrowband (FBW = 4%) bandpass filter centered at 2.46 GHz. As an alternative approach, triangular open-loop resonators have been employed in [127] to design a compact-sized, narrow-passband (FBW = 2.5%) cross-coupled bandpass filter. However, the passband edge attenuation levels had been degraded to 28 dB and 38 dB compared to 60 dB of [123]. Afterward, edge-coupled split-ring resonators have been investigated in [128] to achieve more compactness and improve the passband of the cross-coupled elliptic function filter. The design flexibility has been achieved further in [129] by applying a similarity transformation of the coupling coefficients between the open-loop resonators. As a result, the design of both narrowband (4%) and wideband (8%) efficient cross-coupled filters became available to researchers.

Later, stepped-impedance folded open-loop resonators have been investigated in [130] to reduce the size of the filter as well as to improve the attenuation levels of the selectivity of the filter. Accordingly, a compact size of $0.13\lambda_g \times 0.11\lambda_g$ and two sharp transmission zeros at an attenuation level of 60 dB have been achieved. In this context, microstrip high-low impedance resonant cells have been embedded in the open-loop resonator to achieve a slow-wave feature [131]. This has generated a pair of finite frequency transmission zeros in the

filter response. As a result, a compact size of $0.1705\lambda_g \times 0.1634\lambda_g$ i.e., a size reduction of 34% compared to the conventional square open-loop resonator, and attenuation levels of 35 dB for the lower stopband edge and 30 dB for the upper stopband edge frequency have been reported. This work has been extended further with a different slow-wave structure in periodically loaded high-low impedance microstrip cells in the open-loop resonator [132]. Thus, a compact size of $0.199\lambda_g \times 0.194\lambda_g$ (size reduction of 45%) and rejection levels better than 31.5 dB at the lower stopband and 29 dB at the upper stopband have been achieved. Later, a size reduction of 46% and improved selectivity have been reported in [133]. This has been achieved by employing interdigital and stepped-impedance hairpin resonators in a four-pole cross-coupled filter configuration. As an improvement over [132-133], Tsai et al. [134] have designed a compact four-pole cross-coupled filter by employing open-loop stepped-impedance resonators where a size reduction of 50% has been reported.

Following that, [135] investigated a completely different approach based on the hybrid-coupling path with multiple tunable transmission zeros. A microstrip grounded via-hole has been incorporated in the middle of the open-loop resonator to generate additional transmission zeros along the passband edges. Later, a two-fold tunable cross-coupled open-loop resonator bandpass filter has been proposed by Schuster et al. [136] to simultaneously and independently control both the center frequency of 1.5 GHz to 1.75 GHz with a constant bandwidth of 100 MHz and the bandwidth between 70 MHz and 180 MHz at a fixed center frequency of 1.625 GHz. In this work, thin-film barium strontium titanate (BST) varactors have been employed to achieve the tunability. Very recently, a compact four-pole two-folded cross-coupled square open-loop resonator bandpass filter of size $0.36\lambda_g \times 0.45\lambda_g$ and centered at 2.5 GHz has been proposed [137]. A rejection level of 35 dB has been recorded for the transmission zeros at the passband edges.

From the survey of [123-137], it has been revealed that most of the researchers have focused mainly on four things: (1) compactness of the filter structure, (2) the design of narrowband filters; (3) improvement of skirt selectivity due to the placement of two transmission zeros at the passband edges; and (4) improvement of the rejection level at the passband edges. For most of the work, the insertion loss becomes less than 2 dB, and the return loss becomes greater than 15 dB. However, the effects of such cross-coupled configurations on harmonic suppression have not been addressed.

2.8. Review of Cross-Coupled Bandpass Filters with Harmonics Suppression

Investigation of harmonic suppression in cross-coupled filters was carried out by Lee and Tsai in [138], where the open-end arms of the open-loop resonators have been folded inward and replaced by stepped-impedance resonators (SIRs) to increase the capacitive coupling between the folded arms. As a result, a stopband bandwidth of $2.4f_0$ with a rejection level of 30 dB has been obtained. The study of SIRs has been extended further in [139] to achieve a size reduction of more than 50% compared to the conventional square open-loop resonator filter, and accordingly, a stopband bandwidth of $2.44f_0$ with a rejection level of 19 dB has been obtained. In order to improve both the compactness and the stopband rejection level, Yu et al. [140] embedded an interdigital capacitor structure between the folded arms of the open-loop resonators to increase the slow-wave effects. Accordingly, a stopband rejection bandwidth up to $2.53f_0$ with an attenuation level of 25 dB along with improved skirt selectivity and compact size has been achieved.

Subsequently, an ultra-small (68% smaller than a conventional one) open-loop resonator cross-coupled filter has been designed in [141] by employing a more compact capacitive coupling structure. Besides, skirt selectivity has been improved significantly by the introduction of two sharp transmission zeros at the passband edges, with a rejection level of more than 55 dB. A stopband up to $2.43f_0$ with a rejection level of more than 40 dB has also been reported. In this context, the stopband bandwidth has been extended up to $8.2f_0$ with a rejection level of 30 dB in [142] by properly tuning the impedance and length ratio of the SIRs used for the open-loop resonator cells of the quasi-elliptic cross-coupled filter. The size of the filter is $0.32\lambda_g \times 0.22\lambda_g$. Subsequently, the study of [142] has been carried out further by Lin et al. [143] using dissimilar quarter-wavelength stepped-impedance resonators. A relatively small size of $0.2\lambda_g \times 0.13\lambda_g$ has been achieved with an extended stopband up to $11.4f_0$ with a rejection level better than 27.5 dB. As an alternative approach, Chen et al. [144] proposed a four-pole quasi-elliptic net-type resonator filter with a *FBW* of 3.5% with a stopband bandwidth up to $5f_0$ and a rejection level better than 30 dB. The size of the filter has been reduced by approximately 67% compared to the cross-coupled open-loop resonator filter.

Subsequently, coupled triangular open-loop stepped-impedance resonators have been employed in [145]. The rejection level in the upper stopband has exceeded 21 dB before the spurious passband at $4f_0$. Later, multiple transmission zeros have been incorporated by Kumar and Singh [146] for a cross-coupled compact bandpass filter by loading the open-loop resonators with stubs. The length and locations of the stubs have become the control parameters for those additional transmission zeros in the stopband. As a result, harmonic suppression of up to $3.2f_0$ with a rejection level of 26 dB has been obtained by creating five transmission zeros. In addition, a size reduction of 44% ($0.17\lambda_g \times 0.1\lambda_g$) has been reported compared with the conventional OLR-based filter without stubs. As an alternative approach, U-shaped stepped-impedance resonators have been embedded with source-load coupling in [147] to improve the skirt selectivity and to reduce the size of the cross-coupled filter. Moreover, spurlines have been incorporated at the input and output ports to introduce multiple transmission zeros in the stopband, resulting in an extended stopband up to $4f_0$ and a rejection level of 20 dB. Recently, an ultrawide stopband up to 25 GHz ($4.95f_0$) with a rejection level of 24.5 dB has been reported in [148] by combining a four-pole cross-coupled open-loop resonator filter to improve skirt selectivity and a folded stepped-impedance line with open stubs to suppress the spurious harmonics.

According to a review of parallel-coupled, hairpin-line, and cross-coupled planar bandpass filters, the majority of research has concentrated on the following main areas:

(1) Using various folding techniques, narrowband compact bandpass filters can be designed with better skirt characteristics, low insertion loss, and high return loss in the appropriate passband.

(2) By adding various non-uniform reactive slow-wave perturbations in the linked areas of the filters' resonators and extending the stopband bandwidth for conventional filter architectures, harmonics can be suppressed.

(3) Compact bandpass filter can be designed with harmonics suppression capabilities..

However, there is a compromise between the level of compactness, skirt characteristics, stopband bandwidth, and stopband rejection level in the earlier works. But, with the advancements of modern technology, it has been observed that the demands for miniaturized, narrowband bandpass filters with symmetrical passband response, low insertion loss, sharp skirt characteristics, and suppressed multiband harmonics are highly demanded in wireless

communication systems. Accordingly, the contributions of the present thesis report have the following outcomes:

(1) Design of miniaturized bandpass filters according to the specific applications to enhance the skirt characteristics subject to the symmetric passband.

(2) Analysis of the equivalent lumped element circuits and synthesis of the miniaturized filters.

(3) Investigation of different nonuniform slow-wave and fractal perturbations on the designed compact filter to suppress the second harmonics.

(4) Comparison of different planar structures and subsequent perturbation techniques for multiband harmonics suppression on a compact design.

(5) Design of a narrow passband filter with wide stopband characteristics.

References:

[1] G. Mattaei, L. Young and E. M. T. Jones, "Microwave Filters, Impedance-matching Networks and Coupling Structures," *Artech House*, Norwood, MA, vol. 1, ch.4, pp. 84-94, 1980.

[2] D. M. Pozar, "Microwave Engineering," *John Willey and Sons*, Inc., 4th. ed., ch. 2, pp. 48-59, 2011.

[3] J. S. Hong and M. J. Lancaster, "Microstrip Filters for RF/Microwave Applications," *John Willey & Sons*, Inc., New York, NY, 2001, ISBN 0-471-22161-9, Ch. 3, pp. 29-30, 2001.

[4] W. P. Mason and R. A. Sykes, "The Use of Coaxial and Balanced Transmission Lines in Filters and Wide-Band Transformers for High Radio Frequencies," *Bell System Technical Journal*, vol. 16, no. 3, pp. 275-302, July 1937.

[5] S. Darlington, "Synthesis of reactance 4-Poles which produce prescribed insertion loss characteristics: including special applications to filter design," *Journal of Mathematics and Physics*, vol. 18, no. 1-4, pp. 257-353, April 1939.

[6] R. R. Levy and S. B. Cohn, "A History of Microwave Filter Research, Design, and Development," *IEEE Transactions on Microwave Theory and Techniques*, vol. 32, no. 9, pp. 1055-1067, September 1984.

[7] R. M. Fano und A. W. Lawson, "Microwave Transmission Circuits," *ser. M.I.T. Rad. Lab*., New York, McGraw-Hill, vol. 9, ch. 9 -10, 1948.

[8] P. I. Richards, "Resistor-transmission-line circuits," *Proceedings of the IRE*, vol. 36, no. 2, pp. 217-220, February 1948.

[9] E. H. Bradley, "Design and development of strip-line filters," *IRE Transactions on Microwave Theory and Techniques*, vol. 4, no. 2, pp. 86-93, April 1956.

[10] S. B. Cohn, "Shielded coupled-strip transmission line," *IRE Transactions on Microwave Theory and Techniques*, vol. 3, no. 5, pp. 29-38, October 1955.

[11] W. Menzel, A. Balalem, "Quasi-lumped suspended stripline filters and diplexers," *IEEE transactions on microwave theory and techniques*. vol. 53, no. 10, pp. 3230-3237, October 2005.

[12] J. S. Lim, C. S. Kim, Y. T. Lee, D. Ahn, S. Nam, "Design of lowpass filters using defected ground structure and compensated microstrip line," *Electronics Letters*, vol. 38, no. 22, pp. 1357-1358, October 2002.

[13] L. H. Hsieh, K. Chang, "Compact, low insertion-loss, sharp-rejection, and wide-band microstrip bandpass filters," *IEEE Transactions on Microwave Theory and Techniques*, vol. 51, no. 4, pp. 1241-1246, April 2003.

[14] Y. H. Shu, J. A. Navarro and K. Chang, "Electronically switchable and tunable coplanar waveguide-slotline band-pass filters," *IEEE Transactions on Microwave Theory and Techniques*, vol. 39, no. 3, pp. 548-554, March 1991.

[15] F. Martin, F. Falcone, J. Bonache, R. Marqués, M. Sorolla, "Miniaturized coplanar waveguide stop band filters based on multiple tuned split ring resonators," *IEEE Microwave and Wireless Components Letters*, vol. 13, no. 12, pp. 511-513, December 2003.

[16] R. Azadegan, K. Sarabandi, "Miniature high-Q double-spiral slot-line resonator filters," *IEEE transactions on microwave theory and techniques*, vol. 52, no. 5, pp. 1548-1557, May 2004.

[17] S. K. Remillard, P. O. Radzikowski, S. Cordone, D. S. Applegate, A. Mehrotra, J. D. Kokales, A. Abdelmonem, "A closed slot-line resonator filter," *IEEE microwave and wireless components letters*, vol. 14, no. 5, pp. 234-236, May 2004.

[18] Zhang-Cheng Hao, Wei Hong, Ji-Xin Chen, Xiao-Ping Chen and Ke Wu, "Compact super-wide bandpass substrate integrated waveguide (SIW) filters," *IEEE Transactions on Microwave Theory and Techniques*, vol. 53, no. 9, pp. 2968-2977, September 2005.

[19] X. Chen, W. Hong, T. Cui, K. Wu, "Substrate integrated waveguide (SIW) asymmetric dual-mode filter and diplexer," *International Journal of Electronics*, vol. 92, no. 12, pp. 743-53, December 2005.

[20] S. B. Cohn, "Shielded coupled-strip transmission line," *IRE Transactions on Microwave Theory and Techniques*, vol. 3, no. 5, pp. 29-38, October 1955.

[21] S. B. Cohn, "Direct-coupled-resonator filters," *Proceedings of the IRE*, vol. 45, no. 2, pp. 187-196, February 1957.

[22] S. B. Cohn, "Parallel-coupled transmission-line-resonator filters," *IRE Transactions on Microwave Theory and Techniques*, vol. 6, no. 2, pp. 223-231, April 1958.

[23] G. I. Zysman and A. K. Johnson, "Coupled Transmission Line Networks in an Inhomogeneous Dielectric Medium," *IEEE Transactions on Microwave Theory and Techniques*, vol. 17, no. 10, pp. 753-759, October 1969.

[24] S. Akhtarzad, T. R. Rowbotham and P. B. Johns, "The Design of Coupled Microstrip Lines," *IEEE Transactions on Microwave Theory and Techniques*, vol. 23, no. 6, pp. 486-492, June 1975.

[25] J. E. Adair and G. I. Haddad, "Coupled-Mode Analysis of Nonuniform Coupled Transmission Lines," *IEEE Transactions on Microwave Theory and Techniques*, vol. 17, no. 10, pp. 746-752, October 1969.

[26] V. K. Tripathi, "Asymmetric Coupled Transmission Lines in an Inhomogeneous Medium," *IEEE Transactions on Microwave Theory and Techniques*, vol. 23, no. 9, pp. 734-739, September 1975.

[27] R. W. Jackson and D. M. Pozar, "Full-Wave Analysis of Microstrip Open-End and Gap Discontinuities," *IEEE Transactions on Microwave Theory and Techniques*, vol. 33, no. 10, pp. 1036-1042, October 1985.

[28] K. S. Chin, L. Y. Lin and J. T. Kuo, "New formulas for synthesizing microstrip bandpass filters with relatively wide bandwidths," *IEEE Microwave and Wireless Components Letters*, vol. 14, no. 5, pp. 231-233, May 2004.

[29] K. S. Chin and J. T. Kuo, "Insertion loss function synthesis of maximally flat parallel-coupled line bandpass filters," *IEEE Transactions on Microwave Theory and Techniques*, vol. 53, no. 10, pp. 3161-3168, October 2005.

[30] K. S. Chin, Y. C. Chiou, and J. T. Kuo, "New Synthesis of Parallel-Coupled Line Bandpass Filters With Chebyshev Responses," *IEEE Transactions on Microwave Theory and Techniques*, vol. 56, no. 7, pp. 1516- 1523, July 2008.

[31] R. K. Mongia, I. J. Bahl, P. Bhartia, J. Hong, "RF and Microwave Coupled-Line Circuits," *Artech House*, 2nd Ed., Ch.4, London, 2007.

[32] J. S. Hong and M. J. Lancaster, "Microstrip Filters for RF/Microwave Applications," *John Willey & Sons*, Inc., New York, NY, 2001, ISBN 0-471-22161-9, Ch. 1-4., 2001.

[33] C. Y. Chang and T. Itoh, "A modified parallel-coupled filter structure that improves the upper stopband rejection and response symmetry," *IEEE Transactions on Microwave Theory and Techniques*, vol. 39, no. 2, pp. 310-314, February 1991.

[34] G. Prigent, E. Rius, F. Le Pennec, and S. Le Maguer, "A Design Method for Improvement of λ/4 Coupled Line Narrow Bandpass Filter," *Microwave and Optical Technology Letters*, vol. 39, no. 2, pp. 121-125, October 2003.

[35] C. Jianxin, Y. Mengxia, X. Jun and X. Quan, "Compact microstrip bandpass filter with two transmission zeros," *Electronics Letters*, vol. 40, no. 5, pp. 311-313, March 2004.

[36] W. Wang, J. S. Fu, Y. Lu and Y. Z. Xiong, "Compact Bandpass Filter Design using Folded Coupled-Line Resonators," *Microwave and Optical Technology Letters*, vol. 45, no. 1, pp. 32-35, April 2005.

[37] C. K. Liao and C. Y. Chang, "Modified Parallel-Coupled Filter With Two Independently Controllable Upper Stopband Transmission Zeros," *IEEE Transactions on Microwave Theory and Techniques*, vol. 15, no. 12, pp. 841-843, December 2005.

[38] J. Z. Gu and X. W. Sun, "A Compact Microstrip Bandpass Filter using Folded Parallel-Coupled Lines," *Microwave and Optical Technology Letters*, vol. 48, no. 11, pp. 2328-2330, November 2006.

[39] Y. Zhang, "A Novel Microstrip Slow-Wave Resonator Bandpass Filter for Millimeter Wave Applications," *Microwave and Optical Technology Letters*, vol. 50, no. 7, pp. 1720-1722, July 2008.

[40] C.Y. Kung, Y.C. Chen, C.F. Yang and C.Y. Huang, "Triple-band Parallel Coupled Microstrip Bandpass Filter with Dual Coupled Length Input/Output," *Microwave and Optical technology Letters*, vol. 51, no. 4, pp. 995-997, April 2009.

[41] J. T. Kuo and E. Shih, "Wideband bandpass filter design with three-line microstrip structures," *IEE Proceedings - Microwaves, Antennas and Propagation*, vol. 149, no. 56, pp. 243-247, October 2002.

[42] Z. Zhang, J. Z. Gu, C. Wang and X. W. Sun, "Millimeter Wave Bandpass Filter using Three-Line Microstrip Structures," *Microwave and Optical technology Letters*, vol. 49, no. 1, pp. 40-42, January 2007.

[43] K. C. Yoon and J. C. Lee, "Design of a Compact Wide-Bandwidth Bandpass Filter using a Parallel-Coupled Structure," *Microwave and Optical technology Letters*, vol. 54, no. 11, pp. 2581-2584, November 2012.

[44] H. Shaman and J. S. Hong, "A Novel Microstrip Parallel-Coupled Line Structure for Ultra-wideband Microwave Filters," *Microwave and Optical technology Letters*, vol. 54, no. 11, pp. 2510-2513, November 2012.

[45] X. H. Wang, and H. Zhang, "Novel Balanced Wideband Filters Using Microstrip Coupled Lines," *Microwave and Optical Technology Letters*, vol. 56, no. 5, 1139-1141, May 2014.

[46] C. P. Chen, W. Imashiro, T. Anada and Z. Ma, "Improved Modeling of Parallel-Coupled Three-Line for Wideband Filters," *Microwave and Optical technology Letters*, vol. 56, no. 10, pp. 2392-2395, October 2014.

[47] F. Huang, J. Wang, J. Li, and W. Wu, "Compact microstrip wideband bandpass filter with high selectivity," *Electronics Letters*, vol. 52, no. 8, pp. 626-628, April 2016.

[48] T. Cheng, K. W. Tam, "A wideband bandpass filter with reconfigurable bandwidth based on cross-shaped resonator," *IEEE Microwave and Wireless Components Letters*, vol. 27, no. 10, pp. 909-911, September 2017.

[49] X. K. Bi, C. Teng, P. Cheong, S. K. Ho, K. W. Tam, "Wideband bandpass filters with reconfigurable bandwidth and fixed notch bands based on terminated cross-shaped resonator," *IET Microwaves, Antennas & Propagation*, vol. 13, no. 6, pp. 796-803, February 2019.

[50] D. S. La, X. Guan, H. C. Li, Y. Y. Li, and J. W. Guo, "Design of Broadband Band-Pass Filter with Cross-Coupled Line Structure," *International Journal of Antennas and Propagation*, vol. 2020, no. 5257325, pp. 1- 5, July 2020.

[51] M. Makimoto and S. Yamashita, "Bandpass Filters Using Parallel Coupled Stripline Stepped Impedance Resonators," *IEEE Transactions on Microwave Theory and Techniques*, vol. 28, no. 12, pp. 1413-1417, December 1980.

[52] B. Easter and K. A. Merza, "Parallel-coupled-line filters for inverted-microstrip and suspended-substrate MICs," *Proceedings of 11th IEEE Eur. Microwave Conf. Dig.*, pp. 164-167, September 1981.

[53] S. L. March, "Phase velocity compensation in parallel-coupled microstrip," *Proceedings of IEEE MTT-S Symp. Dig.*, pp. 410-412, June 1982.

[54] A. Riddle, "High performance parallel coupled microstrip filters," *Proceedings of IEEE MTT-S International Microwave Symposium Digest*, New York, NY, USA, vol. 1, pp. 427-430, May 1988.

[55] I. J. Bahl, "Capacitively compensated high performance parallel coupled microstrip filters," *Proceedings of IEEE MTT-S Symp. Dig.*, pp. 679-682, June 1989.

[56] V. Radisic, Y. Qian, R. Coccioli, and T. Itoh, "Novel 2-D photonic bandgap structure for microstrip lines," *IEEE Microwave Guided Wave Lett.*, vol. 8, no. 2, pp. 69-71, February 1998.

[57] F. R. Yang, K. P. Ma, Y. Qian, and T. Itoh, "A uniplanar compact photonic-bandgap (UC-PBG) structure and its applications for microwave circuits," *IEEE Trans. Microwave Theory Tech.*, vol. 47, no. 8, pp. 1509-1514, August 1999.

[58] F. R. Yang, R. Coccioli, Y. Qian, and T. Itoh, "Analysis and application of coupled microstrips on periodically patterned ground plane," *Proceedings of IEEE MTT-S Int. Microwave Symp. Dig.*, Boston, MA, pp.1529-1531, June 2000.

[59] T. Lopetegi, M. A. G. Laso, J. Hernández, M. Bacaicoa, D. Benito, M. J. Garde, M. Sorolla, and M. Guglielmi, "New microstrip 'wiggly-Line' filters with spurious passband suppression," *IEEE Trans. Microwave Theory Tech.*, vol. 49, no. 9, pp. 1593-1598, September 2001.

[60] J. T. Kuo, W. H. Hsu and W. T. Huang, "Parallel Coupled Microstrip Filters With Suppression of Harmonic Response," *IEEE Microwave and Wireless Components Letters*, vol. 12, no. 10, pp. 383-385, October 2002.

[61] J. S. Park, J. S. Yun and D. Ahn, "A design of the novel coupled-line bandpass filter using defected ground structure with wide stopband performance," *IEEE Transactions on Microwave Theory and Techniques*, vol. 50, no. 9, pp. 2037-2043, September 2002.

[62] J. T. Kuo and E. Shih, "Microstrip Stepped Impedance Resonator Bandpass filter With an Extended Optimal Rejection Bandwidth," *IEEE Trans. Microwave Theory Tech*., vol. 51, no. 5, pp. 1554-1559, April 2003.

[63] M. H. Weng, C. H. Pan, C. W. Shao, H. W. Wu and T. H. Huang, "Microstrip Stepped-Impedance Resonator Bandpass Filter with Over-coupled structure for Suppression of Harmonic Response," *Microwave and Optical Technology Letters*, vol. 41, no. 2, pp. 130-133, April 2004.

[64] C. F. Chen, T. Y. Huang and R. B. Wu, "Design of Microstrip Bandpass Filters With Multiorder Spurious-Mode Suppression," *IEEE Trans. Microwave Theory Tech*., vol. 53, no.12, pp. 3788-3793, December 2005.

[65] J. T. Kuo, S. P. Chen and M. Jiang, "Parallel-coupled microstrip filters with over-coupled end stages for suppression of spurious responses," *IEEE Microw. Wireless Compon. Lett.*, vol. 13, no. 10, pp. 440-442, October 2003.

[66] J. T. Kuo, M. Jiang and H.J. Chang, "Design of parallel-coupled microstrip filters with suppression of spurious resonances using substrate suspension," *IEEE Trans. Microwave Theory Tech*., vol. 52, pp. 83-89, 2004.

[67] F. Falcone, T. Lopetegi, J. D. Baena, R. Marques, F. Martin and Sorolla M, "Effective negative-ε stopband microstrip lines based on complementary split-ring resonators," *IEEE Microwave Wireless Compon. Lett*., vol. 14, no. 6, pp. 280-282, June 2004.

[68] B. S. Kim, J. W. Lee, and M. S. Song, "An Implementation of Harmonic-Suppression Microstrip Filters with Periodic Grooves," *IEEE Microwave and Wireless Components Letters*, vol. 14, no.9, pp. 413-415, September 2004.

[69] T. Lopetegi, M. A. G. Laso, F. Falcone, F. Martin, J. Bonache, "Microstrip "Wiggly-Line" Bandpass Filters With Multispurious Rejection," *IEEE Microwave and Wireless Components Letters*, vol. 14, no.11, pp. 531-533, November 2004.

[70] S. Sun and L. Zhu, "Guided-Wave Characteristics of Periodically Nonuniform Coupled Microstrip Lines-Even and Odd Modes," *IEEE Trans. Microw. Th. Tech*., vol. 53, no. 4, pp. 1221-1227, April 2005.

[71] S. Sun and L. Zhu, "Periodically Nonuniform Coupled Microstrip-Line Filters With Harmonic Suppression Using Transmission Zero Reallocation," *IEEE Trans. Microw. Th. Tech*., vol. 53, no. 5, pp. 1817-1822, May 2005.

[72] Meshon Jiang, Meng-Huan Wu and Jen-Tsai Kuo, "Parallel-coupled microstrip filters with over-coupled stages for multispurious suppression," *Proceedings of IEEE MTT-S International Microwave Symposium Digest*, pp. 687-690, 2005.

[73] Il K. Kim, N. Kingsley, M. Morton, R. Bairavasubramanian, J.Papapolymerou, M. M. Tentzeris, and J. G. Yook, "Fractal-Shaped Microstrip Coupled-Line Bandpass Filters for Suppression of Second Harmonic," *IEEE Trans. on Microwave Th. and Tech*., vol. 53, no. 9, pp. 2943-2948, September 2005.

[74] W. L. Chen and G. M. Wang, "Effective Design of Novel Compact Fractal-Shaped Microstrip Coupled-Line Bandpass Filters for Suppression of the Second Harmonic," *IEEE Microwave and Wireless Components Letters*, vol. 19, no. 2, pp. 74-76, February 2009.

[75] J. T. Kuo and M. H. Wu, "Corrugated parallel-coupled line bandpass filters with multispurious suppression," *IET Microwaves, Antennas & Propagation*, vol. 1, no. 3, pp. 718-722, June 2007.

[76] J. T. Kuo, U. H. Lok and M. H. Wu, "Novel Corrugated Coupled-Line Stage with Ideal Frequency Response and Its Application to Bandpass Filter Design with Multi-Harmonic Suppression," *IEEE/MTT-S International Microwave Symposium*, Honolulu, HI, pp. 553-556, 2007.

[77] A M. Moradian and M. Tayarani, "Spurious-Response Suppression in Microstrip Parallel-Coupled Bandpass Filters by Grooved Substrates," *IEEE Transactions on Microwave Theory and Techniques*, vol. 56, no. 7, pp. 1707-1713, July 2008.

[78] T. Yamaguchi, T. Fujii, T. Kawai and I. Ohta, "Parallel-coupled microstrip filters with periodic floating-conductors on coupled-edges for spurious suppression," *Proceedings of IEEE MTT-S International Microwave Symposium Digest*, Atlanta, GA, pp. 531-534, June 2008.

[79] A. S. Mohra, "Coupled Microstrip Line Bandpass Filter with Harmonic Suppression using Right-Angle Triangle Grooves," *Microwave and Optical Technology Letters*, vol. 51, no. 10, pp. 2313-2318, October 2009.

[80] H. Kuan, Y. L. Lin, R. Y. Yang and Y. C. Chang, "A Multilayered Parallel Coupled Microstrip Bandpass Filter With Embedded SIR Cells to Have a Broad Upper Rejection Band," *IEEE Microwave and Wireless Components Letters*, vol. 20, no. 1, pp. 25-27, January 2010.

[81] H. H. Ardakani, S. Fallahzadeh and J. Rashed-Mohassel, "Phase Velocities Equalization of Coupled Microstrip Lines Using Ω-Shaped Particles and Suppression of the Second Harmonic," *IEEE Transactions on Microwave Theory and Techniques*, vol. 60, no. 3, pp. 464-470, March 2012.

[82] M. A. S. Soriano, G. T. Penalva and E. Bronchalo, "Multispurious suppression in parallel-coupled line filters by means of coupling control," *IET microwaves, antennas & propagation*, vol. 6, no. 11, pp. 1269-1276, August 2012.

[83] F. Huang, "Suppression of harmonics in microstrip filters using a combination of techniques," *IEEE Transactions on Microwave Theory and Techniques*, vol. 63, no. 10, pp. 3453-3461, August 2015.

[84] F. C. Chen, H. T. Hu, R. S. Li, J. F. Chen, D. Luo, Q. X. Chu, M. J. Lancaster, "Design of wide-stopband bandpass filter and diplexer using uniform impedance resonators," *IEEE Transactions on Microwave Theory and Techniques*, vol. 64, no. 12, pp. 4192-4203, October 2016.

[85] F. Huang, "Microstrip band-pass filter with - 67 dB stop band up to 8.8 times the pass-band center frequency," *International Journal of Microwave and Wireless Technologies*, vol. 9, no. 10, pp. 1937-44, December 2017.

[86] E. G. Cristal and S. Frankel, "Hairpin-Line and Hybrid Hairpin-Line/ Half-Wave Parallel-Coupled-Line Filters," *IEEE Transactions on Microwave Theory and Techniques*, vol. MTT-20, no. 11, pp. 719-728, November 1972.

[87] B. Easter, "Microstrip Bandpass Filters with Reduced Radiation Effects," *Electronics Letters*, vol. 9, no. 4, pp. 93-94, February 1973.

[88] U. H. Gysel, "New Theory and Design for Hairpin-Line Filters," *IEEE Transactions on Microwave Theory and Techniques*, vol. 22, no. 5, pp. 523-31, May 1974.

[89] J. S. Wong, "Microstrip tapped-line filter design," *IEEE Transactions on Microwave Theory and Techniques*, vol. 27, no. 1, pp. 44-50, January 1979.

[90] M. Sagawa, K. Takahashi, M. Makimoto, "Miniaturized hairpin resonator filters and their application to receiver front-end MICs," *IEEE Transactions on Microwave Theory and Techniques*,; vol. 37, no. 12, pp. 1991-1997, December 1989.

[91] P. Pramanick, "Compact 900-MHz hairpin-line filters using high dielectric constant microstrip line," *International Journal of Microwave and Millimeter-Wave Computer-Aided Engineering*, no. 4, vol. 3, pp. 272-81, July 1994.

[92] Lung-Hwa Hsieh and Kai Chang, "Slow-Wave Bandpass Filters Using Ring or Stepped-Impedance Hairpin Resonators," *IEEE Transactions on Microwave Theory And Techniques*, vol. 50, no. 7, pp. 1795-1800, July 2002.

[93] X. M. Qing, Y. W. Chia, J. Sun, "A novel miniaturized microstrip bandpass filter using a meander-line resonator," *Microwave and Optical Technology Letters*. vol. 32, no. 4, pp. 319-321, February 2002.

[94] Y. Di, P. Gardner, P. S. Hall, H. Ghafouri-Shiraz, J. Zhou, "Multiple-coupled microstrip hairpin-resonator filter," *IEEE microwave and wireless components letters*, vol. 13, no. 12, pp. 532-534, December 2003.

[95] C. L. Huang, C. H. Hsu, C. M. Tsai, "Miniaturization of hairpin bandpass filters using high-permittivity substrate," *Microwave and Optical Technology Letters*, vol. 45, no. 3, pp. 222-225, May 2005.

[96] K. Ma, J. G. Ma, K. S. Yeo, M. A. Do, "A compact size coupling controllable filter with separate electric and magnetic coupling paths," *IEEE Transactions on Microwave Theory and Techniques*, vol. 54, no. 3, pp. 1113-1119, March 2006.

[97] W. H. Tu, "Compact microstrip bandpass filter using modified stepped-impedance hairpin resonator," *Microwave and Optical Technology Letters*, vol. 50, no. 8, pp. 2007-2010, August 2008.

[98] C. H. Shen and C. L. Huang, "Miniaturized hairpin resonator filters using dielectric ceramic substrates," *Microwave and Optical Technology Letters*, vol. 50, no. 3, pp. 620-624, March 2008.

[99] H. Wang and Q. X. Chu, "A narrow-band hairpin-comb two-pole filter with source-load coupling," *IEEE Microwave and Wireless Components Letters*, vol. 20, no. 7, pp. 372-374, June 2010.

[100] X. Ouyang and Q.-X. Chu, "High-Order Quasi-Elliptic Bandpass Filters Using Mixed EM Coupling Hairpin-Comb Resonators," *Journal of Electromagnetic Waves and Applications*, vol. 25, no. 14-15, pp. 1975-1984, January 2011.

[101] X. Gu, L. Yang, X. Bao, C. Yu, and Q. Shi, "A compact hairpin bandpass filter using multilayer stripline folded quarter-wavelength resonators," *Microwave and Optical Technology Letters*, vol. 54, no. 11, pp. 2627-2629, November 2012.

[102] A. Basti, A. Périgaud, S. Bila, S. Verdeyme, L. Estagerie, and H. Leblon, "Design of microstrip lossy filters for receivers in satellite transponders," *IEEE Transactions on Microwave Theory and Techniques*, vol. 62, no. 9, pp. 2014-2024, July 2014.

[103] R. K. Maharjan and N. Y. Kim, "Microstrip bandpass filters using window hairpin resonator and T-feeder coupling lines," *Arabian Journal for Science and Engineering*, vol. 39, no. 5, pp. 3989-97, May 2014.

[104] N. Chami, D. Saigaa, A. Djaiz, R. AlThomali and M. Nedil, "A new miniature microstrip two-layer bandpass filter using aperture-coupled hairpin resonators," *International Journal of Advanced and Applied Sciences*, vol. 4, no. 1, pp. 10-14, January 2017.

[105] D. Swanson, "Port tuning a microstrip-folded hairpin filter," *IEEE Microwave Magazine*, vol. 21, no. 4, pp. 18-28, March 2020.

[106] I. Hong, S. W. Fok, W. W. Choi, K. W. Tam and R. P. Martins, "A novel wiggly-line hairpin filter with 2nd spurious passband suppression," *Proceedings of 34th European Microwave Conference*, vol. 2, pp. 1125-1128, October 2004.

[107] M. L. Her, M. W. Hsu, Y. D. Wu, W. Ko, C. J. Hsu, "A wide rejection bandwidth bandpass filter with stepped-impedance hairpin resonator and interlaced coupled-line," *Microwave and Optical Technology Letters*, vol. 49, no. 3, pp. 542-545, March 2007.

[108] C. Y. Hung, M. H. Weng, Y. K. Su and R. Y. Yang, "A hairpin line wideband bandpass filter design with embedded open stubs," *Microwave and Optical Technology Letters*, vol. 49, no. 4, pp. 934-936, April 2007.

[109] P. Mondal P, A. Chakrabarty A, "Hairpin bandpass filter with extended upper stopband," *Microwave and Optical Technology Letters*, vol. 49, no. 6, pp. 1463-1464, June 2007.

[110] R. N. Baral and P. K. Singhal, "Design of Microstrip Band Pass Fractal Filter for Suppression of Spurious Band," *Radioengineering*, vol. 17, no. 4, December 2008.

[111] L. S. Chen, W. J. Lin, T. H. Huang, M. P. Houng and S. L. Fu, "Harmonic suppression of bandpass filters using open-circuited stubs," *Microwave and Optical Technology Letters*, vol. 50, no. 4, pp. 863-865, April 2008.

[112] W. Shen, W.Y. Yin and X.W. Sun, "Compact Microstrip Tri-Section Bandpass Filters with Mixed Couplings," *Journal of Electromagnetic Waves and Applications*, vol. 24, no. 13, pp. 1807-1816, January 2010.

[113] H. P. Partal, "Cross coupled wiggly line hairpin filters with high selectivity and spurious suppression," *Proceedings of 40th European Microwave Conference*, pp. 1265-1268, September 2010.

[114] W. J. Lin, J. Y. Li, D. B. Lin, L. S. Chen and M. P. Houng, "Multi-suppression of microstrip bandpass filter using split-mode excitations," *Journal of Electromagnetic Waves and Applications*, vol. 24, no. 11-12, pp. 1501-1510, January 2010.

[115] M. Naser-Moghadasi, M. Alamolhoda, B. Rahmati, "Harmonics blocking in hairpin filter using Defected Microstrip Structure," *IEICE Electronics Express*, vol. 8, no. 9, pp. 629-635, April 2011.

[116] J. Ghalibafan, S. Fallahzadeh, N. Komjani and M. Tayarani, "Design of a compact hairpin filter with spurious suppression," *Journal of Electromagnetic Waves and Applications*, vol. 25, no. 7, pp. 1059-1067, January 2011.

[117] A. A. Lotfi-Neyestanak and A. Lalbakhsh, "Improved microstrip hairpin-line bandpass filters for spurious response suppression," *Electronics letters*, vol. 48, no. 14, pp. 858-859, July 2012.

[118] F. Huang, "Suppression of spurious responses in microstrip filters using a reduced number of resistors," *IET microwaves, antennas & propagation*, vol. 6, no. 10, pp. 1128-1135, July 2012.

[119] H.T. Hsu and C. Y. Chiang, "Miniaturization of hairpin resonator filters with improved harmonic suppression by using lumped capacitors," *Proceedings of MTT-S International Microwave Symposium Digest*, pp. 1-4, June 2013.

[120] F. Huang, "Suppression of harmonics in microstrip filters with stagger tuning and voltage redistributions," *IEEE Transactions on Microwave Theory and Techniques*, vol. 62, no. 3, pp. 464-71, February 2014.

[121] J. Marimuthu, K. S. Bialkowski and A. Abbosh, "Compact bandpass filter with sharp passband and wide harmonic suppression using miniaturized coupled structure loaded with stepped-impedance stubs," *Microwave and Optical Technology Letters*, vol. 58, no. 10, pp. 2505-2508, October 2016.

[122] V. K. Killamsetty, B. Mukherjee, "Miniaturised highly selective bandpass filter with very wide stopband using meander coupled lines," *Electronics Letters*. vol. 53, no. 13, pp. 889-890, June 2017.

[123] J. S. Hong and M. J. Lancaster, "Couplings of microstrip square open-loop resonators for cross-coupled planar microwave filters," *IEEE Transactions on Microwave theory and Techniques*, vol. 44, no. 11, pp. 2099-2109, November 1996.

[124] J. S. Hong and M. J. Lancaster, "Compact microwave elliptic function filter using novel microstrip meander open-loop resonators," *Electronics Letters*, vol. 32, no. 6, pp. 563-564, March 1996.

[125] J. S. Hong and M. J. Lancaster, "Design of highly selective microstrip bandpass filters with a single pair of attenuation poles at finite frequencies," *IEEE Transactions on Microwave theory and Techniques*, vol. 48, no. 7, pp. 1098-1107, July 2000.

[126] J. T. Kuo, M. J. Maa and P. H. Lu, "A microstrip elliptic function filter with compact miniaturized hairpin resonators," *IEEE Microwave and Guided Wave Letters*, vol. 10, no. 3, pp. 94-95, March 2000.

[127] S. Chaimool, S. Kerdsumang and P. Akkaraekthalin, "A novel microstrip bandpass filter using triangular open-loop resonators," *Proceedings of 9th Asia-Pacific Conference on Communications (IEEE Cat. No. 03EX732)*, vol. 2, pp. 788-791, September 2003.

[128] S. H. Jang and J. C. Lee, "Design of novel cross-coupling elliptic function filters with the miniaturized edge-coupled split ring resonators," *Microwave and optical technology letters*, vol. 45, no. 6, pp. 495-499, June 2005.

[129] C. S. Ahn, J. Lee and Y. S. Kim, "Design flexibility of an open-loop resonator filter using similarity transformation of coupling matrix," *IEEE microwave and wireless components letters*, vol. 15, no. 4, pp. 262-264, April 2005.

[130] C. F. Chen, T. Y. Huang and R. B. Wu, "Compact microstrip cross-coupled bandpass filters using miniaturized stepped impedance resonators," *Proceedings of Asia-Pacific Microwave Conference*, vol. 1, pp. 1-4, December 2005.

[131] X. C. Zhang, J. Xu and Z. Y. Yu, "Design of quasi-elliptic bandpass filter based on slow-wave open-loop resonators," *Journal of Electromagnetic Waves and Applications*, vol. 22, no. 13, pp. 1849-1856, January 2008.

[132] X. C. Zhang, J. Xu, Z. Y. Yu and Y. L. Dong, "Design of microstrip filter based on slow-wave open-loop resonator," *Microwave and Optical Technology Letters*. vol. 51, no. 4, pp. 1057-1560, April 2009.

[133] C. H. Hsu, C. I. Hsu, C. C. Yu and H. A. Ho, "A compact bandpass filter using interdigital and step-impedance hairpin resonators," *Microwave and Optical Technology Letters*, vol. 52, no. 7, pp. 1493-1495, July 2010.

[134] L. C. Tsai, S. C. Jheng and K. C. Chu, "Design of bandpass filters using miniaturized Stepped-impedance Resonators," *Proceedings of Cross Strait Quad-Regional Radio Science and Wireless Technology Conference*, vol. 1, pp. 567-570, July 26.

[135] J. He, L. Jin and W. Tang, "A Novel Cross-Coupled Filter Through Mixed Coupling Path with Multiple Tunable Transmission Zeros," *Electromagnetics*, vol. 34, no. 8, pp. 608-616, October 2014.

[136] C. Schuster, R. Hu, A. Wiens, M. Maasch, R. Jakoby and H. Maune, "Cross-coupled open-loop resonator bandpass filter with independently tunable center frequency and bandwidth," *Proceedings of 2018 IEEE Radio and Wireless Symposium (RWS)*, pp. 52-55, January 2018.

[137] M. T. El Khorassani, H. Benchakroun, I. Badaout, A. Farkhsi, and N. A. Touhami, "Design of Cross-Coupled Band-Pass Filter Based on Square Open Loop Resonators," *International Journal of Microwave and Optical Technology*, vol. 15, no. 6, pp. 511-516, November 2020.

[138] S. Y. Lee and C. M. Tsai, "New cross-coupled filter design using improved hairpin resonators," *IEEE Transactions on Microwave theory and Techniques*, vol. 48, no. 12, pp. 2482-2490, December 2000.

[139] H. Nam, H. Lee and Y. Lim, "A design and fabrication of bandpass filter using miniaturized microstrip square SIR," *Proceedings of IEEE Region 10 International Conference on Electrical and Electronic Technology. TENCON 2001 (Cat. No. 01CH37239)*, vol. 1, pp. 395-398, August 2001.

[140] J. J. Yu, S. T. Chew, M. S. Leong and B. L. Ooi, "Miniaturized microstrip open-loop filters," *Microwave and optical technology letters*, vol. 35, no. 2, pp. 157-159, October 2002.

[141] S. Jovanovic and A. Nesic, "Microstrip bandpass filter with new type of capacitive coupled resonator," *Electronics Letters*, vol. 41, no. 1, pp. 19-21, January 2005.

[142] C. F. Chen, T. Y. Huang, R. B. Wu, "Design of microstrip bandpass filters with multiorder spurious-mode suppression," *IEEE transactions on microwave theory and techniques*, vol. 53, no. 12, pp. 3788-3793, December 2005.

[143] S. C. Lin, P. H. Deng, Y. S. Lin, C. H. Wang, and C. H. Chen, "Wide-stopband microstrip bandpass filters using dissimilar quarter-wavelength stepped-impedance resonators," *IEEE transactions on microwave theory and techniques*, vol. 54, no. 3, pp. 1011-1018, March 2006.

[144] C. F. Chen, T. Y. Huang and R. B. Wu, "Novel compact net-type resonators and their applications to microstrip bandpass filters," *IEEE transactions on microwave theory and techniques*, vol. 54, no. 2, pp. 755-762, February 2006.

[145] K. S. Chin and D. J. Chen, "Harmonic-suppressing bandpass filter based on coupled triangular open-loop stepped-impedance resonators," *Microwave and Optical Technology Letters*, vol. 52, no. 1, pp. 187-191, January 2010.

[146] N. Kumar and Y. K. Singh, "Compact stub-loaded open-loop BPF with enhanced stopband by introducing extra transmission zeros," *Electronics Letters*, vol. 51, no. 2, pp. 164-166, January 2015.

[147] F. Yan, Y. M. Huang, T. Huang, S. Ding, K. Wang and M. Bozzi, "Transversely Compact Single-Ended and Balanced Bandpass Filters with Source–Load-Coupled Spurlines," *Electronics*, vol. 8, no. 416, pp. 1-13, April 2019.

[148] C. Han, Y. Rao, H. J. Qian and X. Luo, "High-selectivity bandpass filter with wide upper stopband using harmonic suppression structure," *IEEE International Symposium on Radio-Frequency Integration Technology (RFIT)*, pp. 1-3, August 2019.

DESIGN OF FOLDED PARALLEL-COUPLED LINE BANDPASS FILTER

3.1. Theory of Filters

3.1.1. Introduction

Filters play a very important role in many wireless RF/microwave applications, in which demands for RF/microwave filters with higher performance, smaller size, lighter weight, and lower cost have increased. They are generally used to differentiate different frequency spectrums within the applicable electromagnetic regime. As a two-port network, the filter provides perfect transmission, i.e., negligible attenuation for signals in the passband and infinite attenuation in the stopband. An ideal filter should be designed with the following characteristics:

- zero insertion loss and infinite return loss from the output port towards the input port
- infinite stopband attenuation such that all undesired frequencies are completely removed
- symmetrical group delay variation in the passband and steeper skirt characteristics
- linear phase response within the passband and free from spurious passbands or harmonics

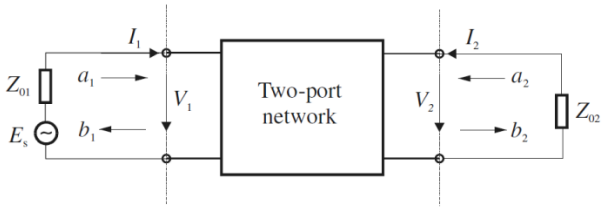

Fig. 3.1. Two-port network equivalent of a filter [1].

Such ideal characteristics cannot be attained practically, and the goal of the filter design is to approximate the ideal requirements within an acceptable tolerance. Most RF/microwave filters are represented by a two-port network, as shown in Fig. 3.1, where V_1, V_2, are the voltages and I_1, I_2 are the currents at ports 1 and 2, respectively. Similarly, Z_{01} and Z_{02} are the terminal impedances, with E_s being the source or generator voltage [1].

Filters are used in all frequency spectrums and are categorized into four main groups [1]:

- A low-pass filter (LPF) that transmits all signals between DC and with an upper cut-off frequency f_c and attenuates all signals with frequencies above f_c.
- A high-pass filter (HPF) that passes all signals with frequencies above the cutoff frequency f_c and rejects signals with frequencies below f_c.
- A band-pass filter (BPF) that passes signals with frequencies in the range of f_1 to f_2 and rejects frequencies outside this range.
- A band-reject or band-stop filter attenuates signals with frequencies in the range of f_1 to f_2 and passes frequencies outside this range.

Depending on the requirements and specifications, filters are designed as active and passive types; analog and digital types; lumped element based and distributed element based; etc. The output power of a passive filter will always be less than the input power, while an active filter allows admissible gain. Two traditional approaches: the transfer function approach or the attenuation function approach are generally applied to describe the characteristics of a passive filter. At low frequencies, the transfer function, $H(\omega)$ is used, while at microwave frequencies the attenuation function, L_A (dB) is preferred to describe the filter's response. The characteristics of the four filter categories are shown in Figs. 3.2(a) - (b) and Figs. 3.3(c) - (h) respectively. Accordingly, $H(\omega)$ and L_A (dB) are defined as [2]

$$H(w) = \frac{V_2(w)}{V_1(w)} \tag{1}$$

$$L_A(dB) = -20\log_{10}\left(\left|\frac{V_2(w)}{V_1(w)}\right|\right) \tag{2}$$

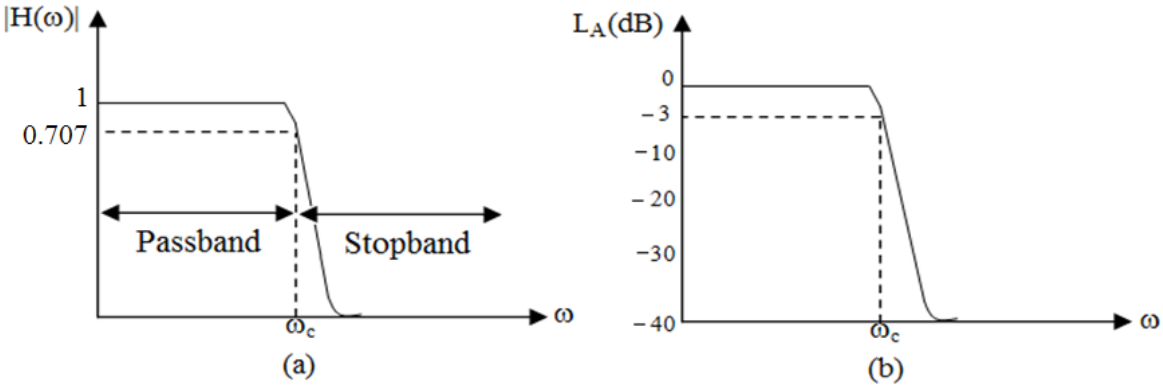

Fig. 3.2. Frequency response of lowpass filter (a) transfer function $|H(\omega)|$ and (b) attenuation function L_A (dB).

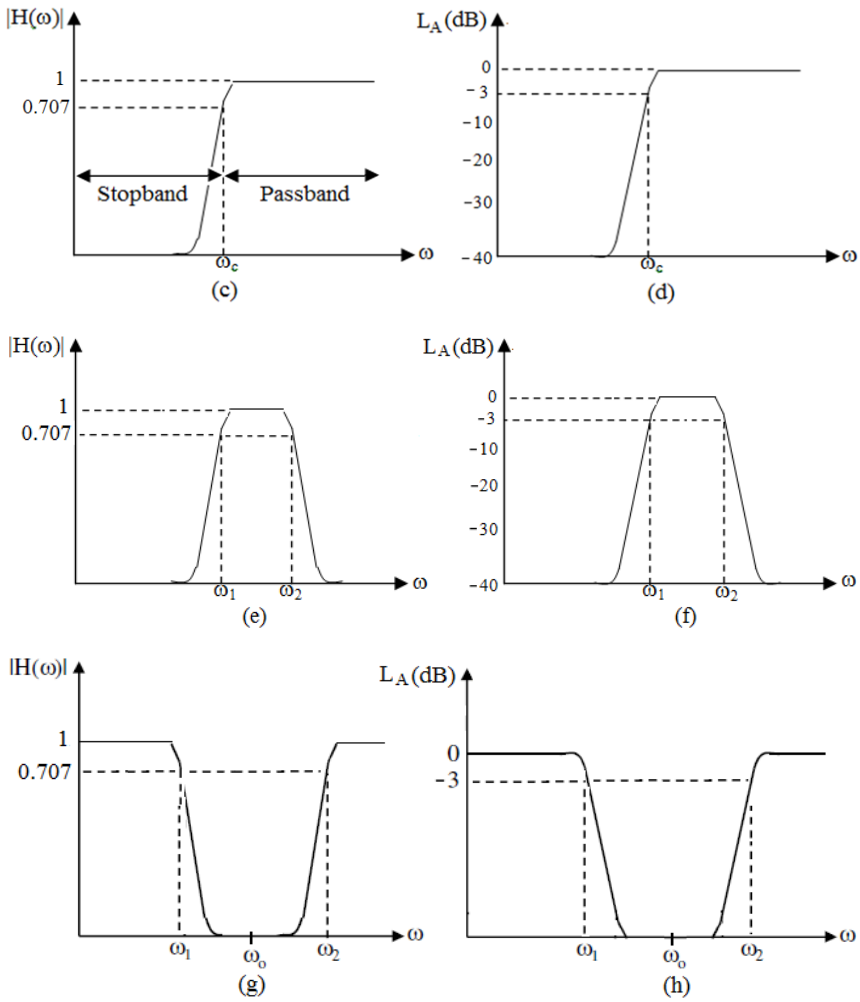

Fig. 3.3. Frequency response of filters (c)-(d) highpass, (e)-(f) bandpass, and (g)-(h) bandstop filter.

3.2. Passive Filter Synthesis by Insertion Loss Method (ILM)

The ideal filter would have no insertion loss and linear phase response in the passband, an infinite attenuation in the stopband, and be matched at the input and output ports [3]. It is impossible to practically build such a filter; therefore, compromises are made among different design constraints. The design by the insertion loss method allows a high degree of control over the filter width, stopband slope, and phase characteristic. Depending on the applications, the necessary trade-off design is evaluated. Various frequency responses are analyzed by the insertion loss method (*ILM*), providing a systematic way to design and synthesize a filter. The *ILM* method also allows filter performance to be improved in a straightforward manner, at the expense of a higher order filter [3]. Here, the filter response is defined by the insertion loss or

power loss ratio (*PLR*), which is defined by the ratio of the power available from source to the power delivered to load, i.e.,

$$PLR(\omega) = \frac{P_{inc}}{P_{Trns}} = \frac{1}{1-\left|\Gamma(\omega)\right|^2} \tag{3}$$

where $\Gamma(\omega)$ is the reflection coefficient looking into the input of the filter network. The insertion loss (*IL*) is expressed in dB as

$$IL = 10\log PLR \tag{4}$$

If $|\Gamma(\omega)|^2$ is an even function of ω, it can be expressed as

$$\left|\Gamma(\omega)\right|^2 = \frac{M(\omega^2)}{M(\omega^2)+N(\omega^2)} \tag{5}$$

where *M* and *N* are real polynomials of the order 2. Substituting equation (5) in (3) it has been obtained as

$$PLR(\omega) = 1 + \frac{M(\omega^2)}{N(\omega^2)} \tag{6}$$

Thus, for a filter to be physically realizable its power loss ratio must be of the form of (6). Moreover, specifying the power loss ratio simultaneously constrains the refection coefficient, $\Gamma(\omega)$.

3.2.1. Types of Transfer Function Polynomials

The two-port filter network, as shown in Fig. 3.1, is described mathematically by the transfer function as $|S_{21}|$. In general, the lossless passive filter network is characterized by the amplitude-squared transfer function, defined as [3]

$$\left|S_{21}(j\Omega)\right|^2 = \frac{1}{1+\varepsilon^2 F_n^2(\Omega)} \tag{7}$$

where ε is a ripple constant, $F_n(\Omega)$ represents a filtering or characteristic function, and Ω is a frequency variable of a lowpass prototype filter that has a cutoff frequency at $\Omega = \Omega_c$ with $\Omega_c = 1$ rad/sec.

3.2.1.1. Butterworth (Maximally Flat) Response

The amplitude-squared transfer function for the Butterworth filter, which has an insertion loss of $L_{Ar} = 3.01$ dB at the cutoff frequency $\Omega_c = 1$ rad/sec, is given by

$$\left|S_{21}(j\Omega)\right|^2 = \frac{1}{1+\Omega^{2n}} \tag{8}$$

Here, the degree or order of the filter is n, corresponding to the number of reactive elements of the lowpass prototype filter. Because the amplitude-squared transfer function defined in (7) has the greatest number of $(2n - 1)$ zero derivatives at $\Omega = 0$, such a response is referred to as maximally flat. Hence, the best response for the maximally flat approximation to the ideal lowpass filter in the passband is at $\Omega = 0$. However, it degrades as Ω approaches the cutoff frequency Ω_c. Fig. 3.4(a) shows a typical Butterworth lowpass prototype filter response and Fig. 3.4(b) depicts its poles distribution plot.

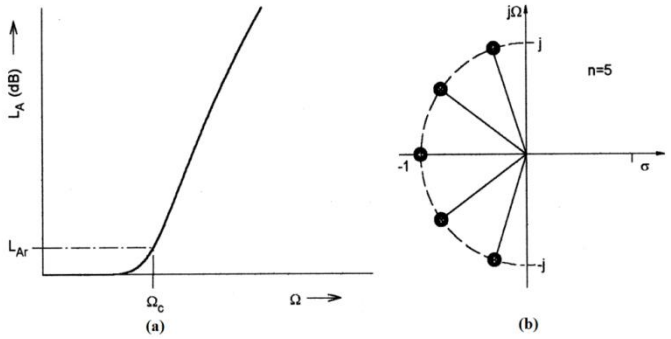

Fig. 3.4. (a) Butterworth or maximally flat lowpass prototype filter's response, (b) pole distribution [3].

Accordingly, a rational transfer function can be constructed from (8) [3] as

$$S_{21}(p) = \frac{1}{\prod_{i=1}^{n}(p - p_i)} \tag{9}$$

with

$$p_i = j\exp\left[\frac{(2i-1)\pi}{2n}\right] \tag{10}$$

According to (9), all the zeros of $S_{21}(p)$ are lying at infinity, and no finite-frequency transmission zero exists. As a result of $|p_i| = 1$ and Arg $p_i = (2i - 1)\pi/2n$, all the poles p_i are equally spaced on the unit circle in the left half-plane.

3.2.1.2. Chebyshev Response

Fig. 3.5(a) illustrates the Chebyshev response exhibiting an equal-ripple passband and a maximally flat stopband. The amplitude-squared transfer function for such a response is [3]

$$\left|S_{21}(j\Omega)\right|^2 = \frac{1}{1 + \varepsilon^2 T_n^2(\Omega)} \tag{11}$$

The ripple constant ε and passband ripple L_{Ar} in dB are related as

$$\varepsilon = \sqrt{10^{0.1L_{Ar}} - 1} \tag{12}$$

In (11), $T_n(\Omega)$ describes the first kind of Chebyshev function of order n. It is defined as

$$T_n(\Omega) = \begin{cases} \cos(n\cos^{-1}\Omega) & |\Omega| \le 1 \\ \cosh(n\cosh^{-1}\Omega) & |\Omega| \ge 1 \end{cases} \tag{13}$$

Similarly to the maximally flat response, all transmission zeros of $|S_{21}(s)|$ are at infinity. Therefore, the Butterworth and Chebyshev filters are referred to as all-pole filters [3].

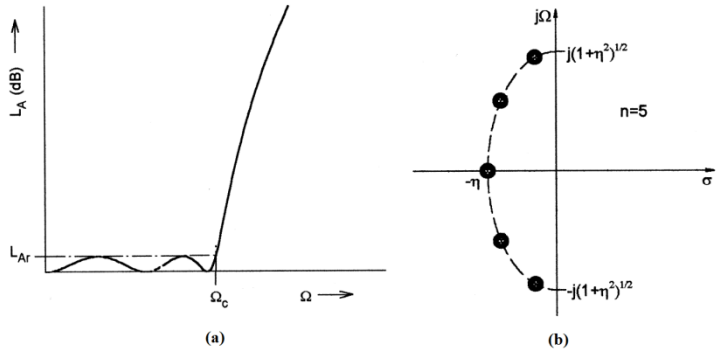

Fig. 3.5. (a) Chebyshev lowpass prototype filter's response, (b) pole distribution [3].

The pole locations for the Chebyshev case, on the other hand, are different and lie on an ellipse in the left half-plane, as shown in Fig. 3.5(b) with

$$\eta = \sinh\left(\frac{1}{n}\sinh^{-1}\frac{1}{\varepsilon}\right) \tag{14}$$

3.2.1.3. Elliptic Function Response

Fig. 3.6 illustrates the elliptic function response, which is equal-ripple in both the passband and stopband. The transfer function for such a response is defined as [3]

$$|S_{21}(j\Omega)|^2 = \frac{1}{1+\varepsilon^2 F_n^2(\Omega)} \tag{15}$$

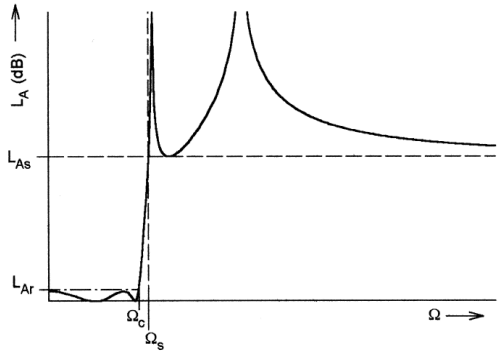

Fig. 3.6. Elliptic function lowpass prototype filter's response [3].

$$F_n(\Omega) = \begin{cases} M \dfrac{\Pi_{i=1}^{n/2}(\Omega_i^2 - \Omega^2)}{\Pi_{i=1}^{n/2}(\Omega_s^2 / \Omega_i^2 - \Omega^2)} & \text{for } n \text{ even} \\ N \dfrac{\Omega \Pi_{i=1}^{(n-1)/2}(\Omega_i^2 - \Omega^2)}{\Pi_{i=1}^{(n-1)/2}(\Omega_s^2 / \Omega_i^2 - \Omega^2)} & \text{for } n \geq 3 \text{ odd} \end{cases} \tag{16}$$

where Ω_i ($0 < \Omega_i < 1$) and $\Omega_s > 1$ represent some critical frequencies; M and N are constants. $F_n(\Omega)$ will oscillate between ±1 for $|\Omega| \leq 1$, and $|F_n(\Omega) = \pm 1$, n is the order of the filter.

3.3. Lowpass Prototype Filters

The lowpass prototype filter is the basic foundation to be used as a template for the designing of any modified filter for different practical applications, which is realized by the transfer functions as discussed in the previous section [1-3]. A lowpass prototype filter is characterized by the element values normalized such that the source resistance or conductance becomes equal to one ($g_0 = 1$) and the angular cutoff frequency to be unity ($\Omega_c = 1$ rad/sec). Figs. 3.7(a)-(b) demonstrate two possible forms of an n-pole lowpass prototype for realizing an all-pole filter response, including Butterworth, Chebyshev, and elliptic responses. In Figs. 3.7(a)-(b), g_i ($i = 1$ to n) represents either a series inductor or a shunt capacitor, where n indicates the number of reactive elements.

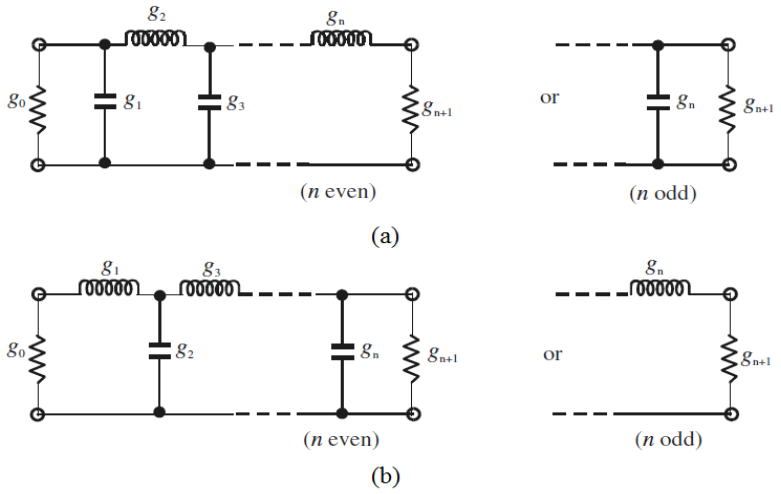

Fig. 3.7. Lowpass prototype filters for all-pole filters with (a) a ladder network structure and (b) its dual [3].

Thus, g_0 can be defined as the source resistance or the source conductance, and g_1 corresponds to the shunt capacitance or the series inductance, respectively. Like that, g_{n+1} corresponds to the load resistance or the load conductance if g_n is the shunt capacitance or the series inductance. Inductance (in Henry), capacitance (in Farad), resistance (in Ohm), and

conductance (in mho) are represented by these g-values. Such a lowpass filter can serve as a prototype to design practical, realizable filters after frequency and element transformations.

3.3.1. Butterworth Lowpass Prototype Filters

The element values for the network of Figs. 3.7(a)-(b) corresponding to the Butterworth or maximally flat lowpass prototype filters with the standard insertion loss L_{Ar} = 3.01 dB at the cutoff Ω_c = 1 rad/sec [3] are computed by (17).

$$\begin{aligned} g_0 &= 1 \\ g_i &= 2\sin\left(\frac{(2i-1)\pi}{2n}\right) \\ g_{n+1} &= 1 \qquad\qquad \text{for } i = 1 \text{ to } n \end{aligned} \tag{17}$$

Table 3.1 gives element values for such filters having n = 1 to 9 [3]. It may be noted that the two-port Butterworth filter has a symmetrical network structure, i.e., $g_0 = g_{n+1}$, $g_1 = g_n$, and so on. To determine the degree of a Butterworth lowpass prototype, a specification that is usually the minimum stopband attenuation L_{As} (dB) at $\Omega = \Omega_s$ for $\Omega_s > 1$ is given. Hence, the order is calculated as

$$n \geq \frac{\log(10^{0.1L_{As}} - 1)}{2\log\Omega_s} \tag{18}$$

Table 3.1. Element values for Butterworth lowpass prototype filters (g_0 = 1, Ω_c = 1 rad/sec, L_{Ar} = 3.01 dB at Ω_c)

n	g_1	g_2	g_3	g_4	g_5	g_6	g_7	g_8	g_9	g_{10}
1	2.0000	1.0								
2	1.4142	1.4142	1.0							
3	1.0000	2.0000	1.0000	1.0						
4	0.7654	1.8478	1.8478	0.7654	1.0					
5	0.6180	1.6180	2.0000	1.6180	0.6180	1.0				
6	0.5176	1.4142	1.9318	1.9318	1.4142	0.5176	1.0			
7	0.4450	1.2470	1.8019	2.0000	1.8019	1.2470	0.4450	1.0		
8	0.3902	1.1111	1.6629	1.9616	1.9616	1.6629	1.1111	0.3902	1.0	
9	0.3473	1.0000	1.5321	1.8794	2.0000	1.8794	1.5321	1.0000	0.3473	1.0

3.3.2. Chebyshev Lowpass Prototype Filters

The element values for the two-port networks of Figs. 3.7(a)-(b), corresponding to the Chebyshev lowpass prototype filter with the transfer function as (11) characterized by the passband ripple L_{Ar} (dB) and the cutoff frequency Ω_c = 1 rad/sec, are computed using the following formulas:

$$g_0 = 1$$

$$g_1 = \frac{2}{\gamma}\sin\left(\frac{\pi}{2n}\right)$$

$$g_1 = \frac{1}{g_{i-1}} \frac{4\sin\left[\frac{(2i-1)\pi}{2n}\right]\sin\left[\frac{(2i-3)\pi}{2n}\right]}{\gamma^2 + \sin^2\left[\frac{(i-1)\pi}{n}\right]} \quad \text{for } i = 2,3, \ldots\ldots n \qquad (19)$$

$$g_{n+1} = \begin{cases} 1 & \text{for } n = \text{odd} \\ \coth^2\left(\frac{\beta}{4}\right) & \text{for } n = \text{even} \end{cases}$$

where,

$$\beta = \ln\left[\coth\left(\frac{L_{Ar}}{17.37}\right)\right]$$

$$\gamma = \sinh\left(\frac{\beta}{2n}\right)$$

Some typical element values for such filters are tabulated in Table 3.2 for various passband ripples L_{Ar}, and for the filter degree of n = 1 to 9. The value of n for a Chebyshev lowpass prototype with the required passband ripple L_{Ar} (dB) and the minimum stopband attenuation L_{As} (dB) at $\Omega = \Omega_s$ is determined by (20) as

$$n \geq \frac{\cosh^{-1}\sqrt{\frac{10^{0.1L_{As}}-1}{10^{0.1L_{Ar}}-1}}}{\cosh^{-1}\Omega_s} \qquad (20)$$

Table 3.2. Element values for Chebyshev lowpass prototype filters (g_0 = 1, Ω_c = 1 rad/sec) [3].

For passband ripple L_{Ar} = 0.01 dB										
n	g_1	g_2	g_3	g_4	g_5	g_6	g_7	g_8	g_9	g_{10}
1	0.0960	1.0								
2	0.4489	0.4078	1.1008							
3	0.6292	0.9703	0.6292	1.0						
4	0.7129	1.2004	1.3213	0.6476	1.1008					
5	0.7563	1.3049	1.5773	1.3049	0.7563	1.0				
6	0.7814	1.3600	1.6897	1.5350	1.4970	0.7098	1.1008			
7	0.7970	1.3924	1.7481	1.6331	1.7481	1.3924	0.7970	1.0		
8	0.8073	1.4131	1.7825	1.6833	1.8529	1.6193	1.5555	0.7334	1.1008	
9	0.8145	1.4271	1.8044	1.7125	1.9058	1.7125	1.8044	1.4271	0.8145	1.0
For passband ripple L_{Ar} = 0.1 dB										
n	g_1	g_2	g_3	g_4	g_5	g_6	g_7	g_8	g_9	g_{10}
1	0.3052	1.0								
2	0.8431	0.6220	1.3554							
3	1.0316	1.1474	1.0316	1.0						
4	1.1088	1.3062	1.7704	0.8181	1.3554					
5	1.1468	1.3712	1.9750	1.3712	1.1468	1.0				
6	1.1681	1.4040	2.0562	1.5171	1.9029	0.8618	1.3554			
7	1.1812	1.4228	2.0967	1.5734	2.0967	1.4228	1.1812	1.0		
8	1.1898	1.4346	2.1199	1.6010	2.1700	1.5641	1.9445	0.8778	1.3554	
9	1.1957	1.4426	2.1346	1.6167	2.2054	1.6167	2.1346	1.4426	1.1957	1.0

3.3.3. Elliptic Function Lowpass Prototype Filters

The elliptic function lowpass prototype filters are characterized by the network structures as shown in Fig. 3.8(a). Here, the finite-frequency transmission zeros are realized by the series of branches of parallel-resonant circuits. This is because they block transmission by having an infinite series impedance (open-circuit) at resonance. In this equation, g_i represents the capacitance of a shunt capacitor for odd i (i = 1, 3,…) and g_i represents the inductance of an inductor for even i (i = 2, 4,…). Similarly, the capacitance of a capacitor in a parallel resonant circuit's series branch is represented by the prime g'_i for even i (i = 2, 4,…).

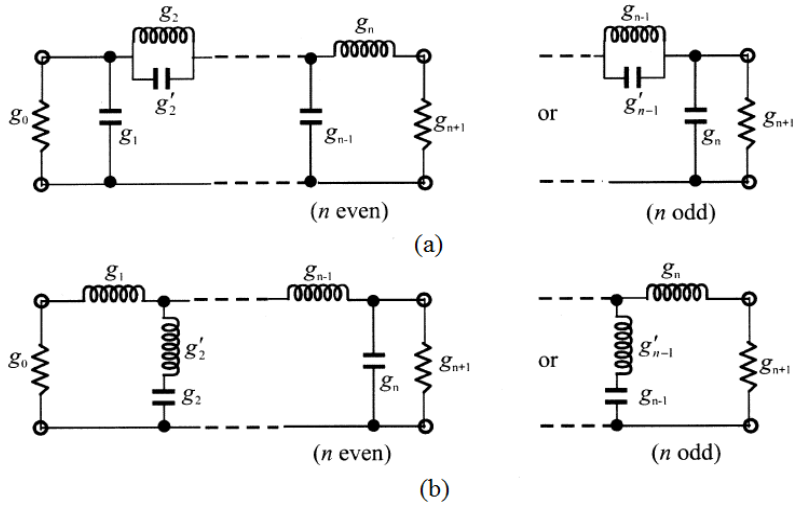

Fig. 3.8. Lowpass prototype filters for elliptic function filters with (a) series parallel-resonant branches, and (b) its dual with shunt series-resonant branches.

For the dual realization form in Fig. 3.8(b), the shunt branches of series-resonant circuits are used for implementing the finite-frequency transmission zeros, since they short out transmission at resonance. In this case, g_i represents the inductance of a series inductor for odd i (i = 1, 3,…) and g_i represents the capacitance of a capacitor for even i (i = 2, 4,…). Similarly, the inductance of an inductor in the series-resonant circuit's shunt branch is represented by primed g'_i for even i (i = 2, 4,…). Table 3.3 tabulates some useful design data for equally terminated ($g_0 = g_{n+1} = 1$) two-port elliptic function lowpass prototype filters shown in Figs. 3.8(a)-(b). These element values are given for a passband ripple L_{Ar} = 0.1 dB, a cut off frequency Ω_c = 1 rad/sec, and various Ω_s, which is the equal-ripple stopband starting frequency. Also, the minimum stopband insertion loss (L_{As} in dB) is required to determine the degree of an elliptic function lowpass prototype with a given specification.

Table 3.3. Element values for elliptic function lowpass prototype filters (Ω_c = 1 rad/sec, L_{Ar} = 0.1 dB) [3].

n	Ω_s	L_{As} dB	g_1	g_2	g_2'	g_3	g_4	g_4'	g_5	g_6	g_6'	g_7
3	1.4493	13.5698	0.7427	0.7096	0.5412	0.7427						
	1.6949	18.8571	0.8333	0.8439	0.3252	0.8333						
	2.0000	24.0012	0.8949	0.9375	0.2070	0.8949						
	2.5000	30.5161	0.9471	1.0173	0.1205	0.9471						
4	1.2000	12.0856	0.3714	0.5664	1.0929	1.1194	0.9244					
	1.2425	14.1259	0.4282	0.6437	0.8902	1.1445	0.9289					
	1.2977	16.5343	0.4877	0.7284	0.7155	1.1728	0.9322					
	1.3962	20.3012	0.5675	0.8467	0.5261	1.2138	0.9345					
	1.5000	23.7378	0.6282	0.9401	0.4073	1.2471	0.9352					
	1.7090	29.5343	0.7094	1.0688	0.2730	1.2943	0.9348					
	2.0000	36.0438	0.7755	1.1765	0.1796	1.3347	0.9352					
5	1.0500	13.8785	0.7081	0.7663	0.7357	1.1276	0.2014	4.3812	0.0499			
	1.1000	20.0291	0.8130	0.9242	0.4934	1.2245	0.3719	2.1350	0.2913			
	1.1494	24.5451	0.8726	1.0084	0.3845	1.3097	0.4991	1.4450	0.4302			
	1.2000	28.3031	0.9144	1.0652	0.3163	1.3820	0.6013	1.0933	0.5297			
	1.2500	31.4911	0.9448	1.1060	0.2694	1.4415	0.6829	0.8827	0.6040			
	1.2987	34.2484	0.9681	1.1366	0.2352	1.4904	0.7489	0.7426	0.6615			
	1.4085	39.5947	1.0058	1.1862	0.1816	1.5771	0.8638	0.5436	0.7578			
	1.6129	47.5698	1.0481	1.2416	0.1244	1.6843	1.0031	0.3540	0.8692			
	1.8182	54.0215	1.0730	1.2741	0.0919	1.7522	1.0903	0.2550	0.9367			
	2.000	58.9117	1.0876	1.2932	0.0732	1.7939	1.1433	0.2004	0.9772			

3.4. Frequency and Element Transformation

In order to obtain frequency characteristics and element values for practical filters based on the lowpass prototype, which has a normalized source resistance/conductance g_0 = 1 and a cutoff frequency Ω_c = 1 rad/sec, frequency and element transformations are required. The frequency transformation helps to perform the mapping from the lowpass prototype frequency-domain Ω to that in the frequency domain ω for the realization of all practical filters responses. Accordingly, all the reactive elements are affected by such a frequency transformation with no effect on the resistive elements. Besides the frequency mapping, impedance scaling is also required to be performed to accomplish the element transformation. As a result, the normalization g_0 = 1 will be removed and the filter will be adjusted to work for any value of the source impedance Z_0. The impedance scaling factor, γ_0 is defined as [3]

$$\gamma_0 = \begin{cases} Z_0 / g_0 & \text{for } g_0 \text{ being the resistance} \\ g_0 / Y_0 & \text{for } g_0 \text{ being the conductance} \end{cases} \tag{21}$$

where $Y_0 = 1/Z_0$ is the source admittance.

Finally, the impedance scaling is applied in a filter network by the conversion formula

$$\begin{aligned} L &\rightarrow \gamma_0 L \\ C &\rightarrow C/\gamma_0 \\ R &\rightarrow \gamma_0 R \\ G &\rightarrow G/\gamma_0 \end{aligned} \tag{22}$$

3.4.1. Lowpass Filter Transformation

The frequency transformation from a lowpass prototype to a practical lowpass filter having a cutoff frequency ω_c in the angular frequency axis ω is simply given by (23).

$$\Omega = \left(\frac{\Omega_c}{\omega_c}\right)\omega \tag{23}$$

Applying (23) together with the impedance scaling yields the element transformation:

$$\begin{aligned} L &= \left(\frac{\Omega_c}{\omega_c}\right)\lambda_0 g \qquad \text{for } g \text{ representing the inductance} \\ C &= \left(\frac{\Omega_c}{\omega_c}\right)\frac{g}{\lambda_0} \qquad \text{for } g_0 \text{ representing the capacitance} \end{aligned} \tag{24}$$

Fig. 3.9 shows the basic element transformation from a lowpass prototype to a practical lowpass filter.

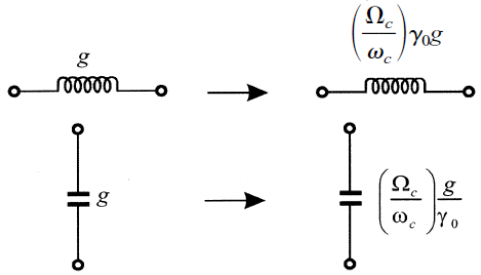

Fig. 3.9. Basic element transformations from a lowpass prototype to a practical lowpass filter.

3.4.2. Bandpass Filter Transformation

The frequency transformation from a lowpass prototype response to a bandpass filter response having a passband bandwidth ω_2 - ω_1, where ω_1 and ω_2 indicate the passband-edge angular frequency, is performed as

$$\Omega = \frac{\Omega_c}{FBW}\left(\frac{\omega}{\omega_0} - \frac{\omega_0}{\omega}\right) \tag{25.a}$$

$$FBW = \frac{\omega_2 - \omega_1}{\omega_0}$$
$$\omega_0 = \sqrt{\omega_1 \omega_2} \tag{25.b}$$

Here, the center angular frequency and the fractional bandwidth are denoted by ω_0 and *FBW*, respectively. By applying the frequency transformation to a reactive element *g* of the lowpass prototype, it is obtained as

$$j\Omega_g \rightarrow j\omega \frac{\Omega_c g}{FBW\omega_0} + \frac{1}{j\omega}\frac{\Omega_c \omega_0 g}{FBW} \tag{26}$$

Here, a series/parallel *LC* resonant circuit in the bandpass filter is being transformed from an inductive/capacitive element *g* in the lowpass prototype. After performing the impedance scaling, the elements for the series *LC* resonator in the bandpass filter are

$$L_s = \left(\frac{\Omega_c}{FBW\omega_0}\right)\gamma_0 g$$
$$C_s = \left(\frac{FBW}{\omega_0 \Omega_c}\right)\frac{1}{\gamma_0 g} \tag{27}$$

where *g* represents the inductance. Similarly, the elements for the parallel *LC* resonator in the bandpass filter are

$$C_p = \left(\frac{\Omega_c}{FBW\omega_0}\right)\frac{g}{\gamma_0}$$
$$L_p = \left(\frac{FBW}{\omega_0 \Omega_c}\right)\frac{\gamma_0}{g} \tag{28}$$

where *g* represents the capacitance. It should be noted that $\omega_0 L_s = 1/(\omega_0 C_s)$ and $\omega_0 L_p = 1/(\omega_0 C_p)$ are held in (27) and (28). The element transformation is shown in Fig. 3.10.

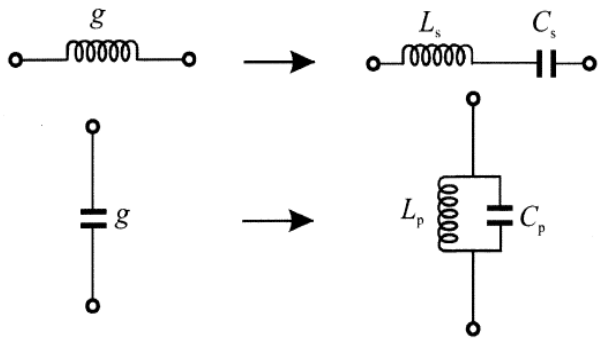

Fig. 3.10. Basic element transformations from a lowpass prototype to a practical bandpass filter.

3.5. Immittance Inverters

Immittance inverters, which are essentially reciprocal two-port linear time-invariant electrical networks, can also be used to realize practical filters. These are used to convert a ladder network consisting of both series and shunt immitances to the equivalent forms with only series or only parallel immitances. An idealized impedance inverter is a two-port network that has a unique property at all frequencies, i.e., if it is terminated in impedance Z_2 on one port, the impedance Z_1 seen at the other port is (29).

$$Z_1 = \frac{K^2}{Z_2} \tag{29}$$

In (29), K is called the characteristic impedance of the inverter, and it is a real quantity. The nature of Z_1 will be conductive or inductive if Z_2 is inductive or conductive. Thus, a phase shift of $\pm 90^o$ or its odd multiple occurs. An ideal impedance inverter is characterized by the *ABCD* matrix expressed as

$$\begin{bmatrix} A & B \\ C & D \end{bmatrix} = \begin{bmatrix} 0 & \mp jK \\ \pm \dfrac{1}{jK} & 0 \end{bmatrix} \tag{30}$$

Likewise, for an ideal admittance inverter, the admittance Y_1 seen looking into one port with an admittance Y_2 connected to the other port, is

$$Y_1 = \frac{J^2}{Y_2} \tag{31}$$

where J is the characteristic admittance of the inverter, which is also a real quantity. Similarly, the admittance inverter exhibits a phase shift of $\pm 90^o$ or its odd multiple. The ideal admittance inverter is characterized by the *ABCD* matrix as

$$\begin{bmatrix} A & B \\ C & D \end{bmatrix} = \begin{bmatrix} 0 & \pm \dfrac{1}{jJ} \\ \mp jJ & 0 \end{bmatrix} \tag{32}$$

3.5.1. Realization of Filters by Immittance Inverters

Fig. 3.11(a) shows the conversion of a series inductance with an inverter on each side to a shunt capacitance, and similarly, Fig. 3.11(b) illustrates the conversion of a shunt capacitance with an inverter on each side to a series inductance. Moreover, the inverters can shift impedance or admittance levels based on their types, either K or J. Such properties of inverters enable a filter circuit to be implemented with microwave structures. The two

common lowpass prototype structures in Figs. 3.7(a)-(b) are converted into the equivalent immittance inverter forms as shown in Fig. 11, where the g_i values are the original prototype element values. The values of Z_0, Z_{n+1}, L_{ai}, Y_0, Y_{n+1}, and C_{ai}, are selected as per the filter's specifications to make it identical to the original prototype, provided that the immittance inverter parameters $K_{i,i+1}$ and $J_{i,i+1}$ are specified as indicated by the equations in Figs. 3.12(a)-(b). These equations are derived by expanding the input immittances of the original prototype networks and the equivalent ones in continued fractions and by equating corresponding terms.

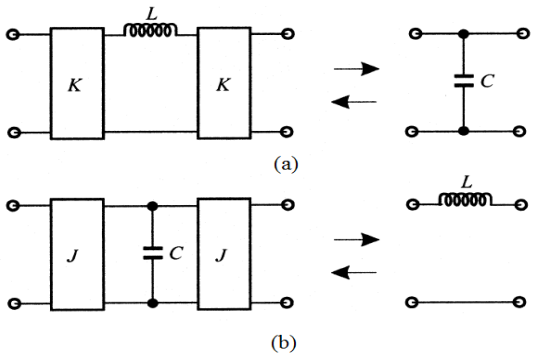

Fig. 3.11. (a) Impedance inverters used to convert a shunt capacitance into an equivalent circuit with series inductance, and (b) admittance inverters used to convert a series inductance into an equivalent circuit with shunt capacitance.

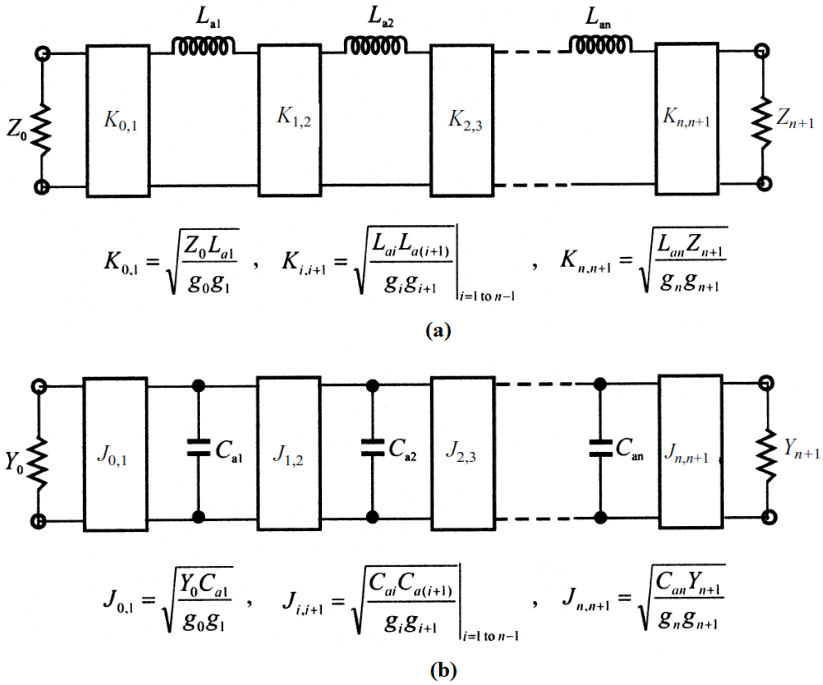

Fig. 3.12. Lowpass prototype filters modified to include immittance inverters: (a) *K*-inverter, and (b) *J*-inverter.

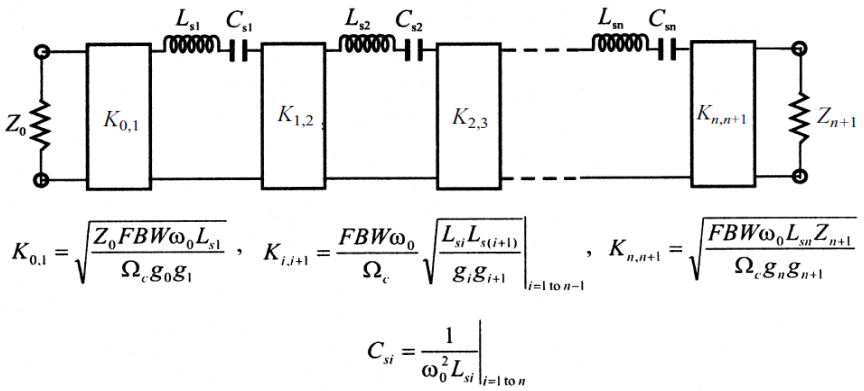

Fig. 3.13. Realization of bandpass filters using impedance (*K*) inverters [3].

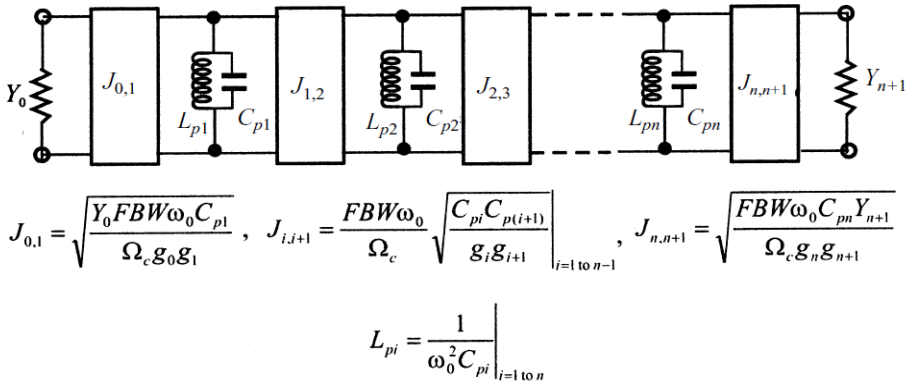

Fig. 3.14. Realization of bandpass filters using admittance (*J*) inverters [3].

Ideally, the immittance inverter parameters are independent of frequency. Thus, the lowpass filter networks in Figs. 3.12(a)-(b) can easily be transformed to other filters by simply applying the element transformation. The realizations of bandpass filters using impedance (*K*) and admittance (*J*) inverters are shown in Fig. 3.13 and Fig. 3.14, respectively. In the case of Fig. 3.13, only series resonators are involved, whereas the filter in Fig. 3.14 consists of only shunt parallel resonators. Due to the assumption that the source impedances are the same in both the filters, no impedance scaling is required, i.e., the scaling factor $\gamma_0 = 1$. Now, viewing L_{ai} as inductive g in Fig. 3.9, and transforming the inductors of the lowpass filter to the series resonators of the bandpass filter, it is obtained as

$$L_{si} = \left(\frac{\Omega_c}{FBWw_0}\right) L_{ai} \qquad (33)$$

$$C_{si} = \frac{1}{w_0^2 L_{si}}$$

$$L_{si} = \left(\frac{\Omega_c}{FBW\omega_0} \right) L_{ai} \qquad (34)$$

$$C_{si} = \frac{1}{\omega_0^2 L_{si}}$$

Replacing L_{ai} in the equations mentioned in Fig. 12(a) with $L_{ai} = (FBW\omega_0/\Omega_c)L_{si}$ yields the equations mentioned in Fig. 3.13. Similarly, the transformations and equations in Fig. 3.14 can be obtained on a dual basis for *J*-inverters.

3.5.2. Practical Realization of Immittance Inverters

The practical immittance inverters are realized by a quarter-wavelength of transmission line with the *ABCD* matrix as in (30) for $K = Z_c$ ohms, where Z_c is the characteristic impedance of the line. Similarly, a quarter-wavelength line can also be used as an admittance inverter with $J = Y_c$, where $Y_c = 1/Z_c$ is the characteristic admittance of the line. The narrow-band nature of the quarter-wavelength line makes it suitable to be used satisfactorily as an immittance inverter for narrow-band filters [3]. Four typical lumped-element immittance inverters are shown in Figs. 3.15(a)-(d). While the inverters in Fig. 3.15(a) and Fig. 3.15(b) are of interest for use as *K*-inverters, those shown in Fig. 3.15(c) and Fig. 3.15(d) are of interest for use as *J*-inverters. The reason is that the negative elements of the inverters could be absorbed into adjacent elements in practical filters.

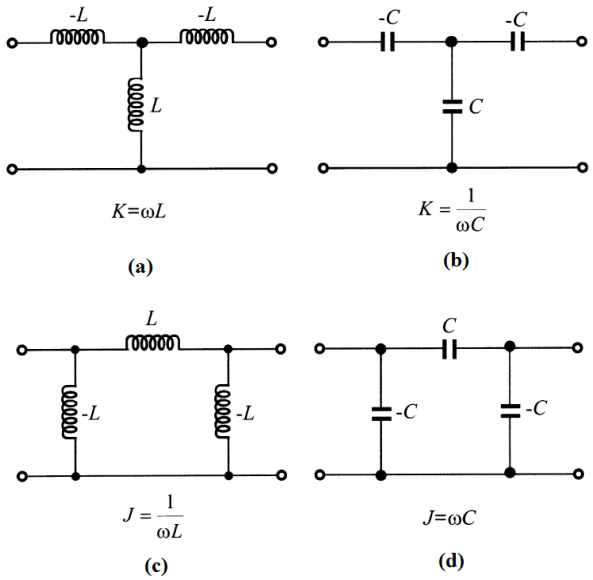

Fig. 3.15. Lumped-element immittance inverters: (a) *L*-based T-network, (b) *C*-based T-network, (c) *L*-based π -network, and (d) *C*-based π -network [3].

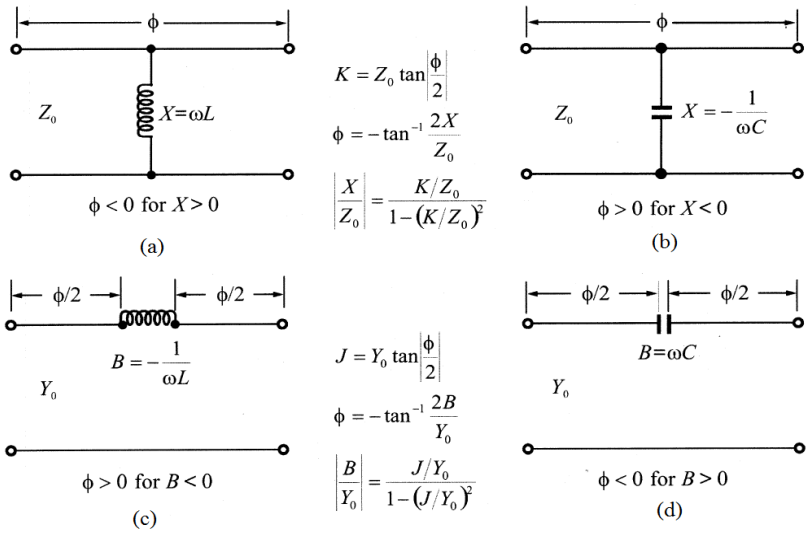

Fig. 3.16. Immittance inverters comprised of lumped and transmission line elements [3].

It can be shown that the inverters in Fig. 3.15(a) and Fig. 3.15(d) have a phase shift (the phase of S_{21}) of $+90^o$, whereas those in Fig. 3.15(b) and Fig. 3.15(c) have a phase shift of-90^o. This is why the different signs appear in the *ABCD* matrix expressions of immittance inverters. Another type of practical immittance inverter is a circuit mixed with lumped and transmission line elements, as shown in Figs. 3.16(a)-(d), where Z_0 and Y_0 are the characteristic impedance and admittance of the line, and φ denotes the total electrical length of the line. Practically, the line with positive or negative electrical length can be added to or subtracted from adjacent lines of the same characteristic impedance. However, the limited bandwidth of the practical immittance inverters limits their applications when the bandwidth of the filter increases.

3.6. Richards' Transformation

Practical microwave filters are designed with distributed transmission line elements. At first, some approximate equivalence between lumped and distributed elements is taken care of. Richards' transformation is an efficient mathematical tool for establishing such equivalence [3]. According to this, distributed networks with commensurate length transmission lines and lumped resistors could be considered in analysis or synthesis as lumped element *LRC* networks following the transformation:

$$t = \tanh\frac{ls}{v_p} \tag{35}$$

In (35), $s = \sigma + j\omega$ is the usual complex frequency variable, and l/v_p is the ratio of the length of the basic commensurate transmission line element to the phase velocity of the wave propagating in such a line. The variable t is a new complex frequency variable, also known as Richards' variable, and (35) is referred to as Richards' transformation. For lossless passive networks, $s = j\omega$ and the Richards' variable is simply expressed by

$$t = j\tan\theta \tag{36}$$

and the electrical length is defined as

$$\theta = \frac{\omega l}{v_p} \tag{37}$$

Assuming that the phase velocity v_p is independent of frequency, which is true for TEM transmission lines, the electrical length is then proportional to frequency and may be expressed as $\theta = \theta_0\omega/\omega_0$, where θ_0 is the electrical length at a reference frequency ω_0. It is convenient for discussion to let ω_0 be the radian frequency at which all line lengths are quarter-wave long, with $\theta_0 = \pi/2$ and to let $\Omega = \tan\theta$, so that

$$\Omega = \tan\left(\frac{\pi}{2}\frac{\omega}{\omega_0}\right) \tag{38}$$

Under Richards' transformation, a close correspondence exists between lumped inductors and capacitors in the s-plane and short- and open-circuited transmission lines in the t-plane. As a one-port inductive element with an impedance $Z = sL$ and Z_c as the characteristic impedance of the line, a lumped inductor can be realized by a short-circuited line element (stub) having an input impedance $Z = tZ_c = jZ_c\tan\theta$. Likewise, a lumped capacitor with an admittance $Y = sC$ corresponds to an open-circuited stub of input admittance $Y = tY_c = jY_c\tan\theta$ and characteristic admittance Y_c. These correspondences are illustrated in Fig. 3.17, and as a consequence, the short-circuited and open-circuited line elements are sometimes referred to as the t-plane inductor and capacitor, respectively, and use the corresponding lumped-element symbols as well. A transmission line of characteristic impedance Z_u has an *ABCD* matrix

$$\begin{bmatrix} A & B \\ C & D \end{bmatrix} = \begin{bmatrix} \cos\theta & jZ_u\sin\theta \\ j\sin\theta/Z_u & \cos\theta \end{bmatrix} \tag{39}$$

which in terms of Richards' variable becomes

$$\begin{bmatrix} A & B \\ C & D \end{bmatrix} = \frac{1}{\sqrt{1-t^2}}\begin{bmatrix} 1 & Z_u t \\ t/Z_u & 1 \end{bmatrix} \tag{40}$$

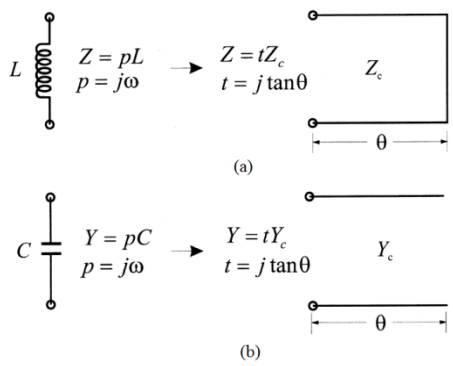

Fig. 3.17. Lumped and distributed element correspondence under Richards' transformation [3].

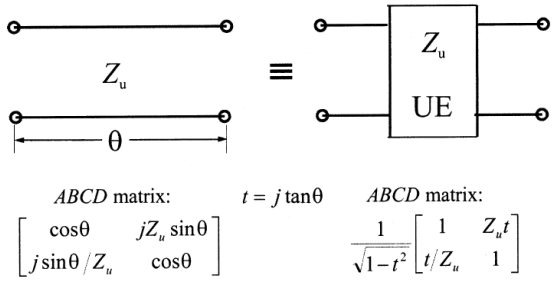

$$\begin{bmatrix} \cos\theta & jZ_u \sin\theta \\ j\sin\theta / Z_u & \cos\theta \end{bmatrix} \qquad \frac{1}{\sqrt{1-t^2}} \begin{bmatrix} 1 & Z_u t \\ t/Z_u & 1 \end{bmatrix}$$

Fig. 3.18. Symbol of a unit element (UE) for Richards' transformation [3].

This line element is referred to as a unit element, hereafter as UE, and its symbol is illustrated in Fig. 3.18. It can be noted that the unit element has a half-order transmission zero at $t = \pm 1$. In order to separate the circuit elements in distributed filters, unit elements are usually employed.

3.7. Kuroda Identities

In general, for the designing of transmission line filters, various network identities are applied to obtain filter networks that are equivalent electrically but that are different in form or in element values. Such transformations provide flexibility to designers to obtain networks that are physically realizable with physical dimensions. The Kuroda identities, shown in Figs. 3.19(a)-(b), form a basis to achieve such transformations, where the commensurate line elements with the same electrical length θ are assumed for each identity. For the Kuroda identities, a unit element with a shunt open-circuited stub or a series short-circuited stub is interchanged with a unit element with a series short-circuited stub or a shunt open-circuited stub.

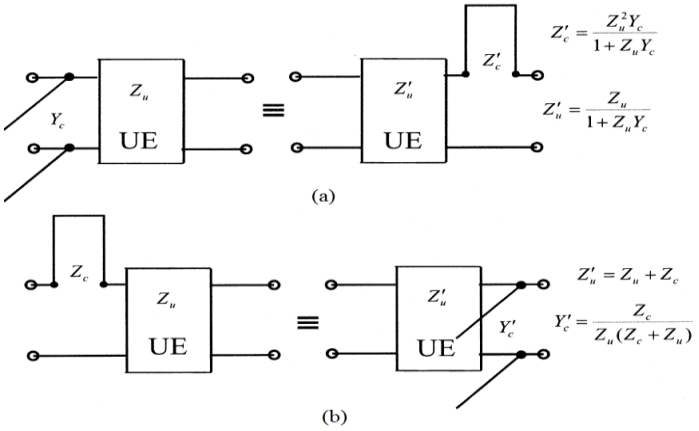

Fig. 3.19. Kuroda identities for a unit element [3].

3.8. Performance Parameters of Filters

The filters are generally characterized by the following parameters:

(1) the roll-off rate ξ (dB/GHz) generally used to measure skirt selectivity defined as:

$$\xi = \frac{\alpha_s - \alpha_c}{f_s - f_c} \tag{41}$$

where α_s is the 30 dB attenuation point and α_c is the 3 dB attenuation point; f_s is the 30 dB stopband frequency and f_c is the 3 dB cutoff frequency.

(2) The relative stopband frequency f_{SB} defined as:

$$RSB = \frac{f_{SBW}}{f_{SC}} \tag{42}$$

where f_{SBW} is the 25 dB stopband bandwidth and f_{SC} is the stopband center frequency.

(3) The suppression factor *SF* is the parameter that indicates the degree of stopband suppression. It is defined as:

$$SF = \frac{SBRL}{10} \tag{43}$$

where *SBRL* is the stopband rejection level of consideration.

(4) The normalized circuit size *NCS* indicates the degree of miniaturization of the filters and it is defined as:

$$NCS = \frac{physical\ size\ \ (length \times width)}{\lambda_g \times \lambda_g} \tag{44}$$

(5) Finally, the figure-of-merit (FOM) is the overall performance index of the proposed filters, and it is defined as:

$$FOM = \frac{\xi \times RSB \times SF}{NCS \times AF} \tag{45}$$

3.9. Parallel-Coupled Line Bandpass Filter

Parallel-coupled bandpass filters are widely used in the transmitters' and receivers' front ends to provide frequency selectivity and efficient transmission of band-limited signals for various wireless communications systems such as satellites, mobile, WLAN, WiMAX, Wi-Fi, electronic warfare, radar, metrology, and remote-sensing systems operating at microwave frequencies. It provides a variety of advantages, like

(1) low insertion loss in the passband
(2) high return loss in the passband
(3) wide range of fractional bandwidth (2% -70%)
(4) simple design procedure
(5) low fabrication and production costs
(6) simple to integrate with other components of the system
(7) fewer circuit area requirements and compact structures

Coupled microstrip lines are the building blocks of such types of filters. Fig. 3.20 illustrates the cross-section of a pair of coupled microstrip lines. In Fig. 3.20, the coupled lines are characterized by their widths W and separation s, whereas h is the thickness and ε_r is the relative dielectric constant of the substrate material. In this structure, the interaction of the electromagnetic fields is responsible for the coupling of signal power from one line to the other. Accordingly, it supports two different quasi-TEM excitation modes called even-mode and odd-mode [1-2].

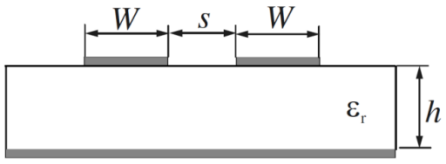

Fig. 3.20. Cross section of a pair of coupled microstrip lines [3].

A magnetic wall or open-circuit plane is generated at the symmetry plane due to the even-mode excitation with equal voltage potentials induced on both the microstrip lines as illustrated in Fig. 3.21(a). However, a symmetric plane of an electric wall i.e., a short circuit plane is created for the odd mode excitation. In this case, opposite voltage potentials are induced on the microstrip lines due to opposite sign charges, as indicated in Fig. 3.21(b).

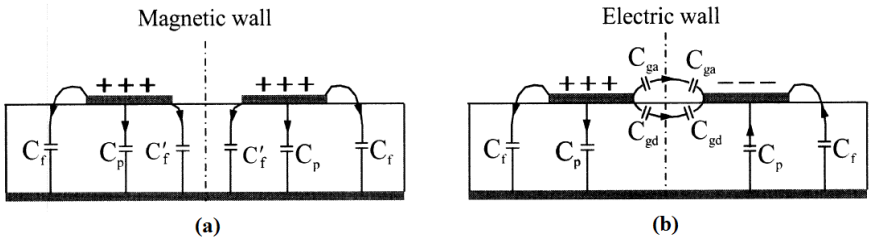

Fig. 3.21. Quasi-TEM modes of a pair of coupled microstrip lines: (a) even mode and (b) odd mode [3].

In general, these two modes will be excited at the same time. However, they propagate with different phase velocities because they are not pure TEM modes. Therefore, the coupled microstrip lines are characterized by their characteristic impedances as well as the effective dielectric constants for the two modes. In spite of the synchronous excitation of these two impure TEM modes during the signal transmission, they propagate with different phase velocities, especially at higher frequencies. It results in two different characteristic impedances (Z_{oe} and Z_{oo}) for the coupled microstrip lines [1]. The phase constant of the odd-mode is comparatively much less than that of the even-mode, and hence, the odd-mode propagates more speedily than the even-mode. Accordingly, spurious passbands, i.e., harmonics, are generated for parallel-coupled line filters. In Fig. 3.21, different capacitances are defined as

(1) even-and odd-mode capacitances C_e and C_o

(2) parallel plate capacitance between the microstrip and the ground plane C_p

(3) fringe capacitance for an uncoupled single microstrip line C_f

(4) modified fringe capacitance for the even-mode of a single line due the presence of another line $C_f^{'}$

(5) fringe capacitances for the even-mode due to the air and dielectric regions across the coupling gap C_{ga} and C_{gd}

Accordingly, the even- and odd-mode characteristics impedances, Z_{oo} and Z_{oe} are determined analytically as [3]

$$Z_{oe} = \left(c\sqrt{C_e^a C_e}\right)^{-1} \tag{46}$$

$$Z_{oo} = \left(c\sqrt{C_o^a C_o}\right)^{-1} \tag{47}$$

where C_e^a and C_o^a are even- and odd-mode capacitances for the coupled microstrip line structure with air as dielectric. Similarly, the modal effective dielectric constants ε_{re} and ε_{ro} are formulated as [3]

$$\varepsilon_{re}^e = \frac{C_e}{C_e^a} \tag{48}$$

$$\varepsilon_{re}^{o} = \frac{C_o}{C_o^a} \tag{49}$$

The structure of a two-port parallel-coupled line section exhibiting the bandpass response is depicted in Fig. 3.22(a). The total port currents, including the even- and odd-mode currents at port-1 and port-3, are I_1 and I_3 respectively, whereas port-2 and port-4 are left open-circuited. Accordingly, a single coupled-line section has been modelled by the equivalent *J*-inverter circuit as shown in Fig. 3.22(b). The electrical length of the coupled-line section has been calculated as $\theta \approx \pi/2$ to correspond to the center frequency of the bandpass response. Fig. 3.23 illustrates the general structure of the N^{th}-order parallel-coupled line bandpass filter.

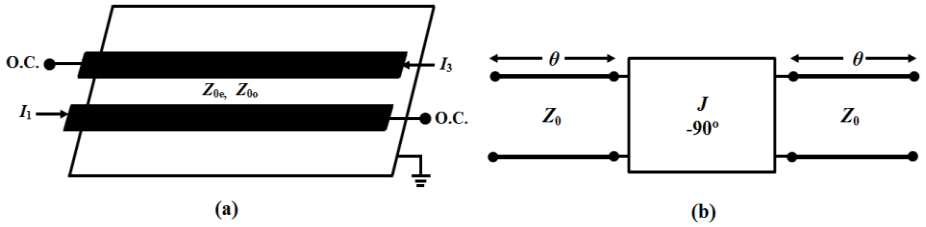

Fig. 3.22. (a) A two-port coupled-line section having a bandpass response, (b) equivalent J-inverter circuit.

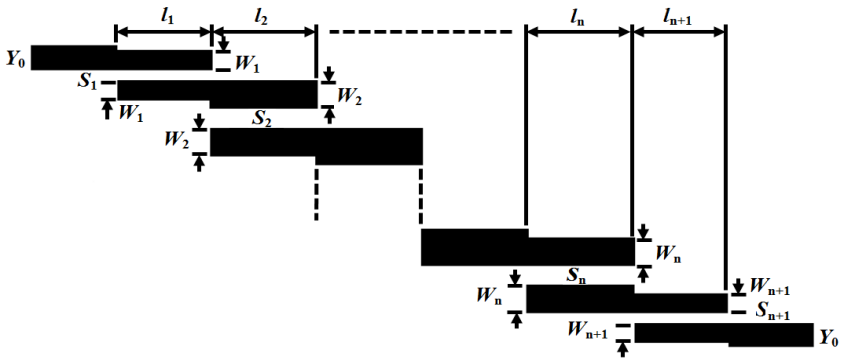

Fig. 3.23. General structure of a parallel-coupled microstrip bandpass filter of order *N*.

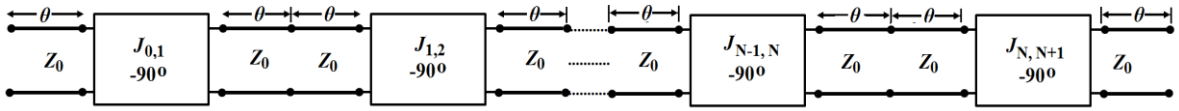

Fig. 3.24. Equivalent *J*-inverter circuit diagram of a parallel-coupled microstrip bandpass filter of order *N*.

The filter has been constructed by placing the half-wavelength line resonators parallel to each other along half of their length in a ladder-type arrangement. As a result, relatively large coupling between the resonators has been achieved, and thus, bandpass filters with a wider bandwidth can be constructed conveniently. The equivalent *J*-inverter circuit of the n^{th}-order parallel-coupled line bandpass filter is depicted in Fig. 3.24. There is a transmission line

section of effectively 2θ in length between any two consecutive *J*-inverters. This line is approximately half-wavelength long near the passband region of the filter.

3.10. Parallel-Coupled Line Bandpass Filters Realizations for WLANs

As information and communications technology (ICT) advances, there is a greater demand for devices that support communication with higher data rates, greater security, and smaller sizes. Local Area Network (LAN) is used to provide a wired connection between devices for data exchange within a specific geographic area. Although it is more secure and less costly, it suffers from poor data rates, limited bandwidth and mobility, and requires regular maintenance and physical access. The popularity of LAN has been replaced by Wireless Local Area Network (WLAN), in which the entire communication is performed on a wireless platform in early 1999. In general, a WLAN network is a collection of computers or other such network devices in a particular location that are connected together wirelessly by communication elements or network elements. Wireless LANs use high-frequency radio signals, infrared beams, or lasers to communicate between workstations, file servers, or hubs. WLAN follows a standard named IEEE 802.11 [4]. This network is used by different mediums to connect personal digital assistants, desktop computers, workstations, printers, mobile phones, etc. WLAN uses IEEE 802.11 specifications that include four subsets of Ethernet-based protocol standards: 802.11a, 802.11b, and 802.11g. Table 3.4 highlights the primary RF characteristics of different standards [5].

Table 3.4. Different WLAN standards.

Standard	Frequency Band (GHz)	Data rate (Mbps)	Channel spacing (MHz)	Receiver sensivity (dBm)	Maximal transmit power (mW)
802.11a	5.0 (5.15-5.35 and 5.725-5.825)	6-54	20	-82 to -65	40/200/800
802.11b	2.4 (2.401-2.483)	1-11	10/25	-76	1000
802.11g	2.4 (2.401-2.483)	6-54	25	-82 to -65	1000

Bandpass filters are one of the most important components for WLAN transceivers. Fig. 3.25 illustrates the typical block diagram of a dual-band WLAN IEEE 802.11 RF transceiver [5].

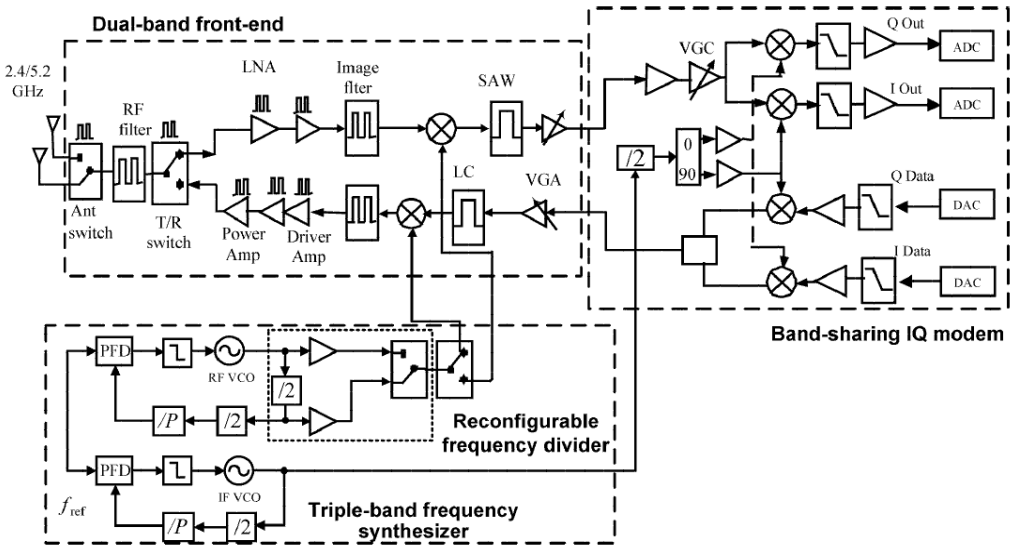

Fig. 3.25. Architecture of the dual-band WLAN RF transceiver [5].

Table 3.5. Specifications of the bandpass filters.

Specifications	**Filter-I**	**Filter-II**
Cut-off frequency, f_0 (GHz)	5.25	2.5
Transfer function type	Chebyshev Type-I	
Fractional bandwidth, Δ (%)	20	
Bandwidth, *BW* (GHz)	4.75-5.80	2.26-2.77
Passband ripple, L_{Ar} (dB)	0.1	
Insertion loss, *IL* (dB)	<2 dB	
Return loss, *RL* (dB)	>15 dB	
Passband attenuation (dB) (L_{As})	>10 dB at 5.15 GHz	>10 dB at 2.4 GHz

Accordingly, Table 3.5 highlights the specifications of the parallel coupled-line bandpass filters applicable for WLAN IEEE 802.11 a/b/g transceivers' front end circuits. The specifications of the substrate material are as follows:

- Name- FR4
- Dielectric constant $\varepsilon_r = 4.4$
- Thickness h =1.6 mm
- Loss tangent tan$\delta = 0.02$

Based on the specifications of Table 3.5, the filters have been designed according to the following steps:

Step 1: **Determination of the order, *N* of the Filter-I:**

From Table 3.5, it has been noted that an attenuation level greater than 10 dB is to be obtained at 5.15 GHz for the proposed filter, and thus, the design has been initiated by

transforming the stopband frequency to the normalized lowpass form i.e. $\omega_c = 1$ (rad/sec) by using (50)-(51) [2] as

$$\omega \leftarrow \frac{1}{\Delta}\left(\frac{\omega}{\omega_0}-\frac{\omega_0}{\omega}\right)=\frac{1}{0.02}\left(\frac{5.15}{5.25}-\frac{5.25}{5.15}\right)=-2.0244 \tag{50}$$

$$\left|\frac{\omega}{\omega_0}\right|-1=\left|-2.0244\right|-1=1.0244 \tag{51}$$

From the attenuation (dB) vs. $\left|\frac{\omega}{\omega_0}\right|-1$ plot given in [Ref. 2, Fig. 8.27] the order of the filter has been chosen as $N = 3$. Accordingly, the lowpass prototype elements are obtained from Table 3.6 as highlighted, i.e., $g_0 = g_4 = 1.0000$, $g_1 = g_3 = 1.0316$, $g_2 = 1.1474$ [3].

Table 3.6. Element values for Chebyshev lowpass prototype filters (L_{Ar} = 0.1 dB, $g_0 = 1$, $\Omega_c = 1$ rad/sec) [3].

n	g_1	g_2	g_3	g_4	g_5	g_6	g_7	g_8	g_9	g_{10}
1	0.3052	1.0								
2	0.8431	0.6220	1.3554							
3	1.0316	1.1474	1.0316	1.0						
4	1.1088	1.3062	1.7704	0.8181	1.3554					
5	1.1468	1.3712	1.9750	1.3712	1.1468	1.0				
6	1.1681	1.4040	2.0562	1.5171	1.9029	0.8618	1.3554			
7	1.1812	1.4228	2.0967	1.5734	2.0967	1.4228	1.1812	1.0		
8	1.1898	1.4346	2.1199	1.6010	2.1700	1.5641	1.9445	0.8778	1.3554	
9	1.1957	1.4426	2.1346	1.6167	2.2054	1.6167	2.1346	1.4426	1.1957	1.0

Step 2: Determination of admittance inverter constants, or characteristic admittances of *J*-inverter (J_n):

The admittance inverter constants (Fig. 3.12b) are determined by the following equations

$$\frac{J_{0,1}}{Y_0}=\sqrt{\frac{\pi}{2}\cdot\frac{\Delta}{g_0 g_1}} \tag{52}$$

$$\frac{J_{n,n+1}}{Y_0}=\sqrt{\frac{\pi}{2}\cdot\frac{\Delta}{g_n g_{n+1}}} \tag{53}$$

$$\frac{J_{j,j+1}}{Y_0}=\frac{\pi\Delta}{2}\cdot\frac{1}{\sqrt{g_j g_{j+1}}} \quad \text{for } j=1 \text{ to } n\text{-}1 \tag{54}$$

In (52)-(54), Y_0 is the characteristic admittance of the microstrip feed line.

Step 3: Determination of the even- and odd-mode characteristic impedances of the coupled microstrip lines (Z_{0e} and Z_{0o}):

The values of Z_{0e} and Z_{0o} are determined by the following equations (55)-(56) for $j = 0$ to n.

$$(Z_{0e})_{j,j+1} = \frac{1}{Y_0}\left[1 + \frac{J_{j,j+1}}{Y_0} + \left(\frac{J_{j,j+1}}{Y_0}\right)^2\right] \tag{55}$$

$$(Z_{0o})_{j,j+1} = \frac{1}{Y_0}\left[1 - \frac{J_{j,j+1}}{Y_0} + \left(\frac{J_{j,j+1}}{Y_0}\right)^2\right] \tag{56}$$

Step 4: Determination of the width (*W*) of the line and gap (*s*) between the lines:

The values of *W* and *s* for each pair of coupled line are determined by following the equations proposed in [6] if width *W*-to-substrate's thickness *h* ratio i.e., $W/h \leq 1$ as:

$$\varepsilon_{re} = \frac{\varepsilon_r + 1}{2} + \frac{\varepsilon_r - 1}{2}\left[\left\{1 + 12\left(\frac{h}{W}\right)\right\}^{-0.5} + 0.04\left(1 - \frac{W}{h}\right)^2\right] \tag{57}$$

If $W/h \geq 1$

$$\varepsilon_{re} = \frac{\varepsilon_r + 1}{2} + \frac{\varepsilon_r - 1}{2}\left\{1 + 12\left(\frac{h}{W}\right)\right\}^{-0.5} \tag{58}$$

Step 5: Determination of guided wavelength and lengths of the resonators

The guided wavelength and the lengths of the resonators are obtained as

$$\lambda_g = \frac{300}{f_0(GHZ)\sqrt{\varepsilon_{re}}} \tag{59}$$

$$l = \frac{\lambda_g}{4} \tag{60}$$

Finally, an approximate length correction of $d = 1.64h$ [2] is to be subtracted from *l* to obtain the final length of each coupled line. Table 3.7 and Table 3.8 list all the calculated parameters for Filter-I. Fig. 3.26 illustrates the layout of a third-order parallel-coupled line bandpass filter. The overall size of the filter is 53.99 mm × 12.23 mm, i.e., 660.19 mm^2 or $1.74\lambda_g \times 0.39\lambda_g$ where λ_g is the guided wavelength at f_0 = 5.25 GHz. Fig. 3.27(a) exhibits the simulated *S*-parameters plots and Fig. 3.27(b) shows the transmission phase angle plot. All the EM and circuit simulation results have been carried out by Zeland_IE3D_v14.10 EM simulator.

Table 3.7. Calculated values of widths and gaps for Filter-I.

j	$J_{j,j+1}/Y_0$	$(Z_{0e})_{j,j+1}$	$(Z_{0o})_{j,j+1}$	W_j (mm)	s_j (mm)	W_s (mm)
0	0.5519	92.8247	37.6347	0.8	0.368	3.083
1	0.2888	68.6103	39.7303	1.152	0.935	
2	0.2888	68.6103	39.7303	1.152	0.935	
3	0.5519	92.8247	37.6347	0.8	0.768	

Table 3.8. Calculated values of lengths for Filter-I.

j	$(\lambda_g)_j$ (mm)	$l_j = \lambda_g/4$ (mm)	$d_j = 1.6h$ (mm)	$l_{j'} = l_j - d_j$ (mm)	l_s (mm)
0	32.128	8.032	0.264	7.768	11
1	31.848	7.962	0.264	7.698	
2	31.848	7.962	0.264	7.698	
3	32.128	8.032	0.264	7.768	

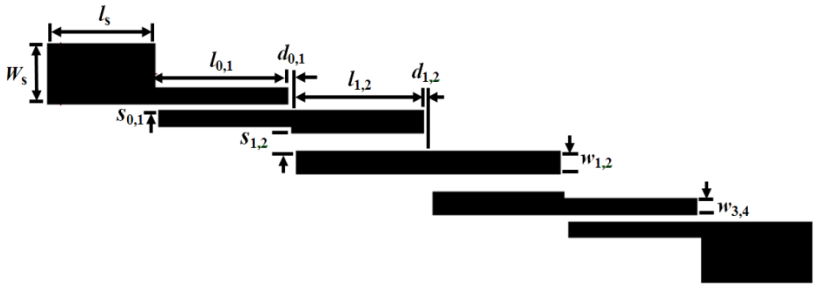

Fig. 3.26. Layout of the third-order conventional parallel-coupled bandpass filter.

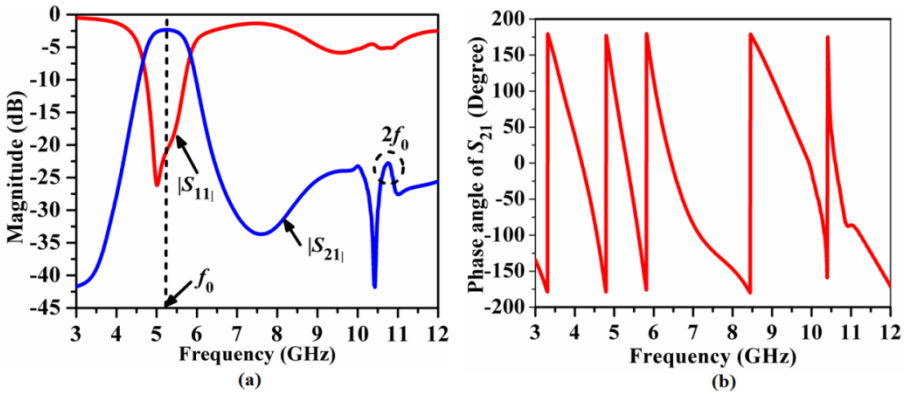

Fig. 3.27. Simulated *S*-parameters plots for a third-order conventional parallel-coupled bandpass filter (*C*-band): (a) magnitude (dB) and (b) phase angle of S_{21} (degree).

It has been observed from Fig. 3.27(a) that insertion loss of 2.2 dB and return loss of 21 dB have been obtained in the desired passband at f_0 = 5.25 GHz. Moreover, a high degree of transmission zero having an attenuation level of 42 dB at 10.5 GHz has been observed, and subsequently, the second harmonic has been observed at 10.75 GHz with an attenuation level of 23 dB due to the dispersive behaviour of the microstrip coupled-line structure. The transmission phase angle plot varies linearly in the passband as illustrated in Fig. 3.27(b). The surface current distribution for the third-order conventional parallel-coupled microstrip-line bandpass filter (PCMLBF) is shown in Figs. 3.28(a)-(b).

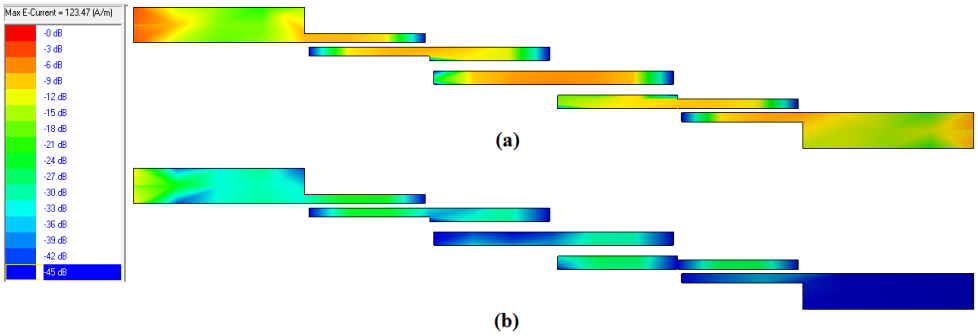

Fig. 3.28. Surface current distribution for third-order parallel-coupled microstrip-line bandpass filter (PCMLBF): (a) at f_0 = 5.25 GHz, and (b) at $2f_0$ = 10.5 GHz.

It has been observed from Fig. 3.28(a) that the surface current has been well distributed from the input port (left side) to the output port (right side) for f_0 = 5.25 GHz. However, due to the presence of a spurious second harmonic in the stopband with a high attenuation level, a comparable amount of current has been able to reach the output port at $2f_0$ = 10.5 GHz, as shown in Fig. 3.28(b). By following the same procedure as discussed, Filter-II (Table 3.5) has been designed, and Tables 3.9 and 3.10 list all the parameter values. Fig. 3.29 shows the layout of the third-order PCMLBF centered at f_0 = 2.5 GHz with optimized dimensions in mm.

Table 3.9. Calculated values of widths and gaps for Filter-II.

j	$J_{j,j+1}/Y_0$	$(Z_{0e})_{j,j+1}$	$(Z_{0o})_{j,j+1}$	$(w/h)_j$	$(s/h)_j$	w_j (mm)	s_j (mm)	w_s (mm)
0	0.499	87.470	37.500	1.180	0.163	0.940	0.3	3.083
1	0.201	62.077	41.967	1.929	0.434	1.543	0.8	
2	0.201	62.077	41.967	1.929	0.434	1.543	0.8	
3	0.499	87.470	37.500	1.180	0.163	0.940	0.3	

Table 3.10. Calculated values of lengths for Filter-II.

j	$(\lambda_g)_j$ (mm)	$l_j=\lambda_g/4$ (mm)	$\Delta l_j=1.65h$ (mm)	$l_j'=l_j-\Delta l_j$ (mm)	l_s (mm)
0	67.845	16.961	0.264	16.697	16
1	66.921	16.730	0.264	16.466	

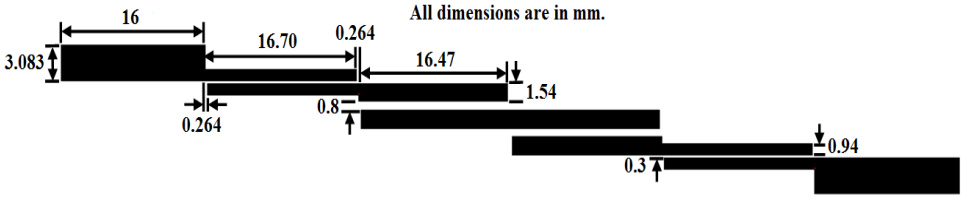

Fig. 3.29. Layout of third-order conventional parallel-coupled microstrip line bandpass filter centered at 2.5 GHz.

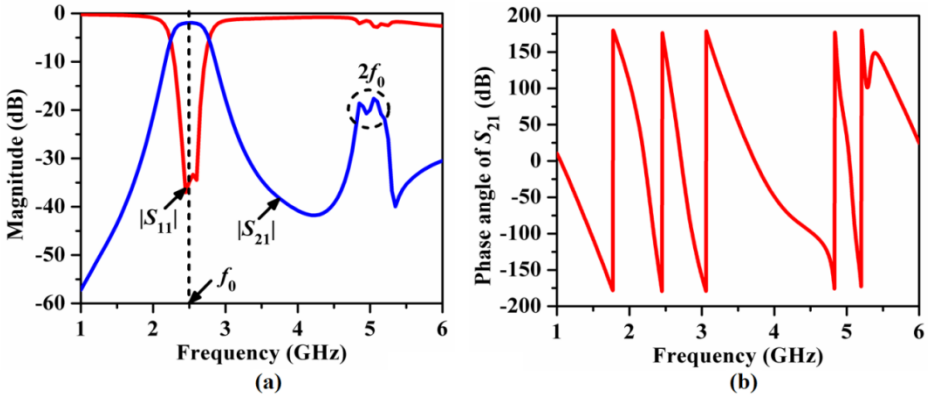

Fig. 3.30. Simulated *S*-parameters plots for a third-order conventional parallel-coupled bandpass filter, (a) magnitude (dB) and (b) phase angle of S_{21} (degree).

The overall size of the filter is 99.4 mm × 12.99 mm, i.e., 1291.21 mm^2 or 1.46λ_g × 0.19λ_g where λ_g is the guided wavelength at f_0 = 2.5 GHz. Fig. 3.30(a) and Fig. 3.30(b) depict the simulated *S*-parameters plots and the transmission phase angle plot respectively for Filter-II. It has been observed from Fig. 3.30(a) that insertion loss of 1.8 dB and return loss of 35 dB have been obtained in the desired passband. Moreover, the second harmonic $2f_0$ has been obtained at 5 GHz with an attenuation level of 16 dB. From Fig. 3.30(b) it has been observed that the transmission phase angle becomes linear as expected in the passband.

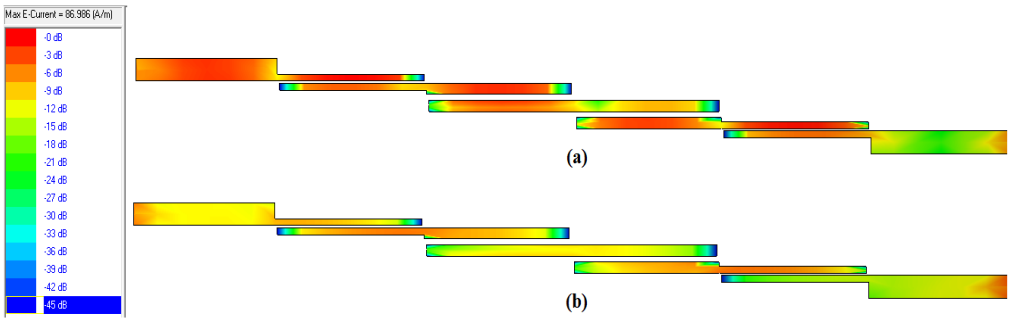

Fig. 3.31. Surface current distribution for third-order parallel-coupled microstrip line (PCML) bandpass filter (a) at f_0 = 2.5 GHz, and (b) at $2f_0$ = 5 GHz.

Fig. 3.31(a)-(b) highlight the surface current distribution for the third-order conventional PCML bandpass filter. It has been observed from Fig. 3.31(a) that the surface current has been distributed densely from the input port to the output port for f_0 = 2.5 GHz. However, large current has been distributed for $2f_0$ = 5 GHz also due to the presence of second harmonic. From these designs it has been revealed that although the passband frequency responses are pretty satisfactory for both the conventional filters, however, generation of

spurious harmonics limits their applications in the stopband. Moreover, the conventional filters occupy very large circuit area, restricting their applications in WLAN. Thus, the size reductions of such filters are utmost necessary which are explained in the next section with folded and inline PCMLBFs and subsequently different methods for harmonics suppression have been investigated.

3.11. Folding Mechanism of the Conventional First-Order PCMLBF

A unit PCML structure of width (w), gap (s) and length (l) with an open-end length correction of 'd' due to the fringing field effects is shown in Fig. 3.32(a). The structure is characterized by even- and odd-mode characteristic impedances Z_{0e}, Z_{0o} and electrical lengths of θ_e and θ_o respectively. The equivalent J-inverter diagram is shown in Fig. 3.32(b). For an open-circuit unit PCML cell, the equivalent Z_{11}, Z_{21} and S_{21} have been derived as [2]

$$Z_{11} = \frac{-j}{2}\left(\frac{Z_{0e}\cos\theta_e \sin\theta_o + Z_{0o}\cos\theta_o \sin\theta_e}{\sin\theta_e \sin\theta_o}\right) \tag{61}$$

$$Z_{21} = \frac{-j}{2}(Z_{0e}\csc\theta_e - Z_{0o}\csc\theta_o) = \frac{-j}{2}\left(\frac{Z_{0e}\sin\theta_o - Z_{0o}\sin\theta_e}{\sin\theta_e \sin\theta_o}\right) \tag{62}$$

$$S_{21} = \frac{2(Z_{0e}\sin\theta_o - Z_{0o}\sin\theta_e)Z_0}{\left[Z_{11}^2 + Z_{11}Z_0 + Z_0^2 - Z_{21}^2\right]*(\sin\theta_e \sin\theta_o)} \tag{63}$$

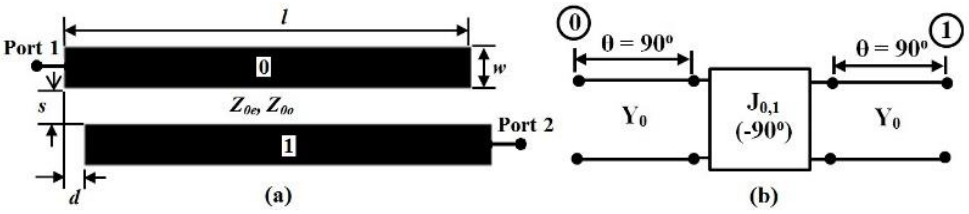

Fig. 3.32. Unit PCML cell: (a) layout, and (b) equivalent J-inverter diagram.

From (61) - (63) the transmission zeros of $|Z_{11}|$, $|Z_{21}|$ and $|S_{21}|$ have been obtained by the conditions

$$P = Z_{0e}\cos\theta_e \sin\theta_o + Z_{0o}\cos\theta_o \sin\theta_e = 0 \tag{64}$$

$$Q = Z_{0e}\sin\theta_o - Z_{0o}\sin\theta_e = 0 \tag{65}$$

and the attenuation poles for all above parameters have been obtained by the condition

$$R = \sin\theta_e \sin\theta_o = 0 \tag{66}$$

i.e., $\theta_e = \theta_o = m\pi$ where m is a positive integer. Fig. 3.33 shows the simulated $|S_{21}|$ (dB) and $|Z_{21}|$ (dB) plots for a unit PCML cell with a resonant frequency of 5.25 GHz. The transmission parameters for a unit PCML cell are obtained as

$$\begin{bmatrix} A_{i,i+1} & B_{i,i+1} \\ C_{i,i+1} & D_{i,i+1} \end{bmatrix} = \begin{bmatrix} \dfrac{P}{Q} & \dfrac{j(Q^2-P^2)}{2QR} \\ j\left(\dfrac{2R}{Q}\right) & \dfrac{P}{Q} \end{bmatrix} \tag{67}$$

where $i = 0$ and 1.

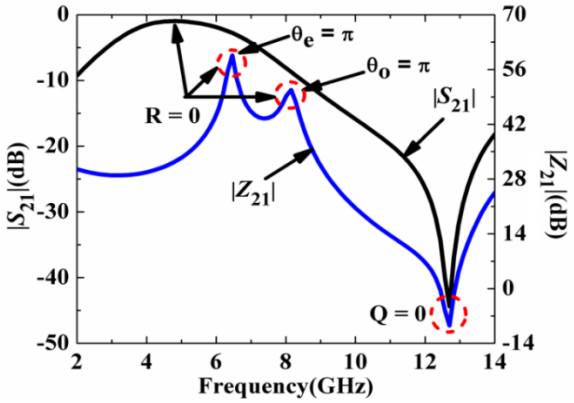

Fig. 3.33. Resonance characteristics of $|S_{21}|$(dB) and (b) $|Z_{21}|$ plots for a unit PCML cell with resonant frequency of 5.25 GHz.

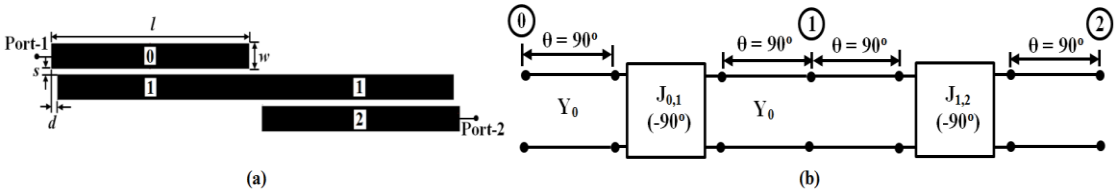

Fig. 3.34. Conventional first-order PCMLBF: (a) Layout and (b) equivalent *J*-inverter diagram.

Fig. 3.34(a) shows the layout of a first-order conventional PCMLBF and Fig. 3.34(b) shows its equivalent *J*-inverter diagram. The equivalent *ABCD* matrix for a first-order conventional PCMLBF is obtained by cascading PCML cells as

$$\begin{bmatrix} A_t & B_t \\ C_t & D_t \end{bmatrix} = \begin{bmatrix} A_{0,1} & B_{0,1} \\ C_{0,1} & D_{0,1} \end{bmatrix} \begin{bmatrix} A_{1,2} & B_{1,2} \\ C_{1,2} & D_{1,2} \end{bmatrix} = \begin{bmatrix} \dfrac{2P^2-Q^2}{Q^2} & \dfrac{jP(Q^2-P^2)}{Q^2R} \\ j\dfrac{4PR}{Q^2} & \dfrac{2P^2-Q^2}{Q^2} \end{bmatrix} \tag{68}$$

Accordingly, the *Z*-parameters of the first-order conventional PCMLBF is highlighted in (69) - (70).

$$Z_{11t} = Z_{22t} = -j\left(\frac{2P^2-Q^2}{4PR}\right) \tag{69}$$

$$Z_{12t} = Z_{21t} = -j\left(\frac{Q^2}{4PR}\right) \tag{70}$$

According to (70), the transmission zero of $|Z_{21t}|$ occurs when $Q = 0$, and the attenuation pole occurs when $P = 0$ or $R = 0$. Accordingly, the equivalent S_{21t} is obtained as

$$S_{21t} = -j\frac{Q^2}{\left(\frac{P}{2Z_0}\right)\left(Q^2 - P^2 + 4Z_0^2R^2\right)} \tag{71}$$

The transmission zero of $|S_{21t}|$ occurs when $Q = 0$, and the attenuation pole occurs when $P = 0$, as in a unit PCML cell, or $P^2 - Q^2 = 4Z_0^2R^2$. Fig. 3.35 shows simulated $|S_{21}|$ (dB) and $|Z_{21}|$ (dB) plots of first-order conventional PCMLBF centered at 5.25 GHz.

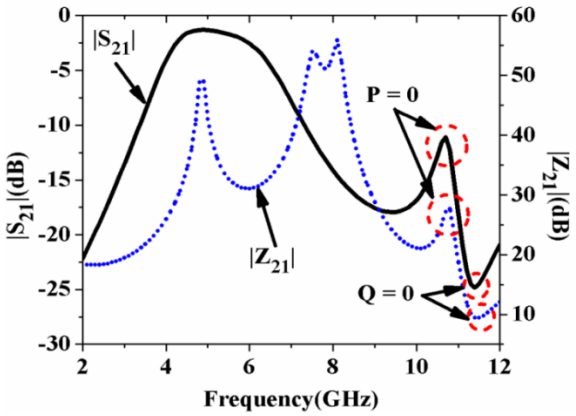

Fig. 3.35. Simulated $|S_{21}|$ (dB) and $|Z_{21}|$ (dB) plots of a first-order conventional PCMLBF (Filter-I).

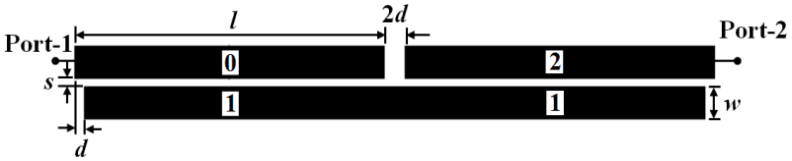

Fig. 3.36. Layout of the first-order folded PCMLBF.

The attenuation poles of $|S_{21}|$ and $|Z_{21}|$ have been observed for the condition $P = 0$ and the transmission zeros for the condition $Q = 0$ around the second harmonic. Subsequently, the design of traditional PCMLBF has been extended to obtain folded PCMLBF as shown in Fig. 3.36, in which the folding process has been carried out by cascading the third quarter-wavelength resonator of conventional PCMLBF (marked as 2) with the first quarter-wavelength resonator (marked as 0) in the transverse plane.

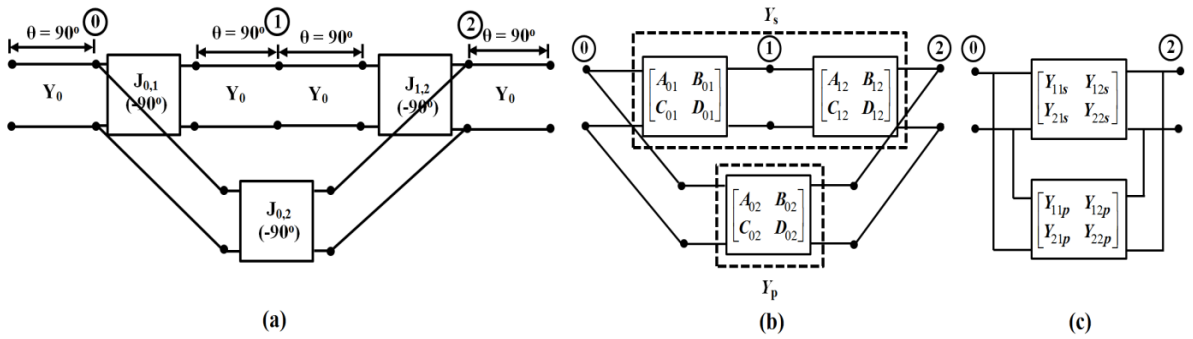

Fig. 3.37. First-order folded PCMLBF: (a) *J*-inverters equivalent diagram, (b) conversion to ABCD parameters, and (c) illustration of *Y*-parameters.

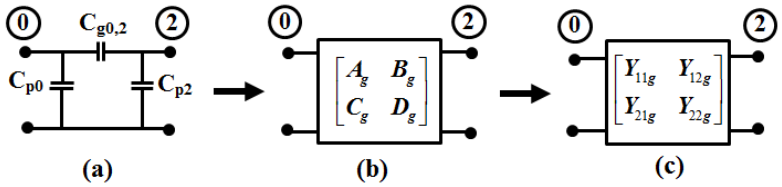

Fig. 3.38. Model of offset gap: (a) equivalent capacitive network, (b) ABCD, and (c) *Y*-parameter.

Accordingly, an offset gap of 2*d* has been created at the plane of symmetry between the in-line resonators, resulting in an additional capacitive coupling. Fig. 3.37(a) shows the equivalent *J*-inverter circuit of the folded PCMLBF, which includes an additional *J*-inverter ($J_{0,2}$) relative to the offset gap. Figure 3.37(b) depicts the transformation of the individual *J*-inverter section to an equivalent ABCD model. The subscript "s" represents series and "*p*" represents parallel paths. However, overall ABCD parameters can't be obtained directly as there has been a shunt network along with a cascading combination. Accordingly, *Y*-parameter transformation has been invoked to take into account the shunt component of *J*-inverter sections as in Fig. 3.37(c). The *J*-inverter ($J_{0,2}$) related to the offset gap has been replaced by the equivalent capacitive π-network as shown in Fig. 3.38, in which $C_{g0,2}$ represents the end-coupling capacitance between the in-line resonators 0 and 2, and C_{p0} and C_{p2} are the equivalent parallel-coupling capacitances between the resonators 0 and 2 and the ground plane of the microstrip structure, respectively. Thus, the equivalent *Y*-parameters of the microstrip gap are obtained by transformation as shown in (72) and (73).

$$Y_{11g} = Y_{22g} = j(B_p + B_g) \tag{72}$$

$$Y_{12g} = Y_{21g} = -jB_g \tag{73}$$

where, $B_p = \omega C_{p0} = \omega C_{p2}$ and $B_g = \omega C_{g0,2}$ with ω is the frequency of operation.

The equivalent *Y*-parameters of the series combination between resonator 0 and 2 are obtained by

$$Y_{11s} = Y_{22s} = -j\frac{(2P^2 - Q^2)R}{P(Q^2 - P^2)} \tag{74}$$

$$Y_{12t} = Y_{21t} = -j\frac{Q^2 R}{P(P^2 - Q^2)} \tag{75}$$

Accordingly, the overall equivalent *Y*-parameters of the first-order folded PCMLBF has been presented in (76) and (77).

$$Y_{11}^{'} = Y_{22}^{'} = -j\left[\frac{(2P^2 - Q^2)R}{P(Q^2 - P^2)} - (B_g + B_p)\right] \tag{76}$$

$$Y_{12}^{'} = Y_{21}^{'} = -j\left[\frac{Q^2 R}{P(P^2 - Q^2)} + B_g\right] \tag{77}$$

The equivalent $Z_{21}^{'}$ parameter of the folded filter has been obtained as

$$Z_{21}^{'} = Z_{12}^{'} = j\left[\frac{Q^2 R + P(P^2 - Q^2)B_g}{P(P^2 - Q^2)\Delta Y^{'}}\right] \tag{78}$$

where,

$$\Delta Y^{'} = Y_{11}^{'}Y_{22}^{'} - Y_{12}^{'}Y_{21}^{'} \tag{79}$$

From (78) it has been observed that the transmission zero of $|Z_{21}^{'}|$ has been obtained by the condition

$$Q^2 = -\frac{P(P^2 - Q^2)B_g}{R} \tag{80}$$

Furthermore, it has been observed that the condition of first-order conventional PCMLBF has been re-established with a zero offset gap, which exhibits $B_g = 0$ and subsequently $Q = 0$. The attenuation pole of first-order folded PCMLBF occurs for either $P = 0$ or $P^2 = Q^2$. Finally, the expression of S_{21} has been formulated as

$$S_{21}^{'} = j\frac{\left[2Q^2 RY_0 + 2B_g Y_0 P(P^2 - Q^2)\right]}{P(P^2 - Q^2)A} \tag{81}$$

where,

$$A = (Y_0 + Y_{11}^{'})^2 - (Y_{12}^{'})^2 \tag{82}$$

From (81) it has been observed that the transmission zero of $S_{21}^{'}$ is occurred at

$$2Q^2 RY_0 + 2B_g Y_0 P(P^2 - Q^2) = 0 \tag{83}$$

It can be noticed that (83) justifies (80). Further, it has been observed that the transmission zero of $S_{21}{}'$ is taken place for $Q = 0$. Accordingly, from (65) it has been obtained as

$$Z_{0e}\sin\theta_o = Z_{0o}\sin\theta_e \tag{84}$$

Moreover, the condition for attenuation pole to occur for S_{21}' is $P = 0$, hence from (64) it has been obtained as

$$\begin{aligned} &Z_{0e}\cos\theta_e\sin\theta_o + Z_{0o}\cos\theta_o\sin\theta_e = 0 \\ &\cos\theta_e = -\cos\theta_o = \cos(n\pi - \theta_o) \\ &\theta_e = n\pi - \theta_o \end{aligned} \tag{85}$$

For the second harmonic, n =1 and $\theta_e = \pi - \theta_o$. Substituting this condition in (84), the condition for harmonic suppression has been obtained as $P = Q = 0$ i.e., $Z_{0e} = Z_{0o}$. Fig. 3.39(a) depicts the simulated $|S_{21}|$ plots for a first-order folded filter, indicating the transmission zero and attenuation pole condition. Fig. 3.39(b) shows the comparison of S-parameters between the first-order conventional and folded PCMLBFs centered at 5.25 GHz with dimensions: l = 7.929 mm, s = 0.2 mm, w = 0.8 mm, d = 0.264 mm. However, the central offset-gap length (d) has incremented to 0.528 mm due to the folding mechanism. It has been observed that the improvement in the skirt characteristics has been overshadowed by the degradation of the second harmonic level in the folded configuration. Accordingly, the variation in in-line gap length (s) on the transmission characteristics of the filter has been investigated at 5.25 GHz for different transverse coupling gaps as highlighted in Fig. 3.40(a). It has been observed from Fig. 3.40(a) that the insertion loss at the upper stopband edge frequency has been increased non-linearly with the incremental offset gap ($2d$).

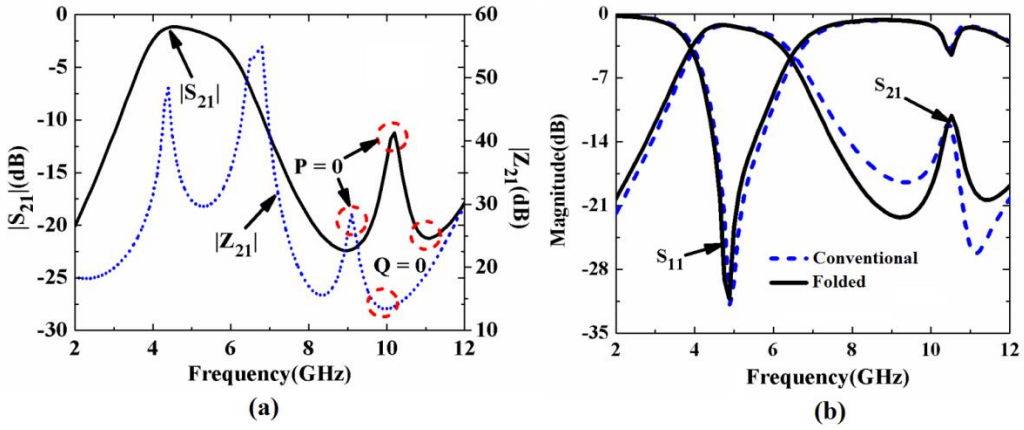

Fig. 3.39 (a) Simulated $|S_{21}|$(dB) and $|Z_{21}|$(dB) plots of an first-order folded PCMLBF, and (b) comparison of S-parameters of first-order conventional vs. folded PCMLBF.

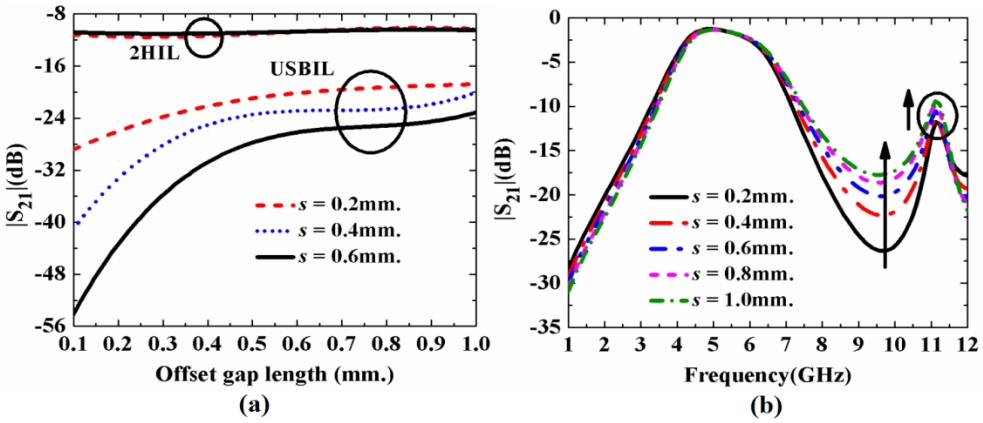

Fig. 3.40 Study of incremental offset gap length (mm.) on (a) upper stopband insertion loss (*USBIL*) and second harmonic insertion loss (2*HIL*), and (b) variation of $|S_{21}|$(dB) for different longitudinal coupling gap (*s*) with constant offset gap length of 0.528 mm.

However, the variation of offset-gap length (*d*) has little effect on second harmonic insertion loss. As a result, Fig. 3.40(b) depicts the variation of $|S_{21}|$ (dB) for various longitudinal coupling gaps (*s*) with a constant offset gap length of 0.528 mm. By following the transmission line theory and conversion procedure [1] the equivalent lumped-elements circuit diagram of the first-order folded PCMLBF has been obtained as shown in Fig. 3.41, in which the offset gap 2*d* has been represented by the equivalent gap capacitive π-network. In Fig. 3.41, $C_{g0,2}$ represents the end-coupling capacitance between the in-line resonators 0 and 2. Moreover, C_{p0} and C_{p2} are the equivalent parallel-coupling capacitances between each of the in-line resonators 0 and 2 and the ground plane of the microstrip structure, respectively.

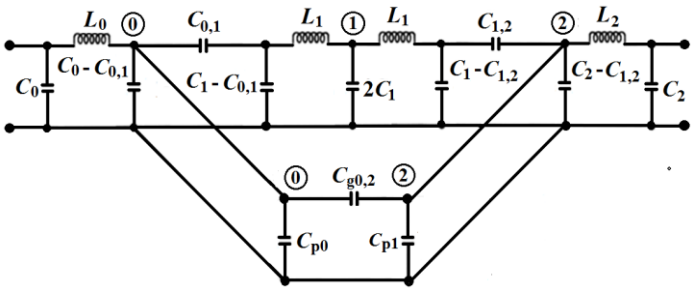

Fig. 3.41. Equivalent lumped-elements circuit diagram of a first-order folded PCMLBF.

In order to investigate the effects of the incremental variation of the microstrip offset gap 2*d* on the equivalent gap capacitances, the layout diagram of the in-line resonators has been depicted in Fig. 3.42(a). Accordingly, the interactions among the open-end fringe field lines have been illustrated in Fig. 3.42(b).

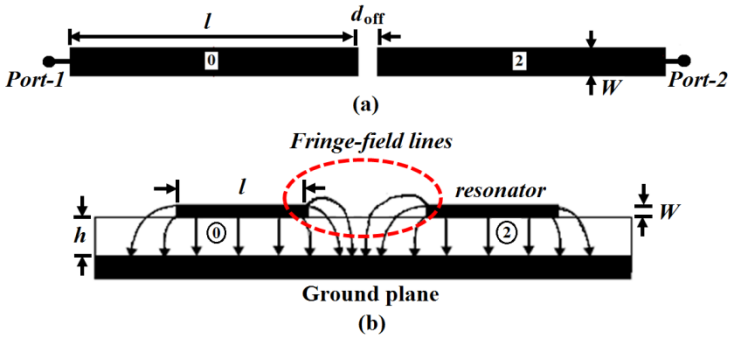

Fig. 3.42. (a) Layout of a pair of in-line microstrip lines, and (b) distribution of open-ends fringe field lines.

The equivalent *Y*-parameters of the said two-port network is expressed as

$$[Y] = \begin{bmatrix} Y_{11} & Y_{12} \\ Y_{21} & Y_{22} \end{bmatrix} \tag{86}$$

The capacitances C_g and C_p are determined based on a narrow-band basis as [1]

$$C_g = -\frac{\mathrm{Im}(Y_{21})}{\omega_0} \tag{87}$$

$$C_p = \frac{\mathrm{Im}(Y_{11} + Y_{21})}{\omega_0} \tag{88}$$

where ω_0 is the angular velocity (rad/sec) at the center frequency f_0. Accordingly, a simulation study has been carried out for the incremental offset gap, d (mm), and the variations of C_g (pF) and C_p (pF) have been depicted in Fig. 3.43.

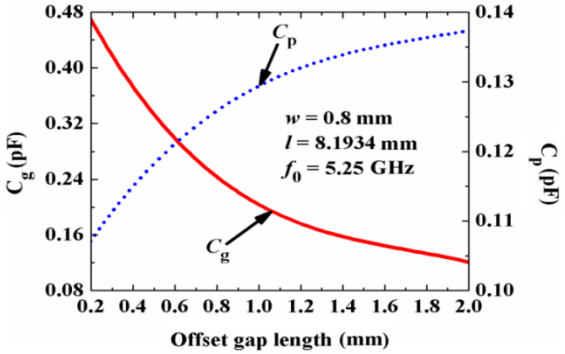

Fig. 3.43. Variation of C_g and C_p (pF) with incremental offset gap, d_{off} (mm).

It has been noticed that the value of C_g has decreased nonlinearly compared to the incremental slope of C_p with the incremental values of d_{off}. This is due to the fact that the interaction between the open-ends fringe-field lines gradually decreases (Fig. 3.42(b)), and accordingly, the coupling between the open-ends of the in-line resonators has been decreased

with the incremental values of d_{off}. Fig. 3.44 compares the EM-simulated and the circuit simulated $|S_{21}|$ (dB) plots of the first-order folded PCMLBF for Filter-I. The lumped element values are calculated by following the transmission line theory [1] and optimized at f_0 = 5.25 GHz. Accordingly, L_0 = 1.724 nH, C_0 = 0.1475 pF, $C_{0,1}$ = 0.2552 pF, $C_{g0,2}$ = 0.0433 pF, $C_{p0,2}$ = 0.0118 pF, Z_0 = 50 Ohm are the final values of the lumped elements. The plots are closely matched in the passband with some mismatches at $2f_0$. Various issues like infinite ground plane for EM simulation, tolerances due to the microstrip open-ends, gaps and bends, and finite conductor loss are the main reasons for such mismatches. The surface current distributions for a first-order folded PCMLBF at f_0 = 5.25 GHz and $2f_0$ = 10.5 GHz are shown in Fig. 3.45(a)-(b).

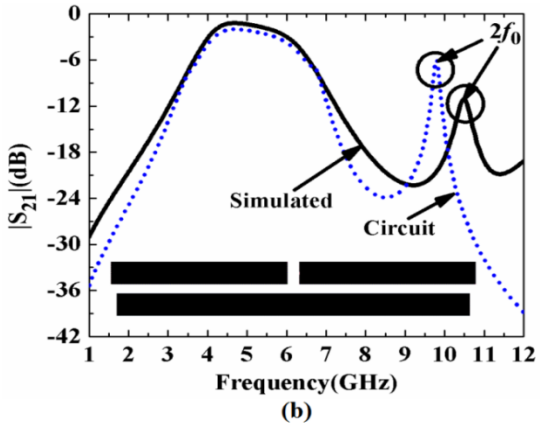

Fig. 3.44. Comparison of $|S_{21}|$ (dB) plots between the simulated and equivalent lumped elements circuit of first-order folded PCMLBF with f_0 = 5.25 GHz.

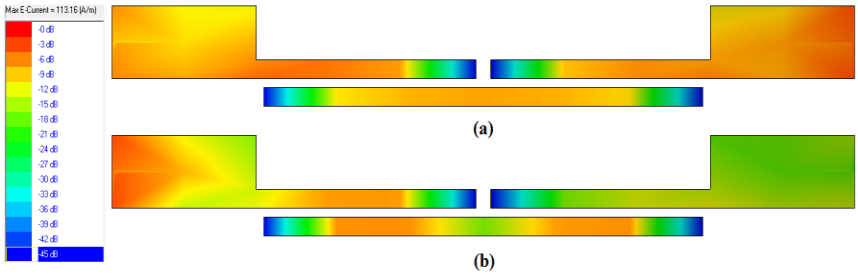

Fig. 3.45. Surface current distribution for first-order PCMLBF: (a) at f_0 = 5.25 GHz, and (b) at $2f_0$ = 10.5 GHz.

It has been observed that the surface current reaches the output port at a large strength at f_0 compared to that at $2f_0$ due to the lower value of attenuation level at $2f_0$. Finally, it can be concluded that the first-order folded filter achieves a size reduction of 35.71% over the conventional filter along with the improvement of passband skirt characteristics. It justifies

the effectiveness of the folding mechanism, which has been extended further for the fourth-order conventional PCMLBF as discussed in the next section.

3.12. Design of Third-Order Folded PCMLBF

By following the same procedure discussed in the previous section, the third-order folded PCMLBF centered at 5.25 GHz has been designed. Fig. 3.46 shows its optimized layout with all dimensions measured in mm. The overall size of the filter is 41.43 mm × 6.7 mm, i.e., 277.58 mm^2 or 1.33λ_g × 0.22λ_g where λ_g is the guided wavelength at f_0 = 5.25 GHz. A significant size reduction of 58% has been achieved over the third-order conventional filter (Fig. 3.26). Fig. 3.47(a) compares the simulated *S*-parameters between these filters. It has been observed that the folded filter exhibits a significant improvement in the upper stopband edge rejection level over the conventional filter. However, the stopband rejection level has been increased to 20 dB due to the folding structure. The variation of simulated $|S_{11}|$ (dB) plots for the folded filter compared to the conventional filter is shown in Fig. 3.47(b), and the maximum return loss in the passband becomes 18 dB for the folded filter, satisfying the specifications.

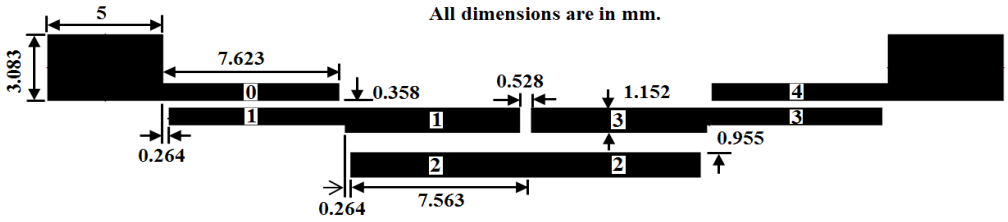

Fig. 3.46. Layout of the third-order folded PCMLBF centered at 5.25 GHz.

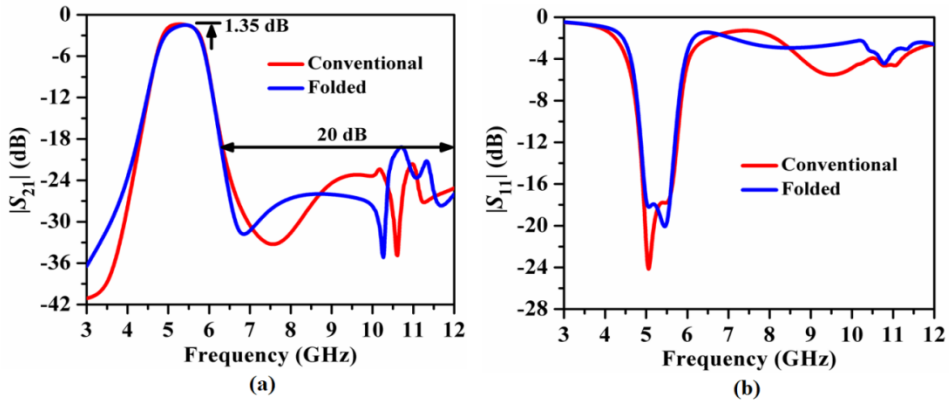

Fig. 3.47. *S*-parameters comparison of conventional and folded filters: (a) $|S_{21}|$ (dB), and (b) $|S_{11}|$ (dB).

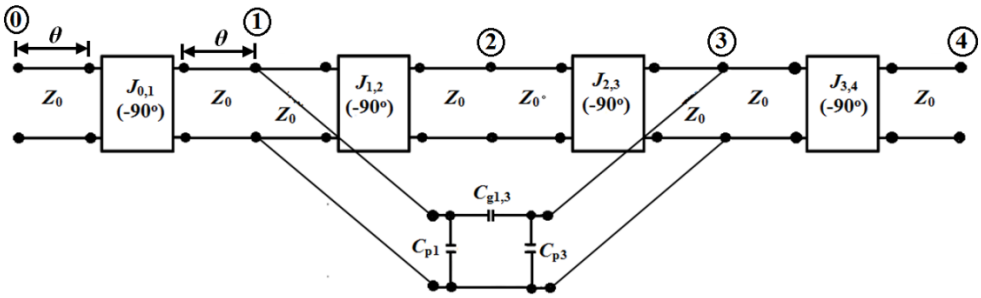

Fig. 3.48. Equivalent *J*-inverter circuit diagram of the third-order folded PCMLBF.

Accordingly, Fig. 3.48 depicts the equivalent *J*-inverter circuit diagram of the folded filter. The $|S_{21}|$ (dB) plots of the simulated and extracted equivalent lumped elements circuit of third-order folded PCMLBF are shown in Fig. 3.49. All the values of the lumped elements have been computed by following the conventional transmission line theory [1] and tuned at f_0. The plots are in close agreement with each other in the passband except for some mismatches at $2f_0$ due to the tolerances mentioned in the previous section (Fig. 3.44).

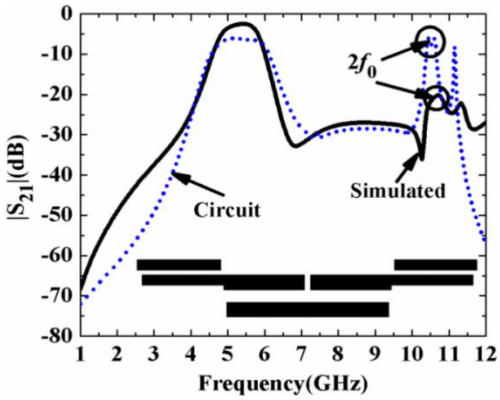

Fig. 3.49. Comparison of $|S_{21}|$ (dB) plots between the simulated and equivalent lumped elements circuit of third-order folded PCMLBF with f_0 = 5.25 GHz.

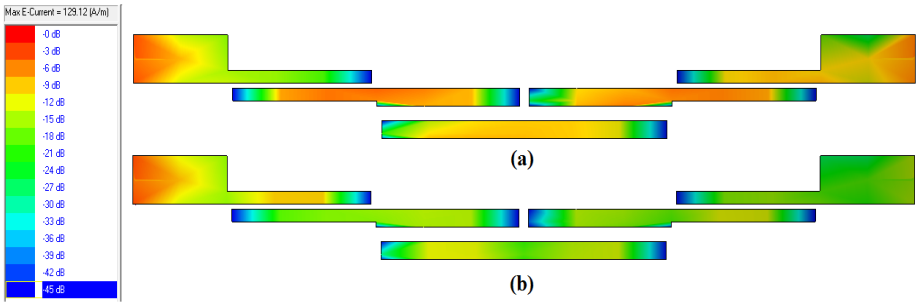

Fig. 3.50. Surface current distribution for the third-order folded PCMLBF at (a) f_0 = 5.25 GHz, and (b) $2f_0$ = 10.5 GHz.

Figs. 3.50(a)-(b) show the surface current distribution for a third-order folded filter with f_0 = 5.25 GHz and $2f_0$ = 10.5 GHz, respectively. It has been observed that the current reaches the output port at a large strength for the passband but slightly less strength at $2f_0$ due to the stopband response. As expected, the current distributions are minimum at the open ends of the couple-lines in both cases.

By following the same procedure, the third-order folded PCMLBF-II centered at 2.5 GHz with specifications as listed in Table 3.5, has been designed and Fig. 3.51 shows its layout with optimized dimensions. The overall size of the filter is 98.58 mm × 7.3 mm i.e., 720.92 mm^2 or 1.44λ_g × 0.11λ_g where λ_g is the guided wavelength at f_0 = 2.5 GHz. A size reduction of 44.17% has been achieved over the conventional filter with the same specifications (Fig. 3.29). Figs. 3.52(a) and (b) compare the simulated *S*-parameters between these two filters. It has been observed from Fig. 3.52(a) that the folded filter exhibits improved skirt characteristics over the conventional filter along with a stopband attenuation level of 17 dB up to 2.8f_0 due to the presence of the second harmonic. However, the return loss (Fig. 3.52(b)) has been decreased for the folded filter below 23 dB compared to the conventional filter.

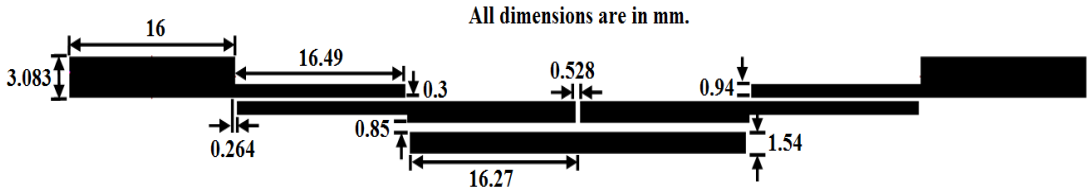

Fig. 3.51. Layout of the third-order folded PCMLBF centered at 2.5 GHz.

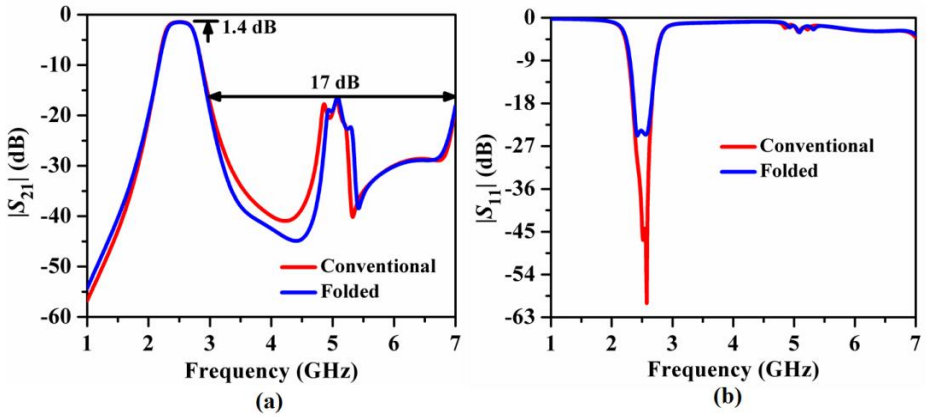

Fig. 3.52. *S*-parameters comparison between the third-order conventional and folded filters: (a) $|S_{21}|$ (dB), and (b) $|S_{11}|$ (dB).

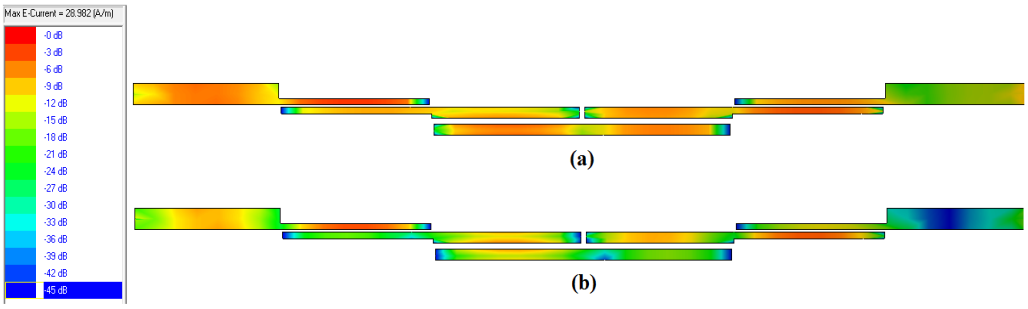

Fig. 3.53. Surface current distribution for the third-order folded PCMLBF: (a) at f_0 = 2.5 GHz, and (b) at $2f_0$ = 5 GHz.

As a result, Figs. 3.53(a)-(b) illustrate the corresponding surface current at f_0 = 2.5 GHz and $2f_0$ = 5 GHz respectively. It has been observed that the current distribution is the highest for the passband, and less in strength at $2f_0$ due to the stopband response. The sizes of the folded filters discussed in this section can be further reduced by modifying their structures to in-line filters as discussed in the next section.

3.13. Design of Third-Order Inline PCMLBF

In this approach, the parallel-coupled line sections of the conventional filter structure centered at 5.25 GHz have been placed alternatively like a zigzag in a single longitudinal plane, resulting in an inline structure as shown in Fig. 3.54. The overall size of the filter is 49.31 mm × 4.63 mm, i.e., 228.31 mm^2 or $1.41\lambda_g \times 0.13\lambda_g$ where λ_g is the guided wavelength at f_0 = 5.25 GHz. Accordingly, size reductions of 65.42% over the conventional filter and 17.75% over the folded filter with the same specifications have been achieved. However, compared to the folded filter structure, three distinct offset gaps of 0.528 mm each have been created in the inline filter. As a result, three additional cross-coupling regions were created along the structure, which has a significant impact on the filter's *S*-parameter responses. The simulated $|S_{21}|$ (dB) plots of the conventional, folded, and inline filters are shown in Fig. 3.55(a). It has been observed that the skirt characteristics have been greatly improved for the inline filter over the folded filter.

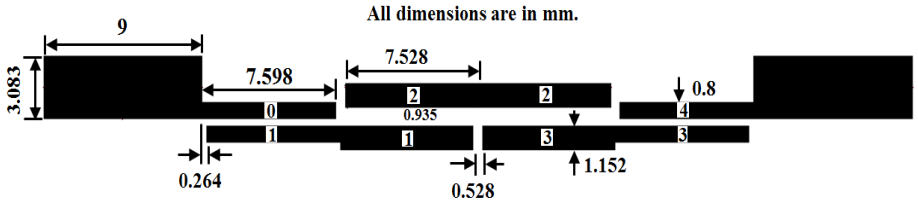

Fig. 3.54. Layout of third-order inline PCMLBF centered at f_0 = 5.25 GHz.

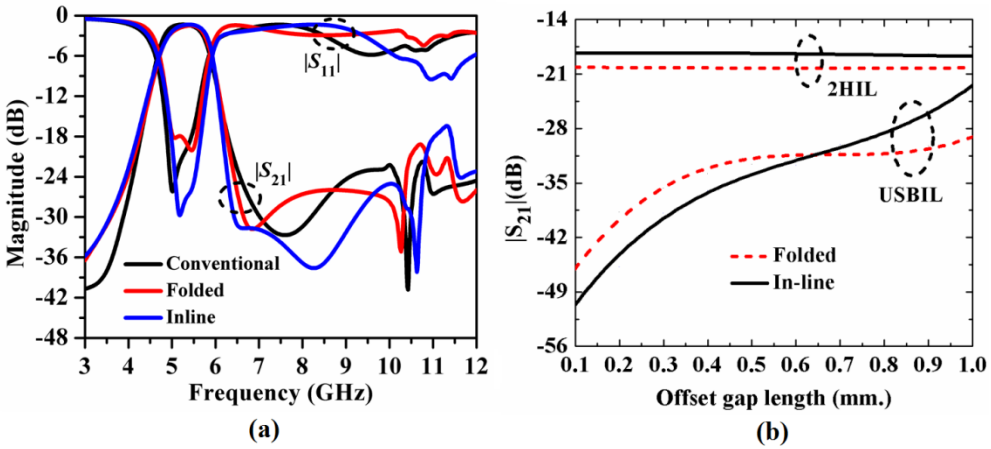

Fig. 3.55. (a) Comparison of *S*-parameters of third-order conventional, folded and inline filters, and (b) study of variation of offset gap length on *USBIL* and 2*HIL*.

However, the attenuation level at $2f_0$ has been increased by 9 dB compared to the folded filter due to the introduction of three offset gaps of dimension 0.528 mm for the inline structure. Accordingly, Fig. 3.55(b) compares the variation of the attenuation levels at the upper stopband edge frequency, i.e., *USBIL*, and at $2f_0$, i.e., 2*HIL*, with the incremental offset gap length (mm) for both the folded and inline filters. It has been observed that in comparison to the folding structure, the in-line structure poses a higher dynamic variation of *USBIL* subject to three distinct offset gaps. The equivalent *J*-inverter circuit of the inline structure has been depicted in Fig. 3.56, including the capacitive couplings corresponding to the offset gaps.

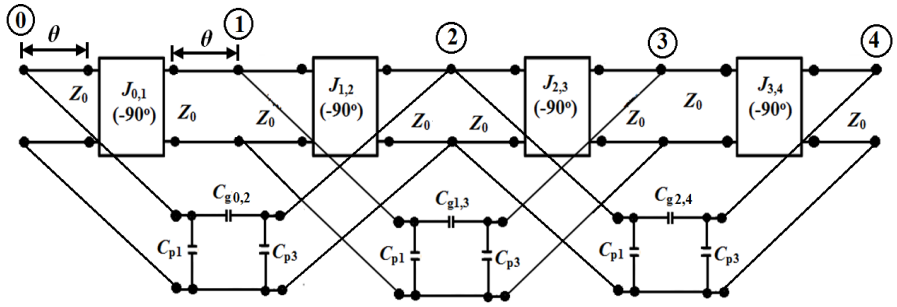

Fig. 3.56. Equivalent *J*-inverters circuit of the third-order inline filter.

Fig. 3.57 compares the $|S_{21}|$ plots between the EM-simulation and the circuit simulation of the third-order inline PCMLBF. The lumped element values have been computed by following the transmission line theory like the folded PCMLBF [1]. Due to some tolerances between the circuit simulation and the EM-simulation, there is some mismatch between the two plots, especially at $2f_0$.

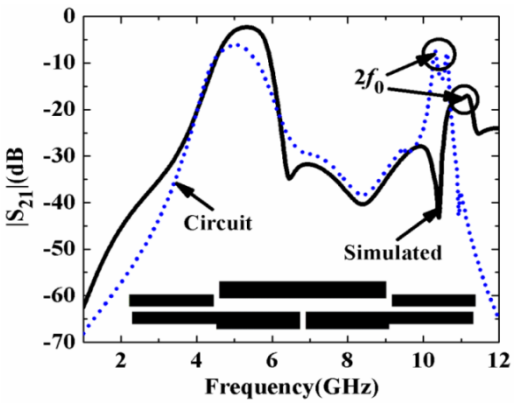

Fig. 3.57. Comparison of $|S_{21}|$ plots between the simulated and equivalent lumped elements circuit of the third-order inline PCMLBF (Filter-I).

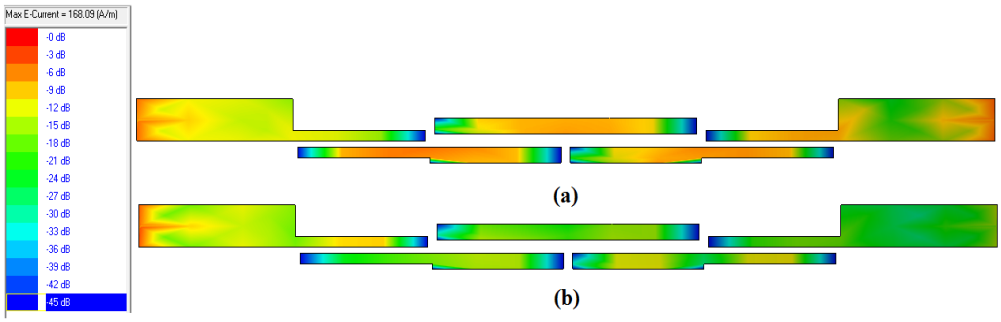

Fig. 3.58. Surface current distribution for the third-order inline PCMLBF (a) at f_0 = 5.25 GHz, and (b) at $2f_0$ = 10.5 GHz.

Figs. 3.58(a)-(b) illustrate the corresponding surface current at f_0=5.25 GHz and $2f_0$ = 10.5 GHz respectively. It has been noticed that due to the presence of the second harmonic frequency with large attenuation loss, the current distribution is of large strength at f_0 as expected and of moderate strength at $2f_0$. By following the same methodology, the third-order inline PCMLBF-II centered at 2.5 GHz with the specifications listed in Table 3.9 has been designed, and its layout with optimized dimensions is shown in Fig. 3.59. The overall size of the filter is 98.58 mm × 4.92 mm, i.e., 485.01 mm^2 or 1.44λ_g × 0.07λ_g where λ_g is the guided wavelength at f_0 = 2.5 GHz. A size reduction of 62.44% has been achieved over the conventional filter (Fig. 3.29) and 32.72% over the folded filter with the same specifications (Fig. 3.51).

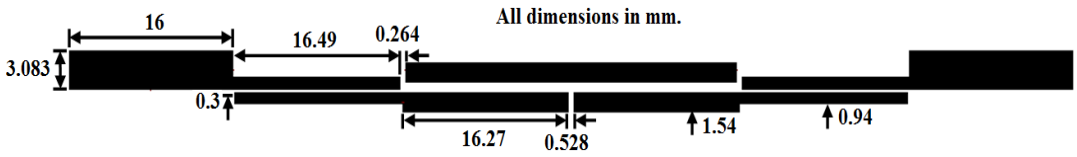

Fig. 3.59. Layout of third-order inline PCMLBF centered at f_0 = 2.5 GHz.

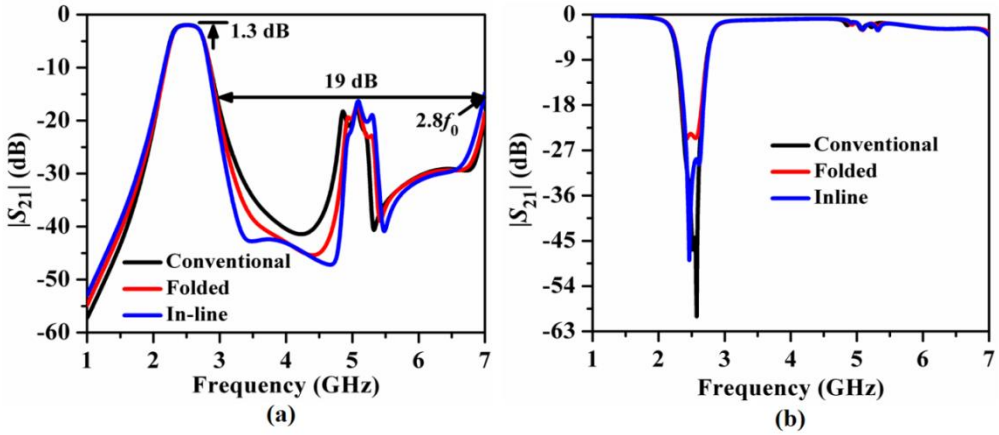

Fig. 3.60. *S*-parameters comparison of the third-order conventional, folded and inline filters centered at 2.5 GHz: (a) $|S_{21}|$ (dB), and (b) $|S_{11}|$ (dB).

Accordingly, Figs. 3.60(a)-(b) compare the simulated S-parameters between these two filters. It has been observed from Fig. 3.60(a) that the inline filter exhibits improved skirt characteristics over the folded filter along with the stopband attenuation level of 19 dB up to $2.8f_0$ due to the presence of the second harmonic. Moreover, the return loss (Fig. 3.60(b)) has been increased for the inline filter to below 30 dB compared to the folded filter. The reason for such improvements in the skirt characteristics and the return loss for the inline filter are three offset gaps compared to one offset gap for the folded filter. This justifies the effectiveness of the inline filter over the folded filter.

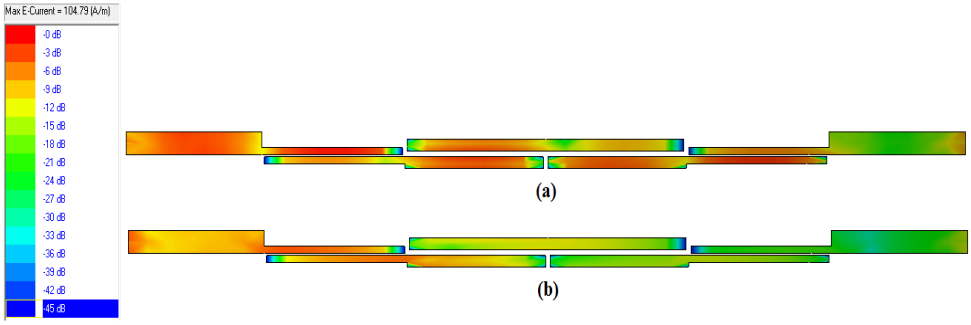

Fig. 3.61. Surface current distribution for the third-order inline PCMLBF (a) at f_0 = 2.5 GHz, and (b) at $2f_0$ = 5 GHz.

Fig. 3.61(a)-(b) illustrate the corresponding surface current distributions at f_0 = 2.5 GHz and $2f_0$ = 5 GHz respectively. The surface current propagates with large strength at the center frequency (f_0) and comparatively less strength at the second harmonic frequency ($2f_0$) as expected. Table 3.11 lists all the parameters characterizing the filters such as ξ = skirt factor, *SBRL* = stopband rejection level, *SBW* = stopband bandwidth as a multiple of f_0,

RSB = relative stopband frequency, *SF* = suppression factor, *NCS* = normalized circuit size, *AF* = architecture factor, and *FOM* = figure-of-merit, already defined in section 3.9. It has been noticed from Table 3.15 that the value of *NCS* is minimum and *FOM* is maximum for the inline filters. It can be concluded that the folded and inline filters have exhibited significant size reductions and improvements in the skirt characteristics compared to the conventional PCMLBF with the same specifications. However, the stopband rejection level is restricted to only 16 dB due to the presence of spurious harmonics. Subsequently, the studies of harmonic suppression by employing different non-uniform perturbations in the folded and inline filters have been carried out in the next section.

Table 3.11. Comparison of all designed bandpass filters.

Type of filter	f_o (GHz)	ξ (dB/GHz)	*SBRL* (dB)	*SBW* (x f_0)	*RSB*	*SF*	*NCS*	*AF*	*FOM*
Conventional	5.25 GHz	21.12	22	2.76	0.744	2.2	1.025	1	33.73
Folded		40.17	20	2.41	0.405	2.1	0.226		151.17
Inline		35.80	17	2.80	0.762	1.7	0.181		256.22
Conventional	2.5 GHz	43.70	18	2.79	0.787	1.8	0.277		223.49
Folded		52.29	17	2.84	0.811	1.7	0.155		465.11
Inline		63.65	16	2.82	0.807	1.6	0.104		790.24

3.14. Harmonic Suppression for PCMLBF

In general, harmonics are generated for a parallel-coupled line filter due to the imbalance between the odd-mode and even-mode phase velocities. The odd-mode phase velocity is much higher than that of the even-mode due to the lower value of the phase constant. Moreover, the odd-mode is excited around the coupled regions between the two parallel-coupled lines and the even-mode is excited along the outer edges of the coupled-lines. So, the objective is to make the two phase velocities close to each other to reduce harmonics. Conventionally, this can be achieved in two ways: by balancing the phase velocities of the two modes or by compensating for the different electrical lengths of both modes by modifying the line shape. There are various methods investigated by the researchers to lower the rejection level of these harmonics, such that:

(1) By cascading a lowpass filter or a notch filter with the bandpass filter [7]. However, the overall size of the RF module in the communication system will be increased

along with the introduction of additional insertion loss. Hence, such a method is not preferable.

(2) By providing over-coupled end stages for the coupled lines [8] to extend the phase length of the odd-mode for the compensation of the phase velocity imbalance. However, the size of the filter increases due to the over-coupling structure, and numerous tuning steps are to be followed to achieve a satisfactory harmonic suppression level.

(3) By introducing various reactive lumped elements like capacitors [9] and inductors [10] to achieve the phase velocity compensation. However, additional fabrication steps are required for soldering of the lumped elements on the microstrip board, which increases the design complexity and creates chances of signal leakage.

(4) By etching the ground plane with different reactive components such as photonic band gaps (PBG) [11], electromagnetic bandgap resonators (EBG) [12] and defected ground structure (DGS) [13]. However, the physical and electrical parameters of the coupled line are to be recalculated for each optimization step, increasing the design complexity. Moreover, additional care has to be taken for the separation of the patterned ground plane from other components of the system. It also increases the fabrication complexity as the ground plane is to be patterned separately, and there may be high chance of the generation of leaky waves due to the discontinuities in the ground plane.

(5) By perturbing the coupled lines with various fractal geometries to utilize their space filling and self-similarity properties, such as the rectangular Koch fractal [14], triangular Koch fractal [15], and quasi-Minkowski fractal [16]. This method greatly reduces the filter size along with the reduction of the suppression level of the spurious harmonics. However, the design and fabrication complexity generally increase as the iteration order of the fractals is increased.

(6) By modifying the width of the coupled lines with continuous sinusoidal shaped wiggly-lines [17]. However, the tuning of the sinusoidal shape of the wiggly-lines becomes difficult. Thus, asymmetrical rectangular perturbations are the alternative structures to suppress the harmonics [18]. These structures are easy to implement and the design complexity is reduced greatly.

(7) By introducing a stepped-impedance resonator (SIR) and tuning the phase length of the even- and odd-modes [19]. However, the recalculation of the electrical lengths for the modes is required in this method.

(8) By incorporating different nonuniform periodic structures like square grooves [20], triangular grooves [21] and interdigital corrugations [22]. In these methods, the odd-mode phase velocities have been reduced by increasing their electrical length, and those of the even-mode have been kept almost unaltered.

3.14.1. Study of Periodic Square Grooves for a Pair of PCML Unit Cell

Of the various methods mentioned above, the simplest method of harmonic suppression is the introduction of periodic grooves [20-21] as the recalculation of the electrical lengths for the even- and odd-modes is not required. In general, in this method, the defects are employed mostly along the coupled edges to slow down the phase velocity of the odd-mode EM wave propagation, affecting that of the even-mode poorly. Out of the various microstrip defects, periodic grooves of regular shapes such as square, rectangular, sawtooth, and quarter-elliptical, etc. are the simplest and easiest to incorporate into the coupled-line structure. In general, the periodic grooves are employed in the coupled regions of the pair of PCML to achieve the Bragg reflection at the second harmonic frequency of $2f_c$ [23]. The Bragg's law of reflection states that when an X-ray is incident onto a crystal surface, its' angle of incidence (θ) will reflect with the same angle of scattering (θ). When the path difference d is equal to a whole number n of the wavelength (λ), constructive interference will occur because the two waves are superimposed with an equal phase angle [24].

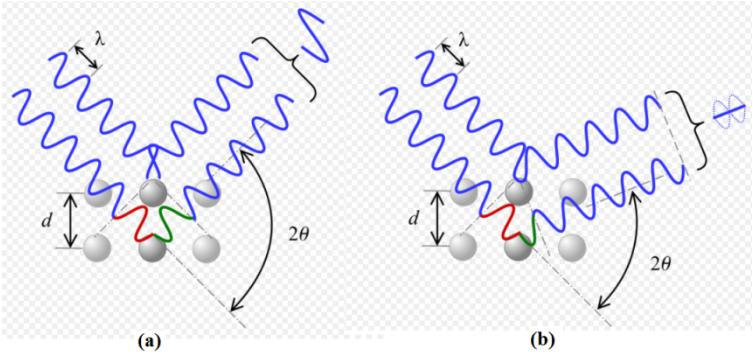

Fig. 3.62. Bragg's reflection: (a) constructive Interference, (b) destructive Interference.

Otherwise, destructive interferences take place between the waves due to their superposition with the opposite phase angle. Figs. 3.62(a)-(b) show examples of this phenomenon. This

feature of Bragg's reflection can be utilized efficiently for the PCML cell pair to achieve phase compensation by employing the slow-wave grooves periodically in the coupled region. As a result, the attenuation level at $2f_0$ can be greatly suppressed. In general, if the wave number of the TEM mode propagating along the horizontal direction from the input port to the output port is *k*, then the condition for Bragg reflection is given by

$$n\lambda = 2d\sin\theta \tag{89.a}$$

$$2D = n\lambda_g \tag{89.b}$$

$$k = \frac{2\pi}{\lambda_g} \tag{89.c}$$

$$2kD = 2\pi n \tag{89.d}$$

In (89.b), *D* is the period of perturbation or beat wavelength [24] and *n* is an integer (1,2,..). If the desired center frequency is f_0 and the guided wavelength is λ_g, then the condition for the generation of Bragg reflection at $2f_0$ is given as

$$\frac{8\pi D}{\lambda_g} = 2\pi \qquad \text{for } n = 1 \tag{90}$$

Thus, the value of *D* is obtained as $\lambda_g/4$. As the building blocks of the parallel coupled-line filter are the quarter-wavelength lines, a single quarter-wavelength microstrip resonator with a single square groove placed at the middle has been depicted in Fig. 3.63.

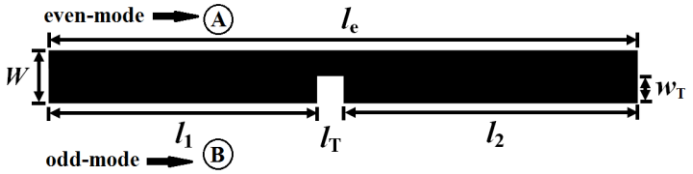

Fig. 3.63. Layout of a single resonator with a single square groove at the middle.

Here, l_e = even-mode physical length, l_T = length of the groove, w_T = width of the groove, *W* = width of the resonator. For a square groove, $l_T = w_T$ and the effective odd-mode physical length l_o is obtained as

$$l_o = l_1 + l_2 + l_T + 2w_T \tag{91}$$

Clearly, as l_o is greater than l_e, the wave slows down while travelling along the odd-mode edge of the resonator (as marked by A) compared to that of the even-mode propagating edge (as marked by B). As the number of grooves increases, the slowing-down phenomenon has also increased, resulting in more phase compensation.

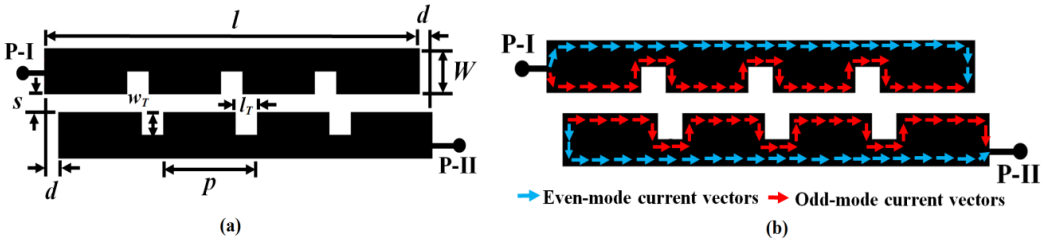

Fig. 3.64. (a) Layout of a pair of unit PCML cell with three square periodic grooves, (b) slowdown phenomenon of the wave vectors along the coupled region.

Fig. 3.64(a) shows the layout of a unit PCML cell with three square grooves at the middle, and Fig. 3.64(b) illustrates the slow-down phenomenon of the wave vectors along the coupled regions. Figs. 3.65(a)-(b) show the resonance characteristics of $|S_{21}|$ (dB) and $|Z_{21}|$ (dB) for a pair of unit PCML cells with a single square groove in the middle of the coupled-lines with $w_T = l_T = W/2$.The second harmonic transmission zero of $|S_{21}|$ (highlighted as $Q = 0$) has been shifted to a lower frequency (highlighted as $Q' = 0$) due to the increment of the odd-mode electrical length, as shown in Fig. 3.65(a)..

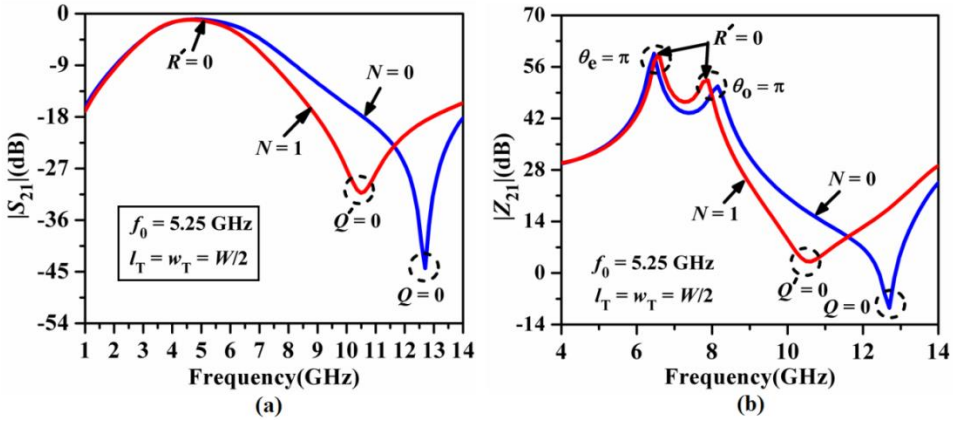

Fig. 3.65. Simulated resonance characteristics of (a) $|S_{21}|$ (dB), and (b) $|Z_{21}|$ (dB) for a unit PCML cell with a single square- groove with $l_T = h_T = W/2$ and $f_0 = 5.25$ GHz.

As a result, the attenuation pole of $|Z_{21}|$ due to $R' = 0$ and $\theta_o = \pi$ shifts more than that due to $\theta_e = \pi$, as shown in Fig. 3.65(b), clearly demonstrating the existence of phase velocity compensation between the even- and odd-modes. As a result of selecting the optimal dimension and number of grooves, the transmission zero of the unit PCML cell $|S_{21}|$ has been placed at the second harmonic frequency $2f_0$, and harmonic suppression could be achieved by grooves.

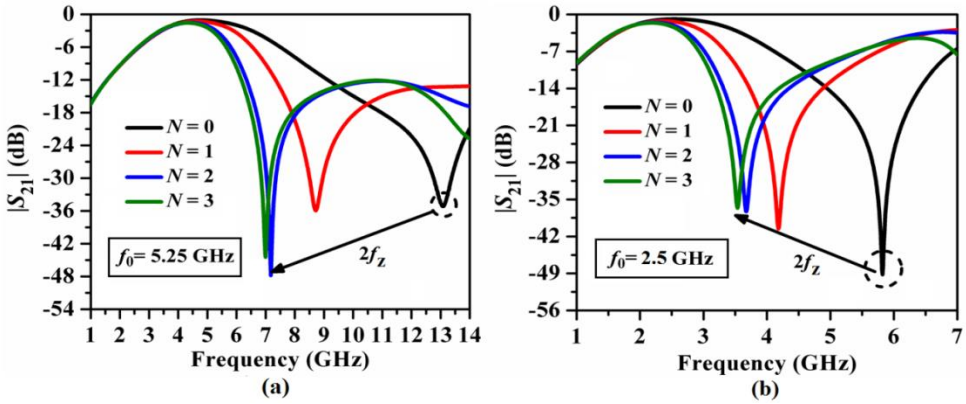

Fig. 3.66. Simulated resonance characteristics of $|S_{21}|$ (dB) for a pair of unit PCML cell with periodic square grooves: (a) f_0 = 5.25 GHz, (b) f_0 = 2.5 GHz.

The research has been expanded in Figs. 3.66(a)-(b) for both PCML cell pairs tuned at f_0 = 5.25 GHz with optimized dimensions of l = 8.193 mm, W = 0.8 mm, s = 0.2 mm and at f_0 = 2.5 GHz with optimized dimensions of l = 16.57, W = 0.94 mm, s = 0.2 mm. For all the PCML cells, an open-end offset length correction of d = 0.264 mm has been employed [1]. Such an open-end length correction is essential for the design to take into account the fringe field effects at the open end-ends of the lines. The transmission zero frequency ($2f_z$) for the second harmonic ($2f_0$) has shifted more to the lower frequency region as the number of grooves increases, as shown in Figs. 3.66(a)-(b).However, the attenuation levels at $2f_z$ in dB have been detoriated for f_0 = 5.25 GHz and incremented for f_0 = 2.5 GHz. This is due to the fact that the length of the line is less for f_0 = 5.25 GHz and hence the grooves are placed very close to each other, resulting in cross-coupling between two adjacent grooves. However, the length of the line for f_0 = 2.5 GHz is quite large and the grooves are placed periodically with a sufficient gap, reducing the chances of cross-coupling.

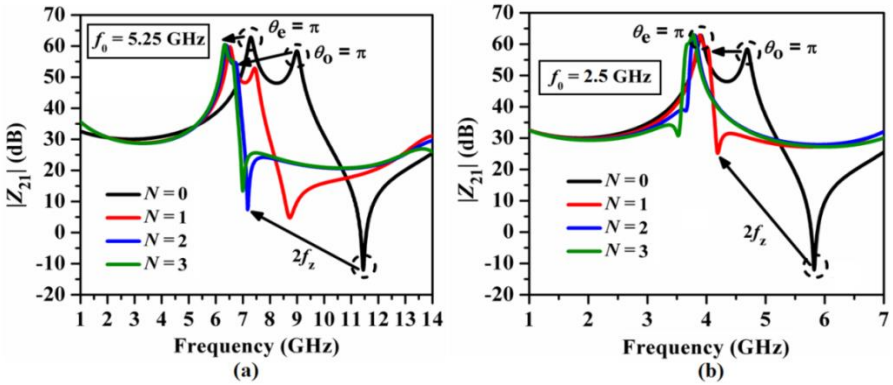

Fig. 3.67. Simulated resonance characteristics of $|Z_{21}|$ (dB) for a pair of unit PCML cell with periodic square grooves: (a) f_0 = 5.25 GHz, (b) f_0 = 2.5 GHz.

As a result, Figs. 3.67(a)-(b) show how the periodic grooves affect the even- and odd-mode resonant frequencies of $|Z_{21}|$ (dB) for the coupled lines at f_0 = 5.25 GHz and f_0 = 2.5 GHz, respectively. It has been observed that although both the resonant frequencies have been shifted to lower frequency regions with incremental N, the odd-mode resonant frequency for $\theta_0 = \pi$ has been shifted mostly compared to the even-mode resonant frequency for $\theta_e = \pi$. This justifies the ability to achieve modal phase velocity compensation for the PCML pair through the periodic square grooves. The surface current distribution for the pair of unit PCML cells with three periodic square grooves has been highlighted in Fig. 3.68(a) at f_0 = 5.25 GHz and $2f_z$ = 7 GHz. It has been observed that the strength of the surface current is maximum at f_0 = 5.25 GHz due to the center frequency (passband) and minimum at $2f_z$ = 7 GHz (stopband) due to the decrement of the corresponding attenuation level. The knowledge obtained from the study of unit PCML cell pairs with square grooves has been extended further for the third-order folded PCMLBF in the next section.

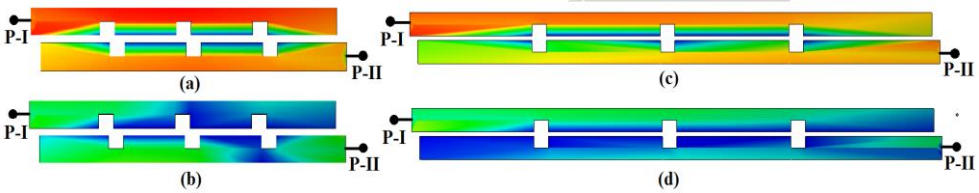

Fig. 3.68. Surface current distribution for a pair of unit PCML cell with periodic square grooves for N = 3 at (a) f_0 = 5.25 GHz, and (b) $2f_z$ = 7 GHz (Fig. 3.66(a)), (c) f_0 = 2.5 GHz and (b) $2f_z$ = 3.4 GHz (Fig. 3.66(b)).

3.14.2. Third-Order Folded PCMLBF with Periodic Square Grooves

The general layout of the third-order folded PCMLBF with a single square groove has been depicted in Fig. 3.69 with the input port P-I and the output port P-II. The parametric studies for the third-order folded PCMLBFs centered at 5.25 GHz and 2.5 GHz have been depicted in Figs. 3.70(a)-(b) respectively. The dimension of the groove has been considered as $w_T = l_T = W/2$, where W is the width of the lines. It has been observed that a sharp transmission zero, highlighted as $2f_z$, has been observed at 9.65 GHz with an attenuation level of 46 dB for the filter centered at 5.25 GHz with N = 2.

Fig. 3.69. Layout of the third-order folded PCMLBF with a single square groove.

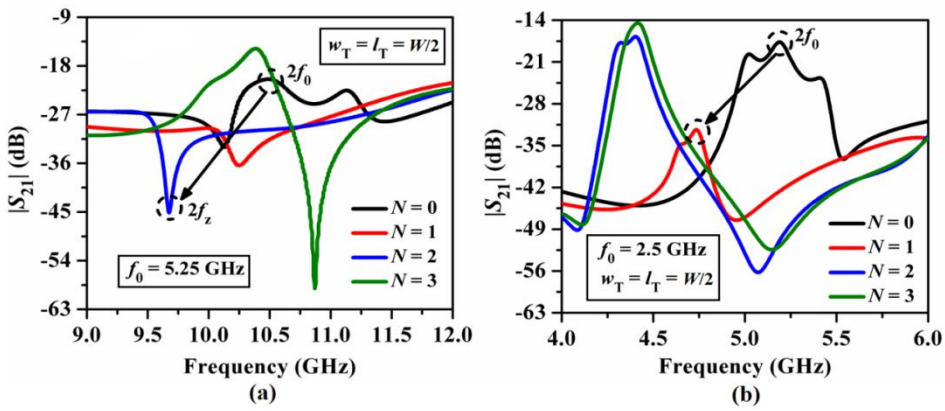

Fig. 3.70. Effects of periodic square grooves on the second harmonic suppression for the third-order folded PCMLBF with at (a) f_0 = 5.25 GHz, and (b) f_0 = 2.5 GHz.

However, the attenuation level at $2f_0$ for the filter centered at 2.5 GHz has been suppressed to 32 dB from 17 dB for N = 1. Accordingly, the optimum number of square grooves has been chosen as N = 2 for the *C*-band filter and N = 1 for the *S*-band filter. After numerous trial-and-error tuning steps, the layouts of the final filters with optimized groove dimensions were designed for two different frequency bands, as shown in Figs. 3.71(a)-(b). The overall size of the *C*-band filter is 41.97 mm × 6.42 mm, i.e., 269.24 mm^2 or 1.31λ_g × 0.2λ_g where λ_g is the guided wavelength at f_0 = 5.25 GHz. A size reduction of 59.22% has been achieved over the conventional filter and 3% over the folded filter, both having the same specifications. The overall size of the *S*-band filter is 95.59 mm × 6.65 mm, i.e., 663.97 mm^2 or 1.4λ_g × 0.1λ_g where λ_g is the guided wavelength at f_0 = 2.5 GHz.

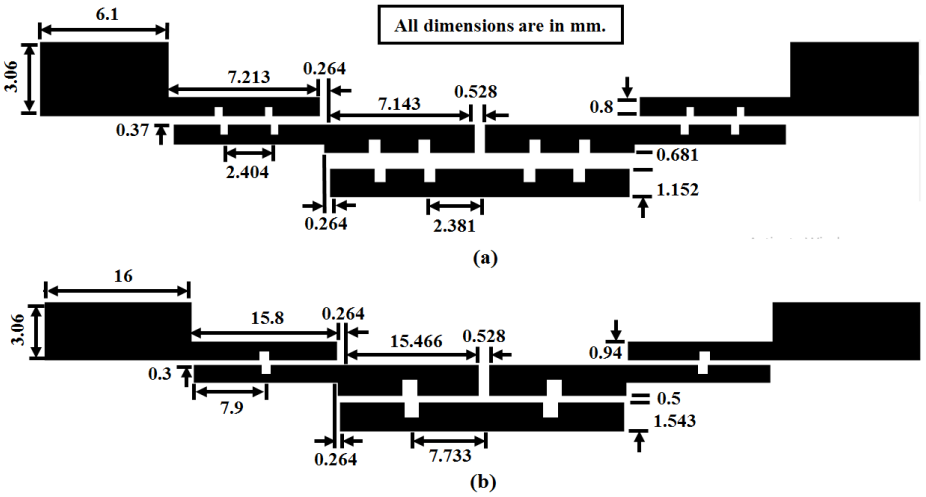

Fig. 3.71. Layout of third-order folded PCMLBFs with periodic square grooves centered at (a) f_0 = 5.25 GHz, and (b) f_0 = 2.5 GHz.

A size reduction of 48.58% has been achieved over the conventional filter and 7.9% over the folded filter with the same specifications. Figs. 3.72(a)-(b) compare the simulated *S*-parameter plots between the third-order folded filters with and without grooves for *C*-band and *S*-band respectively. It has been observed that a sharp transmission zero f_z has occurred at 6.35 GHz with an attenuation level of 41 dB for the *C*-band filter. This justifies the improvement of the skirt characteristics for the folded filter with grooves. In addition, another transmission zero $2f_z$ has occurred at 10.2 GHz with an attenuation level of 45 dB. The stopband rejection level of 26 dB up to $2.06f_0$ has been obtained for the *C*-band filter.

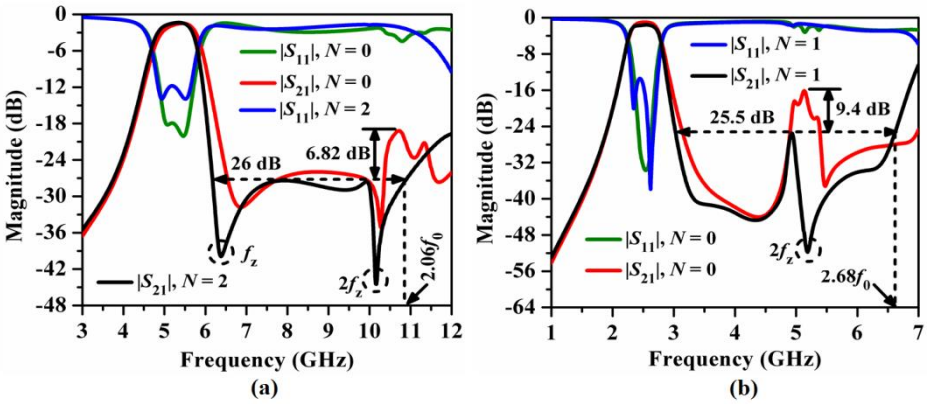

Fig. 3.72. Simulated *S*-parameters plots of the third-order folded PCMLBFs with periodic square grooves centered at (a) f_0 = 5.25 GHz, and (b) f_0 = 2.5 GHz.

The relative harmonic suppression performance is 35.55%. Although no significant transmission zero has occurred for the *S*-band filter, the stopband rejection level of 25.5 dB up to $2.68f_0$ has been obtained along with the improved skirt characteristics. Also, the relative harmonic suppression performance has been calculated as 58.38%. For both the filters, the passband insertion losses are less than 2 dB and the return losses are more than 15 dB, validating the effectiveness of the passband responses of such filters. Figs. 3.73(a)-(b) show the surface current distribution of the C-band filter, while Figs. 3.73(c)-(d) show the surface current distribution of the *S*-band filter. It has been observed that the strength of the surface current is maximum at f_0 = 5.25 GHz and 2.5 GHz and minimum at $2f_0$ = 10.5 GHz and 5 GHz due to the suppression of the harmonic attenuation level.

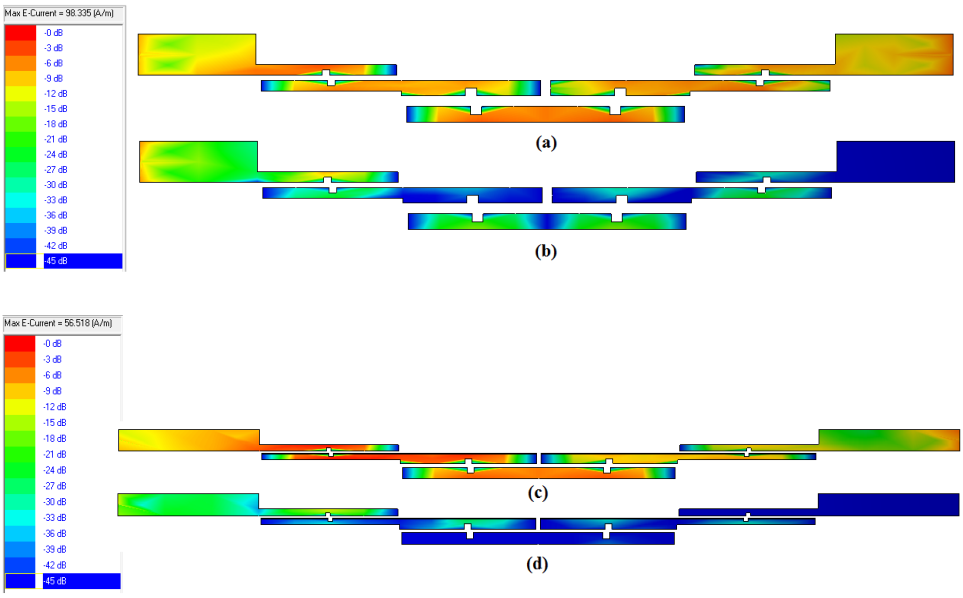

Fig. 3.73. Surface current distribution for the third-order folded PCMLBF with periodic square groove at (a) f_0 = 5.25 GHz, and (b) $2f_0$ = 10.5 GHz (Filter-I), (c) f_0 = 2.5 GHz, and (d) $2f_0$ = 5 GHz (Filter-II).

3.14.3. Third-Order Inline PCMLBF with Periodic Square Grooves

The effects of periodic square grooves on the harmonic suppression performance of third-order inline PCMLBFs in both *C*-band and *S*-band have been investigated using the same methodology. The general layout of the third-order inline PCMLBF with a single square groove at the middle has been depicted in Fig. 3.74 with the input port P-I and the output port P-II.

Fig. 3.74. Layout of the third-order inline PCMLBF with a single square groove.

From the parametric study of Figs. 3.75 (a)-(b), it has been observed that maximum suppression of the second harmonic's attenuation level has been obtained with N = 1 for both the *C*-band and *S*-band filters. As a result, the optimized dimensions of the inline filters are shown in Figs. 3.76(a)-(b), respectively. The overall size of the *C*-band filter is 39.03 mm × 4.47 mm i.e., 174.5 mm^2 or 1.26λ_g × 0.14λ_g and that of the *S*-band filter is 95.4 mm × 4.9 mm i.e., 467.5 mm^2 or 1.4λ_g × 0.07λ_g. A size reduction of 73.57% and 63.8% has been achieved over the conventional filters, 23.57% and 3.6% over the inline filters without grooves having the same specifications.

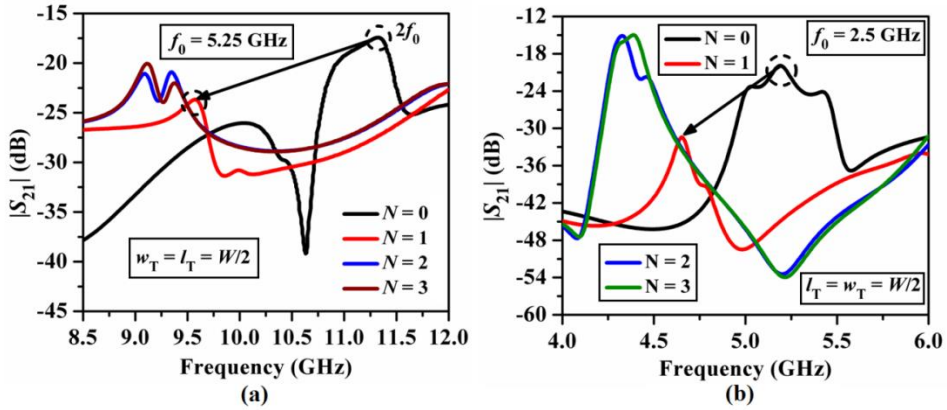

Fig. 3.75. Effects of periodic square grooves on the second harmonic suppression for the third-order inline PCMLBF with at (a) f_0 = 5.25 GHz, and (b) f_0 = 2.5 GHz.

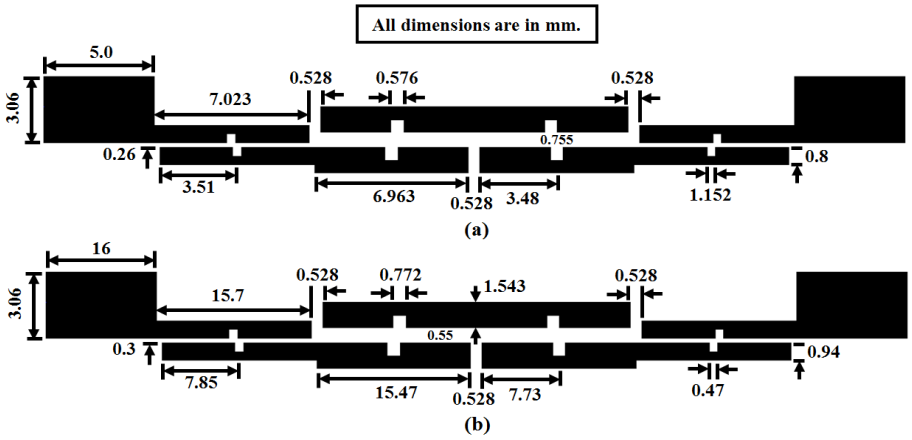

Fig. 3.76. Layout of third-order inline PCMLBFs with periodic square groove centered at (a) f_0 = 5.25 GHz, and (b) f_0 = 2.5 GHz.

Figs. 3.77(a)-(b) show a comparison of the simulated S-parameter plots of inline PCMLBFs with and without grooves. It has been observed that a stopband up to $2.29f_0$ with a rejection level of 27 dB for the *C*-band inline filter and a stopband up to $2.68f_0$ with a rejection level of 30 dB for the *S*-band inline filter along with improved skirt characteristics have been obtained. The relative harmonic suppression performance has been obtained at 68.8% and 66.7%, respectively, compared to the inline filters without grooves. For both the filters, the insertion losses become less than 2 dB and the return losses become more than 25 dB. The surface current distributions for the designed inline filters in *C*-band and *S*-band are elaborated in Figs. 3.78(a)-(b) and Figs. 3.79(a)-(b), respectively, with large strengths at f_0 = 5.25 GHz and f_0 = 2.5 GHz and minimum strengths at $2f_0$ = 10.5 GHz and $2f_0$ = 5 GHz, as expected.

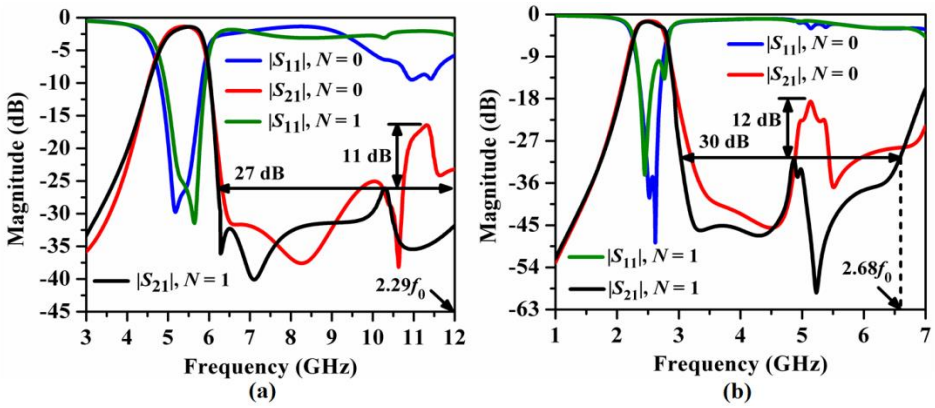

Fig. 3.77. Comparison of the simulated *S*-parameters plots of the third-order inline PCMLBFs with and without periodic square grooves centered at (a) f_0 = 5.25 GHz and (b) f_0 = 2.5 GHz.

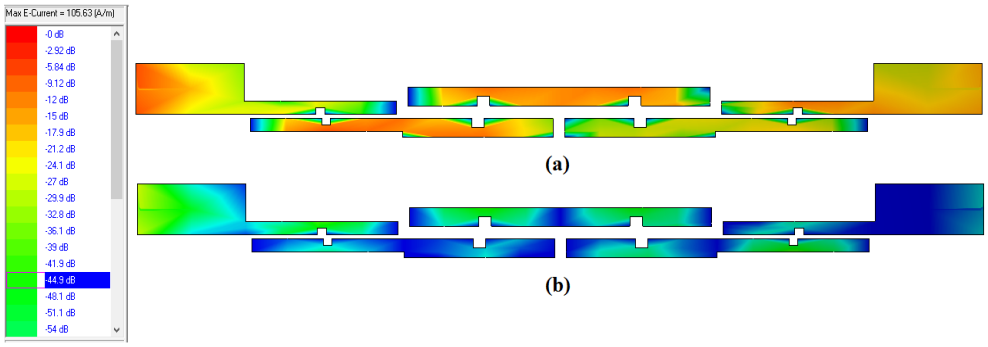

Fig. 3.78. Surface current distribution for the third-order inline PCMLBF with periodic square groove at (a) f_0 = 5 GHz, and (b) $2f_0$ =10.5 GHz.

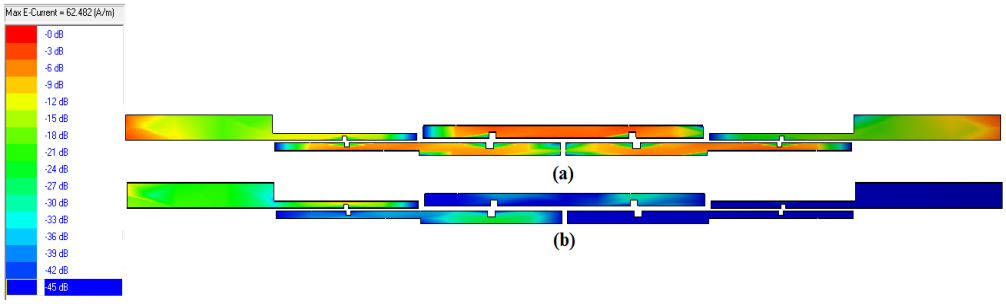

Fig. 3.79. Surface current distribution for the third-order inline PCMLBF with periodic square groove at (a) f_0 = 2.5 GHz, and (b) $2f_0$ = 5 GHz.

3.14.4. Harmonic Suppression for the Third-Order Folded PCMLBF by Periodic Rectangular Grooves-Simulation Study

In the previous section, it has been concluded that periodic square shapes are quite capable of suppressing the attenuation level at $2f_0$ for both folded and inline filters. However, the suppression level is limited to 27 dB for the *C*-band filter and 30 dB for the inline filter.

Moreover, the study has been focused mainly on the square-shaped grooves. The effects of the variation in length and width of the periodic grooves have not been investigated. Thus, the study of periodic grooves has been further extended for rectangular grooves in this section. Four different length (l_T) and width (w_T) combinations for the grooves have been considered. The combinations are:

- Case 1: $l_T = W/2$, $w_T = W/2$
- Case 2: $l_T = W/2$, $w_T = 3W/4$
- Case 3: $l_T = 3W/4$, $w_T = W/2$
- Case 4: $l_T = 3W/4$, $w_T = 3W/4$

Here, W is the width of the coupled-lines. The layout of a pair of unit PCML cells with three periodic rectangular grooves is shown in Fig. 3.80, and the corresponding resonant characteristics of $|S_{21}|$ (dB) with $l_T = 3W/4$ and $w_T = W/2$ for both the *C*-band and *S*-band filters are shown in Figs. 3.81(a)-(b).

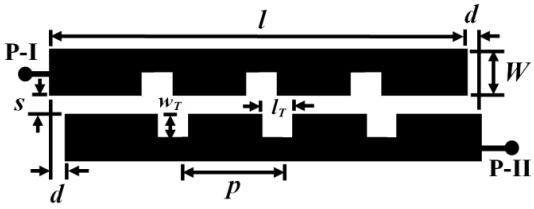

Fig. 3.80. Layout of a pair of unit PCML cell with rectangular shaped periodic grooves.

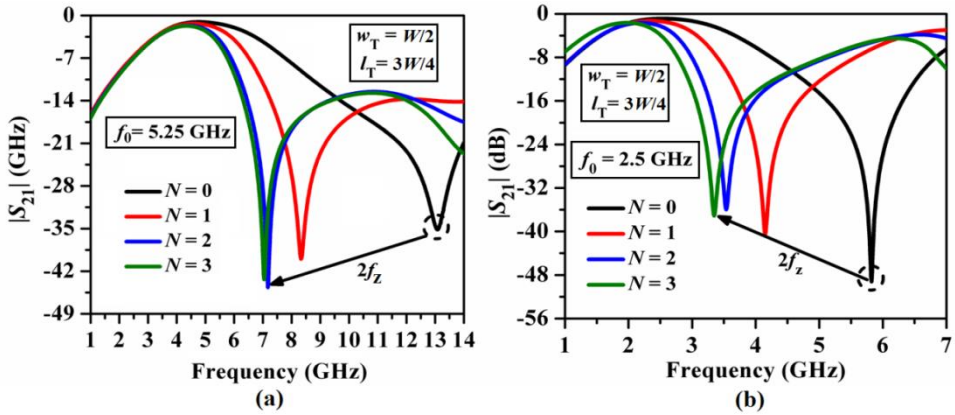

Fig. 3.81. Simulated resonance characteristics of $|S_{21}|$ (dB) for a pair of unit PCML cell with periodic rectangular grooves: (a) f_0 = 5.25 GHz, and (b) f_0 = 2.5 GHz.

From the resonance characteristics, it has been observed that the second harmonic transmission zeros $2f_z$ have been shifted to lower frequency regions for both the filters with incremental N due to the increment of the effective odd-mode electrical length. However, the attenuation level at $2f_z$ has been increased for the *C*-band filter and decreased for the *S*-band

filter due to the difference in the amount of cross-couplings between the adjacent grooves. As a result, the phase compensation between the even-mode and odd-mode resonant peaks for $|Z_{21}|$ (dB) plots is shown in Figs. 3.82(a)-(b). It can be concluded that the odd-mode resonant peaks shift more compared to the even-mode resonant peaks, just like the square grooves. The layout of the third-order folded PCMLBF with a single rectangular groove is shown in Fig. 3.83.

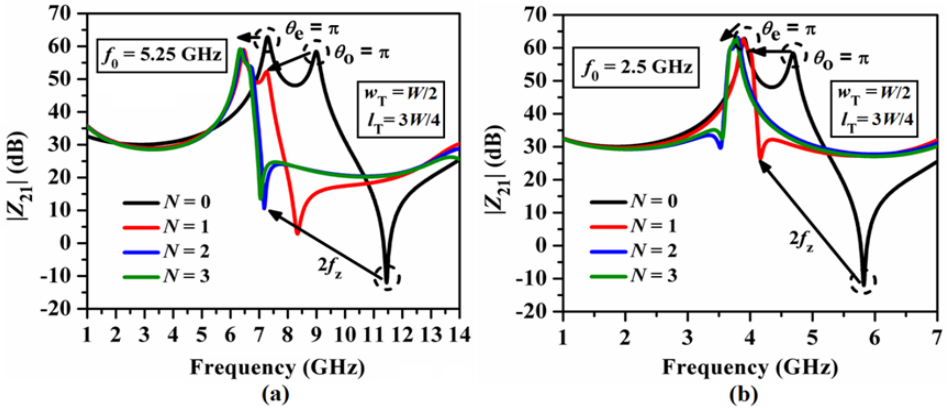

Fig. 3.82. Simulated resonance characteristics of $|Z_{21}|$ (dB) for a pair of unit PCML cell with periodic rectangular grooves: (a) f_0 = 5.25 GHz, (b) f_0 = 2.5 GHz.

Fig. 3.83. Layout of the third-order folded PCMLBF with a single rectangular groove placed at the middle.

The effects of periodic rectangular grooves on the second harmonic suppression performance of third-order folded PCMLBFs are investigated in Figs. 3.84(a)-(b) by increasing the number of grooves with dimensions of $l_T = 3W/4$ and $w_T = W/2$. It has been noticed that maximum suppression of second harmonic's attenuation level has been obtained for $N = 2$ for *C*-band filter and $N = 1$ for *S*-band filter. Accordingly, four different cases have been studied with these optimum number of grooves for the folded filters and mentioned in Figs. 3.85(a)-(b). The optimum dimensions of grooves have been obatined as $l_T = 3W/4$, $w_T = W/2$ (Case 3) for both the filters as it gives the maximum suppression of the harmonics' attenuation levels. Finally, the optimized dimensions of the folded filters with periodic rectangular grooves have been obtained in Figs. 3.86(a)-(b) respectively. The overall size of the *C*-band filter is 42.18 mm × 6.3 mm i.e., 265.73 mm^2 or $1.36\lambda_g \times 0.2\lambda_g$ and that of the *S*-band filter is 95.4 mm × 6.92 mm i.e., 660.17 mm^2 or $1.4\lambda_g \times 0.1\lambda_g$.

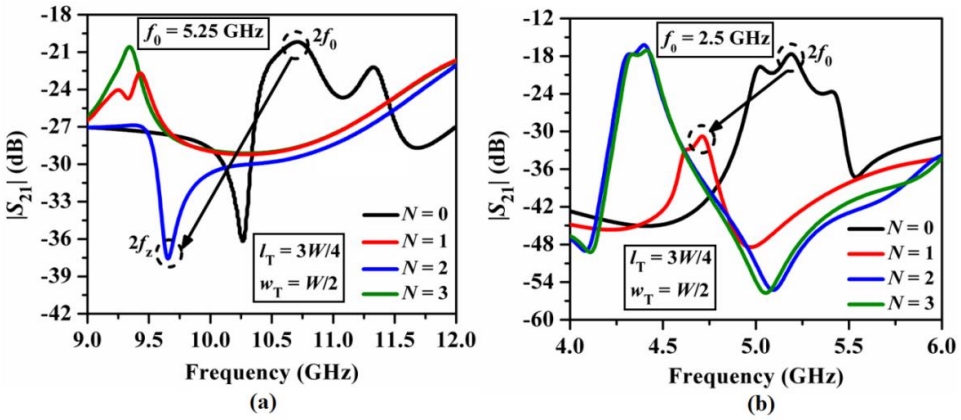

Fig. 3.84. Effects of periodic rectangular grooves on the second harmonic suppression for the third-order folded PCMLBF with at (a) f_0 = 5.25 GHz, and (b) f_0 = 2.5 GHz.

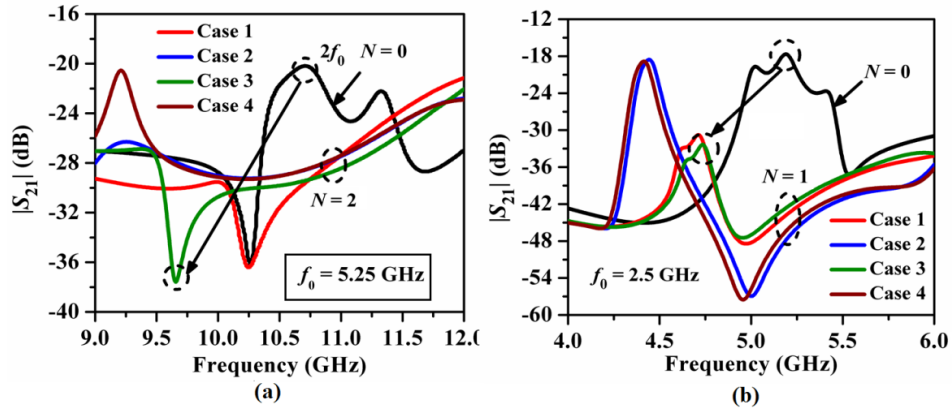

Fig. 3.85. Parametric simulation study for a third-order folded PCMLBF with a single rectangular groove with different dimensions at (a) f_0 = 5.25 GHz, and (b) f_0 = 2.5 GHz.

Accordingly, size reductions of 59.7%, 48.9% have been achieved over the conventional filters, 4.27%, 12.6% over the folded filters without grooves have been obtained. The comparison of the simulated *S*-parameters plots for the folded filters with and without grooves has been illustrated in Fig. 3.87(a)-(b). It has been observed that a stopband up to $2.1f_0$ with a rejection level of 30 dB for *C*-band folded filter along with the improved skirt characteristics with transmission zero f_z having attenuation level of 45 dB have been obtained. Moreover, another transmission zero $2f_z$ has been obtained at 10.3 GHz justifying the harmonics suppression ability of the rectangular grooves. Similarly, a stopband up to $2.68f_0$ with a rejection level of 28 dB have been obtained for the *S*-band folded filter. The relative harmonic suppression performances have been obtained as 66.7% and 64.7% respectively compared to the folded filters without grooves.

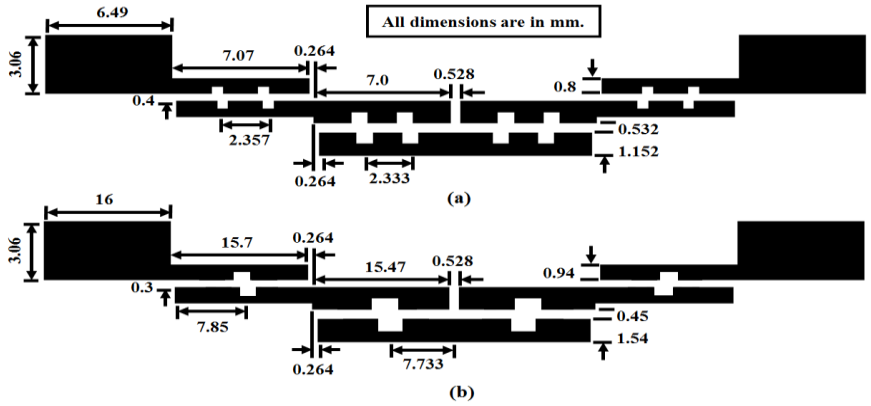

Fig. 3.86. Layout of third-order folded PCMLBF with periodic rectangular grooves centered at (a) f_0 = 5.25 GHz, and (b) f_0 = 2.5 GHz.

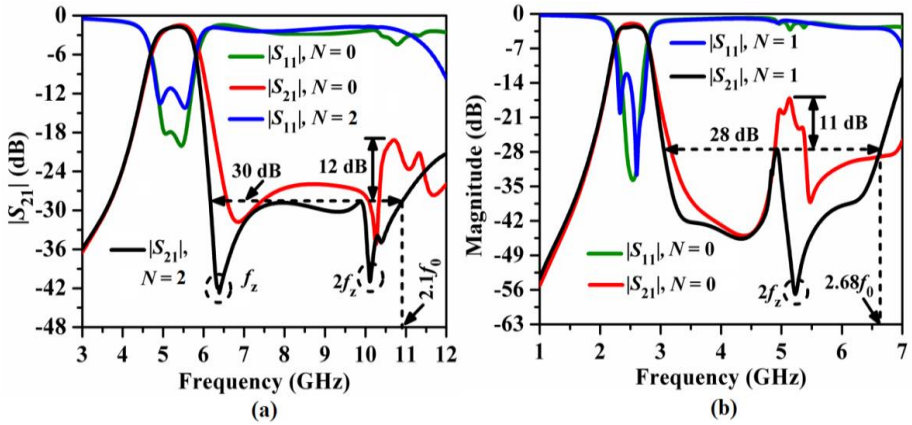

Fig. 3.87. Simulated *S*-parameters plots of the third-order folded PCMLBF with periodic rectangular grooves centered at (a) f_0 = 5.25 GHz, and (b) f_0 = 2.5 GHz.

3.14.4.1. Fabricated Prototype

To validate the performance of the designed filters the prototype of *C*-band folded filter with two rectangular grooves have been fabricated as shown in Fig. 3.88(a) and the experimental set up for the S-parameters measurements has been explained in Fig. 3.88(b)-(c). The measurement has been carried out in Agilent Technologies Keysign N9928A vector network analyzer by following the procedure described below.

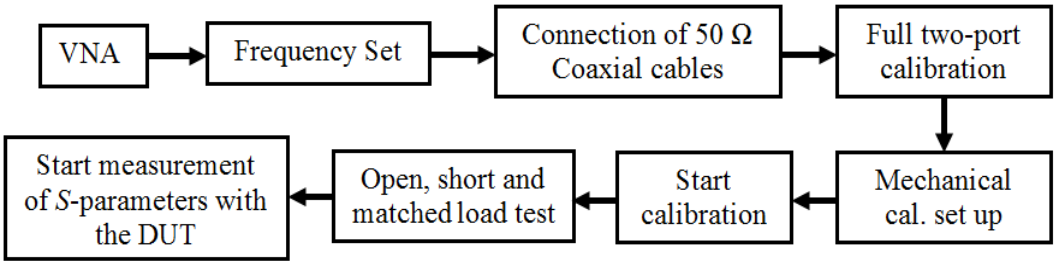

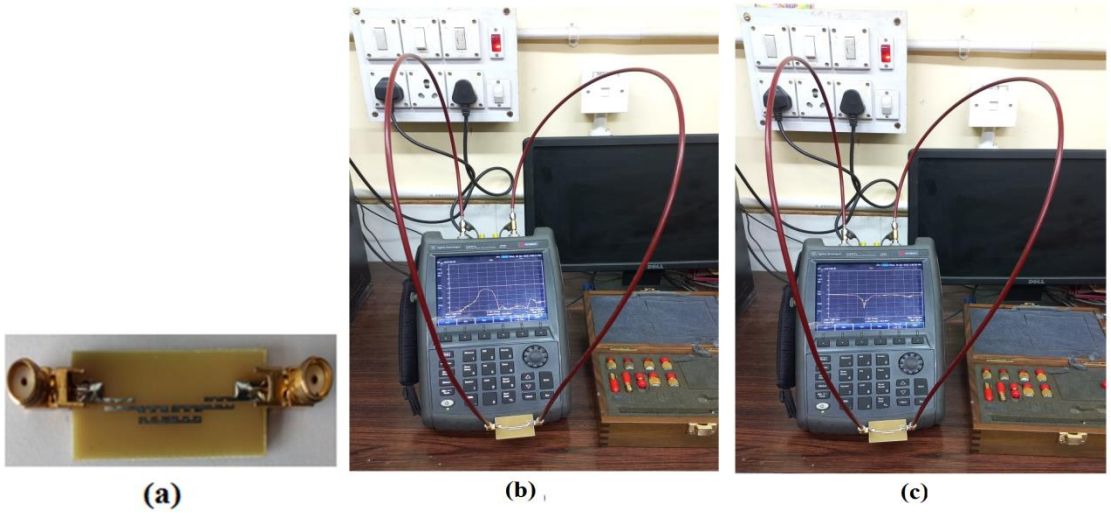

Fig. 3.88. (a) Fabricated prototype, (b) experimental set up for $|S_{21}|$ (dB) measurement, and (c) $|S_{11}|$ (dB) measurement for the 3rd -order folded PCMLBF with rectangular grooves with f_0 = 5.25 GHz.

3.14.4.2. Comparison of EM Simulation vs. Measurement Results

The comparison between the simulated and measured *S*-parameters plots has been illustrated in Figs. 3.89(a)-(b). It has been observed from Fig. 3.89(a) that the measured and the simulated $|S_{21}|$ plots are in good agreement in the passband. A sharp transmission zero f_z with an attenuation level of 48 dB has been obtained at 6.6 GHz, justifying the improvement of the skirt characteristics of the proposed folded filter with grooves. Moreover, a stopband up to $1.87f_0$ with a rejection level below 36 dB and up to $2.29f_0$ below a rejection level of 30 dB has been recorded for the measured response. The measured insertion loss of 1.1 dB and the measured return loss of 18 dB (Fig. 3.89(b)) have been obtained for the designed folded filter with grooves. Figs. 3.90(a)-(b) depict the surface current distribution for the *C*-band third-order folded PCMLBF with periodic rectangular grooves.

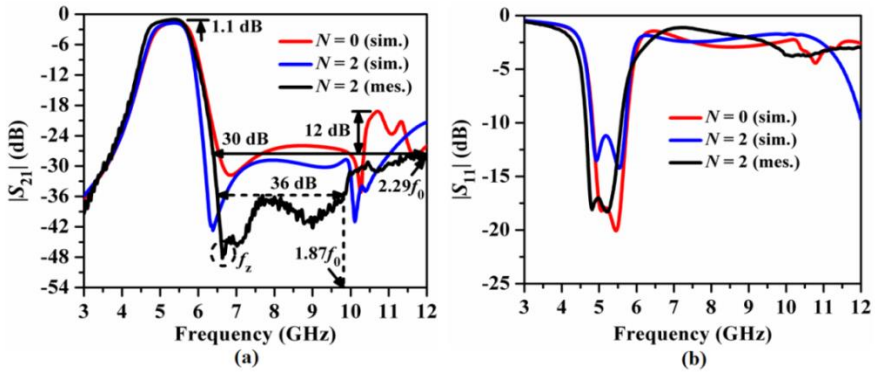

Fig. 3.89. Simulated vs. measured *S*-parameters plots of the third-order folded PCMLBF with periodic rectangular grooves centered at f_0 = 5.25 GHz: (a) $|S_{21}|$ (dB) and (b) $|S_{11}|$ (dB) [25].

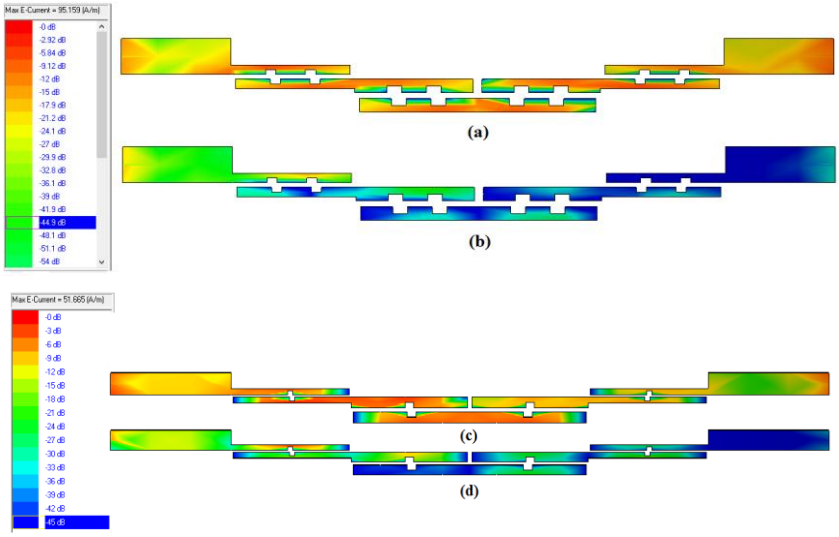

Fig. 3.90. Surface current distribution for the third-order folded PCMLBF with periodic rectangular grooves at (a) f_0 = 5.25 GHz, (b) $2f_0$ = 10.5 GHz, (c) f_0 = 2.5 GHz, and (d) $2f_0$ = 5 GHz.

It has been observed that the surface current is distributed with a large strength at f_0 = 5.25 GHz and it becomes minimum at $2f_0$ = 10.5 GHz due to the suppression of the harmonic.

3.14.5. Third-Order Inline PCMLBF by Periodic Rectangular Grooves

By following the same methodology, the study has been extended to the third-order inline PCMLBFs in both *C*-band and *S*-band. The general layout of the third-order inline PCMLBF with a single rectangular groove at the middle has been depicted in Fig. 3.91 with the input port P-I and the output port P-II. The effects of rectangular grooves with dimensions of l_T = 3W/4, w_T = *W*/2 (Case 3) on the suppression of the second harmonic's attenuation level are shown in Figs. 3.92(a)-(b). It has been observed that maximum suppression has been achieved for N = 1 for both the filters. Thus, this has been chosen as the optimum value of the groove's number. As a result, four different cases of the previously mentioned groove dimension have been studied further for the inline filters, and their comparative $|S_{21}|$ plots are highlighted in Figs. 93(a)-(b), respectively. From this study, Case 3 has been chosen as the optimum combination of groove dimensions as it gives the maximum suppression of harmonic attenuation levels for both the filters. Finally, the optimized dimensions for the third-order inline filters operating at *C*- and *S*-band have been obtained as shown in Figs. 3.94(a)-(b). The overall size of the *C*-band filter is 39.03 mm × 4.57 mm i.e., 178.45 mm^2 or 1.26λ_g × 0.15λ_g and that of the *S*-band filter is 95.4 mm × 4.9 mm i.e., 467.5 mm^2 or 1.4λ_g × 0.07λ_g.

Fig. 3.91. Layout of the third-order inline PCMLBF with a single rectangular groove.

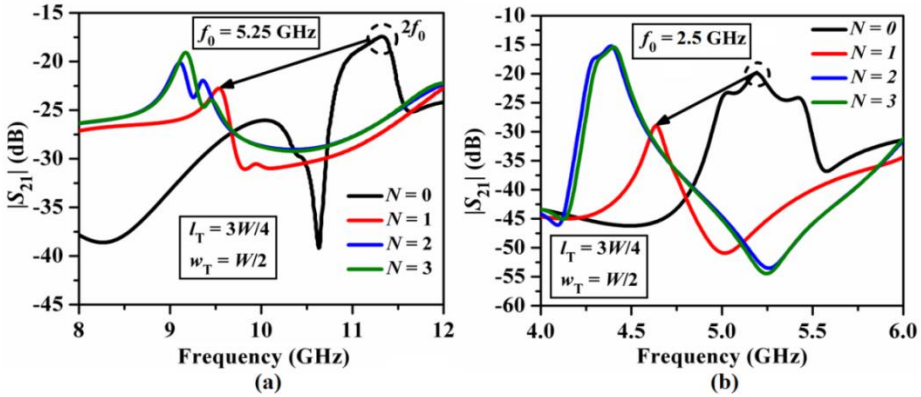

Fig. 3.92. Effects of periodic rectangular grooves on the second harmonic suppression for the third-order inline PCMLBF with at (a) f_0 = 5.25 GHz, and (b) f_0 = 2.5 GHz.

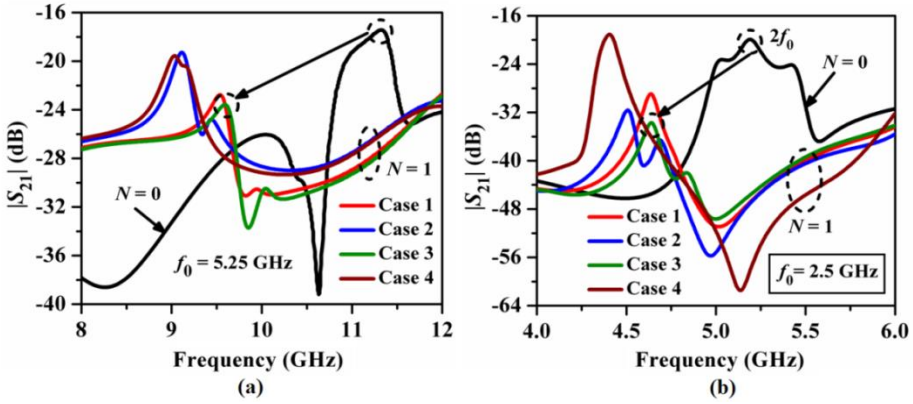

Fig. 3.93. Parametric simulated study for a third-order inline PCMLBF with a single rectangular groove with different dimensions at (a) f_0 = 5.25 GHz, and (b) f_0 = 2.5 GHz.

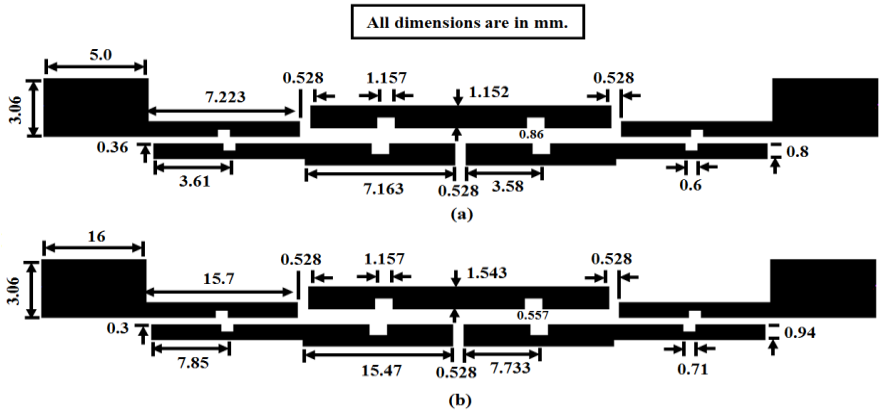

Fig. 3.94. Layout of optimized third-order inline PCMLBF with periodic rectangular grooves centered at (a) f_0 = 5.25 GHz, and (b) f_0 = 2.5 GHz.

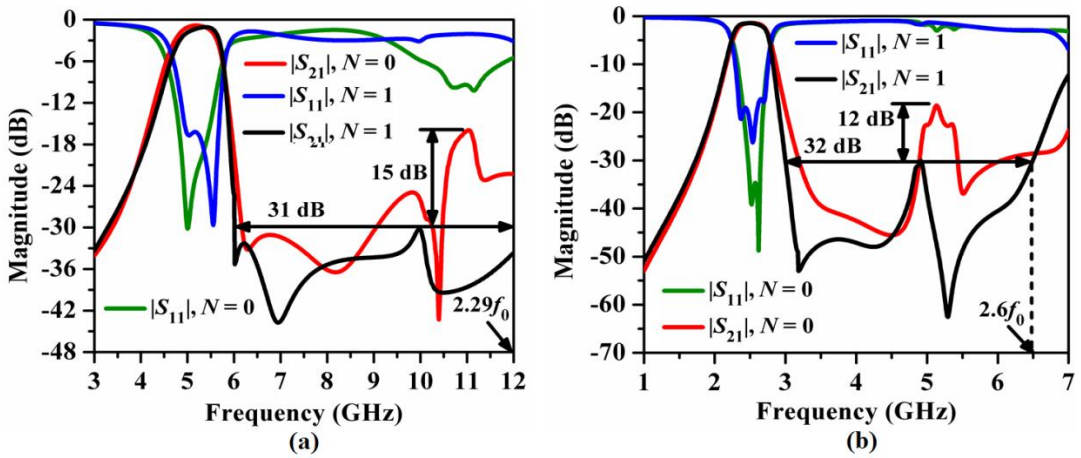

Fig. 3.95. Simulated *S*-parameters plots of the third-order inline PCMLBF with periodic rectangular grooves centered at (a) f_0 = 5.25 GHz and (b) f_0 = 2.5 GHz.

Accordingly, size reductions of 73%, 63.8% over the conventional filters, 21.9%, and 3.6% over the inline filters without grooves have been achieved. Figs. 3.95(a)-(b) show a comparison of the simulated S-parameter plots of inline PCMLBFs with and without grooves. It has been observed that a stopband up to $2.29f_0$ with a rejection level of 31 dB for the *C*-band inline filter and a stopband up to $2.6f_0$ with a rejection level of 32 dB for the *S*-band inline filter along with improved skirt characteristics have been obtained.

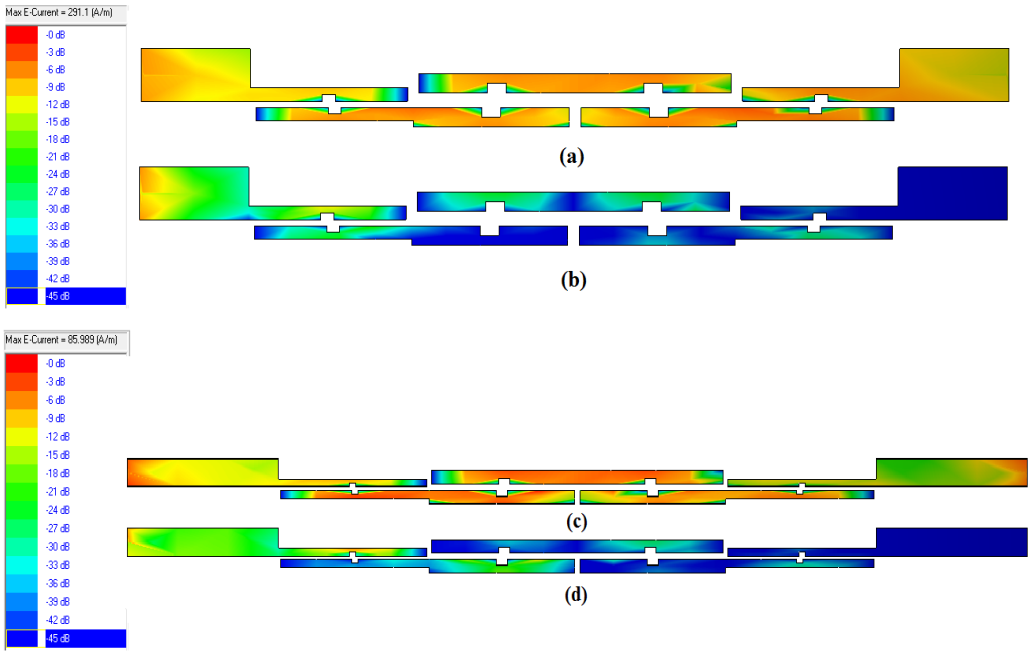

Fig. 3.96. Surface current distribution for the third-order inline PCMLBF with periodic rectangular grooves at (a) f_0 = 5.25 GHz, and (b) $2f_0$ = 10.5 GHz.

The relative harmonic suppression performance has been obtained as 93.75% and 60%, respectively, compared to the inline filters without grooves. For both the filters, the insertion losses become less than 2 dB and the return losses become more than 18 dB. The surface current distribution for the designed inline filters in *C*-band and *S*-band is shown in Figs. 3.96(a)-(d), with large strengths at f_0 = 5.25 GHz and 2.5 GHz and minimum strengths at $2f_0$ = 10.5 GHz and 5 GHz, as expected.

3.14.6. Harmonic Suppression for the Third-Order Folded PCMLBF by Periodic Sawtooth Grooves

It has been revealed from the previous sections that for both the square and rectangular grooves, the surface current flow changes its direction abruptly at the sharp bends of 90^o at the corners of the grooves. This may cause signal diffraction at the edges of the grooves and increase the chance of more cross-coupling between two adjacent grooves. This problem will be severe for the *C*-band filter, where the resonator length is quite small compared to the *S*-band filter. To avoid such an abrupt change of current flow direction and to reduce the radiation effects, the square and rectangular grooves are modified to sawtooth grooves as shown in Fig. 3.97. Accordingly, the sawtooth grooves have been employed for folded and inline PCMLBFs to achieve more harmonic suppression performance. In general, the sawtooth groove forms a right-angled triangle with the dimensions of square and rectangular grooves. Thus, the signal rises smoothly to the vertex of the groove along the hypotenuse edge and then flows in a forward direction in the line. This reduces the chance of radiations of signal which frequently occur in square and rectangular groove due to their sharp perpendicular bent edges.

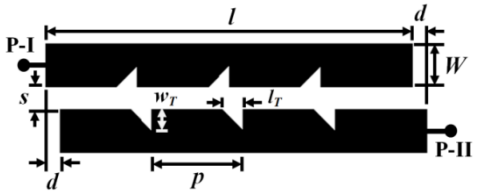

Fig. 3.97. Layout of a pair of unit PCML cell with three periodic sawtooth shaped grooves.

Fig. 3.98. Layout of the third-order folded PCMLBF with a single sawtooth groove.

The general layout of the third-order inline PCMLBF with a single sawtooth groove at the middle has been depicted in Fig. 3.98 with the input port P-I and the output port P-II. As a result, for the *C*-band and *S*-band folded filters, the effects of sawtooth grooves with dimensions of $l_T = W/2$ and $w_T = W/2$ (Case 1) on the suppression of second harmonic attenuation level are shown in Figs. 3.99(a)-(b).

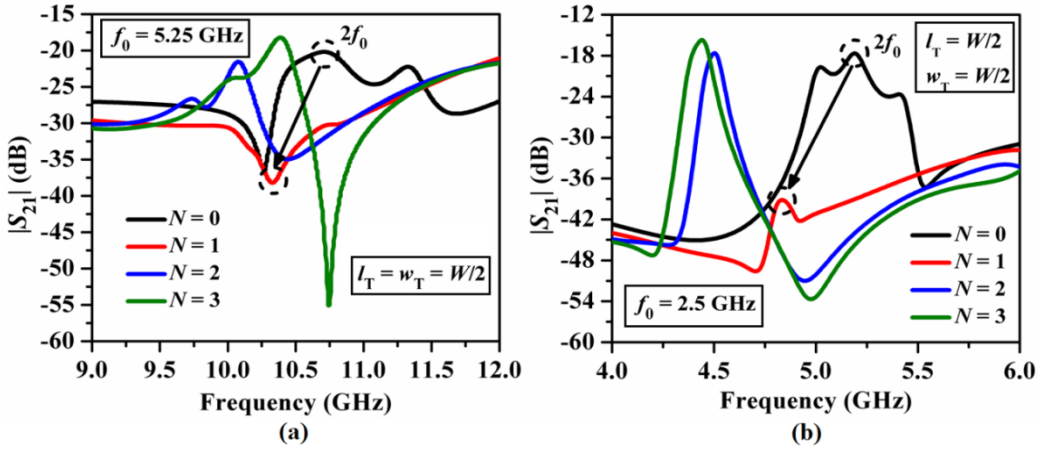

Fig. 3.99. Effects of periodic sawtooth grooves on the second harmonic suppression for the third-order folded PCMLBF with at (a) f_0 = 5.25 GHz, and (b) f_0 = 2.5 GHz.

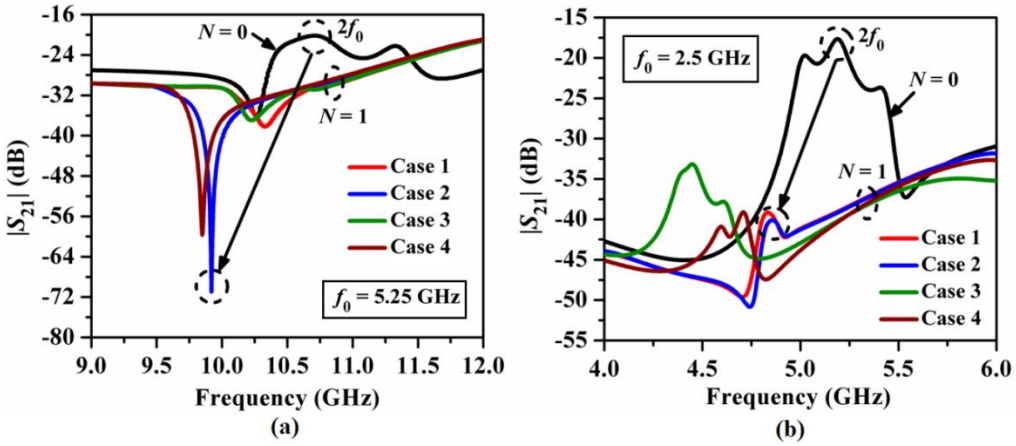

Fig. 3.100. Parametric simulated study for a third-order folded PCMLBF with a single sawtooth groove with different dimensions at (a) f_0 = 5.25 GHz, and (b) f_0 = 2.5 GHz.

It has been observed that maximum suppression has been achieved for $N = 1$ for both the filters. Thus, this has been chosen as the optimum value of the groove's number. As a result, the variations of the sawtooth groves' base (l_T) and height (w_T) have been investigated for third-order folded filters such as the rectangular groove in Figs. 3.100(a)-(b). From this study, Case 2, i.e., $l_T = W/2$, $w_T = 3W/4$, has been chosen as the optimum combination of groove

dimensions as it gives the maximum suppression of harmonics for both the filters. Finally, Figs. 3.101(a)-(b) show the optimized dimensions of the folded filters with periodic sawtooth grooves. The overall size of the *C*-band filter is 42.58 mm × 6.36 mm, i.e., 270.64 mm^2 or 1.37λ_g × 0.2λ_g and that of the *S*-band filter is 96.96 mm × 6.87 mm, i.e., 666.12 mm^2 or 1.42λ_g × 0.1λ_g. A size reduction of 59% and 48.4% has been achieved over the conventional filters, and 2.5% and 7.6% over the folded filters without grooves, having the same specifications.

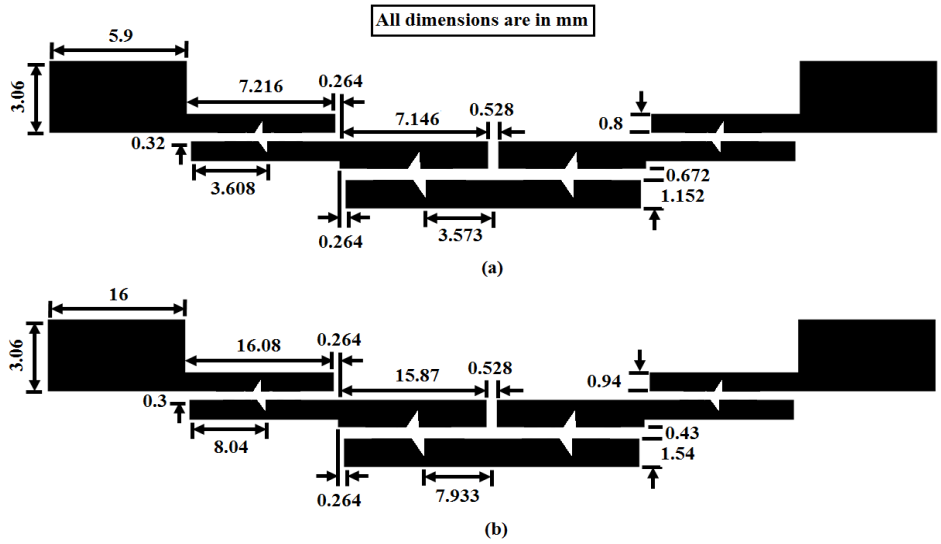

Fig. 3.101. Layout of optimized third-order folded PCMLBF with periodic sawtooth groove centered at (a) f_0 = 5.25 GHz, and (b) f_0 = 2.5 GHz [39].

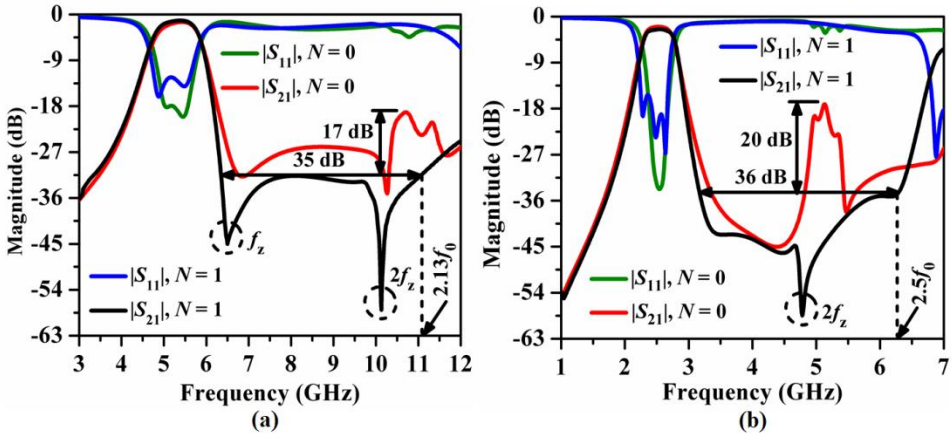

Fig. 3.102. Simulated *S*-parameters plots of the third-order folded PCMLBF with periodic sawtooth grooves centered at (a) f_0 = 5.25 GHz and (b) f_0 = 2.5 GHz [26].

The simulated *S*-parameter plots of folded PCMLBFs with and without grooves are shown in Figs. 3.102(a)-(b). It has been observed that a stopband up to 2.13f_0 with a rejection level of 35 dB for the *C*-band folded filter and a stopband up to 2.5f_0 with a rejection level of 36 dB

for the *S*-band folded filter along with improved skirt characteristics have been obtained. In addition, sharp transmission zero peaks with an attenuation level of 58 dB at 10.2 GHz for the *C*-band filter and that of 57 dB at 4.8 GHz for the *S*-band filter have been obtained. It clearly justifies the effectiveness of the sawtooth groove over square and rectangular grooves with respect to stopband rejection performance. For both the designed filters with sawtooth grooves, the insertion losses become less than 2 dB and the return losses become more than 18 dB. Figs. 3.103(a)-(d) depicts the surface current distribution for the *C*-band third-order folded PCMLBF with periodic sawtooth grooves. It has been observed that the surface current distribution is maximum at f_0 = 5.25 GHz and 2.5 GHz and minimum at $2f_0$ = 10.5 GHz and 5 GHz due to the suppression of the harmonic.

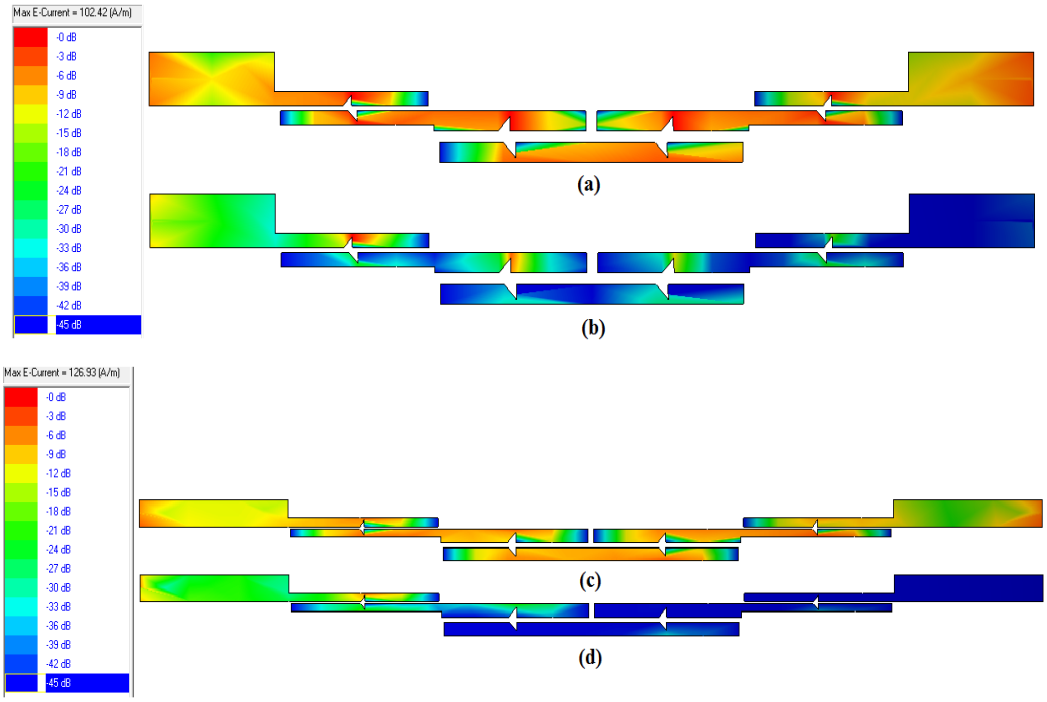

Fig. 3.103. Surface current distribution for the third-order folded PCMLBF with periodic sawtooth groove at (a) f_0 = 5.25 GHz, and (b) $2f_0$ = 10.5 GHz.

3.14.7. Third-Order Inline PCMLBF by Periodic Sawtooth Grooves

By following the same methodology, the study of periodic sawtooth grooves has been extended to the third-order inline PCMLBFs in both *C*-band and *S*-band. The general layout of the third-order inline PCMLBF with a single sawtooth groove at the middle has been depicted in Fig. 3.104 with the input port P-I and the output port P-II. Figs. 105(a)-(b) show the effects of sawtooth grooves with dimensions of $l_T = W/2$, $w_T = W/2$ (Case 1) on the

suppression of the attenuation level of the second harmonic. It has been observed that maximum suppression has been achieved for N = 1 for both the filters. Thus, the optimum value of the groove's number has been chosen as one. As a result, four different cases of groove dimension were investigated further for inline filters, and their comparative $|S_{21}|$ plots are shown in Figs. 106(a)-(b).

Fig. 3.104. Layout of the third-order inline PCMLBF with a single sawtooth groove.

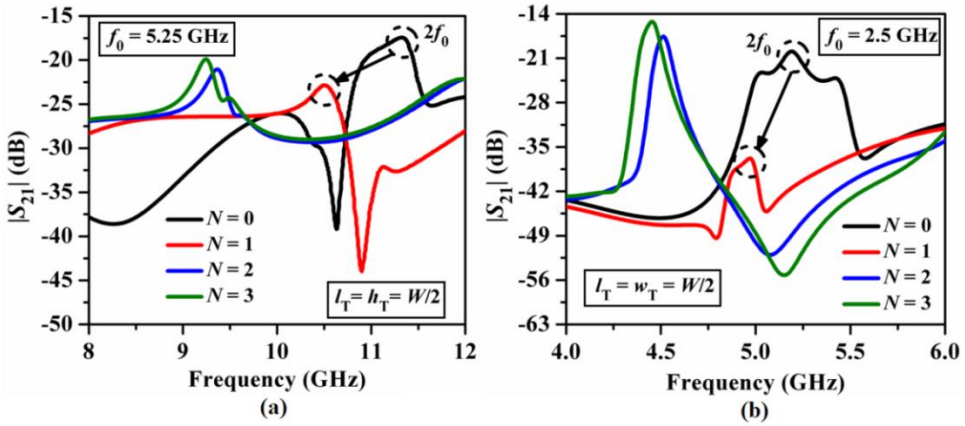

Fig. 3.105. Effects of periodic sawtooth grooves on the second harmonic suppression for the third-order inline PCMLBFs centered at (a) f_0 = 5.25 GHz, and (b) f_0 = 2.5 GHz.

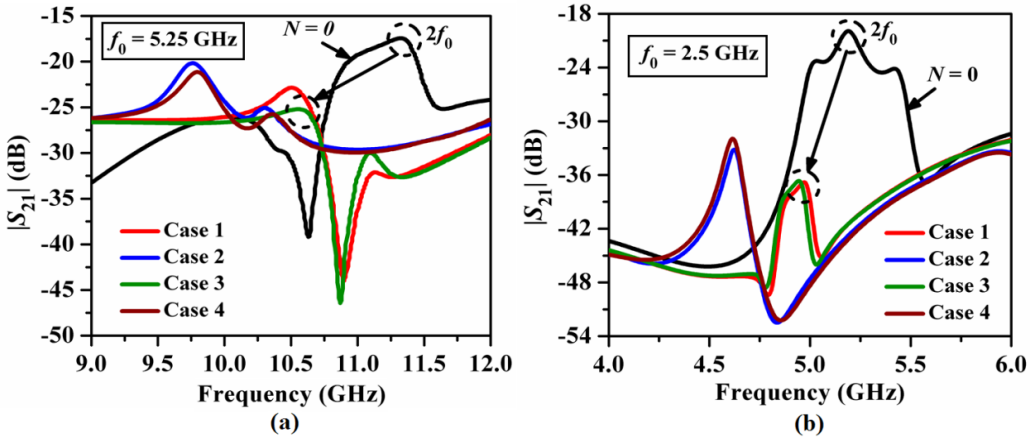

Fig. 3.106. Parametric simulated study for the third-order inline PCMLBFs with a single sawtooth groove with different dimensions at (a) f_0 = 5.25 GHz, and (b) f_0 = 2.5 GHz.

From this study, Case 3, i.e., l_T = 3W/2, w_T = W/2, has been chosen as the optimum combination of groove dimensions, as this case gives the maximum suppression of harmonics for both the filters. Finally, in Figs. 3.107(a)-(b), the optimized dimensions for third-order

inline filters operating in the *C*- and *S*-bands have been obtained. The overall size of the *C*-band filter is 41.43 mm × 4.57 mm, i.e., 189.42 mm^2 or 1.33λ_g × 0.15λ_g and that of the *S*-band filter is 97.8 mm × 4.9 mm, i.e., 479.2 mm^2 or 1.43λ_g × 0.07λ_g. A size reduction of 71.3% and 62.9% has been achieved over the conventional filters, and 17% and 2.2% over the inline filters without grooves, having the same specifications.

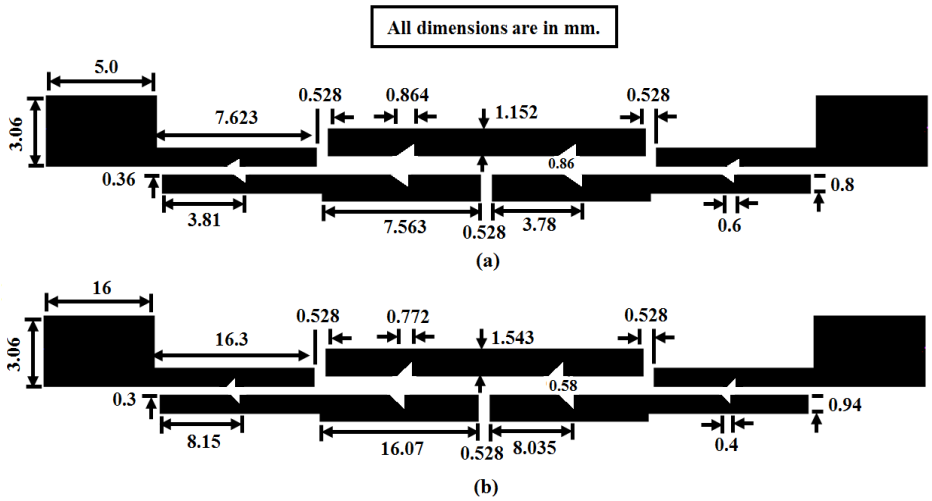

Fig. 3.107. Layout of optimized third-order inline PCMLBF with periodic sawtooth groove centered at (a) f_0 = 5.25 GHz and (b) f_0 = 2.5 GHz.

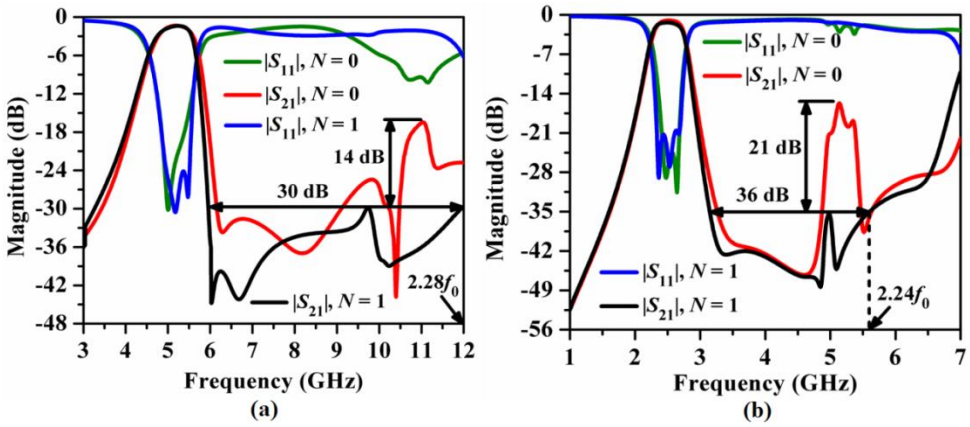

Fig. 3.108. Simulated *S*-parameters plots of the third-order inline PCMLBF with periodic sawtooth grooves centered at (a) f_0 = 5.25 GHz and (b) f_0 = 2.5 GHz.

Figs. 3.108(a)-(b) show a comparison of simulated *S*-parameter plots for inline PCMLBFs with and without grooves. It has been observed that a stopband up to 2.28f_0 with a rejection level of 30 dB for the *C*-band inline filter and a stopband up to 2.24f_0 with a rejection level of 36 dB for the *S*-band inline filter along with improved skirt characteristics have been obtained.

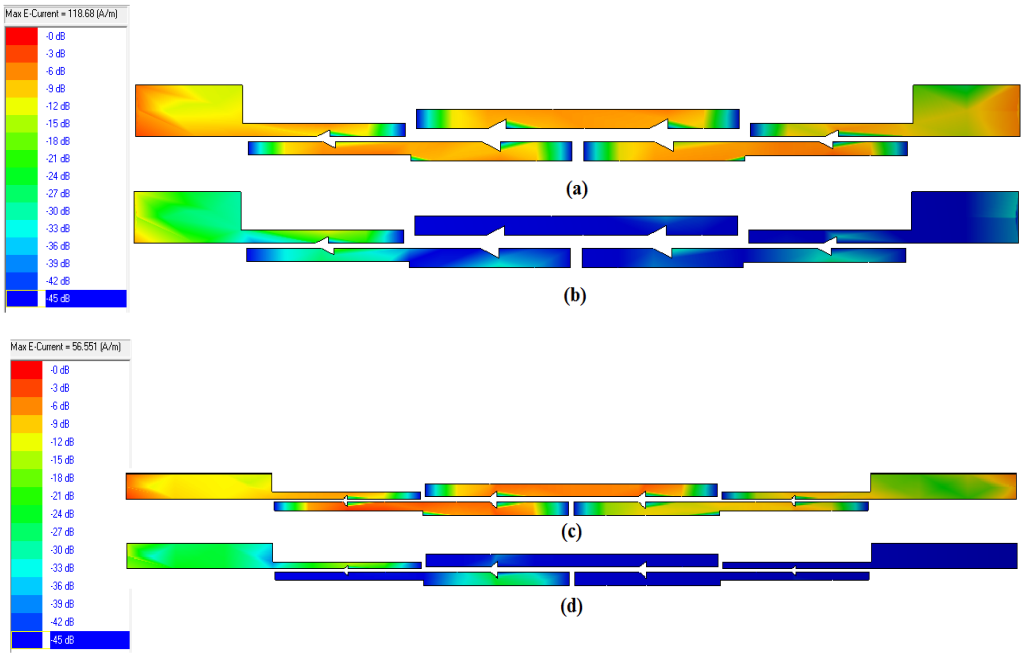

Fig. 3.109. Surface current distribution for the third-order inline PCMLBF with periodic sawtooth groove at (a) f_0 = 5.25 GHz, and (b) $2f_0$ = 10.5 GHz.

For both the filters, the insertion losses become less than 2 dB and the return losses become more than 25 dB. As a result, Figs. 3.109(a)-(d) depicts the surface current distribution for *C*-band and *S*-band inline filters with periodic sawtooth grooves. It has been observed that the surface current distribution is maximum at f_0 = 5.25 GHz and 2.5 GHz due to the passband response and minimum at $2f_0$ = 10.5 GHz and 5 GHz due to the suppression of the harmonic in the stopband. It can be concluded from this section that periodic sawtooth grooves have exhibited improved harmonic suppression performance and skirt characteristics for both the *C*-band and *S*-band folded and inline filters compared to the periodic square and rectangular grooves.

3.14.8. Harmonic Suppression for the Third-Order Folded PCMLBF by Periodic Quarter-elliptical Grooves-Simulation Study

Although the sawtooth periodic groove has exhibited improvement in harmonic suppression performance, the chance of radiation from the straight hypotenuse section and sharp pointed edge of the sawtooth groove still remains for the surface current flow. Accordingly, the sawtooth groove has been modified to a quarter-elliptical groove in which the hypotenuse of the sawtooth groove has been chamfered by a smooth curve to reduce the chance of radiation.

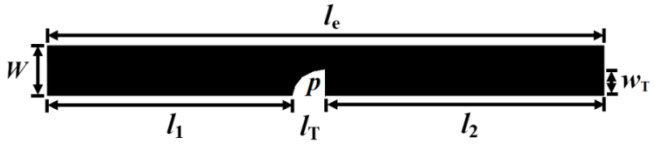

Fig. 3.110. Layout of a single quarter-wavelength line with a single quarter-elliptical periodic groove.

Fig. 3.110 shows the layout of a quarter-wavelength line with a single quarter-elliptical groove placed at the middle. Here, l_e is the even-mode physical length and p is the arc length of the groove. From Fig. 3.110 the odd-mode physical length l_o is obtained as

$$l_o = l_1 + p + w_T + l_2 = l_e + (p + w_T - l_T) \tag{92}$$

According to S. Ramanujan's formula [40] the arc length, p of the quarter-elliptical groove can be written as

$$p = \frac{\pi}{4}\left[3(l_T + w_T) - \sqrt{(3l_T + w_T)(l_T + 3w_T)}\right] \tag{93}$$

Putting (93) in (94) and considering N as the number of such periodic grooves, l_o is written as

$$l_o = l_e + N(p + w_T - l_T) \tag{94}$$

$$l_o = l_e + N\left[\frac{\pi}{4}\left\{3(l_T + w_T) - \sqrt{(3l_T + w_T)(l_T + 3w_T)}\right\} + w_T - l_T\right] \tag{95}$$

If $l_T = w_T = W/2$ and $N = 1$, then $l_o = l_e + 0.7854W$, which is identical to the quarter-circular groove with radius $W/2$. In general, the periodicity of grooves is given by $l/(N+1)$, where l is the length of the resonator and N is the number of grooves. For $N = 2$, the periodicity of grooves is $l/3$ and, for $N = 3$, the periodicity will be $l/4$. It can be clearly understood that $l_o > l_e$ and thus, the odd-mode electrical length increases over that of the even-mode, resulting in the slowdown of the odd-mode phase velocity compared to the even-mode phase velocity. Fig. 3.111 depicts the layout of a unit PCML cell with three periodic quarter-elliptical grooves.

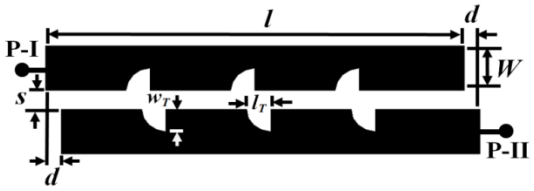

Fig. 3.111. Layout of a pair of unit PCML cell with quarter-elliptical shaped periodic grooves.

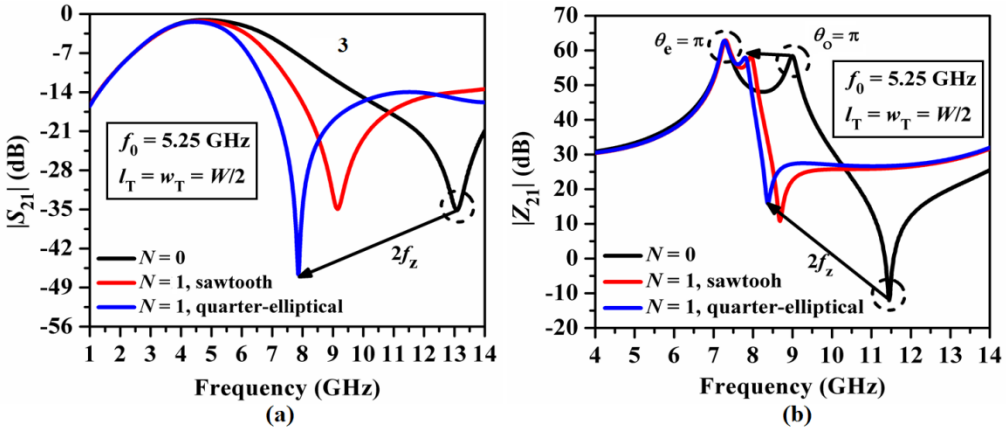

Fig. 3.112. Comparison of simulated resonance characteristics for a unit PCML cell with a single sawtooth and quarter-elliptical groove centered at f_0 = 5.25 GHz: (a) $|S_{21}|$ (dB) and (b) $|Z_{21}|$ (dB).

The resonance characteristics of $|S_{21}|$ (dB) and $|Z_{21}|$ (dB) are compared in Figs. 3.112(a)-(b) between the unit PCML cell centered at f_0 = 5.25 GHz with a single sawtooth and quarter-elliptical groove with dimensions of $l_T = w_T = W/2$ placed in the middle. It has been observed from Fig. 3.112(a) that the second harmonic transmission zero $2f_z$ has been shifted more to the lower frequency region with a decreased attenuation level from 35 dB (N = 0) to 48 dB than that for the sawtooth groove. Furthermore, as shown in Fig. 3.112(b), the odd-mode resonant peak ($\theta_o = \pi$) of the $|Z_{21}|$ (dB) plot shifts to a lower frequency than the sawtooth groove. This clearly justifies the effectiveness of the quarter-elliptical groove to achieve more phase velocity compensation than the sawtooth groove. Accordingly, the general layout of the third-order folded PCMLBF with a single sawtooth groove at the middle has been depicted in Fig. 3.113 with the input port P-I and the output port P-II. A detailed parametric analysis has been performed for the third-order filter centered at 5.25 GHz with different length and width combinations of the groove and with different numbers of grooves. Results have been compared to obtain the optimum dimensions of the grooves as shown in Fig. 3.114(a) for N = 1. It has been observed that a sharp transmission of zero $2f_z$ has occurred at 9.6 GHz with an attenuation level of 53 dB for the groove with dimensions of $l_T = W/2$, $w_T = 3W/4$.

Fig. 3.113. Layout of the third-order folded PCMLBF with a single quarter-elliptical shaped groove.

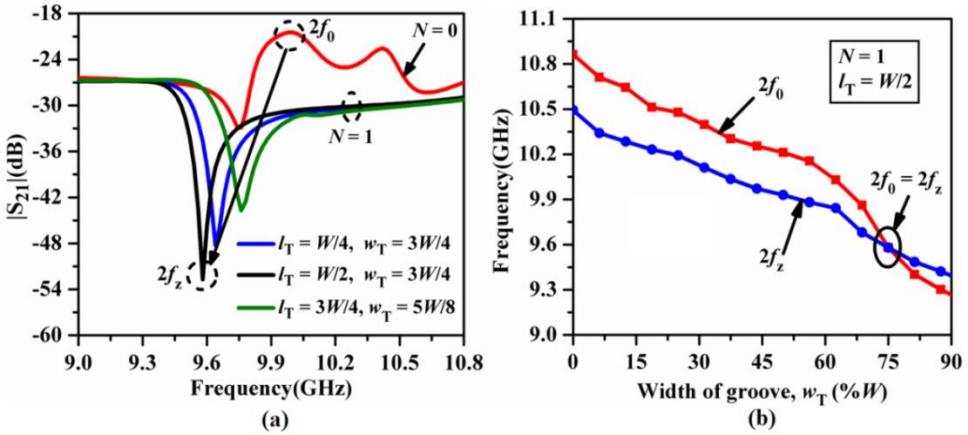

Fig. 3.114. (a) Parametric simulated study for the third-order folded PCMLBF centered at f_0 = 5.25 GHz with a single quarter-elliptical groove having different dimensions, and (b) phase compensation plot.

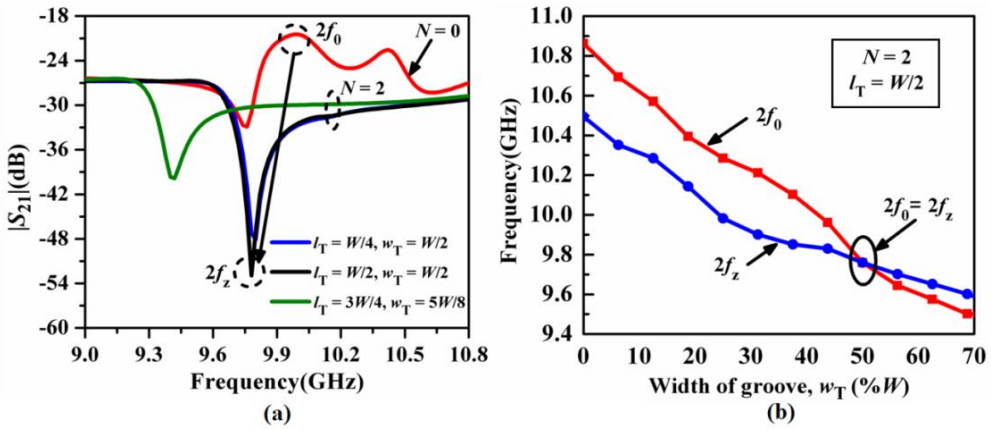

Fig. 3.115. (a) Parametric simulated study for the third-order folded PCMLBF centered at f_0 = 5.25 GHz with two periodic quarter-elliptical grooves having different dimensions, and (b) phase compensation plot.

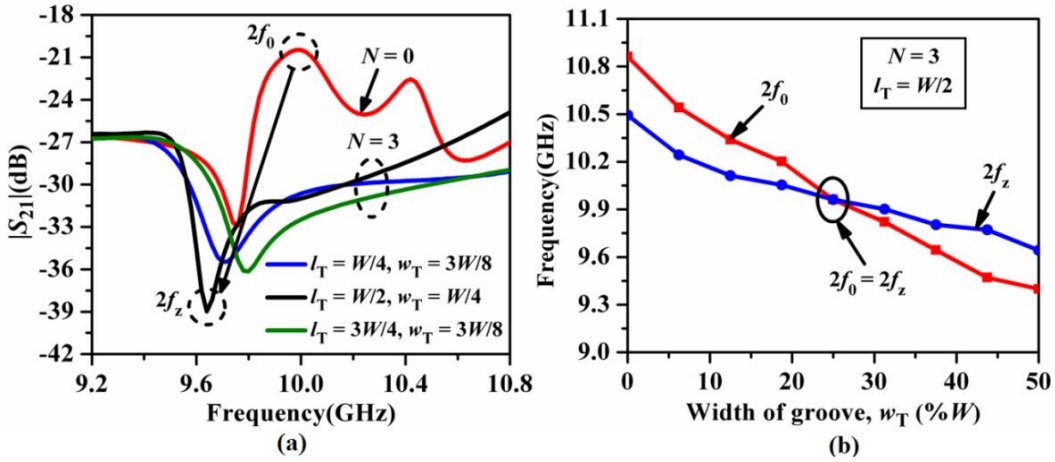

Fig. 3.116. (a) Parametric simulated study for the third-order folded PCMLBF centered at f_0 = 5.25 GHz with three periodic quarter-elliptical grooves having different dimensions, and (b) phase compensation plot.

It is further supported by the phase compensation plot in Fig. 3.114(b), which shows the variations of the second harmonic frequency $2f_0$ and transmission zero 2fz for incremental w_T (%) with $l_T = W/2$. It can be observed that the phase compensation ($2f_0 = 2f_z$) has been achieved for w_T = 75% of W, i.e., for $w_T = 3W/4$. Similarly, a sharp transmission of zero $2f_z$ was observed at 9.75 GHz with an attenuation level of 54 dB for $N = 2$ with dimensions of $l_T = w_T = W/2$, as shown in Figs. 3.115(a)-(b), and at 9.63 GHz with an attenuation level of 40 dB for $N = 3$ with dimensions of $l_T = W/2$, $w_T = W/4$, as shown in Figs. 3.116(a)-(b). It may be further noticed that as the number of grooves has been increased, the value of w_T has also been decreased along with an increment of the attenuation level at $2f_z$. This happens due to the introduction of additional cross-coupling between the adjacent cells with an increased periodicity of grooves.

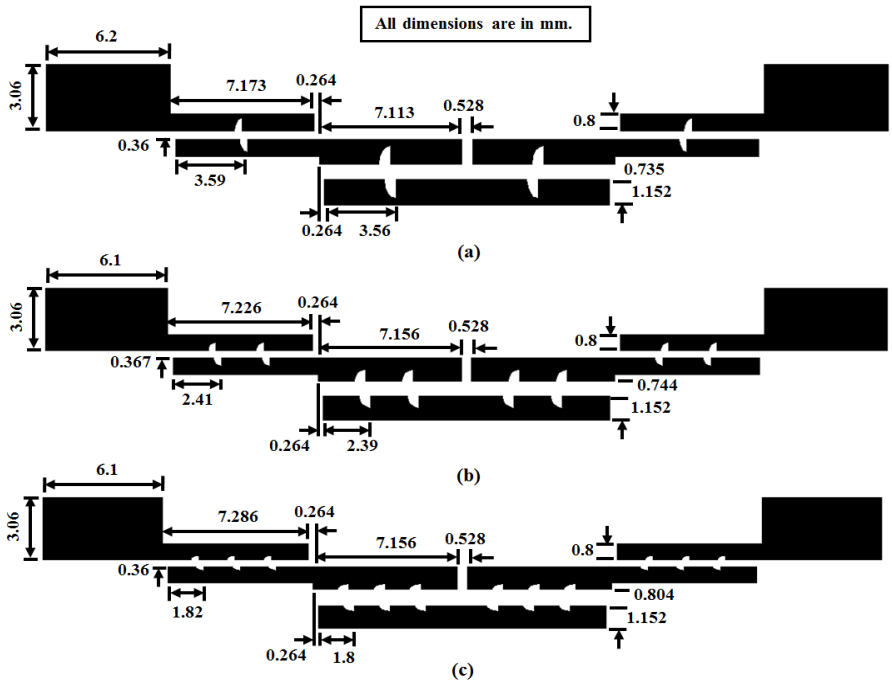

Fig. 3.117. Layout of optimized third-order folded PCMLBFs with periodic quarter-elliptical grooves centered at f_0 = 5.25 GHz: (a) $N = 1$, (b) $N = 2$ and (c) $N = 3$.

Finally, Figs. 3.117(a)-(c) show the optimized dimensions for the third-order folded filters with N = 1, 2, and 3 and f_0 = 5.25 GHz. The overall size of the filters is 42.03 mm × 6.46 mm, i.e., 271.47 mm^2 or $1.35\lambda_g \times 0.21\lambda_g$ for $N = 1$, 42.02 mm × 6.53 mm, i.e., 274.39 mm^2 or $1.35\lambda_g \times 0.21\lambda_g$ for $N = 2$, and 41.6 mm × 5.38 mm, i.e., 223.81 mm^2 or $1.35\lambda_g \times 0.21\lambda_g$ for $N = 3$. Accordingly, size reductions of 58.9%, 58.4%, and 66.1% have been achieved over the conventional filters without grooves having the same specifications.

3.14.8.1. Fabricated Prototype

Prototypes for the designed folded filters with N = 1, 2, and 3 are shown in Figs. 3.118(a)-(c). All prototypes have been tested experimentally on the Agilent N9928A vector network analyzer by following the experimental procedure mentioned in 3.14.4.1.

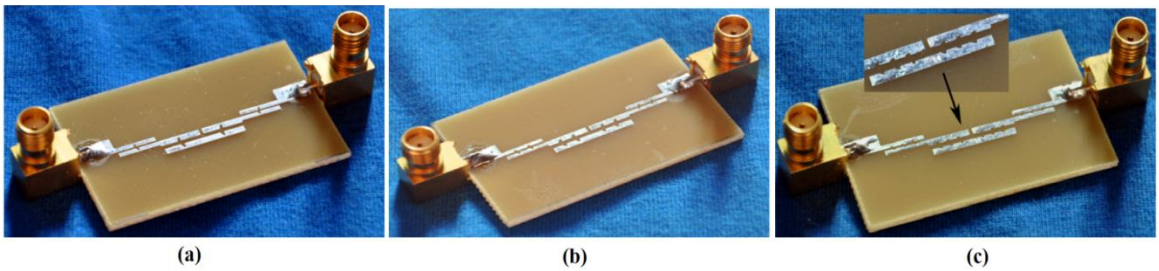

Fig. 3.118. Fabricated prototypes of the third-order PCMLBFs with periodic quarter-elliptical grooves centered at f_0 = 5.25 GHz: (a) N = 1, (b) N = 2, and (c) N = 3 [27].

3.14.8.2. Comparison of EM simulation vs. Measurement Results

Figs. 3.119(a)-(c) show a comparison of the simulated and measured S-parameter plots.

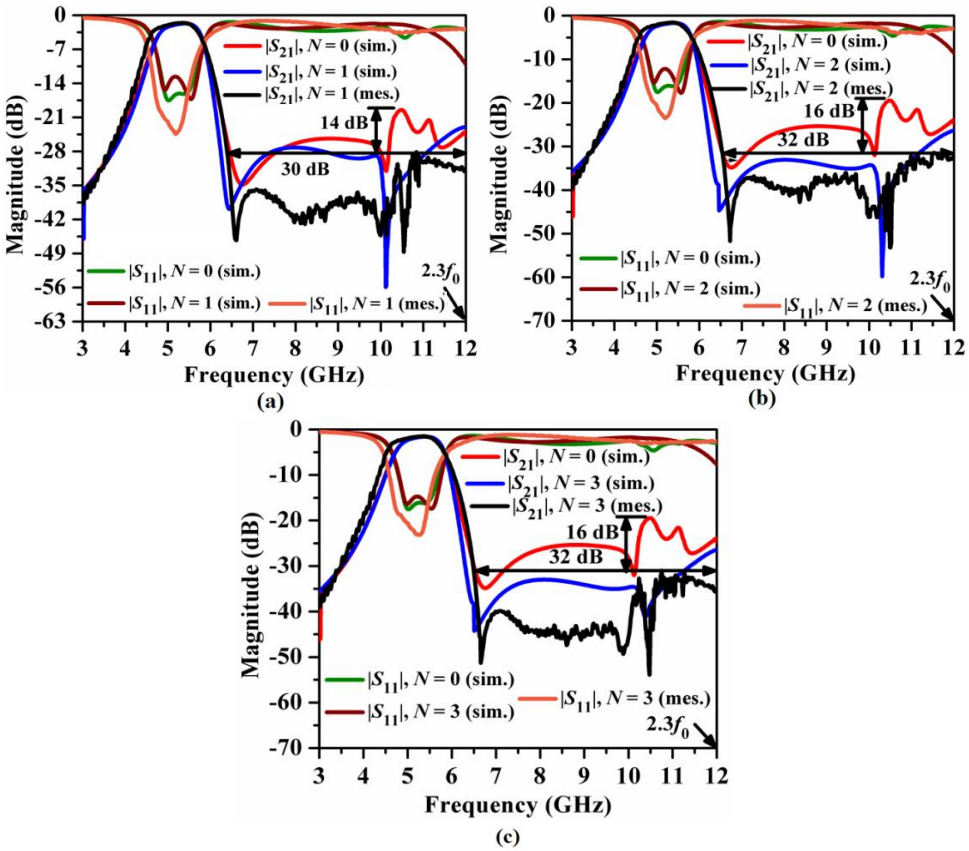

Fig. 3.119. Comparison of the simulated vs. measured S-parameters plots of the third-order folded PCMLBFs with periodic quarter-elliptical grooves centered at f_0 = 5.25 GHz: (a) N = 1, (b) N = 2, (c) N = 3 [27].

The measured and simulated $|S_{21}|$ plots are in good agreement in the passband, as shown in Fig. 3.119(a). For all the filters, a sharp transmission zero has been obtained at the upper passband edge with an attenuation level of more than 45 dB, justifying the improvement of the skirt characteristics with quarter-elliptical grooves. Moreover, stopbands up to $2.3f_0$ with rejection levels below 30 dB have been recorded in the measured responses for all the filters. It has been further noticed that flat stopbands from the upper passband edges up to $2f_0$ with rejection levels below 36 dB have been obtained for the filters. Besides, measured insertion loss of less than 1.4 dB and return loss of better than 20 dB have been obtained. The surface current distributions for the *C*-band folded filter with $N = 3$ are shown in Figs. 3.120(a)-(b). It has been discovered that the surface current is strongest at $f_0 = 5.25$ GHz (passband) and weakest at $2f_0 = 10.5$ GHz (stopband).

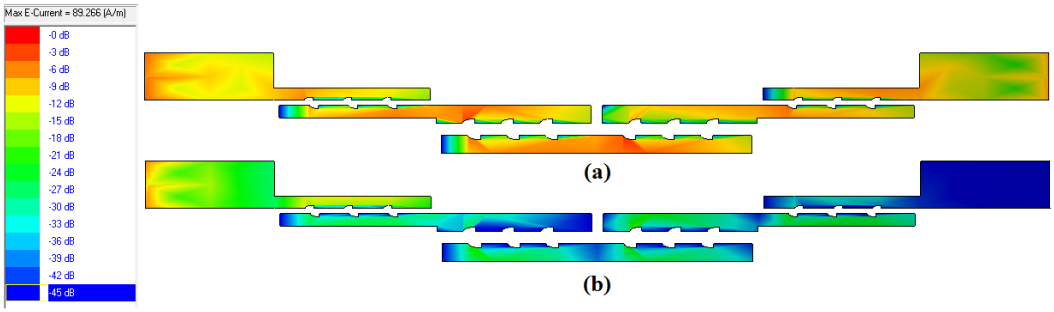

Fig. 3.120. Surface current distribution for the third-order folded PCMLBF with three periodic quarter-elliptical grooves at (a) $f_0 = 5.25$ GHz, and (b) $2f_0 = 10.5$ GHz.

The optimized dimensions for third-order folded filters with periodic quarter-elliptical grooves centered at 2.5 GHz are shown in Figs. 3.121(a)-(c). The study of quarter-elliptical grooves has been extended to the *S*-band folded filters centered at 2.5 GHz. The parametric study of Figs. 3.122(a)-(c) yielded the optimum dimensions of the quarter-elliptical grooves as $l_T = W/4$, $w_T = 3W/4$ for $N = 1$, $l_T = W/2$, $w_T = W/4$ for $N = 2$, and $l_T = 3W/4$, $w_T = W/4$ for $N = 3$. As a result, Figs. 3.122(a)-(c) show the optimized layouts of the third-order folded PCMLBFs with periodic quarter-elliptical grooves centered at $f_0 = 2.5$ GHz: (a) $N = 1$, (b) $N = 2$, and (c) $N = 3$. The overall dimensions of the filters are 96.2 mm × 7.0 mm, which equates to 672.44 mm^2 or $1.41\lambda_g \times 0.1\lambda_g$ for $N = 1$, 96.9 mm × 7.09 mm, which equates to 687.02 mm^2 or $1.42\lambda_g \times 0.1\lambda_g$ for $N = 2$, and 96.4 mm × 7.07 mm, which equates to 681.55 mm^2 or $1.41\lambda_g \times 0.1\lambda_g$ for $N = 3$. Accordingly, size reductions of 47.9%, 46.8%, and 47.2% have been obtained, respectively, over the conventional filters.

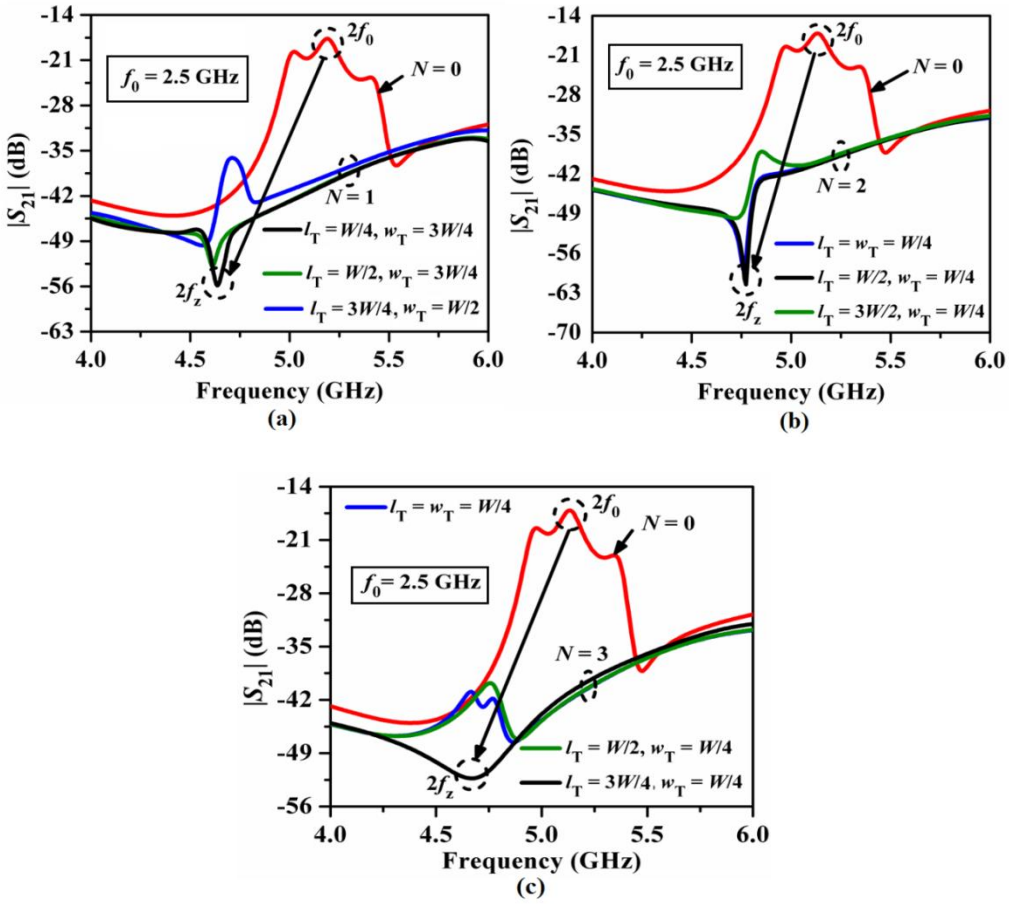

Fig. 3.121. (a) Parametric simulated study for the third-order folded PCMLBF centered at f_0 = 2.5 GHz with periodic quarter-elliptical grooves having different dimensions.

The simulated *S*-parameter plots of the folded PCMLBFs with and without grooves with the optimum dimensions are shown in Figs. 3.123(a)-(c). It has been observed that stopbands up to 2.4f_0 with rejection levels of 32 dB, 32 dB, and 33 dB for N = 1, 2, and 3 have been obtained respectively. Moreover, sharp transmission zeros have been obtained at 2f_0 = 5 GHz with attenuation levels of more than 50 dB for all filters. The surface current distributions for the folded filter at f_0 = 2.5 GHz and 2f_0 = 5 GHz are shown in Figs. 3.124(a)-(b). The currents flow with large strength for the passbands and with weak strength for the stopbands for all the filters due to their harmonics suppression performance.

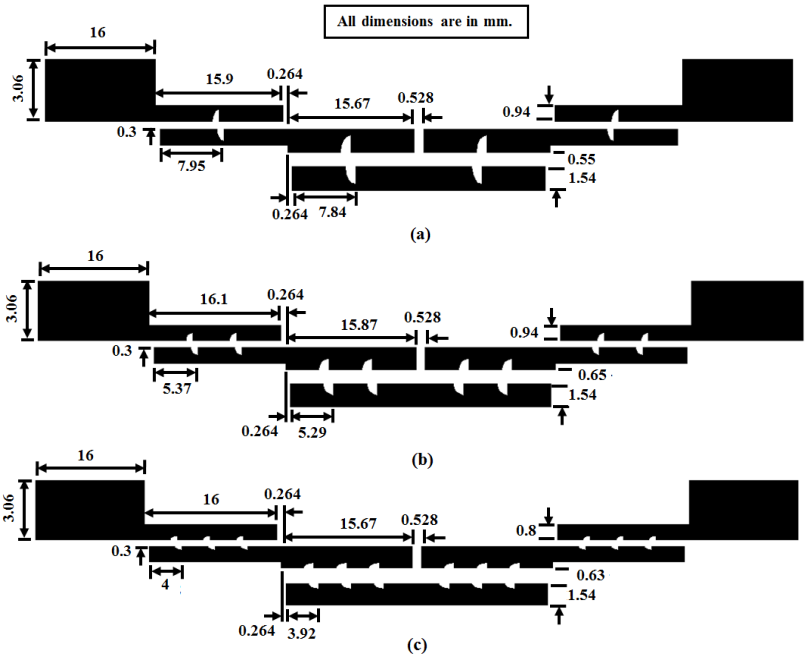

Fig. 3.122. Layout of optimized third-order folded PCMLBFs with periodic quarter-elliptical grooves centered at f_0 = 2.5 GHz: (a) N = 1, (b) N = 2, and (c) N = 3.

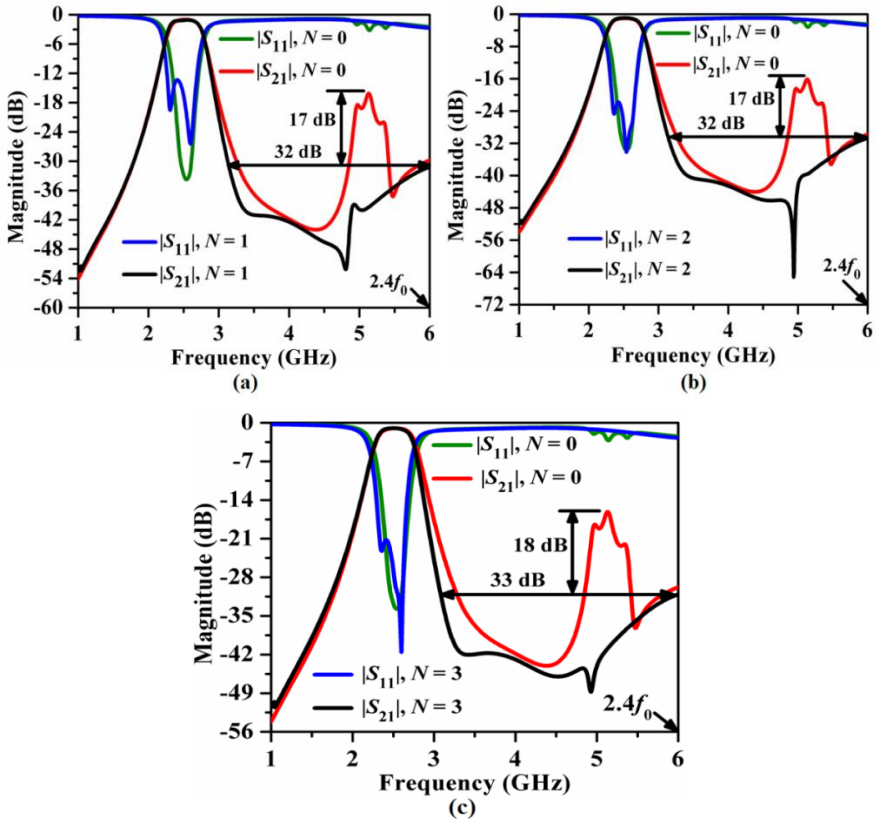

Fig. 3.123. Comparison of the simulated *S*-parameters plots of the third-order folded PCMLBFs with periodic quarter-elliptical grooves centered at f_0 = 2.5 GHz: (a) N = 1, (b) N = 2, and (c) N = 3.

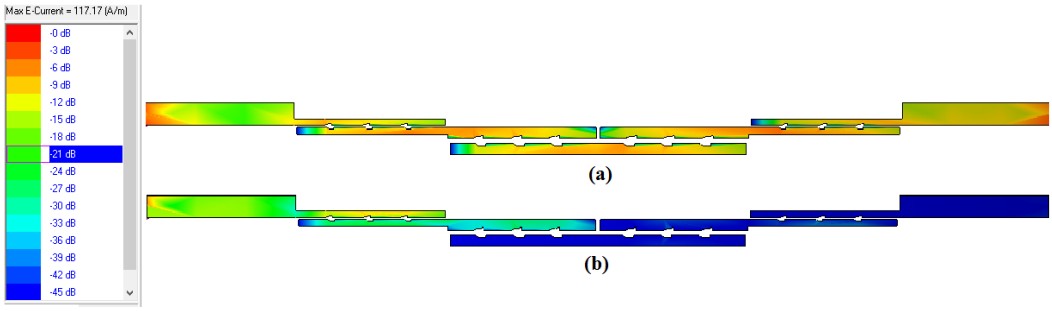

Fig. 3.124. Surface current distribution for the third-order folded PCMLBF with three periodic quarter-elliptical grooves respectively at (a) f_0 = 2.5 GHz, and (b) $2f_0$ = 5 GHz.

3.14.9. Third-Order Inline PCMLBF by Periodic Quarter-elliptical Grooves

By following the same methodology, the study of periodic quarter-elliptical grooves has been extended to the third-order inline PCMLBF centered at f_0 = 5.25 GHz. As a result of the parametric study shown in Figs. 3.125(a)-(c), the optimum dimensions of the quarter-elliptical grooves are $l_T = W/4$, $w_T = W/2$ for N = 1, $l_T = 3W/4$, $w_T = W/4$ for N = 2, and $l_T = W/4$, $w_T = W/2$ for N = 3.

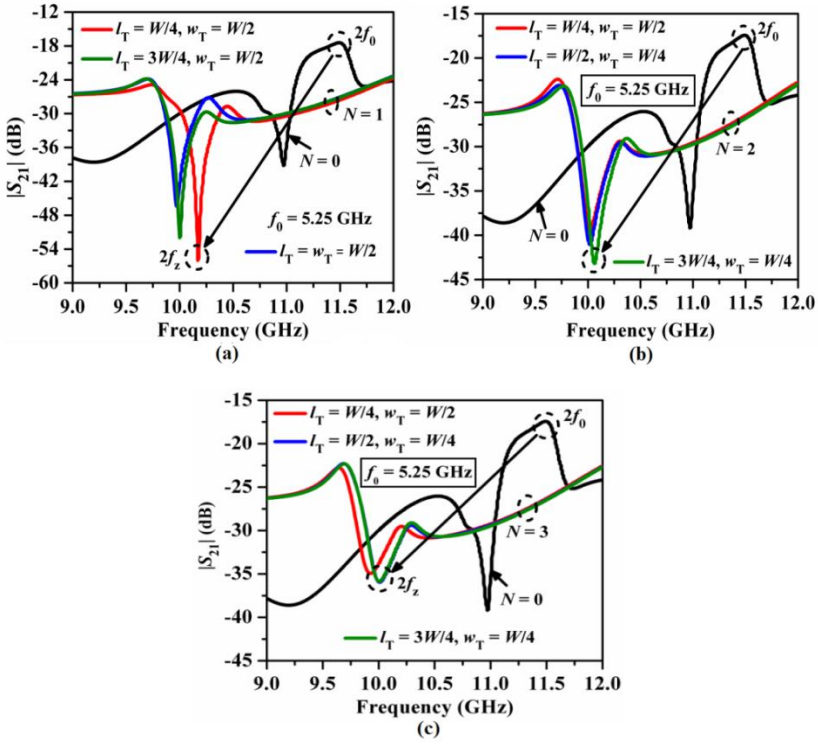

Fig. 3.125. (a) Parametric simulated study for the third-order inline PCMLBF centered at f_0 = 5.25 GHz with periodic quarter-elliptical grooves having different dimensions.

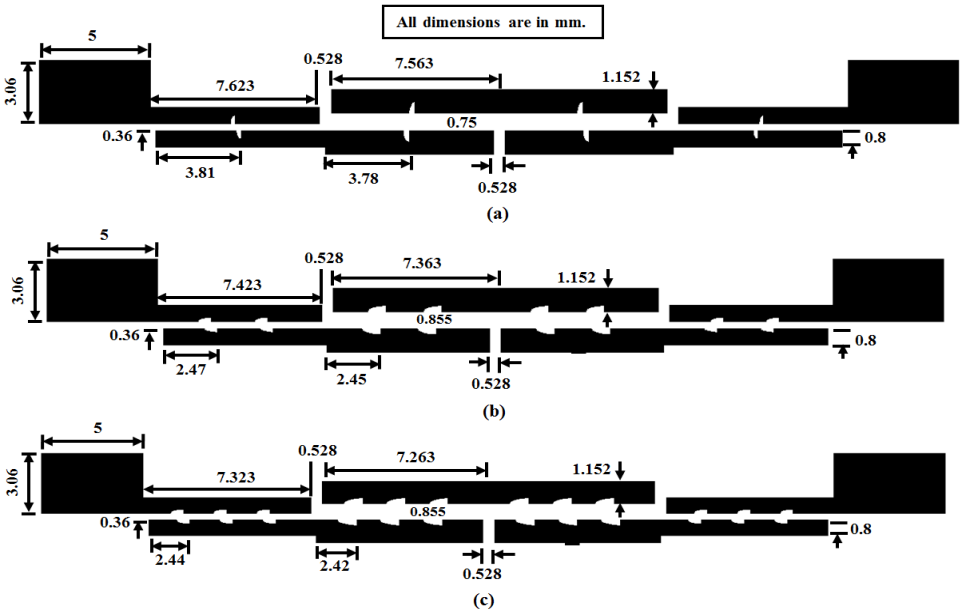

Fig. 3.126. Layout of optimized third-order folded PCMLBFs with periodic quarter-elliptical grooves centered at f_0 = 5.25 GHz: (a) N = 1, (b) N = 2 and (c) N = 3.

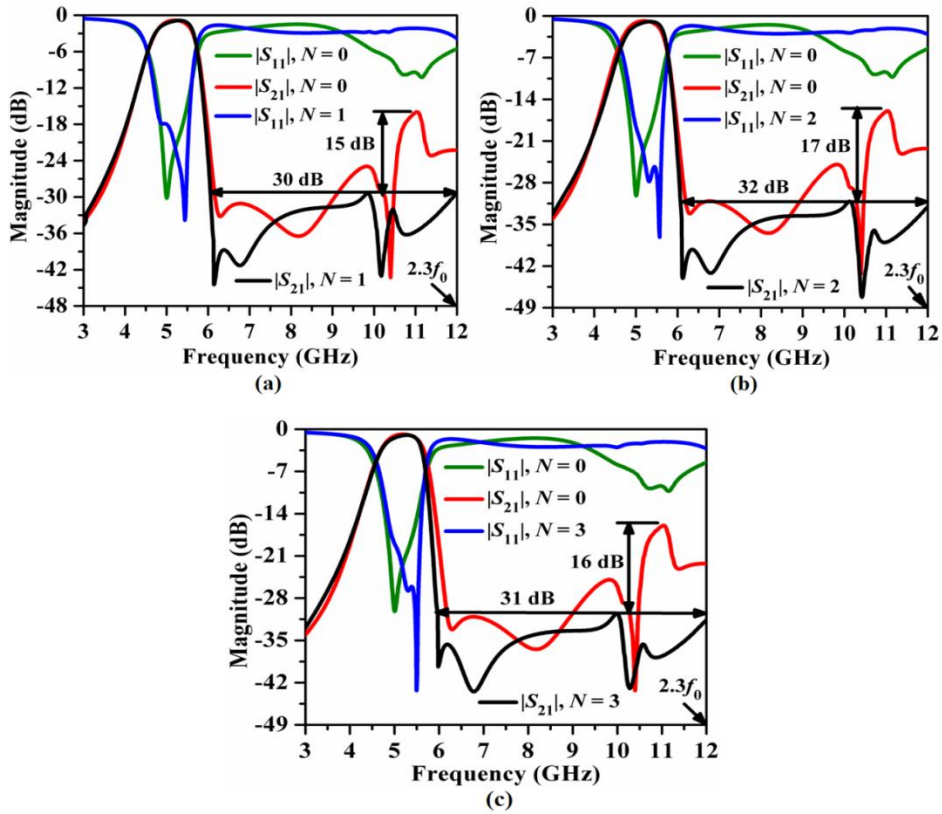

Fig. 3.127. Comparison of the simulated *S*-parameters plots of the third-order inline PCMLBFs with periodic quarter-elliptical grooves centered at f_0 = 5.25 GHz: (a) N = 1, (b) N = 2, (c) N = 3.

Finally, the optimized dimensions for the third-order inline filters with grooves are shown in Figs. 3.126(a)-(c) after optimizing the design parameters. The overall sizes of the filters are 41.43 mm × 4.57 mm, i.e., 189.42 mm^2 or 1.33λ_g × 0.15λ_g for N = 1, 40.63 mm × 4.57 mm, i.e., 185.68 mm^2 or 1.31λ_g × 0.15λ_g for N = 2, and 40.23 mm × 4.57 mm, i.e., 183.85 mm^2 or 1.3λ_g × 0.15λ_g for N = 3. The simulated S-parameter plots of inline PCMLBFs with and without grooves with the optimum dimensions are shown in Figs. 3.127(a)-(c). It has been observed that stopbands up to 2.3f_0 with rejection levels of 30 dB, 32 dB, and 31 dB for N = 1, 2 and 3 have been obtained respectively. The surface current distributions for the folded filters with grooves have been depicted in Fig. 3.128(a)-(b) for N = 3.

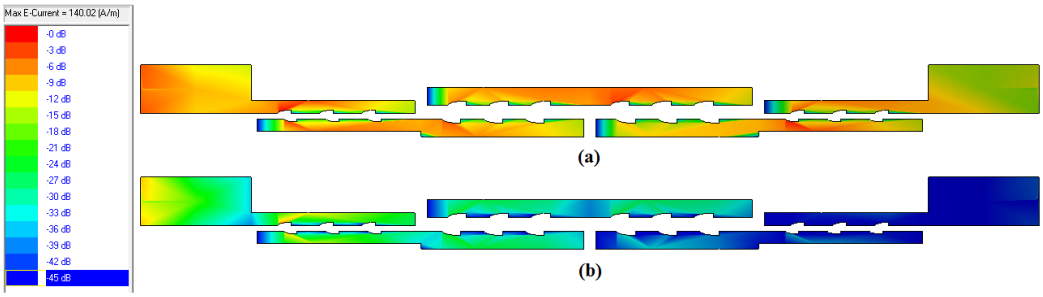

Fig. 3.128. Surface current distribution for the third-order inline PCMLBF with three quarter-elliptical grooves at (a) f_0 = 5.25 GHz, and (b) 2f_0 = 10.5 GHz.

It has been observed that there has been a higher degree of concentration of surface current at f_0 = 5.25 GHz (passband) and it becomes minimum at 2f_0 = 10.5 GHz (stopband) due to the harmonic suppression. Following that, the parametric study for the inline filters with quarter-circular grooves centered at f_0 = 2.5 GHz is shown in Figs. 3.129(a)-(c) for N = 1, 2, and 3 respectively. Accordingly, the optimum dimensions of the grooves have been selected as l_T = W/2, w_T = 3W/4 for N = 1, l_T = W/2, w_T = W/4 for N = 2, and l_T = 3W/4, w_T = W/4 for N = 3. Finally, optimized dimensions for third-order inline filters with grooves are shown in Figs. 3.130 (a)-(c). The overall sizes of the filters are 95.4 mm × 4.87 mm, i.e., 464.6 mm^2 or 1.4λ_g × 0.07λ_g for N = 1, 98.6 mm × 4.9 mm, i.e., 483.14 mm^2 or 1.44λ_g × 0.07λ_g for N = 2, and 96.2 mm × 4.9 mm, i.e., 471.38 mm^2 or 1.41λ_g × 0.1λ_g for N = 3. Accordingly, size reductions of 64%, 62.6%, and 63.5% have been obtained, respectively, over the conventional filters.

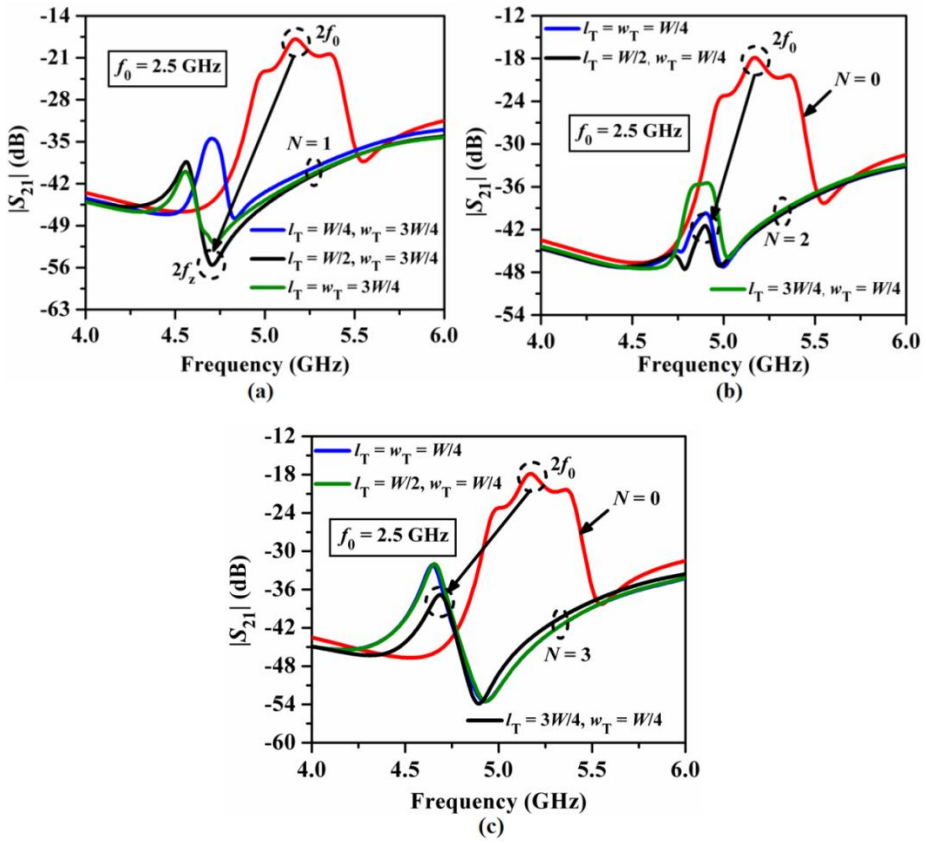

Fig. 3.129. (a) Parametric simulated study for the third-order inline PCMLBF centered at f_0 = 2.5 GHz with periodic quarter-elliptical grooves having different dimensions.

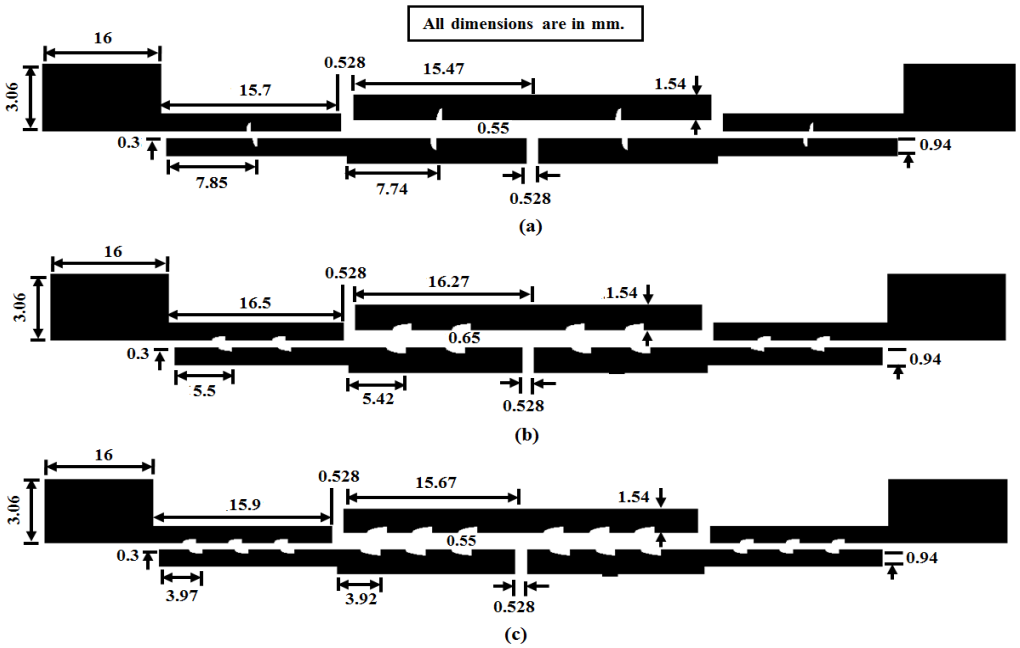

Fig. 3.130. Layout of optimized third-order inline PCMLBFs with periodic quarter-elliptical grooves centered at f_0 = 2.5 GHz: (a) N = 1, (b) N = 2 and (c) N = 3.

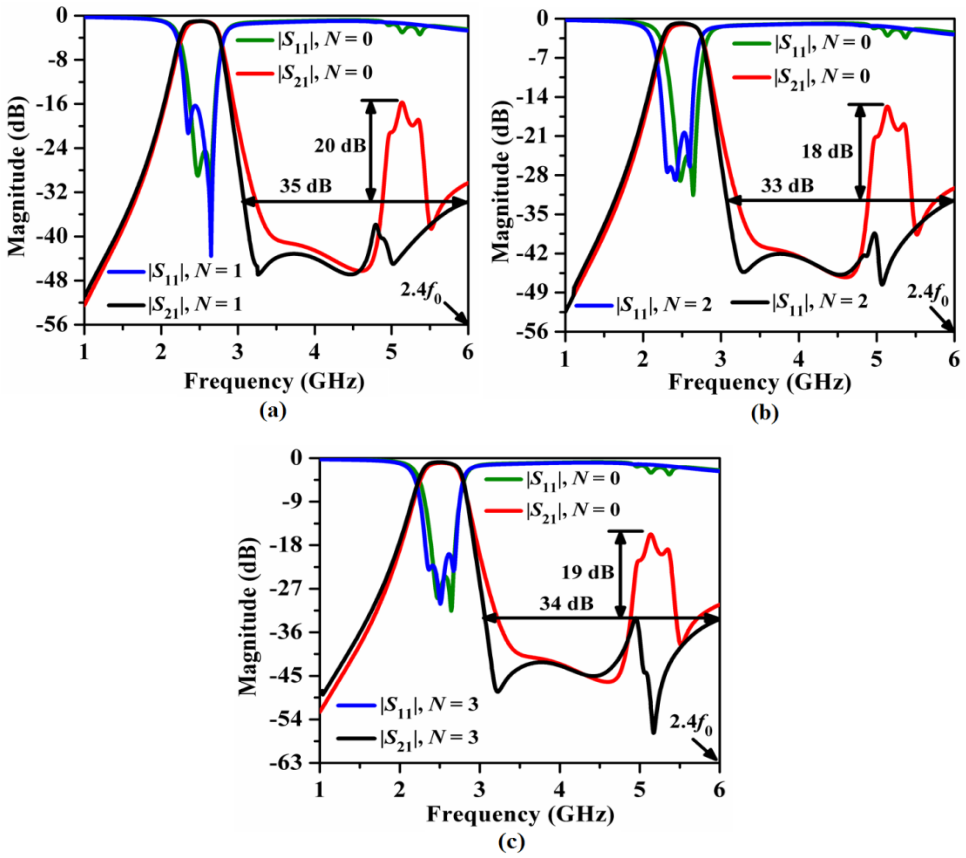

Fig. 3.131. Comparison of the simulated *S*-parameters plots of the third-order inline PCMLBFs with periodic quarter-elliptical grooves centered at f_0 = 2.5 GHz: (a) N = 1, (b) N = 2, and (c) N = 3.

The simulated *S*-parameter plots of inline PCMLBFs with and without grooves with the optimum dimensions are shown in Figs. 3.131(a)-(c). It has been observed that stopbands up to $2.4f_0$ with rejection levels of 35 dB, 33 dB, and 34 dB for N = 1, 2 and 3 have been obtained respectively. The attenuation levels at $2f_0$ have been suppressed to 20 dB, 18 dB, and 19 dB, respectively for the filters. Estimated insertion losses of less than 1.5 dB and return losses greater than 25 dB Figs. 3.132(a)-(b) show the surface current distributions for the N = 3 filter at f_0 = 2.5 GHz and $2f_0$ = 5 GHz. The currents flow with large strength for the passbands and in weak strength for the stopbands for all the filters due to their harmonics suppression performance. Table 3.12 and Table 3.13 illustrate the calculated values of all the design parameters as defined in section 3.10.

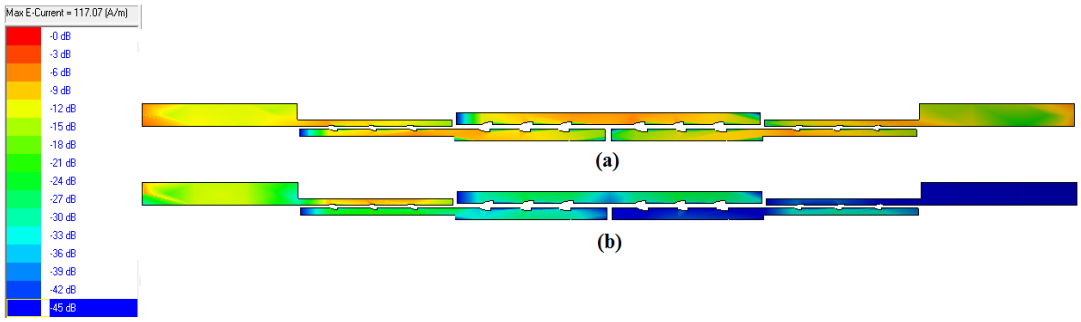

Fig. 3.132. Surface current distribution for the third-order inline PCMLBF with three periodic quarter-elliptical grooves respectively at (a) f_0 = 5.25 GHz, and (b) $2f_0$ = 10.5 GHz.

Table 3.12. Comparison of all designed folded PCMLBFs with grooves.

f_o (GHz)	Type of periodic groove	ξ (dB/GHz)	*SBRL* (dB)	*SBW* (x f_0)	*RSB*	*SF*	*NCS*	*AF*	*FOM*
5.25	square	45	26	2.06	1.27	2.6	0.28	1	530.68
	rectangular	15	30	2.29	1.34	3	0.27		223.33
	sawtooth	45	35	2.13	1.29	3.5	0.27		752.5
	quarter-elliptical	27	32	2.3	1.28	3.2	0.28		394.97
2.5	square	67.5	25.5	2.68	1.4	2.55	0.14		1721.25
	rectangular	54	28	2.68	1.37	2.8	0.13		1593.42
	sawtooth	54	36	2.5	1.3	3.6	0.143		1767.27
	quarter-elliptical	67.5	33	2.4	1.3	3.3	0.1		2895.75

Table 3.13. Comparison of all designed inline PCMLBFs with grooves.

f_o (GHz)	Type of periodic groove	ξ (dB/GHz)	*SBRL* (dB)	*SBW* (x f_0)	*RSB*	*SF*	*NCS*	*AF*	*FOM*
5.25	square	54	27	2.29	1.32	2.7	0.18	1	1069.2
	rectangular	67.5	31	2.29	1.34	3.1	0.19		1475.8
	sawtooth	54	30	2.28	1.33	3.0	0.2		1077.3
	quarter-elliptical	54	32	2.3	1.33	3.2	0.19		1209.6
2.5	square	90	30	2.68	1.43	3.0	0.1		3861
	rectangular	90	32	2.6	1.38	3.2	0.1		3974.4
	sawtooth	90	36	2.24	1.244	3.6	0.1		4030.56
	quarter-elliptical	90	35	2.4	1.33	3.5	0.1		4189.5

It has been noticed that the Figure of Merit (*FOM*) becomes maximum for the *C*-band folded filter with a square groove and for the *S*-band folded filter with a quarter-elliptical groove. Similarly, the Figure of Merit (*FOM*) becomes maximum for the *C*-band inline filter with rectangular groove and for the *S*-band inline filter with quarter-elliptical groove. From this section, it has been concluded that periodic square, rectangular, sawtooth, and quarter-elliptical grooves have efficiently suppressed the second harmonic attenuation level below 30 dB with stopband bandwidth extended up to $2.3f_0$.

3.15. Harmonic Suppression by Periodic Corrugations

3.15.1. Folded PCMLBF with Periodic Square Shaped Corrugations-Simulation Study

From the study of harmonics suppression by periodic grooves, it has been noticed that the suppression level of the harmonics has been restricted to 30 dB up to $2.3f_0$. In order to obtain an improvement in the suppression level by providing more slow-wave structure for the odd-mode, periodic corrugations have been investigated in this section. Due to the corrugated structure [22], the even and odd modes of symmetric PCMLs are turned into *c*-mode and π-mode, respectively. The general layout of a PCML cell with square periodic corrugations has been depicted in Fig. 3.133, where l = length of the line, l_T = length of the slot, w_T = width of the slot, w_B = width of the base line segment on which the slots are to be placed periodically, S_T = coupling gap between the two corrugated parallel line segments, d = length correction due to open-end fringe field effects. Maximum π -mode energy propagates along the central corrugated slots with a lower degree of phase constant β_π, while c-mode energy propagates along the outer metallic edge of the PCML with a higher degree of phase constant β_c. The effective electrical length of the π-mode increases over that of the *c*-mode. This phenomenon is depicted in Figs. 3.134(a)-(b), which show the distribution of surface current density vectors.

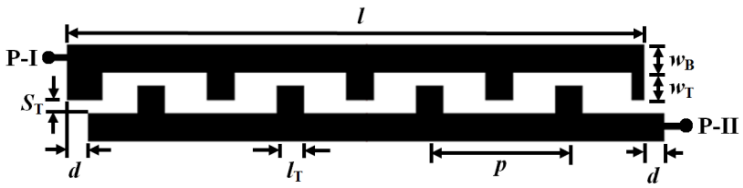

Fig. 3.133. Layout of a unit PCML cell with periodic square shaped corrugations.

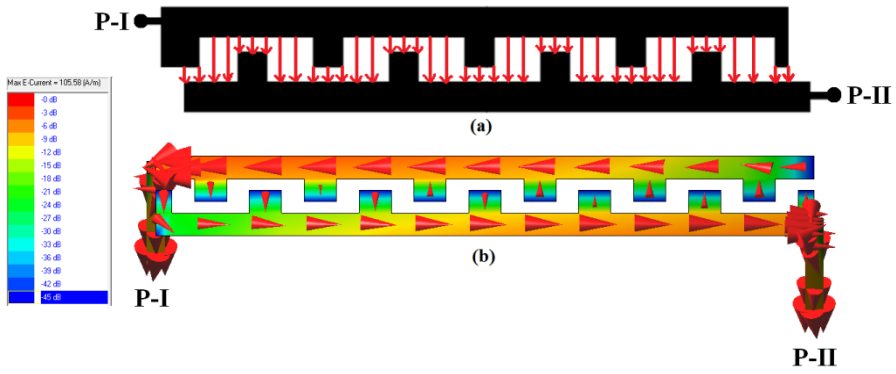

Fig. 3.134. (a) Distribution of electric filed lines for a unit PCML cell with periodic square shaped corrugations, and (b) distribution of surface current distribution at f_0 = 5.25 GHz.

Thus, phase velocity compensation between the π - and c-modes has been effectively achieved by properly selecting the optimum number of periodic corrugations with their optimum dimensions. Figs. 3.135(a) and (b) show a comparison of wideband resonance characteristics of $|S_{21}|$ dB and $|Z_{11}|$ dB for a unit PCML cell tuned at f_0 = 5.25 GHz with periodic square-shaped corrugations. It has been observed from Fig. 3.135(a) that the second harmonic transmission zero frequency $2f_z$ has been shifted to a lower frequency region with incremental values of the pair of periodic corrugations (N). The reason for this is that the effective electrical length of the -mode is greater than that of the c-mode. Likewise, the resonant peak (θ_o) of π-mode in the $|Z_{21}|$ (dB) plot has been shifted towards the c-mode resonant peak (θ_e) in Fig. 3.135 (b), exhibiting the phase compensation between these two modes. Accordingly, three different parametric studies for the corrugations have been performed for C-band filter to understand the effects of variations of different parameters such as S_T (Fig. 3.136(a)), l_T (Fig. 3.136(b)), and w_T (Fig. 3.136(c)).

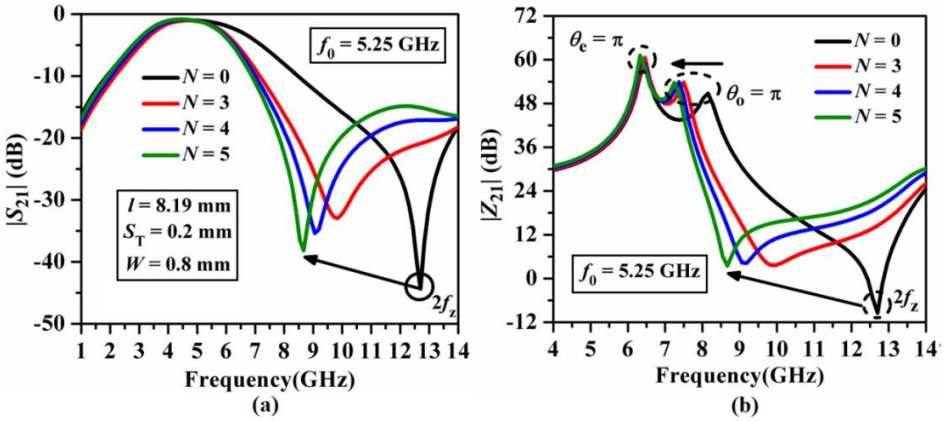

Fig. 3.135. Comparison of simulated resonance characteristics for a unit PCML cell centered at f_0 = 5.25 GHz with periodic square shaped corrugations: (a) $|S_{21}|$ (dB), and (b) $|S_{11}|$ (dB).

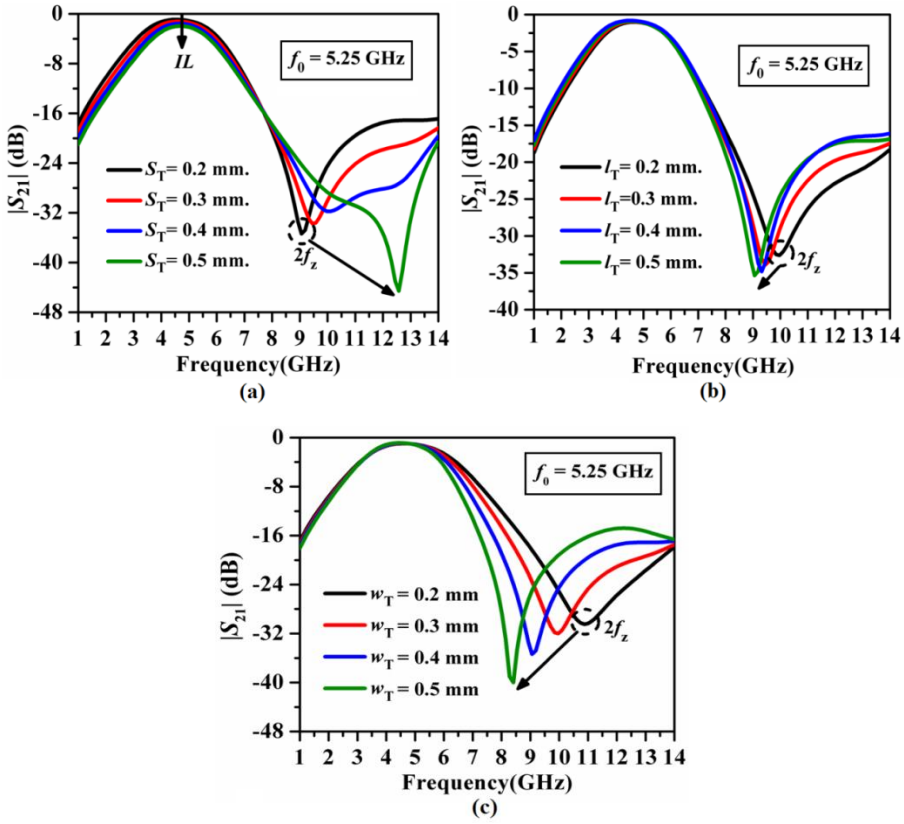

Fig. 3.136. Variations of simulated $|S_{21}|$ (dB) for a unit PCML cell centered at f_0 = 5.25 GHz with periodic square shaped corrugations for (a) different values of S_T (mm), (b) different values of l_T (mm), and (c) different values of w_T (mm), N = 5, w_B = 0.4 mm.

From Fig. 3.136 (a), it has been noticed that the location of $2f_z$ has been shifted to a higher frequency with a decrement in its attenuation level as the value of S_T increases with a constant value of l_T = w_T = 0.4 mm. This is due to the fact that the degree of coupling between the corrugated lines reduces with incremental values of S_T. Thus, the value of S_T should be kept as low as practicable. Moreover, from Fig. 3.136(b), it has been noticed that the location of $2f_z$ has been shifted to a lower frequency region with a degradation in the attenuation level as the value of l_T increases for a constant value of S_T = 0.2 mm and w_T = 0.4 mm. This is because the corrugations come closer to each other, increasing the cross-coupling between the adjacent slots. However, from Fig. 3.136 (c), it has been noted that the attenuation level at $2f_z$ has been reduced rapidly with the shifting of $2f_z$ to a lower frequency region as the value of w_T increases for constant values of S_T = 0.2 mm and l_T = 0.4 mm. This is due to the fact that the depth of the slots is increased, resulting in a slow propagation rate of the π-mode signals through the central corrugations.

Accordingly, the square corrugations have been employed for the third-order folded PCMLBF as in Fig. 3.137. According to the parametric study shown in Figs. 3.138(a)-(c), transmission zero $2f_z$ occurred with minimum attenuation levels of $l_T = w_T = W/2$ for $N = 3$, and $l_T = W/4$, $w_T = W/2$ for $N = 4$ and 5, respectively. Thus, these dimensions of the corrugations have been chosen as the optimum values. The optimized dimensions of the final folded filters are shown in Figs. 3.139(a)-(c). The overall sizes of the filters are 42.94 mm × 6.0 mm, i.e., 257.64 mm^2 or $1.34\lambda_g \times 0.19\lambda_g$ for $N = 3$, 42.42 mm × 6.06 mm, i.e., 257.07 mm^2 or $1.32\lambda_g \times 0.19\lambda_g$ for $N = 4$, and 42.42 mm × 6.1 mm, i.e., 258.76 mm^2 or $1.32\lambda_g \times 0.19\lambda_g$ for $N = 5$.

Fig. 3.137. General layout diagram for the third-order PCMLBF with periodic square shaped corrugations.

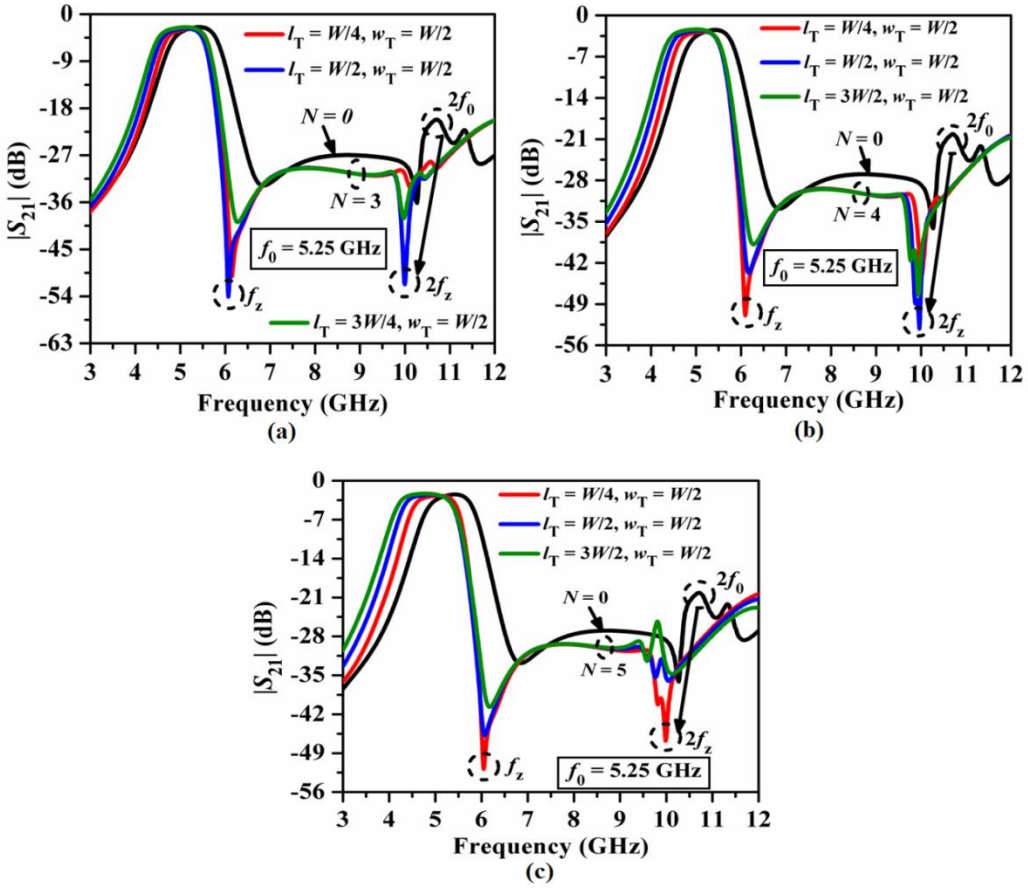

Fig. 3.138. Parametric simulated study for the folded PCMLBF centered at $f_0 = 5.25$ GHz with periodic square shaped corrugations: (a) $N = 3$, (b) $N = 4$, and (c) $N = 5$.

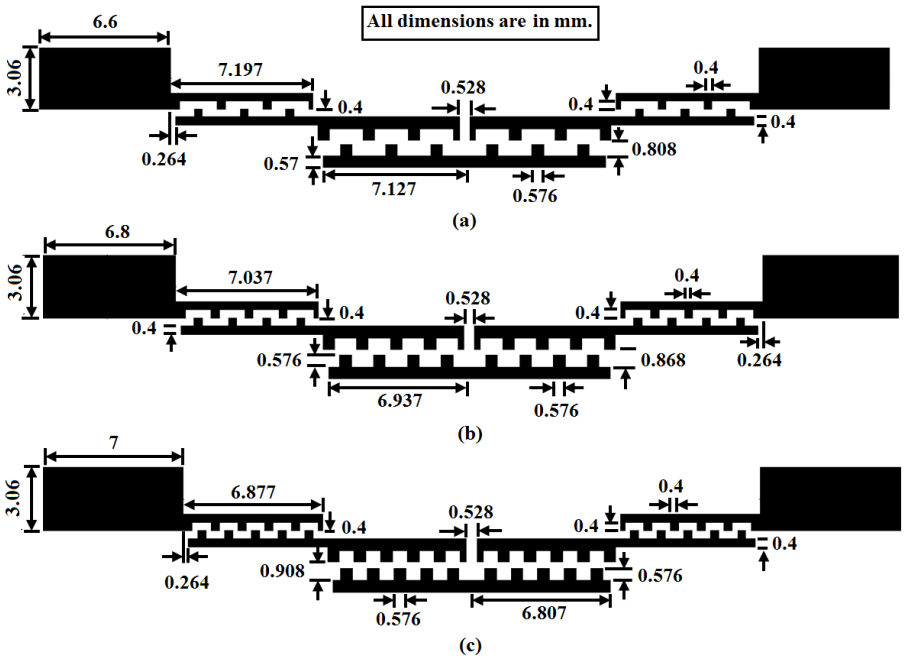

Fig. 3.139. Optimized layout of the folded PCMLBF centered at f_0 = 5.25 GHz with periodic square shaped corrugations: (a) N = 3, (b) N = 4, and (c) N = 5.

Accordingly, size reductions of 61%, 61.1% and 60.8% have been obtained respectively over the conventional filters. Figs. 3.140(a)-(b) compare the simulated *S*-parameters plots for all the folded filters with corrugations and that of without corrugations. Therefore, it has been observed that the maximum stopband bandwidth up to $2.1f_0$ with the rejection level of 33 dB have been obtained for N = 3. Two sharp transmission zeros f_z and $2f_z$ have been observed at 6.4 GHz and 10.5 GHz respectively with an attenuation level of 60 dB and 48 dB. For all the designed filters the return loss becomes more than 16 dB.

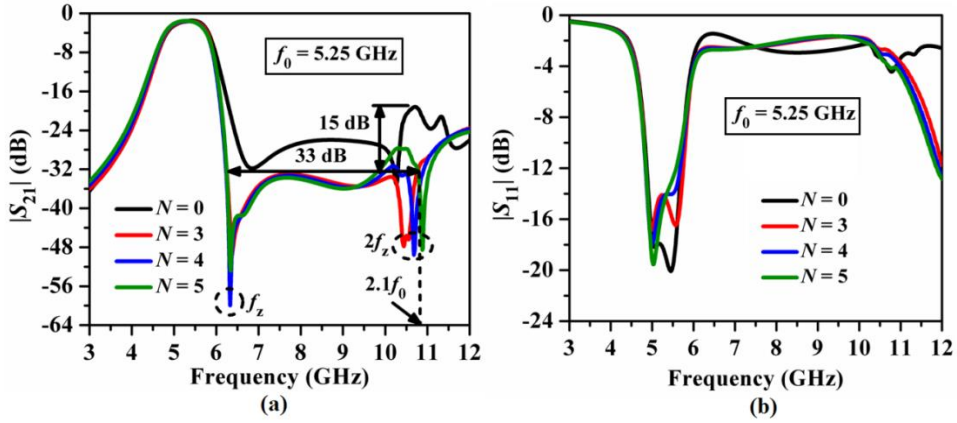

Fig. 3.140. Comparison of simulated *S*-parameters plots for the optimized folded PCMLBF centered at f_0 = 5.25 GHz with periodic square shaped corrugations: (a) $|S_{21}|$ (dB), and (b) $|S_{11}|$ (dB).

3.15.1.1. Fabricated Prototype for C-band Filter

Accordingly, the fabricated prototype for the third-order folded PCMLBF with three pairs of square corrugations is shown in Fig. 3.141 on FR4 laminate.

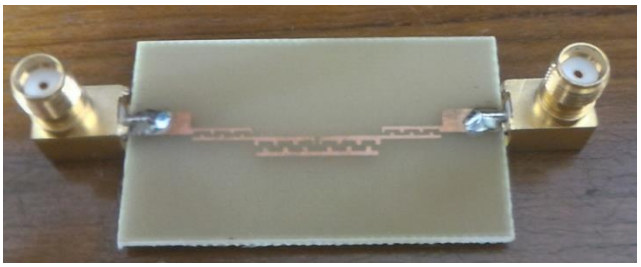

Fig. 3.141. Fabricated prototype of the third-order PCMLBF centered at f_0 = 5.25 GHz with three pair of periodic square shaped corrugations [28].

3.15.1.2. Comparison of EM simulation vs. Measurement Results

The comparison of simulated and measured *S*-parameters plots is highlighted in Figs. 3.142(a)-(b). The experimental procedure has been carried out in the similar way of 3.14.4.1. It has been observed that two sharp transmission zeros f_z and $2f_z$ have been observed at 6.2 GHz and 10.5 GHz, respectively, with an attenuation level of 45 dB and 56 dB for the measured result of $|S_{21}|$ (dB). A stopband up to $2.3f_0$ with a rejection level of 33 dB has been achieved. Moreover, the passband insertion loss and return loss (Fig. 3.142(b)) have been recorded as less than 1.2 dB and more than 23 dB, respectively. Figs. 3.143(a)-(b) show the surface current distribution for the filter, with a strong current distribution at f_0 = 5.25 GHz and a minimum current distribution at $2f_0$ = 10.5 GHz due to the generation of the transmission zero at $2f_z$.

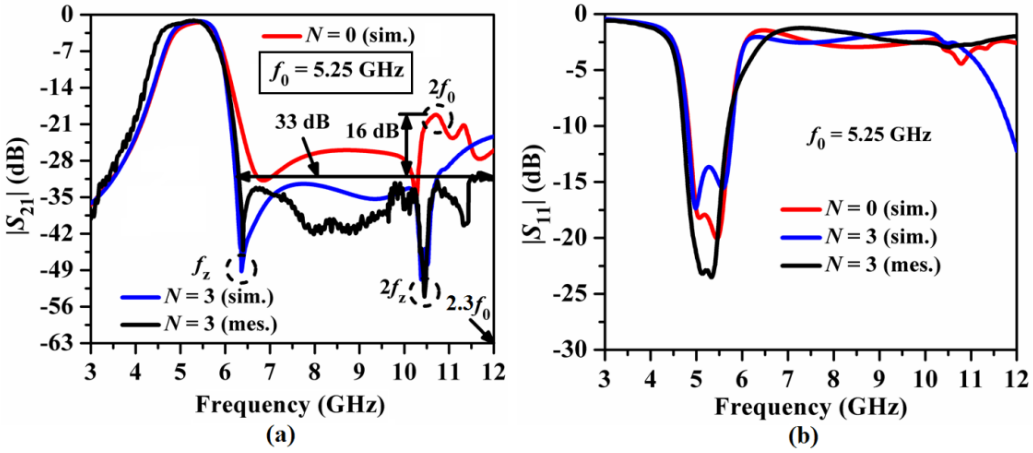

Fig. 3.142. Comparison of the simulated vs. measured *S*-parameters plots of the third-order folded PCMLBF at f_0 = 5.25 GHz with three pair of periodic square shaped corrugations: (a) $|S_{21}|$ (dB) and (b) $|S_{11}|$ (dB) [28].

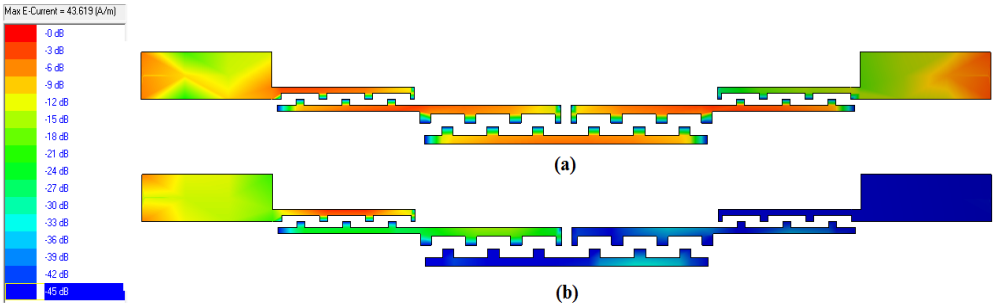

Fig. 3.143. Surface current distribution for the third-order folded PCMLBF cell with three pair of periodic square shaped corrugations at (a) f_0 = 5.25 GHz, and (b) $2f_0$ = 10.5 GHz.

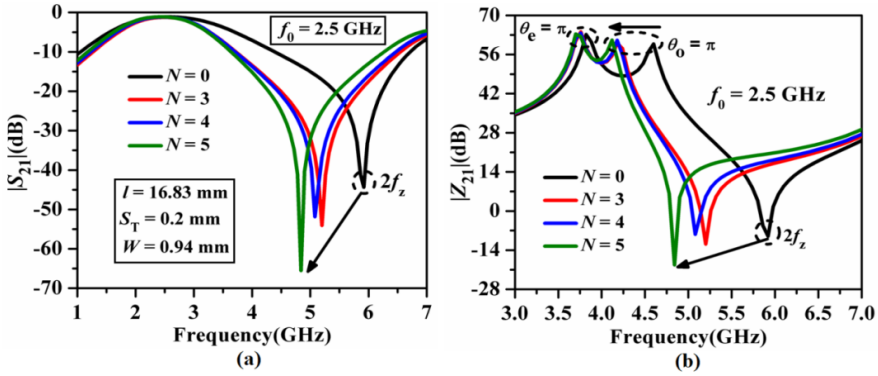

Fig. 3.144. Comparison of simulated resonance characteristics for a unit PCML cell centered at f_0 = 2.5 GHz with periodic square shaped corrugations: (a) $|S_{21}|$ (dB), and (b) $|S_{11}|$ (dB).

The study has been extended further for the S-band filter centered at 2.5 GHz to investigate the ability of the corrugations in harmonic suppression, as shown in Figs. 3.144(a)-(b). It could be observed from Fig. 3.144(a) that the location of $2f_z$ has been shifted to a lower frequency with decreased attenuation level as N increases, just like in the C-band filter. Moreover, the odd-mode resonant peak of $|Z_{21}|$ (dB) has been shifted more compared to that of π-mode due to the slow-wave nature of corrugations. As a result of the parametric study of third-order folded PCMLBF at 2.5 GHz shown in Figs. 3.145 (a)-(c), the optimum corrugation dimensions have been chosen as $l_T = 3W/4$, $w_T = W/2$ for N = 4 and 5, and $l_T = w_T = W/2$ for N = 6. As a result, Figs. 3.146(a)-(c) show the optimized layouts of the third-order folded filters centered at 2.5 GHz with N = 4, 5, and 6. The overall dimensions of the filters are 97.18 mm × 6.39 mm, which equates to 620.98 mm^2 or $1.42\lambda_g \times 0.09\lambda_g$ for N = 5, 95.38 mm × 5.66 mm, which equates to 540.29 mm^2 or $1.4\lambda_g \times 0.08\lambda_g$ for N = 6, and 96.58 mm × 6.35 mm, which equates to 612.94 mm^2 or $1.41\lambda_g \times 0.09\lambda_g$ for N = 7. Accordingly, size reductions of 49%, 55.7%, and 49.8% have been obtained, respectively,

over the conventional filters. The comparison of the simulated *S*-parameter plots for all the folded filters with corrugations and the folded filter without corrugations has been explored in Figs. 3.147(a)-(b). It has been observed that maximum stopband bandwidth up to $2.4f_0$ with a rejection level of 35 dB has been obtained for $N = 6$.

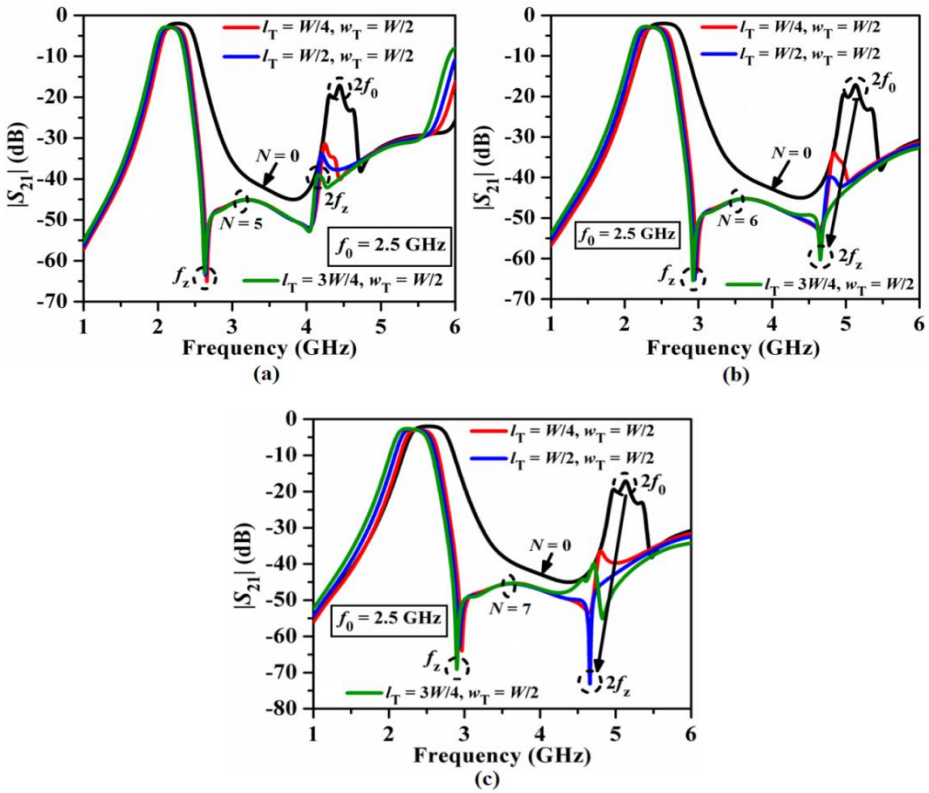

Fig. 3.145. Parametric simulated study for the folded PCMLBF centered at $f_0 = 2.5$ GHz with periodic square shaped corrugations: (a) $N = 3$, (b) $N = 4$, and (c) $N = 5$.

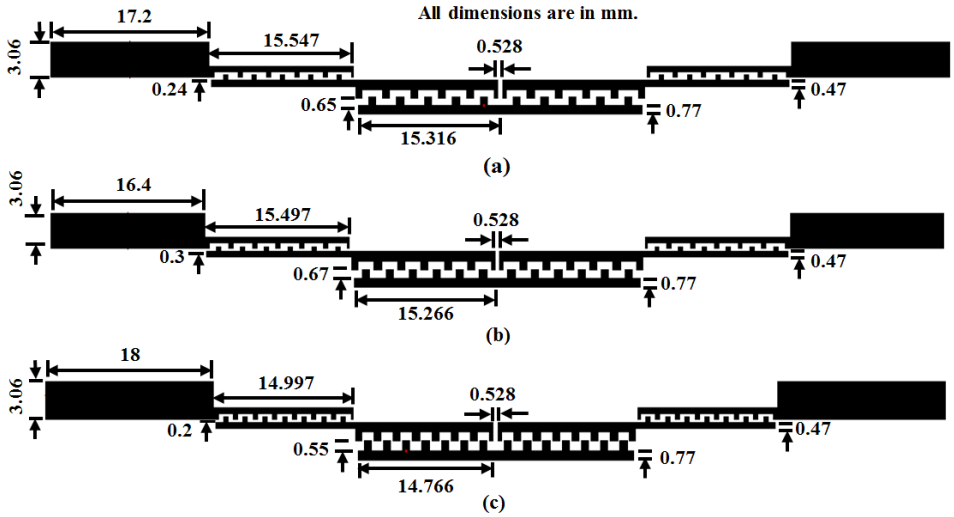

Fig. 3.146. Optimized layout of the folded PCMLBF centered at $f_0 = 2.5$ GHz with periodic square shaped corrugations: (a) $N = 5$, (b) $N = 6$, and (c) $N = 7$.

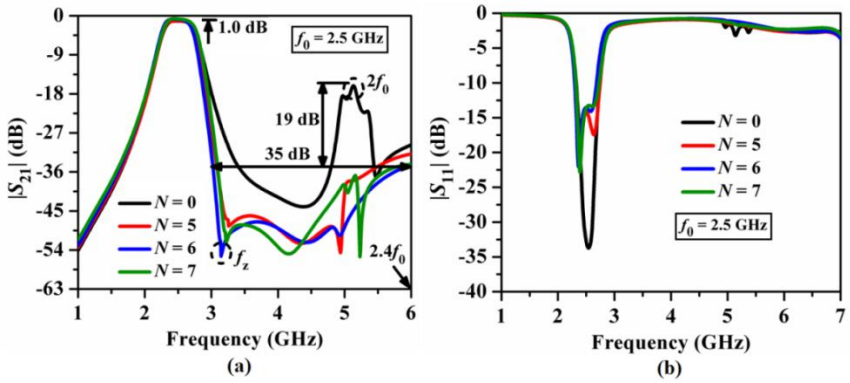

Fig. 3.147. Comparison of simulated *S*-parameters plots for the optimized folded PCMLBF centered at f_0 = 2.5 GHz with periodic square shaped corrugations: (a) $|S_{21}|$ (dB), and (b) $|S_{11}|$ (dB).

The attenuation level at $2f_0$ has been suppressed by 23 dB over the conventional filter. A sharp transmission zero f_z has occurred at 3.2 GHz with an attenuation level of 56 dB, indicating the improvement of the skirt characteristics of the filter. For all the designed filters, the return loss becomes more than 15 dB, as highlighted in Fig. 3.147(b).

3.15.1.3. Fabricated Prototype for S-band Filter

To validate the performance of the filter, the fabricated prototype for the third-order folded PCMLBF with six pairs of square corrugations is shown in Fig. 3.148.

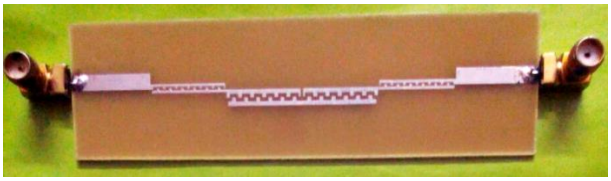

Fig. 3.148. Fabricated prototype of the third-order folded PCMLBF centered at f_0 = 2.5 GHz with six pair of periodic square shaped corrugations [29].

3.15.1.4. Comparison of EM simulation vs. Measurement Results

Figs. 3.149(a)-(b) compare simulated and measured S-parameter plots. The experimental procedure has been carried out in the similar way of 3.14.4.1. It has been observed that two sharp transmission zeros f_z and $2f_z$ have been observed at 3.3 GHz and 4.8 GHz, respectively, with an attenuation level of 62 dB and 60 dB for the measured result of $|S_{21}|$ (dB). A stopband up to $2.4f_0$ with a rejection level of 39 dB has been achieved. Moreover, the passband insertion loss and return loss (Fig. 3.149(b)) have been recorded as less than 1.1 dB and more than 25 dB, respectively. The surface current distribution for the filter has been explored in Fig. 3.150.

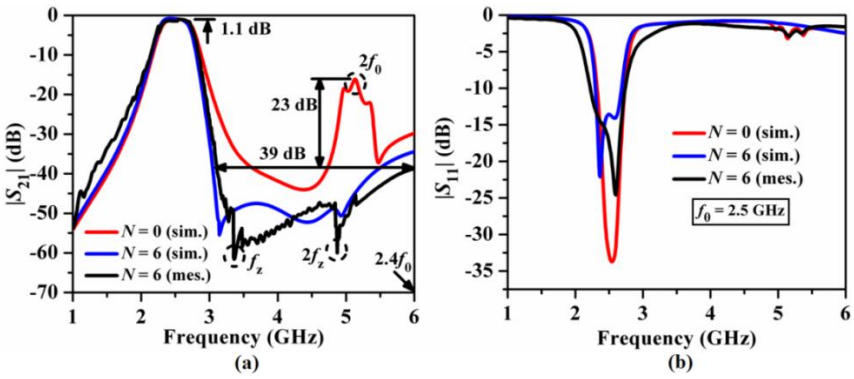

Fig. 3.149. Comparison of the simulated vs. measured *S*-parameters plots of the third-order folded PCMLBF at f_0 = 2.5 GHz with six pair of periodic square shaped corrugations: (a) $|S_{21}|$ (dB) and (b) $|S_{11}|$ (dB) [29].

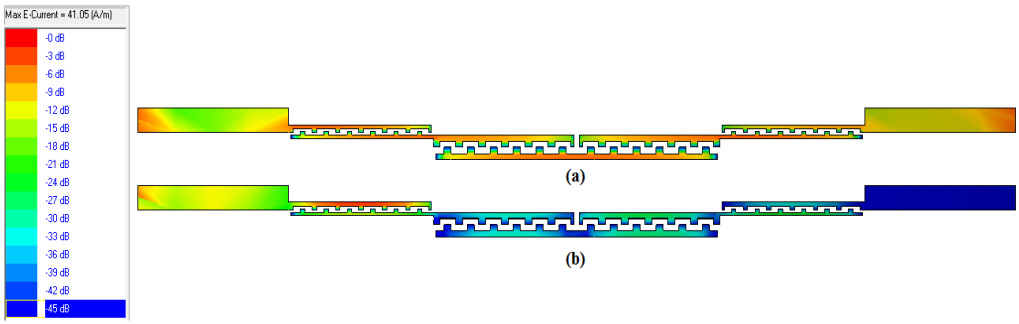

Fig. 3.150. Surface current distribution for the third-order folded PCMLBF cell with six pair of periodic square shaped corrugations at (a) f_0 = 2.5 GHz, (b) $2f_0$ = 5 GHz.

It has been noticed that the current distributes at a large strength at f_0 = 5.25 GHz with a minimum current distribution at $2f_0$ = 10.5 GHz due to the generation of the transmission zero $2f_z$.

3.15.2. Inline PCMLBF with Periodic Square Shaped Corrugations

The study of square shaped corrugations in harmonic suppression has been extended further for the inline PCMLBF centered at 5.25 GHz, and the optimum dimensions of the corrugations have been obtained by the parametric study as $l_T = W/4$, $w_T = W/2$ for N = 3, 4 and 5. Finally, the dimensions of the overall inline filters, including feed ports, are shown in Figs. 3.151(a)-(c). The overall sizes of the filters are 40.23 mm × 3.76 mm, i.e., 151.26 mm^2 or $1.26\lambda_g \times 0.12\lambda_g$ for N = 3, 36.32 mm × 3.76 mm, i.e., 136.56 mm^2 or $1.13\lambda_g \times 0.12\lambda_g$ for N = 4, and 35.92 mm × 3.76 mm, i.e., 135.06 mm^2 or $1.12\lambda_g \times 0.12\lambda_g$ for N = 5. Accordingly, size reductions of 77.1%, 79.3%, and 79.5% have been obtained, respectively, over the conventional filters. As a result, Figs. 3.152(a)-(b) shows a comparison of the

simulated *S*-parameters plots for the designed inline filters with square corrugations. It has been observed from Fig. 3.152(a) that two sharp transmission zeros, f_z and $2f_z$, have been observed at 6.0 GHz and 10.5 GHz, respectively, with an attenuation level of 45 dB and 42 dB. A stopband up to $2.15f_0$ with a rejection level of 35 dB has been achieved for $N = 4$ as the best result. Furthermore, the passband insertion loss (Fig. 3.152(a)) and return loss (Fig. 3.152(b)) were less than 1.1 dB and greater than 30 dB, respectively.

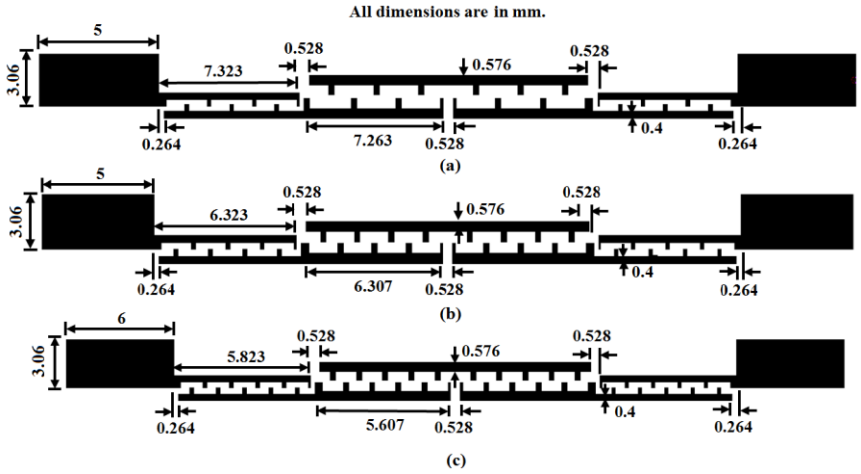

Fig. 3.151. Optimized layout of the inline PCMLBF centered at f_0 = 5.25 GHz with periodic square shaped corrugations: (a) $N = 3$, (b) $N = 4$, and (c) $N = 5$.

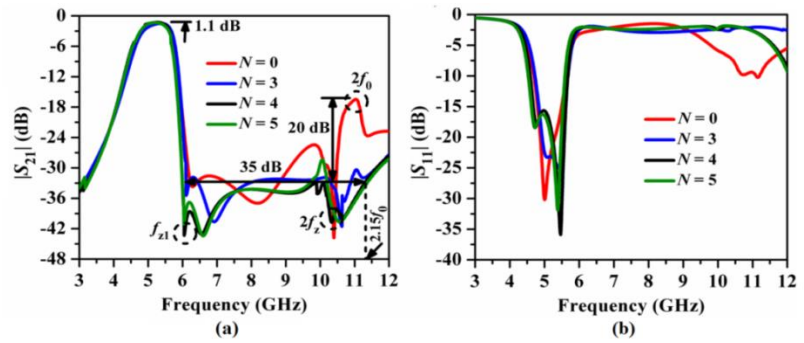

Fig. 3.152. Comparison of *S*-parameters plots for the optimized inline PCMLBF centered at f_0 = 5.25 GHz with periodic square shaped corrugations: (a) $|S_{21}|$ (dB, and (b) $|S_{11}|$ (dB).

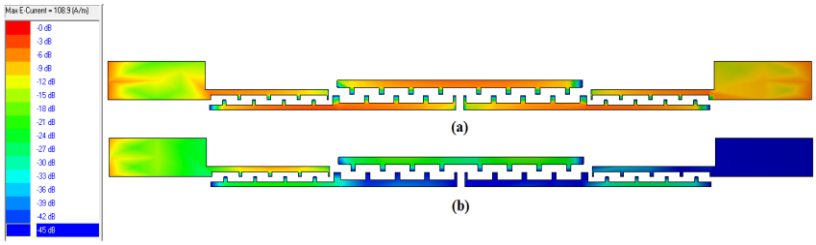

Fig. 3.153. Surface current distribution for the third-order inline PCMLBF cell with four pair of periodic square shaped corrugations at (a) f_0 = 5.25 GHz, and (b) $2f_0$ = 10.5 GHz.

In Fig. 3.153, the surface current distribution for the inline filter with four pairs of periodic corrugations has been explored, and it has been observed that the current strength has been increased at f_0 = 5.25 GHz and decreased at $2f_0$ = 10.5 GHz due to the suppression of harmonics. Following that, the inline PCMLBFs centered at 2.5 GHz with square corrugations were optimally designed, as shown in Figs. 3.154(a)-(c) for N = 3, 4, and 5, respectively. The overall sizes of the filters are 99.2 mm × 3.78 mm, i.e., 374.98 mm^2 or 1.45λ_g × 0.06λ_g for N = 3, 99 mm × 3.78 mm, i.e., 374.22 mm^2 or 1.45λ_g × 0.06λ_g for N = 4, and 98.18 mm × 3.78 mm, i.e., 371.11 mm^2 or 1.44λ_g × 0.06λ_g for N = 5. Accordingly, size reductions of 69.27%, 69.3%, and 69.6% have been obtained, respectively, over the conventional filters. In Figs. 3.155(a)-(b), the simulated S-parameter plots for the designed inline filters with square corrugations are compared. It has been noted from Fig. 3.155(a) that stopband bandwidth up to 2.08f_0 with a rejection level of 41 dB and that up to 2.08f_0 with a rejection level of 35 dB has been obtained for N = 4.

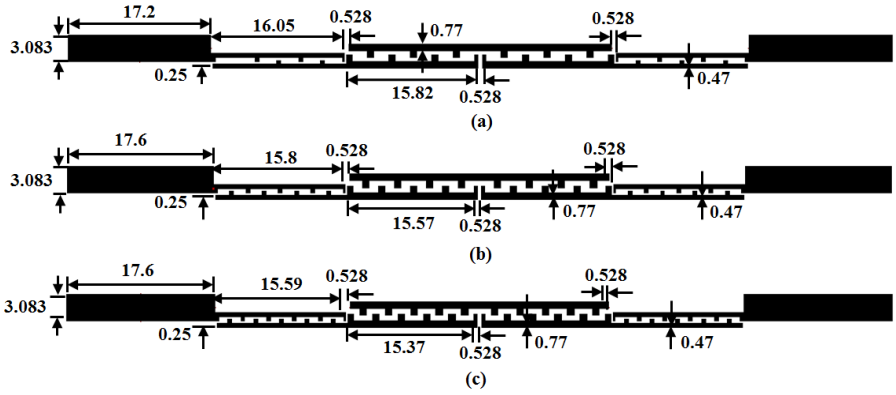

Fig. 3.154. Optimized layout of the inline PCMLBF centered at f_0 = 2.5 GHz with periodic square shaped corrugations: (a) N = 3, (b) N = 4, and (c) N = 5.

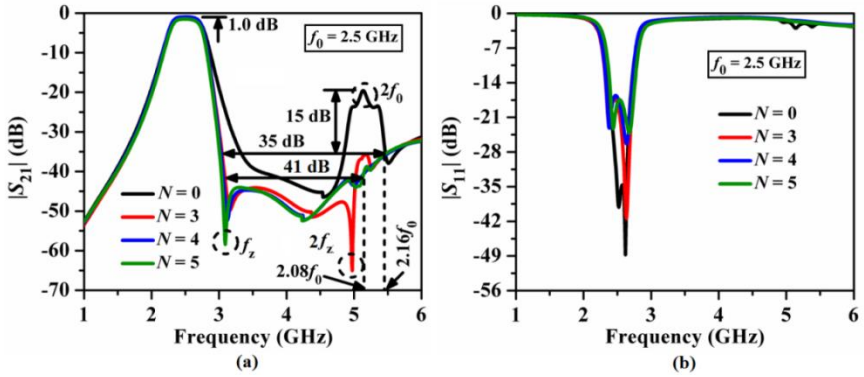

Fig. 3.155. Comparison of simulated S-parameters plots for the optimized inline PCMLBF centered at f_0 = 2.5 GHz with periodic square shaped corrugations: (a) |S_{21}| (dB), and (b) |S_{11}| (dB).

Two sharp transmission zeros, f_z and $2f_z$ have occurred at 3.2 GHz and 5 GHz with attenuation levels of 60 dB and 65 dB, respectively. The attenuation level at $2f_0$ for the inline filter without corrugations has been suppressed by 15 dB with corrugations. For all the designed filters, the return loss becomes more than 20 dB, as exhibited in Fig. 3.155(b).

3.15.2.1. Fabricated Prototype for S-band Filter

Accordingly, the fabricated prototype for the third-order inline PCMLBF with four pairs of square corrugations is shown in Fig. 3.156 on FR4 substrate.

Fig. 3.156. Fabricated prototype of the third-order inline PCMLBF centered at f_0 = 2.5 GHz with four pair of periodic square shaped corrugations [29].

3.15.2.2. Comparison of EM simulation vs. Measurement Results

By following the similar experimental procedure as in 3.14.4.1., the comparison of simulated and measured S-parameter plots is explored in Figs. 3.157(a)-(b). It has been observed that two sharp transmission zeros f_z and $2f_z$ have been observed at 3.3 GHz and 4.8 GHz, respectively, with an attenuation level of 62 dB and 58 dB for the measured result of $|S_{21}|$ (dB). A stopband up to $2.12f_0$ with a rejection level of 42 dB has been achieved. The attenuation level at $2f_0$ has been suppressed by 22 dB over the inline filter without corrugations. Furthermore, the passband insertion loss (Fig. 3.157(a)) and return loss (Fig. 3.157(b)) were less than 1.05 dB and more than 20 dB, respectively.

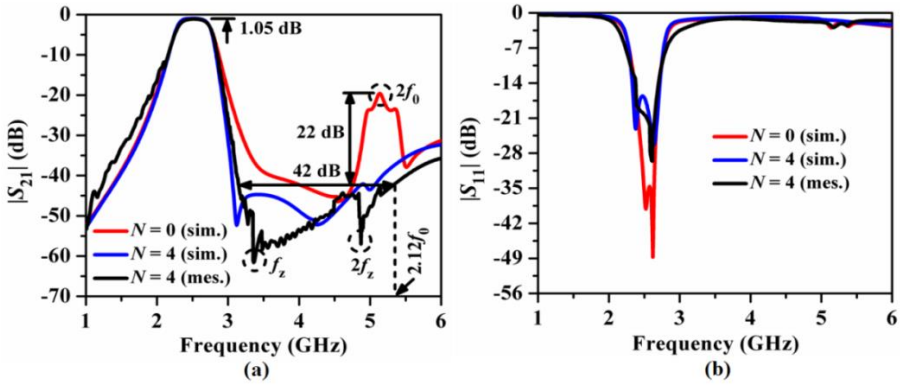

Fig. 3.157. Comparison of the simulated vs. measured *S*-parameters plots of the third-order folded PCMLBF at f_0 = 2.5 GHz with six pair of periodic square shaped corrugations: (a) $|S_{21}|$ (dB), and (b) $|S_{11}|$ (dB) [29].

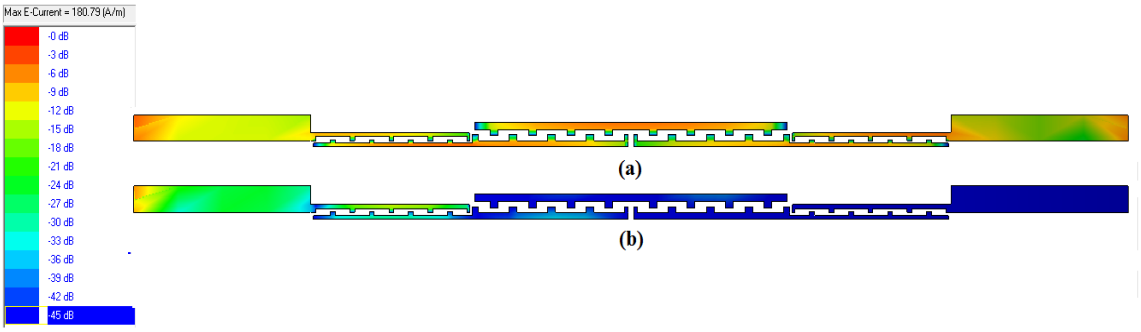

Fig. 3.158. Surface current distribution for the third-order inline PCMLBF cell with four pair of periodic square shaped corrugations at (a) f_0 = 2.5 GHz, and (b) $2f_0$ = 5.0 GHz.

The surface current distribution plot of the N = 4 inline filter (Figs. 3.158(a)-(b)) revealed that the surface current was distributed strongly due to the passband response and very weakly due to the stopband with multiple transmission zeros.

3.15.3. Harmonic Suppression by Periodic Triangular Shaped Corrugations

It can be concluded from the previous section that square corrugations are quite capable of suppressing the harmonics to a significant rejection level for both folded and inline filters in both *S*-and *C*-bands. As an alternative approach, the square shaped corrugations have been modified by triangular shaped corrugations as highlighted in Fig. 3.159 to reduce the dispersion effects due to the sharp bent edges of the square slots. The triangular corrugations are characterized by the base length l_T, height or altitude w_T, and periodicity p. Fig. 3.160 illustrates the improvement of the surface current vector distribution for triangular corrugations over square corrugations.

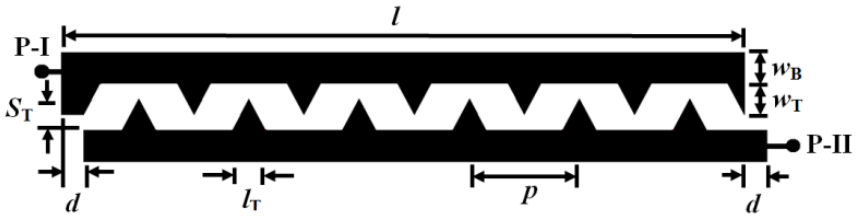

Fig. 3.159. Layout of a unit PCML cell with periodic triangular shaped corrugations.

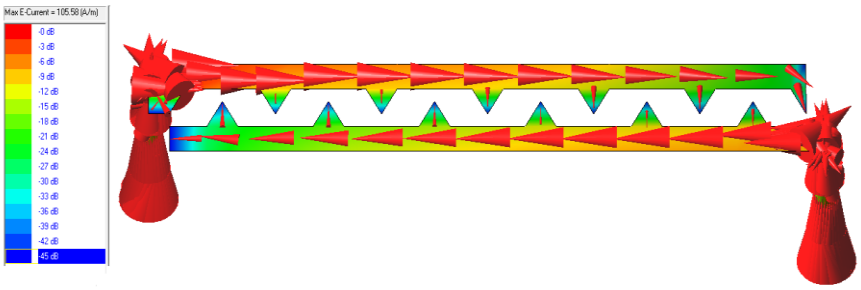

Fig. 3.160. Surface current vectors distribution for a unit PCML cell with six pair of periodic isosceles triangular shaped corrugations.

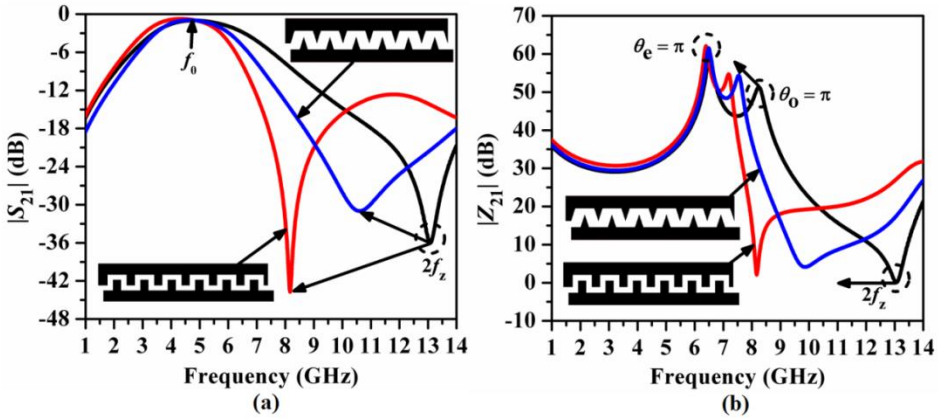

Fig. 3.161. Comparison of simulated resonance characteristics for a unit PCML cell centered at f_0 = 5.25 GHz with periodic square and triangular shaped corrugations: (a) $|S_{21}|$ (dB) and (b) $|S_{11}|$ (dB).

It has been noticed that the strength of the current vectors increases strongly at the feed ports and along the base arm of the coupled lines. The resonance characteristics of a unit PCML cell centered at 5.25 GHz with six pairs of periodic square and triangular corrugations are compared in Fig. 3.161(a)-(b).According to Fig. 3.161(a), the second transmission zero $2f_z$, like the square corrugations, has been shifted to a lower frequency region by the triangular corrugations. However, the attenuation level at $2f_z$ has been increased due to the reduction in the area of the effective conductive surface due to the triangular shape compared to that of a square shape. The -mode resonant peak has been shifted towards the c-mode resonant peak for triangular corrugations, indicating phase velocity compensation ability, as shown in Fig. 3.161(b). Accordingly, the layout of the third-order folded PCMLBF with five pairs of periodic triangular corrugations is depicted in Fig. 3.162. Finally, the parametric study shown in Figs. 3.163(a)-(c) yielded the optimum dimensions of the corrugations as $l_T = W/2$ and $w_T = W/2$ for N = 3, 4, and 5. As a result, the optimized layouts of the folded filters, as shown in Figs. 3.164(a)-(c), have been obtained. The overall sizes of the filters are 43.16 mm × 6.36

mm, which equates to 274.45 mm^2 or 1.35λ_g × 0.2λ_g for N = 3, 42.96 mm × 6.42 mm, which equates to 276 mm^2 or 1.34λ_g × 0.2λ_g for N = 4, and 42.76 mm × 6.36 mm, which equates to 272.12 mm^2 or 1.33λ_g × 0.2λ_g for N = 5.

Fig. 3.162. Typical layout of the third-order folded PCMLBF with ten triangular corrugations.

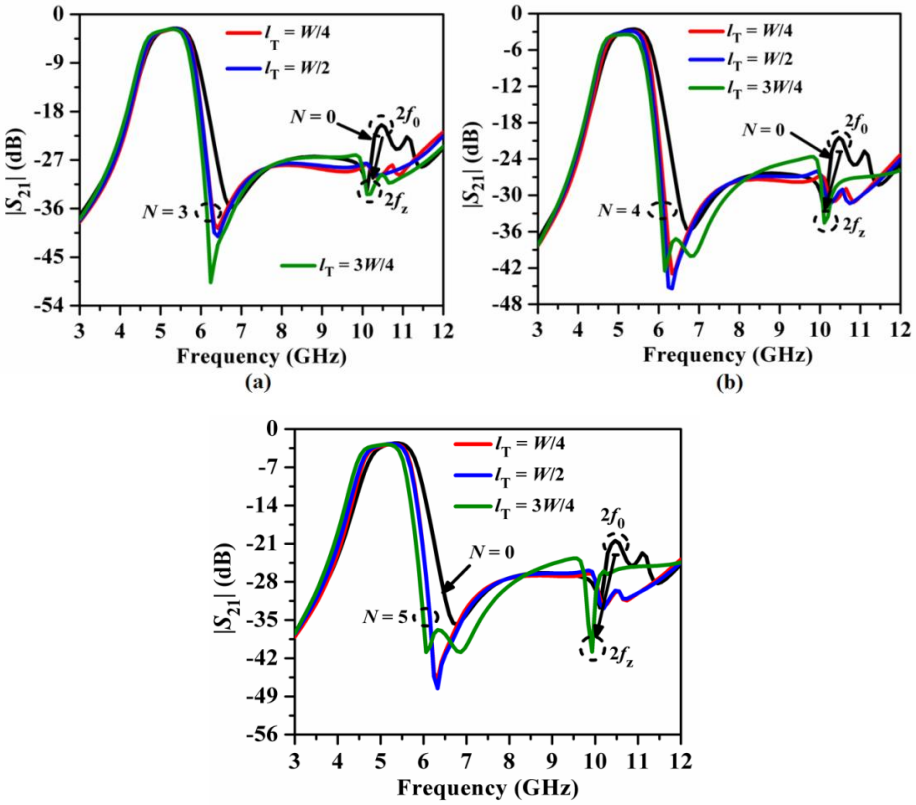

Fig. 3.163. Parametric simulated study for the folded PCMLBF centered at f_0 = 5.25 GHz with periodic triangular shaped corrugations: (a) N = 3, (b) N = 4, and (c) N = 5, (w_T = W/2 for all studies).

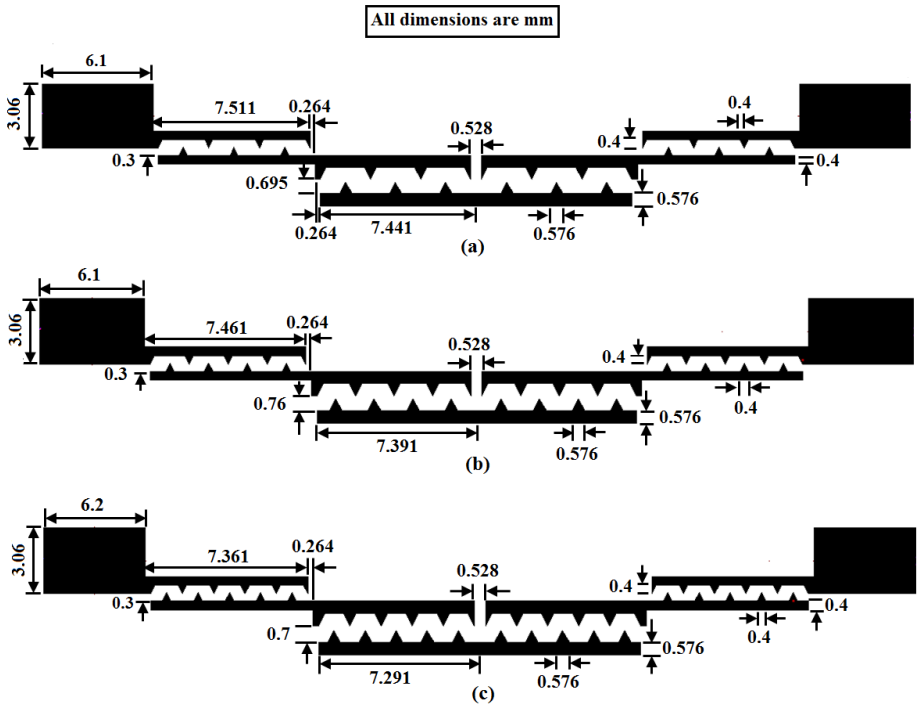

Fig. 3.164. Optimized layout of the folded PCMLBF centered at f_0 = 5.25 GHz with periodic triangular shaped corrugations: (a) N = 3, (b) N = 4, and (c) N = 5.

Accordingly, size reductions of 58.4%, 58.2%, and 58.8% have been obtained over the conventional filters. Figs. 3.165(a)-(b) show a comparison of the simulated *S*-parameter plots for folded filters with triangular corrugations. It has been noted from Fig. 3.165(a) that a stopband bandwidth up to $2.08f_0$ with a rejection level of 35 dB has been obtained for N = 5. Two sharp transmission zeros, f_z and $2f_z$, have occurred at 6.4 GHz and 10.5 GHz with attenuation levels of 53 dB and 64 dB, respectively. The skirt characteristics of the filter and the stopband harmonic suppression performance have been improved significantly due to the placement of such transmission zeros. For all the filters, the return loss becomes more than 20 dB, as explored in Fig. 3.165(b).

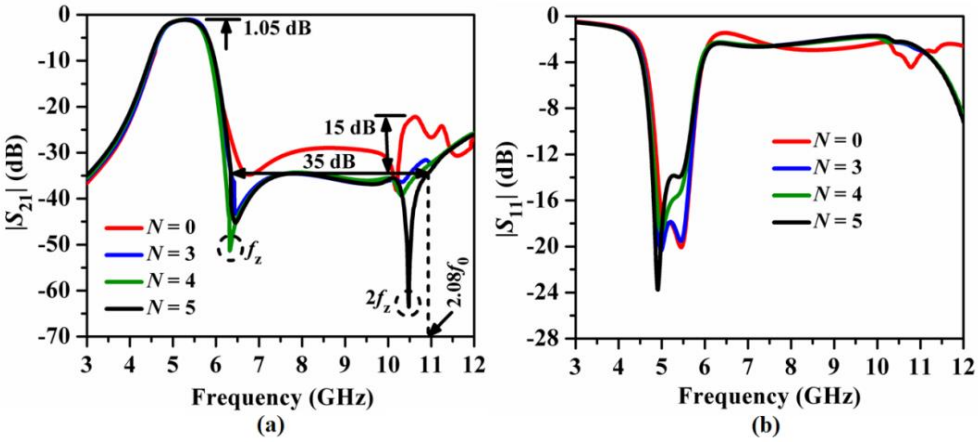

Fig. 3.165. Comparison of simulated *S*-parameters plots for the optimized inline PCMLBF centered at f_0 = 5.25 GHz with different values of *N*: (a) $|S_{21}|$ (dB), and (b) $|S_{11}|$ (dB).

3.15.3.1. Fabricated Prototype

Accordingly, the fabricated prototype for the third-order folded PCMLBF with five pairs of triangular corrugations is shown in Fig. 3.166 based on FR4 laminate.

Fig. 3.166. Fabricated prototype of the third-order folded PCMLBF centered at f_0 = 5.25 GHz with triangular shaped corrugations having *N* = 5 [30].

3.15.3.2. Comparison of EM simulation vs. Measurement Results

By following the similar experimental procedure as in 3.14.4.1., the comparison of simulated and measured S-parameter plots is explored in Figs. 3.167(a)-(b). Fig. 3.167(a) shows that, similar to the simulated results, two sharp transmission zeros, f_z and $2f_z$, were observed at 6.7 GHz and 10.4 GHz with attenuation levels of 64 dB and 62 dB, respectively, for the measured result of $|S_{21}|$ (dB).

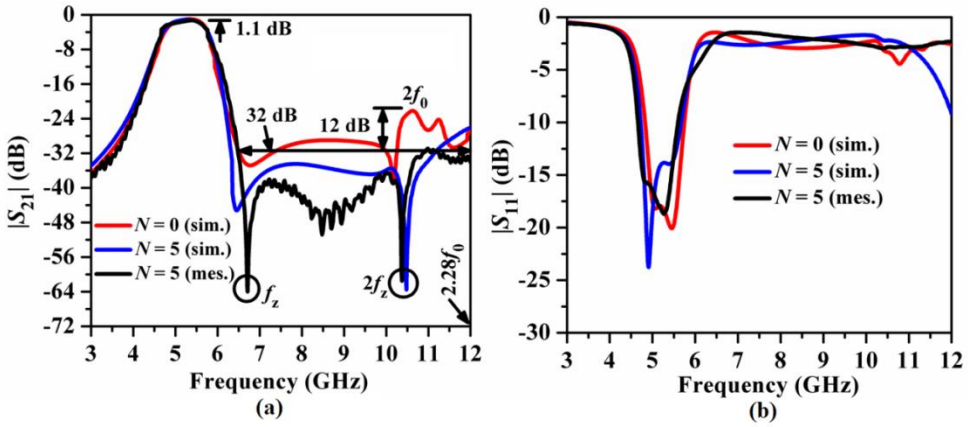

Fig. 3.167. Comparison of the simulated vs. measured *S*-parameters plots of the third-order folded PCMLBF at f_0 = 5.25 GHz with five pair of periodic triangular shaped corrugations: (a) $|S_{21}|$ (dB), and (b) $|S_{11}|$ (dB) [30].

Accordingly, a stopband up to $2.28f_0$ with a rejection level of 32 dB has been achieved. The attenuation level at $2f_0$ has been suppressed by 12 dB over the folded filter without corrugations. Moreover, the measured passband insertion loss and return loss (Fig. 3.167(b)) have been recorded as less than 1.1 dB and more than 18 dB, respectively. The surface current distribution plot of the folded filter with N = 5 (Fig. 3.168(a)-(b)) revealed that the surface current was propagated strongly by the passband response and very weakly by the stopband response.

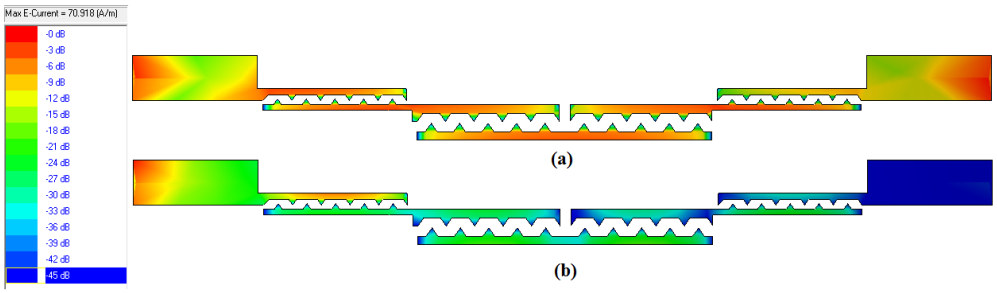

Fig. 3.168. Surface current distribution for the third-order folded PCMLBF cell with five pair of periodic triangular shaped corrugations at (a) f_0 = 5.25 GHz, (b) $2f_0$ = 10.5 GHz.

Following that, the previous design of triangular corrugations for the folded *S*-band PCMLBF centered at 2.5 GHz was extended further, and the optimized layouts of the final filters with N = 6, 7, and 8 are shown in Figs. 3.169(a)-(c). The overall sizes of the filters are 96.6 mm × 6.17 mm, which equates to 596.48 mm^2 or $1.41\lambda_g \times 0.09\lambda_g$ for N = 6, 95.18 mm × 6.12 mm, which equates to 582.96 mm^2 or $1.39\lambda_g \times 0.09\lambda_g$ for N = 7, and 93.38 mm × 6.12 mm, which equates to 571.93 mm^2 or $1.37\lambda_g \times 0.09\lambda_g$ for N = 8. Accordingly, size reductions of 51.1%, 52.2%, and 53.1% have been obtained over the conventional filters. In Figs. 3.170(a)-(b), the

simulated *S*-parameter plots for all the folded filters with corrugations and the folded filter without corrugations are compared. It has been observed that maximum stopband bandwidth up to $2.56f_0$ with a rejection level of 35 dB has been obtained for $N = 8$. A sharp transmission zero of $2f_z$ has occurred at 4.87 GHz with an attenuation level of 65 dB, indicating the improved harmonic suppression by triangular corrugations.

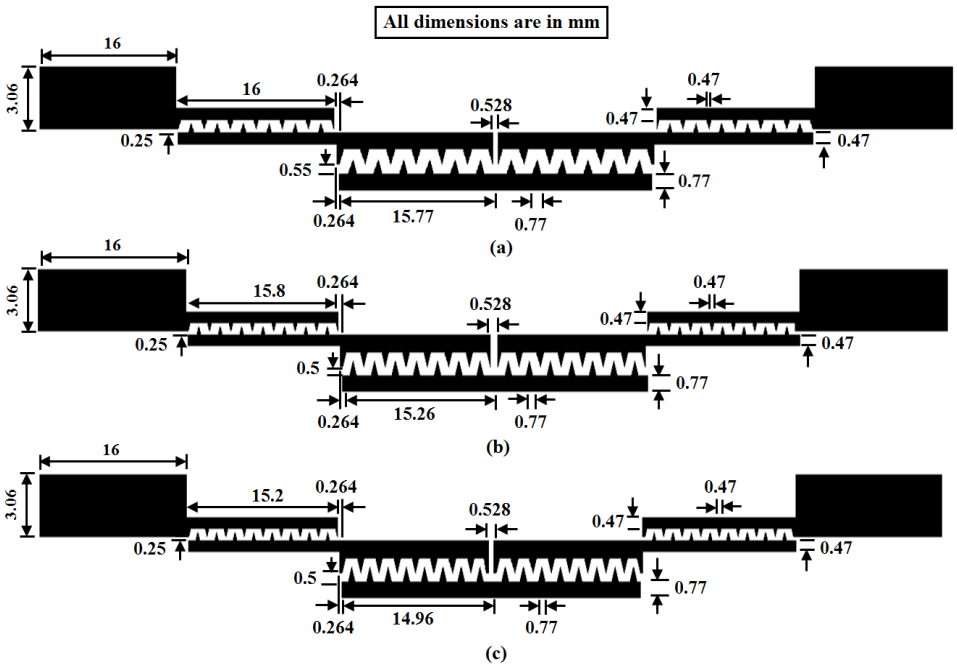

Fig. 3.169. Optimized layout of the third-order folded PCMLBF centered at $f_0 = 5.25$ GHz with periodic triangular shaped corrugations: (a) $N = 6$, (b) $N = 7$, and (c) $N = 8$.

The attenuation level at $2f_0$ for the folded filter without corrugations has been suppressed by 19 dB by introducing corrugations. As a result, at $f_0 = 5.25$ GHz and $2f_0 = 10.5$ GHz, the surface current distribution of the folded filter with $N = 8$ has been investigated in Fig. 3.171(a)-(b). It has been revealed that the surface current propagates strongly due to the passband response and very weakly due to the stopband response, as expected.

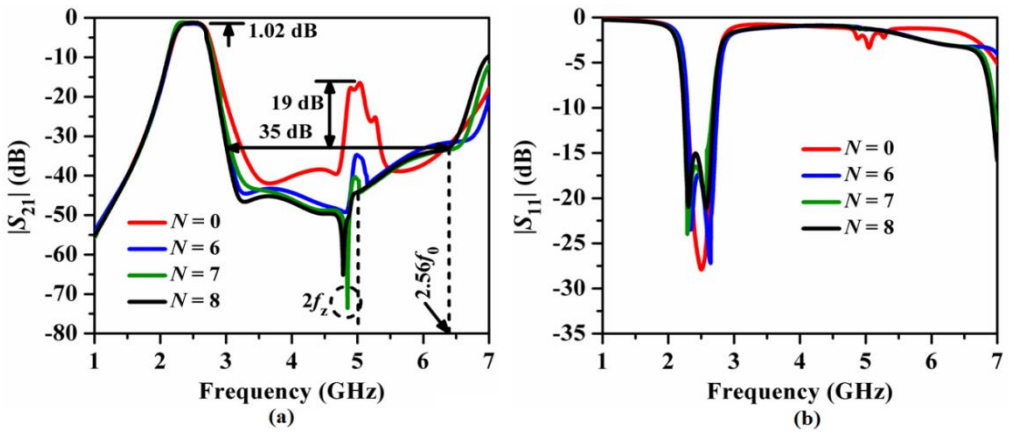

Fig. 3.170. Comparison of simulated *S*-parameters plots for the optimized third-order folded PCMLBF centered at f_0 = 2.5 GHz with periodic triangular shaped corrugations: (a) $|S_{21}|$ (dB) and (b) $|S_{11}|$ (dB).

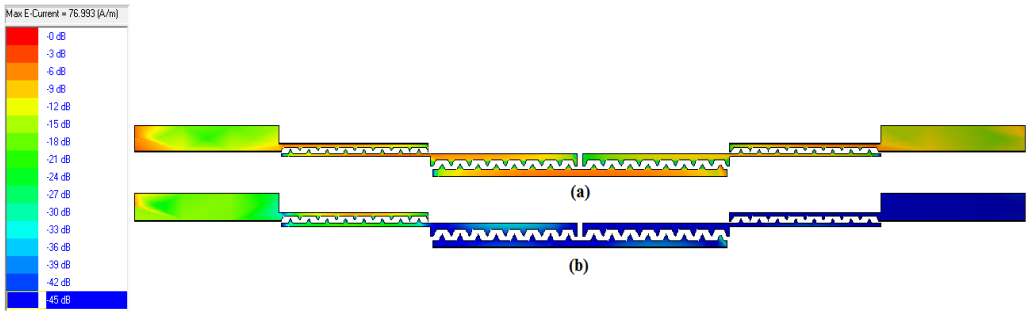

Fig. 3.171. Surface current distribution for the third-order folded PCMLBF cell with eight pair of periodic triangular shaped corrugations at (a) f_0 = 2.5 GHz, and (b) $2f_0$ = 5.0 GHz.

3.15.4 Inline PCMLBFs with Triangular Shaped Corrugations

From the study of folded PCMLBFs with triangular corrugations, it has been concluded that the triangular corrugations exhibit significant improvement in skirt characteristics and harmonic suppression level compared to square corrugations. Thus, the knowledge was applied to the inline PCMLBF centered at 5.25 GHz, and the optimum corrugation dimensions were obtained using the parametric study of Figs. 3.172(a)-(c) as $l_T = W/2$, $w_T = W/2$ for N = 3, 4, and 5, respectively. Finally, the overall dimensions of the inline filters, including feed ports, are shown in Figs. 3.173(a)-(c). The overall sizes of the filters are 45.5 mm × 3.76 mm, i.e., 171.08 mm^2 or $1.42\lambda_g \times 0.12\lambda_g$ for N = 3, 45.09 mm × 3.76 mm, i.e., 169.54 mm^2 or $1.41\lambda_g \times 0.12\lambda_g$ for N = 4, and 44.74 mm × 3.76 mm, i.e., 168.21 mm^2 or $1.4\lambda_g \times 0.12\lambda_g$ for N = 5. Accordingly, size reductions of 74.1%, 74.3%, and 74.5% have been obtained, respectively, over the conventional filters.

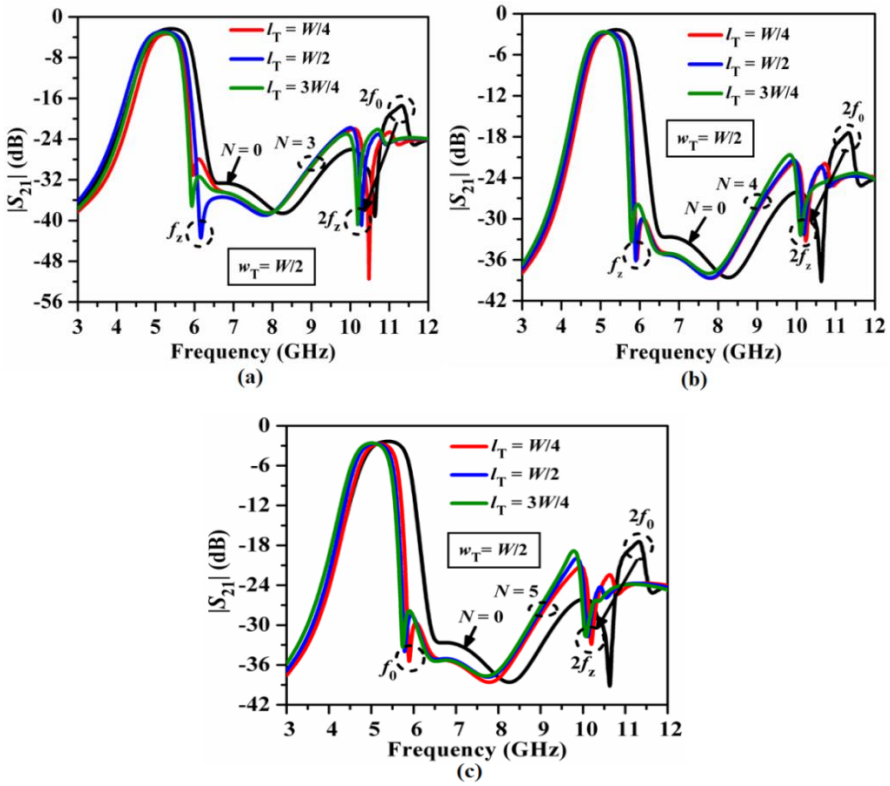

Fig. 3.172. Parametric simulated study for the third-order inline PCMLBF centered at f_0 = 5.25 GHz with periodic triangular shaped corrugations: (a) N = 3, (b) N = 4, and (c) N = 5.

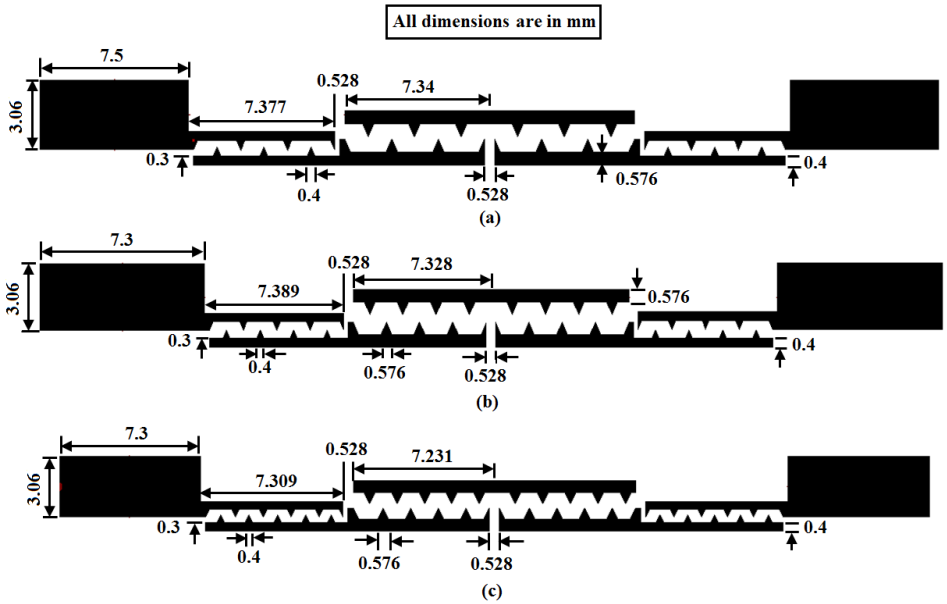

Fig. 3.173. Optimized layout of the third-order inline PCMLBF centered at f_0 = 5.25 GHz with periodic triangular shaped corrugations: (a) N = 3, (b) N = 4, and (c) N = 5.

The comparison of the simulated *S*-parameters plots for the designed inline filters with triangular corrugations is shown in Fig. 3.174(a)-(b). It has been noted from Fig. 3.174(a) that

a stopband bandwidth up to $2.13f_0$ with a rejection level of 32 dB has been obtained for $N = 4$. Two sharp transmission zeros, f_z and $2f_z$ have occurred at 6.1 GHz and 10.5 GHz with attenuation levels of 52 dB and 49 dB, respectively. Accordingly, the skirt characteristics and harmonic suppression performance of the inline filter have been improved. The return loss becomes more than 20 dB, as exhibited in Fig. 3.174(b).

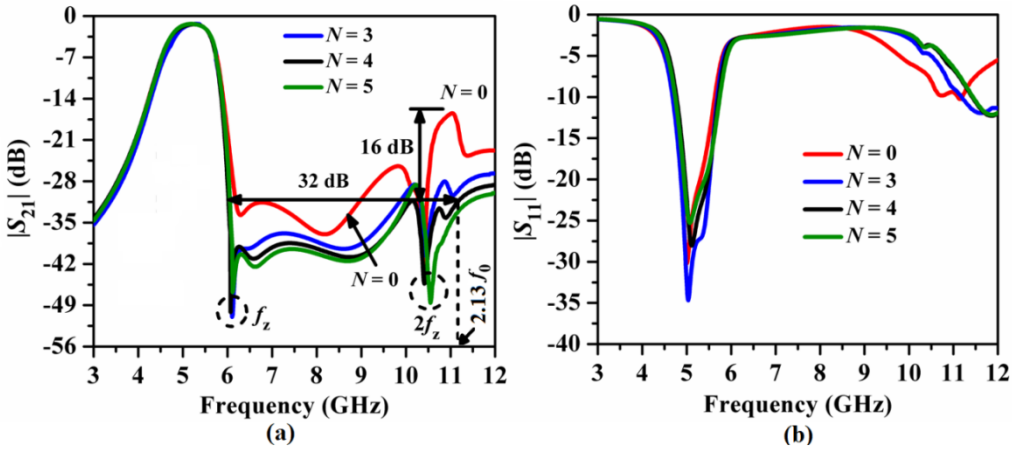

Fig. 3.174. Comparison of simulated *S*-parameters plots for the optimized third-order inline PCMLBF centered at $f_0 = 5.25$ GHz with periodic triangular shaped corrugations: (a) $|S_{21}|$ (dB), and (b) $|S_{11}|$ (dB).

3.15.4.1. Fabricated Prototype

Fig. 3.175 shows the fabricated prototype for the third-order inline PCMLBF with four pairs of triangular corrugations.

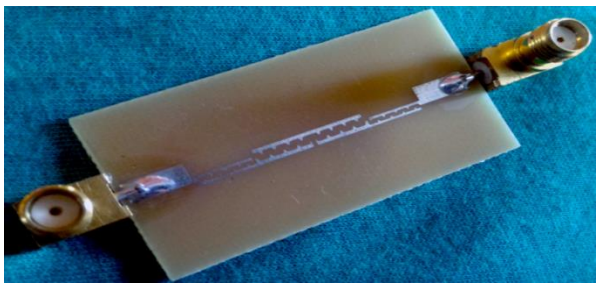

Fig. 3.175. Fabricated prototype of the third-order inline PCMLBF centered at $f_0 = 5.25$ GHz with four pair of periodic triangular shaped corrugations [30].

3.15.4.2. Comparison of EM simulation vs. Measurement Results

By following the similar experimental procedure as in 3.14.4.1., the comparison of simulated and measured *S*-parameter plots is explored in Figs. 3.176(a)-(b). It has been observed from Fig. 3.176(a) that a sharp transmission zero f_z with an attenuation level of 52 dB has occurred at 6.2 GHz in measurement.

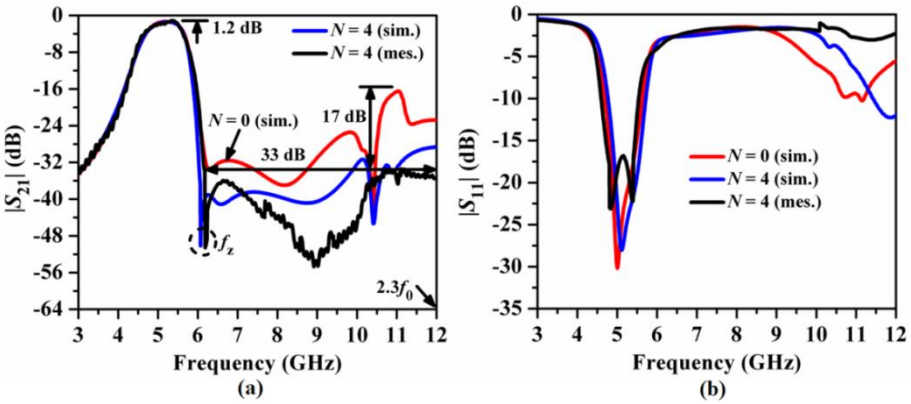

Fig. 3.176. Comparison of the simulated vs. measured *S*-parameters plots of the third-order inline PCMLBF at f_0 = 5.25 GHz with four pair of periodic triangular shaped corrugations: (a) $|S_{21}|$ (dB), and (b) $|S_{11}|$ (dB).

Moreover, a wide stopband up to $2.3f_0$ has been recorded with a rejection level of 33 dB has been achieved. Very interestingly, a deep valley with a rejection level below 36 dB has occurred between the upper passband edge and $2f_0$. Besides, the attenuation level at $2f_0$ has been suppressed by 17 dB over the folded filter without corrugations. The fabricated filter has a passband insertion loss of 1.2 dB and a return loss of 17 dB (Fig. 3.176(b)). The surface current distributions for the inline filter with N = 4 at f_0 and $2f_0$ have been depicted in Figs. 3.177(a) and (b) respectively. It can be concluded that the current strength is maximum at f_0 due to the passband and minimum at $2f_0$ due to the harmonic suppression performance in the stopband.

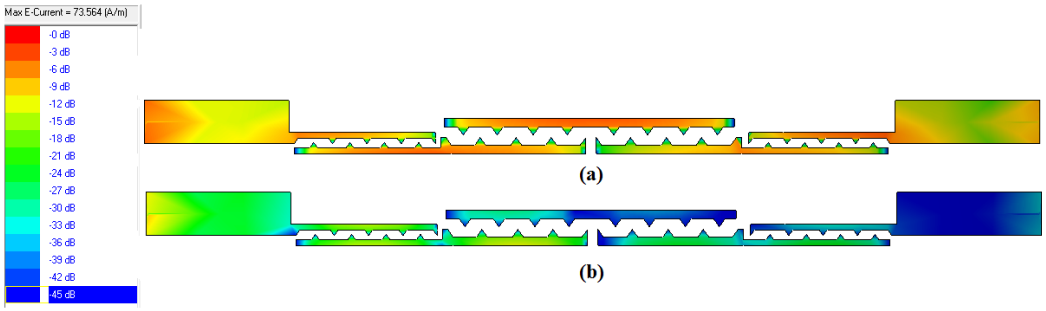

Fig. 3.177. Surface current distribution for the third-order inline PCMLBF cell with four pair of periodic triangular shaped corrugations at (a) f_0 = 5.25 GHz, (b) $2f_0$ = 10 GHz.

Following that, the inline PCMLBFs centered at 2.5 GHz with triangular corrugations were optimally designed, as shown in Figs. 3.178(a)-(c) for N = 6, 7, and 8, respectively. The overall sizes of the filters are 95.4 mm × 3.83 mm, i.e., 365.38 mm^2 or $1.4\lambda_g \times 0.06\lambda_g$ for N = 6, 95.6 mm × 3.83 mm, i.e., 366.15 mm^2 or $1.4\lambda_g \times 0.06\lambda_g$ for N = 7, and 90.8 mm × 3.83 mm, i.e., 347.75 mm^2 or $1.34\lambda_g \times 0.06\lambda_g$ for N = 8.

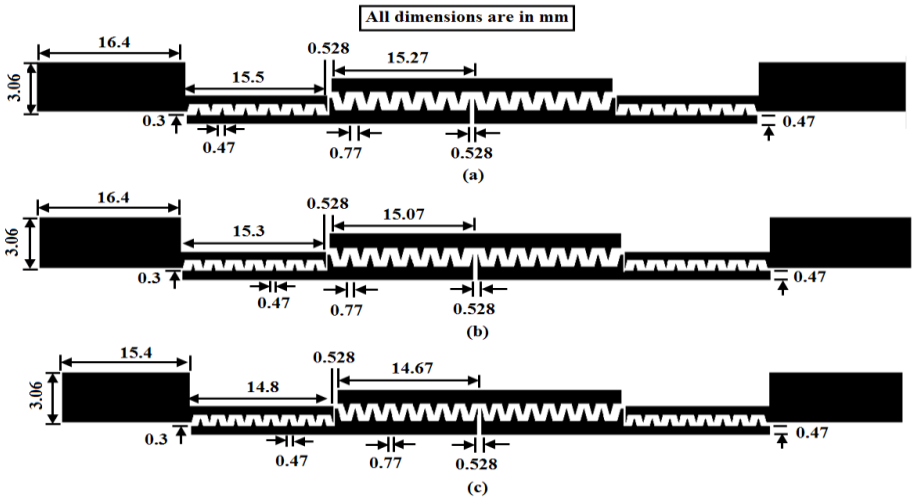

Fig. 3.178. Optimized layout of the third-order inline PCMLBF centered at f_0 = 2.5 GHz with periodic triangular shaped corrugations: (a) N = 6, (b) N = 7, and (c) N = 8.

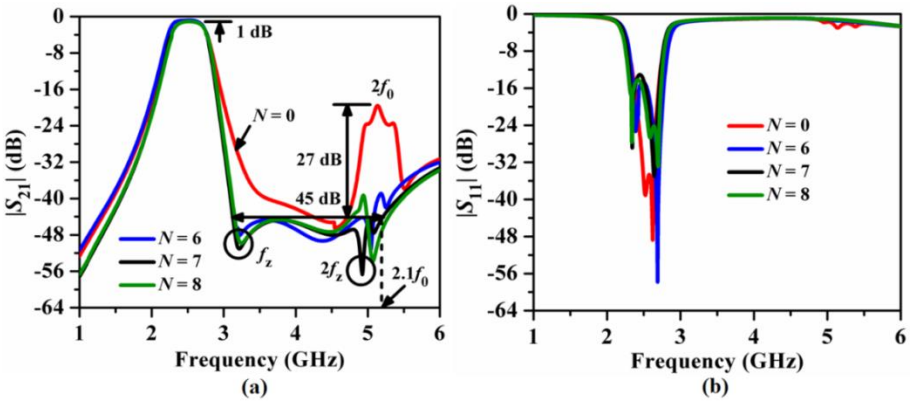

Fig. 3.179. Comparison of simulated *S*-parameters plots for the optimized third-order inline PCMLBF centered at f_0 = 2.5 GHz with periodic triangular shaped corrugations: (a) $|S_{21}|$ (dB) and (b) $|S_{11}|$ (dB).

Accordingly, size reductions of 70%, 70%, and 71.5% have been obtained, respectively, over the conventional filters. The comparison of the simulated *S*-parameters plots for the designed inline filters centered at 2.5 GHz with triangular corrugations has been highlighted in Figs. 3.179(a)-(b). It has been observed from Fig. 3.179(a) that a stopband bandwidth up to $2.1f_0$ with a rejection level of 45 dB has been obtained for N = 7. Two sharp transmission zeros, f_z and $2f_z$ have occurred at 3.2 GHz and 4.9 GHz with attenuation levels of 51 dB and 57 dB, respectively. Accordingly, improvements in the skirt characteristics and harmonic suppression performance of the inline filter with triangular corrugations (N = 7) have been obtained. From the plots, it has been observed that among all the previous designs, the maximum stopband rejection level has occurred with triangular corrugations. The return

losses become more than 16 dB, as exhibited in Fig. 3.179(b) for all the inline filters centered at 2.5 GHz. Accordingly, the surface current distributions for the inline filter with $N = 7$ at f_0 and $2f_0$ have been plotted in Figs. 3.180(a)-(b) respectively.

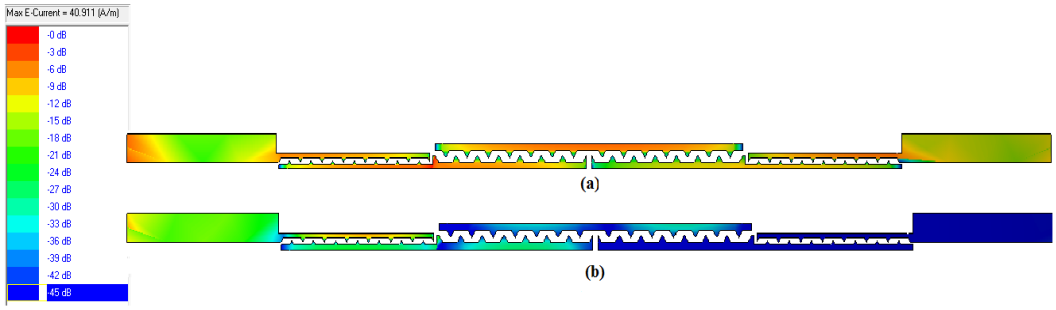

Fig. 3.180. Surface current distribution for the third-order inline PCMLBF cell with seven pair of periodic triangular shaped corrugations at (a) $f_0 = 2.5$ GHz, and (b) $2f_0 = 5$ GHz.

It can be concluded that the current strength is maximum at f_0 due to the passband and minimum at $2f_0$ due to the harmonic suppression performance in the stopband. Tables 3.14 and 3.15 tabulate all the parameters for the folded and inline filters with square and triangular corrugations. It has been noticed that the Figure of Merit (*FOM*) becomes maximum for both the *C*-band and *S*-band folded filters with square corrugations. However, the Figure of Merit (*FOM*) becomes maximum for both the *C*-band and *S*-band inline filters with triangular corrugations. As a result, square corrugations work well for *C*-band filters and triangular corrugations work well for *S*-band filters. From this section, it has been concluded that periodic square and triangular corrugations have efficiently suppressed the second harmonic attenuation level below 35 dB with stopband bandwidth extended up to $2.56f_0$. The validation of the proposed filters has been performed by fabricating some of the prototypes and testing them experimentally. The measured responses are in good agreement with the simulated results.

Table 3.14. Comparison of all designed folded PCMLBFs with corrugations.

f_o (GHz)	*Type of corrugations*	ξ (dB/GHz)	*SBRL* (dB)	*SBW* (x f_0)	*RSB*	*SF*	*NCS*	*AF*	*FOM*
5.25	square	45	33	2.3	1.34	3.3	0.26	1	765.35
	triangular	33.75	32	2.28	1.30	3.2	0.28		501.43
2.5	square	90	39	2.4	1.32	3.9	0.12		3861
	triangular	90	35	2.56	1.36	3.5	0.12		3570

Table 3.15. Comparison of all designed inline PCMLBFs with corrugations.

f_o (GHz)	*Type of corrugations*	ξ (dB/GHz)	*SBRL* (dB)	*SBW* (x f_0)	*RSB*	*SF*	*NCS*	*AF*	*FOM*
5.25	square	90	35	2.15	1.3	3.5	0.14	1	2925
	triangular	67.5	33	2.3	1.31	3.3	0.28		1042.15
2.5	square	90	35	2.16	1.23	3.5	0.08		4843.12
	triangular	135	45	2.1	1.22	4.5	0.08		9264.38

3.16. Harmonic Suppression by Asymmetric perturbations

3.16.1 Study of Unit PCML Cell

From the previous section, it has been concluded that periodic corrugations can effectively suppress the harmonics. However, the performance of the filters has been degraded as the number of corrugations increases due to the additional cross-couplings between the closely placed adjacent slots. Moreover, the fabrication limitations are imposed if the gap between the slots is reduced. Subsequently, as an alternative approach, mode velocity normalization has been carried out by modulating the characteristic impedance of the propagating wave with the inclusion of rectangular perturbations along the width of the line, akin to the sinusoidal perturbations of [17]. Thus, the complexity of sinusoidal perturbations has been replaced by employing rectangular perturbations. Construction of the edge patterns has been initiated by segmenting the complete line into three equal sections of $l/3$, i.e., of wavelength $\lambda_{g0}/12$ where λ_{g0} is the guided wavelength at the center frequency (f_0). As shown in Figs. 3.181(a)-(d), rectangular perturbation has been introduced symmetrically in the edges of the middle section of the line.

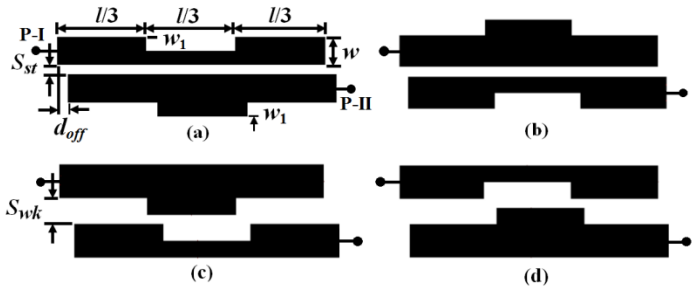

Fig. 3.181. Unit PCML cell with different types of perturbations: (a) Type-1, (b) Type-II, (c) Type-III, and (d) type-IV.

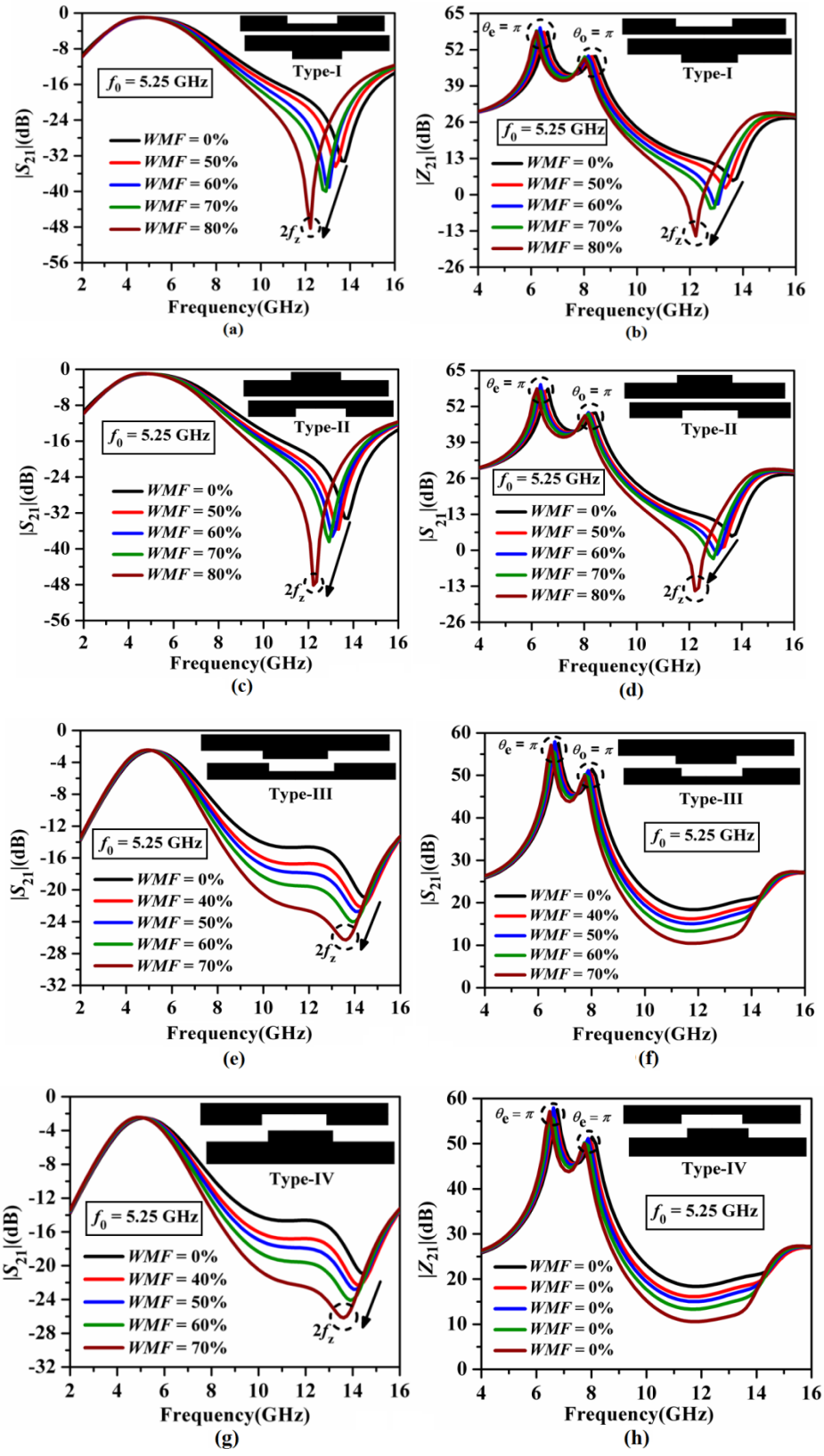

Fig. 3.182. Simulated resonance characteristics for $|S_{21}|$ (dB) and $|Z_{21}|$ (dB) of the PCML cell centered at f_0 = 5.25 GHz with the perturbation of (a)-(b) Type-I, (c)-(d) Type-II, (e)-(f) Type-III, and (g)-(h) Type-IV.

The perturbations introduced at the outer edges in Figs. 3.181(a)-(b) exhibit a strong coupling around the coupled edges, and the corresponding structures are labeled Type-I and Type-II. Similarly, Fig. 3.181(c)-(d) depicts the weak coupling geometry with perturbed coupled-edges, and the corresponding structures are designated as Type-III and Type-IV. Figs. 3.182(a)-(h) shows the effects of the width modulation factor, defined as $WMF = w_1/w$ (%), on the resonance characteristics of $|S_{21}|$ (dB) and $|Z_{21}|$ (dB) for various structures. It has been observed that the inherent transmission zero ($2f_z$) of the unit PCML cell has been shifted to a lower frequency region due to the modulation of the width by asymmetric perturbations with incremental values of *WMF*. Moreover, the odd-mode resonance peak of $|Z_{21}|$ (dB) has been shifted to a lower frequency region than that of the even-mode, resulting in modal phase velocity compensation. Better surface current distributions for a unit PCML cell with different types of perturbations are plotted in Figs. 3.183(a)-(d) to better understand the effects of perturbations. For all the cases, it has been observed that the current vectors are concentrated densely through the narrow segment of the coupled lines, resulting in a slow-wave effect for the signal. Accordingly, the pair of unit PCML cells with perturbations of different types has been taken care of to achieve the desired characteristics, elaborated in the next section.

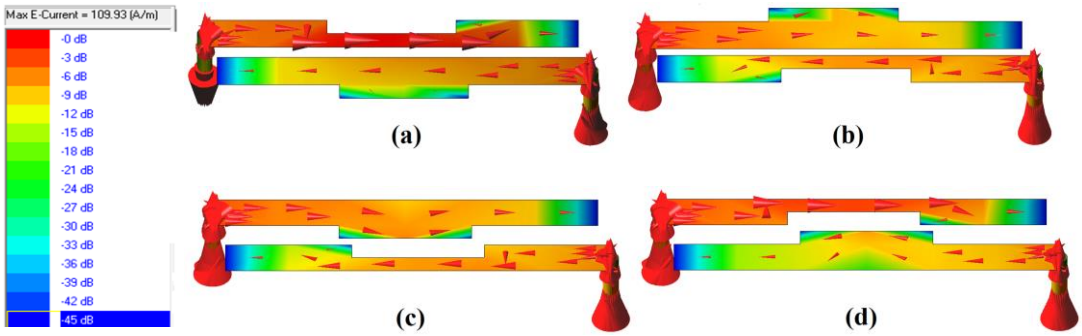

Fig. 3.183. Distribution of surface current vectors for a unit PCML cell with different perturbations: (a) Type-I, (b) Type-II, (c) Type-III, and (d) Type-IV.

3.16.2. Study of Pair of PCML Cells with Perturbations

The concept of rectangular perturbations has been incorporated into the pair of PCML cells to achieve the transmission zero for harmonic suppression. The layouts of the strongly coupled first-order folded filter structures with perturbations as Type I, denoted by 1, and Type II, denoted by 2, are shown in Fig. 3.184(a)-(d). Four possible cases have been considered and

named as Case 1 (1-1), Case 2 (2-2), Case 3 (1-2) and Case 4 (2-1). However, Case 3 and Case 4 are identical. Similarly, Figs. 3.185(a)-(d) depicts the layouts of weakly coupled first-order folded filter structures with Type III, denoted by 3, and Type IV, denoted by 4. Four possible cases have been considered and called Case 5 (3-3), Case 6 (4-4), Case 7 (3-4) and Case 8 (4-3). In this case, too, Case 7, and Case 8 are identical. Figs. 3.186(a)-(b) show a comparison of $|S_{21}|$ (dB) plots for all of these cases with WMF = 50%.

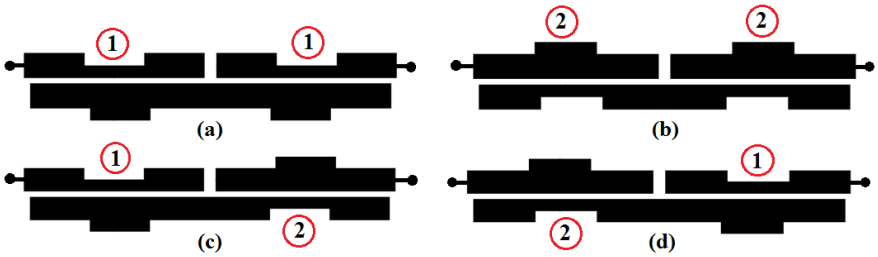

Fig. 3.184. Possible combinations of pair of PCML cells with perturbations: (a) Case 1, (b) Case 2, (c) Case 3, and (d) Case 4. Case 3 and Case 4 are identical.

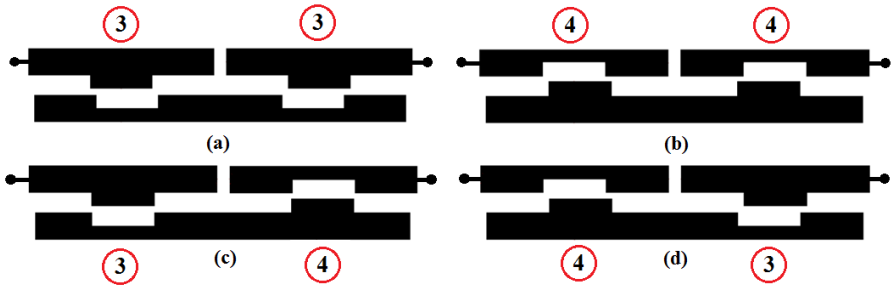

Fig. 3.185. Possible combinations of pair of PCML cells with perturbations: (a) Case 5, (b) Case 6, (c) Case 7, and (d) Case 8. Case 7 and Case 8 are identical.

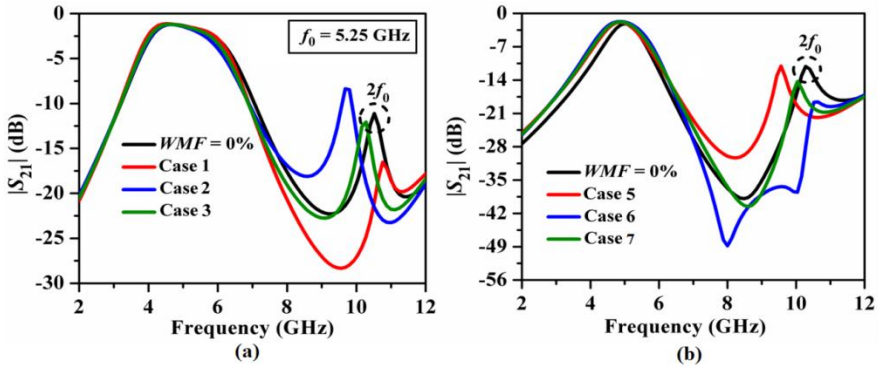

Fig. 3.186. Comparison of simulated $|S_{21}|$ (dB) plots for (a) Case 1, Case 2, and Case 3, (b) Case 5, Case 6 and Case 7.

It has been observed that Case 1 and Case 6 have exhibited maximum suppression of second harmonic attenuation level. As a result, by varying the values of WMF, the study has been

extended further in Figs. 3.187(a)-(b) for Case 1 and Case 6, respectively. It has been revealed that the second harmonic resonance peak ($2f_0$) has been suppressed completely for *WMF* = 80% for both Case 1 and Case 6. Following that, Figs. 3.188(a)-(b) show the surface current distribution profile for the first-order folded filter structure at f_0 = 5.25 GHz, with *WMF* = 50% in Case 1 and Case 6, respectively. It has been observed that the current vectors are concentrated strongly throughout the structure due to the passband response.

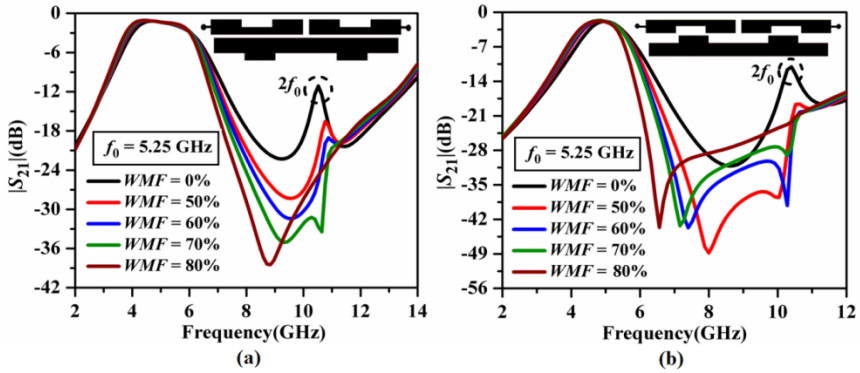

Fig. 3.187. Parametric study for a pair of PCML cells with of Case 1 (strong coupled), (b) Case 6 (weak coupled).

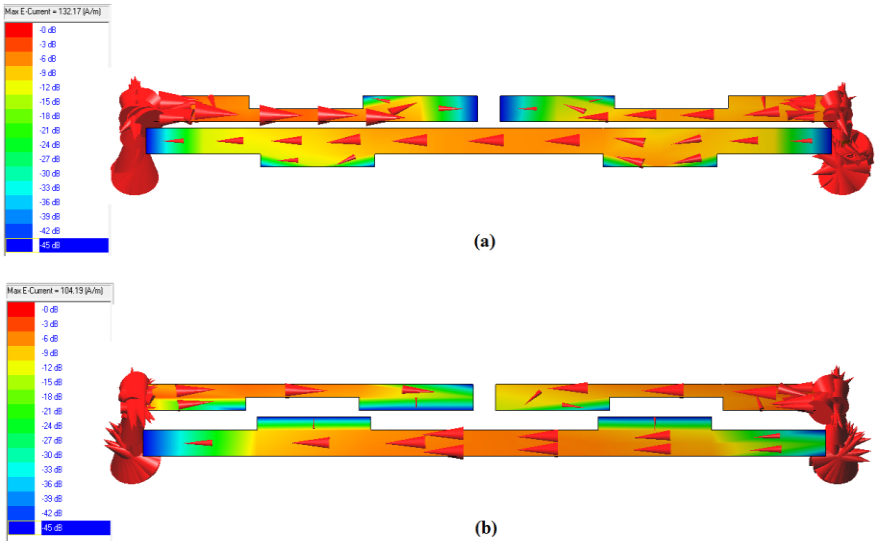

Fig. 3.188. Surface current distribution for a pair of PCML cells with (a) Case 1 (strong coupled), and (b) Case 6 (week coupled) at f_0 = 5.25 GHz.

It can be concluded from this section that the asymmetric perturbations can effectively suppress the second harmonic's attenuation level for a particular value of *WMF*. Thus, the study has been investigated further for the third-order folded and inline filters in the next section.

3.16.3 Study of Third-Order Folded PCMLBF with Perturbations

Four different cases of perturbations have been studied by choosing Type 1 and Type 2 as input and output ports. As a result, 16 perturbed filter combinations with middle resonators replaced by Type III and Type IV are shown in Figs. 3.189-3.192.

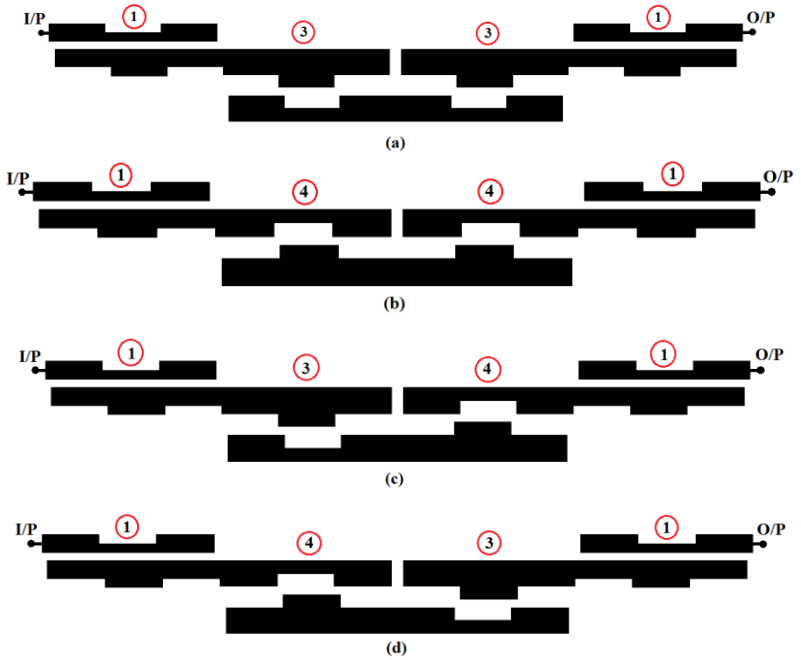

Fig. 3.189. Layouts of third-order folded bandpass filter with different combinations of asymmetric perturbations: (a) 1-3-3-1, (b) 1-4-4-1, (c) 1-3-4-1, and (d) 1-4-3-1.

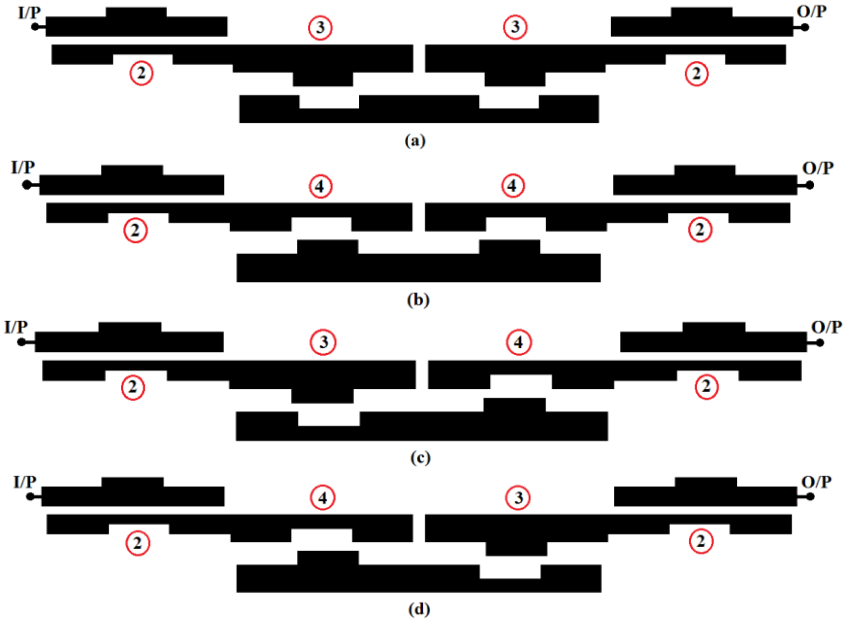

Fig. 3.190. Layouts of third-order folded bandpass filter with different combinations of asymmetric perturbations: (a) 2-3-3-2, (b) 2-4-4-2, (c) 2-3-4-2, and (d) 2-4-3-2.

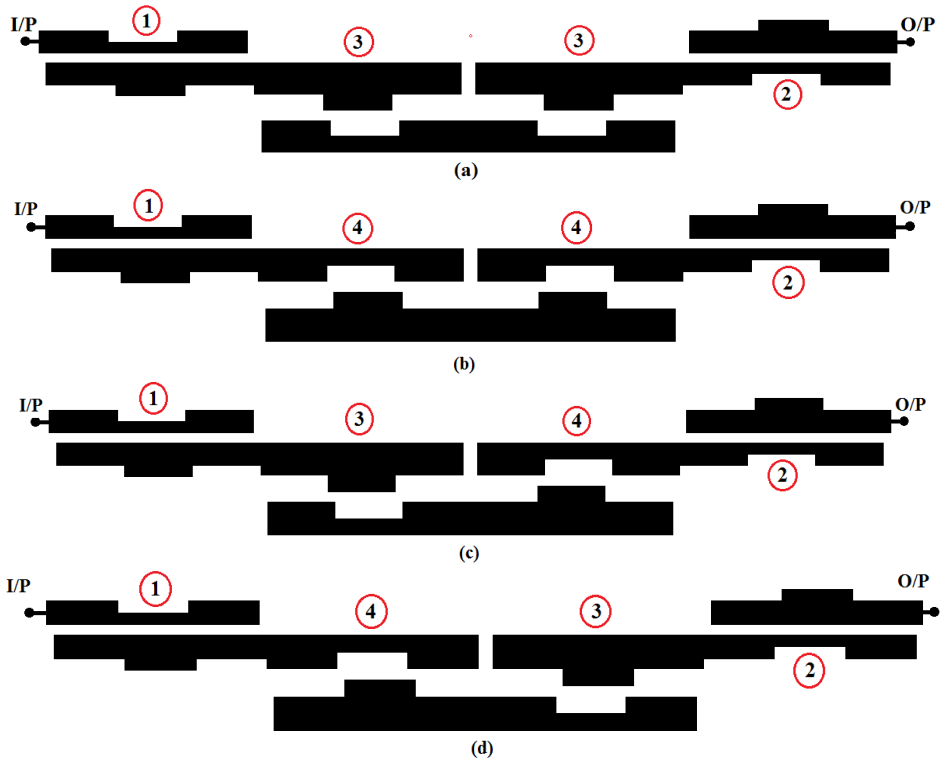

Fig. 3.191. Layouts of third-order folded bandpass filter with different combinations of asymmetric perturbations: (a) 1-3-3-2, (b) 1-4-4-2, (c) 1-3-4-2, and (d) 1-4-3-2.

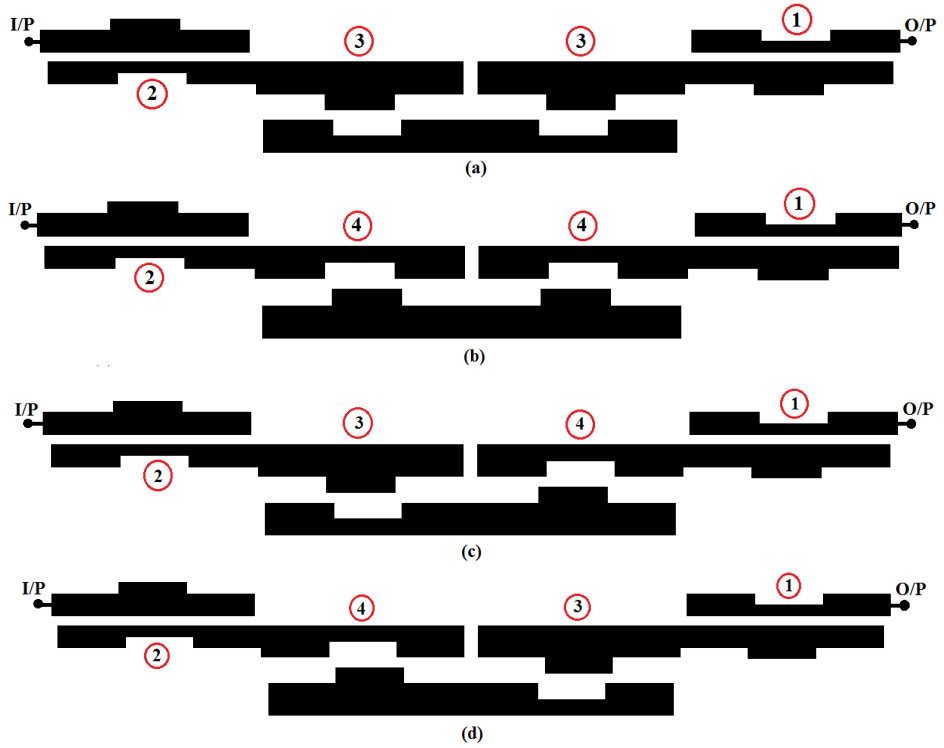

Fig. 3.192. Layouts of third-order folded bandpass filter with different combinations of asymmetric perturbations: (a) 2-3-3-1, (b) 2-4-4-1, (c) 2-3-4-1, and (d) 2-4-3-1.

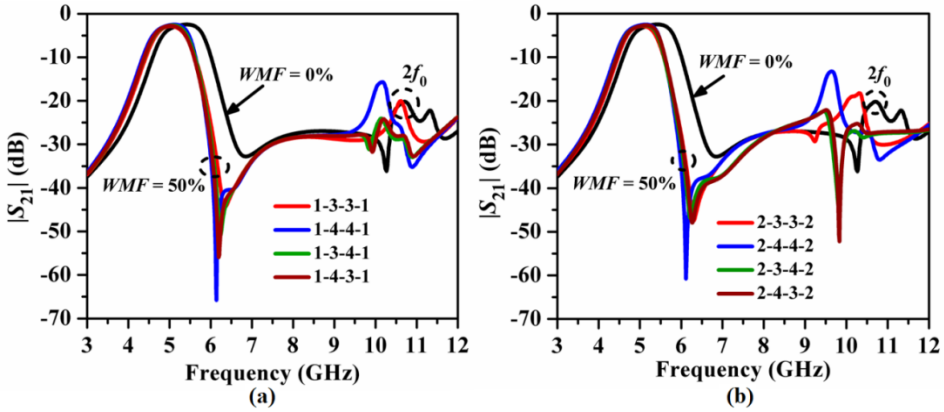

Fig. 3.193. Simulated Parametric study for a third-order folded bandpass filter centered as 5.25 GHz with asymmetric perturbations: (a) input and output port as Type I, and (b) input and output port as Type II.

Figs. 3.193(a)-(b) show a comparison of $|S_{21}|$ (dB) plots for different perturbation combinations with the same input and output ports, either Type I or Type II. It has been observed that the combinations 1-4-3-1 and 2-4-3-2 have exhibited the maximum harmonic suppression. As a result, Figs. 3.194(a)-(b) compare $|S_{21}|$ (dB) plots for various combinations of Type 1 and Type II input and output ports. It has been observed that the combinations 1-3-4-2 and 2-4-3-1 have exhibited the maximum harmonic suppression. Subsequently, all these best cases have been compared in Fig. 3.195(a) and it has been concluded that the combination 1-3-4-2 has exhibited the maximum suppression of harmonic attenuation level. This optimum case 1-3-4-2 has been studied further in Fig. 3.195(b) by varying the value of *WMF* and the optimum value of *WMF* has been chosen as 50% as it has exhibited the best harmonic suppression performance.

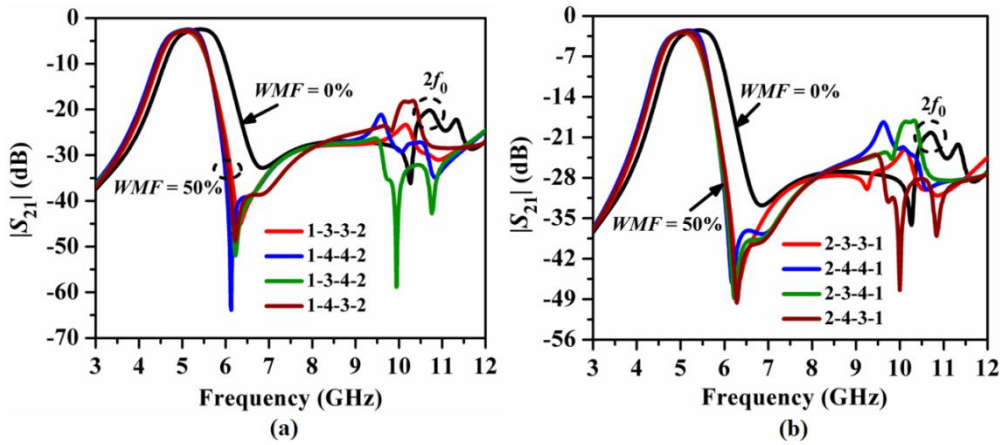

Fig. 3.194. Simulated parametric study for a third-order folded bandpass filter centered as 5.25 GHz with asymmetric perturbations: (a) input port as 1 and output port as 2, and (b) input port as 2 and output port as 1.

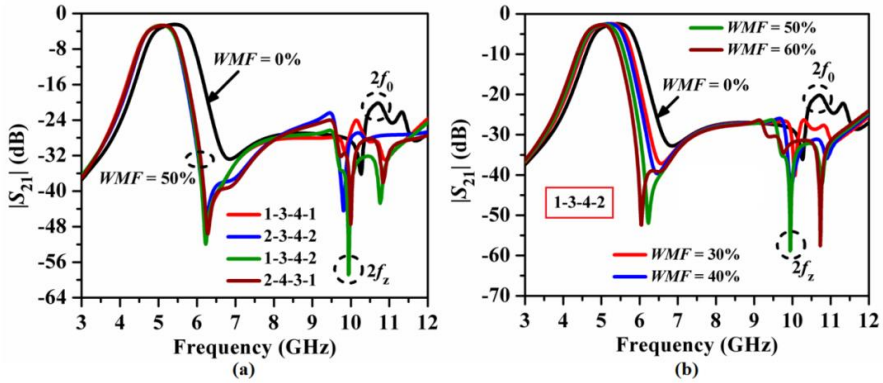

Fig. 3.195. (a) Comparison of simulated $|S_{21}|$ (dB) plots of all best cases of asymmetric perturbations for a third-order folded bandpass filter centered as 5.25 GHz, and (b) simulated parametric study for 1-3-4-2 combination.

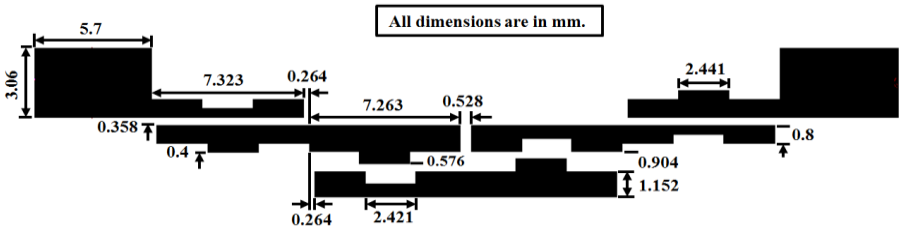

Fig. 3.196. Optimized layout for the third-order bandpass filter centered at f_0 = 5.25 GHz with 1-3-4-2 type of asymmetric perturbations.

Finally, the dimensions of the optimized folded filter based on the 1-3-4-2 case including feed ports have been obtained in Fig. 3.196. The overall size of the filter is 41.63 mm × 6.63 mm, i.e., 275.84 mm^2 or 1.34λ_g × 0.21λ_g. Accordingly, size reductions of 58.3% have been obtained over the conventional filter.

3.16.3.1. Fabricated Prototype

Fig. 3.197 shows the photograph of the fabricated prototype on FR4 substrate material.

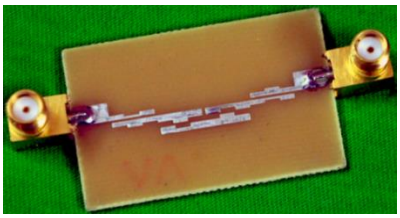

Fig. 3.197. Fabricated prototype of the third-order folded bandpass filter with asymmetric perturbation of 1-3-4-2 combination [32].

3.16.3.2. Comparison of EM simulation vs. Measurement Results

Figs. 3.198(a)-(b) shows a comparison of the simulated and measured *S*-parameter plots for the fabricated filter. The experimental procedure is same as elaborated in 3.14.4.1.

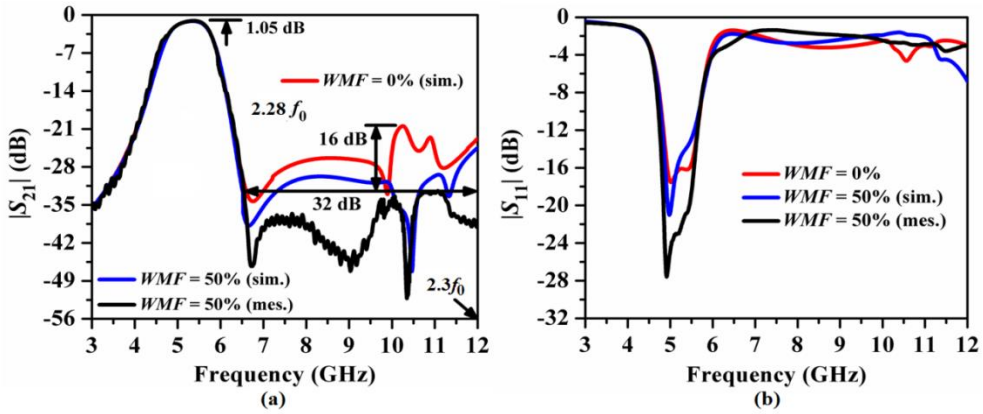

Fig. 3.198. Comparison between the simulated and measured *S*-parameters plots for the third-order folded bandpass filter with asymmetric perturbation of 1-3-4-2 combination: (a) $|S_{21}|$ (dB) and (b) $|S_{11}|$ (dB) [32].

According to Fig. 3.198(a), a stopband bandwidth of up to $4.8f_0$ with a rejection level of 32 dB was obtained in the measurement for the $|S_{21}|$ (dB) plot. Moreover, the second harmonic attenuation level has been degraded by 16 dB compared to the folded filter without perturbation. The skirt characteristics of the fabricated filter have been improved greatly by the introduction of the sharp transmission zero at the upper passband edge at 6.7 GHz with the attenuation level of 46 dB. The measured insertion loss has been recorded as 1.05 dB and the return loss has been recorded as 28 dB from Fig. 3.198(b). Figs. 3.199(a)-(b) illustrate the surface current distribution for the final folded filter with perturbations at f_0 = 5.25 GHz and $2f_0$ = 10.5 GHz. It has been clearly observed that the surface current reaches the output port with large strength for the passband; however it becomes minimum for the stopband due to the suppression of harmonics. Following that, the research was expanded for the *S*-band filter with a center frequency of 2.5 GHz, as shown in Figs. 3.200(a)-(b) for Type I and Type II as both input and output ports, and in Figs. 3.201(a)-(b) for Type I as input port with Type II as output port and vice versa. The best combinations with respect to maximum harmonics suppression have become 1-4-4-1 and 2-3-4-2, 1-3-4-2 and 2-4-3-1 respectively.

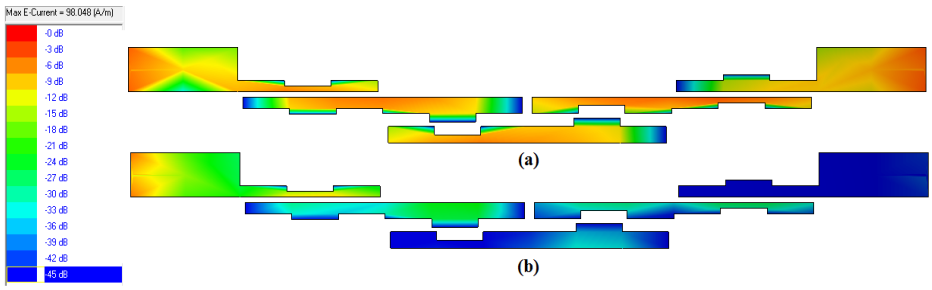

Fig. 3.199. Surface current distribution for the third-order folded bandpass filter with asymmetric perturbation of 1-3-4-2 combination at (a) f_0 = 5.25 GHz, and (b) $2f_0$ = 10.5 GHz.

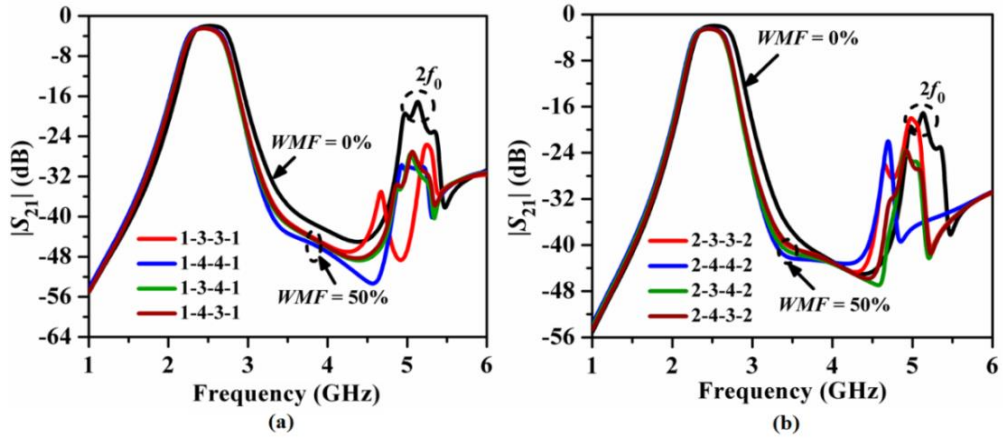

Fig. 3.200. Simulated parametric study for the third-order folded bandpass filter centered as 2.5 GHz with asymmetric perturbations: (a) input and output port as 1, and (b) input and output port as 2.

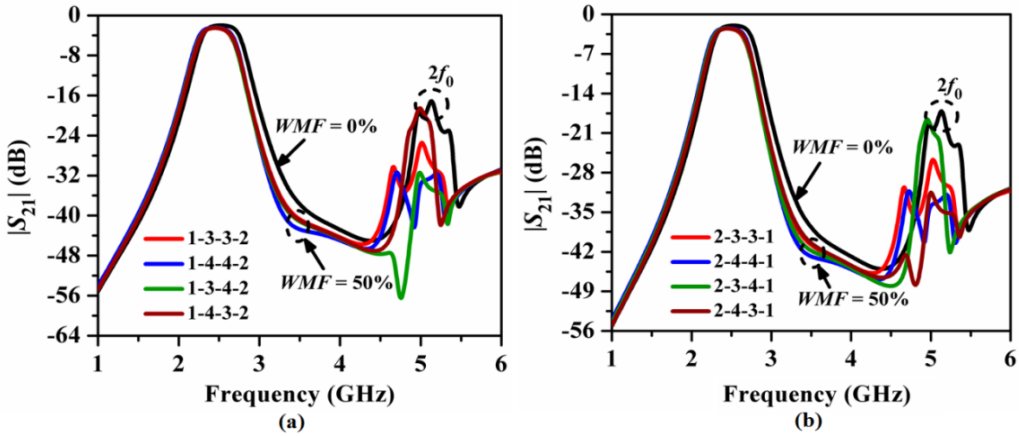

Fig. 3.201. Simulated parametric study for the third-order folded bandpass filter centered as 2.5 GHz with asymmetric perturbations: (a) input port as 1 and output port as 2, and (b) input port as 2 and output port as 1.

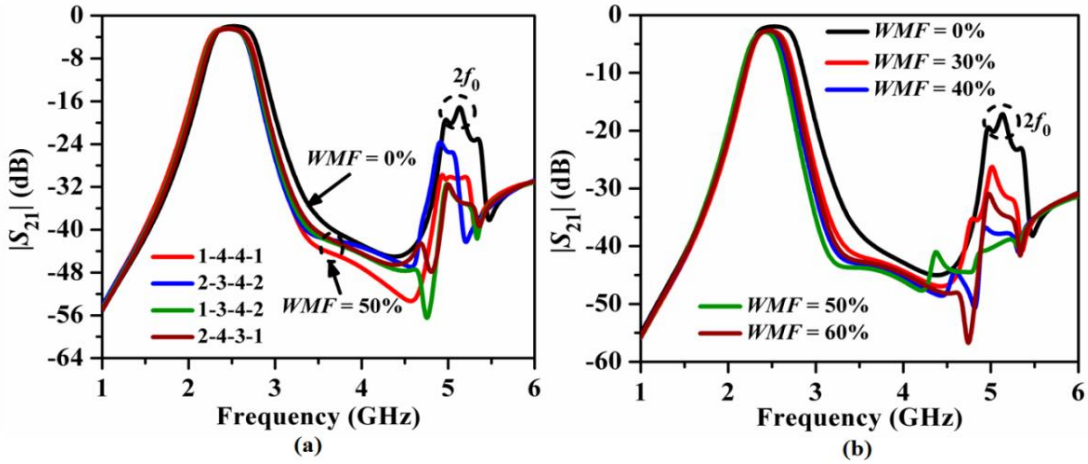

Fig. 3.202. (a) Comparison of simulated $|S_{21}|$ (dB) plots of all best cases from the parametric study, and (b) comparison of $|S_{21}|$ (dB) plots for different values of *WMF* for 1-3-4-2 case.

Subsequently, all the best cases have been compared in Fig. 3.202 (a), and it has been revealed that the combination 1-3-4-2 exhibits the maximum harmonic suppression. Thus, the parametric study for such a case has been carried out in Fig. 3.202(b) for different values of *WMF* to determine the optimum dimension. Maximum harmonic suppression was obtained with *WMF* = 50% for the 1-3-4-2 case, as shown in Fig. 3.202(b), and the dimensions of the final folded filter with perturbation were optimized as a result.

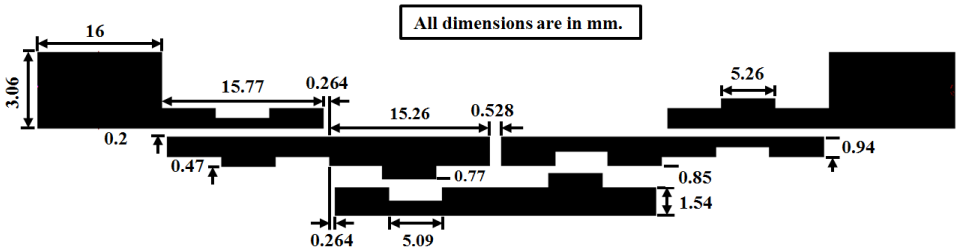

Fig. 3.203. Optimized layout for the third-order bandpass filter centered at f_0 = 2.5 GHz with 1-3-4-2 type of asymmetric perturbations.

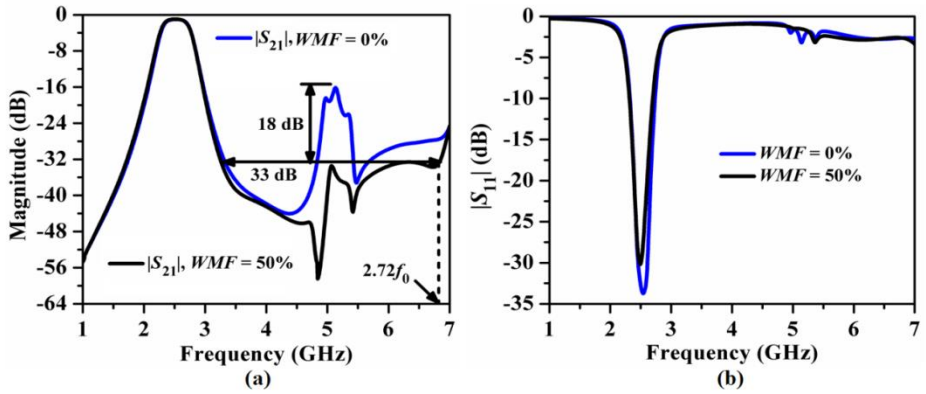

Fig. 3.204. Comparison of simulated *S*-parameters plots for the optimized third-order folded bandpass filter with asymmetric perturbation of 1-3-4-2 combination (*WMF* = 50%) and without perturbation: (a) $|S_{21}|$ (dB), and (b) $|S_{11}|$ (dB).

The final optimized layout is depicted in Fig. 3.203. The overall size of the filter is 95.11 mm × 7.2 mm, i.e., 684.44 mm^2 or 1.39λ_g × 0.11λ_g. Accordingly, size reductions of 47% have been obtained over the conventional filter. Figs. 3.204(a)-(b) show a comparison of the simulated *S*-parameter plots for the designed folded filter with perturbation. It has been observed from Fig. 3.204(a) that a stopband bandwidth up to 2.72f_0 with a rejection level of 33 dB has been obtained in simulation. Two sharp transmission zeros at 4.8 GHz and 5.5 GHz have occurred at attenuation levels of 59 dB and 45 dB, respectively. This justifies the ability of the final filter to generate transmission zeros in the stopband due to the asymmetric

perturbation. Fig. 3.205 illustrates the surface current distribution of the folded filter with perturbation. Surface current is strongly distributed from the input port to the output port at f_0 = 5.25 GHz due to the passband response, whereas less current reaches the output port at f_0 = 10.5 GHz due to harmonic suppression in the stopband.

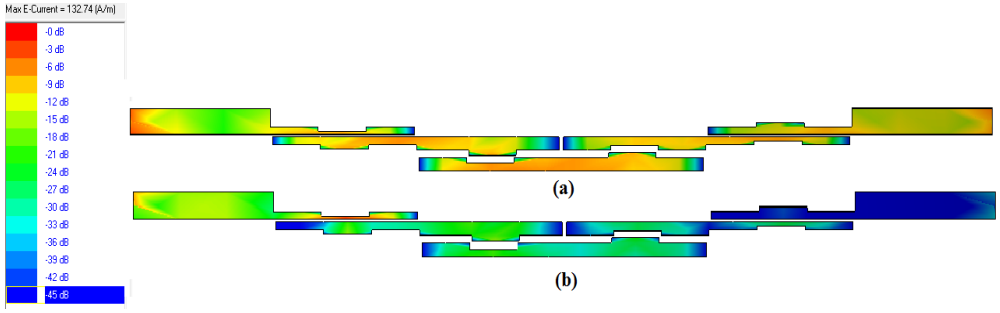

Fig. 3.205. Surface current distribution for the third-order folded bandpass filter with 1-3-4-2 case: (a) f_0 = 2.5 GHz and (b) $2f_0$ = 5.0 GHz.

3.16.4. Study of Third-Order Inline PCMLBF with Perturbations

The study of asymmetric perturbation has been carried out for third-order inline filters. Accordingly, 16 possible combinations of perturbed inline filters have been constructed with middle coupled-resonators replaced by Type III and Type IV and end coupled-resonators replaced by Type I and Type II. Figs. 3.206(a)-(d) depict layouts with Type I input and output ports, Figs. 3.207(a)-(d) depict layouts with Type II input and output ports, Figs. 3.208(a)-(d) depict layouts with Type I as input and Type II as an output port, and Figs. 3.209(a)-(d) depict layouts with Type II as input and Type I as an output port. From the corresponding parametric studies of all the combinations as highlighted in Fig. 3.210-Fig. 3.211, it has been revealed that maximum suppression of harmonics has occurred for 1-3-4-1, 2-3-4-2, 1-4-3-2, and 3-2-4-1 combinations. As a result, Fig. 3.212(a) compares all such best combinations, and it has been discovered that 2-3-4-1 has the highest suppression of the harmonic's attenuation level. Finally, the parametric study of the 2-3-4-1 case for different values of *WMF* has been performed in Fig. 3.212(b) and it has been revealed that maximum suppression of harmonic attenuation level has been obtained for *WMF* = 40%. The optimized layout of the third-order inline filter with 2-3-4-1 combination and *WMF* = 40% is shown in Fig. 3.213. The overall size of the filter is 41.75 mm × 4.57 mm i.e., 190.8 mm^2 or 1.34λ_g × 0.15λ_g. Accordingly, size reductions of 71% have been obtained over the conventional filter.

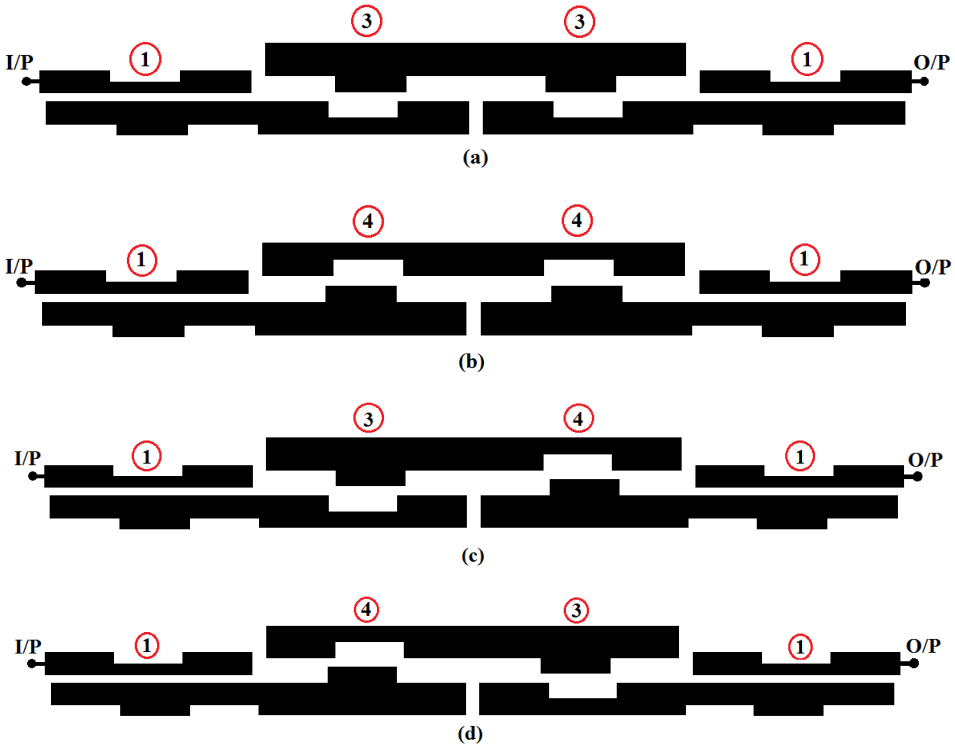

Fig. 3.206. Layouts of third-order inline bandpass filter with different combinations of asymmetric perturbations: (a) 1-3-3-1, (b) 1-4-4-1, (c) 1-3-4-1, and (d) 1-4-3-1.

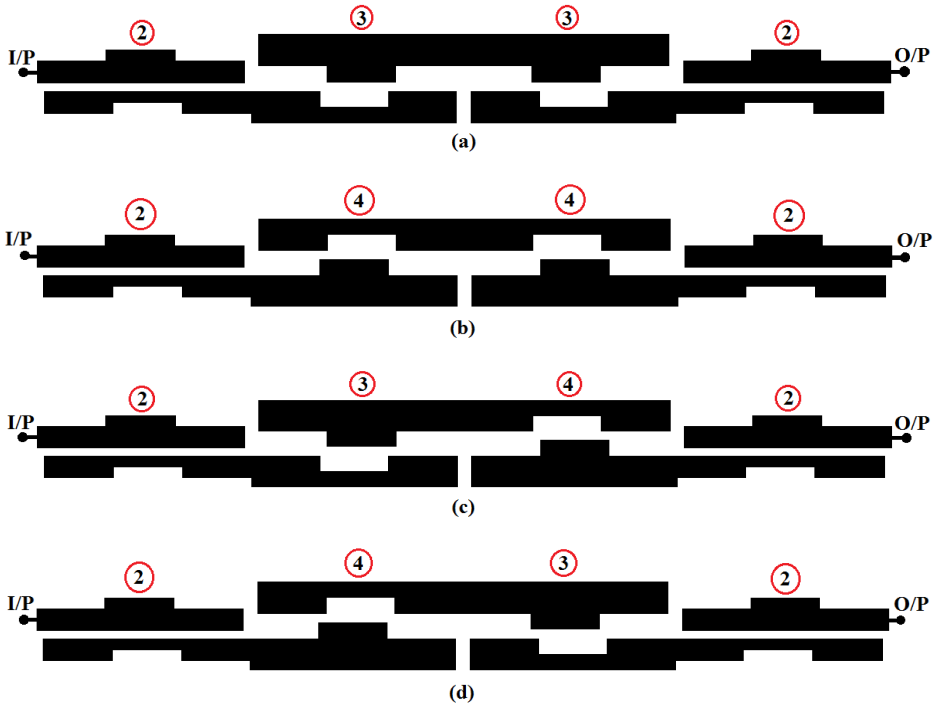

Fig. 3.207. Layouts of third-order inline bandpass filter with different combinations of asymmetric perturbations: (a) 2-3-3-2, (b) 2-4-4-2, (c) 2-3-4-2, and (d) 2-4-3-2.

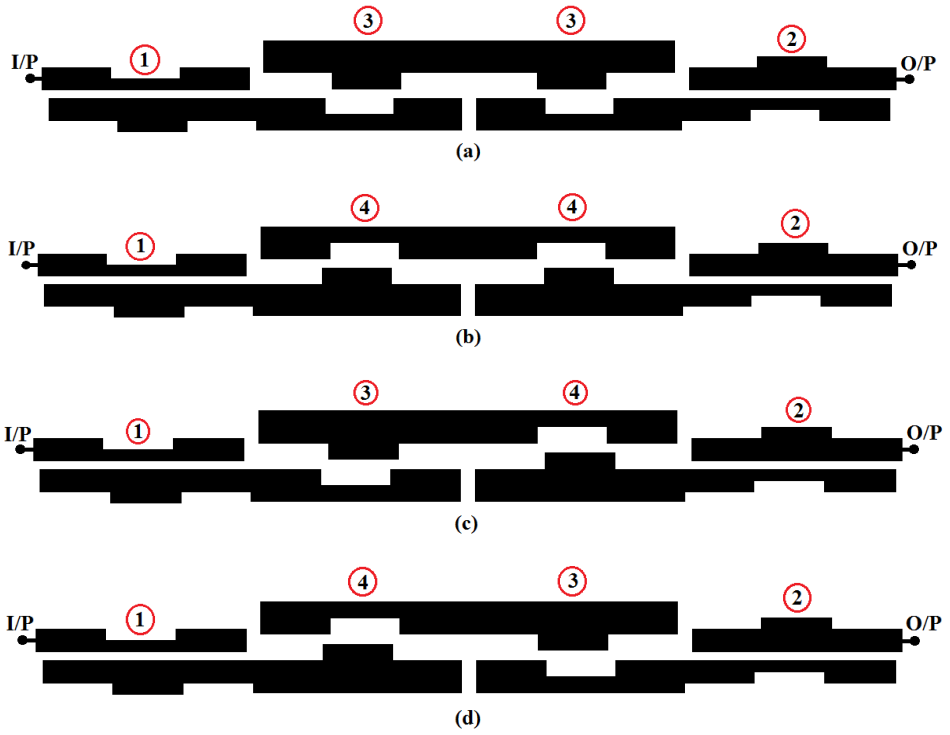

Fig. 3.208. Layouts of third-order inline bandpass filter with different combinations of asymmetric perturbations: (a) 1-3-3-2, (b) 1-4-4-2, (c) 1-3-4-2, and (d) 1-4-3-2.

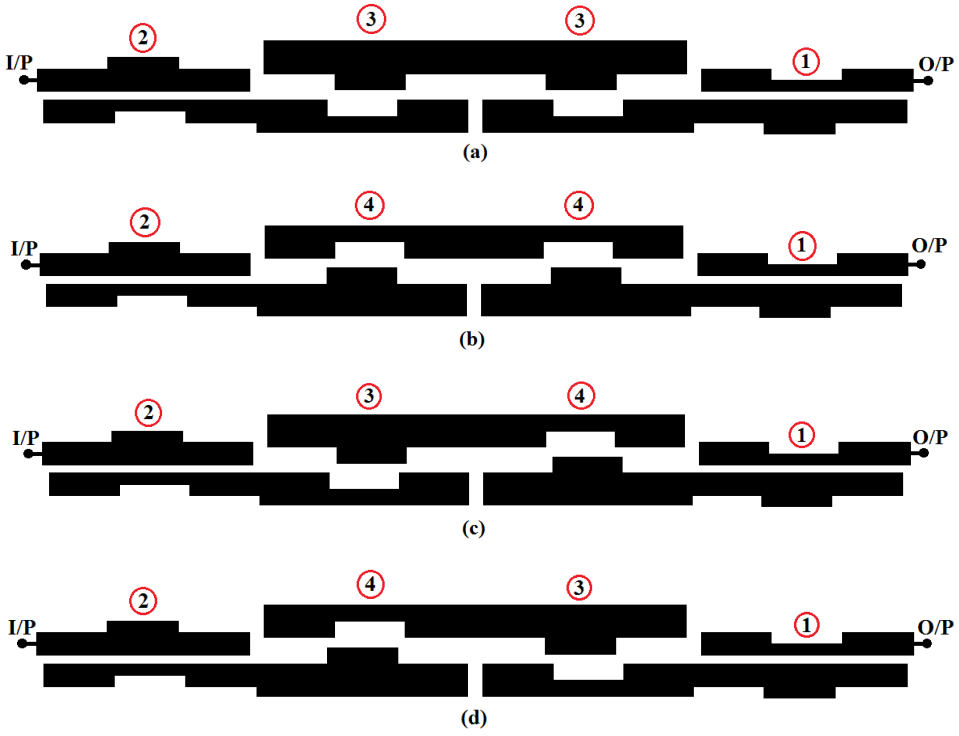

Fig. 3.209. Layouts of third-order inline bandpass filter with different combinations of asymmetric perturbations: (a) 2-3-3-1, (b) 2-4-4-1, (c) 2-3-4-1, and (d) 2-4-3-1.

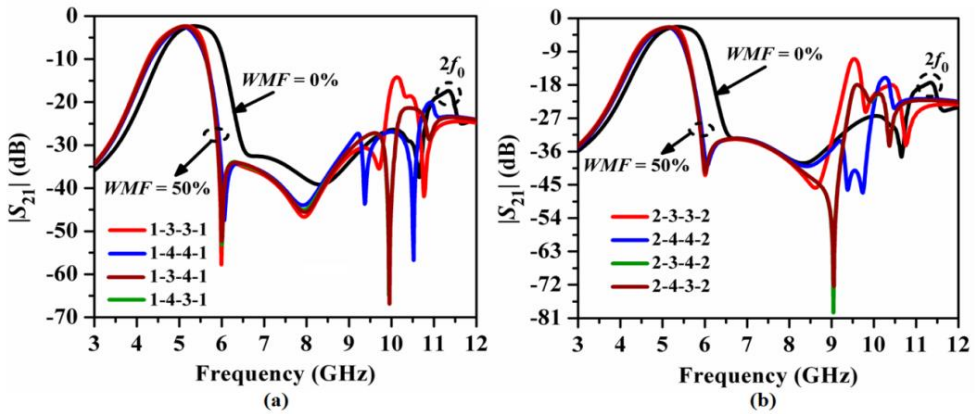

Fig. 3.210. Simulated parametric study for the third-order folded bandpass filter centered as 5.25 GHz with asymmetric perturbations: (a) input and output port as 1 and (b) input and output port as 2.

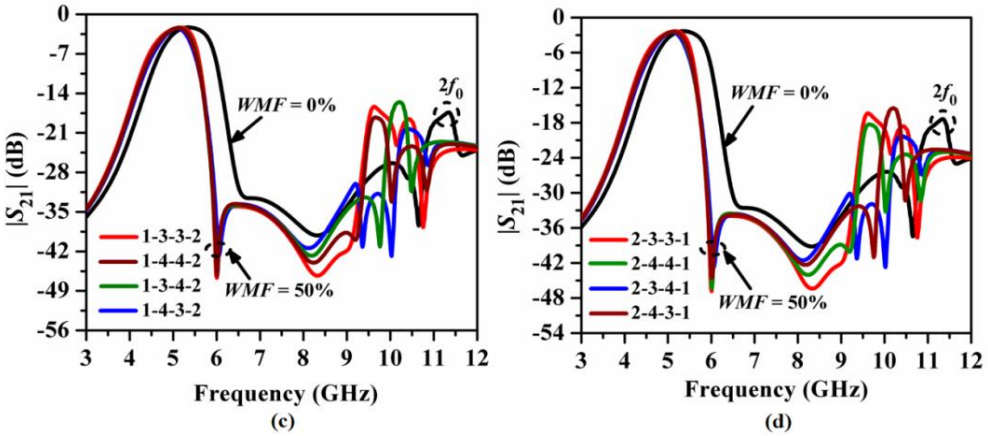

Fig. 3.211. Simulated parametric study for the third-order folded bandpass filter centered as 5.25 GHz with asymmetric perturbations: (a) input port as 1 and output port as 2, and (b) input port as 2 and output port as 1.

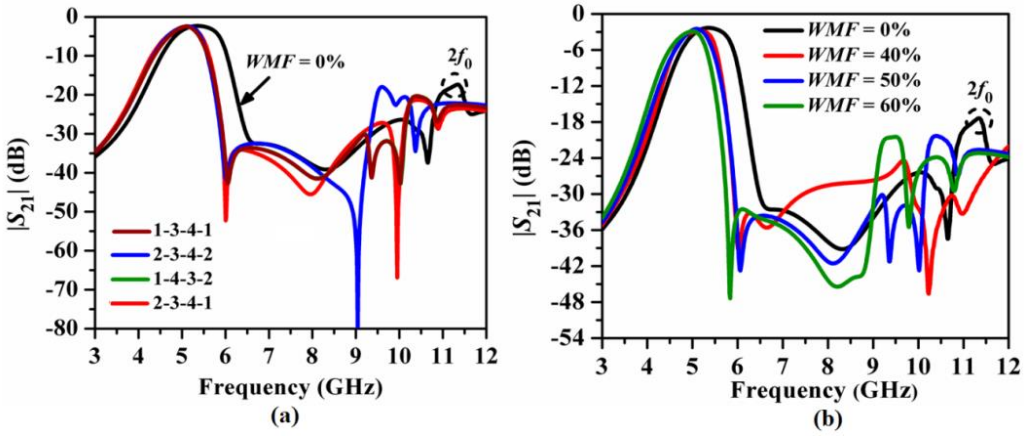

Fig. 3.212. (a) Comparison of simulated $|S_{21}|$ (dB) plots of all best cases of asymmetric perturbations for a third-order inline bandpass filter centered as 5.25 GHz, and (b) parametric study for 2-3-4-1 combination.

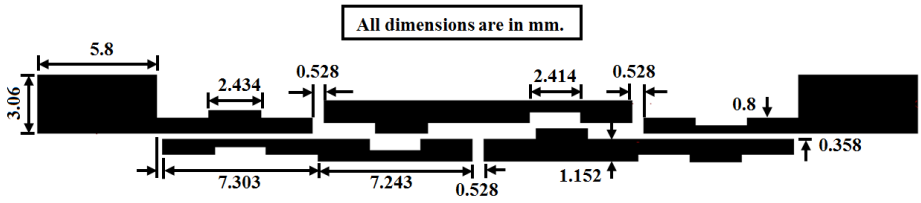

Fig. 3.213. Optimized layout for the third-order bandpass inline filter centered at f_0 = 5.25 GHz with 2-3-4-1 type of asymmetric perturbations.

3.16.4.1. Fabricated Prototype

Fig. 3.214 shows the fabricated prototype of the final inline filter with perturbation.

Fig. 3.214. Fabricated prototype of the third-order inline bandpass filter with asymmetric perturbation of 2-3-4-1 combination [33].

3.16.4.2. Comparison of EM simulation vs. Measurement Results

Figs. 3.215(a)-(b) show a comparison of the simulated and measured *S*-parameter plots for the designed inline filter with perturbation. The experimental procedure has been carried out in the similar way of 3.14.4.1. According to Fig. 3.215(a), a stopband with a rejection level of 33 dB up to 2.4f_0 was recorded in the measurement. Two sharp transmission zeros at 6.3 GHz and 10.6 GHz with attenuation levels of 44 dB and 55 dB have been obtained.

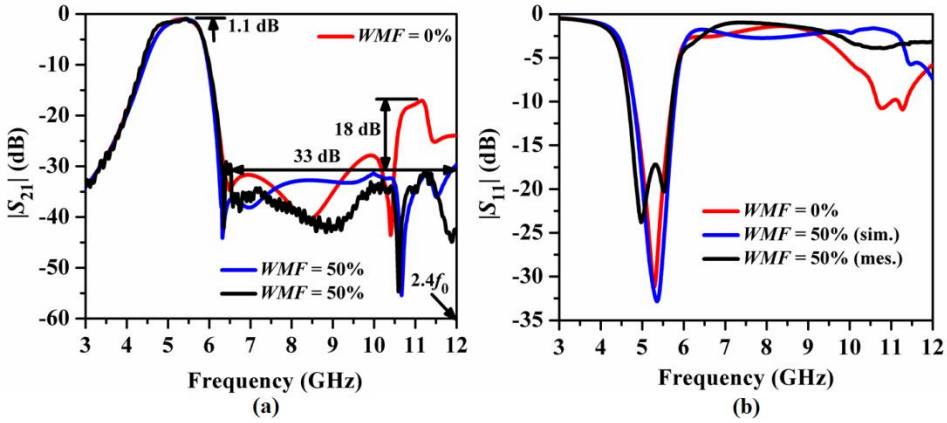

Fig. 3.215. Comparison between the simulated and measured *S*-parameters plots for the third-order inline bandpass filter with asymmetric perturbation of 2-3-4-1 combination: (a) $|S_{21}|$ (dB) and (b) $|S_{11}|$ (dB) [33].

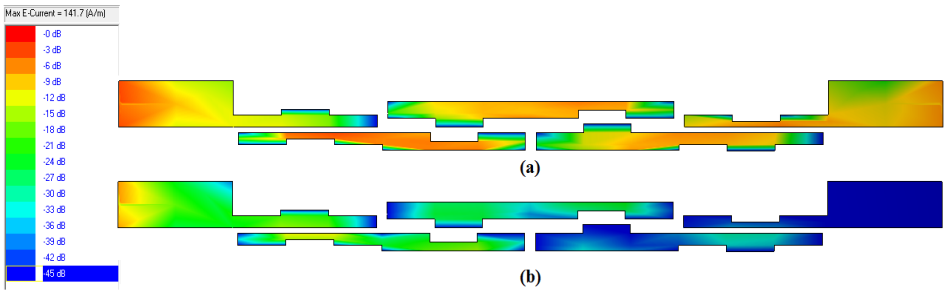

Fig. 3.216. Surface current distribution for the third-order inline bandpass filter with 2-3-4-1 case: (a) f_0 = 5.25 GHz and (b) $2f_0$ = 10.5 GHz.

Thus, the skirt characteristics of the filter have been improved significantly over the folded filter without perturbation. In addition, the second harmonic's attenuation level has been degraded by 18 dB by the perturbation. The measured insertion loss has been recorded as 1.1 dB. Moreover, maximum return loss has been measured as 23 dB from Fig. 3.215(b). Figs. 3.216(a)-(b) show the surface current distribution for the inline filter with perturbation at f_0 = 5.25 GHz and $2f_0$ = 10.5 GHz, respectively. It has been revealed that the surface current distributes strongly from the input port to the output port due to the passband and very weakly due to the harmonic suppression in the stopband.

To justify the effectiveness of the asymmetric perturbation on the suppression of harmonics attenuation level, the study has been carried out further for an *S*-band inline filter centered at 2.5 GHz. According to the parametric studies shown in Figs. 3.217(a)-(b) and Figs. 3.218(a)-(b), the combinations 1-3-4-1, 2-3-3-2, 1-4-3-2, and 2-3-4-1 have the greatest suppression of the second harmonic's attenuation levels. As a result, all such best cases were further compared in Fig. 3.219(a), and the combination 2-3-4-1 was chosen as the best case among other best cases. Finally, the parametric study for different values of *WMF* has been carried out in Fig. 3.219(b). It has been revealed that maximum harmonic suppression has occurred with *WMF* = 60% for the 2-3-4-1 combination. Accordingly, the optimized dimensions of the final inline filter with perturbation have been obtained as depicted in Fig. 3.220. The overall size of the filter is 94.58 mm × 4.9 mm, i.e., 463.44 mm^2 or 1.39λ_g × 0.07λ_g. Accordingly, size reductions of 64% have been obtained over the conventional filter. The comparison of the simulated *S*-parameter plots for the third-order inline filters with and without perturbation is shown in Figs. 3.221(a)-(b). It has been observed from Fig. 3.221(a) that a stopband with a rejection level of 33 dB up to 2.4f_0 has been obtained.

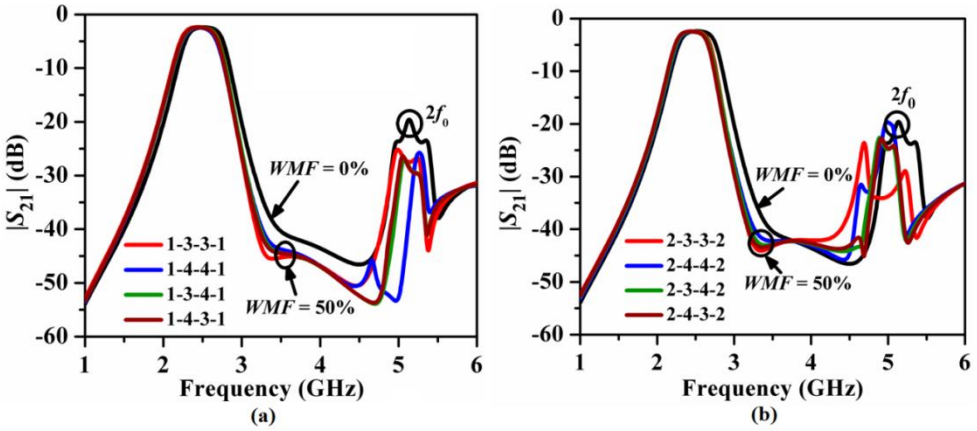

Fig. 3.217. Simulated parametric study for the third-order inline bandpass filter centered as 2.5 GHz with asymmetric perturbations: (a) input and output port as 1, and (b) input and output port as 2.

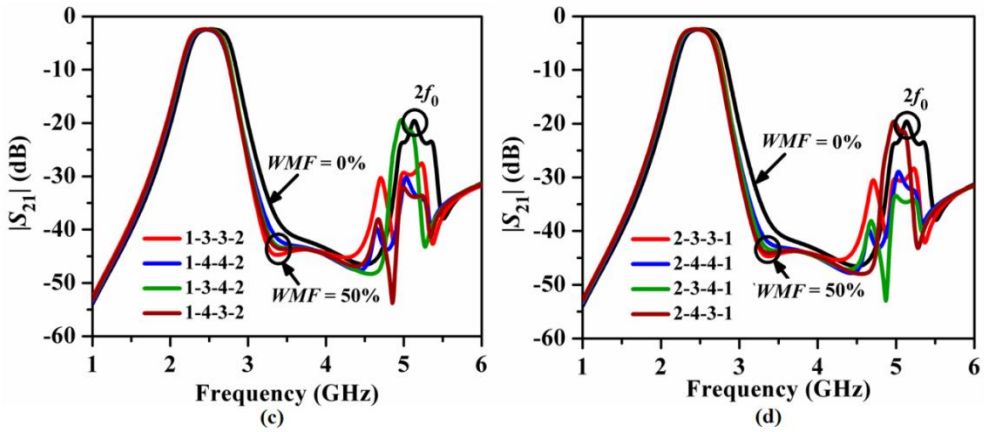

Fig. 3.218. Simulated parametric study for the third-order inline bandpass filter centered as 2.5 GHz with asymmetric perturbations: (a) input port as 1 and output port as 2, and (b) input port as 2 and output port as 1.

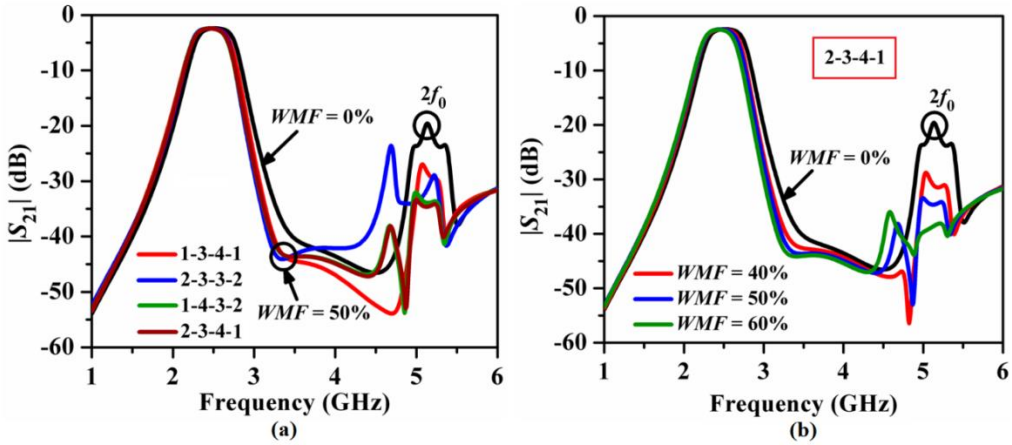

Fig. 3.219. (a) Comparison of simulated $|S_{21}|$ (dB) plots of all best cases of asymmetric perturbations for a third-order inline bandpass filter centered as 2.5 GHz, and (b) parametric study for 2-3-4-1 combination.

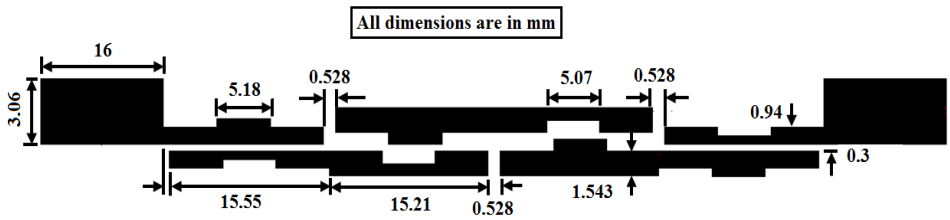

Fig. 3.220. Optimized layout for the third-order bandpass inline filter centered at f_0 = 2.5 GHz with 2-3-4-1 type of asymmetric perturbations.

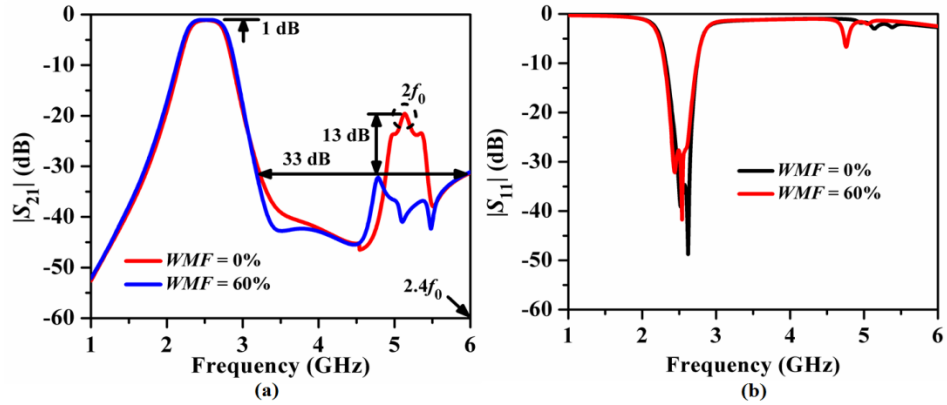

Fig. 3.221. Simulated *S*-parameters plots for the optimized third-order inline bandpass filter with asymmetric perturbation of 2-3-4-1 combination: (a) $|S_{21}|$ (dB), and (b) $|S_{11}|$ (dB) .

The skirt characteristics of the filter have been improved significantly over the folded filter without perturbation due to the sharp slope of the transition at the upper passband edge. Moreover, transmission zeros have occurred in the stopband, resulting in an improvement in the stopband performance of the filter. In addition, the second harmonic's attenuation level has been degraded by 13 dB by the perturbation over the filter without perturbation. The passband insertion loss becomes 1.0 dB and the return loss becomes more than 30 dB (Fig. 3.221(b)).

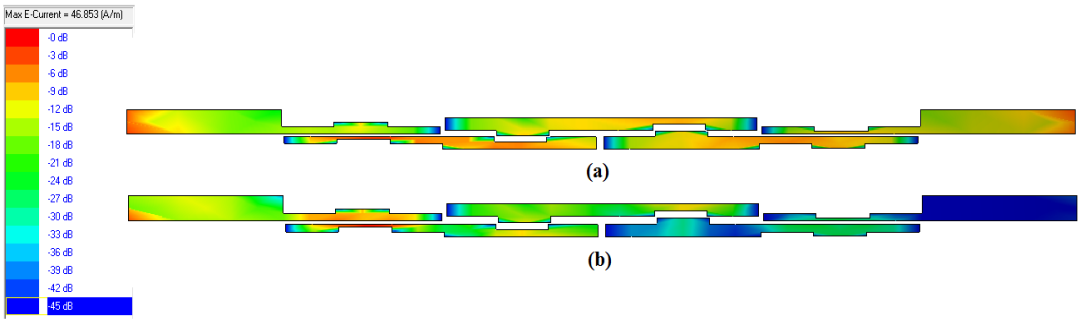

Fig. 3.222. Surface current distribution for the third-order inline bandpass filter with 2-3-4-1 case: (a) f_0 = 5.25 GHz, and (b) $2f_0$ = 10.5 GHz.

The surface current distribution for the inline filter with perturbation is plotted in Figs. 3.222(a)-(b) at f_0 = 2.5 GHz and $2f_0$ = 5 GHz, respectively, where surface current concentrations at the output port are observed for the passband and harmonics region. Table 3.16 tabulates all the parameters for the folded and inline filters with asymmetric perturbation. It has been noticed that the Figure of Merit (*FOM*) becomes greater for both the *C*-band and *S*-band inline filters with perturbation compared to folded filters with perturbation. From this section, it has been concluded that asymmetric perturbation has efficiently suppressed the second harmonic attenuation level to 33 dB with stopband bandwidth extended up to $2.4f_0$. The validation of the proposed filters has been performed by experimental observations. The measured responses are in good agreement with the simulated results.

Table 3.16. Comparison of all designed PCMLBFs with asymmetric perturbation.

f_o (GHz)	Type of filter	ξ (dB/GHz)	*SBRL* (dB)	*SBW* (x f_0)	*RSB*	*SF*	*NCS*	*AF*	*FOM*
5.25	folded	30	32	2.3	1.34	3.3	0.28	1	473.79
	inline	45	33	2.4	1.35	3.3	0.2		1002.38
2.5	folded	54	33	2.72	1.3	3.3	0.15		1544.4
	inline	67.5	33	2.4	1.29	3.3	0.1		2873.48

3.17. Harmonic Suppression by Koch Fractals

3.17.1. Study of Unit PCML Cell with Fractals

Generally, a fractal is a fragmented geometric shape that can be subdivided into parts, each of which is a reduced-size copy of the whole. Fractals are generally self-similar and independent of scale. The Koch fractal geometry, named after the mathematician Helge Von Koch, has been characterized by two primary properties, such as the iteration factor and the iteration order [14]. The iteration factor represents the construction law of the fractal geometry generation, whereas the iteration order indicates how many iteration processes are to be carried out. Fig. 3.223 shows the Koch fractal island shape with an iteration factor, *IF* = ¼ in which each edge of the island is a Koch curve. The zeroth iteration of the Koch Island structure (Fig. 3.223(a)) is a perfect square, called pre-fractal geometry. The iteration order of the fractal geometry gradually increases by following the same fragmental procedure. This is typically called the self-similarity property of the fractal. According to the space filling

property, the fractal geometry can fill a limited area as the iteration order increases and occupies the same area regardless of the order. Moreover, the space-filling property of the fractal increases the electrical length of each Koch edge, decreasing the resonant frequency. By self-similarity, a portion of the fractal geometry always resembles the first order geometry. This feature encourages the miniaturization of the overall structure. Moreover, such a space-filling property has a larger effect on the harmonic frequency than the fundamental dominant resonant frequency. This is because the electrical length of the Koch curve at the harmonic is shorter than that of the dominant mode [27]. Therefore, these two properties have been used effectively to suppress the harmonics along with the miniaturization of the filter's size.

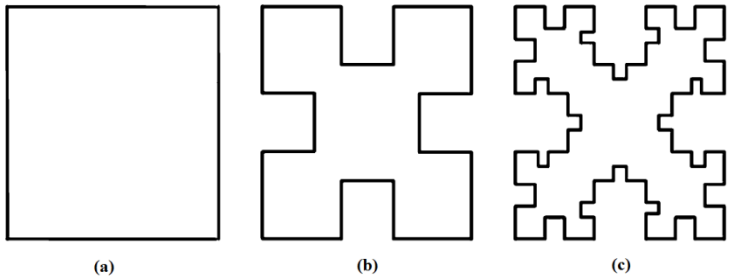

Fig. 3.223. Koch fractal island shape with iteration factor *IF* = 1/4. (a) Zeroth iteration order, (b) First iteration order, and (c) Second iteration order.

Figs. 3.224(a)-(c) depict the layouts of the unit PCML cells with Koch rectangular fractal. In Fig. 3.224(a) *l* and *w* represent the length and width of the coupled-lines, *s* represents the coupling gap between them and *d* is the open-end length correction due to fringing fields. By introducing fractals in parallel-coupled lines the physical length of the resonator remains constant, but the effective electrical length increases. For iteration order *IO* = 1 of Fig. 3.224(b) rectangular Koch slits are indented at the middle and at the open end center of the lines. The process has been repeated for iteration order *IO* = 2 in Fig. 3.224(b). The comparison of simulated $|S_{12}|$ (dB) plots for the unit PCML cell tuned at 5.25 GHz with different iteration orders of Koch fractal has been carried out in Fig. 3.225(a). It has been observed that the inherent transmission zero point ($2f_z$) has been shifted away from the second harmonic frequency as the iteration order of fractal shape has been increased. This is due to the fact that as the iteration order increases, the length around the perimeter increases and accordingly, the effective electrical length of the geometry have been also increased.

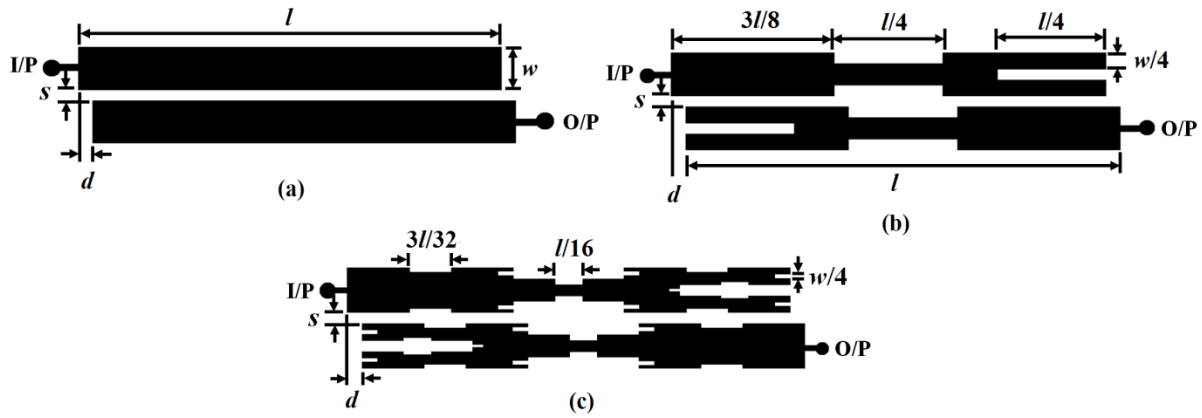

Fig. 3.224. Layouts of unit PCML cells with Koch fractal: (a) zeroth iteration order, (b) first iteration order, and (c) second iteration order.

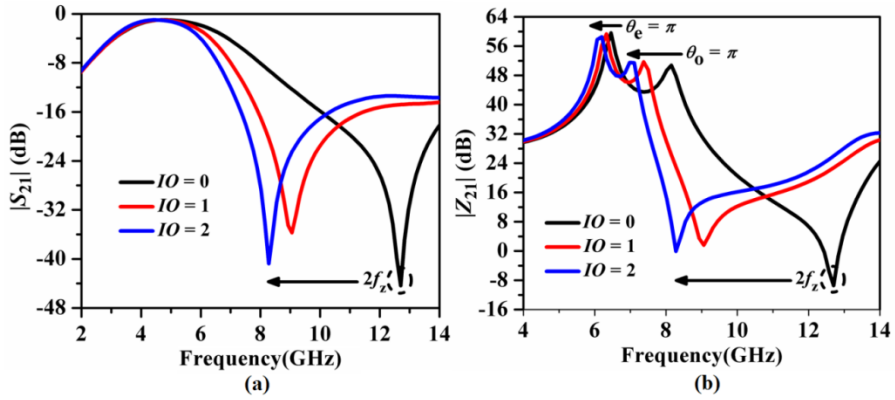

Fig. 3.225. Comparison of simulated (a) $|S_{21}|$ (dB), and (b) $|Z_{21}|$ (dB) plots for a unit PCML cell with Koch fractal for different iteration order.

However, the physical perimeter length remains constant and, as a result, the transmission zero point ($2f_z$) shifts to the low frequency. By controlling the location of the null point, the second harmonic can be suppressed by using the space filling property. According to Fig. 3.225(b) of $|Z_{21}|$ (dB) plots for the unit PCML cell with fractal, the resonant peak due to the odd-mode ($\theta_o = \pi$) shifts more to the lower frequency than that due to the even-mode ($\theta_e = \pi$). This justifies the ability of the Koch fractal to exhibit the modal phase velocity compensation. The surface current distribution plots for the unit PCML cell at 5.25 GHz, shown in Figs. 3.226(a)-(c), further validate the effectiveness of the Koch fractal. It has been observed that the current vectors have concentrated strongly while propagating along the narrow slits created due to fractal. The study of fractals has been extended further for the pair of PCML cells in the next section.

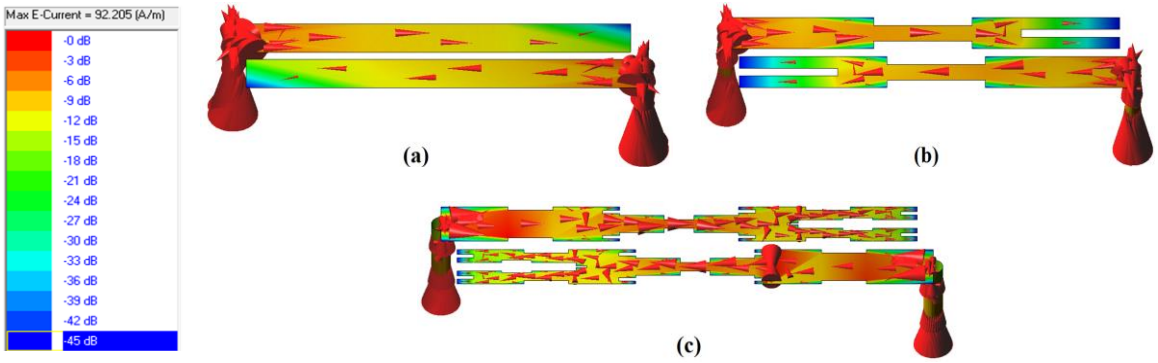

Fig. 3.226. Surface current distribution for a unit PCML cell with Koch fractal for different iteration order at f_0 = 5.25 GHz, (a) *IO* = 0, (b) *IO* = 1, and (c) *IO* = 2.

3.17.2. Study of Pair of PCML Cells with Koch Fractals

The layouts of the pairs of PCML cells with *IO* = 0, 1, and 2 are shown in Figs. 3.227(a)-(c). The comparison of the simulated $|S_{21}|$ (dB) plots has been explored in Fig. 3.228. A few significant observations have been obtained from the plots, such as a transmission zero (f_z) has occurred for *IO* = 1 at 7.4 GHz with an attenuation level of 40 dB and at 6.4 GHz with an attenuation level of 34 dB. It justifies that (1) the skirt characteristics of the first-order folded filter have been improved by the fractals, (2) the attenuation level at the second harmonic ($2f_0$) has been reduced from 10 dB (*IO* = 0) to 21 dB for *IO* = 1 and to 25 dB for *IO* = 2, (3) a very sharp transmission zero ($2f_z$) has occurred at 9.2 GHz with an attenuation level of 54 dB for *IO* = 1.

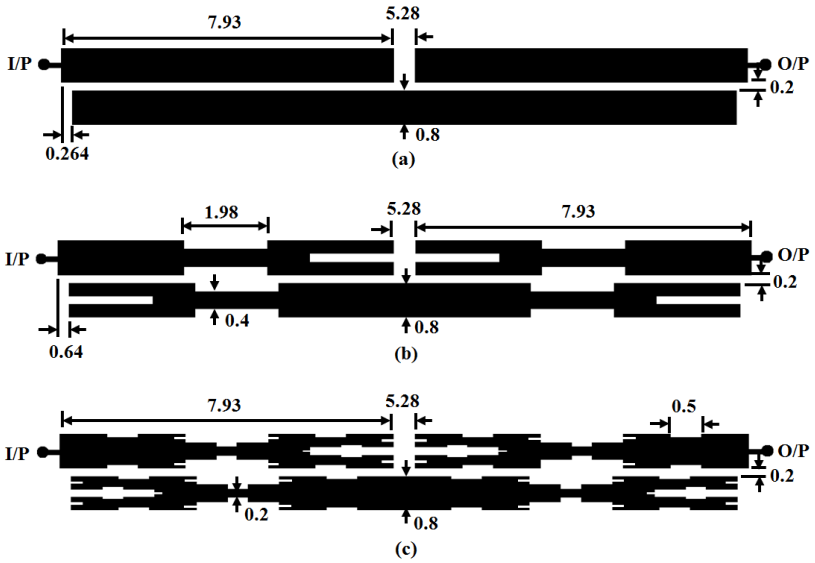

Fig. 3.227. Layouts of pair of PCML cells with Koch fractal: (a) zeroth iteration order, (b) first iteration order, and (c) second iteration order.

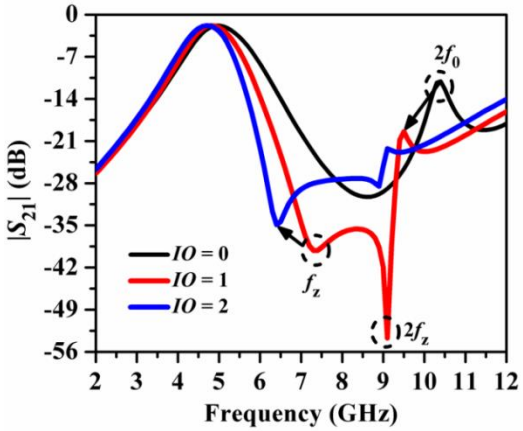

Fig. 3.228. Comparison of simulated $|S_{21}|$ (dB) plots for a pair of unit PCML cells with Koch fractal for different iteration order.

However, the attenuation level at $2f_z$ has been increased to 23 dB for IO = 2, compared to that for IO = 1. It can be concluded from these observations that Koch fractal has the ability to suppress the harmonic's attenuation level along with improvement of the skirt characteristics. Figs. 3.229(a)-(c) at f_0 = 5.25 GHz and Figs. 3.230(a)-(c) at $2f_0$ = 10.5 GHz show the distribution of surface currents for the first-order filter structure with different IO values.

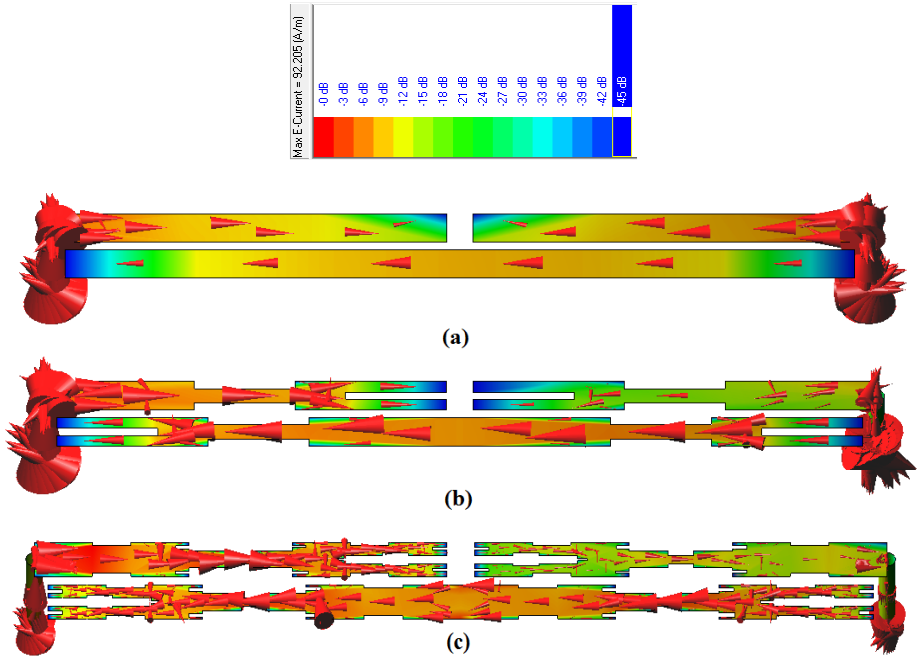

Fig. 3.229. Surface current distribution for a pair of unit PCML cells with Koch fractal for different iteration order at f_0 = 5.25 GHz, (a) IO = 0, (b) IO = 1, and (c) IO = 2.

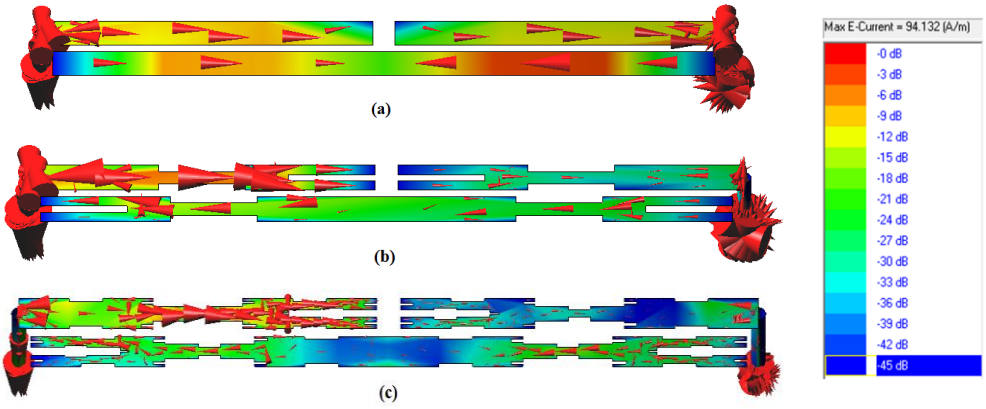

Fig. 3.230. Surface current distribution for a pair of unit PCML cells with Koch fractal for different iteration order at f_0 = 10.5 GHz, (a) *IO* = 0, (b) *IO* = 1 and (c) *IO* = 2.

3.17.3. Study of Third-Order Folded PCMLBF with Koch Fractals

The optimized layout of the third-order folded filter with a Koch fractal of *IO* = 1 and centered at 5.25 GHz (*C*-band) is shown in Fig. 3.231. The overall size of the filter is 41.65 mm × 6.57 mm i.e., 273.81 mm^2 or 1.34λ_g × 0.21λ_g. Accordingly, a size reduction of 58.5% has been obtained over the conventional filter.

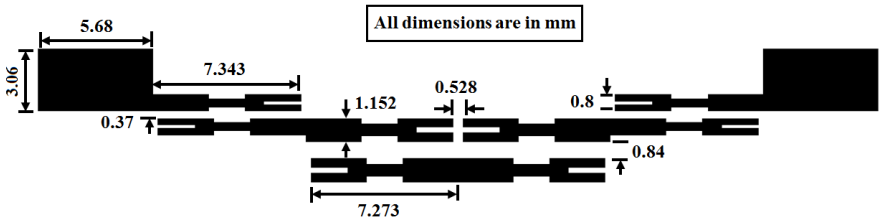

Fig. 3.231. Layout of the optimized third-order folded PCMLBF centered at 5.25 GHz with Koch fractal for iteration order *IO* = 1.

3.17.3.1. Fabricated Prototype

The fabricated prototype based on FR4 laminate is shown in Fig. 3.232.

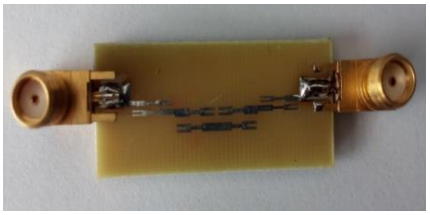

Fig. 3.232. Fabricated prototype of the third-order folded PCMLBF centered at 5.25 GHz with Koch fractal for iteration order *IO* = 1 [34].

3.17.3.2. Comparison of EM simulation vs. Measurement Results

The comparison of the simulated and measured *S*-parameter plots is shown in Figs. 3.233(a)-(b). The experimental procedure has been carried out in the similar way of 3.14.4.1. A stopband rejection level of 32 dB up to $2.3f_0$ has been recorded from the measurement results. Moreover, the attenuation level of the second harmonic has been degraded by 16 dB due to fractal. A sharp transmission zero has been obtained at the upper stopband edge frequency of 6.5 GHz with an attenuation peak of 42 dB. Besides, multiple transmission zeros have been observed throughout the entire stopband up to $2.4f_0$, resulting in the improvement of the stopband performance of the filter by fractals. The passband insertion loss has been recorded as 1.1 dB and the passband return loss has been obtained as 22 dB (Fig. 3.233(b)).

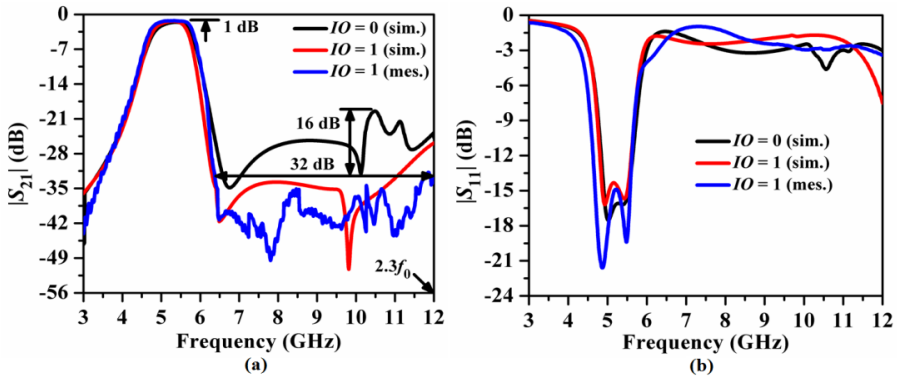

Fig. 3.233. Comparison of simulated vs. measured S-parameters plots for the third-order folded PCMLBF centered at 5.25 GHz with Koch fractal for iteration order *IO* = 1, (a) $|S_{21}|$ (dB), and (b) $|S_{11}|$ (dB) [47].

Figs. 3.234(a)-(b) show the surface current distribution at f_0 = 5.25 GHz and $2f_0$ = 10.5 GHz, respectively. It has been clearly observed that the surface current propagates strongly towards the output port at 5.25 GHz due to the passband response and very poorly at 10.5 GHz due to the suppression of the harmonic by fractal. Subsequently, the optimized dimensions of the third-order folded filter with fractal of *IO* = 2 has been obtained as depicted in Fig. 3.235.

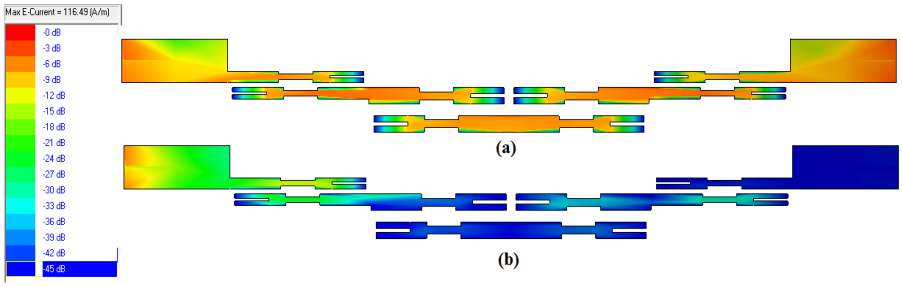

Fig. 3.234. Surface current distribution for the third-order folded PCMLBF with Koch fractal for iteration order *IO* = 1, (a) at f_0 = 5.25 GHz, and (b) at $2f_0$ = 10.5 GHz.

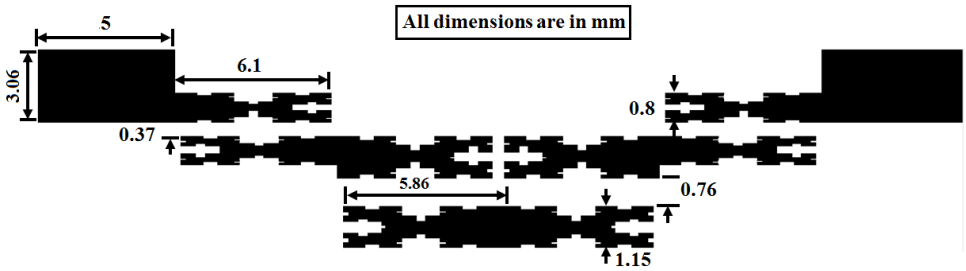

Fig. 3.235. Layout of the optimized third-order folded PCMLBF centered at 5.25 GHz with Koch fractal for iteration order *IO* = 2.

The overall size of the filter is 34.98 mm × 6.49 mm, i.e., 227.16 mm^2 or 1.12λ_g × 0.21λ_g. Accordingly, a size reduction of 65.6% has been obtained over the conventional filter. The simulated *S*-parameter plots for the designed folded filters with fractal (*IO* = 0, 1, and 2) are shown in Figs. 3.236(a)-(b). A stopband rejection level of 33 dB up to 2f_0 has been observed for *IO* = 2. However, a sharp transmission zero attenuation level of 52 dB has been obtained at 6.4 GHz by exploring the improvement of the skirt characteristics over *IO* = 0 and 1. Besides, a second transmission zero at an attenuation level of 46 dB at 10 GHz has been obtained for *IO* = 2. Although this attenuation level is less than that of *IO* = 1 (52 dB). This is due to the additional inductive and capacitive effects generated by the greater number of bends and notches for *IO* = 2 compared to *IO* = 1. Figs. 3.237(a)-(b) show the surface current distribution at f_0 = 5.25 GHz and 2f_0 = 10.5 GHz, respectively.

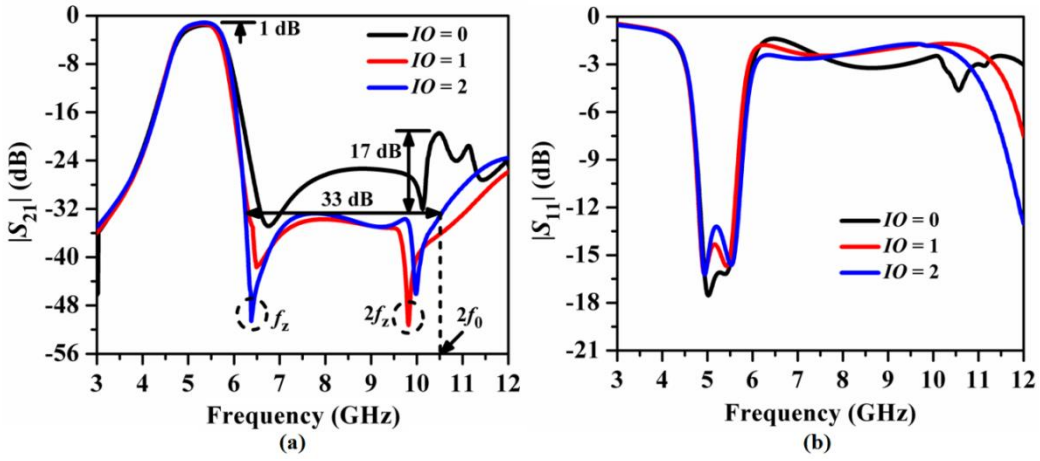

Fig. 3.236. Comparison of **s**imulated *S*-parameters plots for the third-order folded PCMLBF centered at 5.25 GHz with Koch fractal for different iteration orders: (a) $|S_{21}|$ (dB), and (b) $|S_{11}|$ (dB).

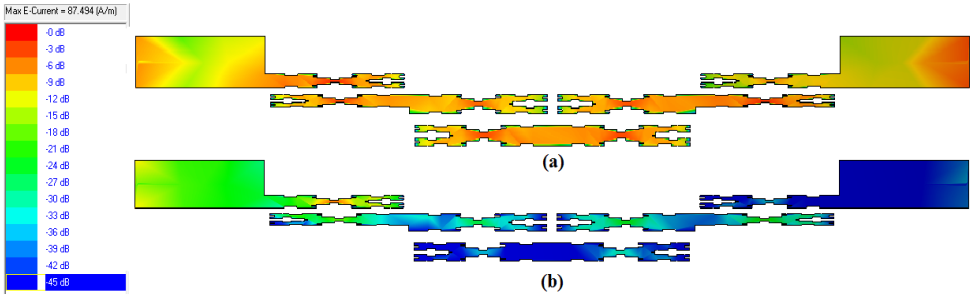

Fig. 3.237. Surface current distribution for the third-order folded PCMLBF with Koch fractal for iteration order IO = 2, (a) at f_0 = 5.25 GHz and (b) at $2f_0$ = 10.5 GHz.

It has been noticed that the surface current propagates strongly towards the output port at 5.25 GHz due to the passband response and very poorly at 10.5 GHz due to the suppression of the harmonic by fractal. The passband insertion loss becomes 1 dB and the return loss becomes more than 15 dB for the filters with fractals. Subsequently, the Koch fractal has been employed for the S-band folded filter centered at 2.5 GHz by following the same design mechanism. Figs. 3.238(a)-(b) show the optimized layouts for the folded filter with IO = 1 and IO = 2. The overall size of the folded filter with IO = 1 is 95.59 mm × 6.99 mm, i.e., 668.17 mm^2 or 1.4λ_g × 0.1λ_g. Accordingly, a size reduction of 48.3% has been obtained over the conventional filter. The overall size of the folded filter with IO = 2 is 90.18 mm × 6.92 mm, i.e., 624.62 mm^2 or 1.32λ_g × 0.1λ_g and a size reduction of 48.3% has been obtained over the conventional filter.

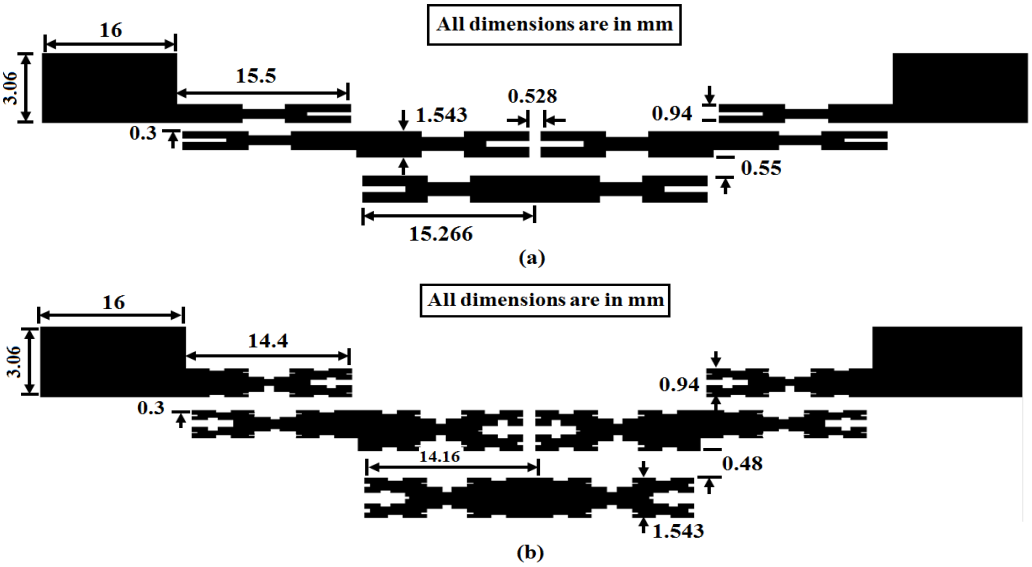

Fig. 3.238. Layout of the optimized third-order folded PCMLBFs centered at 2.5 GHz with Koch fractal for iteration order: (a) IO = 1, and (b) IO = 2.

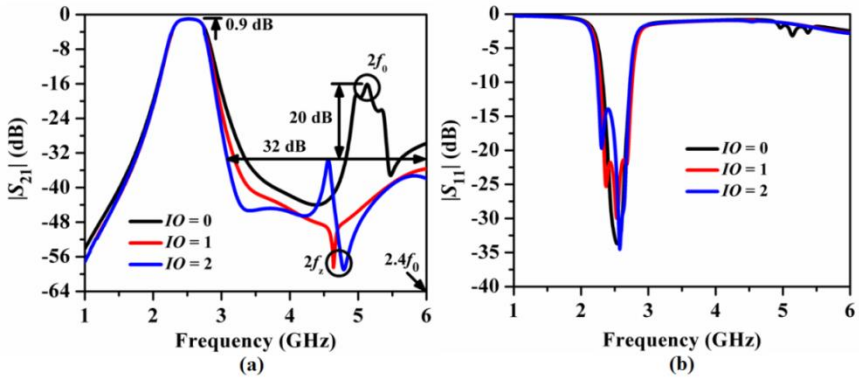

Fig. 3.239. Comparison of **s**imulated *S*-parameters plots for the third-order folded PCMLBF centered at 2.5 GHz with Koch fractal for different iteration orders: (a) $|S_{21}|$ (dB), and (b) $|S_{11}|$ (dB).

Figs. 3.239(a)-(b) compare the simulated *S*-parameter plots for the designed folded filters with fractal (*IO* = 0, 1, and 2). It has been observed that stopband rejection levels of 35 dB for *IO* = 1 and 32 dB for *IO* = 2 up to $2.4f_0$ have been obtained. Moreover, a sharp transmission zero attenuation level of 59 dB has been obtained at 4.6 GHz for *IO* = 1. However, the skirt characteristics have been improved significantly for *IO* = 2 over *IO* = 0 and 1. Besides, the second harmonic attenuation level has been degraded by 20 dB due to the fractals. It can be concluded from the above observations that as the iteration order of the fractal increases, the skirt characteristics of the folded filter have improved gradually, but the performance of the harmonic suppression degrades.

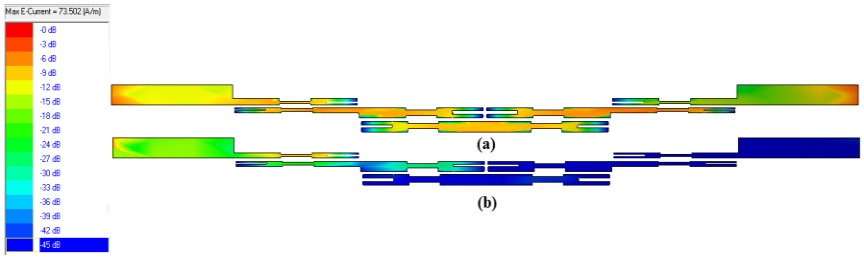

Fig. 3.240. Surface current distribution for the third-order folded PCMLBF with Koch fractal for iteration order *IO* = 1, (a) at f_0 = 2.5 GHz, and (b) at $2f_0$ = 5 GHz.

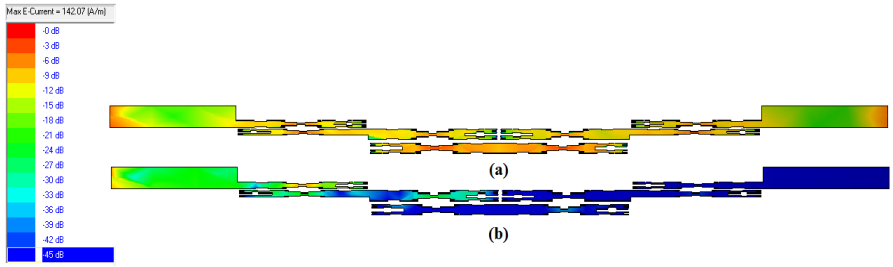

Fig. 3.241. Surface current distribution for the third-order folded PCMLBF with Koch fractal for iteration order *IO* = 2, (a) at f_0 = 2.5 GHz, and (b) at $2f_0$ = 5 GHz.

Figs. 3.240(a)-(b) and Figs. 3.241(a)-(b) show the surface current distribution at f_0 = 5.25 GHz and $2f_0$ = 10.5 GHz for *IO* = 1 and 2, respectively. It has been noticed that the surface current propagates strongly towards the output port at 5.25 GHz due to the passband response and very poorly at 10.5 GHz due to the suppression of the harmonic by fractal for both the cases.

3.17.4. Study of Third-Order Inline PCMLBF with Koch Fractals

In this section, Koch fractals have been employed for the third-order inline filters to justify the effectiveness of the Koch fractals for harmonics' suppression for such filters. Fig. 3.242 shows the optimized dimensions of the third-order inline PCMLBF centered at f_0 = 5.25 GHz with *IO* = 1, and Fig. 3.243 shows the fabricated prototype. The overall size of the folded filter is 40.49 mm × 4.53 mm, i.e., 183.42 mm^2 or $1.3\lambda_g \times 0.15\lambda_g$ and a size reduction of 73.5% has been obtained over the conventional filter.

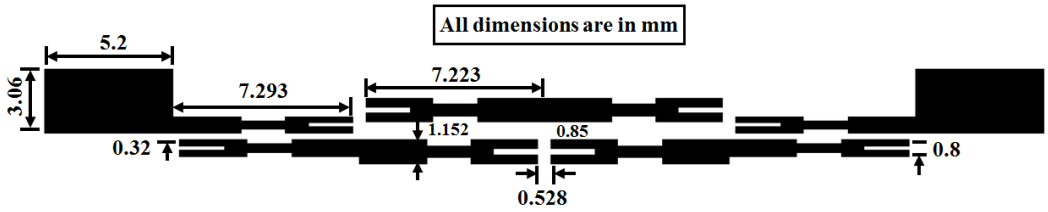

Fig. 3.242. Layout of the optimized third-order inline PCMLBF centered at 5.25 GHz with Koch fractal for iteration order *IO* = 1.

3.17.4.1. Fabricated Prototype

The fabricated prototype of the third-order inline PCMLBF centered at 5.25 GHz with Koch fractal for iteration order *IO* = 1 is shown in Fig. 3.243.

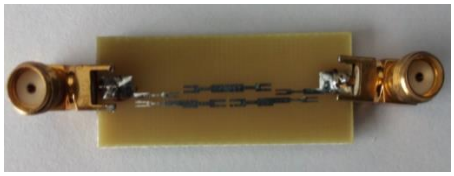

Fig. 3.243. Fabricated prototype of the third-order inline PCMLBF centered at 5.25 GHz with Koch fractal for iteration order *IO* = 1 [34].

3.17.4.1. Comparison of EM simulation vs. Measurement Results

The simulated and measured *S*-parameter plots for the fabricated inline filter with fractal are shown in Figs. 3.244(a)-(b). The experimental procedure has been carried out in the similar

way of 3.14.4.1. It has been observed that a stopband rejection level of 30 dB up to $2.3f_0$ has been obtained. Furthermore, at 6.5 GHz, a sharp transmission zero with an attenuation level of 53 dB was obtained, indicating that the skirt characteristics of the filter were improved by fractal. Moreover, multiple transmission zeros have occurred in the stopband, justifying the improved harmonic suppression performance by the fractal. The passband insertion loss becomes 1 dB and the return loss becomes more than 17 dB for the filters with fractals.

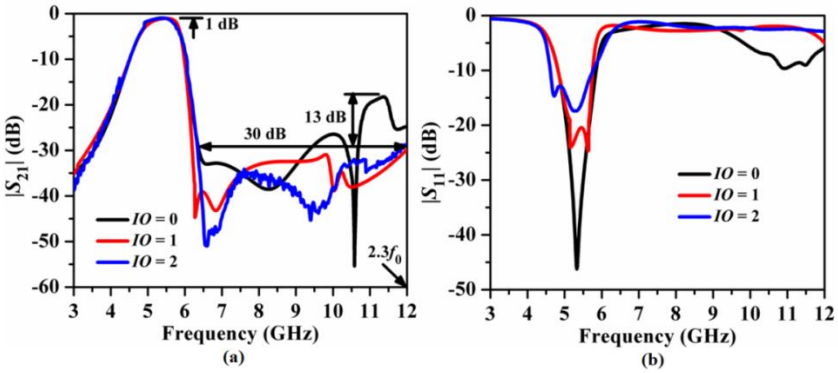

Fig. 3.244. Comparison of **s**imulated vs. measured *S*-parameters plots for the third-order inline PCMLBF centered at 5.25 GHz with Koch fractal for iteration order IO = 1, (a) $|S_{21}|$ (dB), and (b) $|S_{11}|$ (dB).

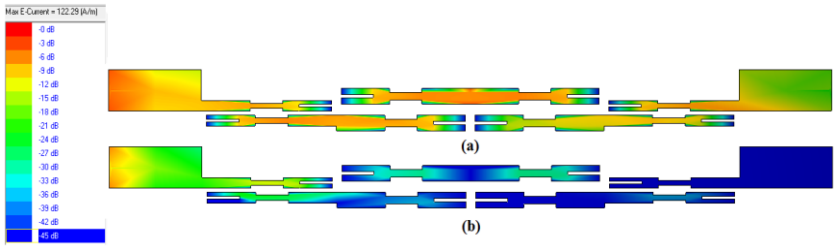

Fig. 3.245. Surface current distribution for the third-order inline PCMLBF with Koch fractal for iteration order IO = 1, (a) at f_0 = 5.25 GHz and (b) at $2f_0$ = 10.5 GHz.

As a result, Figs. 3.245(a)-(b) investigate the surface current distribution at f_0 = 5.25 GHz and $2f_0$ = 10.5 GHz, respectively. It has been observed that the surface current propagates towards the output port from the input port with a large strength at 5.25 GHz due to the passband and very weak strength at 10.5 GHz due to the stopband. Fig. 3.246 depicts the optimized dimensions of the third-order inline filter with a Koch fractal of IO = 2. The overall size of the inline filter is 41.88 mm × 4.58 mm, i.e., 191.89 mm^2 or $1.34\lambda_g \times 0.15\lambda_g$ and a size reduction of 71% has been obtained over the conventional filter. Figs. 3.247(a)-(b) compare the simulated S-parameter plots for inline filters with fractal (IO = 0, 1, and 2). It has been observed that stopband rejection levels of 32 dB up to $2.3f_0$ have been obtained for both IO = 1 and 2.

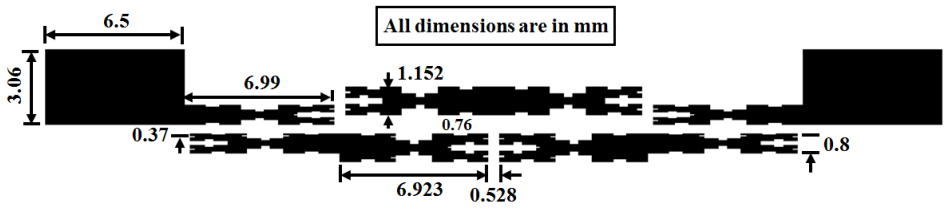

Fig. 3.246. Layout of the optimized third-order inline PCMLBF centered at 5.25 GHz with Koch fractal for iteration order *IO* = 2.

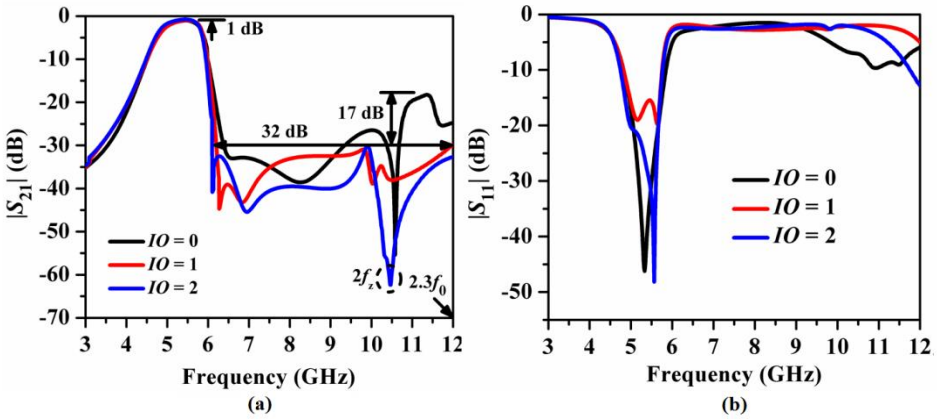

Fig. 3.247. Comparison of simulated *S*-parameters plots for the third-order inline PCMLBF centered at 5.25 GHz with Koch fractal for different iteration orders, (a) $|S_{21}|$ (dB), and (b) $|S_{11}|$ (dB).

Besides, the second harmonic attenuation level has been degraded by 17 dB due to the fractals. Moreover, two sharp transmission zeros of attenuation levels of 43 dB and 46 dB have been obtained at 6.1 GHz for *IO* = 1 and 6.3 GHz for *IO* = 2, respectively. However, a second sharp transmission zero $2f_z$ has been obtained for *IO* = 2 with an attenuation level of 64 dB at 10.5 GHz. This justifies the effectiveness of Koch fractals for harmonic suppression. As a result, the surface current distributions at f_0 = 5.25 GHz and 2f0 = 10.5 GHz have been investigated in Figs. 3.248(a)-(b) for *IO* = 2.

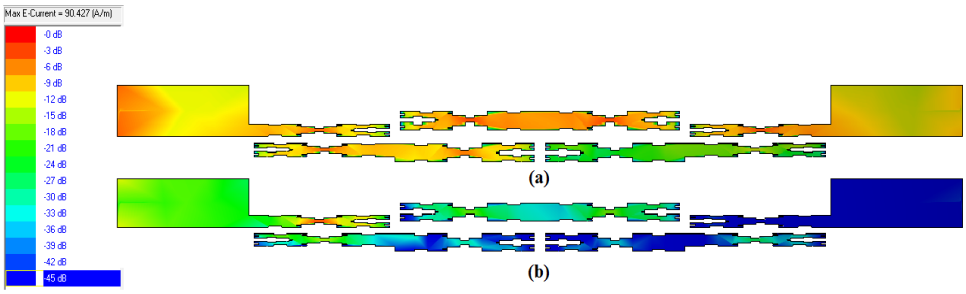

Fig. 3.248. Surface current distribution for the third-order inline PCMLBF with Koch fractal for iteration order *IO* = 2, (a) at f_0 = 5.25 GHz, and (b) at $2f_0$ = 10.5 GHz.

Just like the inline filter with *IO* = 1, the surface current concentrates more at 5.25 GHz due to the passband response and pretty less at 10.5 GHz. The optimized dimensions of the third-order inline filters centered at f_0 = 2.5 GHz with fractals of *IO* = 1 and *IO* = 2 were obtained using the same methodology, as shown in Figs. 3.249(a)-(b). The overall size of the inline filter with *IO* = 1 becomes 94.6 mm × 4.9 mm, i.e., 463.84 mm^2 or 1.38λ_g × 0.07λ_g and a size reduction of 64.1% has been obtained over the conventional filter.

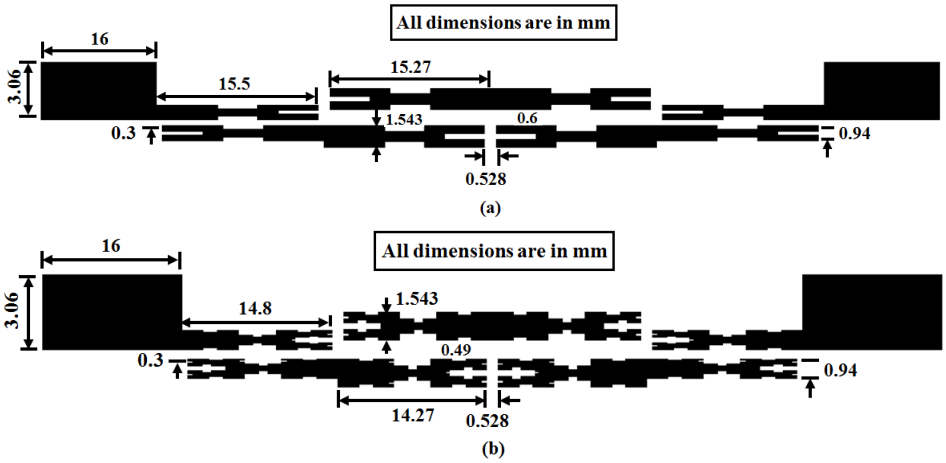

Fig. 3.249. Layout of the optimized third-order inline PCMLBFs centered at 2.5 GHz with Koch fractal for (a) *IO* = 1, and (b) *IO* = 2.

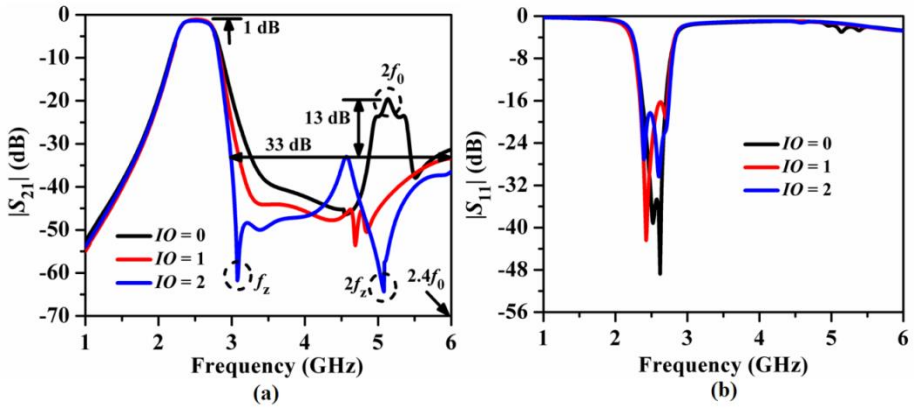

Fig. 3.250. Comparison of simulated *S*-parameters plots for the third-order inline PCMLBF centered at 2.5 GHz with Koch fractal for different iteration orders, (a) $|S_{21}|$ (dB), and (b) $|S_{11}|$ (dB).

However, the overall size of the inline filters with *IO* = 2 becomes 91.2 mm × 4.9 mm, i.e., 447.17 mm^2 or 1.34λ_g × 0.07λ_g and a size reduction of 65.4% has been obtained over the conventional filter. As a result, Figs. 3.250(a)-(b) compare the simulated S-parameter plots for inline filters with fractal (*IO* = 0, 1, and 2). It has been observed that stopband rejection levels of 33 dB up to 2.4f_0 have been obtained for both *IO* = 1 and 2. Besides, the second

harmonic attenuation level has been degraded by 13 dB due to the fractal. Moreover, the skirt characteristics of the inline filters have been improved significantly for IO = 2 over IO = 0 and 1 due to the generation of a very sharp transmission zero attenuation level of 63 dB at 3.1 GHz. Moreover, another sharp transmission of zero $2f_z$ has been obtained for IO = 2 with an attenuation level of 65 dB. Such generation of transmission zero justifies the effectiveness of Koch fractals for harmonic suppression. The designed inline filter with fractal has a passband insertion of 1.0 dB and a return loss of 26 dB.

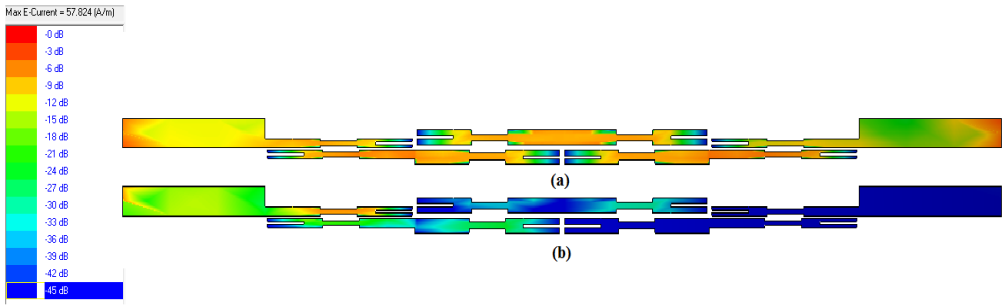

Fig. 3.251. Surface current distribution for the third-order inline PCMLBF with Koch fractal for iteration order IO = 1, (a) at f_0 = 2.5 GHz, and (b) at $2f_0$ = 5 GHz.

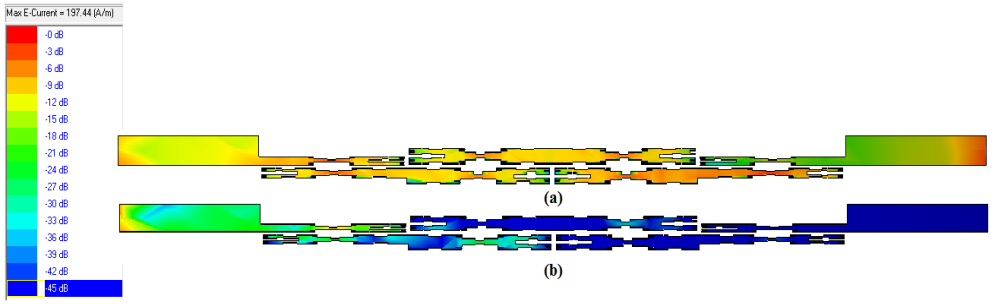

Fig. 3.252. Surface current distribution for the third-order inline PCMLBF with Koch fractal for iteration order IO = 2, (a) at f_0 = 2.5 GHz, and (b) at $2f_0$ = 5 GHz.

According to the surface current distribution plots shown in Fig. 3.251(a)-(b) for IO = 1 and Fig. 3.252(a)-(b) for IO = 2, the surface current distributes well in strength at f_0 = 2.5 GHz due to the passband and reaches the output port with a very weak strength due to the stopband performance of the fractal based filters for both IO = 1 and 2. Table 3.17 tabulates all the parameters for the folded and inline filters with the Koch fractal. It has been noticed that the Figure of Merit (*FOM*) becomes greater for both the *C*-band and *S*-band inline filters with perturbation than for folded filters with perturbation. It can be concluded from Table 3.17 that the *FOM* values become maximum for the inline filters centered at both 5.25 GHz and 2.5 GHz with IO = 2.

Table 3.17. Comparison of all designed PCMLBFs with Koch fractal.

f_o (GHz)	*Type of filter*	*IO*	ξ (dB/GHz)	*SBRL* (dB)	*SBW* (x f_0)	*RSB*	*SF*	*NCS*	*AF*	*FOM*
5.25	folded	1	38.57	32	2.3	1.31	3.2	0.282	1	573
		2	38.57	33	2	1.24	3.3	0.234		675
	inline	1	67.5	30	2.3	1.30	3.0	0.189		1393
		2	90	30	2.3	1.33	3.0	0.198		1814
2.5	folded	1	54	32	2.4	1.3	3.2	0.143		1571
		2	90	32	2.4	1.34	3.2	0.134		2880
	inline	1	67.5	33	2.4	1.3	3.3	0.099		2925
		2	135	33	2.4	1.3	3.3	0.096		6033

3.18. Harmonic Suppression by Minkowski Fractals

3.18.1. Generation of Minkowski Fractals

It has been observed from the previous section that due to space filling and self-similarity properties, Koch fractal geometries have the capability to suppress the inherent spurious harmonics of the parallel-coupled line filters along with the miniaturization of the filter size. Moreover, the upper passband edge skirt characteristics have been greatly improved by the generation of a sharp transmission zero with a large attenuation level as the iteration order of the filter increases. However, the design difficulty and fabrication difficulty arise with higher iteration order due to narrow coupling gaps between the slots of the fractal pattern. Moreover, interaction of the fringe field lines in the gaps degrades the harmonic suppression performance of the filter. As a remedy to these difficulties, the quasi Minkowski fractal is an attractive alternative to the Koch fractal. Due to their easy generation procedure and weak sensitivity to fabrication tolerances, Minkowski fractals are very effective for designing compact filters. Minkowski fractals were introduced first in 1885, where fractals are generated using an Iterated Function System (IFS), based on the application of a series of affine transformations (w) defined as

$$w\begin{pmatrix} x_1 \\ x_2 \end{pmatrix} = \begin{pmatrix} a & b \\ c & d \end{pmatrix}\begin{pmatrix} x_1 \\ x_2 \end{pmatrix} + \begin{pmatrix} e \\ f \end{pmatrix} = Ax + t \tag{96}$$

Here, x_1 and x_2 are the coordinates of the point x.

Also, *a*, *b*, *c*, and *d* control rotation and scaling of the fractal segment, while *e* and *f* control linear translation. The column matrix, *t* is a translation on the plane. A can be written as

$$A = \begin{pmatrix} r_1 \cos\theta_1 & -r_2 \sin\theta_2 \\ r_1 \sin\theta_1 & r_2 \cos\theta_2 \end{pmatrix} \tag{97}$$

In the special case where $r_1 = r_2 = r$, $0 < r < 1$, and $\theta_1 = \theta_2 = \theta$, the transformation is a contractive similarity, where *r* is the scale factor and θ is the rotation angle. The generation of quasi-Minkowski fractal geometry is shown in Figs. 3.253(a)-(b), where *l* is the length of the initiator.The values of *a* and *b* will decide the length of the horizontal and vertical segments of the generator.

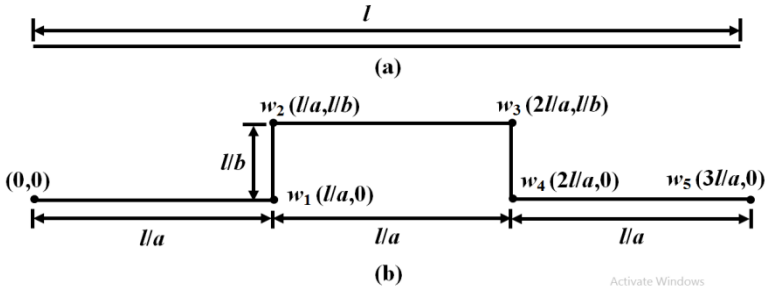

Fig. 3.253. Generation of quasi-Minkowski fractal shape on a line: (a) Initiator with iteration order, *IO* = 0 and (b) generator geometry with *IO* = 1.

In the classical Minkowski fractal, the IFSs are applied to the vertical as well as horizontal segments. However, for convenience in designing parallel-coupled lines, a quasi-Minkowski fractal has been used, because the IFSs are applied only to the horizontal segments. Here, the initiator is placed along the *x*-axis with the left starting point at the origin. Accordingly, the generator geometry is produced by applying the set of affine linear transformations, {*wn*} of (96), to the initial geometry, *K*. The set {*wn*} is characterized by the coordinates as shown in Fig. 3.253(b). Subsequently, the Hutchinson operator is defined as (98), in which *i* is the index number of the line segments.

$$W(K) = \sum_{i=1}^{5} w_i(K) \tag{98}$$

The IFS transformation coefficients for the generator of quasi-Minkowski fractals with iteration order $IO = 1$ have been formulated in (99) - (103).

$$w_1\begin{pmatrix} x_1 \\ x_2 \end{pmatrix} = \begin{pmatrix} \frac{1}{a}\cos 0^o & -\frac{1}{a}\sin 0^o \\ \frac{1}{a}\sin 0^o & \frac{1}{a}\cos 0^o \end{pmatrix}\begin{pmatrix} x_1 \\ x_2 \end{pmatrix} + \begin{pmatrix} 0 \\ 0 \end{pmatrix} = \begin{pmatrix} \frac{1}{a} & 0 \\ 0 & \frac{1}{a} \end{pmatrix}\begin{pmatrix} x_1 \\ x_2 \end{pmatrix} + \begin{pmatrix} 0 \\ 0 \end{pmatrix} \tag{99}$$

$$w_2\begin{pmatrix} x_1 \\ x_2 \end{pmatrix} = \begin{pmatrix} \frac{1}{b}\cos 90^o & -\frac{1}{b}\sin 90^o \\ \frac{1}{b}\sin 90^o & \frac{1}{b}\cos 90^o \end{pmatrix}\begin{pmatrix} x_1 \\ x_2 \end{pmatrix} + \begin{pmatrix} \frac{1}{a} \\ 0 \end{pmatrix} = \begin{pmatrix} 0 & -\frac{1}{b} \\ \frac{1}{b} & 0 \end{pmatrix}\begin{pmatrix} x_1 \\ x_2 \end{pmatrix} + \begin{pmatrix} \frac{1}{a} \\ 0 \end{pmatrix} \tag{100}$$

$$w_3\begin{pmatrix} x_1 \\ x_2 \end{pmatrix} = \begin{pmatrix} \frac{1}{a}\cos 0^o & -\frac{1}{a}\sin 0^o \\ \frac{1}{a}\sin 0^o & \frac{1}{a}\cos 0^o \end{pmatrix}\begin{pmatrix} x_1 \\ x_2 \end{pmatrix} + \begin{pmatrix} \frac{1}{a} \\ \frac{1}{b} \end{pmatrix} = \begin{pmatrix} \frac{1}{a} & 0 \\ 0 & \frac{1}{a} \end{pmatrix}\begin{pmatrix} x_1 \\ x_2 \end{pmatrix} + \begin{pmatrix} \frac{1}{a} \\ \frac{1}{b} \end{pmatrix} \tag{101}$$

$$w_4\begin{pmatrix} x_1 \\ x_2 \end{pmatrix} = \begin{pmatrix} \frac{1}{b}\cos(-90^o) & -\frac{1}{b}\sin(-90^o) \\ \frac{1}{b}\sin(-90^o) & \frac{1}{b}\cos(-90^o) \end{pmatrix}\begin{pmatrix} x_1 \\ x_2 \end{pmatrix} + \begin{pmatrix} \frac{2}{a} \\ \frac{1}{b} \end{pmatrix} = \begin{pmatrix} 0 & \frac{1}{b} \\ -\frac{1}{b} & 0 \end{pmatrix}\begin{pmatrix} x_1 \\ x_2 \end{pmatrix} + \begin{pmatrix} \frac{2}{a} \\ \frac{1}{b} \end{pmatrix} \tag{102}$$

$$w_5\begin{pmatrix} x_1 \\ x_2 \end{pmatrix} = \begin{pmatrix} \frac{1}{a}\cos 0^o & -\frac{1}{a}\sin 0^o \\ \frac{1}{a}\sin 0^o & \frac{1}{a}\cos 0^o \end{pmatrix}\begin{pmatrix} x_1 \\ x_2 \end{pmatrix} + \begin{pmatrix} \frac{2}{a} \\ 0 \end{pmatrix} = \begin{pmatrix} \frac{1}{a} & 0 \\ 0 & \frac{1}{a} \end{pmatrix}\begin{pmatrix} x_1 \\ x_2 \end{pmatrix} + \begin{pmatrix} \frac{2}{a} \\ 0 \end{pmatrix} \tag{103}$$

Table 3.18. IFS transformation coefficients for $IO = 1$.

w_i	a_i	b_i	c_i	d_i	e_i	f_i
w_1	$1/a$	0	0	1/a	0	0
w_2	0	$-1/b$	$1/b$	0	$1/a$	0
w_3	$1/a$	0	0	$1/a$	$1/a$	$1/b$
w_4	0	$1/b$	$-1/b$	0	$2/a$	$1/b$
w_5	$1/a$	0	0	$1/a$	$2/a$	0

Table 3.18 lists the IFS transformation coefficients for the generator with iteration order $IO = 1$ (normalized to unit length). Here, a_i, b_i, c_i, d_i, e_i and f_i are the values of A, B, C, D, E, and F for the line segment i. The generator is characterized by Hausdorff-Besicovitch dimension (D) equal to $ln4/ln3$, i.e., 1.262, and an iteration order $IO = 1$. These properties have been utilized in designing a miniaturized parallel-coupled microstrip line bandpass filter (PCMLBF) in which the parallel lines are modified with fractals at the edges. Accordingly,

the even-and odd-mode characteristic impedances are being modulated to achieve the phase velocity compensation between these modes.

3.18.2. Analysis of a Unit PCML Cell with Minkowski Fractals

The resonance characteristics of a single quarter-wavelength line with Minkowski fractals were investigated using the equivalent odd-and even-mode structure depicted in Figs. 3.254(a)-(c). The odd-mode input-impedance, Z_{ino}, and even-mode input-impedance, Z_{ine}, observed at port T_1-T_1' were calculated using conventional transmission-line theory and are expressed as

$$Z_{ino} = jZ_1\left[\frac{Z_1\tan\left(\frac{\theta}{3}\right)+Z_2\tan\left(\frac{\theta}{3}\right)}{Z_1-Z_2\tan\left(\frac{\theta}{6}\right)\tan\left(\frac{\theta}{3}\right)}\right] \tag{104}$$

$$Z_{ine} = jZ_1\frac{\left[Z_1\cot\left(\frac{\theta}{3}\right)-Z_2\tan\left(\frac{\theta}{6}\right)\right]}{Z_1+Z_2\cot\left(\frac{\theta}{6}\right)\tan\left(\frac{\theta}{3}\right)} \tag{105}$$

Here, Z_1 is the characteristic impedance of the left and right part, and Z_2 is the characteristic impedance of the middle part of the line with the electrical length, θ.

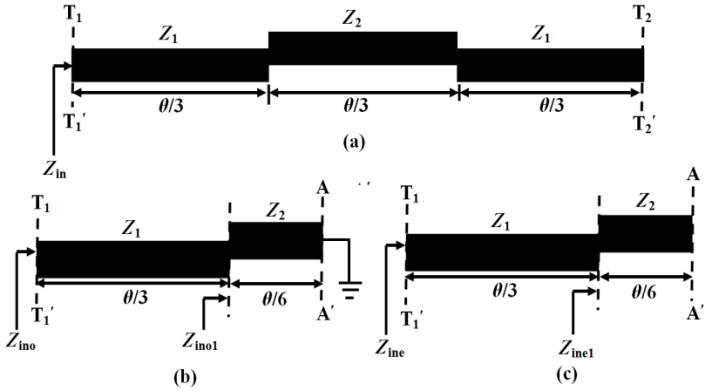

Fig. 3.254. (a) Layout of a single line with Minkowski fractals for iteration order *IO* = 1; (b) odd-mode equivalent structure; and (c) even-mode equivalent structure.

The resonance condition of the modes has been determined by setting $Z_{ino} = Z_{ine} = \infty$ in (104) and (105) are obtained as (106) and (107) respectively as

$$\tan\left(\frac{\theta_{po}}{6}\right)\tan\left(\frac{\theta_{po}}{3}\right) = \frac{Z_1}{Z_2} = K \tag{106}$$

$$\cot\left(\frac{\theta_{pe}}{6}\right)\tan\left(\frac{\theta_{pe}}{3}\right)=-\frac{Z_1}{Z_2}=-K \tag{107}$$

For a special case, if the impedance ratio, K = 1, the modal resonant frequencies, f_{po} and f_{pe} are obtained as (108) and (109).

$$\theta_{po}=(2n-1)\pi$$
$$f_{po}=\frac{(2n-1)c}{2l\sqrt{\varepsilon_{re}}},n=1,2,3... \tag{108}$$

$$\theta_{pe}=2n\pi$$
$$f_{pe}=\frac{nc}{l\sqrt{\varepsilon_{re}}},n=1,2,3... \tag{109}$$

Figs. 3.255(a)-(c) show layouts of the unit PCML cell with Minkowski fractal for iteration orders *IO* = 0, 1, and 2. In Figs. 3.256(b)-(c), fractals have been employed in the outer-and coupled-edges of both the parallel-coupled lines by the same amount of indentation in the same direction.

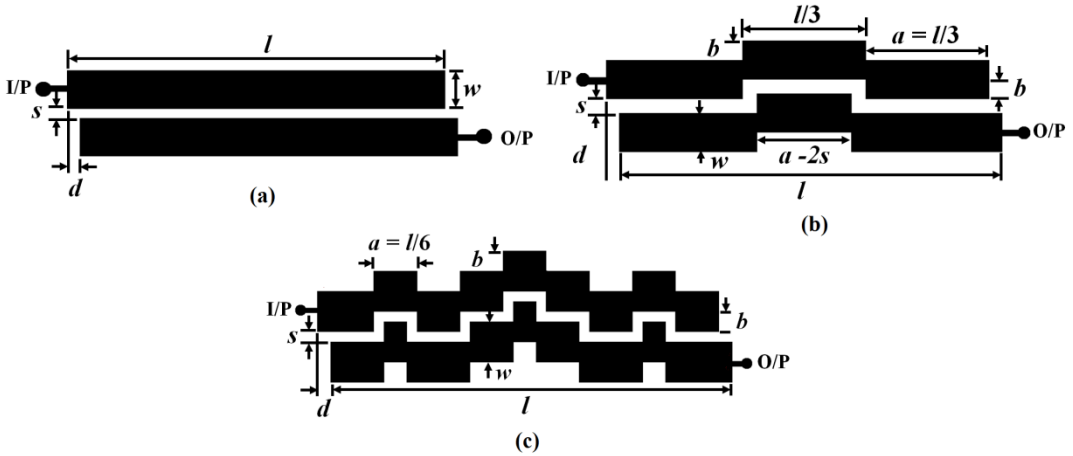

Fig. 3.255. Layouts of the unit PCML cell with Minkowski fractal for iteration order (a) *IO* = 0, (b) *IO* = 1, and (c) *IO* = 2.

However, the lower line has been modified with fractals such that a uniform gap is maintained throughout the structure. In general, for complete self-similar geometry, $a = b = l/3$. However, the parallel-coupled line does not possess self-similar geometry as the width of the line is much smaller than its length. Hence, the value of a has been fixed to three and that of b has been varied in proportion to the width of coupled-lines (w).

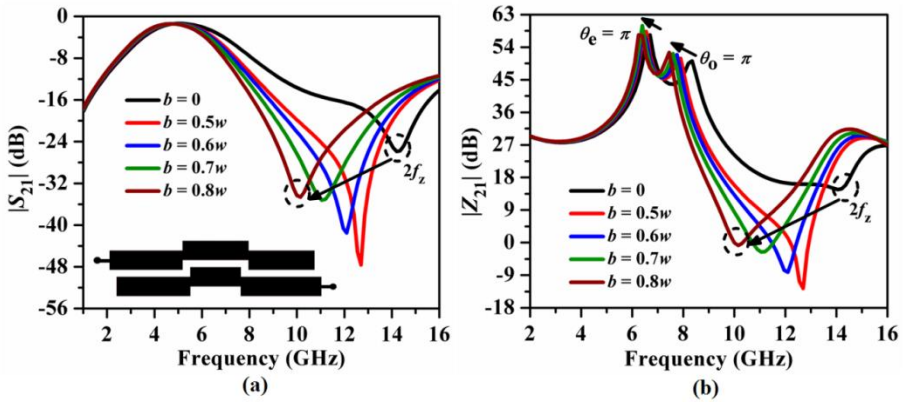

Fig. 3.256. Comparison of simulated (a) $|S_{21}|$ (dB) and (b) $|Z_{21}|$ (dB) plots for the unit PCML cell with Minkowski fractal for iteration order IO = 1.

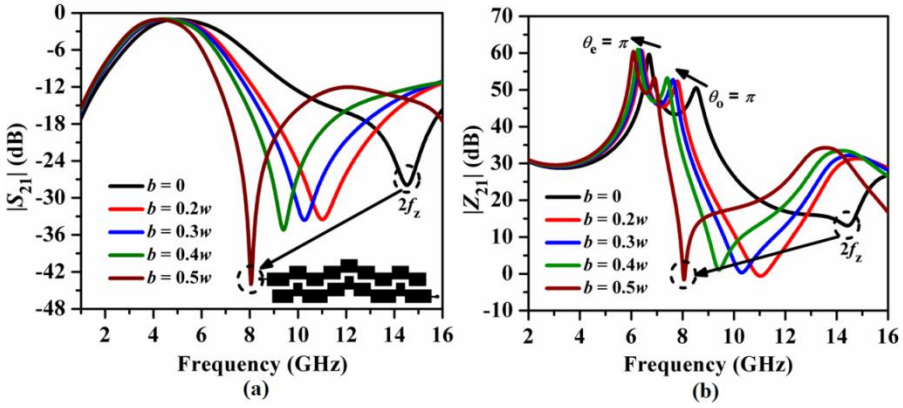

Fig. 3.257. Comparison of simulated (a) $|S_{21}|$ (dB) and (b) $|Z_{21}|$ (dB) plots for the unit PCML cell with Minkowski fractal for iteration order IO = 2.

Figs. 3.256(a)-(b) show the effects of b variation on $|S_{21}|$ (dB) and $|Z_{21}|$ (dB) for l = 7.52 mm, s = 0.2 mm, w = 0.8 mm, d = 0.264 mm, and f_0 = 5.25 GHz, respectively. It has been observed from Fig. 3.256(a) that the transmission zero point ($2f_z$) shifts to a lower frequency region subject to incremental b. This phenomenon is due to the space-filling property of the fractal geometry as the physical length at the line edges has been shortened, resulting in the miniaturization of the space. By properly tuning the value of b, the transmission zero point has been placed exactly at the second harmonic frequency (10.5 GHz) for b = 0.7w. As a result, the resonant peaks for odd-mode electrical length $\theta_o = \pi$ of the $|Z_{21}|$ (dB) plot shift more to the lower frequency region than those for even-mode, i.e., $\theta_e = \pi$, as shown in Fig. 3.256(b). This is due to the increase in odd-mode electrical length compared to that of even-mode, which justifies more reduction in phase velocity of odd-mode compared to even-mode. This phenomenon enables the fractal structure to suppress the harmonic attenuation

level for the PCML cell. For *IO* = 2, a similar phenomenon can be seen in Figs. 257(a)-(b). However, the location of $2f_z$ shifts more rapidly to the lower frequency along with the degradation of the attenuation level. As a result, the odd-mode resonant peak of the $|Z_{21}|$ (dB) plot approaches the even-mode peak more quickly, resulting in more phase velocity compensation between the modes. This is because the overall electrical length of the PCML cells increases greatly due to *IO* = 2, and as a result, the physical length of the cell decreases after tuning back to the dominant resonant frequency. Thus, the size of the cell is reduced compared to *IO* = 1 for the same resonant frequency. In this way, both miniaturization of the cell and modal phase velocity compensation have been achieved effectively by the Minkowski fractal.

The surface current distribution plots for the unit PCML cell with *IO* = 0, 1, and 2 at the resonant frequency of f_0 = 5.25 GHz are shown in Figs. 3.258(a)-(c). It has been observed that the current vectors are congested in the perturbed parts of the PCML cell due to fractal iteration during propagation from the input port to the output port. Accordingly, such unit PCML cells have been cascaded to design the first-order PCMLBF as discussed in the next section.

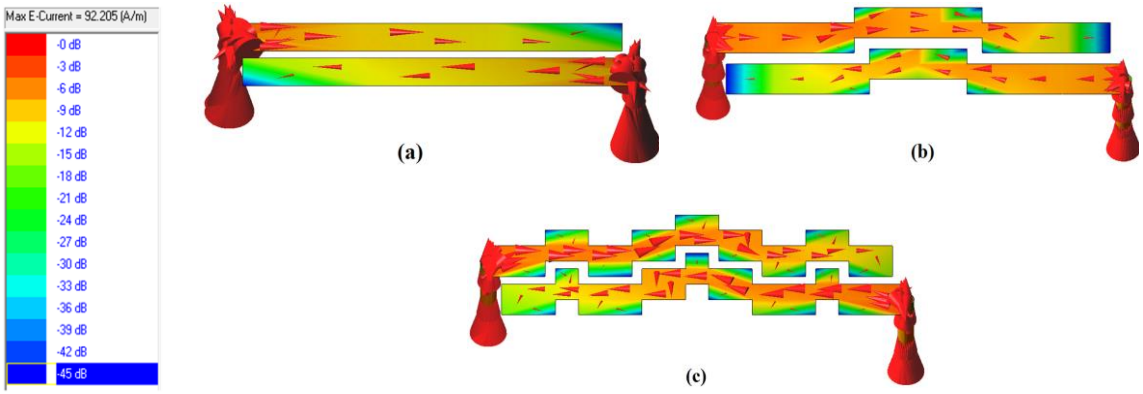

Fig. 3.258. Surface current distribution for the unit PCML cell with Minkowski fractal at f_0 = 5.25 GHz for (a) *IO* = 0, (b) *IO* = 1, and (c) *IO* = 2.

3.18.3. Study of Pair of PCML Cells with Minkowski Fractal

Figs. 3.259(a)-(c) show the layout of the first-order PCMLBF with *IO* = 0, 1, and 2. As a result, Figs. 3.260(a)-(b) compare the $|S_{21}|$ (dB) plots for various values of b in terms of *w*. It has been observed that the second harmonic peak has disappeared completely for $b = 0.5w$ for both *IO* = 1 and 2. Moreover, a sharp transmission of zero $2f_z$ has been generated at 7.5 GHz with an attenuation level of 51 dB for *IO* = 1 and at 6.8 GHz with an attenuation level of

60 dB for *IO* = 2. Thus, with the increase in iteration order, it can be concluded that the location of the transmission zero decreases and its corresponding attenuation level has been degraded too.

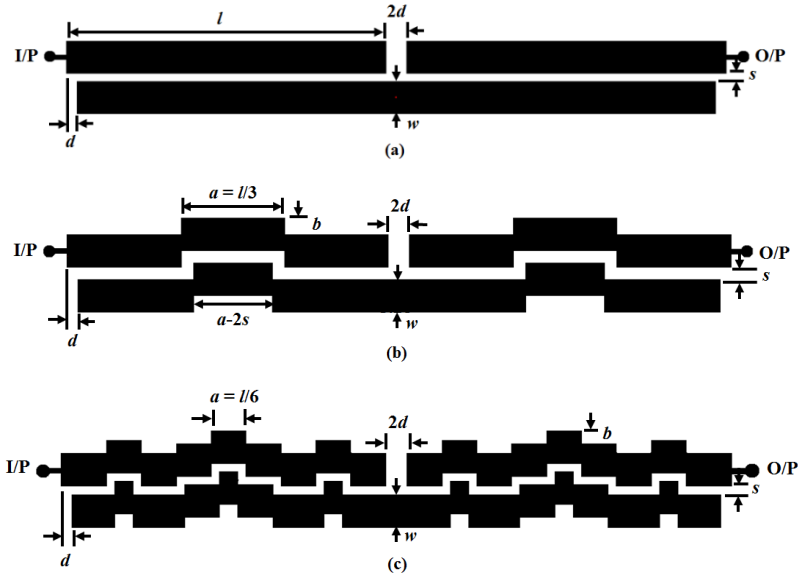

Fig. 3.259. Layouts of the pair of PCML unit cells with Minkowski fractal for iteration order (a) *IO* = 0, (b) *IO* = 1, and (c) *IO* = 2.

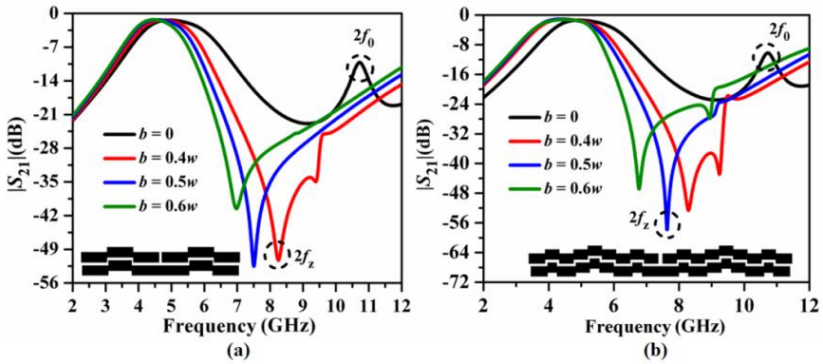

Fig. 3.260. Comparison of simulated $|S_{21}|$ (dB) plots for the pair of unit PCML cells with Minkowski fractal for (a) *IO* = 1, and (b) *IO* = 2.

Surface current distributions at f_0 = 5.25 GHz have been plotted in Figs. 3.261(a)-(c) to better understand the effects of fractal. It has been revealed that the current vectors propagate with a large strength from the input port to the output port due to the passband response. As a result, Figs. 3.262(a)-(c) depict the distribution of surface current vectors at 10.5 GHz for *IO* = 0, 7.5 GHz for *IO* = 1, and 6.8 GHz for *IO* = 2. It has been observed that the surface current propagates to the output port with a minimum strength for both *IO* = 1 and *IO* = 2 due to the suppression of the second harmonic. Subsequently, the quasi Minkowski fractal has been

employed on the third-order folded PCMLBF for the suppression of the second harmonic in the next section.

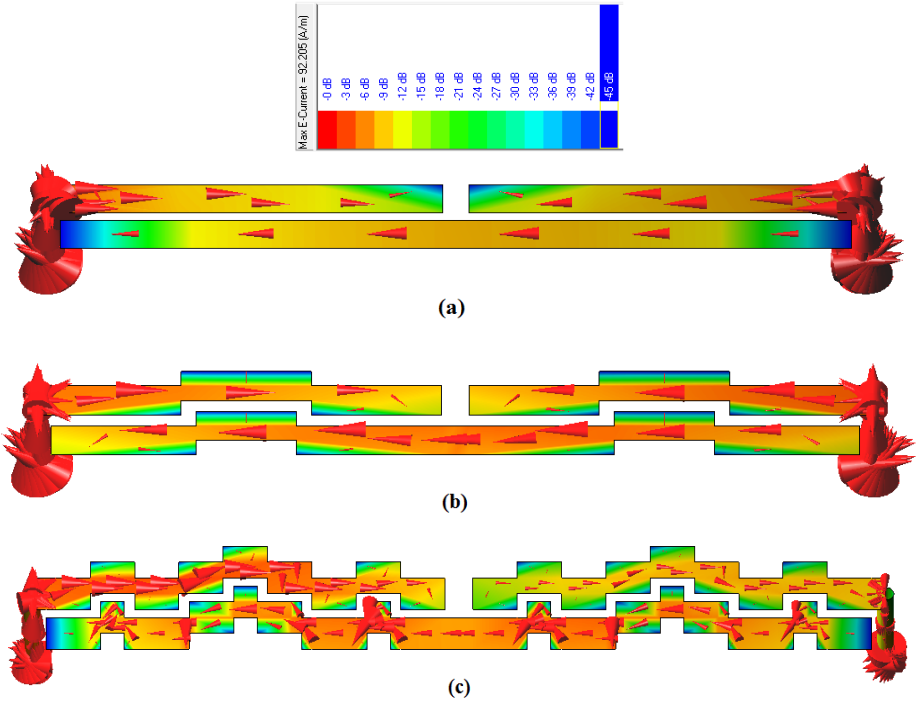

Fig. 3.261. Surface current distribution for the pair of unit PCML cells with Minkowski fractal at f_0 = 5.25 GHz for (a) *IO* = 0, (b) *IO* = 1, and (c) *IO* = 2.

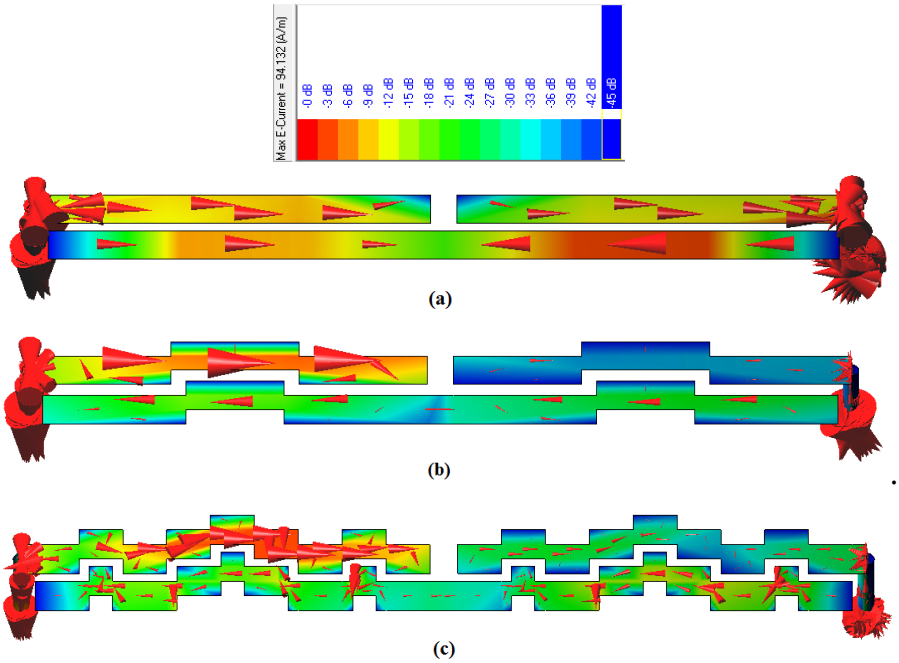

Fig. 3.262. Surface current distribution for the pair of unit PCML cells with Minkowski fractal at f_0 = 10.5 GHz for (a) *IO* = 0, (b) *IO* = 1, and (c) *IO* = 2.

3.18.4. Study of Third-Order Folded PCMLBF with Minkowski Fractal

The general layouts of the third-order folded PCMLBF with quasi Minkowski fractal with *IO* = 1 and 2 are shown in Figs. 3.263(a)-(b). The parametric study for the third-order folded PCMLBF for incremental *b* in terms of w is shown in Figs. 3.264(a)-(b). It has been observed from Fig. 3.264(a) that a sharp transmission zero f_z has occurred at 6 GHz with an attenuation level of 71 dB for $b = 0.4w$ and a sharp second transmission zero $2f_z$ at 9.4 GHz with an attenuation level of 64 dB for $b = 0.6w$.

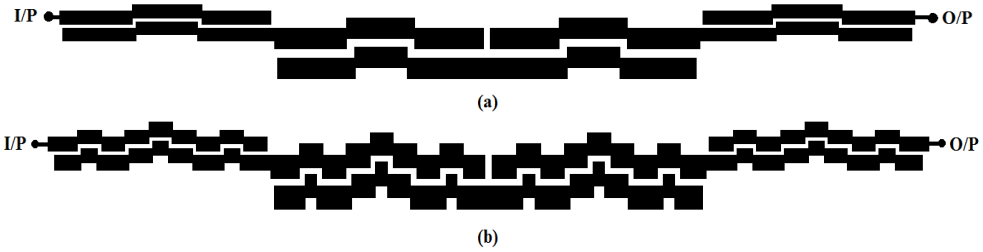

Fig. 3.263. Layout of the third-order folded PCMLBF with Minkowski fractal for (a) *IO* = 1, and (b) *IO* = 2.

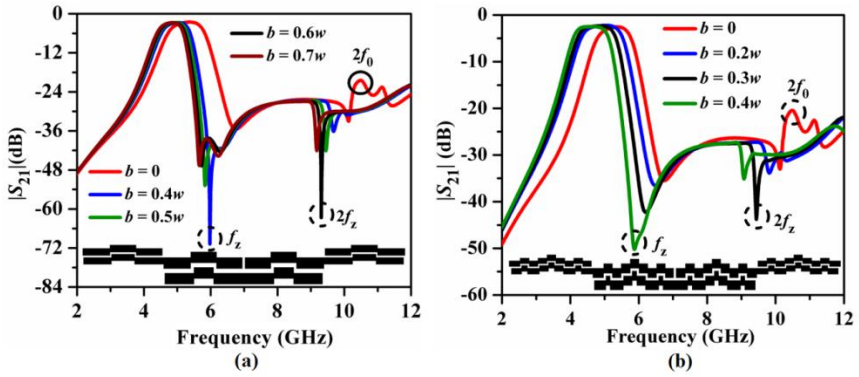

Fig. 3.264. Simulated parametric study for the third-order folded PCMLBF with Minkowski fractal for (a) *IO* = 1, and (b) *IO* = 2.

Similarly, in Fig. 3.264 (b), a sharp transmission zero f_z has occurred at 5.9 GHz with an attenuation level of 50 dB for $b = 0.4w$ and a sharp second transmission zero $2f_z$ at 9.6 GHz with an attenuation level of 45 dB for $b = 0.3w$. It can be concluded from the parametric studies that the Minkowski fractals are capable of improving the skirt characteristics of the filter as well as suppressing the second harmonic completely for some specific value of *b* for the fractal. Accordingly, $b = 0.5w$ and $b = 0.3w$ have been chosen as the optimum values for the final folded filter with *IO* = 1 and *IO* = 2 respectively to improve the skirt characteristics of the filter and suppress second harmonics. The final optimized layout of the third-order folded filters with Minkowski fractal of *IO* = 1 is depicted in Fig. 3.265.

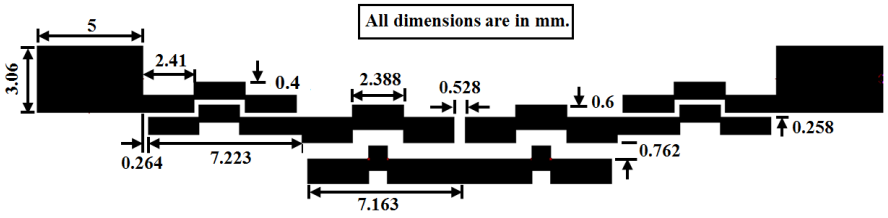

Fig. 3.265. Layouts for the third-order folded PCMLBFs with Minkowski fractal for $IO = 1$ and $b = 0.5w$.

3.18.4.1. Fabricated Prototype- C Band

The fabricated prototype on FR4 laminate is shown in Fig. 3.266. The overall size of the folded filter with $IO = 1$ becomes 39.8 mm × 6.38 mm, i.e., 254.08 mm^2 or $1.28\lambda_g \times 0.2\lambda_g$ and a size reduction of 61.5% has been obtained over the conventional filter.

Fig. 3.266. Fabricated prototype of the third-order folded PCMLBFs with Minkowski fractal for $IO = 1$ [35].

3.18.4.2. Comparison of EM simulation vs. Measurement Results

Figs. 3.267(a)-(b) show simulated vs. measured $|S_{21}|$ (dB) plots. The experimental procedure has been carried out in the similar way of 3.14.4.1. It has been observed from Fig. 3.267(a) that a stopband bandwidth of $2.23f_0$ with a rejection level of 33 dB has been achieved.

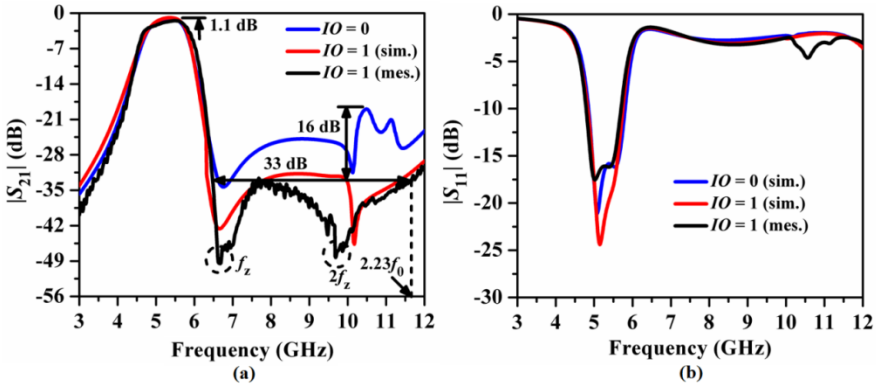

Fig. 3.267. Comparison of simulated vs. measured *S*-parameters for the third-order folded PCMLBF with Minkowski fractal for $IO = 1$, (a) $|S_{21}|$ (dB), and (b) $|S_{11}|$ (dB) [48].

Two sharp transmission zeros, f_z and $2f_z$, have been generated at 6.6 GHz and 9.5 GHz with attenuation levels of 51 dB and 49 dB, respectively. Accordingly, the second harmonic attenuation level has been suppressed by 16 dB due to fractal geometry incorporation. The

measured passband insertion loss was 1.1 dB, and the return loss was 15 dB (Fig. 3.267(b)). Finally, the optimized layout of the third-order folded filter with Minkowski fractal of *IO* = 2 is depicted in Fig. 3.268. The overall size of the folded filter with *IO* = 2 becomes 38.63 mm × 5.79 mm, i.e., 223.67 mm^2 or 1.24λ_g × 0.19λ_g and a size reduction of 66% has been obtained over the conventional filter. The simulated S-parameters for the folded filters with *IO* = 1 and 2 are shown in Fig. 3.269(a)-(b). A stopband extended up to 2.23f_0 with a rejection level of 32 dB has been recorded for *IO* = 2. Moreover, two sharp transmission zeros, f_z and 2f_z, have been generated at 6.5 GHz and 10.3 GHz with attenuation levels of 56 dB and 49 dB, respectively.

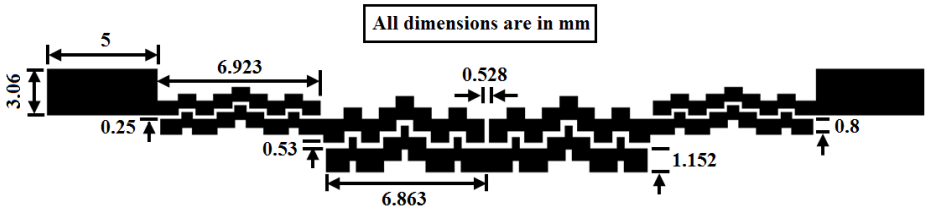

Fig. 3.268. Layouts for the third-order folded PCMLBFs with Minkowski fractal for *IO* = 2, and *b* = 0.3*w*.

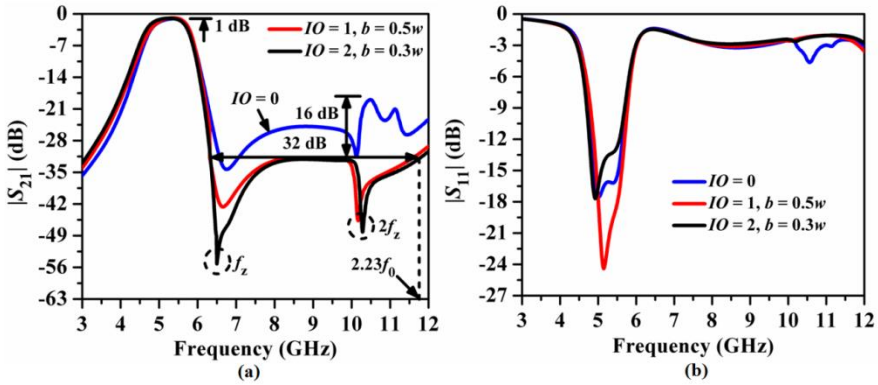

Fig. 3.269. Comparison of simulated *S*-parameters for the third-order folded PCMLBF with Minkowski fractal for different iteration orders: (a) $|S_{21}|$ (dB), and (b) $|S_{11}|$ (dB).

It indicates that the Minkowski fractal with *IO* = 2 has exhibited enhanced skirt characteristics and improved harmonic suppression over the folded filter with *IO* = 1. The surface current distribution plots for the third-order folded PCMLBF with Minkowski fractal for *IO* = 1 and 2 have been explored in Fig. 3.270 and Fig. 3.271, respectively. It has been revealed that for both the cases, the surface current is distributed with large strength at f_0 = 5.25 GHz due to the passband and with very little strength at 2f_0 = 10.5 GHz due to the harmonic suppression. Following that, the parametric study for the third-order *S*-band folded filter centered at 2.5 GHz is shown in Figs. 3.272(a)-(b) for *IO* = 1 and 2, respectively.

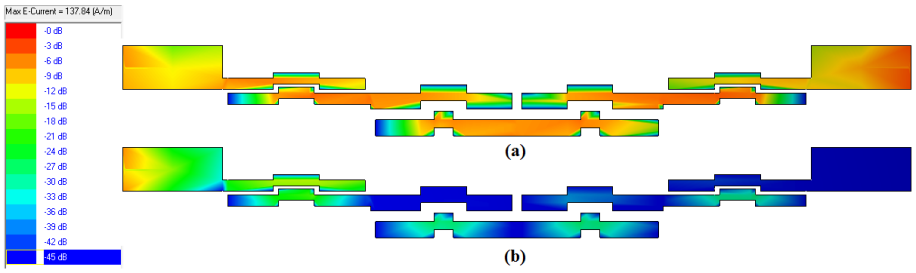

Fig. 3.270. Surface current distribution for the third-order folded PCMLBF with Minkowski fractal for *IO* = 1.

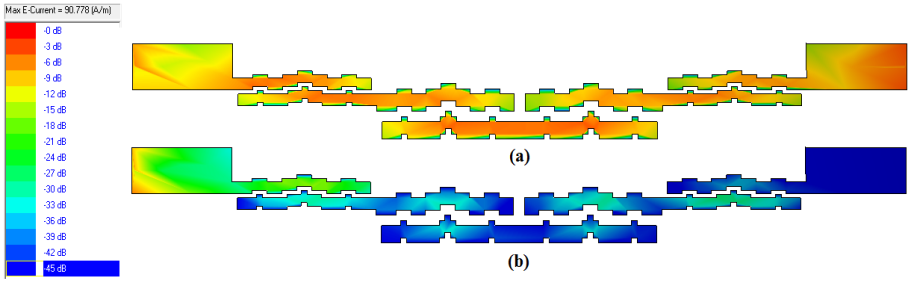

Fig. 3.271. Surface current distribution for the third-order folded PCMLBF with Minkowski fractal for *IO* = 2.

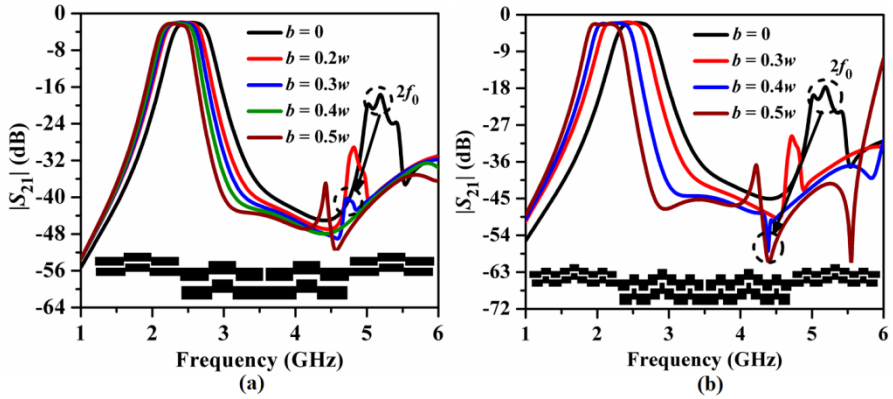

Fig. 3.272. Parametric study for the third-order folded PCMLBF centered at f_0 = 2.5 GHz with Minkowski fractal for (a) *IO* = 1, and (b) *IO* = 2.

It has been observed that maximum suppression of harmonics has occurred with $b = 0.3w$ for *IO* = 1 and with b = 0.4w for *IO* = 2. As a result, the optimized dimensions of the third-order folded filter centered at 2.5 GHz are shown in Figs. 3.273(a)-(b). The overall size of the folded filter with *IO* = 1 becomes 96.6 mm × 7.15 mm, i.e., 690.34 mm^2 or $1.41\lambda_g \times 0.1\lambda_g$ and a size reduction of 43.4% has been obtained over the conventional filter.

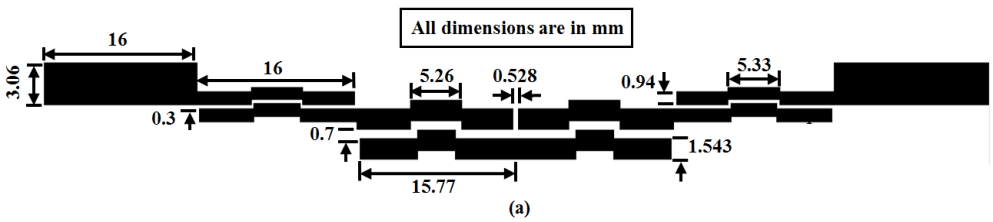

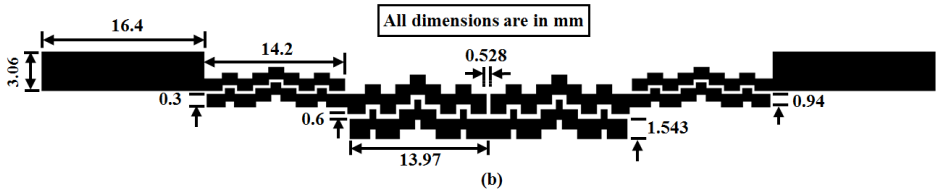

Fig. 3.273. Layouts for the third-order folded PCMLBFs centered at 2.5 GHz with Minkowski fractal for (a) IO = 1, b = 0.4w and (b) IO = 2, b = 0.5w.

Similarly, the overall size of the folded filter with IO = 2 becomes 90.2 mm × 7.05 mm, i.e., 635.6 mm^2 or 1.32λ_g × 0.1λ_g and a size reduction of 48% has been obtained over the conventional filter. As a result, Figs. 3.274(a)-(b) show a comparison of the simulated S-parameter plots for IO = 0, 1, and 2. It has been noticed that a stopband bandwidth of 2.12f_0 has been obtained with a rejection level of 36 dB for the filter with IO = 1 and with the same rejection level up to 2.3f_0 for IO = 2. However, a sharp transmission zero has occurred at 4.8 GHz with an attenuation level of 59 dB for IO = 1, compared to that of 46 dB at 5 GHz for IO = 2. Moreover, the attenuation level at the second harmonic for IO = 0 has been suppressed by 20 dB due to the fractal. The passband return loss of 1.0 dB and a return loss of more than 24 dB for IO = 1 and 14 dB for IO = 2 have been obtained accordingly.

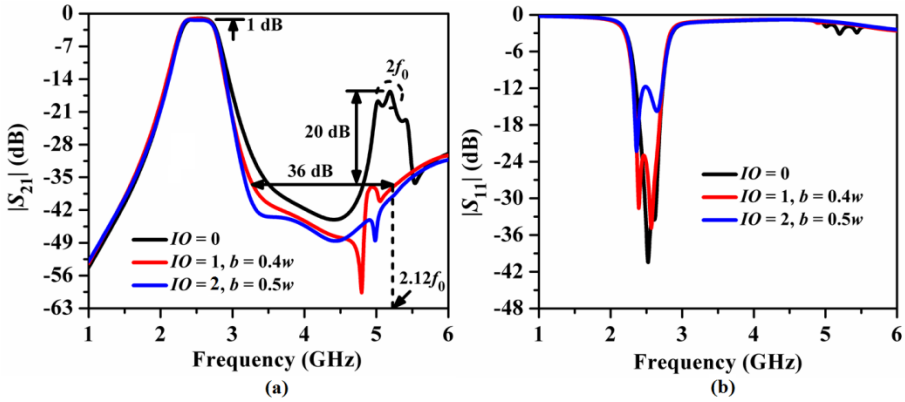

Fig. 3.274. Comparison of simulated S-parameters for the third-order folded PCMLBF centered at 2.5 GHz with Minkowski fractal for different iteration orders, (a) $|S_{21}|$ (dB), and (b) $|S_{11}|$ (dB).

3.18.4.3. Fabricated Prototype- S Band

The fabricated prototypes of the designed filters are shown in Figs. 3.275(a)-(b) respectively.

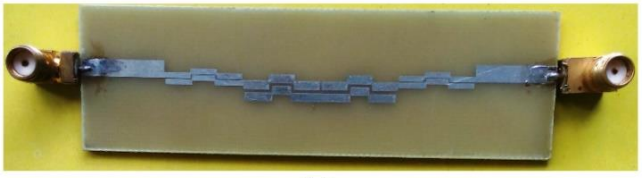

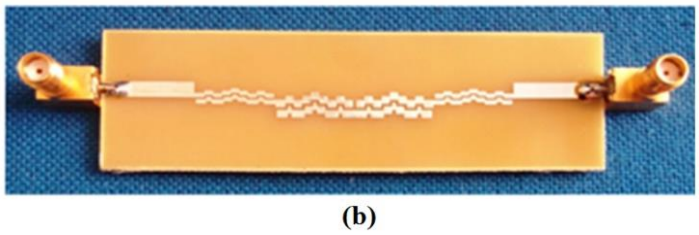

(b)

Fig. 3.275. Fabricated prototypes of the third-order folded PCMLBFs centered at 2.5 GHz with Minkowski fractal for (a) *IO* = 1, and (b) *IO* = 2 [36].

3.18.4.4. Comparison of EM simulation vs. Measurement Results

For *IO* = 1, the experimental results were compared to the simulated results in Figs. 3.276(a)-(b). The experimental procedure has been performed in the similar way of 3.14.4.1. From Fig. 3.276 (a), it has been obtained that a stopband with a rejection level of 37 dB has been obtained up to 2.3f_0. Two sharp transmission zeros, f_z and 2fz, have been generated at 3.3 GHz and 5.3 GHz with attenuation levels of 55 dB and 63 dB. Moreover, the attenuation level at 2f_0 has been suppressed by 21 dB due to the fractal. The skirt characteristics have been improved significantly over the folded filter without fractal. The passband insertion loss has been obtained as 1.1 dB and the return loss has been recorded as 20 dB from Fig. 3.276(b). As a result, the experimental validation for *IO* = 2 is shown in Figs. 3.277(a)-(b). It has been revealed that a stopband rejection level of 40 dB up to 2.12f_0 has been obtained in measurement for *IO* = 2. Similar to *IO* = 1, two sharp transmission zeros f_z and 2f_z with attenuation levels of 58 dB and 55 dB have been generated. Moreover, the attenuation level at 2f_0 has been suppressed by 24 dB due to fractal. The measured insertion loss was 1.05 dB, and the measured return loss was more than 20 dB (Fig. 3.277(b)).

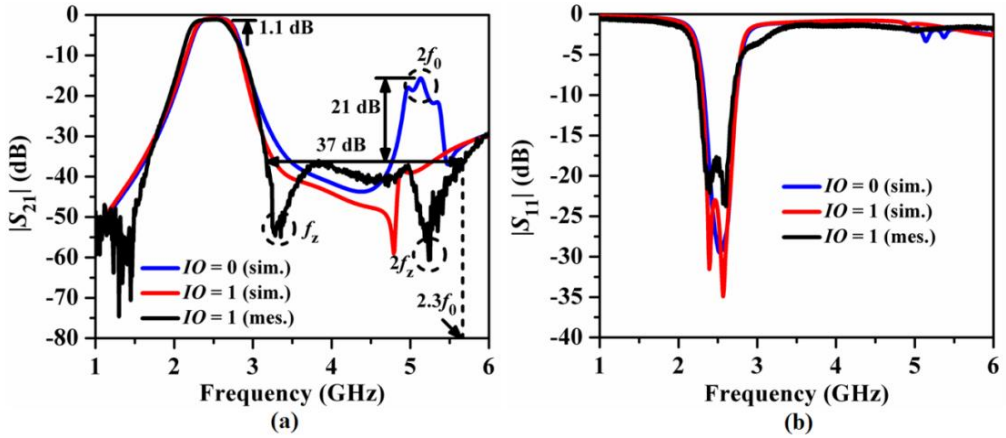

Fig. 3.276. Comparison of simulated vs. measured *S*-parameters for the third-order folded PCMLBF centered at 2.5 GHz with Minkowski fractal for *IO* = 1, (a) $|S_{21}|$ (dB), and (b) $|S_{11}|$ (dB) [36].

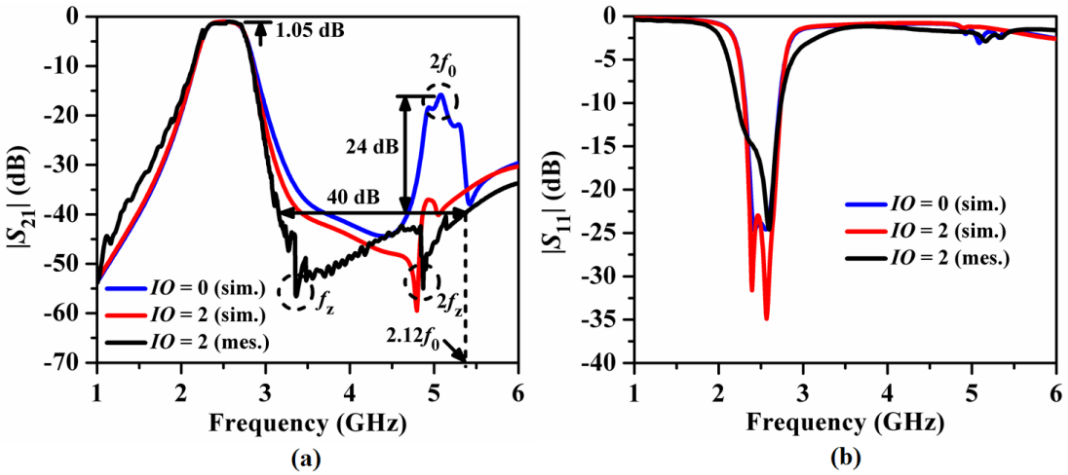

Fig. 3.277. Comparison of simulated vs. measured *S*-parameters for the third-order folded PCMLBF centered at 2.5 GHz with Minkowski fractal for *IO* = 2, (a) $|S_{21}|$ (dB), and (b) $|S_{11}|$ (dB) [36].

As a result, Figs. 3.278(a)-(b) and Figs. 3.279(a)-(b) show the surface current distributions at f_0 = 2.5 GHz and $2f_0$ = 5 GHz for *IO* = 1 and *IO* = 2, respectively. Subsequently, quasi-Minkowski fractals have been employed for the third-order inline filters centered at 5.25 GHz and 2.5 GHz.

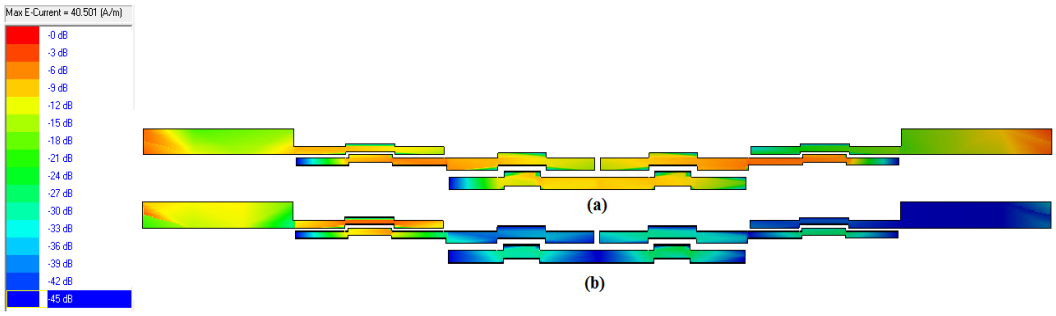

Fig. 3.278. Surface current distribution for the third-order folded PCMLBF with Minkowski fractal for *IO* = 1: (a) f_0 = 2.5 GHz, and (b) $2f_0$ = 5 GHz.

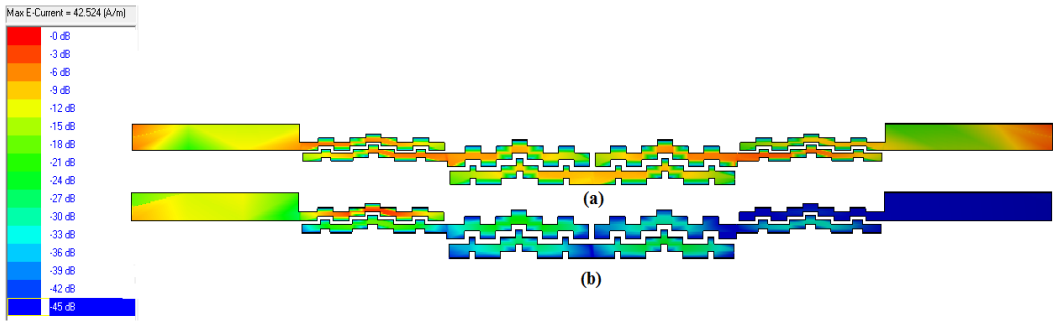

Fig. 3.279. Surface current distribution for the third-order folded PCMLBF with Minkowski fractal for *IO* = 2: (a) f_0 = 2.5 GHz, and (b) $2f_0$ = 5 GHz.

3.18.5. Study of Third-Order Inline PCMLBF with Minkowski Fractal

Figs. 3.280(a)-(b) shows the layouts of the third-order inline PCMLBF with quasi Minkowski fractal with *IO* = 1 and 2, respectively. The parametric study for the third-order inline PCMLBF centered at f_0 = 5.25 GHz for incremental b in terms of w is shown in Figs. 3.281(a)-(b).

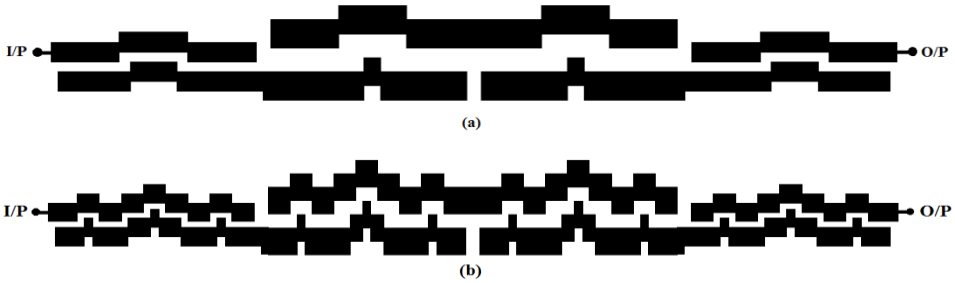

Fig. 3.280. Layout of the third-order folded PCMLBF with Minkowski fractal for (a) *IO* = 1, and (b) *IO* = 2.

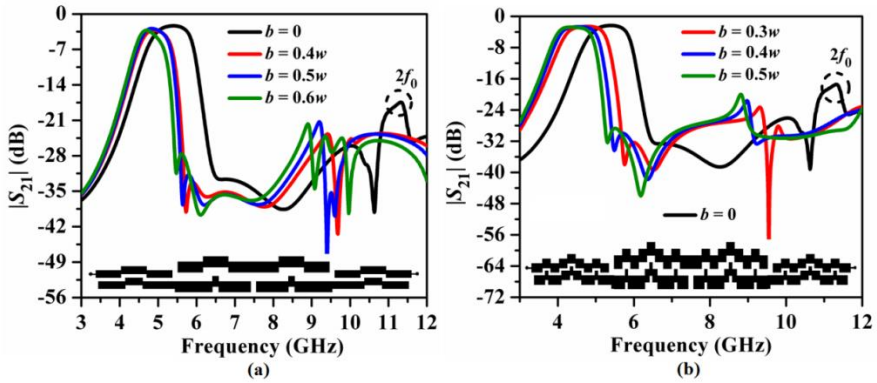

Fig. 3.281. Simulated parametric study for the third-order inline PCMLBF centered at f_0 = 5.25 GHz with Minkowski fractal for (a) *IO* = 1, and (b) *IO* = 2.

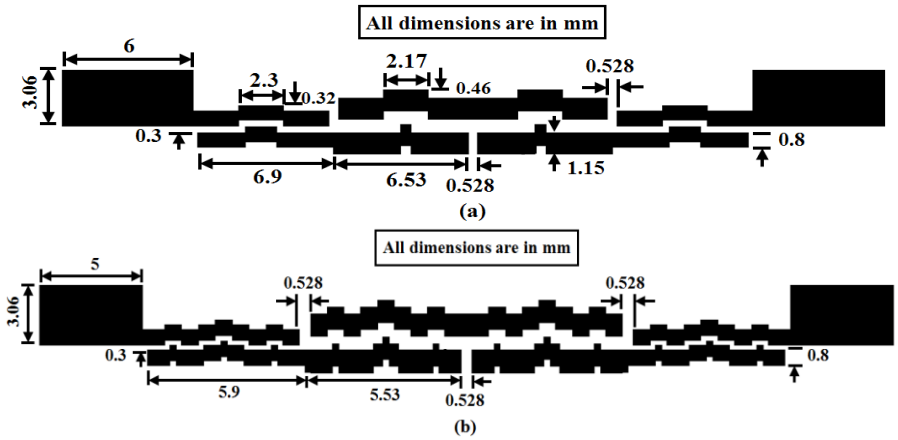

Fig. 3.282. Layouts for the third-order inline PCMLBFs centered at 5.25 GHz with Minkowski fractal for (a) *IO* = 1, *b* = 0.4*w*, and (b) *IO* = 2, *b* = 0.3*w*.

According to Fig. 3.281(a)-(b), b = 0.4w at IO = 1 and b = 0.3w at IO = 2 achieve the best suppression of the attenuation level at $2f_0$. Figs. 3.282(a)-(b) show the final optimized layouts of the third-order inline filters with Minkowski fractals of IO = 1 and IO = 2. The overall size of the inline filter with IO = 1 becomes 39.9 mm × 4.5 mm, i.e., 180 mm^2 or 1.28λ_g × 0.14λ_g and a size reduction of 72.7% has been obtained over the conventional filter. Similarly, the overall size of the inline filter with IO = 2 becomes 33.92 mm × 4.5 mm, i.e., 153 mm^2 or 1.09λ_g × 0.14λ_g and a size reduction of 76.8% has been obtained over the conventional filter.

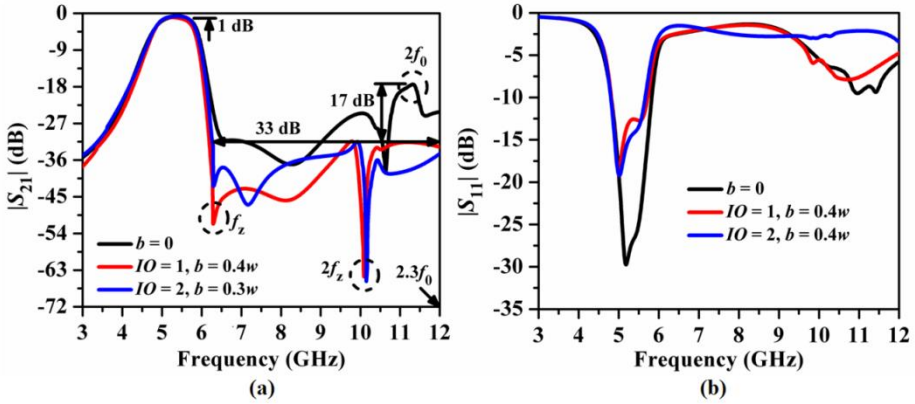

Fig. 3.283. Comparison of simulated *S*-parameters for the third-order inline PCMLBF centered at 5.25 GHz with Minkowski fractal for different iteration orders: (a) $|S_{21}|$ (dB), and (b) $|S_{11}|$ (dB).

As a result, Figs. 3.283(a)-(b) shows a comparison of the simulated S-parameter plots for IO = 0, 1, and 2. It has been noticed that a stopband bandwidth of 2.3f_0 has been obtained with a rejection level of 33 dB for both filters with IO = 1 and IO = 2. However, a sharp transmission zero f_z has occurred at 6.2 GHz with an attenuation level of 51 dB for IO = 1, compared to that of 43 dB for IO = 2. Besides, the attenuation level at the second harmonic for IO = 0 has been suppressed by 17 dB due to the fractal. For both the filters, a second transmission zero $2f_z$ has been generated at 10.2 GHz with a rejection level of 65 dB. As shown in Fig. 3.283(b), a passband return loss of 1 dB and a return loss of more than 15 dB for both IO = 1 and IO = 2 were obtained. The surface current distribution plots for the third-order inline PCMLBF with Minkowski fractal for IO = 1 and 2 have been explored in Fig. 3.284 and Fig. 3.285, respectively. It has been revealed that for both the cases, the surface current is distributed with large strength at f_0 = 5.25 GHz due to the passband and with very little strength at $2f_0$ = 10.5 GHz due to the harmonic suppression. Following that, the parametric study for the third-order S-band inline filter centered at 2.5 GHz is shown in Figs. 3.286(a)-(b) for IO = 1 and 2, respectively.

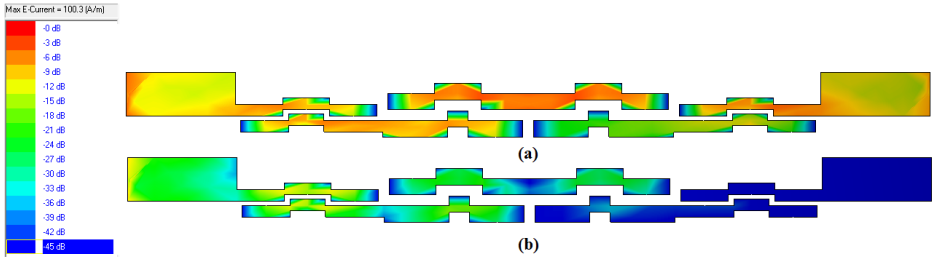

Fig. 3.284. Surface current distribution for the third-order inline PCMLBF centered at 5.25 GHz with Minkowski fractal for *IO* = 1.

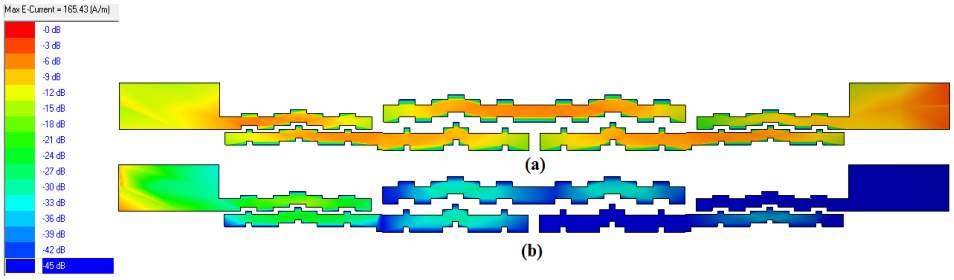

Fig. 3.285. Surface current distribution for the third-order inline PCMLBF centered at 5.25 GHz with Minkowski fractal for *IO* = 2.

It has been observed that maximum suppression of harmonics has occurred with $b = 0.6w$ for *IO* = 1 and with $b = 0.3w$ for *IO* = 2. As a result, the optimized dimensions of the third-order inline filters centered at 2.5 GHz are shown in Figs. 3.287(a)-(b). The overall size of the folded filter with *IO* = 1 becomes 94.6 mm × 4.9 mm, i.e., 463.8 mm^2 or $1.39\lambda_g \times 0.07\lambda_g$ and a size reduction of 64% has been obtained over the conventional filter. Similarly, the overall size of the folded filter with *IO* = 2 becomes 89.6 mm × 4.9 mm, i.e., 439.3 mm^2 or $1.31\lambda_g \times 0.07\lambda_g$ and a size reduction of 66% has been obtained over the conventional filter.

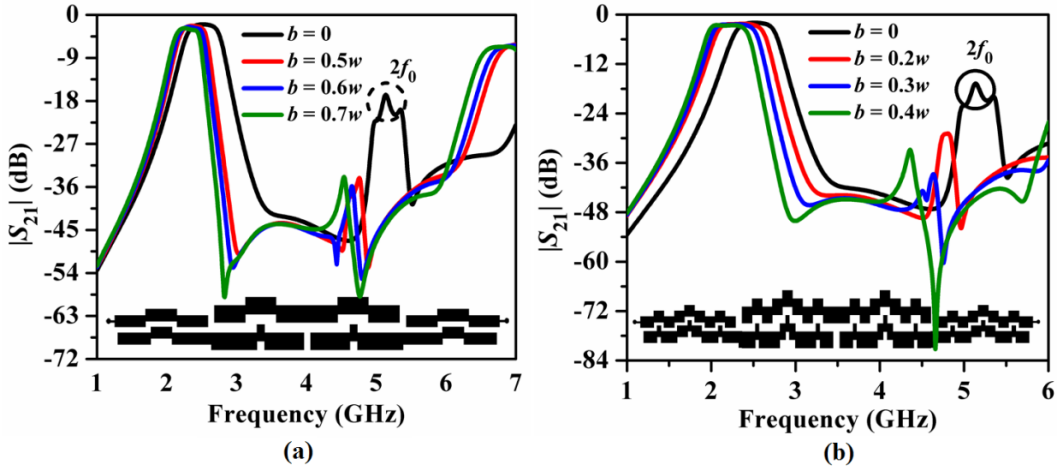

Fig. 3.286. Parametric study for the third-order inline PCMLBF centered at f_0 = 2.5 GHz with Minkowski fractal for (a) *IO* = 1, and (b) *IO* = 2.

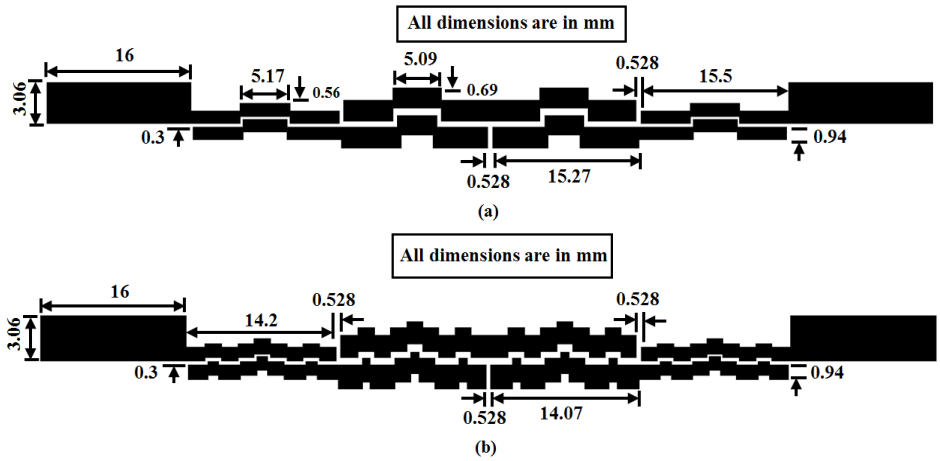

Fig. 3.287. Layouts for the third-order inline PCMLBFs centered at 2.5 GHz with Minkowski fractal for (a) IO = 1, b = 0.6w and (b) IO = 2, b = 0.3w.

In addition, Figs. 3.288(a)-(b) shows a comparison of the simulated S-parameter plots with IO = 0, 1, and 2. It has been noticed that a stopband bandwidth of 2.4f_0 has been obtained with a rejection level of 33 dB for the inline filter having IO = 1, and 36 dB of rejection level up to 2.3f_0 for the filter with IO = 2. Two sharp transmission zeros have occurred at 3.3 GHz and 4.9 GHz with attenuation levels of 47 dB and 57 dB for IO = 2. This shows that the harmonic suppression performance has been improved for the inline filter with IO = 2 compared to IO = 1. The attenuation level at 2f_0 has been suppressed by 21 dB due to the fractal. As a result, Figs. 3.289(a)-(b) and Figs. 3.290(a)-(b) show the surface current distributions at f_0 = 2.5 GHz and 2f_0 = 5 GHz for IO = 1 and IO = 2, respectively. It has been noticed that the surface current propagates with large strength for the passband and weak strength for the stopband due to the harmonic rejection performance.

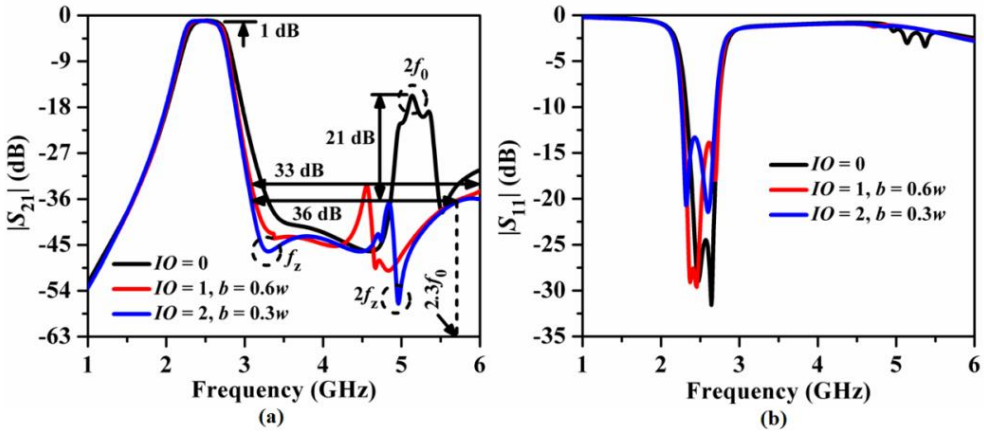

Fig. 3.288. Comparison of simulated S-parameters for the third-order inline PCMLBF centered at 2.5 GHz with Minkowski fractal for different iteration orders: (a) |S_{21}| (dB), and (b) |S_{11}| (dB).

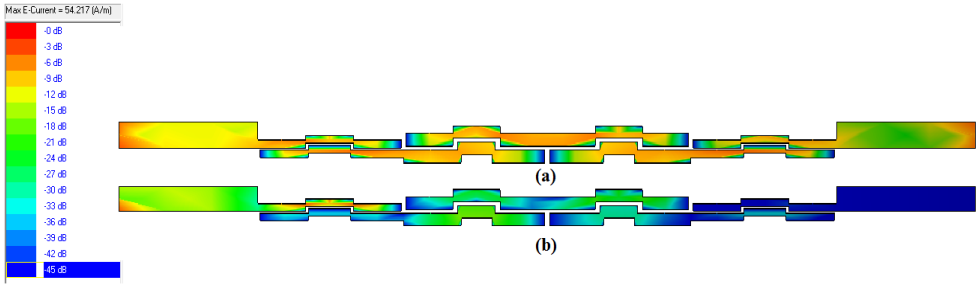

Fig. 3.289. Surface current distribution for the third-order inline PCMLBF centered at 2.5 GHz with Minkowski fractal for *IO* = 1.

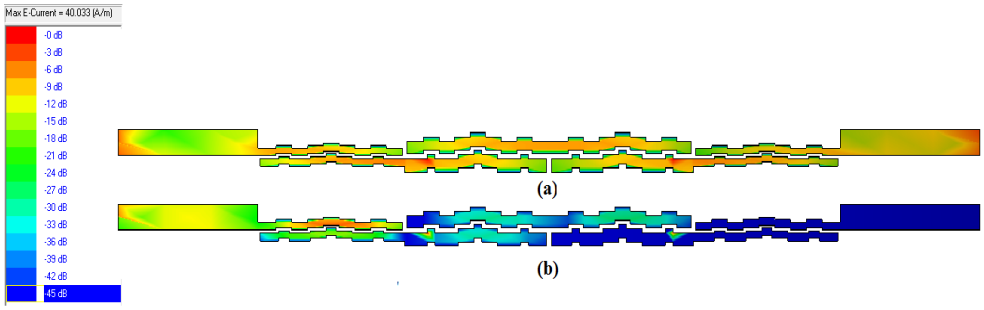

Fig. 3.290. Surface current distribution for the third-order inline PCMLBF centered at 2.5 GHz with Minkowski fractal for *IO* = 2.

Table 3.19 tabulates all the parameters for the folded and inline filters with quasi Minkowski fractals. It has been noticed that the Figure of Merit (*FOM*) becomes greater for both the *C*-band and *S*-band inline filters with perturbation than for folded filters with perturbation. It can be concluded from Table 3.19 that the *FOM* values become maximum for the inline filters centered at both 5.25 GHz and 2.5 GHz with *IO* = 2.

Table 3.19. Comparison of all designed PCMLBFs with quasi Minkowski fractal.

f_o (GHz)	Type of filter	*IO*	ξ (dB/GHz)	*SBRL* (dB)	*SBW* (x f_0)	*RSB*	*SF*	*NCS*	*AF*	*FOM*
5.25 GHz	folded	1	38.57	33	2.23	1.38	3.3	0.262	1	670
		2	38.57	32	2.23	1.39	3.2	0.231		743
	inline	1	45	33	2.3	1.31	3.3	0.186		1046
		2	45	33	2.3	1.31	3.3	0.158		1231
2.5 GHz	folded	1	67.5	36	2.1	1.1	3.6	0.148		1806
		2	67.5	36	2.2	1.12	3.6	0.136		2001
	inline	1	67.5	33	2.4	1.3	3.3	0.099		2925
		2	67.5	36	2.3	1.3	3.6	0.094		3361

Table 3.20. Comparison of all the best folded PCMLBFs.

Types of perturbations	**C-band filter (f_0 = 5.25 GHz)**	**S-band filter (f_0 = 2.5 GHz)**
Periodic grooves	Sawtooth, *FOM* = 753	Quarter elliptical, *FOM* = 2896
Periodic Corrugations	Square, *FOM* = 764	Square, *FOM* = 3861
Asymmetric perturbations	*FOM* = 474	*FOM* = 1544
Koch fractal	*IO* = 2, *FOM* = 675	*IO* = 2, *FOM* = 2880
Minkowski fractal	*IO* = 2, *FOM* = 743	*IO* = 2, *FOM* = 2001

Table 3.21. Comparison of all the best inline PCMLBFs.

Types of perturbations	**C-band filter (f_0 = 5.25 GHz)**	**S-band filter (f_0 = 2.5 GHz)**
Periodic grooves	Quarter elliptical, *FOM* = 1210	Quarter elliptical, *FOM* = 4190
Periodic Corrugations	Square, *FOM* = 2925	Triangular, *FOM* = 9264
Asymmetric perturbations	*FOM* = 1002	*FOM* = 2874
Koch fractal	*IO* = 2, *FOM* = 1814	*IO* = 2, *FOM* = 6033
Minkowski fractal	*IO* = 2, *FOM* = 1231	*IO* = 2, *FOM* = 3361

From this section, it can be concluded that quasi Minkowski fractals are quite capable of suppressing the harmonic rejection level well below 35 dB, up to $2.3f_0$ for both the folded and inline filters. Accordingly, different harmonic suppression methods have been compared in Table 3.20 and Table 3.21 for the folded and inline filters operating in the *C* and *S* bands. It can be concluded that among all the types of perturbations, periodic corrugations exhibit the best performance with respect to *FOM* values for both folded and inline filters for both the bands. However, triangular corrugations exhibit the highest *FOM* value of 9264 for the *S*-band inline filter. In this chapter, different types of perturbations, such as periodic grooves, periodic corrugations, asymmetric perturbations, Koch fractals, and Minkowski fractals, have been studied in detail. Two filters centered at 5.25 GHz (*C*-band) and 2.5 GHz (*S*-band) have been designed, fabricated, and tested experimentally. It has been observed that all the types of perturbations are capable of suppressing the harmonic level below 30 dB. However, the stopband rejection bandwidth has been restricted to $2.4f_0$ for both the filters. Moreover, it has been observed that periodic corrugations have exhibited the maximum suppression of harmonic attenuation level in addition to the miniaturization of the filter size. Accordingly,

the study of periodic corrugations has been extended further in the next section to extend the stopband bandwidth with an improved stopband rejection level.

3.19. Multispurious Harmonics Suppression by Trapezoidal Corrugations

3.19.1. Study of Unit PCML Cell

In this section, the ideas of the over-coupled stages [8] and the corrugated coupled stages [22] have been extended to design miniaturized bandpass filters [22] with an improved rejection level up to the fourth harmonic. The corrugated stages with rectangular corrugations proposed in [22] have been modified with trapezoidal-shaped corrugations to minimize the edge diffraction. In [28-30], the concept of phase velocity compensation has been obtained between even-and odd-mode by relocating the transmission zeros subject to periodic square and triangular corrugations in folded and inline coupled-line filters. In such works, the effects of corrugations on higher order harmonics have not been studied. The rectangular and square corrugations in [28-29] exhibit an abrupt transition at the corners for the surface current, and in [30], the triangular corrugations with sharp edges at the vertices result in the constriction of the path for the surface current. Fig. 3.291(a) shows the layout of a unit PCML cell where trapezoidal corrugations have been introduced, and Fig. 3.291(b) depicts the layout of a unit PCML cell with six periodic trapezoidal corrugations on the coupled edges. It may be further noted that when $a = b$, the trapezoidal corrugation becomes a rectangular corrugation. For simplicity of the design, the values of base width w_B and height h_T have been fixed to $w/2$, where w is the width of the coupled-line. By varying the value of a with b equals to w, the area of the trapezoidal corrugations has been varied, which effectively changes the degree of coupling between the corrugated lines. As a result, the phase velocity of the odd-mode has been compensated more, while the phase velocity of the even-mode has remained almost unchanged, as shown in Fig. 3.292 for $|Z_{21}|$ (dB) plots for the PCML tuned at f_0 = 2.5 GHz. It has been further observed from Fig. 3.292 that the second transmission zero $2f_z$ has been shifted to a lower frequency by the maximum amount compared to those for square and triangular corrugations. Traditionally, an ideal quarter-wavelength PCML cell (Fig. 3.291(a)) has inherent transmission zeros at $2mf_0$ for the electrical coupling length of the coupled-lines of 180^o [3]. Similarly, the line with a length of $\lambda/6$ at f_0 has an electrical length multiple of 180^o that exhibits zeros at $3mf_0$ [22].

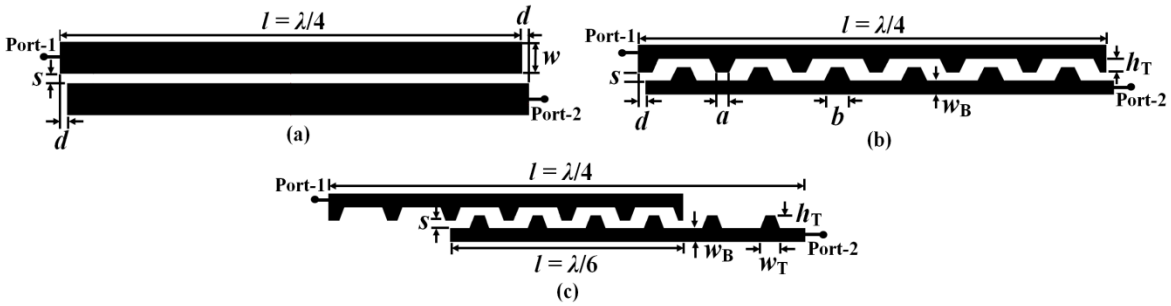

Fig. 3.291. Layout of unit PCML cell:(a) no corrugations, (b) trapezoidal corrugations with coupling periods of 6 for $2f_0$ and $4f_0$ transmission zeros, and (c) coupling periods of 4/6 for $3f_0$ transmission zero placement.

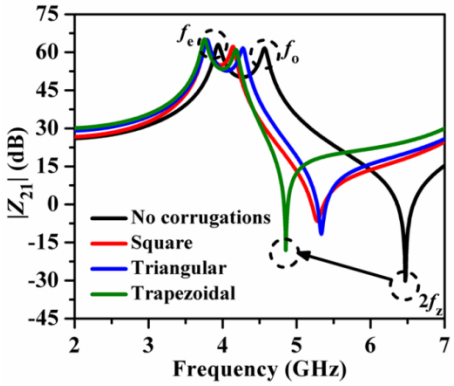

Fig. 3.292. Comparison of simulated $|Z_{21}|$ (dB) for unit PCML cell with square, triangular and trapezoidal corrugations.

Hence, for generating zeros at eve-order harmonics such as $2f_0$, $4f_0$, $6f_0$, and $8f_0$ simultaneously with the same corrugated coupled-line structure, six periods of the corrugations have been chosen as shown in Fig. 3.291(b). However, the odd-order harmonics are unaffected according to the distributed characteristics of the quarter-wavelength line. Thus, by optimizing the coupling periods of the corrugations, the inherent transmission zeros have been allocated at the harmonics of the desired center frequency. Accordingly, by coupling four periods of six corrugations (4/6 x $\lambda/4 = \lambda/6$), the transmission zero has been placed at $3f_0$ as shown in Fig. 3.291(c). Fig. 3.293(a)-(c) depicts the placement of second, third, and fourth harmonic transmission zeros in a unit PCML cell by varying the a/b values of the trapezoidal corrugations. The dimensions of the coupled lines at the corrugations have been taken as l = 16.833 mm, $w = w_T = b$ = 0.94 mm, s = 0.3 mm, d = 0.264 mm, $h_T = w_B = w/2$ = 0.47 mm, N = 6 for f_0 = 2.5 GHz. It has been observed that the values of a/b for exact placement of second, third, and fourth harmonic transmission zeros are 0.3, 0.4, and 0.5, respectively.

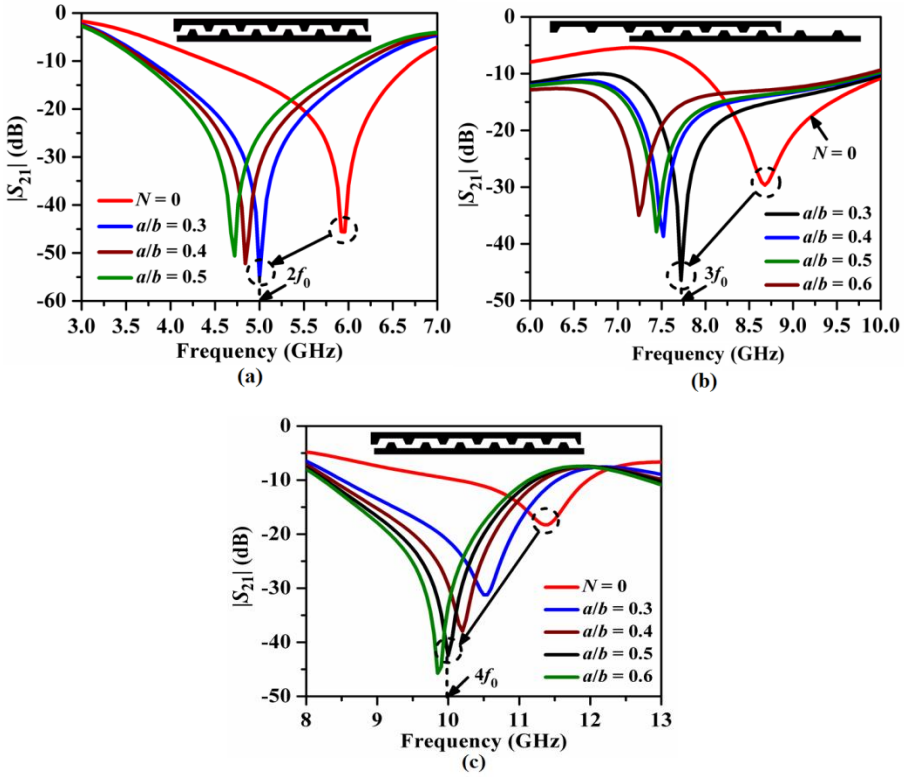

Fig. 3.293. Placement of transmission zeros by varying the values of a/b for the simulated $|S_{21}|$ (dB) plots: (a) at $2f_0$ = 5 GHz, (b) at $3f_0$ = 7.5 GHz and (c) at $4f_0$ = 10 GHz.

Subsequently, such unit PCML cells have been cascaded in a folded structure to design the third-order folded filter for harmonics suppression.

3.19.2. Third-Order Folded Bandpass Filter with Trapezoidal Corrugations

Figs. 3.294(a)-(b) show the general structure of a third-order folded filter with trapezoidal corrugations for multispurious harmonics suppression. Firstly, maximum suppression at $2f_0$ and $4f_0$ by trapezoidal corrugations has been studied by varying the value of a/b with the assumptions that $w_B = h_T = w/2$, $b = w$ and $N = 6$ as highlighted in Fig. 3.295(a). It has been observed that maximum suppression at $2f_0$ and $4f_0$ has been obtained for $a/b = 0.5$. Moreover, three sharp transmission zeros (f_z, 2fz, and $3f_z$) have occurred. Accordingly, the parametric study has been continued in Fig. 3.295(b) for $3f_0$ suppression for the structure shown in and it has been observed that optimum suppression for $2f_0$, $3f_0$, and $4f_0$ has been achieved for $a/b = 0.5$. Besides, seven transmission zeros f_z - $7f_z$ have occurred, justifying the effectiveness of the structure. Figs. 3.296(a)-(b) show the final optimized layouts with all dimensions in millimeters. The overall size of Filter-I becomes 88.18 mm × 5.53 mm, i.e., 488.05 mm^2 or

$1.29\lambda_g \times 0.08\lambda_g$ and that of Filter-II becomes 96.4 mm × 5.36 mm, i.e., 517.15 mm^2 or $1.41\lambda_g \times 0.08\lambda_g$. Accordingly, size reductions of 62% and 60% have been achieved over the conventional filter. Figs. 3.297(a)-(b) show the simulated S-parameter plots for the final filters Filter-I and Filter-II. According to Fig. 3.297(a), Filter-II has a wide stopband up to $4.68f_0$ and a rejection level of 27 dB. The attenuation level at $3f_0$ has been suppressed by 21 dB. The passband insertion loss becomes 0.9 dB and the passband return loss becomes more than 15 dB for both the filters, as highlighted in Fig. 3.297(b).

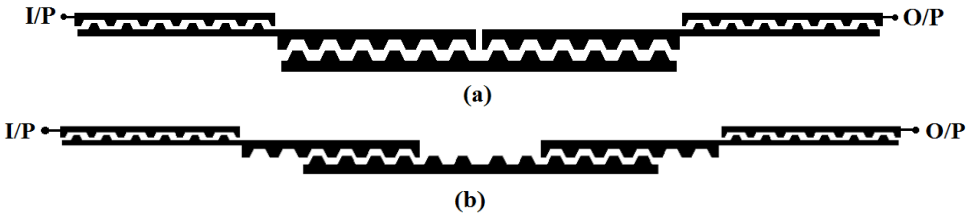

Fig. 3.294. General structure of third-order folded bandpass filter with trapezoidal corrugations: (a) $2f_0$ and $4f_0$ suppression (Filter-I), and (b) for multispurious suppression (Filter-II).

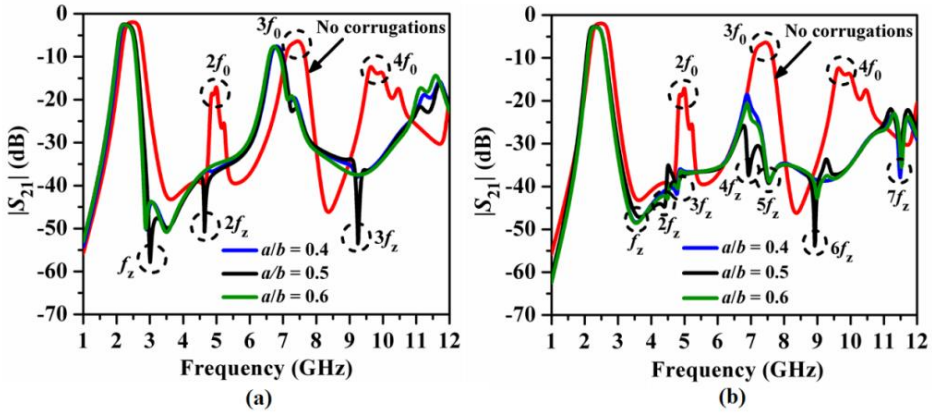

Fig. 3.295. Simulated parametric study for third-order folded filters with trapezoidal corrugations having different value of a/b: (a) for $2f_0$ and $4f_0$ suppression (Filter-I), and (b) for multispurious suppression (Filter-II).

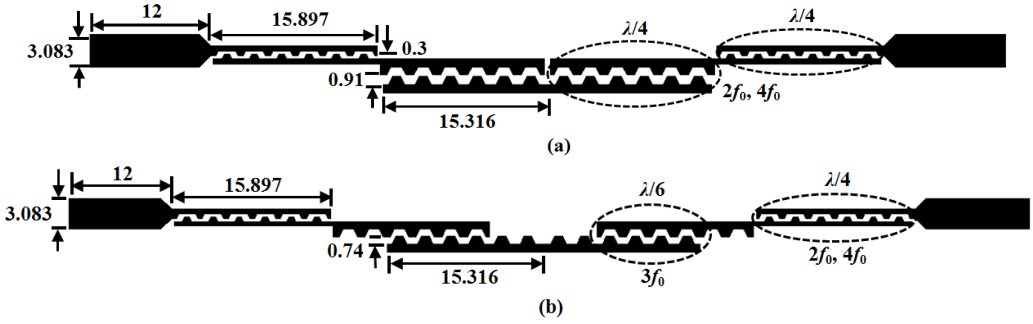

Fig. 3.296. Final optimized layouts of the third-order folded filters with trapezoidal corrugations: (a) for $2f_0$ and $4f_0$ suppression (Filter-I), and (b) for multispurious suppression (Filter-II). All dimensions are in mm.

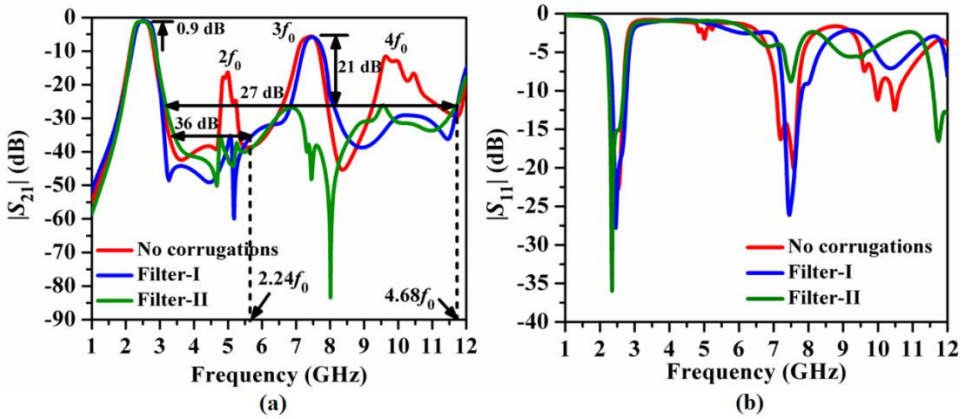

Fig. 3.297. Comparison of simulated *S*-parameters plots for the third-order folded filters with trapezoidal corrugations: (a) $|S_{21}|$ (dB) and (b) $|S_{11}|$ (dB).

3.19.2.1. Fabricated Prototype- Folded Filter

To validate the simulated results, a prototype of Filter-II has been fabricated as shown in Fig. 3.298.

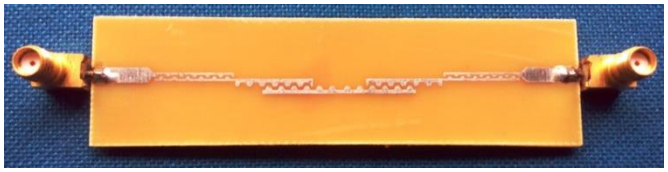

Fig. 3.298. Fabricated prototype of Filter II [37].

3.19.2.2. Comparison of EM simulation vs. Measurement Results

The fabricated prototype has been tested on VNA N9928A by Keysight Technologies by following the similar way of 3.14.4.1. In Figs. 3.299(a)-(b), the experimental results were compared to the simulated results.

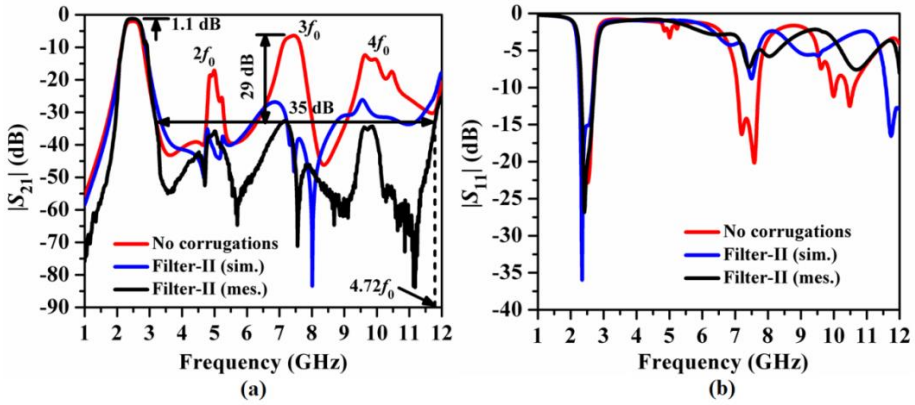

Fig. 3.299. Comparison between the simulated vs. measured *S*-parameters plots for the third-order folded filter (Filter-II) with trapezoidal corrugations: (a) $|S_{21}|$ (dB) and (b) $|S_{11}|$ (dB) [50].

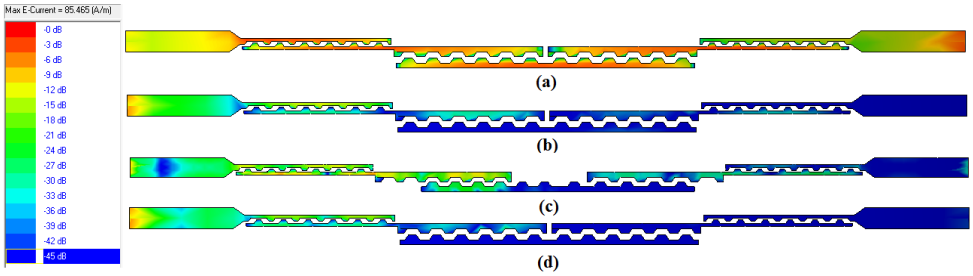

Fig. 3.300. Distribution of surface current for the third-order folded filter (Filter-II) with trapezoidal corrugations: (a) at f_0 = 2.5 GHz, (b) at $2f_0$ = 5 GHz, (c) at $3f_0$ = 7.5 GHz, and (c) at $4f_0$ = 10 GHz.

In measurement, a wide stopband up to $4.72f_0$ with a rejection level of 35 dB was obtained, as shown in Fig. 3.299(a). Moreover, the attenuation level at $3f_0$ has been suppressed by 29 dB and multiple sharp transmission zeros have occurred in the stopband, improving the performance of the filter. The passband insertion loss has been recorded as 1.1 dB. As a result of Fig. 3.299(b), the passband return loss is greater than 20 dB. The surface current distributions for Filter-II at f_0, $2f_0$, $3f_0$, and $4f_0$ are shown in Figs. 3.300(a)-(d). It has been observed that the surface current reaches the output port with maximum strength at f_0. However, due to suppression, the current distributions for $2f_0$, $3f_0$, and $4f_0$ have been reduced. The study was expanded for folded filters with a center frequency of 5.25 GHz (*C*-band) to validate the performance of trapezoidal corrugations on harmonics suppression in other frequency bands, and the final optimized layouts are shown in Figs. 3.301(a)-(b) with a/b = 0.4. The overall size of Filter-I becomes 42.23 mm × 4.67 mm, i.e., 197.07 mm^2 or $1.2\lambda_g \times 0.13\lambda_g$ and that of Filter-II becomes 47.1 mm × 4.62 mm, i.e., 217.6 mm^2 or $1.24\lambda_g \times 0.13\lambda_g$. Accordingly, size reductions of 70% and 67% have been achieved over the conventional filter. The simulated *S*-parameters are shown in Figs. 3.302(a)-(b).

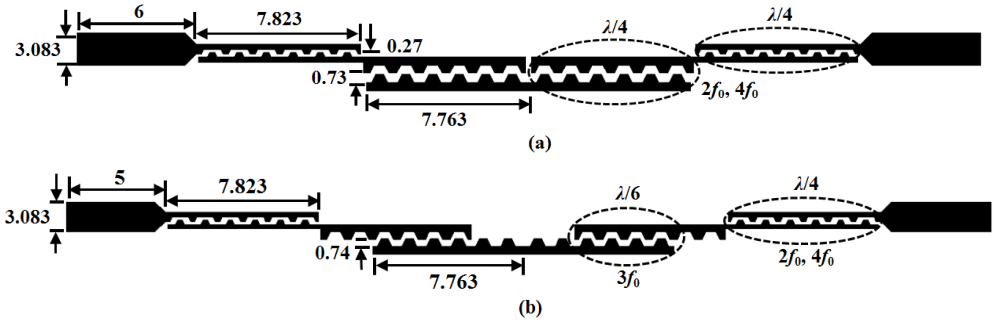

Fig. 3.301. Optimized layouts of the third-order folded filters centered at f_0 = 5.25 GHz with trapezoidal corrugations: (a) for $2f_0$ and $4f_0$ suppression (Filter-I) and (b) for multispurious suppression (Filter-II). All dimensions are in mm.

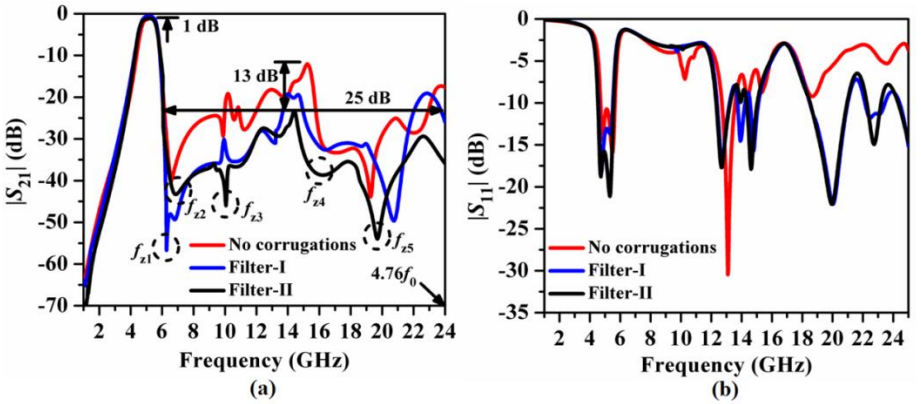

Fig. 3.302. Comparison of simulated *S*-parameters plots for the third-order folded filters centered at 5.25 GHz with trapezoidal corrugations: (a) $|S_{21}|$ (dB) and (b) $|S_{11}|$ (dB).

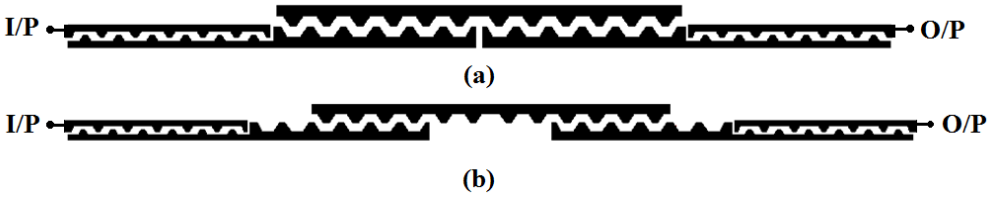

Fig. 3.303. General structure of third-order inline bandpass filter with trapezoidal corrugations: (a) $2f_0$ and $4f_0$ suppression (Filter-III), and (b) for multispurious suppression (Filter-IV).

It has been observed that, similar to the *S*-band filters described earlier, a wide stopband up to $4.76f_0$ with a rejection level of 25 dB has been obtained for Filter-II. The attenuation level at $3f_0$ has been suppressed by 13 dB. Moreover, multiple transmission zeros have occurred in the stopband. The passband insertion loss becomes 1.0 dB and the return loss becomes more than 15 dB, as explored in Fig. 3.302(b). Furthermore, the trapezoidal corrugation-based folded filters, Filter-III and Filter-IV, as shown in Figs. 3.303(a)-(b), have been modified to inline filters.

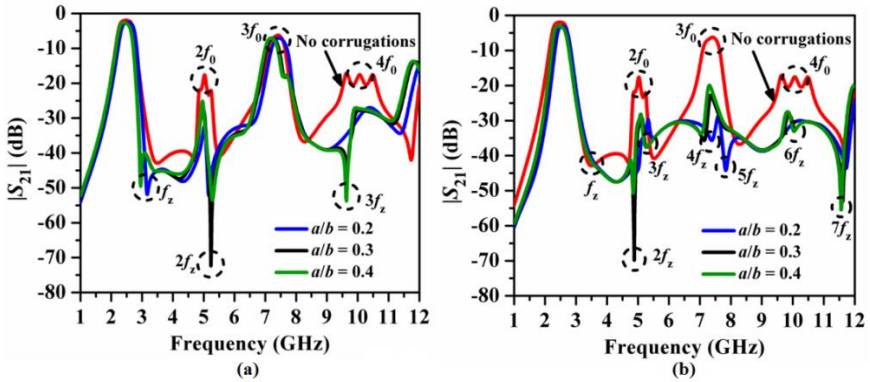

Fig. 3.304. Simulated parametric study for the third-order *S*-band inline filters with trapezoidal corrugations: (a) for $2f_0$ and $4f_0$ suppression (Filter-III), and (b) for multispurious suppression (Filter-IV).

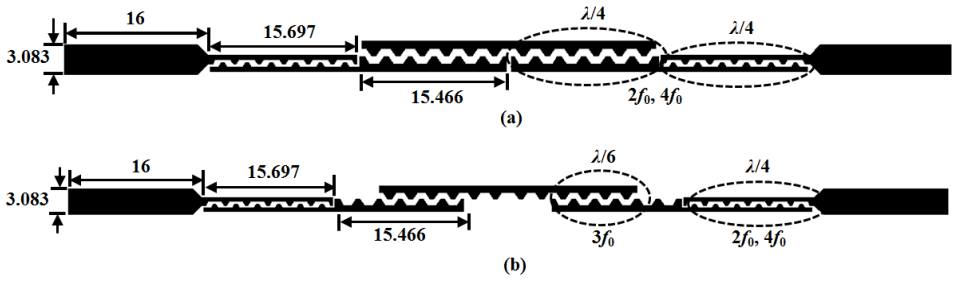

Fig. 3.305. Final optimized layouts of the third-order inline filters with trapezoidal corrugations: (a) for $2f_0$ and $4f_0$ suppression (Filter-III), and (b) for multispurious suppression (Filter-IV). All dimensions are in mm.

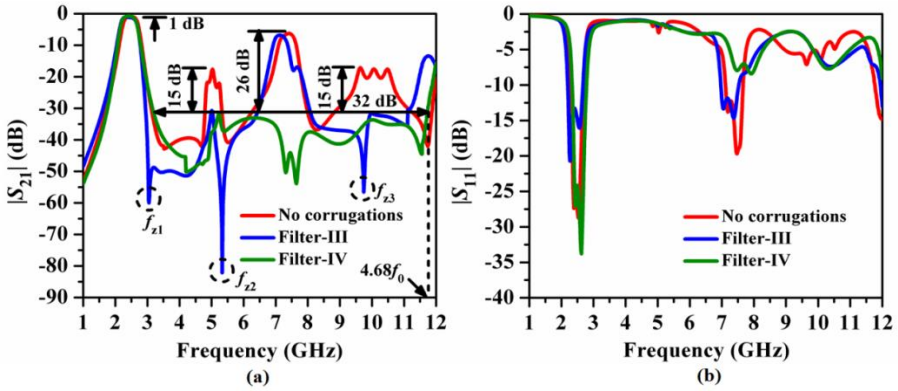

Fig. 3.306. Comparison of simulated *S*-parameters plots for the third-order inline filters with trapezoidal corrugations: (a) $|S_{21}|$ (dB), and (b) $|S_{11}|$ (dB).

As a result, parametric studies for various a/b values are shown in Figs. 3.304(a) and (b). The optimum value of a/b has been chosen as 0.3 for both the filters. The layouts with optimized dimensions in mm of the final inline filters have been depicted in Figs. 3.305(a)-(b). The overall size of Filter-III becomes 96.58 mm × 3.08 mm, i.e., 297.47 mm^2 or 1.41λ_g × 0.045λ_g and that of Filter-IV becomes 105.52 mm × 3.08 mm, i.e., 325.01 mm^2 or 1.55λ_g × 0.045λ_g. Accordingly, size reductions of 55% and 51% have been achieved over the conventional filter. The simulated *S*-parameters have been compared in Figs. 3.306(a)-(b). It has been observed that a wide stopband up to 4.68f_0 with a rejection level of 32 dB has been obtained for Filter-IV. The attenuation levels at $2f_0$ and $4f_0$ have been suppressed by 15 dB and those at $3f_0$ by 26 dB. However, multiple transmission zeros such as f_z, $2f_z$, and $3f_z$ have occurred in the stopband for Filter-III. Accordingly, the skirt characteristics have been enhanced with corrugations over the conventional inline filter. The passband insertion loss becomes 1.0 dB and the return loss becomes more than 15 dB, as explored in Fig. 3.306(b).

3.19.2.3. Fabricated Prototype- Inline Filter

To validate the simulated results, a prototype of Filter-IV has been fabricated as shown in Fig. 3.307.

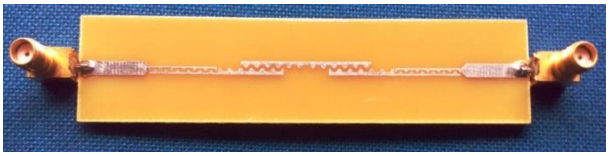

Fig. 3.307. Fabricated prototype of Filter IV [37].

3.19.2.4. Comparison of EM simulation vs. Measurement Results

The fabricated prototype has been tested on VNA N9928A by Keysight Technologies. Figs. 3.308(a)-(b) show a comparison of experimental and simulated *S*-parameter plots. In measurement, a wide stopband up to $4.8f_0$ with a rejection level of 36 dB was obtained, as shown in Fig. 3.308(a).

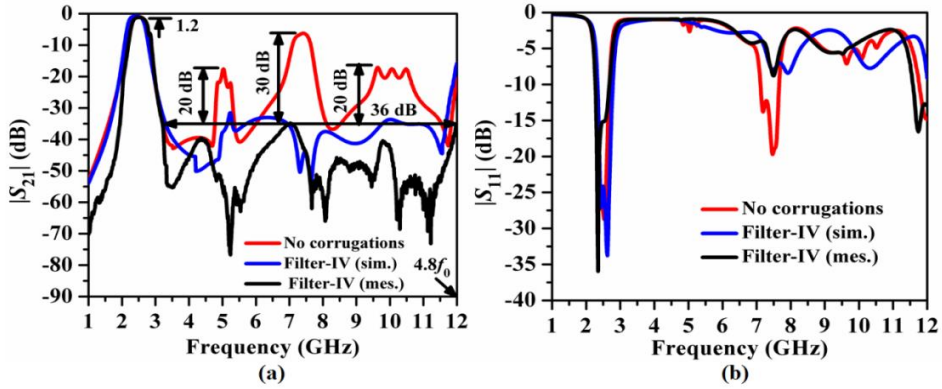

Fig. 3.308. Comparison between the simulated vs. measured *S*-parameters plots for the third-order inline filter (Filter-IV) with trapezoidal corrugations: (a) $|S_{21}|$ (dB) and (b) $|S_{11}|$ (dB) [37].

Moreover, the attenuation levels at $2f_0$ and $4f_0$ have been suppressed by 20 dB and those at $3f_0$ by 30 dB. Multiple sharp transmission zeros have occurred in the stopband, improving the stopband performance of the filter. The passband insertion loss has been recorded as 1.2 dB. As a result, the passband return loss has been calculated to be greater than 15 dB using Fig. 3.308(b). Figs. 3.309(a)-(d) depicts the surface current distributions for Filter-IV at f_0, $2f_0$, $3f_0$, and $4f_0$. It has been observed that the surface current reaches the output port with maximum strength at f_0 and the current distributions for $2f_0$, $3f_0$, and $4f_0$ have been reduced. The investigation for the *C*-band filter (f_0 = 5.25 GHz) has been expanded, and the optimized layouts for Filter-III and Filter-IV are shown in Figs. 3.310(a)-(b).

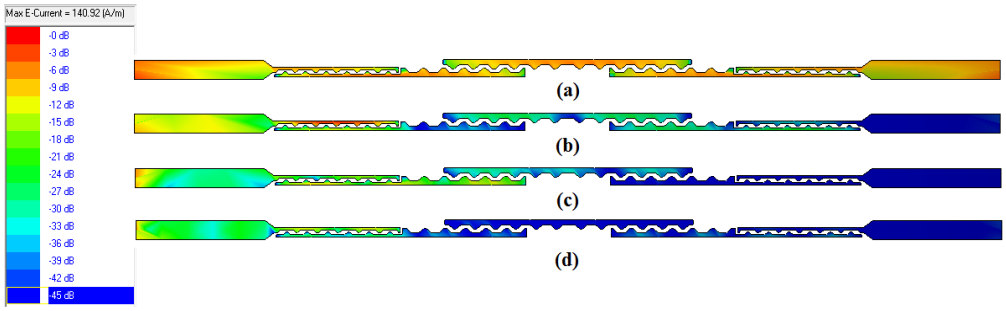

Fig. 3.309. Distribution of surface current for the third-order inline filter (Filter-IV) with trapezoidal corrugations: (a) at f_0 = 2.5 GHz, (b) at $2f_0$ = 5 GHz, (c) at $3f_0$ = 7.5 GHz, and (c) at $4f_0$ = 10 GHz.

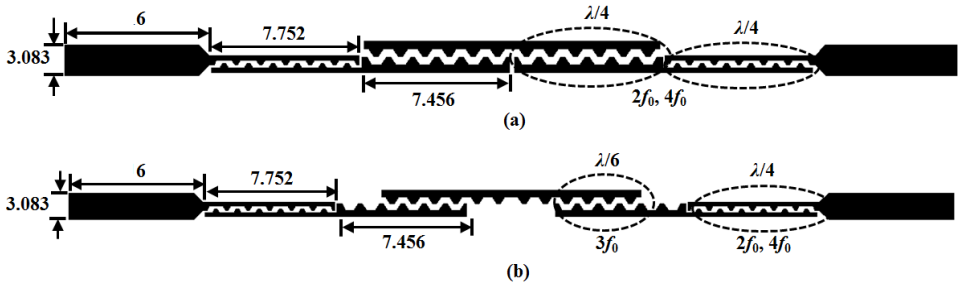

Fig. 3.310. Final optimized layouts of the third-order inline filters centered at f_0 = 5.25 GHz with trapezoidal corrugations: (a) for $2f_0$ and $4f_0$ suppression (Filter-III) and (b) for multispurious suppression (Filter-IV). All dimensions are in mm.

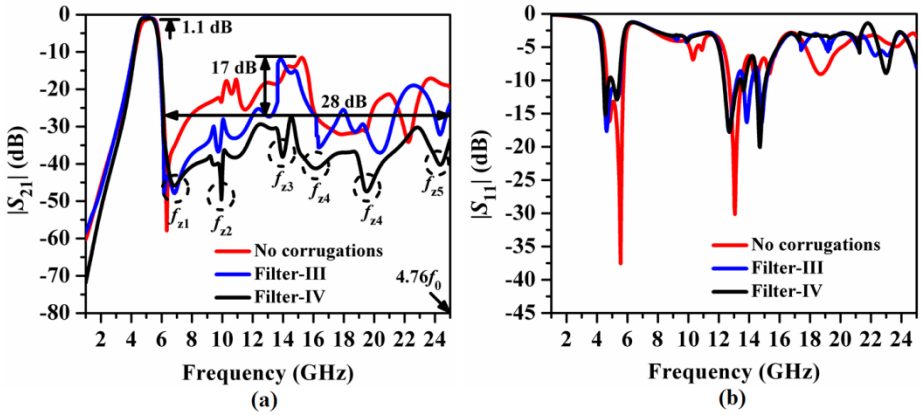

Fig. 3.311. Comparison of simulated *S*-parameters plots for the third-order inline filters centered at f_0 = 5.25 GHz with trapezoidal corrugations: (a) $|S_{21}|$ (dB) and (b) $|S_{11}|$ (dB).

The overall size of Filter-III becomes 42.23 mm × 3.08 mm, i.e., 130.07 mm^2 or $1.2\lambda_g \times 0.045\lambda_g$ and that of Filter-IV becomes 47 mm × 3.08 mm, i.e., 144.76 mm^2 or $1.33\lambda_g \times 0.045\lambda_g$. Accordingly, size reductions of 80% and 78% have been achieved over the conventional filter. Following that, Figs. 3.311(a)-(b) compares simulated *S*-parameter plots for inline filters centered at f_0 = 5.25 GHz with and without corrugations.

According to Fig. 3.311(a), Filter-IV has a wide stopband up to $4.76f_0$ and a rejection level of 28 dB. Moreover, the attenuation level at $3f_0$ has been suppressed by 17 dB. Multiple sharp transmission zeros (f_{z1}-f_{z5}) have occurred in the stopband, justifying the improvement in the stopband performance of the filter. The passband insertion loss has been obtained as 1.1 dB and the passband return loss has been obtained as more than 12 dB, highlighted in Fig. 3.311(b).

Table 3.22. Comparison of all designed PCMLBFs with trapezoidal corrugations.

Type of Filter		***f_o*** **(GHz)**	***ξ*** **(dB/GHz)**	***SBRL*** **(dB)**	***SBW*** **(x f_0)**	***RSB***	***SF***	***NCS***	***AF***	***FOM***
Folded	Filter-I	2.5	24.55	32	2.68	0.735	3.2	0.105	1	549.9
	Filter-II		30	35	4.72	1.147	3.5	0.111		1085
	Filter-I	5.25	14.21	27	2.51	1.045	2.7	0.159		252.2
	Filter-II		15	25	4.76	1.205	2.5	0.175		258.2
Inline	Filter-III	2.5	33.75	32	2.56	0.723	3.2	0.064		1220
	Filter-IV		27	36	4.8	1.137	3.6	0.047		2351
	Filter-III	5.25	12.27	25	2.55	0.735	2.5	0.105		214.7
	Filter-IV		9.64	28	4.76	1.205	2.8	0.117		278

Table 3.22 lists all the filters' parameters to compare their performances. It has been observed that an inline filter (Filter-IV) centered at 2.5 GHz exhibits the maximum figure-of-merit (*FOM*) value among all other designed filters. It can be concluded from this chapter that folded and inline parallel-coupled line filters provide very compact structures with a size reduction of more than 50% over the conventional filter. However, the presence of spurious harmonics restricts their applications. Accordingly, various harmonics suppression methods have been studied in detail for such filters, and as an optimum result, a wide stopband up to $4.8f_0$ with a rejection level of more than 30 dB has been achieved by trapezoidal corrugations. However, the sizes of the folded and inline filters designed so far are still quite large, restricting their applications to some advanced modern wireless systems where compactness is the utmost requirement. Thus, compact hairpin-line filter topology with harmonic suppression performance has been chosen to be studied as the extension of the present work in the next chapter.

References:

[1] G. Mattaei, L. Young and E. M. T. Jones, "Microwave Filters, Impedance- matching Networks and Coupling Structures," *Artech House, Norwood*, MA, vol. 1, ch.4, 84-94, pp.1980.

[2] D. M. Pozar, "Microwave Engineering," *John Willey and Sons*, Inc., 4th. ed., ch. 2, pp. 48-59, 2011.

[3] J. S. Hong and M. J. Lancaster, "Microstrip Filters for RF/Microwave Applications," *John Willey & Sons, Inc.*, New York, NY, 2001, ISBN 0-471-22161-9, Ch. 3, pp. 29-30, 2001.

[4] A P. I. Mak, S. P. U, and R. P. Martins, "Transceiver architecture selection–review, state-of-the-art survey and case study," *Analog-Baseband Architectures And Circuits For Multistandard And Low voltage Wireless Transceivers, Analog Circuits and Signal Processing*, Springer, Dordrecht, doi: 10.1007/978-1-4020-6433-3_2, pp. 9 - 40, 2007.

[5] S. F. Chang, W. L. Chen, S. C. Chang, C. K. Tu, C. L. Wei, C. H. Chien, C. H. Tsai, J. Chen, and A. Chen, "A dual-band RF transceiver for multistandard WLAN applications," *IEEE Transactions on Microwave Theory and Techniques*, vol. 53, no. 3, pp. 1048-1055, March 2005.

[6] S. Akhtarzad, T. R. Rowbotham, and P. B. Johns, "The Design of Coupled Microstrip Lines," *IEEE Transactions on Microwave Theory and Techniques*, vol. 23, no. 6, pp. 486-492, June 1975.

[7] A. Manchec, C. Quendo, E. Rius, C. Person, and J. F. Favennec, "Synthesis of dual behavior resonator (DBR) filters with integrated low-pass structures for spurious responses suppression," *IEEE microwave and wireless components letters*, vol. 16, no. 1, pp. 4-6, December 2005.

[8] M. A. S. Soriano, G. T. Penalva, and E. Bronchalo, "Multispurious suppression in parallel-coupled line filters by means of coupling control," *IET Microw. Antennas Propag*., vol. 6, Iss. 11, pp. 1269-1276, July 2012.

[9] M. Orellana, J. Selga, P. Vélez, M. Sans, A. Rodríguez, J. Bonache, V. E. Boria, and F. Martin, "Design of capacitively loaded coupled-line bandpass filters with compact size and spurious suppression," *IEEE Transactions on Microwave Theory and Techniques*, vol. 65, no. 4, pp. 1235-1248, January 2017.

[10] R. Phromloungsri, M. Chongcheawchamnan, and I. D. Robertson, "Inductively compensated parallel coupled microstrip lines and their applications," *IEEE transactions on microwave theory and techniques*, vol. 54, no. 9, pp. 3571-3582, August 2006.

[11] M. N. Mollah, N. C. Karmakar, and J. S. Fu, "Uniform circular photonic bandgap structures (PBGSs) for harmonic suppression of a bandpass filter," *AEU-International Journal of Electronics and Communications*, vol. 62, no. 10, pp. 717-724, November 2008.

[12] S. Parvez, N. Sakib, and M. N. Mollah, "Investigation on EBG structures: A critical analysis to optimize the performance of asymmetric couple-line bandpass filter," *In Proceedings of The 8th International Conference on Software, Knowledge, Information Management and Applications* (SKIMA 2014), pp. 1-7, Decemeber 2018.

[13] M. L. Her, W. Ko, M. W. Hsu, Y. L. Wang, and C. J. Hsu, "Parallel-coupled bandpass filters with broad rejection band using interdigital fingers and DGS," *Microwave and Optical Technology Letters*, vol. 48, no. 4, pp. 705-707, April 2006.

[14] I. K. Kim, N. Kingsley, M. Morton, R. Bairavasubramanian, J. Papapolymerou, M. M. Tentzeris, and J. G. Yook, "Fractal-shaped microstrip coupled-line bandpass filters for suppression of second harmonic," *IEEE Transactions on Microwave Theory and Techniques*, vol. 53, no. 9, pp. 2943-2948, September 2005.

[15] W. L. Chen and G. M. Wang, "Effective design of novel compact fractal-shaped microstrip coupled-line bandpass filters for suppression of the second harmonic," *IEEE Microwave and Wireless Components Letters*, vol. 19, no. 2, pp. 74-76, February 2009.

[16] A. A. Lotfi-Neyestanak and A. Lalbakhsh, "Improved microstrip hairpin-line bandpass filters for spurious response suppression," *Electronics letters*, vol. 48, no. 14, pp. 858-859, July 2012.

[17] T. Lopetegi, M. A. Laso, J. Hernandez, M. Bacaicoa, D. Benito, M. J. Garde, M. Sorolla, and M. Guglielmi, "New microstrip wiggly-line filters with spurious passband suppression," *IEEE Transactions on microwave theory and techniques*, vol. 49, no. 9, pp. 1593-1598, September 2001.

[18] S. W. Fok, P. Cheong, K. W. Tam, and R. Martins, "A novel microstrip bandpass filter design using asymmetric parallel coupled-line," *In Proceedings of IEEE International Symposium on Circuits and Systems*, pp. 404-407, May 2005.

[19] C. F. Chen, T. Y. Huang, and R. B. Wu, "Design of microstrip bandpass filters with multiorder spurious-mode suppression," *IEEE transactions on microwave theory and techniques*, vol. 53, no. 12, pp. 3788-3793, December 2005.

[20] S. Sun and L. Zhu, "Periodically nonuniform coupled microstrip-line filters with harmonic suppression using transmission zero reallocation," *IEEE transactions on microwave theory and techniques*, vol. 53, no. 5, pp. 1817-1822, May 2005.

[21] A. S. Mohra, "Coupled microstrip line bandpass filter with harmonic suppression using right-angle triangle grooves," *Microwave and Optical Technology Letters*, vol. 51, no. 10, pp. 2313-2318, October 2009.

[22] J. T. Kuo and M. H. Wu, "Corrugated parallel-coupled line bandpass filters with multispurious suppression," *IET Microwaves, Antennas & Propagation*, vol. 1, no. 3, pp. 718-722, June 2007.

[23] W. H. Bragg, W. L. Bragg, "The reflection of X-rays by crystals," *Proceedings of the Royal Society of London. Series A, Containing Papers of a Mathematical and Physical Character*, vol. 88, no. 605, pp. 428-438, July 1913.

[24] B. S. Kim, J. W. Lee, and M. S. Song, "An Implementation of Harmonic-Suppression Microstrip Filters with Periodic Grooves," *IEEE Microwave and Wireless Components Letters*, vol. 14, no.9, pp 413-415, September 2004.

[25] T.K. Das, and S.Chatterjee, "Performance of periodic grooves on harmonic rejection in C band folded edge coupled microstrip band pass filters," *Proceedings of International Conference on Computational Science and Engineering (ICCSE2016)***,** pp. 205-209, October 2016, Kolkata, India.

[26] T.K. Das and S.Chatterjee, "Design of a compact symmetrical C-Band Micro Strip Band Pass Filter with Periodic Sawtooth Grooves," *Special Issue of INROADS, International Conference IAET-2016*, vol. 5, no. 1, pp. 254-259, January 2016,Jaipur, India.

[27] T. K. Das and S. Chatterjee, "Improved Stopband Rejection in Compact Microstrip Filters by Transmission Zero Reallocation," *Proceedings of IEEE International Conference (CALCON 2020)*, February 2020, Kolkata, India, pp. 10–14, 9106476.

[28] T. K. Das and S. Chatterjee, "Spurious Harmonic Suppression in a Compact Parallel-Coupled Microstrip Line Bandpass Filter using Square Shaped Corrugations," *Proceedings of URSI-RCRS 2017*, March 2017, Tirupati, India.

[29] T. K. Das and S. Chatterjee, "Phase Velocity Compensation in Compact Coupled-Line Bandpass Filter with Square Corrugations," *Book chapter of Social Transformation–A Digital Way in Communications in Computer and Information Science*, Springer Nature, Singapore Pte. Ltd. 2018, CSI 2017, January 2018, 836, pp. 29–41.

[30] T.K. Das and S. Chatterjee, "Spurious Harmonic Suppression in a Folded Parallel-Coupled Microstrip Bandpass Filter by using Triangular Corrugations," *Proceedings of Devices for Integrated Circuit (DevIC 2017)*, March 2017, Kalyani, India, pp. 391–395, 8073977.

[31] T. K. Das and S. Chatterjee, "Improved second harmonic suppression in a compact coupled-line bandpass filter with triangular corrugations," *Microsystem Technologies*, vol. 25, no. 5, pp. 1945-1956, May 2018, DOI: 10.1007/s00542-018-3940-0.

[32] T. K. Das and S. Chatterjee, "Spurious harmonic suppression in compact coupled-line bandpass filter with asymmetric perturbations," *International Journal of Electronics*, vol. 107, no. 4, pp. 576-595, 2020, DOI:10.1080/00207217.2019.1672801.

[33] T. K. Das and S. Chatterjee, "Harmonic Suppression in an In-line Chebyshev Bandpass Filter by Asymmetrical Perturbations," *Proceedings of IEEE MTT-S International Conference (IMaRC 2017)*, December 2017, Ahmedabad, India, 2017, pp. 1–5, 8449689.

[34] T. K. Das and S. Chatterjee, "2nd Harmonic Suppression in Parallel-Coupled Microstrip Bandpass Filter by using Koch Fractals," *Proceedings of INDICON 2016*, December 2016, Bengaluru, India.

[35] S. Chatterjee, T. K. Das, and B. Gupta, "Harmonic Suppression in In-line Parallel-Coupled Microstrip Bandpass Filter by Minkowski Fractals," *Proceedings of 17th Mediterranean Microwave Symposium (MMS 2017)*, November 2017, Marseille, France, 8497142.

[36] T. K. Das and S. Chatterjee, "Compact coupled-line microstrip bandpass filter with spurious passband suppression using Minkowski fractal," *Proceedings of URSI Regional Conference on Radio Science (URSI-RCRS 2020)*, February 2020, Varanasi, India, 9113422.

[37] S. Chatterjee and T. K. Das, "Multispurious Harmonic Suppression in Compact Coupled-Line Bandpass Filters by Trapezoidal Corrugations," *Proceedings of 18th Mediterranean Microwave Symposium (MMS 2018)*, October 2018, Istanbul, Turkey, pp. 149-152, 8611809.

DESIGN OF FOLDED HAIRPIN-LINE BANDPASS FILTER

4.1. Introduction

From the previous chapter it has been observed that folded and inline parallel-coupled line bandpass filters are quite capable to suppress the spurious harmonics up to $4.8f_0$ with a rejection level better than 35 dB by using trapezoidal corrugations. However, the size of the filter increases proportionately, restricting its applications for wireless systems. Moreover, the fractional bandwidth of the filter is pretty large (20%). Thus, the designing of a narrowband (less than 10%), compact sized, and high selectivity bandpass filter with multispurious suppression ability still becomes a challenge. Practically, it is not possible to design narrowband filter by parallel-coupled line filter topology due to the increase of coupling gaps between the coupled lines, resulting the increase of insertion loss and decrease of return loss in the desired passband. Also, the size of the filter will increase proportionality. Accordingly, hairpin-line filter topology has been chosen to design the filter with the above mentioned features. The objectives of the present work have been set as follows:

1) Design of a conventional hairpin-line bandpass filter with fractional bandwidth less than 10% applicable for WLAN.
2) Reduction of size of the conventional hairpin-line filter by folding mechanism.
3) Incorporation of different nonuniform perturbations and reactive structures as studied for folded and inline parallel-coupled line filters for multispurious suppression.

4.1.1. Design of Third-Order Conventional Hairpin-Line Bandpass Filter

Microstrip hairpin line filters have been widely employed in the wireless communication systems like WLAN, WiMAX, Radar, mobile and cellular communication systems due to their compact sizes and narrow passband response compared to the parallel-coupled line filters as highlighted in the previous chapter. The hairpin line filters have been devised by folded U-shaped half-wavelength resonators for circuit-size reduction compared to the

conventional parallel-coupled line structure [1]. Moreover, the design procedures for hairpin-line filter are very simple. Besides, the implementation, fabrication and integration of such filters with other components become much simpler due to the absence of any via to ground or any lumped elements. Table 4.1 lists the specifications of the proposed *S*-band hairpin-line filter applicable for modern WLAN systems. In this chapter all the studies have been focused only for the *S*-band filter due to the availability of fabrication resources as the filter size of *C*-band filter is pretty small.

Table 4.1. Specifications of the hairpin-line bandpass filter.

Parameters	Specifications
Cut-off frequency, f_0 (GHz)	2.5
Transfer function type	Chebyshev Type-I
Fractional bandwidth, Δ (%)	8
Bandwidth, *BW* (GHz)	2.402-2.602
Passband ripple, L_{Ar} (dB)	0.1
Insertion loss, *IL* (dB)	<2 dB
Return loss, *RL* (dB)	>15 dB
Passband attenuation (dB) (L_{As})	>20 dB at 2.6 GHz

The specifications of the FR4 epoxy substrate material are: dielectric constant, ε_r = 4.4, loss tangent, tanδ = 0.02 and thickness, h = 1.6 mm. The basic procedures for designing the conventional hairpin-line filter are described as follows:

Step 1: Determination of the order of the filter

The order of the filter (N) of Chebyshev Type-I has been computed three by following the procedure as mentioned in the previous chapter (Section 3.10). Accordingly, the element values g_i's of the equivalent lowpass filter prototype have been determined.

Step 2: Determination of the coupling coefficients

The coupling coefficients between the adjacent resonators have been calculated by following (1) where i = 1 to N-1.

$$M_{i,i+1} = \frac{FBW}{\sqrt{g_i g_{i+1}}} \tag{1}$$

Step 3: Determination of the external quality factors

The external quality factors for the input and output resonators have been calculated by following (2).

$$Q_{e1} = Q_{eN} = \frac{g_0 g_1}{FBW} = \frac{g_N g_{N+1}}{FBW} \tag{2}$$

Step 4: Determination of the resonator's length

The resonator length is about $\lambda_{g0}/4$ long with λ_{g0} as the guided wavelength at the center frequency.

Step 5: Determination of the tapped line feed port location

The width of the tapped line feed ports has been calculated corresponding to the characteristic impedance of 50 Ohm for FR4 substrate. The tapping point t is calculated according to (3) [1].

$$t = \frac{2l}{\pi}\sin^{-1}\left(\sqrt{\frac{\pi Z_0}{2Z_r Q_e}}\right) \tag{3}$$

In (3), Z_r is the characteristic impedance of the hairpin-line, Z_0 is the terminating impedance. Fig. 4.1(a) illustrates the layout of a unit hairpin-line cell and Fig. 4.1(b) shows its equivalent transmission-line structure. The spacing between the two arms of a folded hairpin resonator has been set as double of the width w to minimize the cross-coupling between the folded arms.

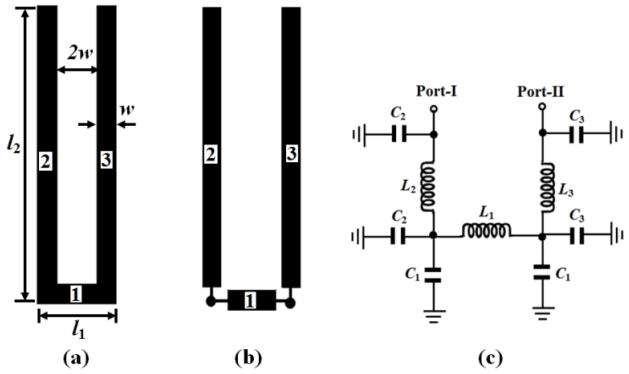

Fig. 4.1. (a) Unit hairpin-line cell, (b) equivalent transmission-line structure, and (c) equivalent *LC*-circuit diagram.

Accordingly, by following the conventional transformation procedures of transmission line to its equivalent lumped elements [1], the circuit diagram of Fig. 4.1(c) has been obtained. The dimensions of the unit hairpin-line cell as highlighted in Fig. 4.1(a) have been computed as l_1 = 4 mm and l_2 = 14.07 mm as per Step 4 corresponding to f_0 = 2.5 GHz. The value of w has been chosen as 1.0 mm corresponding to the characteristic impedance of Z_r = 88 Ohm. Accordingly, the equivalent lumped elements have been determined as L_1= 2.5033 nH, L_2 = L_3 = 5.8571 nH, C_1 = 0.1355 pF, C_2 = C_3 = 0.5502 pF. Fig. 4.2 compares the EM simulation vs. circuit simulation $|S_{11}|$ (dB) plots for a unit hairpin-line cell tuned at 2.5 GHz.

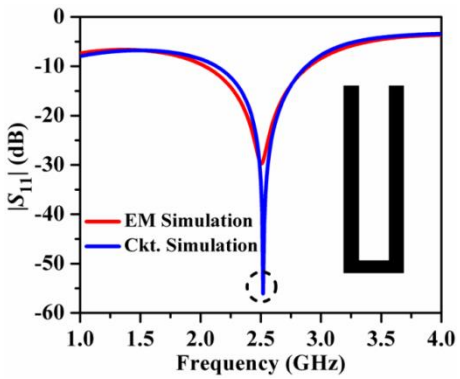

Fig. 4.2. Comparison of EM simulated vs. circuit simulated $|S_{11}|$ (dB) plots for a unit hairpin-line cell.

It has been observed that the plots are matching closely to each other, except that the attenuation level at f_0 = 2.5 GHz has become 57 dB for circuit simulation akin to 29 dB for EM simulation. Subsequently, the conventional hairpin-line bandpass filter centered at 2.5 GHz has been designed by following the steps discussed early. Based on the specifications listed in Table 4.1, the order of the filter has been obtained as N = 3. Afterward, the element values of the equivalent lowpass filter prototype have been determined as g_0 = g_4 = 1.0, g_1 = g_3 = 0.6291, g_2 = 0.9702 [1]. The values of the coupling coefficients have been calculated as $M_{1,2}$ and $M_{2,3}$ = 0.1024. Fig. 4.3(a) illustrates the design curve obtained by full-wave EM simulations in IE3D for the coupling coefficient M with the coupling gap S between the two adjacent folded resonators. From the design curve the value of S = 0.86 mm has been obtained corresponding to the desired coupling coefficients, $M_{1,2}$ and $M_{2,3}$ = 0.1024. Fig. 4.3(b) illustrates the layout of the conventional third-order hairpin line bandpass filter centered at 2.5 GHz.

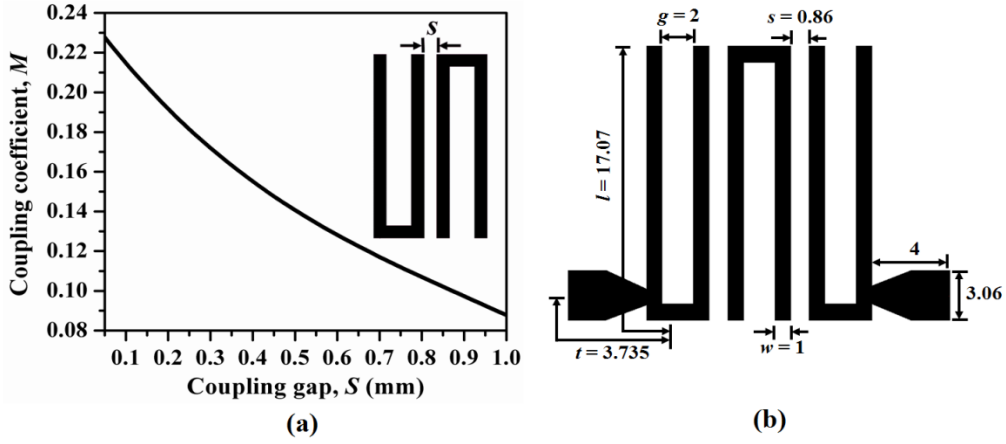

Fig. 4.3. (a) Variation of the coupling coefficient M vs. coupling gap S (mm) for the pair of conventional hairpin-line cell, (b) optimized layout of the third-order conventional hairpin-line bandpass filter.

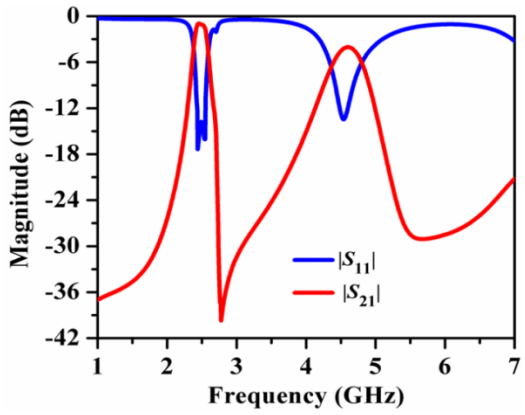

Fig. 4.4. Simulated *S*-parameters plots of the third-order conventional hairpin-line bandpass filter.

The overall size of the filter is 327.32 mm^2 i.e., $0.36\lambda_g \times 0.25\lambda_g$ where λ_g is the guided wavelength at f_0 = 2.5 GHz. Accordingly, Fig. 4.4(a) highlights the simulated *S*-parameters plots for the optimized filter. It has been observed that the filter exhibits sharp skirt characteristics with upper stopband edge rejection level of 37 dB. However, the second harmonic attenuation level becomes 4.0 dB. The passband insertion loss has been obtained as 1.1 dB and return loss becomes more than 15 dB. Accordingly, Fig. 4.5 depicts the equivalent lumped elements circuit diagram of the third-order conventional hairpin-line bandpass filter (CHLF) based on conventional transmission line theory [3].

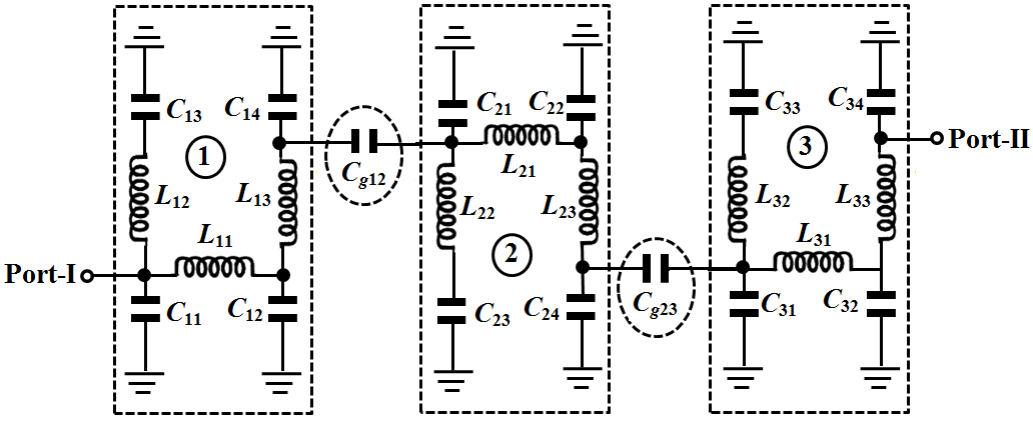

Fig. 4.5. Equivalent lumped elements circuit diagram of the third-order conventional hairpin-line filter.

The conversion procedures from microstrip lines to equivalent lumped elements are discussed as follows: The conversion procedures from microstrip lines to equivalent lumped elements are discussed as follows:

Step 1: Determination of the equivalent lumped inductance (*L*) and capacitance (*C*) values for microstrip resonator

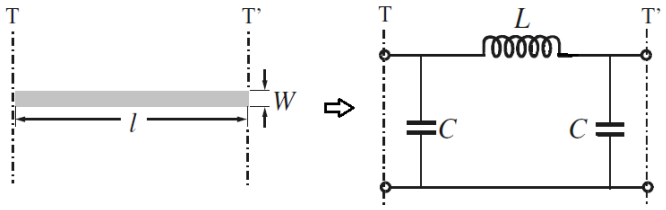

Fig. 4.6. Conversion of microstrip resonator to equivalent *LC* circuit.

Fig. 4.6 illustrates the conversion of a single microstrip line to equivalent LC lumped circuit and the values are computed by (4)-(5).

$$L(nH) = (Z_0 / W) * \sin\left(\frac{2\pi l}{\lambda_g}\right) \tag{4}$$

$$C(pF) = \frac{1}{W * Z_0} \tan\left(\frac{\pi l}{\lambda_g}\right) \tag{5}$$

Step 2: Determination of the equivalent lumped inductance (*L*) and capacitance (*C*) values for microstrip bend

Fig. 4.7 illustrates the conversion of a microstrip bend to equivalent LC lumped circuit and the values are computed by (6)-(7).

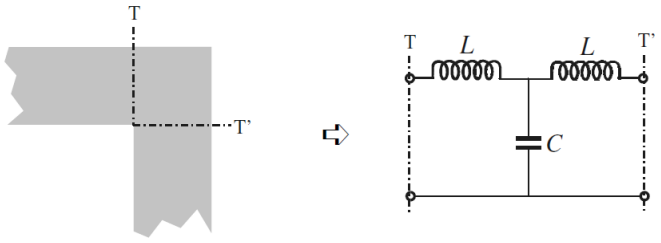

Fig. 4.7. Conversion of microstrip bend to equivalent *LC* circuit.

$$\frac{C}{W}(pF/m) = \begin{cases} \dfrac{(14\varepsilon_r + 12.5)W/h - (1.83\varepsilon_r - 2.25)}{\sqrt{W/h}} + \dfrac{0.02\varepsilon_r}{W/h} & \text{for } W/h < 1 \\ (9.5\varepsilon_r + 1.2)W/h + 5.2\varepsilon_r & \text{for } W/h \geq 1 \end{cases} \tag{6}$$

$$\frac{L}{h}(nH/m) = 100\left\{4\sqrt{\frac{w}{h}} - 4.21\right\} \tag{7}$$

Step 3: Determination of the equivalent capacitance (*C*) values for microstrip gap

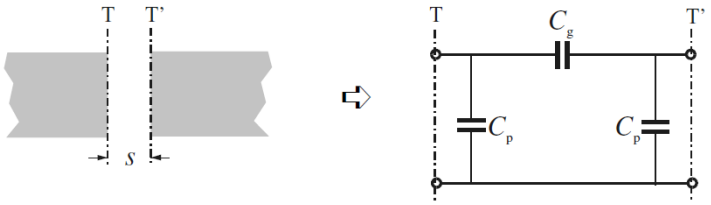

Fig. 4.8. Conversion of microstrip gap to equivalent *C* circuit.

$$\begin{aligned} C_p &= 0.5C_e \\ C_g &= 0.5C_o - 0.25C_e \end{aligned} \tag{8}$$

where

$$\begin{aligned} \frac{C_o}{W}(pF/m) &= \left(\frac{\varepsilon_r}{9.6}\right)^{0.8}\left(\frac{s}{W}\right)^{m_o}\exp(k_o) \\ \frac{C_e}{W}(pF/m) &= 12\left(\frac{\varepsilon_r}{9.6}\right)^{0.9}\left(\frac{s}{W}\right)^{m_e}\exp(k_e) \end{aligned} \tag{9}$$

$$\begin{aligned} m_o &= \frac{W}{h}\left[0.619\log(W/h) - 0.3853\right] \\ k_o &= 4.26 - 1.453\log(W/h) \end{aligned} \quad \text{for } 0.1 \le s/W \le 1.0 \tag{10}$$

$$\begin{aligned} m_e &= 0.8675 \\ k_e &= 2.043\left(\frac{W}{h}\right)^{0.12} \end{aligned} \quad \text{for } 0.1 \le s/W \le 0.3 \tag{11}$$

$$\begin{aligned} m_e &= \frac{1.565}{(W/h)^{0.16}} - 1 \\ k_e &= 1.97 - \frac{0.03}{W/h} \end{aligned} \quad \text{for } 0.3 \le s/W \le 1.0 \tag{12}$$

Fig. 4.8 illustrates the conversion of a microstrip gap to equivalent lumped capacitor circuit and the values are computed by (8)-(12).

Step 4: Determination of the equivalent capacitance (*C*) value for microstrip open end

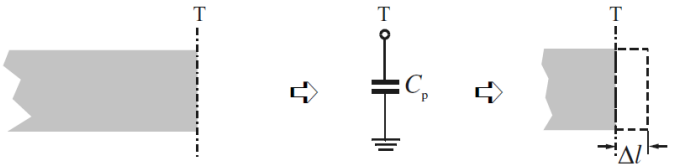

Fig. 4.9. Conversion of microstrip open end to equivalent *C* circuit.

$$C_p = \frac{\Delta l \sqrt{\varepsilon_{re}}}{cZ_0} \tag{13}$$

where $\Delta l = 0.165h$

The L values (nH) and C values (pF) are calculated as follows: L_{i1} = 1.1033 nH, L_{i2} = L_{i3} = 4.6428 nH, C_{i1} = C_{i2} = 0.797 pF, C_{i3} = 0.6615 pF, C_{i4} = 0.6883 pF, C_{g12} = C_{g34} = 0.0759 pF, and C_{g23} = 0.6615 pF where i = 1, 2, and 3. Accordingly, Fig. 4.10(a) compares the circuit vs. EM simulated $|S_{21}|$ (dB) plots. It has been observed that the plots are in good agreement in the passband.

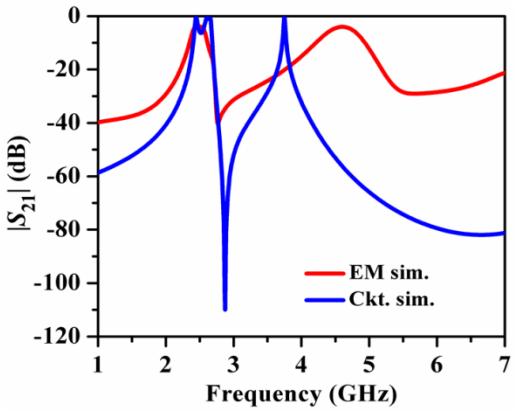

Fig. 4.10. Comparison between the EM simulated vs. the circuit simulated $|S_{21}|$ (dB) plots.

Figs. 4.11(a)-(b) elaborate the distribution of the surface current density of the final hairpin-line filter at 2.5 GHz and at 4.7 GHz respectively. It has been revealed that the surface current reaches the output port with higher degree of strength at 2.5 GHz due to the anticipated passband and also at 4.7 GHz due to the presence of second harmonic frequency.

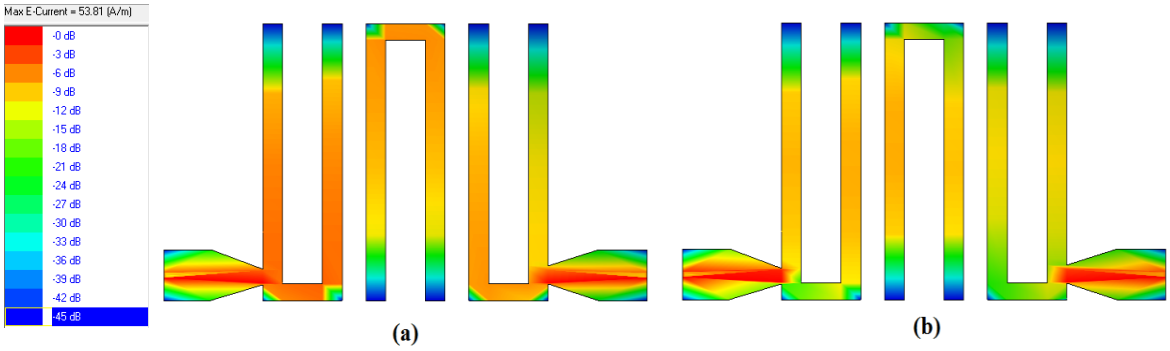

Fig. 4.11. Distribution of the surface current density of the third-order conventional hairpin-line bandpass filter: (a) at 2.5 GHz, and (b) at 4.7 GHz.

4.1.2. Design of Third-Order Folded Hairpin-Line Bandpass Filter

The overall size of the designed third-order conventional hairpin-line filter is pretty large, making it unsuitable for WLAN applications. Accordingly, the size reduction has been achieved by replacing the conventional hairpin-line unit cell with double folded hairpin-line cell as highlighted in Figs. 4.12(a)-(c). In Fig. 4.12(c) the open-end arms of the hairpin-line has been folded inward symmetrically (T-T′ plane) with inner coupling gap equals to the width of the resonator.

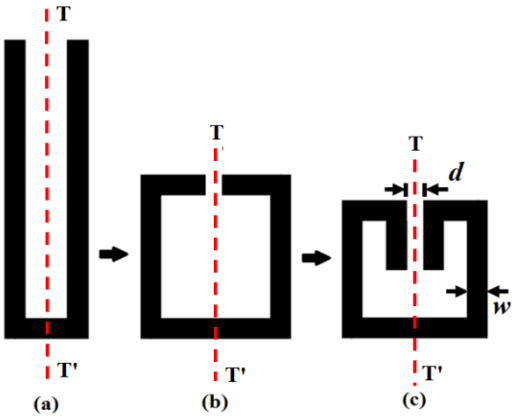

Fig. 4.12. Folding mechanism of the conventional hairpin-line: (a) conventional, (b) first-order folding, and (c) second-order folding.

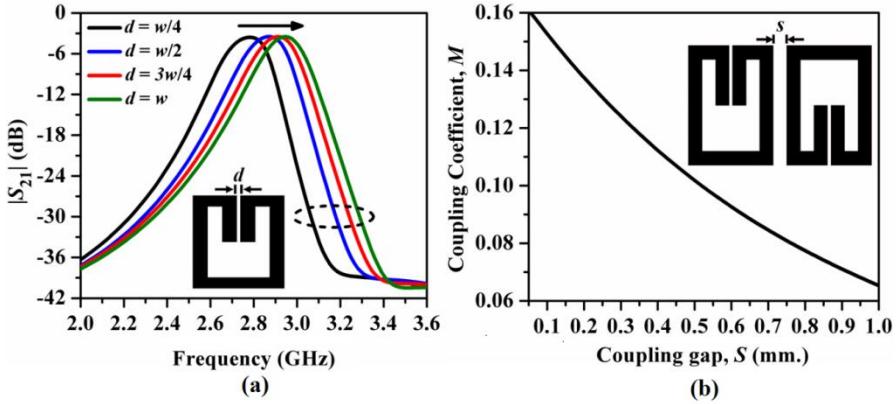

Fig. 4.13. (a) Variation of the simulated $|S_{21}|$ (dB) for different values of the cross-coupling gap d (mm) of a unit FHL cell, and (b) variation of the coupling coefficient M vs. coupling gap S (mm) for the pair of FHL cells.

Accordingly, in Fig. 4.13(a) a parametric study has been carried out for the cross-coupling gap d between the two folded arms with respect to width w and it has been noticed that the location of the center frequency has been shifted to higher frequency with incremental value of d. Thus, the optimum value of d has been chosen as $w/4$ i.e., 0.25 mm. Fig. 4.13(b) illustrates the design curve obtained by full-wave EM simulations for the coupling coefficient

M to determine the spacing S between the two adjacent folded hairpin resonators as highlighted in the inset layout diagram. Accordingly, the value of S has been optimized to 0.53 mm corresponding to $M_{1,2} = M_{2,3} = 0.1024$. Fig. 4.14(a) shows the layout of a tuned double-folded hairpin line bandpass filter with all dimensions are in mm and Fig. 4.14(b) compares the S-parameters plots with the conventional hairpin line filter. The size of the filter is 263.83 mm^2 i.e., $0.41\lambda_g \times 0.14\lambda_g$ and accordingly, a size reduction of 19.4% has been achieved. It has been observed that the skirt characteristics of the folded filter have been improved with upper stopband edge rejection level of 43 dB at 3.75 GHz. Additionally, the second harmonic frequency has been shifted to 5.8 GHz from 4.5 GHz compared to the conventional hairpin line filter due to the folded structure.

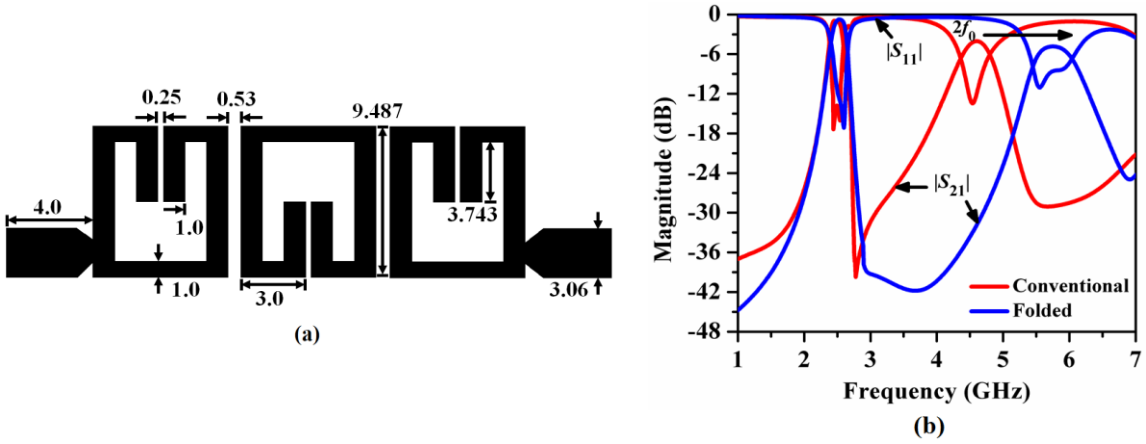

Fig. 4.14. (a) Optimized layout of the third-order folded hairpin-line bandpass filter, and (b) comparison of simulated S-parameters plots between the third-order conventional vs. folded hairpin-line bandpass filter.

This is because the effective coupling areas between the adjacent folded resonators have been reduced due to the folding of the arms. Accordingly, the mutual coupling factor M also has been strongly related with the reduction of coupling area. However, the corresponding attenuation level has been degraded a little from 3.5 dB to 5 dB due to the folding. The surface current distributions for the designed folded filter are exhibited in Figs. 4.15(a)-(b) for 2.5 GHz and 5.8 GHz. It has been concluded from this section that the folded hairpin resonators exhibit improved skirt characteristics and shifting of harmonics to higher frequency region along with a compact structure. However, the attenuation level at $2f_0$ becomes 6 dB which is still very larger restricting its application for WLAN receiver.

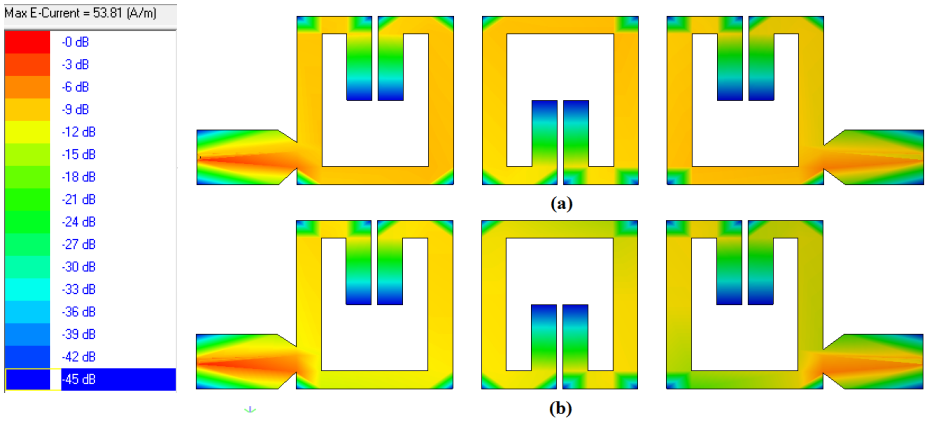

Fig. 4.15. Distribution of the surface current density of the third-order folded hairpin-line bandpass filter: (a) at 2.5 GHz, and (b) at 5.8 GHz.

Subsequently, periodic square grooves have been incorporated in the coupled arms between the folded cells to suppress the attenuation level at the second harmonic as discussed in the next section.

4.1.3. Harmonic Suppression for the Third-Order Folded Hairpin-Line Bandpass Filter by Periodic Grooves

Traditionally, for a coupled line microstrip filter structure, the odd-mode of the EM wave propagates with a higher phase velocity compared to the even-mode as already discussed in Chapter 3. As a result, asymmetrical passband response and spurious harmonics are generated in this type of filters [2-3]. Accordingly, periodic grooves have been inserted to the coupled edges of the parallel resonators to achieve the phase velocity compensation as studied in [4] for a folded hairpin-line filter. Figs. 4.16(a)-(d) depict the structure of a unit folded cell with different number of periodic grooves. The height and width of the groove are represented by H_T and W_T respectively. Implementing the idea of [4], the parametric study for the double-folded hairpin-line filter (Fig. 4.14(a)) with periodic square grooves has been performed to determine the optimum dimension as highlighted in Figs. 4.17(a)-(d).

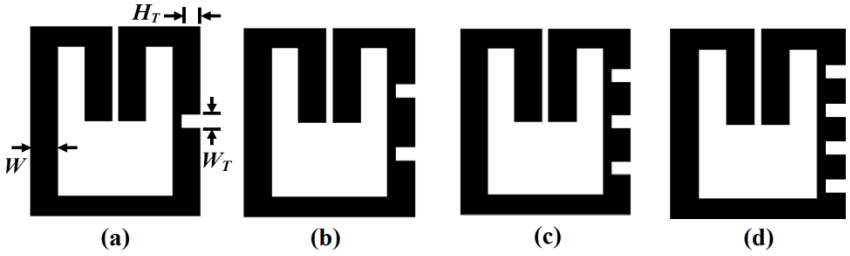

Fig. 4.16. Structure of a unit folded cell with different number of periodic grooves.

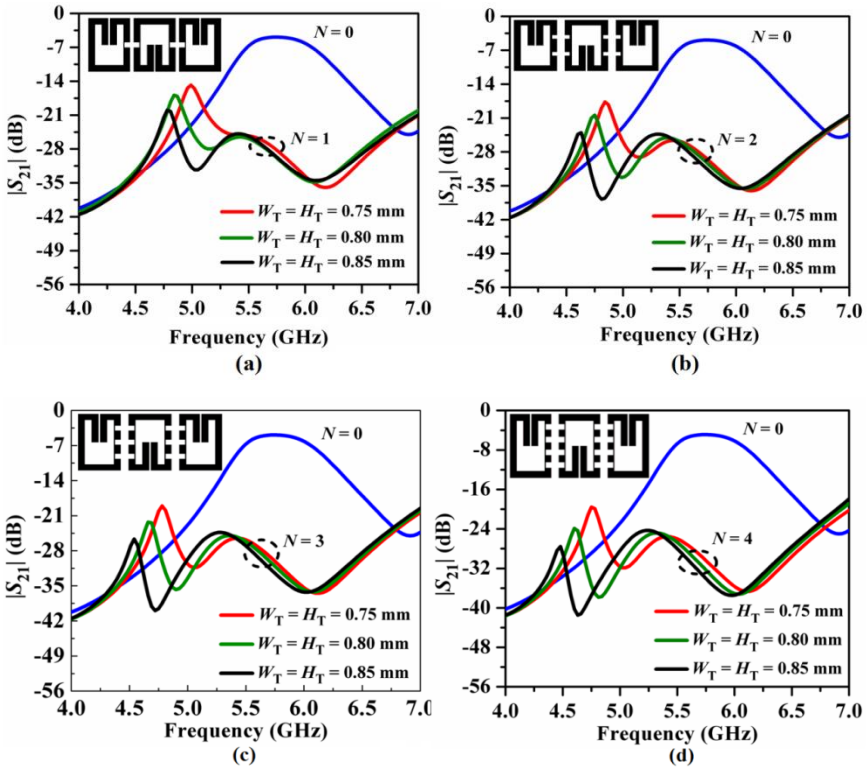

Fig. 4.17. Simulated parametric study for the third-order folded hairpin-line bandpass filter with square periodic grooves: (a) N = 1, (b) N = 2, (c) N = 3, and (4) N = 4.

It has been observed from the parametric study that the width W_T and height H_T equal to 0.85 mm gives the maximum suppression of second harmonic for all the cases. Accordingly, Fig. 4.18(a) shows the layout of the optimized double-folded hairpin line bandpass filter with three square periodic groves as the optimum design and all dimensions are in mm.

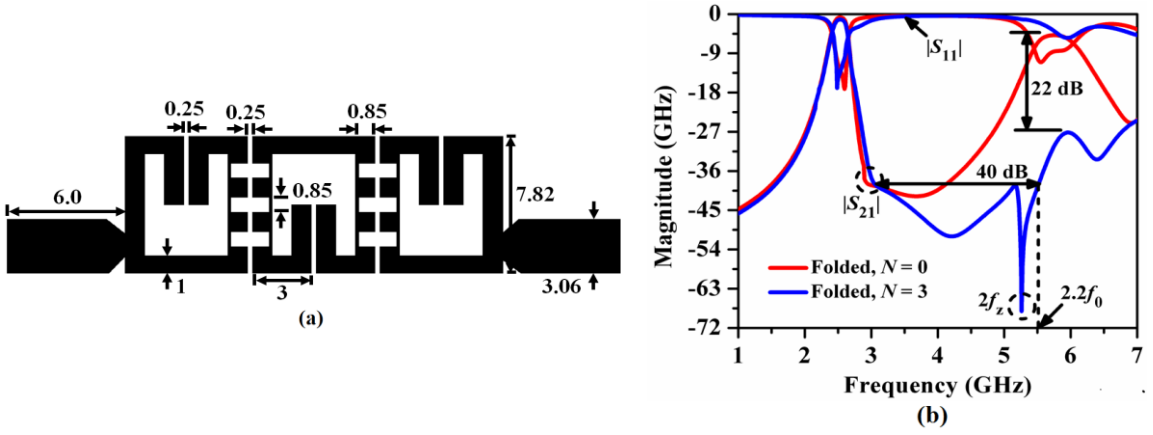

Fig. 4.18. (a) Optimized layout of the third-order folded hairpin-line bandpass filter with three periodic square grooves, and (b) comparison of simulated *S*-parameters for folded filter with and without grooves.

The size of the filter is 244.38 mm^2 i.e., 0.46λ_g × 0.11λ_g and accordingly, a size reduction of 25% compared to the conventional hairpin-line filter has been achieved. Fig. 4.18(b) compares the *S*-parameters plots between the folded filters without any groove and with three periodic grooves. It has been observed that the folded filter with three periodic grooves exhibits a sharp transmission zero 2f_z at 5.25 GHz (near 2f_0 of 5.0 GHz) with a maximum attenuation level of 67 dB. A wide stopband with a rejection level below 40 dB has been obtained up to 2.2f_0. Moreover, the attenuation level degrades to 22 dB at 6 GHz justifying the ability of periodic grooves to suppress the harmonic. In addition, the filter exhibits a return loss of 18 dB and an insertion loss of 1.1 dB in the desired passband.

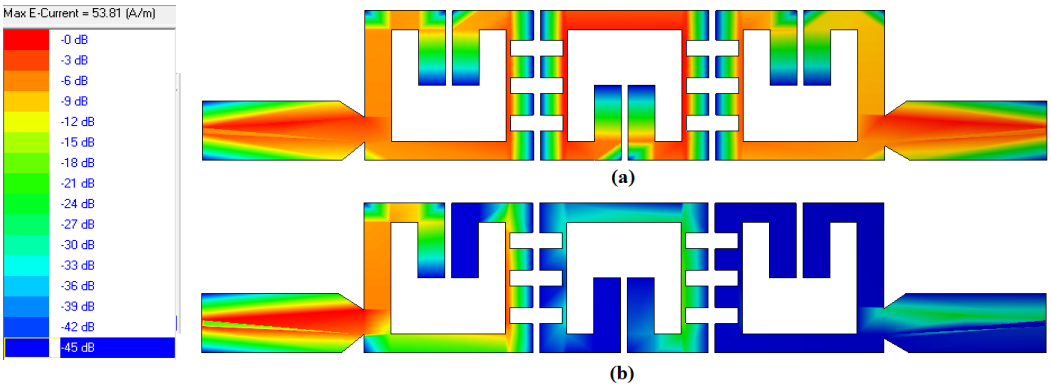

Fig. 4.19. Distribution of the surface current density of the third-order folded hairpin-line bandpass filter with three periodic square grooves: (a) at 2.5 GHz, and (b) at 5.0 GHz.

From the surface current distribution plot at 2.5 GHz (Fig. 4.19(a)) it has been revealed that the surface current has higher degree of strength due to the passband response compared to that at 5.0 GHz (Fig. 4.19(b)) related to the second harmonic's attenuation level. Table 4.2 illustrates the filters' parameters to compare their performances, which concludes that the folded filter with square grooves exhibits satisfactory figure-of-merit value compared to the filters without groove. It can be concluded from this section that the third-order folded hairpin-line filter with periodic square groove exhibits improved performance regarding size reduction and harmonic suppression. However, the skirt characteristics and selectivity of the designed filter needs more improvement. Moreover, the stopband rejection bandwidth is limited up to only 2.2f_0. Accordingly, the order of the filter has been increased in the next section by keeping the filter's specifications unchanged to achieve more stopband bandwidth with improved rejection level along with improvement in the skirt selectivity.

Table 4.2. Determination of different filter's parameters.

f_o (GHz)	*Type of filter*	ξ (dB/GHz)	*SBRL* (dB)	*SBW* (x f_0)	*RSB*	*SF*	*NCS*	*AF*	*FOM*
2.5	Conventional	38.57	4	2.8	0.92	0.4	0.07	1	202.77
	Folded, $N = 0$	28.42	5	2.8	0.902	0.5	0.057		224.87
	Folded, $N = 3$	14.59	40	2.2	0.588	4	0.052		659.92

4.2. Design of Fourth-Order Folded Hairpin-Line Bandpass Filter

Since the order of the filter has been increased to four, the element values of the equivalent lowpass filter prototype have been determined as $g_0 = 1.0000$, $g_1 = 0.7129$, $g_2 = 1.2004$, $g_3 = 1.3213$, $g_4 = 0.6476$, $g_5 = 1.1008$ [1]. The external quality factors of the first and fourth resonators and the coupling coefficients between the adjacent resonators have been determined as $Q_{e1} = Q_{e4} = 8.9113$, $M_{1,2} = M_{3,4} = 0.0865$, $M_{2,3} = 0.0635$. The coupling coefficients have been extracted from the design curve shown in Fig. 4.20(a) by performing the full-wave EM-simulation in IE3D. Accordingly, the spacing between the adjacent cells has been extracted as $S_{1,2} = S_{3,4} = 1.15$ mm for $M_{1,2} = M_{3,4} = 0.0865$, and $S_{2,3} = 1.35$ mm for $M_{2,3} = 0.0635$. Fig. 4.20(b) illustrates the layout with optimized dimensions in mm. All the edges have been tapered to reduce the radiation effects for the abrupt change of surface current flow. The overall size of the filter is 434 mm^2 i.e., $0.42\lambda_0 \times 0.22\lambda_0$.

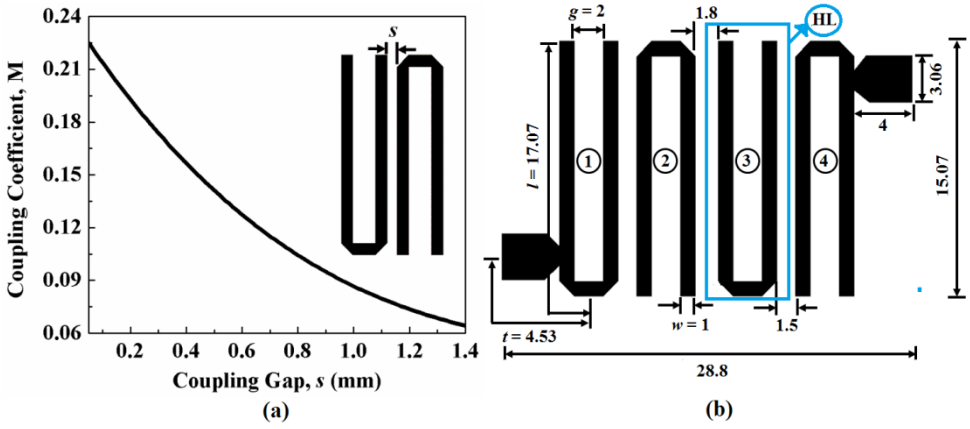

Fig. 4.20. (a) Design curve obtained for the coupling coefficient, and (b) layout of the fourth-order conventional hairpin-line filter (CHLF).

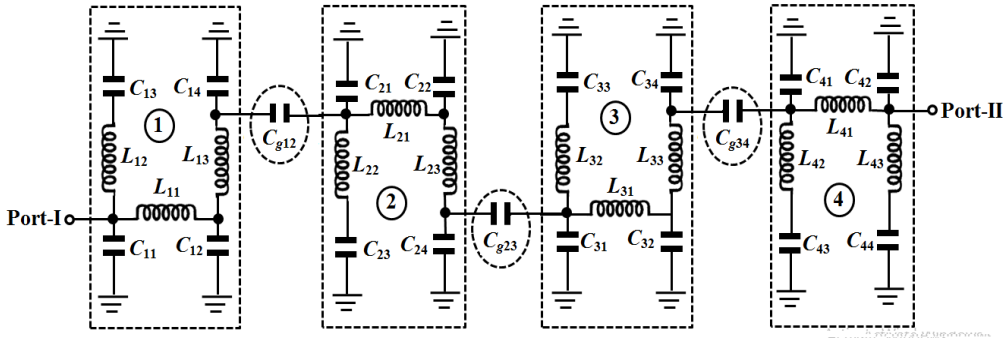

Fig. 4.21. Equivalent lumped elements circuit diagram of the fourth-order conventional hairpin-line filter (CHLF).

Fig. 4.21 depicts the equivalent lumped elements circuit diagram of the fourth-order conventional hairpin-line bandpass filter (CHLF) based on conventional transmission line theory [2]. The L values (nH) and C values (pF) are calculated as follows: L_{i1} = 1.1033 nH, L_{i2} = L_{i3} = 4.6428 nH, C_{i1} = C_{i2} = 0.797 pF, C_{i3} = 0.6615 pF, C_{i4} = 0.6883 pF, C_{g12} = C_{g34} = 0.0759 pF, and C_{g23} = 0.6615 pF where i = 1, 2, 3, 4. Accordingly, Fig. 4.22(a) compares the circuit vs. EM simulated $|S_{21}|$ (dB) plots. It has been observed that the plots are in good agreement in the passband.

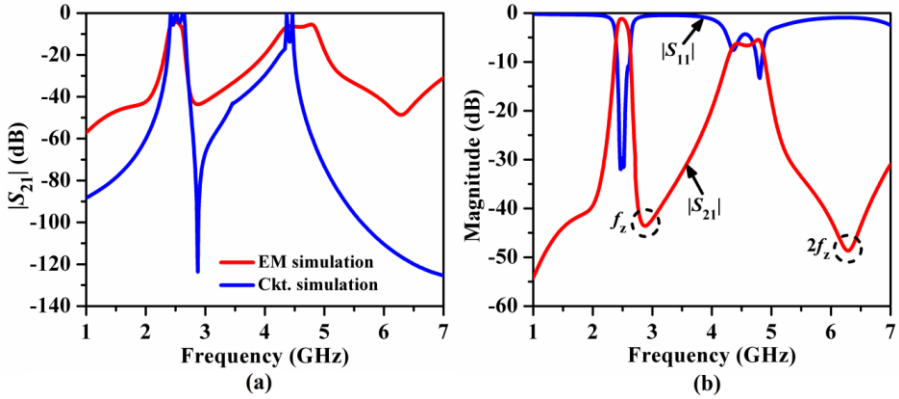

Fig. 4.22. (a) Comparison of circuit vs. EM simulated $|S_{21}|$ (dB) plots and (b) simulated S-parameters plots of the optimized fourth-order conventional hairpin-line filter (CHLF) [5].

Accordingly, Fig. 4.22(b) shows the S-parameters plots for the final filter. It has been observed that the filter exhibits sharp skirt characteristics with an upper stopband-edge rejection level (f_z) of 43 dB at 2.85 GHz. The passband insertion loss of 1.12 dB and return loss of 33 dB have been obtained. However, a wide spurious second harmonic passband has been generated at 4.8 GHz with an attenuation level of 6 dB. The presence of such harmonic degrades the performance of the CHLF in modern WLAN wireless systems. Moreover, the

size of the filter restricts its applications in a miniaturized circuit arrangement. Accordingly, the next objectives have been set as follows: (1) at first, reduction of filter size by the folding approach as already employed for the third-order filter and (2) secondly, suppression of the attenuation level at the second harmonic by Minkowski fractal as already discussed in Chapter 3 for parallel-coupled line filter.

4.2.1. Design of Fourth-Order Folded Hairpin-Line Bandpass Filter

The size of the CHLF has been reduced by folding the open-end arms symmetrically (T-T' plane) to the inward direction as shown in Figs. 4.23(a)-(c). Accordingly, from the wideband resonant characteristic for double-folded cell (FHL) as shown in Fig. 4.23(d), it has been observed that the fundamental odd-mode resonant frequency of a half-wavelength line occurs at f_0 = 2.5 GHz, and that of the even-mode occurs at 5.7 GHz near to $2f_0$. In general, both the modes are excited simultaneously, and hence, the propagation has been occurred with different phase velocities due to the hybrid TEM-mode. Such phenomenon has been elaborated by the vector surface current distribution of the FHL-cell in Figs. 4.24(a)-(c).

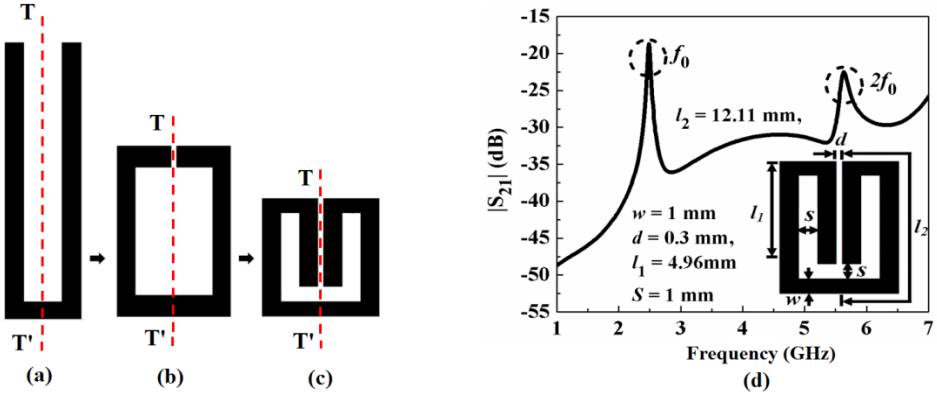

Fig. 4.23. Folding mechanism of the hairpin-line cell: (a) Conventional; (b) first-order folding; (c) second-order folding; and (d) simulated resonance frequency plot of $|S_{21}|$ (dB).

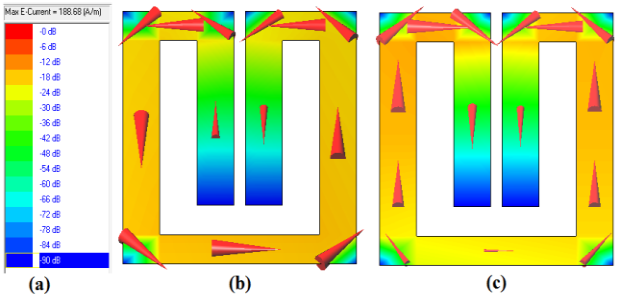

Fig. 4.24. Surface vector-current distribution in a unit FHL cell: (a) colour palette, (b) distribution at 2.5 GHz, and (c) distribution at 5.7 GHz.

It has been observed that the vector currents directions are same along the entire structure at 2.5 GHz (odd-mode, anti-clockwise) and opposite to each other at 5.7 GHz (even-mode). The layout of a unit FHL-cell with different design parameters is shown in Fig. 4.25(a) and the equivalent transmission-line model is extracted in Fig. 4.25(b). The unit FHL-cell is segmented into four lines of length l_1, l_2, l_3, and l_4 respectively. Fig. 4.25(c) illustrates the equivalent lumped-element circuit diagram of the unit FHL-cell. The L values (nH) and C values (pF) are determined as follows: $L_1 = 2.5999$ nH, $L_2 = L_7 = 2.939$ nH, $L_3 = L_6 = 1.0675$ nH, $L_4 = L_5 = 2.6255$ nH, $C_{p1} = C_{p2} = 0.4734$ pF, $C_{p3} = C_{p6} = 0.3574$ pF, $C_{p4} = C_{p5} = 0.3204$ pF, $C_{p7} = C_{p8} = 0.2193$ pF and $C_{g1} = 0.0331$ pF.

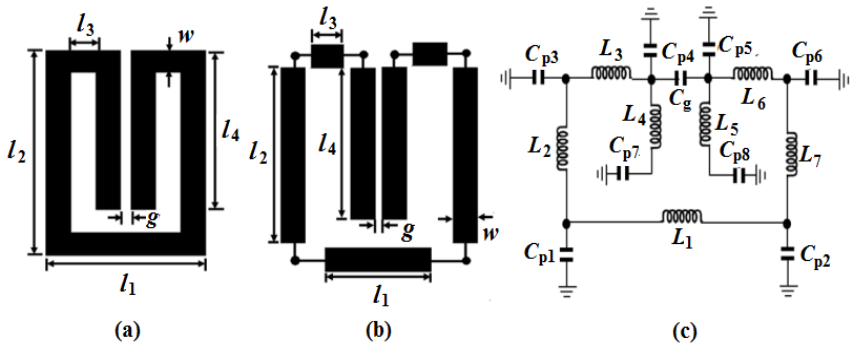

Fig. 4.25. (a) Unit FHL-cell, (b) equivalent transmission-line structure, and (c) equivalent *LC*-circuit diagram.

Fig. 4.26(a) compares the resonant characteristics of $|S_{11}|$ (dB) between the EM-simulation and circuit-simulation of a unit FHL-cell. It has been observed that the plots are in good agreement to each other and a deep attenuation pole has been occurred at 2.5 GHz with attenuation level of 67 dB for circuit simulation akin to 31 dB for EM simulation.

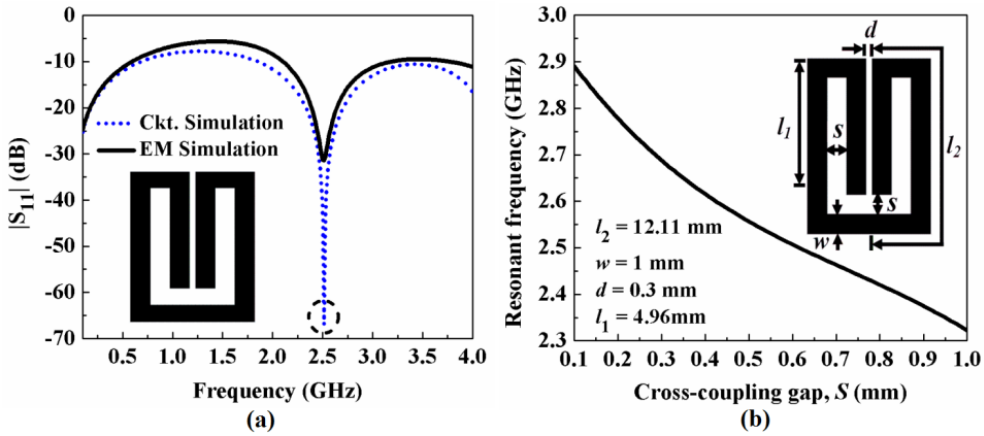

Fig. 4.26. (a) Comparison of $|S_{11}|$ (dB) plots between the EM-simulation and *LC* circuit-simulation, (b) variation of simulated resonance frequency (f_0) vs. internal cross-coupling gap (S).

Accordingly, Fig. 4.26(b) highlights the variation of f_0 for incremental values of the internal cross-coupling gap, S (mm) with constant values of l_1, l_2, w, and d as highlighted in the inset figure. It has been observed that there has been resonant frequency decreases with incremental S. This is due to the diminished effects of cross-coupling between the folded arms and the side arms of the folded cell. Subsequently, such FHL cells have been cascaded in alternative pattern to design the fourth-order folded hairpin-line bandpass filter (FHLBF). From the design curve for the coupling-coefficient M vs. coupling gap s as plotted in Fig. 4.27(a), the spacing between the two adjacent FHL-cells has been determined as $s_{1,2} = s_{3,4}$ = 0.62 mm for $M_{1,2} = M_{3,4}$ = 0.0865, and $s_{3,4}$ = 1.07 mm for $M_{2,3}$ = 0.0635. Fig. 4.27(b) shows the layout of the fourth-order FHLBF. The size of the filter is 306.42 mm^2 i.e., $0.53\lambda_0 \times 0.12\lambda_0$ and accordingly, size reduction of 29.5% has been achieved over the fourth-order conventional filter.

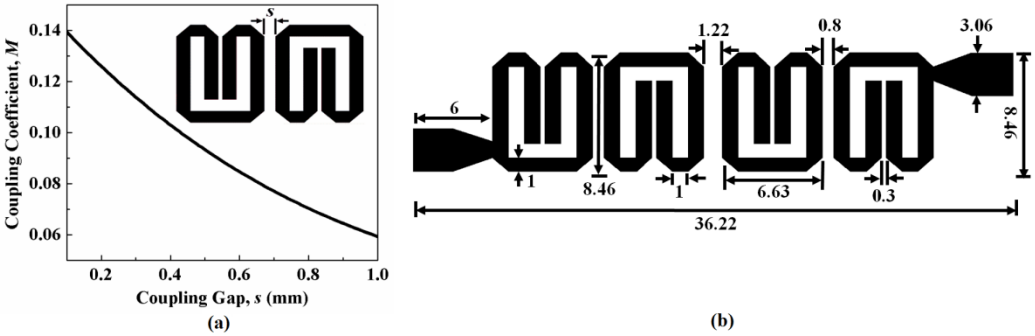

Fig. 4.27. (a) Design curve for the coupling coefficient, and (b) layout of the fourth-order FHLBF.

Figs. 4.28(a)-(b) illustrate the vector surface current distribution in a fourth-order folded filter at f_0 = 2.5 GHz and $2f_0$ = 5.0 GHz. In the fourth-order FHLBF, both the electric coupling (odd-mode) and magnetic coupling (even-mode) have been occurred between the adjacent coupled-arms of two FHL-cells. For the current distribution at 2.5 GHz as shown in Fig. 4.28(a), the electric coupling dominates over the magnetic coupling, resulting the passband. For the current distribution at 5.0 GHz (Fig. 4.28(b)) the magnetic coupling dominates over the electric coupling due to the presence of harmonic. Fig. 4.29 shows the equivalent lumped-element circuit diagram of the fourth-order FHLBF. The equivalent L values (nH) and C values (pF) for the FHL cells and the coupling gaps are calculated as: L_{i1}= 2.5999, $L_{i2} = L_{i7}$ = 2.939, $L_{i3} = L_{i6}$ = 1.0675, $L_{i4} = L_{i5}$ = 2.6255, $C_{pi1} = C_{pi2}$ = 0.4734, $C_{pi3} = C_{pi6}$ = 0.3574, $C_{pi4} = C_{pi5}$ = 0.3204, $C_{pi7} = C_{pi8}$ = 0.2193, and C_{gi} = 0.0331, $C_{g12} = C_{g34}$ = 0.3456, C_{g23} = 0.1235, where i = 1, 2, 3, 4.

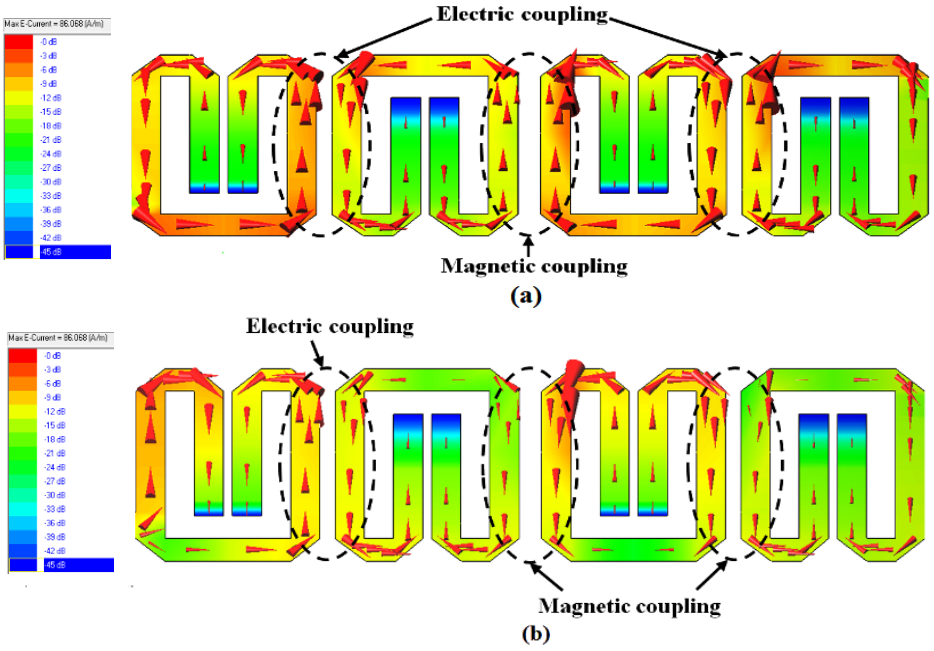

Fig. 4.28. Surface current vectors distribution in a fourth-order FHLBF: (a) at f_0 = 2.5 GHz and (b) at $2f_0$ = 5 GHz.

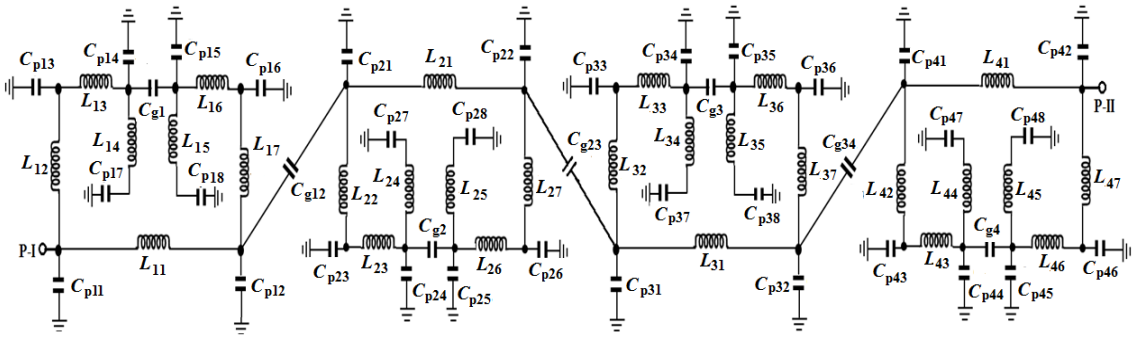

Fig. 4.29. Equivalent *LC*-circuit diagram of the fourth-order FHLBF.

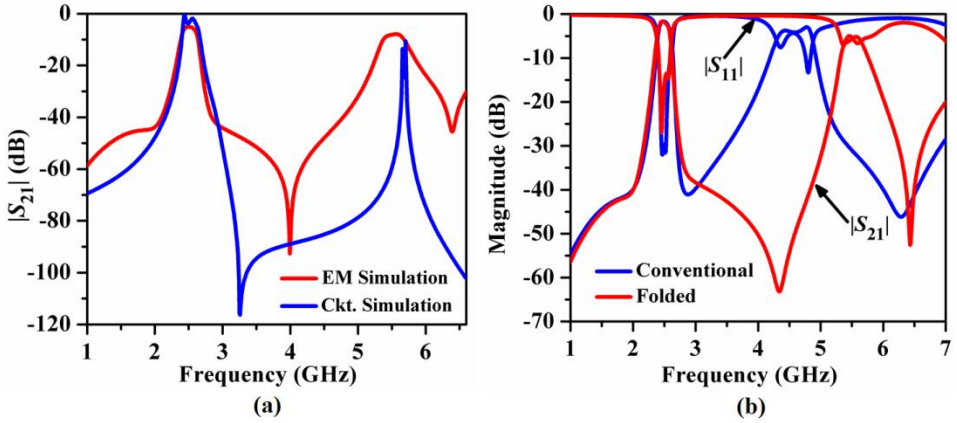

Fig. 4.30. (a) Comparison of $|S_{21}|$ (dB) plots between EM-simulation and circuit-simulation and (b) comparison of simulated *S*-parameters plots between the fourth-order conventional and folded hairpin-line filters.

Fig. 4.30(a) compares the EM-simulated and circuit-simulated $|S_{21}|$ plots. It has been observed the plots are in good agreement in the passband. However, the stopband response including the second harmonic is not matched well due to the problems mentioned in the earlier section. Fig. 4.30(b) compares the simulated *S*-parameters between the fourth-order conventional and folded filters. It has been observed that the passband becomes well separated from the second spurious passband for the folded filter due to the generation of a sharp transmission zero at 4.3 GHz with an attenuation level of 63 dB. Besides, the second harmonic frequency has been shifted to 5.75 GHz from 4.55 GHz. This has been occurred due to the decrement of the effective coupling area between the adjacent coupled-arms of two FHL cells. However, the attenuation level at $2f_0$ has becomes 6 dB which is still pretty large. Accordingly, the inclusion of quasi-Minkowski fractals at the coupled edges of the adjacent resonators and its effect on harmonic suppression has been studied in the following section.

4.2.2. Harmonic Suppression for the Fourth-Order Folded Hairpin-Line Bandpass Filter by Minkowski Fractal

From previous chapter (Section 3.18) it has been revealed that Minkowski fractal is quite capable to suppress the harmonics suppression for parallel-coupled line filter along with the reduction in filter's size due to its space filling and self-similarity properties. Such knowledge has been carried out for the fourth-order folded bandpass filter as follows. Figs. 4.31(a)-(b) shows the generation of quasi-Minkowski fractal geometry where l is the length of the initiator. The values of a and b will decide the length of the horizontal and vertical segments of the generator. Accordingly, the equivalent *LC*-circuit of a half-wavelength resonator tuned at 2.5 GHz with Minkowski fractal is depicted in Fig. 4.32(a) and its $|S_{21}|$ (dB) have been compared with the EM simulation results in Fig. 4.32(b). The values of the lumped elements have been determined as $L_{1f} = L_{2f} = L_{3f} = 4.397$ nH, $C_{1f} = C_{3f} = 0.428$ pF, $C_{2f} = 0.907$ pF. It has been observed that the results have been matched well at $f_0 = 2.5$ GHz with a sharp attenuation peak of 5.52 dB. Fig. 4.33(a) shows the layout of the unit FHL cell with quasi-Minkowski fractals. Here, $a = 2.553$ mm, $l = 7.66$ mm, $s = 1$ mm, $w = 1$ mm, $d = 0.3$mm. Fig. 4.31(b) illustrates the effects of fractals on f_{po} and f_{pe} for the unit FHL-cell with incremental b and constant a.

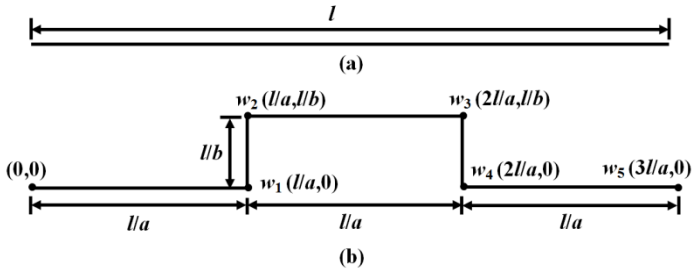

Fig. 4.31. Generation of quasi-Minkowski fractal shape on a line: (a) initiator with iteration order, $n = 0$ and (b) generator geometry with $n = 1$.

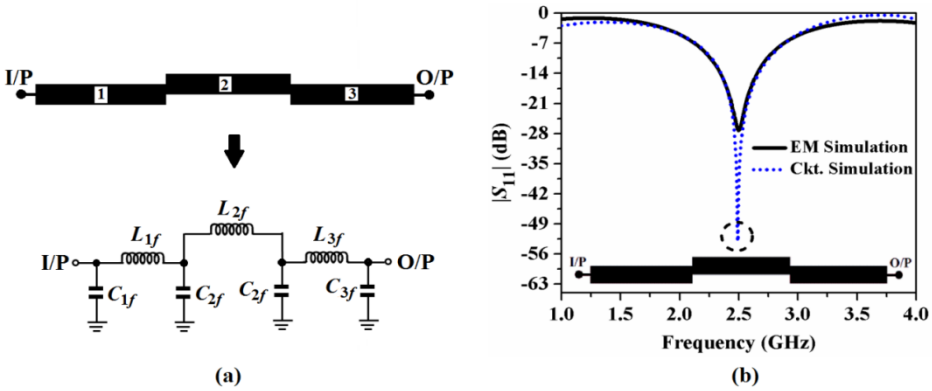

Fig. 4.32. (a) Equivalent *LC*-circuit of half-wavelength resonator with quasi-Minkowski fractals for iteration order, $n = 1$; and (b) comparison of $|S_{21}|$ (dB) plots between the EM-simulation and the circuit-simulation.

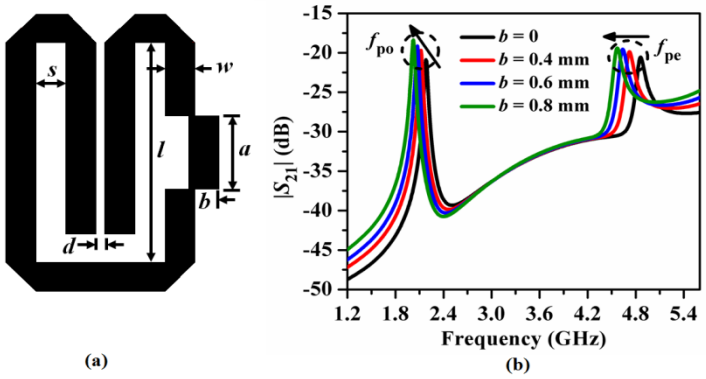

Fig. 4.33. (a) Layout of a unit FHL cell with quasi-Minkowski fractals of iteration order, $n = 1$, and (b) effects of fractals on odd- and even-mode resonance frequencies of the simulated $|S_{21}|$ (dB) plots.

It has been observed that both the modal-resonant frequencies have been shifted towards lower frequency region due to the space-filling nature and slow-wave property of the fractal. The equivalent *LC*-circuit of a unit FHL cell with quasi-Minkowski fractals has been depicted in Fig. 4.34(a) and consequently, the comparison of $|S_{21}|$ (dB) plots between the EM-simulation and the circuit-simulation has been illustrated in Fig. 4.34(b).

The elements values of FHL cell are the same as Fig. 4.25 and those for fractal-based resonator are the same as Fig. 4.30(a). It has been observed from Fig. 4.34(b) that circuit and EM simulation results are closely matching in nature.

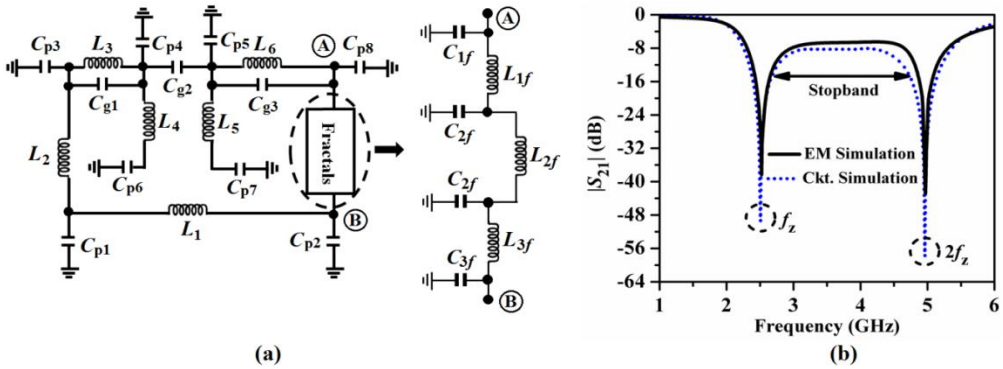

Fig. 4.34. (a) Equivalent lumped elements circuit diagram of a unit FHL cell with fractal and (b) comparison of $|S_{21}|$ (dB) plots between the EM-simulation and the circuit-simulation.

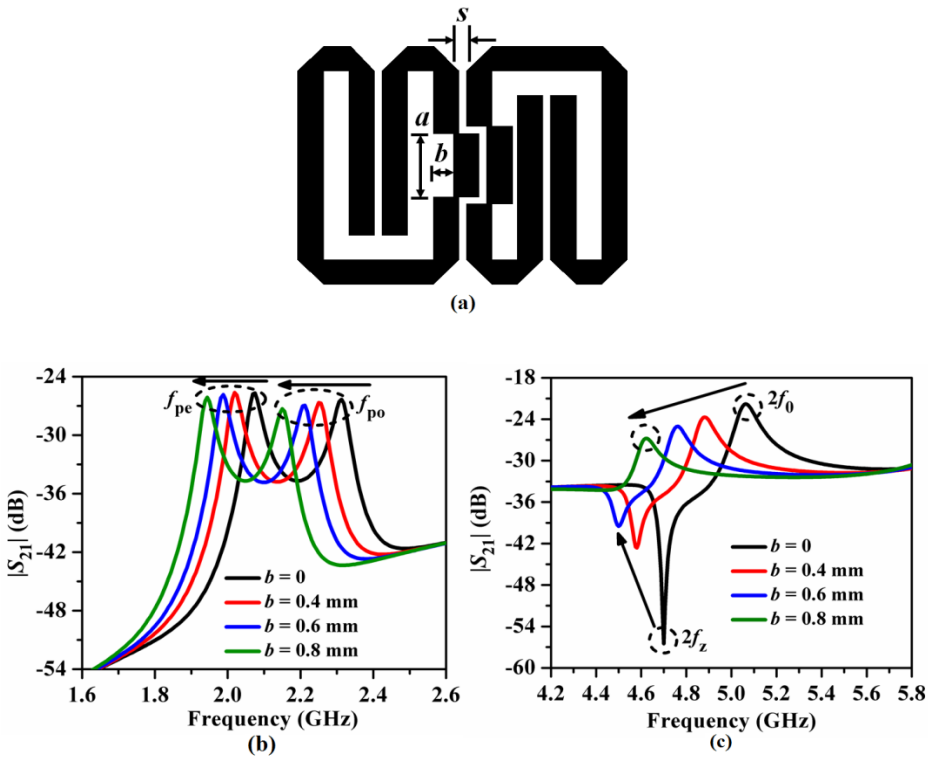

Fig. 4.35. (a) Layout of a pair of FHL cells with Minkowski fractals of n = 1, (b) effects of fractals on f_{po} and f_{pe}, and (c) effects of fractals on $2f_0$ and $2f_z$ for the simulated $|S_{21}|$ (dB) plots.

Two resonant peaks f_z and $2f_z$ with an attenuation level more than 52 dB and 60 dB have been obtained exactly at 2.5 GHz and 5 GHz. However, the attenuation level at $2f_z$ has been degraded more compared to that at f_z due to the bandstop nature of the fractal. A flat stopband

with attenuation level of 9 dB has been obtained between f_z and $2f_z$ due to the modal phase velocities compensation by fractal. The fractals based unit FHL cells are placed alternately in Fig. 4.35(a) to obtain a pair of FHL cells. For achieving self-similar geometry with fractals, the criteria are to be chosen as $a = b = l/3$. However, the parallel-coupled lines do not possess self-similar geometry as the width of the lines is much smaller than its length. Hence, the value of a has been fixed to $l/3$ and that of b has been varying in proportion of w. Accordingly, Fig. 4.35(b) illustrates the variation of f_{po} and f_{pe} for different values of b with the same dimension of a unit FHL cell. It has been observed from Fig. 4.35(b) that both f_{po} and f_{pe} have been shifted to lower frequency regions with an incremental value of b due to the space filling property of the Minkowski fractal. Fig. 4.35(c) exhibits the variation of second harmonic transmission zero, $2f_z$, and harmonic frequency $2f_0$ with incremental values of b. Therefore, the optimum value of b has been chosen as 0.8 mm. The distribution of surface current vectors for a pair of folded cells with fractal (n = 1) has been elaborated in Figs. 4.36(a)-(b) at f_{po} = 1.95 GHz and f_{pe} = 2.15 GHz respectively. It has been observed that the vectors are unidirectional for even-mode and in reverse directional for odd-mode around the coupling regions between the cells as anticipated. Fig. 4.37(a) highlights the effects on f_{po} and f_{pe} due to the incremental value of s for fixed value of a and b. It has been observed that the resonant frequencies are approaching towards each other as the coupling gap increases and hence, the coupling coefficient decreases nonlinearly. It can be concluded that the Minkowski fractal has achieved the phase velocity compensation which is primarily desired for suppressing the second harmonic attenuation level effectively.

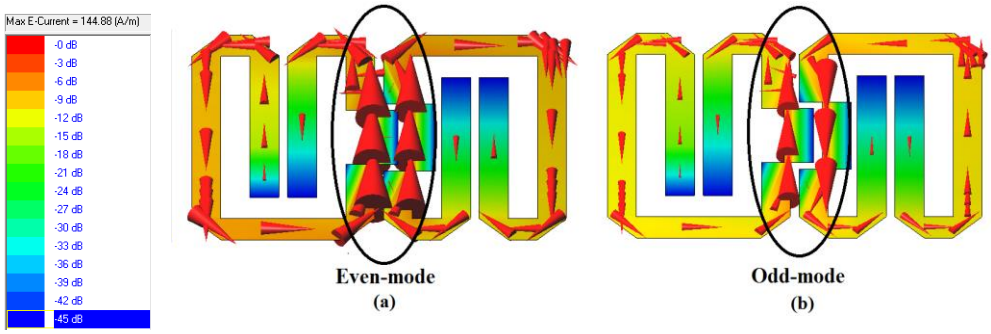

Fig. 4.36. Surface current distribution vectors for a pair of FHL cells with Minkowski fractals of n = 1 with b = 0.8 mm: (a) at f_{pe} = 1.95 GHz and (b) at f_{po}= 2.15 GHz.

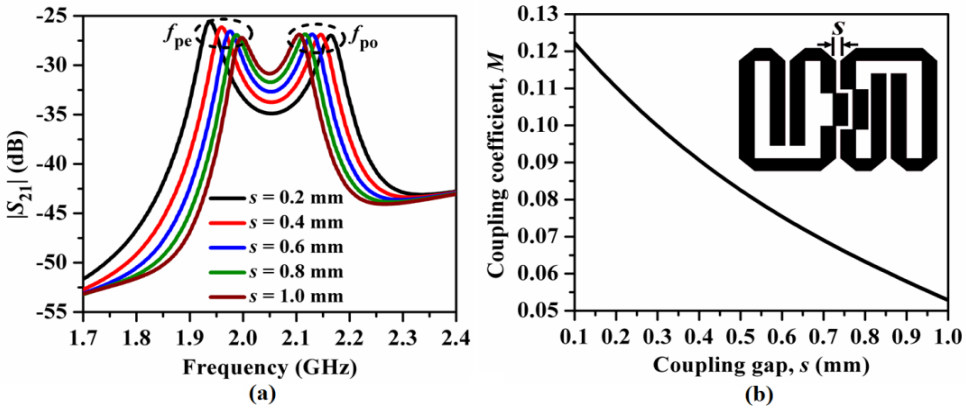

Fig. 4.37. (a) Effects of fractals on f_{po} and f_{pe} for the simulated $|S_{21}|$ (dB) plots with incremental coupling gap, s for a FHL-pair and (b) variation of coupling coefficient M vs. s.

Accordingly, the desired values of s are obtained from the design curve of coupling coefficient vs. coupling gap as shown in Fig. 4.37(b) as $s_{12} = s_{23} = 0.46$ mm for the coupling coefficient $M_{12} = 0.0865$ and $s_{23} = 0.78$ mm for $M_{23} = 0.0635$. The study of a pair of fractals based FHL-cells has been extended further to design the fourth-order FHLBF. The structure and *LC* block-diagram of the fourth-order FHLBF with fractals has been depicted in Figs. 4.38(a)-(b), where the individual FHL cell with fractals has been marked as FHL-*i*, $i = 1$ to 4 and the coupling capacitances between them have been modeled by C_{12}, C_{23}, and C_{34} based on Fig. 4.34(a). The comparison of $|S_{21}|$ (dB) plots between the EM simulation and the circuit simulation has been highlighted in Fig. 4.39.

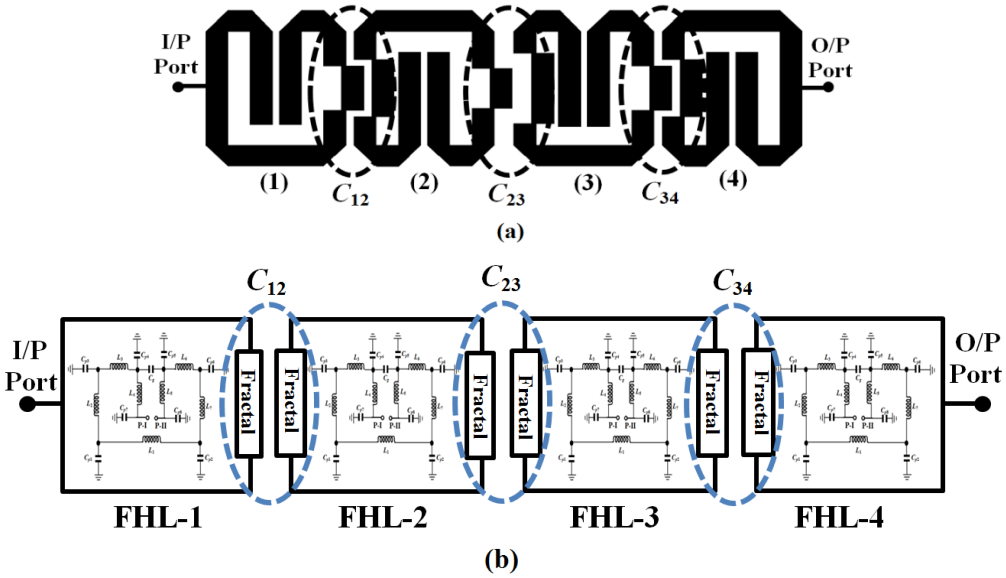

Fig. 4.38. (a) Structure of a fourth-order FHLBF with fractals and (b) equivalent block diagram with *LC* model.

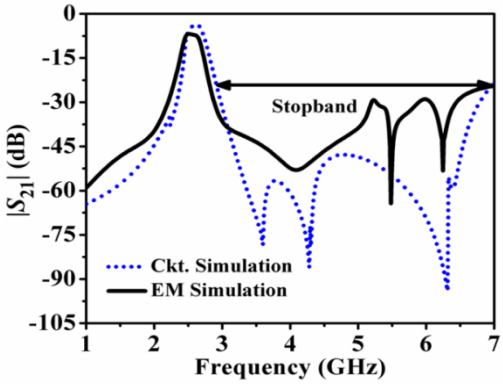

Fig. 4.39. Comparison of $|S_{21}|$ (dB) plots between EM-simulation and circuit-simulation for fourth-order folded filter with fractal.

It has been observed that the passbands have been matched well; however, the stopband response of the circuit simulation has been exhibited better rejection level over EM simulation. Accordingly, the final optimized design has been depicted in Fig. 4.40(a). The location of the feed port has been determined by performing the EM simulation to match the calculated values of the external quality factors i.e., $Q_{e1} = Q_{e4} = 8.9113$. The overall size of the filter is 306 mm^2 i.e., $0.59\lambda_0 \times 0.11\lambda_0$. Accordingly, size reduction of 30% has been achieved over the conventional filter.

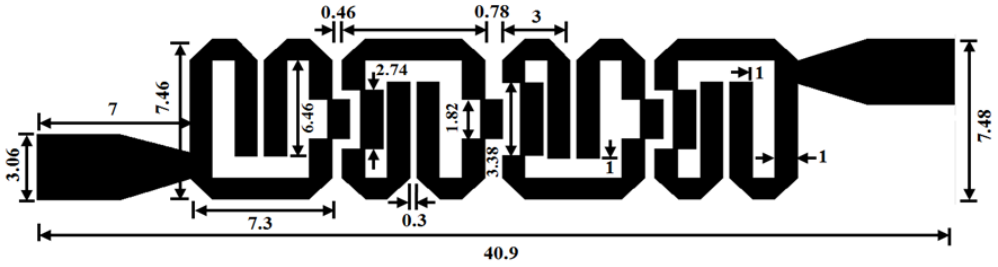

Fig. 4.40. Layout of the fourth-order FHLBF with fractals with dimensions in mm.

4.2.2.1. Fabricated Prototype

The photograph of the fabricated filter is shown in Fig. 4.41.

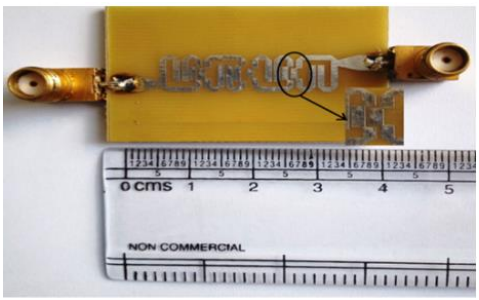

Fig. 4.41. Photograph of the fabricated prototype.

4.2.2.2. Comparison of EM simulation vs. Measurement Results

The experiment has been carried out in the Agilent N9928A vector network analyzer in the similar way of 3.14.4.1 and the measured vs. simulation *S*-parameters plots have been highlighted in Fig. 4.42(a)-(b). It has been observed in experimental verification that the center frequency of the fabricated filter has been shifted to 2.4 GHz instead of 2.5 GHz and it occurs due to the coupling inaccuracy during the PCB fabrication process and the tolerances incurred due to the SMA connectors.

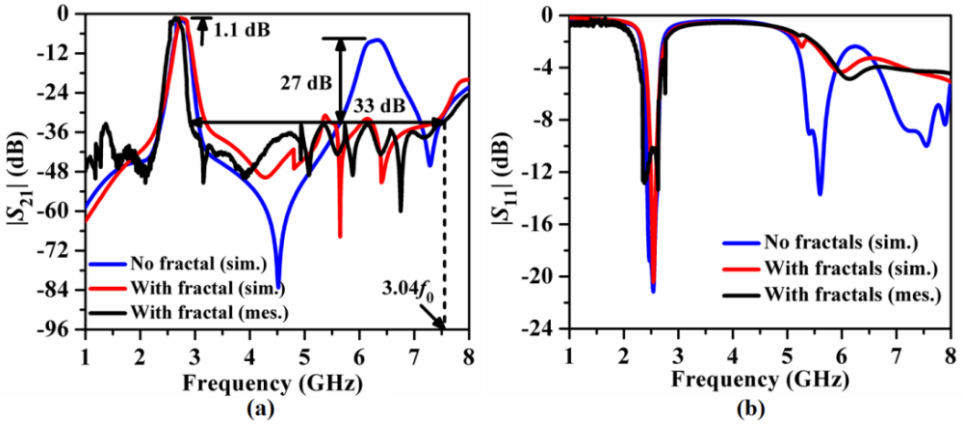

Fig. 4.42. Measured vs. simulated comparison: (a) $|S_{21}|$ (dB) plots and (b) $|S_{11}|$ (dB) plots [6].

A wide stopband with a rejection level below 33 dB has been obtained up to $3.04f_0$. Besides, degradation of 27 dB in the attenuation level at $2f_0$ has been obtained. Fig. 4.42(b) explores the comparison between the simulated and measured $|S_{11}|$ (dB) for the final filter and it has been observed that the passband return loss becomes more than 12 dB in the passband for the measurement result.

Table 4.3. Determination of different filters' parameters.

f_0 (GHz)	*Type of filter*	ξ (dB/GHz)	*SBRL* (dB)	*SBW* (x f_0)	*RSB*	*SF*	*NCS*	*AF*	*FOM*
2.5 GHz	Conventional	90	5	2.8	0.686	0.5	0.093	1	331.94
	Folded, (no fractal)	77	5	2.8	0.693	0.5	0.066		404.25
	Folded, (with fractal)	77	33	3.04	0.691	3.3	0.066		2660.35

Table 4.3 illustrates the filters' parameters to compare their performances and fractal based folded filter exhibits the highest figure-of-merit (*FOM*). Few observations can be listed from this section as follows:

(1) The size of the proposed filter can be further reduced by the folding approach as there are still some vacant spaces inside the inner region of the folded cell.
(2) The fractional bandwidth of the designed filter is 8% which can be reduced further to design a narrowband filter.
(3) Minkowski fractal is capable to suppress the harmonics level to 33 dB. Such attenuation level can be enhanced further.
(4) Lastly, the stopband bandwidth is limited to only third harmonic frequency.

By considering the above observations the objectives of the next work have been set as follows:

(1) more reduction of size of the filter by utilizing the inner vacant space of the folded cell
(2) spurline has been studied in the next section to improve the performance of the filter, especially regarding the harmonics' suppression level.
(3) extension of the stopband beyond fourth harmonic.

4.2.3. Compact Fourth-Order Folded Hairpin-Line Bandpass Filter

Table 4.4 illustrates the specifications of modified Chebyshev Type-I hairpin-line bandpass filter. Accordingly, the element values of the equivalent lowpass filter prototype have been determined as $g_0 = 1.0000$, $g_1 = 0.7129$, $g_2 = 1.2004$, $g_3 = 1.3213$, $g_4 = 0.6476$, $g_5 = 1.1008$ [1]. The external quality factors of the first and fourth cells and the coupling coefficients between the adjacent hairpin-line (HL) cells placed in hybrid coupling mode have been obtained as $Q_{e1} = Q_{e4} = 17.82$, $M_{1,2} = M_{3,4} = 0.0432$, $M_{2,3} = 0.0318$. The width of the tapped-line feed-ports has been calculated as 3.06 mm corresponding to the characteristic impedance of 50 Ω.

Table 4.4. Specifications of the modified hairpin-line bandpass filter.

Parameters	Specifications
Cut-off frequency, f_0 (GHz)	2.5
Transfer function type	Chebyshev Type-I
Fractional bandwidth, Δ (%)	4
Bandwidth, *BW* (GHz)	2.45-2.55
Passband ripple, L_{Ar} (dB)	0.01
Insertion loss, *IL* (dB)	<2 dB
Return loss, *RL* (dB)	>15 dB
Passband attenuation (dB) (L_{As})	>30 dB at 2.8 GHz

Figs. 4.43(a)-(c) illustrates the mechanism to achieve compact folded hairpin-line cell by utilizing the inner space. Each FHL cell has been obtained by folding the open ends of the

conventional HL cell by folding once symmetrically (about T-T′ plane) towards each other (Fig. 4.43(b)) and then by folding further towards the inward direction (Fig. 4.43(c)). The dimensions of the conventional hairpin-line line are l = 17.07 mm, w = 1 mm, t = 2 mm [1]. The total area occupied by the HL cell is 60.28 mm^2 and accordingly, those for the FHL cell have been and determined as $l_1 = l_3$ = 2.3 mm, l_2 = 9.11 mm, l_4 = 8.81 mm, w = 1 mm, and cross-coupling gap between the folded arms d = 0.3 mm. The total area occupied by the FHL cell is 44.64 mm^2 and accordingly size reduction of 26% has been achieved compared to HL cell. All the dimensions of HL and FHL cells have been tuned to f_0 = 2.5 GHz. The resonant characteristics of the unit FHL cell for different values of d have been compared in Fig. 4.43(d).

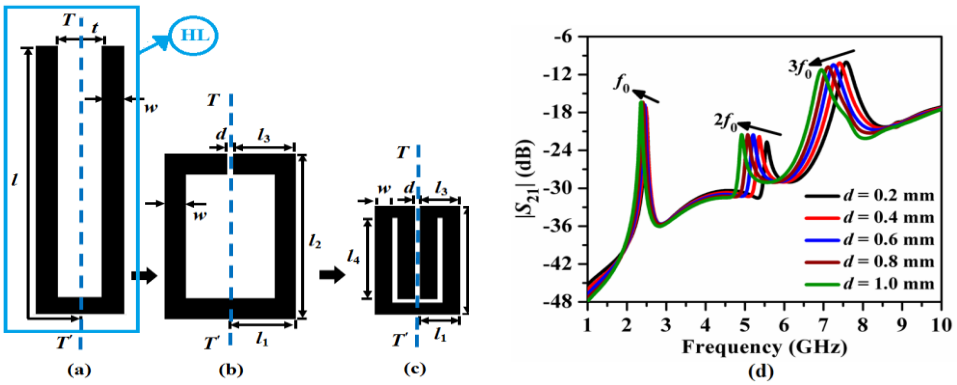

Fig. 4.43. Folding mechanism of hairpin-line cell: (a) conventional HL cell, (b) first-order folding, (c) second-order folding (FHL), and (d) resonance characteristics for the simulated $|S_{21}|$ (dB) plot of a unit FHL cell.

The value of the second harmonic frequency $2f_0$ has been decreased with increased attenuation level and the value of third harmonic frequency $3f_0$ has been decreased with degradation in attenuation level. This is due to the degradation of the amount of cross-coupling between the folded arms as d has increased. Accordingly, the value of d has been chosen as low as 0.3 mm by keeping the fabrication tolerance. The initial values of coupling gaps between the adjacent cells have been extracted from the design curve of Fig. 4.44 as $s_{1,2} = s_{3,4}$ = 1.35 mm for $M_{1,2} = M_{3,4}$ = 0.0432, and $s_{2,3}$ = 1.68 mm for $M_{2,3}$ = 0.0318. Fig. 4.45 shows the layout with optimized dimensions in mm. The size of the filter is 328.35 mm^2 i.e., 0.51λ_g x 0.14λ_g and accordingly, a size reduction of 24.34% over the conventional hairpin-line fitter has been achieved. Figs. 4.46(a)-(b) show the wideband simulated S-parameters plots in the IE3D EM solver of the proposed folded filter. It has been observed that a sharp transmission zero (marked as f_z) has been obtained between the desired passband and the

second harmonic spurious passband with an attenuation level of 50 dB. The attenuation levels at $2f_0$ and $3f_0$ become 9 dB and 3 dB. Accordingly, Fig. 4.46(b) compares the $|S_{21}|$ (dB) plot between the folded filters of Fig. 4.27(b) and Fig. 4.44.

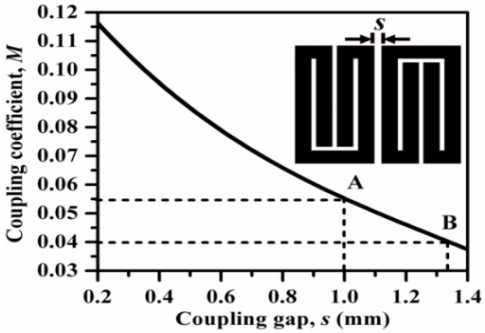

Fig. 4.44. Design curve obtained by full-wave EM simulations for the coupling coefficient *M* for the fourth-order folded hairpin-line bandpass filter.

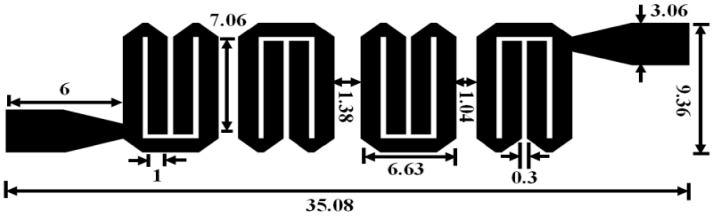

Fig. 4.45. Layout of the third-order compact folded hairpin-line bandpass filter.

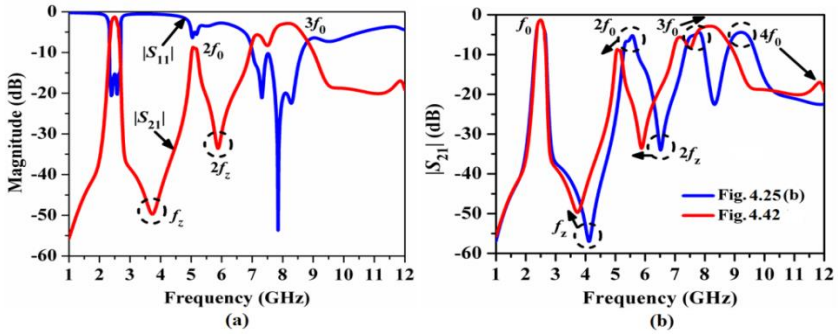

Fig. 4.46. (a) Simulated *S*-parameters plots for the proposed compact folded hairpin-line filter and (b) comparison of simulated $|S_{21}|$ (dB) plots between the folded filter of Fig. 4.25(b) and the compact filter.

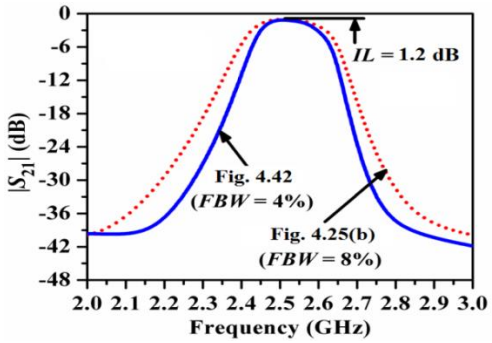

Fig. 4.47. Comparison between the simulated passband responses of the folded filters with *FBW* = 8% and 4%.

It has been observed that the attenuation level at the transmission zero (marked by f_z) has been increased by 7 dB in the proposed compact filter due to the additional cross-coupling of the field lines for a small cross-coupling gap inside the cell. Moreover, the attenuation level at $2f_0$ has been degraded by 5 dB and the second transmission zero (marked by $2f_z$) has been shifted to 6 GHz from 6.7 GHz due to the additional capacitive effects in the cross-coupling gap. The attenuation level at $3f_0$ has been increased by 3.5 dB along with shifting to a higher frequency region. Fig. 4.47 compares the simulated passband responses of the proposed folded filter with the filter shown in Fig. 4.27(b). It has been observed that the passband bandwidth becomes narrow than that of Fig. 4.27(b) with the insertion loss of 1.8 dB at f_0 = 2.5 GHz. Figs. 4.48(a)-(c) illustrate the surface current plots at f_0 = 2.5 GHz and $2f_0$ = 5.2 GHz.

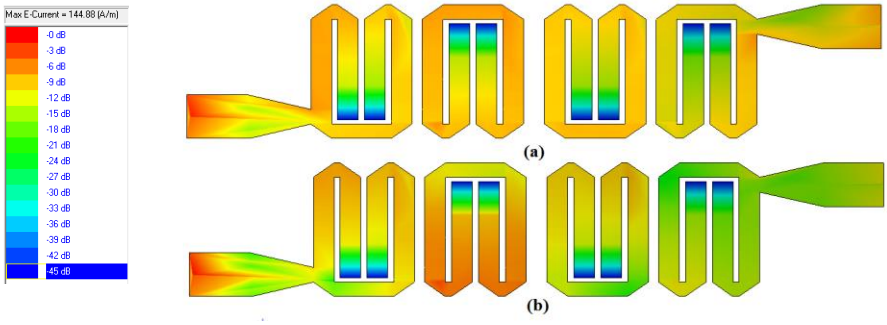

Fig. 4.48. Distribution of surface current for the fourth-order folded bandpass filter: (a) at 2.5 GHz and (b) at 5.2 GHz.

Subsequently, the challenge becomes suppression of such harmonics' attenuation levels by the inclusion of spurlines at the coupled edges of the adjacent resonators of the folded filter as discussed in the following section.

4.3. Harmonics Suppression by Spurline for Compact Fourth-Order Folded Hairpin-Line Bandpass Filter

4.3.1. Resonance Characteristics of Spurline

The spurline is a defected structure, which is realized by introducing one L-shape slot in the microstrip line [7-12]. It consists of a pair of coupled microstrip lines joined together at one end with the other end of one of the lines being left open as shown in Fig. 4.49(a). It exhibits virtually non-dispersive behavior, characterized by the electromagnetic fields of the odd-mode of propagation. The conventional spurline has been characterized by the length of the

open-end line l_{sp}, open-end discontinuity gap g, width w, line width w_1, resonator length l as highlighted by the indications *a*, *b*, and *c* in Fig. 4.49(a). The center frequency f_0 of the stopband of the spurline bandstop filter is determined by l_{sp}. However, the skirt selectivity and bandwidth are determined by g.

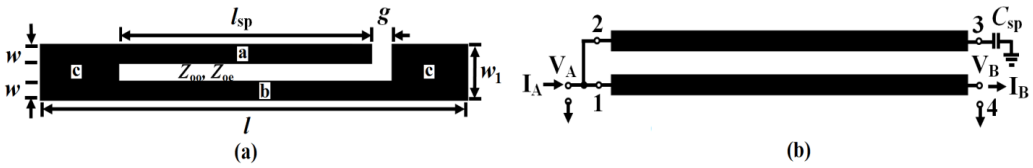

Fig. 4.49. L-shaped spurline, (a) microstrip layout diagram, (b) transmission line structure.

The physical length of the spurline has been approximated by Bates [11] as (14):

$$l_{sp} = \frac{c}{4 f_0 \sqrt{\varepsilon_{effo}}} - \Delta l \tag{14}$$

$$\Delta l = \frac{C_{sp} Z_{oo} c}{\sqrt{\varepsilon_{effo}}} \tag{15}$$

In (14) c is the speed of light, ε_{effo} is the effective dielectric constant of the odd-mode, Z_{oo} is the characteristic impedance of the odd-mode, C_{sp} is the total parasitic capacitance at the end of the open line at resonance due to the gap g and Δl is the effective extension of the open line caused by g. The chain matrix of the two-port L-shaped spurline network as shown in Fig. 4.48(b) has been derived as (16). In (16), Z_{oo} and Z_{oe} are the odd- and even-mode characteristic impedances; θ_{oo} and θ_{oe} are the odd- and even-mode electrical lengths respectively of the coupled-line section.

$$\begin{bmatrix} V_A \\ I_A \end{bmatrix} = \begin{bmatrix} \cos\theta_{oe} & \frac{j}{2}\left(Z_{0e}\sin\theta_{oe} + Z_{oo}\tan\theta_{oo}\cos\theta_{oe}\right) \\ j\frac{2}{Z_{oe}}\sin\theta_{oe} & \cos\theta_{oe} - \frac{Z_{oo}}{Z_{oe}}\sin\theta_{oe}\tan\theta_{oo} \end{bmatrix} \begin{bmatrix} V_B \\ I_B \end{bmatrix} \tag{16}$$

Here, the terminal voltage conditions are considered as $V_1 = V_2 = V_A$, $V_4 = V_B$ and terminating current conditions are considered as $I_A = I_1 + I_2$, $I_B = -I_4$, and $I_3 = 0$. By assuming $\theta_{oo} = \theta_{oe} = \theta$, (16) has been modified as (17).

$$\begin{bmatrix} V_A \\ I_A \end{bmatrix} = \begin{bmatrix} \cos\theta & j\left(\frac{Z_{oo} + Z_{oe}}{2}\right)\sin\theta \\ j\frac{2}{Z_{oe}}\sin\theta & \cos\theta - \frac{Z_{oo}}{Z_{oe}}\sin\theta\tan\theta \end{bmatrix} \begin{bmatrix} V_B \\ I_B \end{bmatrix} \tag{17}$$

The equivalent $|S_{21}|$ has been derived by the parameters conversion [1] and expressed as

$$|S_{21}|^2 = \frac{1}{4Z_0^2}\left(a^2 + b^2 \sin^2\theta\right) \tag{18}$$

$$a = 2Z_0 \cos\theta - \frac{Z_{oo}Z_0}{Z_{oe}} \tan\theta \sin\theta \tag{19}$$

$$b = \frac{Z_{oo} + Z_{oe}}{2} + \frac{2Z_0^2}{Z_{oe}} \tag{20}$$

Fig. 4.50 illustrates the $|S_{21}|$ (dB) plot for the L-shaped spurline according to (18) for different values of g. The values of Z_{oe} and Z_{oo} in (17) have been calculated as 131.37 Ω and 44.8 Ω for g = 0.1 mm, 135.36 Ω and 61.87 Ω for g = 0.3 mm, and 142.1 Ω and 77.4 Ω for g = 0.5 mm respectively [1].

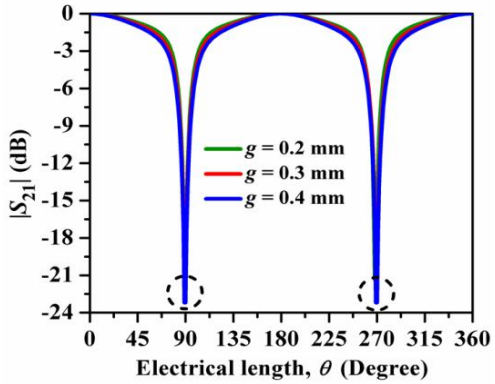

Fig. 4.50. Variation of $|S_{21}|$ (dB) vs. electrical length θ (Degree) of L-spurline for different values of g (mm).

The value of the width w_1 of the resonator has been chosen as 1.0 mm (Z_0 = 84 Ω) which is same as that of the unit FHL cell and accordingly, the value of spurline width w has been calculated as $w = (w1 - g)/2$. The transmission zeros of $|S_{21}|$ according to (18) have been obtained by setting $|S_{21}| = 0$ under the condition of $\theta = (2i\text{-}1)\pi/2$, for i = 1, 2, 3,…..$(2n+1)$, where n is a positive integer. It has been observed that low value of g has significantly improved the skirt selectivity of the passband and subsequently reduced the bandwidth. Thus, the values of g and θ are to be chosen adequately for desirable bandstop performance to place transmission zeros at the location of harmonics.

Fig. 4.51(a) shows the equivalent lumped elements circuit diagram of the L-shaped spurline based on the transmission line theory [1]. In this circuit, L_1 and L_2 represent the lumped inductors equivalent to the parallel-coupled lines of the spurline structure; C_1 represents the lumped capacitor equivalent to the coupling gap between the two coupled lines

and the π-network consisting of C_2, C_3, and C_4 represent the open-end coupling gap of the spurline. The required values of all these elements have been obtained based on the transmission line theory [1] and tuned accordingly by performing the circuit simulation in IE3D to meet the resonant characteristics of the spurline.

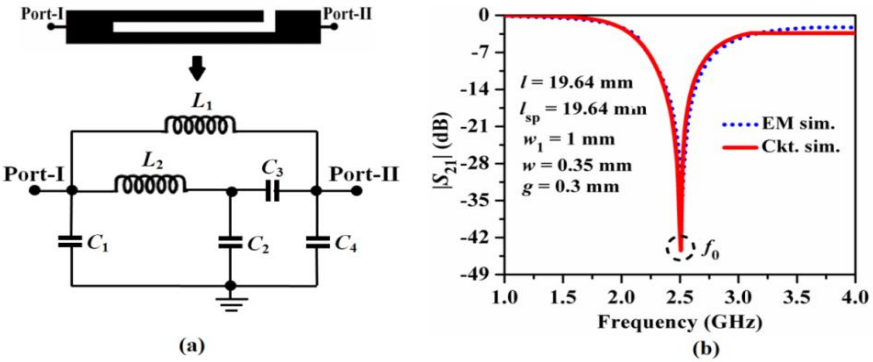

Fig. 4.51. (a) Equivalent lumped elements circuit diagram of the L-shaped spurline, (b) comparison of $|S_{21}|$ (dB) plots between the EM simulation and the circuit simulation.

The values of the lumped elements have been calculated as $L_1 = L_2 = 4.86$ nH, $C_1 = 0.392$ pF, $C_2 = 0.632$ pF, $C_3 = 0.03$ pF, $C_4 = 0.634$ pF equivalent to the microstrip line dimensions: $l_1 = 19.64$ mm, $w_1 = 1$ mm, $w = 0.35$ mm, $g = 0.3$ mm and $l_{sp} = 17.64$ mm for $f_0 = 2.5$ GHz. Fig. 4.51(b) shows the comparison of $|S_{21}|$ (dB) between the EM simulation and the circuit simulation of the spurline. It has been observed that the plots are in good agreement at the bandstop resonant frequency $f_0 = 2.5$ GHz. Fig. 4.52(a) illustrates the variation of $|S_{21}|$ (dB) with the incremental values of inductance $L_1 = L_2 = L$. The stopband resonant peak frequency f_0 has been shifted to the lower frequency regions due to the increment of the L values of the resonant circuit. Accordingly, the dependence of f_0 on L has been depicted in Fig. 4.52(b). It has been observed that f_0 has been decreased exponentially as the value of L increases with constant values C_1, C_2, C_3, and C_4. This is due to the inverse proportional relation between f_0 and L. Accordingly, the optimum value of L has been obtained as 4.86 nH for $f_0 = 2.5$ GHz. Subsequently, the variation of f_0 vs. the incremental values of the capacitances C_3 (pF) and $C_2 = C_4 = C$ (pF) have been highlighted in Figs. 4.53(a) and (b) respectively. It has been noticed that f_0 decreases linearly with incremental C_3 and exponentially with incremental C. As C_3 correspond to the equivalent open-end gap capacitance of the spurline, the open-end fringe fields' effects have been increased with its increment values and accordingly f_0 has been decreased.

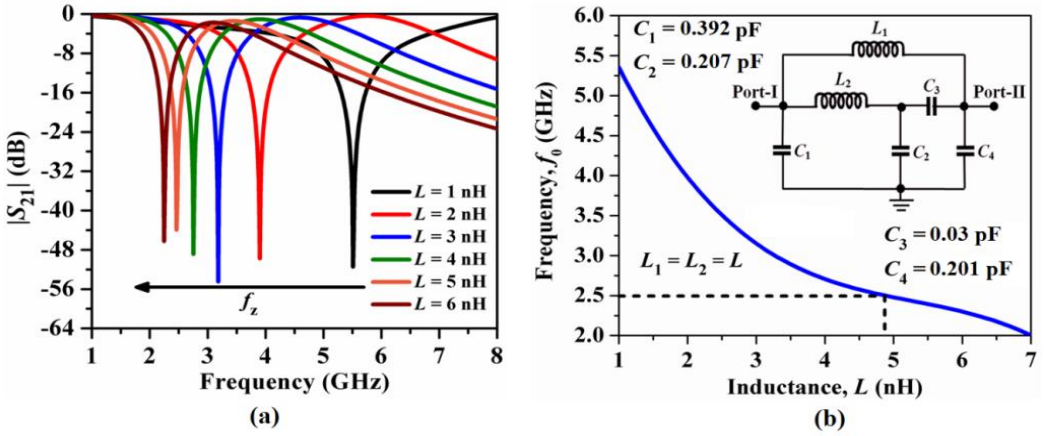

Fig. 4.52. (a) Variation of simulated $|S_{21}|$ (dB) with incremental values of L (nH), (b) variation of f_0 (GHz) with incremental values of L (nH).

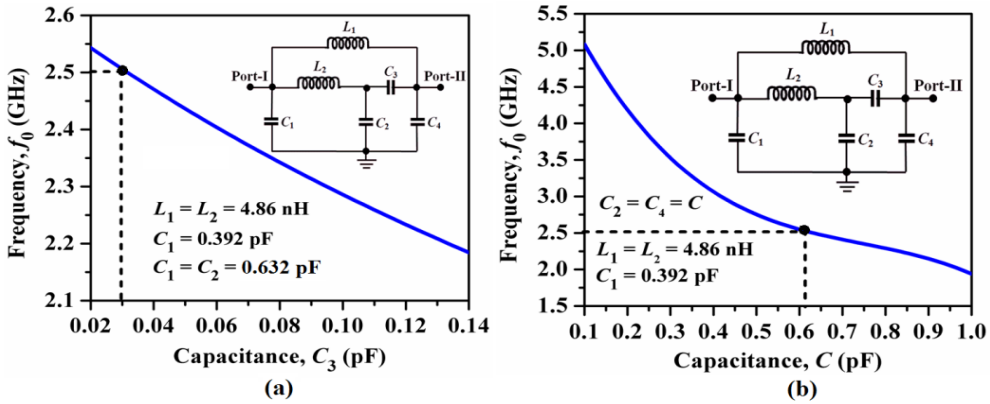

Fig. 4.53. Variation of f_0 (GHz) with incremental values of (a) C_3 (pF), (b) $C_2 = C_4 = C$ (pF).

Moreover, the C_2 and C_4 are the equivalent coupling capacitances between the two resonators of the spurline slot and their values have been increased with the increase of the length of the slot. Thus, f_0 has been decreased exponentially with their incremental values. Accordingly, the optimum values of C_3 and C have been determined as 0.392 pF and 0.632 pF respectively corresponding to f_0 = 2.5 GHz. Hence, it can be concluded from the above study that the bandstop resonant frequency of the spurline can be tuned exactly at the desired frequency by adjusting the dimension of the spurline. It can be concluded from this section that the L-shaped spurline exhibits excellent bandstop resonance characteristics by introducing transmission zeros for optimum values of l_{sp}, g, and w. Accordingly, this feature of L-shaped spurline has been studied further in the following section for the folded hairpin-line cells which are the building blocks of the fourth-order folded filter to achieve harmonic suppression.

4.3.2. Resonance Characteristics of Unit FHL Cell with L-Spurline

The layout of a folded hairpin-line cell with an L-shaped spurline introduced in the right-side arm as indicated by l_3 is shown in Fig. 4.54(a). Such unit FHL cells are in general cascaded to design a higher order filter. For conventional parallel-coupled line structure, the odd-mode phase velocity is more than that of even-mode due to the inhomogeneous microstrip structure. Accordingly, spurious harmonics are generated. The primary objective to incorporate the spurline in the FHL cell is to utilize its slow-wave property for phase velocity compensation between these two modes and the ability to generate transmission zeros in the stopband due to the bandstop nature. From the literature study of spurline it has been revealed that the electromagnetic energy stored by the resonant structure has been mainly determined by the odd-mode of propagation. Thus, the spurline has been employed to the right arm of the FHL cell which is to be coupled with the left arm of the next FHL cell in the final fourth-order filter. The spur-line length ratio, α has been defined as (21).

$$\alpha = \frac{l_3 + g}{l_1 - 2w_1} \tag{21}$$

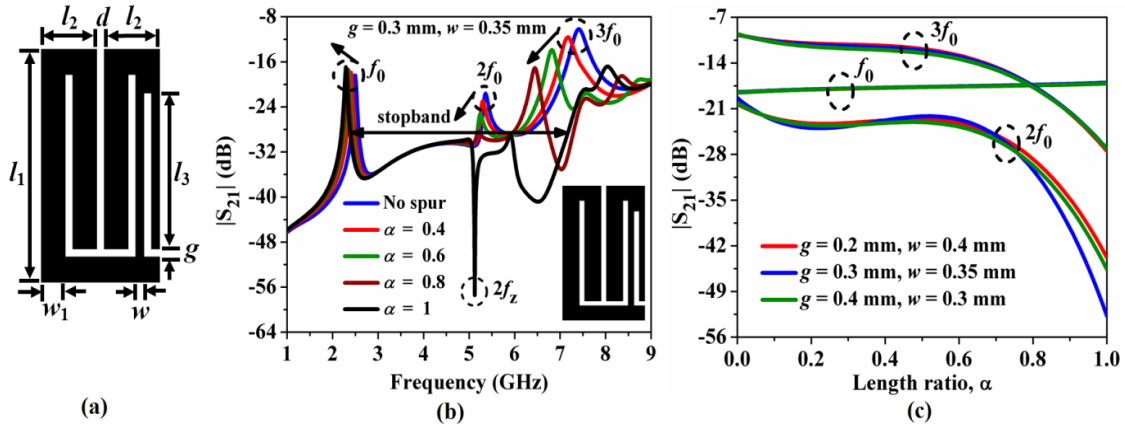

Fig. 4.54. Unit FHL cell with spurline: (a) layout, (b) simulated resonant characteristics, (c) variation of simulated $|S_{21}|$ (dB) with incremental value of α.

The resonant characteristics of the unit FHL cell with spurline have been studied in Fig. 4.54(b). The dimensions of the FHL cell with spurline have been chosen for the study as l_1 = 9.11 mm, l_2 = 2.3 mm, d = 0.3 mm, w_1 = 1 mm, g = 0.3 mm, w = 0.35 mm. It has been observed that the attenuation levels at $2f_0$ and $3f_0$ have been gradually degraded with the incremental value of α while those at f_0 have been increased due to the strong cross-coupling between the two coupled arms of the spurline. Moreover, f_0 has been shifted to lower values

due to the increase in the effective electrical length of the hairpin-line. A sharp transmission zero marked as $2f_z$ has been observed at 5.2 GHz with the attenuation level of 59 dB for α = 1. This justifies the harmonics suppression ability of the FHL cell with spurline. Fig. 4.54(c) illustrates the variation of $|S_{21}|$ (dB) with incremental values of α for different combinations of g and w values. It has been observed that the variation of $|S_{21}|$ at f_0 is almost unaffected with α. However, the values of $|S_{21}|$ at $2f_0$ and $3f_0$ have been decreased nonlinearly and attained a minimum value for α = 1 with g = 0.3 mm. Figs. 4.55(a)-(c) elaborate the vector surface current density distribution for a unit FHL cell with spurline at f_0, $2f_0$, and $3f_0$. Maximum current density vectors have been traveled through the left arm of the spurline at f_0. However, the current distribution has been diminished at all the open ends as expected. The strength of the current density has been decreased significantly at $2f_0$ and $3f_0$ due to their decreased attenuation levels (refer to Fig. 4.54(c)).

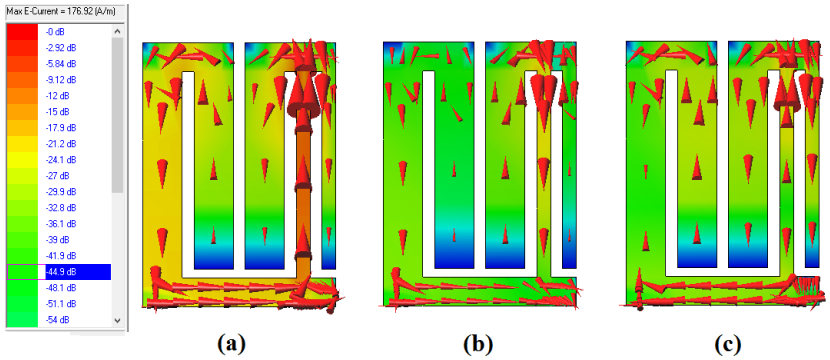

Fig. 4.55. Surface current density distribution for a unit FHL cell with spurline at (a) f_0 = 2.5 GHz, (b) $2f_0$ = 5.0 GHz, and (c) $3f_0$ = 7.5 GHz.

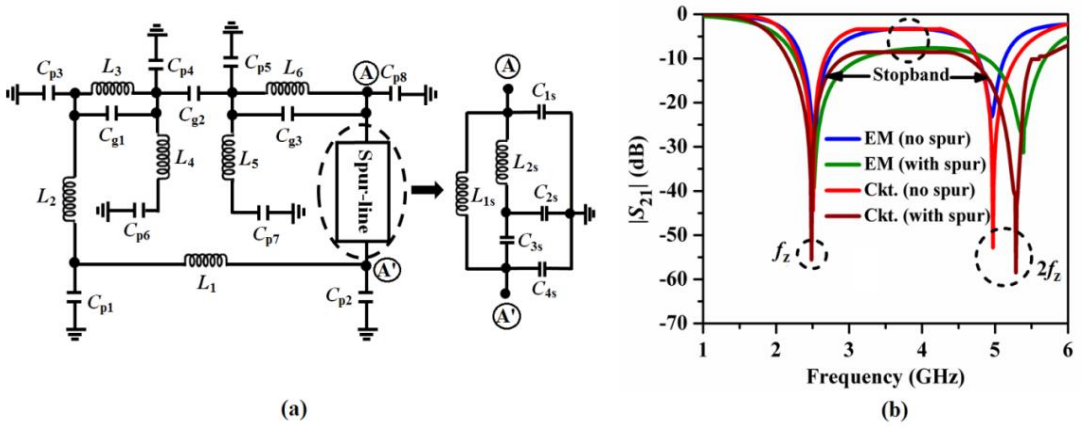

Fig. 4.56. Unit FHL cell with spurline, (a) equivalent lumped elements circuit diagram, (b) comparison of $|S_{21}|$ (dB) variations between the EM simulation and the circuit simulation.

Table 4.5. Values of the equivalent lumped elements of the unit FHL cell with spurline.

L	nH	C_p	pF	Others C	pF
L_1	2.43	C_{p1}	0.45	$C_{g1} = C_{g2} = C_{g3}$	0.02
L_2	2.30	C_{p2}	0.17	C_{1s}	0.39
$L_3 = L_6$	1.17	$C_{p3} = C_{p8}$	0.36	C_{2s}	0.21
$L_4 = L_5$	3.68	$C_{p4} = C_{p5}$	0.08	C_{3s}	0.03
$L_{1s} = L_{2s}$	5.36	$C_{p6} = C_{p7}$	0.28	C_{4s}	0.20

The equivalent lumped elements circuit diagram of a unit FHL cell with spurline has been shown in Fig. 4.56(a) and the comparison of $|S_{21}|$ (dB) between the EM simulation and the circuit simulation has been illustrated in Fig. 4.56(b). It has been observed that there has been a close match between the EM simulation and the circuit simulation plots for both the cases, especially in the passband. Table 4.5 lists the values of the equivalent lumped elements tuned at f_0. It can be concluded from these studies that the spurline has suppressed the higher-order harmonics attenuation levels effectively for a unit FHL cell. Accordingly, the study has been extended further for a pair of FHL cells in the following section.

4.3.3. Resonance Characteristics of a Pair of FHL Cells with L-Spurline

The unit FHL cells with spurlines have been cascaded symmetrically in a hybrid mode of coupling to obtain a pair of FHL cells with a coupling gap (S). Two different types of spurline configurations between the coupled arms of the FHL cells such as asymmetrical L-spurline, and the symmetrical L-spurline highlighted in Fig. 4.57(a) and Fig. 4.58(a) respectively. The dimensions of the pair of the FHL cells are the same as those for the unit FHL cell. For the dimensions of the spurline, the value of the open-end gap and the slot gap has been chosen uniformly as 0.3 mm. Accordingly, the length of the spurline has been incremented to study the effects of spurline's slow-wave nature and bandstop properties on the wideband resonant characteristics of the FHL cells as illustrated in Fig. 4.57(b) and Fig. 4.58(b) respectively. It has been observed from Fig. 4.57(b) that for the case FHL cells pair with the asymmetrical L-shaped spurline a wide stopband of attenuation level of 32 dB has been obtained up to 7.3 GHz for $\alpha = 1$. In addition, two transmission zeros $2f_z$ at 5 GHz with an attenuation level of 43 dB and $3f_z$ at 5.9 GHz with an attenuation level of 38 dB have been obtained. Accordingly, from Fig. 4.58(b) it has been observed that for the case of symmetrical L-shaped spurline two sharp transmission zeros $2f_z$ and $3f_z$ have been occurred at 5 GHz and 5.7 GHz in the stopband with the attenuation levels of 40 dB and 46 dB respectively.

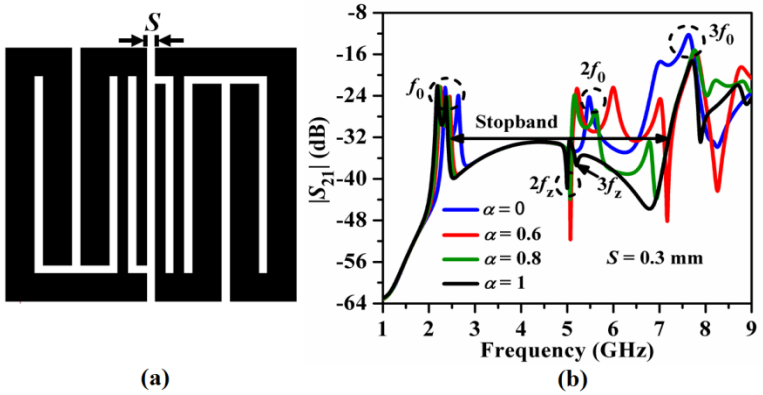

Fig. 4.57. Pair of FHL cells with asymmetrically placed L-shaped spurline: (a) layout and (b) wideband resonant characteristics of simulated $|S_{21}|$ (dB) plots.

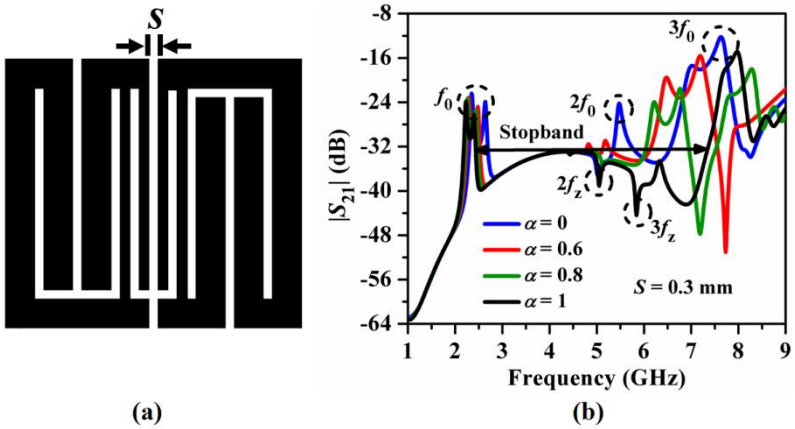

Fig. 4.58. Pair of FHL cells with symmetrically placed L-shaped spurline: (a) layout and (b) wideband resonant characteristics of simulated $|S_{21}|$ (dB) plots.

Besides, $3f_0$ has been shifted to a higher frequency region with degradation in the attenuation level by 6 dB, justifying the ability of maximum suppression harmonics by the symmetrical L-shaped spurline over asymmetrical configuration. Hence, it has been selected for the final fourth-order filter design. Fig. 4.59(a) illustrates the effects of different length ratios on the even- and odd-mode resonant frequencies f_e and f_o respectively for a pair of FHL cells with symmetrical L-shaped spurline. It has been observed that f_e shifts more to lower frequency compared to f_o. Accordingly, the difference between f_o and f_e reduces to 0.17 GHz for α = 1 from 0.29 GHz for a pair of FHL cells without L-spurline. This justifies the effectiveness of the spurline to attain the modal phase compensation for harmonic suppression. The variations f_e, f_o, $2f_z$, $2f_0$, $3f_z$, and $3f_0$ with the incremental value of α have been illustrated in Fig. 4.59(b). It has been observed that the transmission zero $2f_z$ approaches $2f_0$ with the incremental values of α and finally merges at α = 0.7. This justifies the ability of modal phase velocity

compensation by the spurline. A similar phenomenon has been happened for $3f_e$ and $3f_o$ due to the dispersive nature of the spurline. Accordingly, the effects on $|S_{21}|$ (dB) for different frequency parameters have been highlighted in Fig. 4.60.

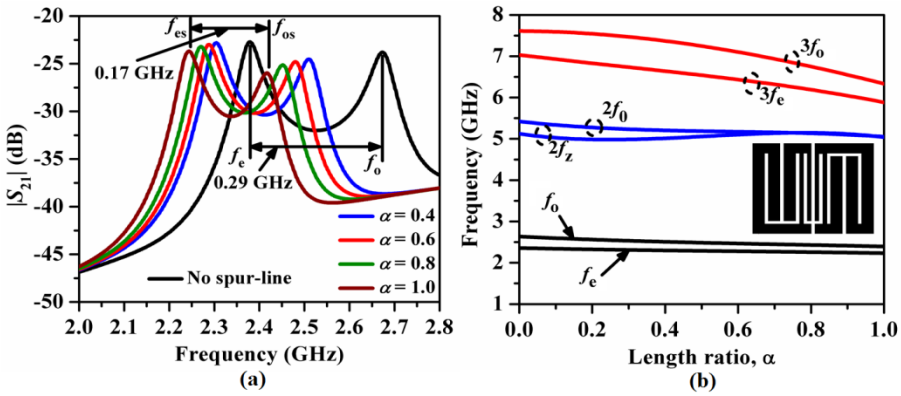

Fig. 4.59. (a) Variation of resonant frequencies f_e and f_o of simulated $|S_{21}|$ (dB), (b) variation of different frequency parameters with α.

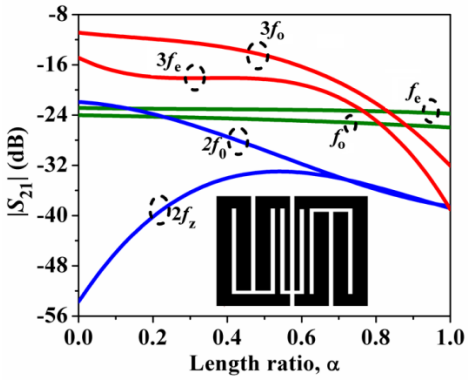

Fig. 4.60. Effects on simulated $|S_{21}|$ (dB) for with the variation of attenuation levels with α.

It has been noticed that the values $|S_{21}|$ have been degraded at $2f_0$ and $3f_0$. For more justification, the vector surface current density distribution profile for the pair of FHL cells at f_e = 2.24 GHz and f_o = 2.42 GHz for α = 1 has been demonstrated in Figs. 4.61(a)-(b). It has been observed that the current vectors are propagating unidirectional for even-mode and in reverse direction for odd-mode as expected. Accordingly, Fig. 4.62(a)-(b) elaborate the distribution of surface current for the pair of FHL cells at $2f_z$ = 5.05 GHz and $3f_z$ = 5.84 GHz (refer to Fig. 5.58(b)) due to the suppression in their attenuation levels by spurline. It can be concluded from this section that the spurline with optimum dimensions can suppress the attenuation levels at higher-order harmonics and subsequently such FHL cells with spurline have been cascaded in hybrid mode to design the fourth-order filter.

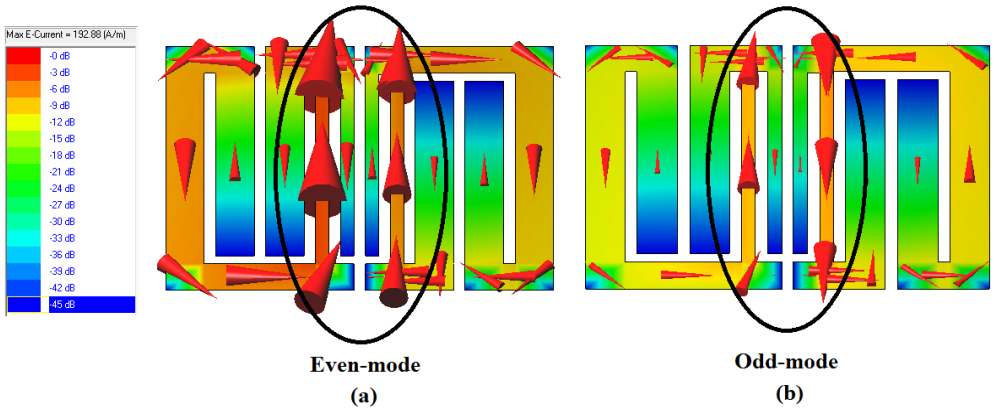

Fig. 4.61. Distribution of surface current vectors for a pair of FHL cells with spurline at (a) f_e = 2.24 GHz, (b) f_o = 2.42 GHz.

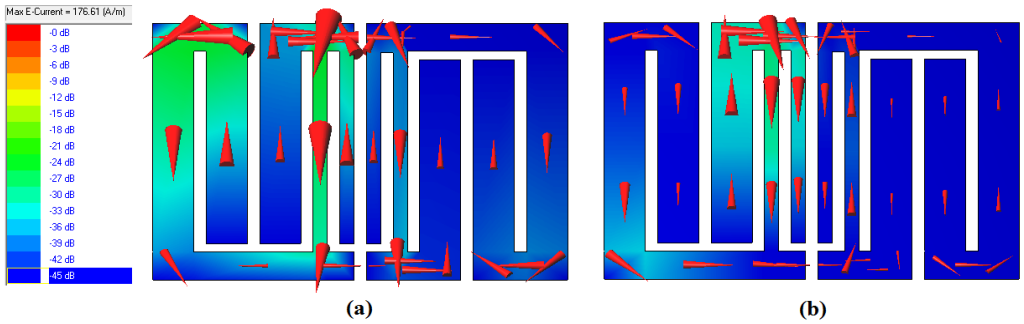

Fig. 4.62. Distribution of surface current vectors for a unit FHL cell with spurline at (a) $2f_0$ = 5.0 GHz and (c) $3f_0$ = 7.5 GHz.

4.3.4. Fourth-Order Bandpass Filter with L-Spurline

Three fourth-order FHLBFs have been designed by incorporating the spurlines symmetrically in different coupling regions namely (1) Filter-I with middle pair-spurline, (2) Filter-II with end pairs-spurline, and (3) Filter-III with all pairs-spurline. Accordingly, the initial values of the coupling gap *s* between the adjacent FHL cells with spurline have been obtained from the design graph of the coupling coefficient (*M*) as shown in Fig. 4.63.

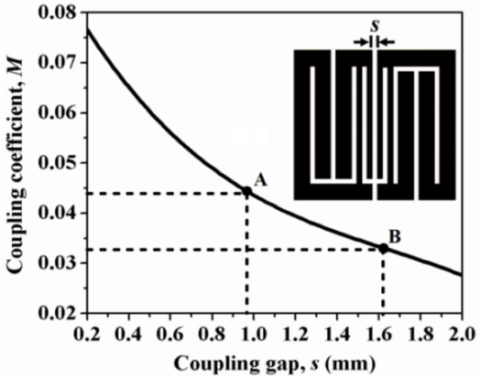

Fig. 4.63. Design curve for *M* vs. *s* (mm) for a pair of FHL cells with spurline.

The optimum values of α = 0.6, g = 0.3 mm and w = 0.35 mm have been chosen for the final filters. The dimensions of the individual FHL cell along with the spurline have been determined from the parametric study. Figs. 4.64(a)-(c) depict the optimized layouts of the final filters. The sizes of the designed filters are 351.2 mm^2, 351.2 mm^2, and 354.63mm^2 i.e., 0.59λ_g × 0.13λ_g, 0.59λ_g × 0.13λ_g, and 0.62λ_g × 0.12λ_g respectively. Accordingly, size reductions of 19.1%, 19.1%, and 18.29% have been obtained compared to conventional hairpin-line filter.

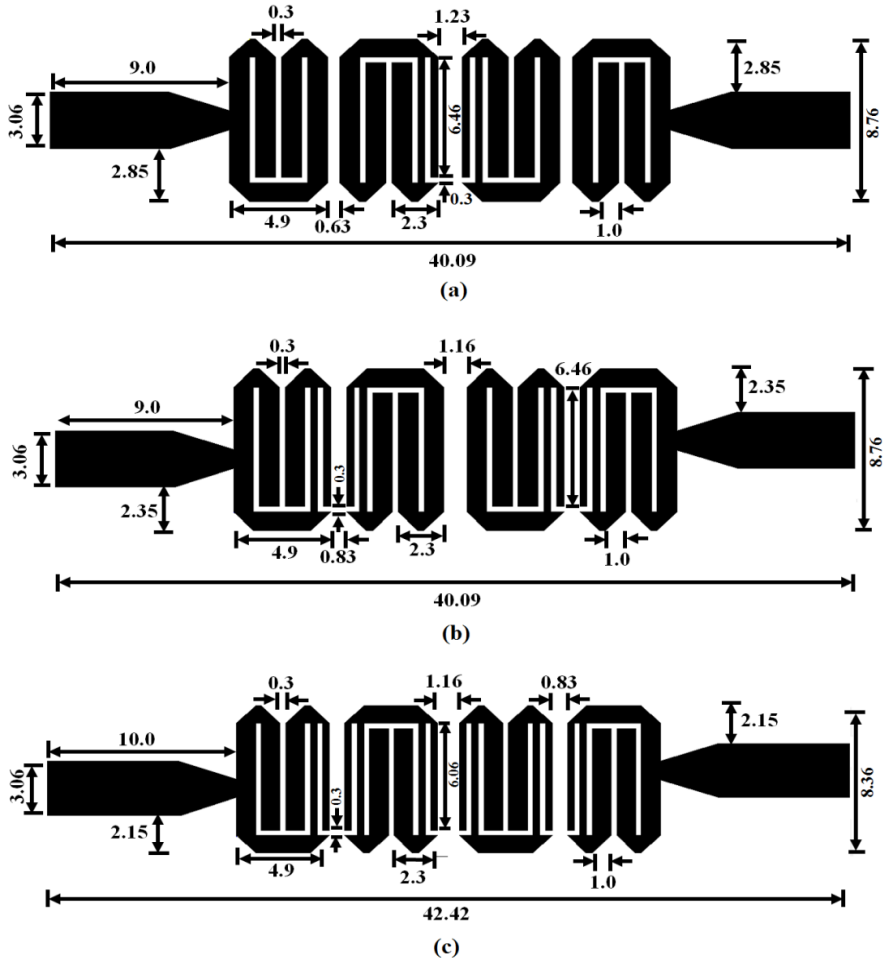

Fig. 4.64. Layouts of fourth-order folded hairpin-line filters: (a) Filter-I with middle pair-spurline, (b) Filter-II with end pairs-spurline, and (c) Filter-III with all pairs-spurline.

The layout diagram of the fourth-order FHLBF with spurline between all FHL cells has been depicted in Fig. 4.65 where the individual FHL cell with spurline has been marked as *FHL-i*, *i* = 1 to 4 and the coupling capacitances between them have been modeled by C_{12}, C_{23}, and C_{34}. Accordingly, the equivalent lumped elements circuit diagram has been obtained as shown in Fig. 4.66 by following the conventional transmission line theory [1-2].

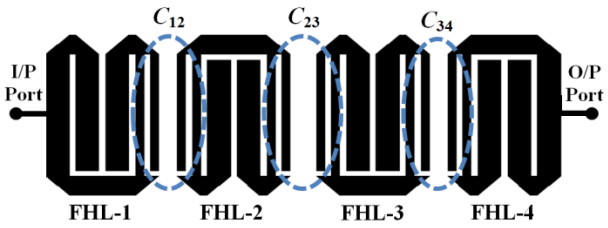

Fig. 4.65. General layout of the fourth-order FHLBF with spurline between all FHL cells.

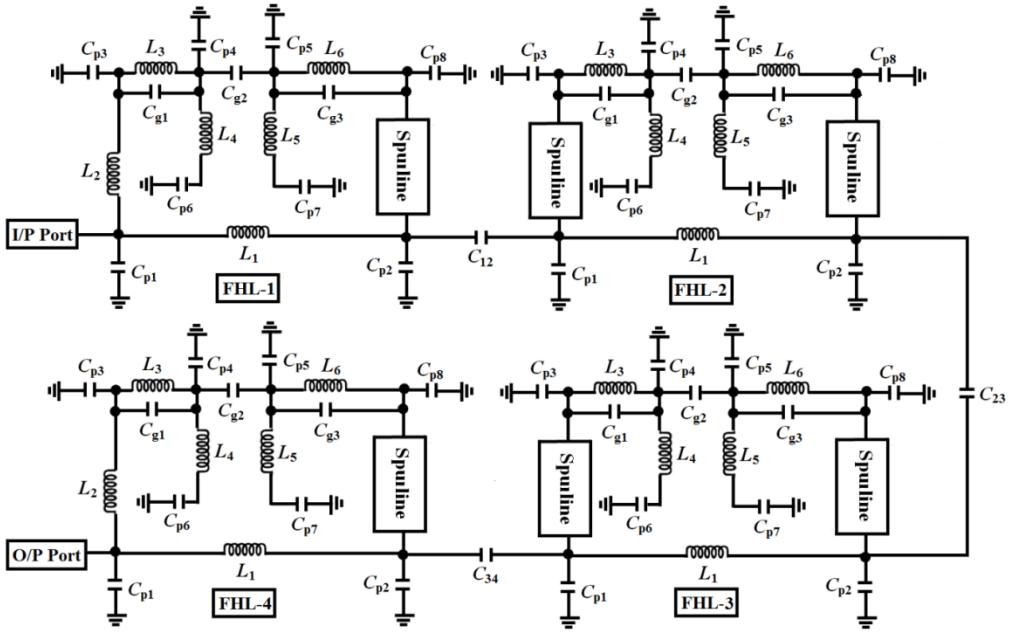

Fig. 4.66. Equivalent lumped elements circuit diagram for the fourth-order FHLBF with spurline placed symmetrically between all FHL cells.

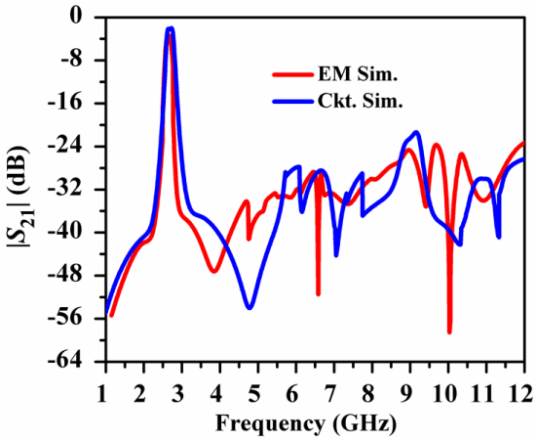

Fig. 4.67. Comparison between EM simulation and circuit simulation.

The lumped elements' values are same as listed in Table 4.5 for FHL cells. Fig. 4.66 explores the comparison of $|S_{21}|$ (dB) plots between the EM simulation and the circuit simulation.

From Fig. 4.67 it has been observed that quite satisfactory agreement has been obtained between the two simulated plots, especially in the passband. There are mismatches between the plots due to the simulation constraints as discussed early.

4.3.4.1. Fabricated Prototypes

Figs. 4.68(a)-(c) show the fabricated prototypes of the proposed filters. The experiment has been carried out in the Agilent N9928A vector network analyser in the similar way of 3.14.4.1.

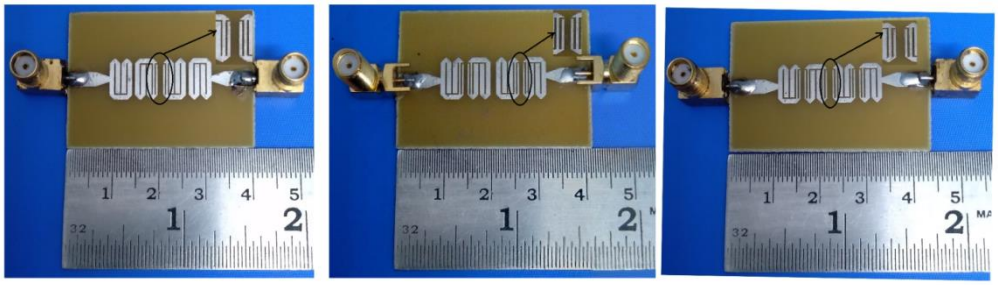

Fig. 4.68. Fabricated prototypes filters: (a) Filter-I, (b) Filter-II, (c) Filter-III [13].

4.3.4.2. Comparison of EM simulation vs. Measurement Results

The comparison of measured vs. simulation $|S_{21}|$ (dB) plots have been highlighted in Figs. 4.69(a)-(b). The insertion loss has been recorded as 1.18 dB, 1.15 dB, and 1.2 dB for the filters respectively.The high value (>1 dB) of the insertion loss has been occurred due to the lossy nature of FR4 substrate along with some experimental tolerances incurred due to the coaxial cable and SMA connectors during measurements. The measured vs. simulated $|S_{11}|$ (dB) plots have been highlighted in Fig. 4.70(a). It has been observed that for all the designed filters the input reflection coefficient in the desired passband becomes better than 15 dB. Fig. 4.70(b) compares the group delay (ns) plots of $|S_{21}|$ for all the fabricated filters and satisfactory symmetrical responses have been observed in the desired passbands of the filters. It can be concluded from this section that the conventional L-spurline are quite capable to suppress the spurious harmonics' attenuation level below 35 dB up to $4.68f_0$. To study the effects of spurline further in more detail for folded hairpin line filter, conventional L-spurline has been modified by T-spurline in the next section.

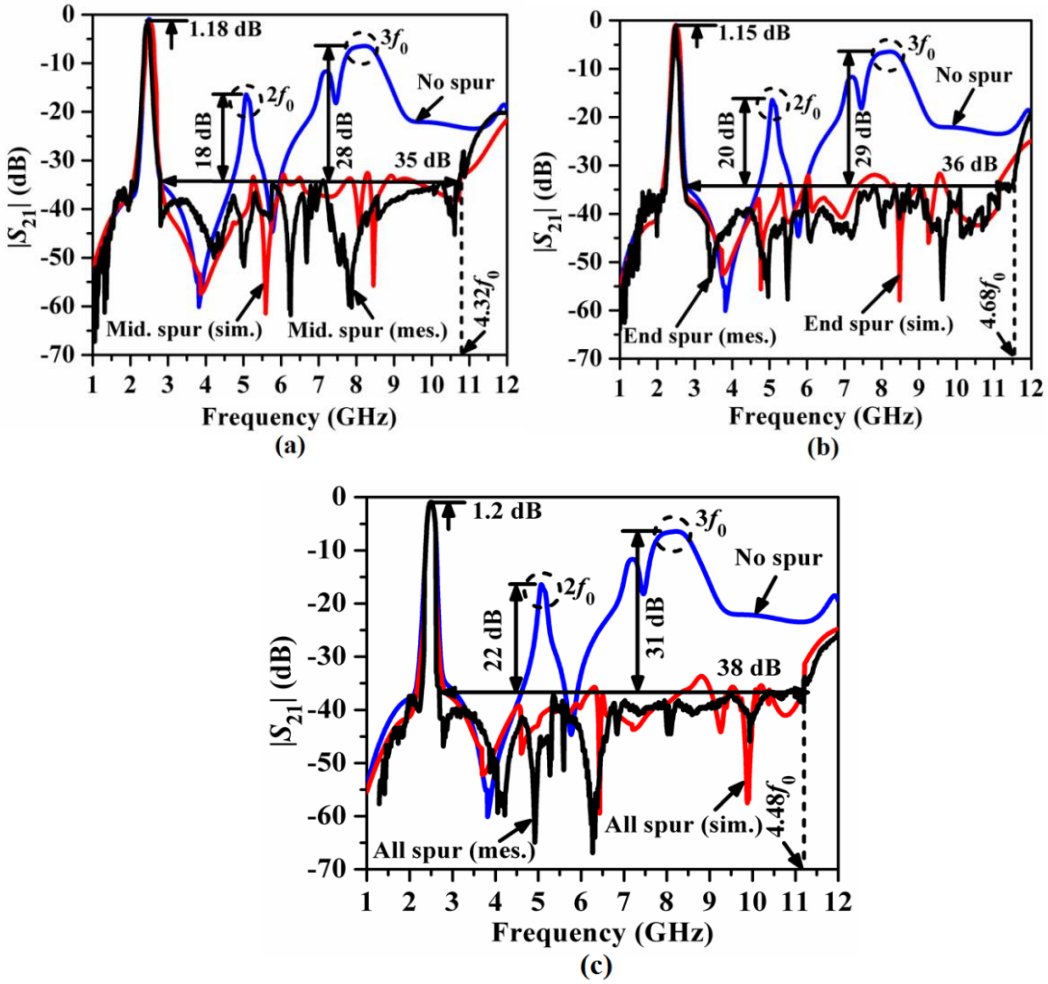

Fig. 4.69. Comparison between simulated vs. measurements results of $|S_{21}|$ (dB) for folded filters, (a) Filter-I, (b) Filter-II, and (c) Filter-III.

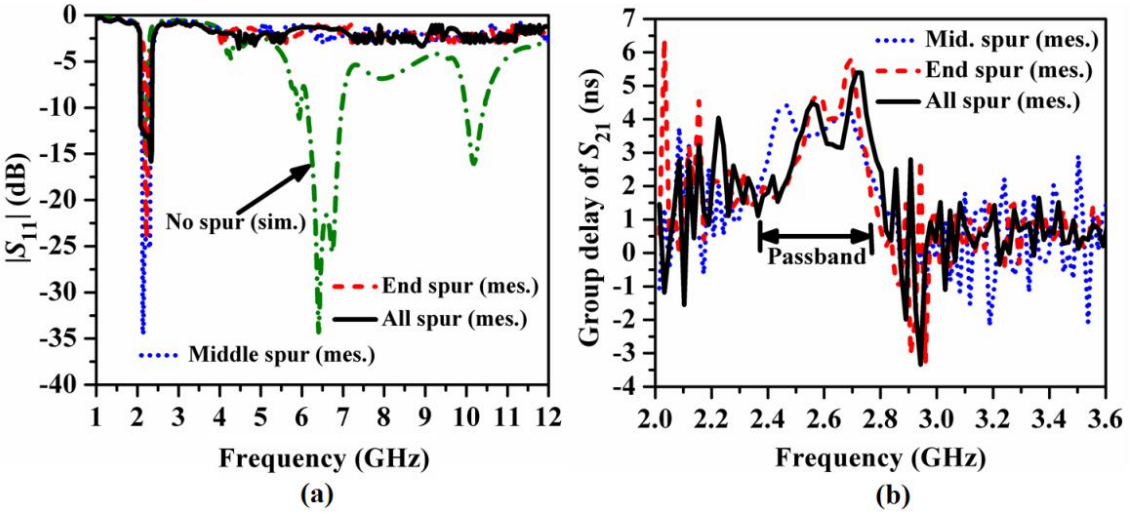

Fig. 4.70. Comparison between simulated vs. measurements results for three fabricated filters: (a) $|S_{11}|$ (dB) and (b) group delay of S_{21} (ns).

4.4. Harmonics Suppression by T-Spurline for the Folded Hairpin-Line Bandpass Filter

4.4.1. Resonance Property of T-Spurline

The T-shaped spur-line structure has been obtained by placing two L-shaped spurlines opposite to each other about the symmetry line in the middle. Two types of T-spurline have been proposed namely (1) outer T-shaped spurline (OTSP) (Fig. 4.71(a)) and (2) double T-shaped spurline (DTSP) (Fig. 4.71(c)). The equivalent transmission line structures are depicted in Fig. 4.71(b) and Fig. 4.71(d) respectively. The equivalent chain matrix of the conventional L-shaped spurline has been obtained in (22) by assuming $\theta_{oo} = \theta_{oo} = \theta$. In (22) Z_{oo} and Z_{oe} are the odd- and even-mode characteristic impedances, θ_{oo} and θ_{oo} are the odd- and even-mode electrical lengths respectively of the coupled line section.

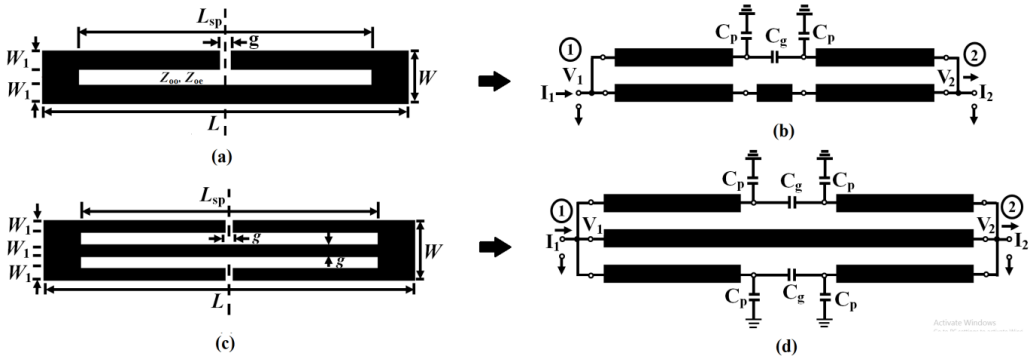

Fig. 4.71. (a) Layout diagram of outer T-shaped spurline (OTSP), (b) transmission line structure, (c) Layout diagram of double T-shaped spurline (DTSP), and (d) layout diagram.

$$\begin{bmatrix} A & B \\ C & D \end{bmatrix} = \begin{bmatrix} \cos\theta & j\left(\dfrac{Z_{oo}+Z_{oe}}{2}\right)\sin\theta \\ j\dfrac{2}{Z_{oe}}\sin\theta & \cos\theta - \dfrac{Z_{oo}}{Z_{oe}}\sin\theta\tan\theta \end{bmatrix} \tag{22}$$

Here, the terminal voltage conditions are $V_1 = V_2 = V_A$, $V_3 = 0$ and $V_4 = V_B$. The equivalent chain matrix of OTSP has been obtained by cascading two chain matrix of L-spurline as

$$\begin{bmatrix} A_T & B_T \\ C_T & D_T \end{bmatrix} = \begin{bmatrix} A_L & B_L \\ C_L & D_L \end{bmatrix}.\begin{bmatrix} D_R & B_R \\ C_R & A_R \end{bmatrix} \tag{23}$$

$$\begin{bmatrix} A_T & B_T \\ C_T & D_T \end{bmatrix} = \begin{bmatrix} 1-2k\sin^2\theta & jkZ_{oe}\sin\theta\cos\theta \\ j\dfrac{4\tan\theta}{Z_{oe}}(1-k\sin^2\theta) & 1-2k\sin^2\theta \end{bmatrix} \tag{24}$$

where,

$$k = \frac{Z_{oe} + Z_{oo}}{Z_{oe}} \tag{25}$$

The suffix *T* stands for total; *L* stands for the left side and *R* stand for the right side of the symmetry line of the T-spurline. The equivalent $|S_{21}|$ has been derived by the parameters conversion [1] and expressed as

$$\left|S_{21}\right|^2 = \frac{1}{4Z_0^2}\left(p^2 + q^2 \sin^2\theta\right) \tag{26}$$

where,

$$p = 2Z_0(1 - 2k\sin^2\theta) \tag{27a}$$

$$q = kZ_{oe}\cos\theta + \frac{4Z_0^2}{Z_{0e}}\cos\theta\left(1 - k\sin^2\theta\right) \tag{28b}$$

Fig. 4.72(a) illustrates the $|S_{21}|$ (dB) plot for the outer T-shaped spurline (OTSP) structure according to (26) for different values of the spurline gap, *g*. The transmission zeros have been obtained under the condition of $\theta = (2i\text{-}1)\pi/2$, for $i = 1, 2, 3, \ldots (2n+1)$, where *n* is a positive integer. It has been observed that the small value of *g* has significantly improved the skirt selectivity of the passband. By following the same method, the equivalent chain matrix of a double T-shaped spurline (DTSP) as shown in Fig. 4.71(c) has been determined as (29).

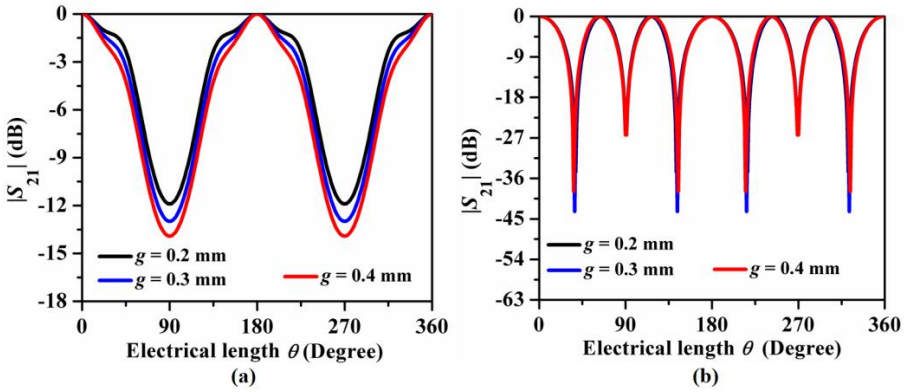

Fig. 4.72. Variation of $|S_{21}|$ (dB) vs. electrical length, θ (Degree) of the T-shaped spurline for different values of spurline gap, *g* (mm) for (a) OTSP, (b) DTSP based.

$$\begin{bmatrix} A_{Td} & B_{Td} \\ C_{Td} & D_{Td} \end{bmatrix} = \begin{bmatrix} \dfrac{1}{1 - 2k\sin^2\theta} & -j\dfrac{Z_{oe}k\sin\theta\cos\theta}{2(1 - 2k\sin^2\theta)} \\ j\dfrac{8\tan\theta(1 - k\sin^2\theta)}{Z_{oe}(1 - 2k\sin^2\theta)} & \dfrac{1}{1 - 2k\sin^2\theta} \end{bmatrix} \tag{29}$$

$$\left|S_{21}\right|^2 = \frac{1}{4Z_0^2}\left(m^2 + n^2 \sin^2\theta\right) \tag{30}$$

where,

$$m = \frac{2Z_0}{1 - 2k\sin^2\theta} \tag{31}$$

$$n = \frac{16{Z_o}^2(1 - k\sin^2\theta) - Z_{oe}^2 k\cos^2\theta}{2Z_{oe}(1 - 2k\sin^2\theta)\cos\theta} \tag{32}$$

The equivalent $|S_{21}|$ has been derived by the parameters conversion and expressed as (30). Fig. 4.72(b) shows the $|S_{21}|$ (dB) plot for a double T-shaped spurline structure according to (17).The transmission zeros have been obtained under the condition of $\theta = (2i\text{-}1)\pi/4$, for i = 1, 2, 3, ….. ($2n$+1), where n is a positive integer. Moreover, it has been observed that the skirt selectivity of the passband of the resonance plots has been improved and bandwidth has been reduced for a DTSP compared to the OTSP structure. Thus, the values of g and θ are to be chosen adequately for desirable bandstop performance to place a transmission zero at the harmonic frequencies.

The effects of spurline gap capacitance have not been considered in the above analysis as no current will flow across the gap at resonance and the voltage developed across it becomes zero (Fig. 4.71(a)). In general, a capacitive effect is provided by the spurline slot and an inductive effect is exhibited by the narrow line. Accordingly, an improvement over the effective inductance and capacitance of the microstrip line has been obtained, resulting in an increment of the effective permittivity of the dielectric substrate. It can be concluded from this section that the T-shaped spurline structure exhibits excellent bandstop resonance characteristics by introducing transmission zeros for the appropriate length of the spurline (θ) along with the optimum value of g. This feature of T-shaped spurline has been studied further in the following section for the folded hairpin-line cells which are the building blocks of narrowband fourth-order folded filter. The equivalent circuit of the OTSP and DTSP are shown in Fig. 4.73(a) where the resonant characteristics are modeled by a parallel *RLC* resonant circuit. In Fig. 4.73(a), R has been included for the radiation effect and conductor loss and L resonator have been considered corresponding to the spurline. Based on the transmission line theory and the spectral domain approach, the circuit parameters can be extracted using the following equations (33) - (35) [13].

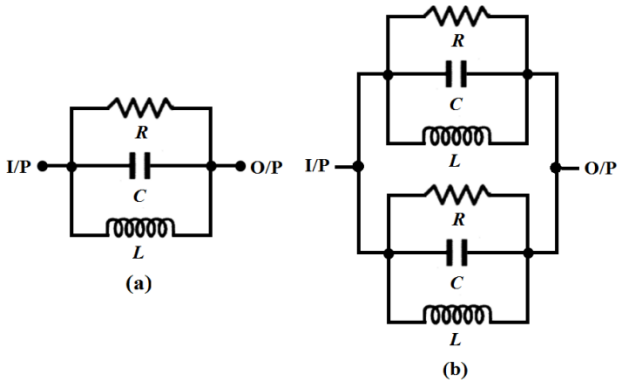

Fig. 4.73. Equivalent lumped elements circuit diagrams of (a) OTSP and (b) DTSP based spurline.

Here, Z_0 is the 50 Ω characteristic impedance of the transmission-line and Δf is the 3 dB bandwidth of simulated $|S_{21}|$.

$$R = 2Z_0(1/|S_{21}|-1)|_{f=f_0} \tag{33}$$

$$C = \frac{\sqrt{0.5(R+2Z_0)^2 - 4Z_0^2}}{2.83\pi Z_0 R\Delta f} \tag{34}$$

$$L = \frac{1}{4(\pi f_0)^2 C} \tag{35}$$

The comparison between EM simulated and circuit simulated plots of $|S_{21}|$ (dB) for a half-wavelength OTSP based line (Fig. 4.71(a)) and DTSP based line (Fig. 4.71(c)) tuned at the resonant frequency f_0 = 2.5 GHz with dimensions: L = 37.64 mm, L_{sp} = 37.04 mm, W = 1.0 mm, W_1 = 0.35 mm, g = 0.3 mm has been illustrated in Fig. 4.74(a)-(b) respectively.

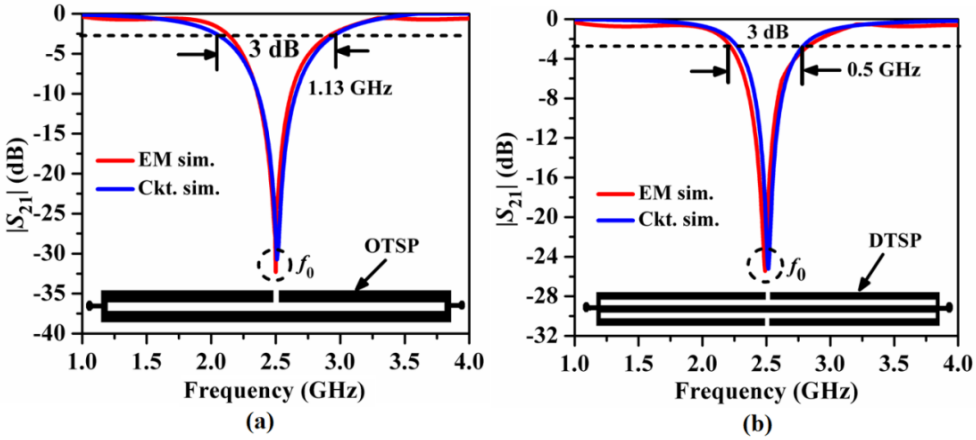

Fig. 4.74. Comparison of EM simulated vs. circuit simulated $|S_{21}|$ (dB) plots of (a) OTSP and (b) DTSP based line.

The circuit parameters have been calculated as L = 0.410 nH, C = 1.929 pF, R = 3.125 kΩ for OTSP based line with $|S_{21}|$ = 33 dB at f_0 and Δf = 0.85 GHz, and L = 0.301 nH, C = 2.626 pF, R = 4.167 kΩ for DTSP based line with $|S_{21}|$ = 27 dB at f_0 and Δf = 0.62 GHz. It has been observed from Figs. 4.74(a)-(b) that the value of Δf for 3 dB insertion loss in circuit simulation has been decreased by 55.8% (from 1.13 GHz to 0.5 GHz) for DTSP based line compared to OTSP based line. This is owing to the increment of the capacitance (C) and decrement of the inductance for the DTSP based line over OTSP based line. However, the attenuation level at f_0 has been increased from 33 dB to 27 dB (18.2 %) for DTSP based line over OTSP based line. This has been occurred due to the reduction of effective conducting surface area and hence, the surface current density distribution along the line has been diminished. Figs. 4.75(a)-(d) show the variation of R (KΩ), C (pF), L (nH) and f_0 (GHz) for a T-shaped spur-line with incremental length ratio L_{sp}/L. It has been observed that resistance varies asymmetrically due to the variation of the effective surface area of the conductor.

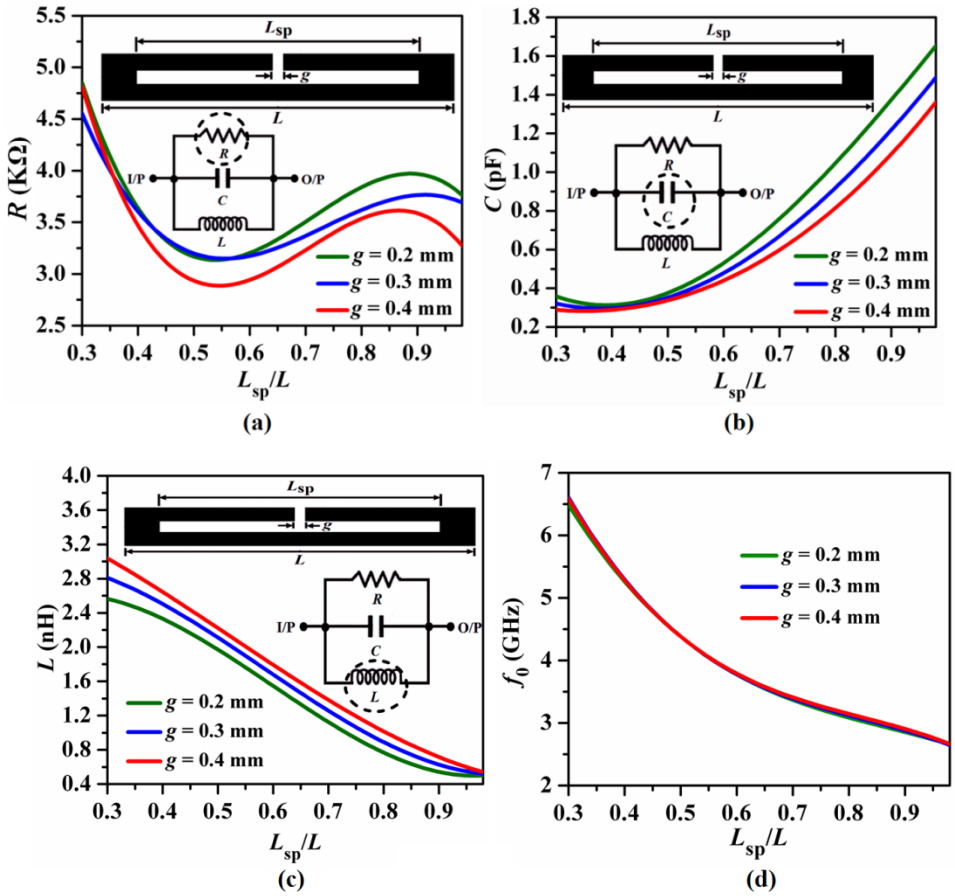

Fig. 4.75. Variation of (a) R (KΩ), (b) C (pF), (c) L (nH), and (d) f_0 (GHz) for a T-shaped spurline with incremental length ratio L_{sp}/L.

The value of C increases exponentially due to the additional cross-couplings in the slot. The value of L decreases exponentially due to the reduction of the width of the line and f_0 decreases exponentially due to the increment of the effective electrical path of the spurline. From the above study, it can be concluded that the OTSP based line has exhibited more improvement in the attenuation level at the resonant frequency over the DTSP based line. However, the selectivity of the passband has been improved significantly for the DTSP based line. Accordingly, these unique features of T-shaped spurline have been utilized for a folded hairpin-line cell to design fourth-order fitter as discussed in the next section.

4.4.2. Resonance Characteristics of Unit FHL Cell with T-Spurline

The structures of a folded hairpin line cell with three different types of T-shaped spurlines introduced in the coupling arm (right-side) are shown in Figs. 4.76(a)-(c). The spurlines have been named as outer T-shaped (OTSP), inner T-shaped (ITSP), and double T-shaped (DTSP) according to their locations. The resonant characteristics of the unit FHL cell with different T-shaped spurlines have been studied in Fig. 4.77.

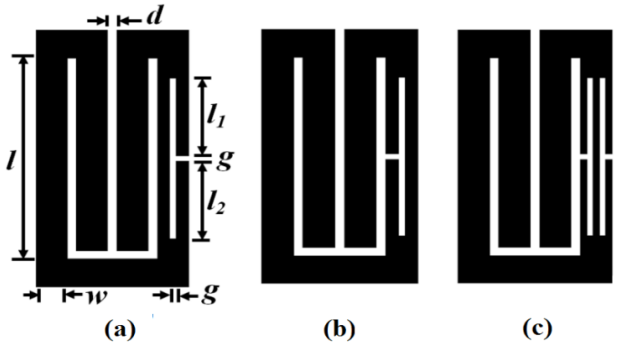

Fig. 4.76. Layout of unit folded hairpin-line cell with spur-lines: (a) OTSP, (b) ITSP, and (c) DTSP.

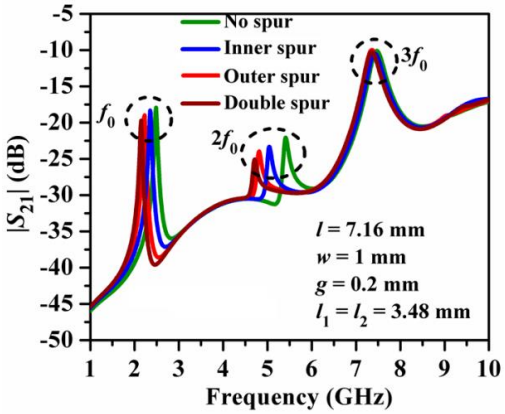

Fig. 4.77. Resonant characteristics of the simulated $|S_{21}|$ (dB) plots for a unit FHL cell with different types of T-spurline.

The dimensions of the unit FHL cells has been chosen as l = 7.16 mm, w = 1 mm, d = 0.3 mm, g = 0.3 mm for OTSP and ITSP cases and g = 0.2 mm for DTSP case. It has been observed that the attenuation levels of the second harmonic frequency $2f_0$ have been degraded for all the cases with a minimum for DTSP based FHL cell. However, the spurline has a minimum effect on the third harmonic frequency $3f_0$. Moreover, the fundamental frequency, f_0 has been shifted to a lower frequency region due to the increase in the effective electrical length of the line due to the defected microstrip slot. The equivalent lumped elements circuit of a unit FHL cell with OTSP based and DTSP based spur-line has been depicted in Figs. 4.78(a)-(b). The right arm of the FHL cell has been modified by the equivalent RLC parallel resonant circuit of the outer T-shaped spurline as shown in Fig. 4.78(a). It has been noted from Fig. 4.78(b) that two OTSP based spurline OTSP-L and OTSP-R have been connected in parallel to obtain a DTSP-based spurline circuit. Table 4.6 lists the values of the lumped elements. The value of the resistor has been calculated as R_{sp} = 3.448 kΩ. The comparisons between the EM simulated and the circuit simulated plots of $|S_{21}|$ (dB) for unit FHL cell with OTSP and DTSP based spurline in Figs. 4.79(a)-(b) respectively.

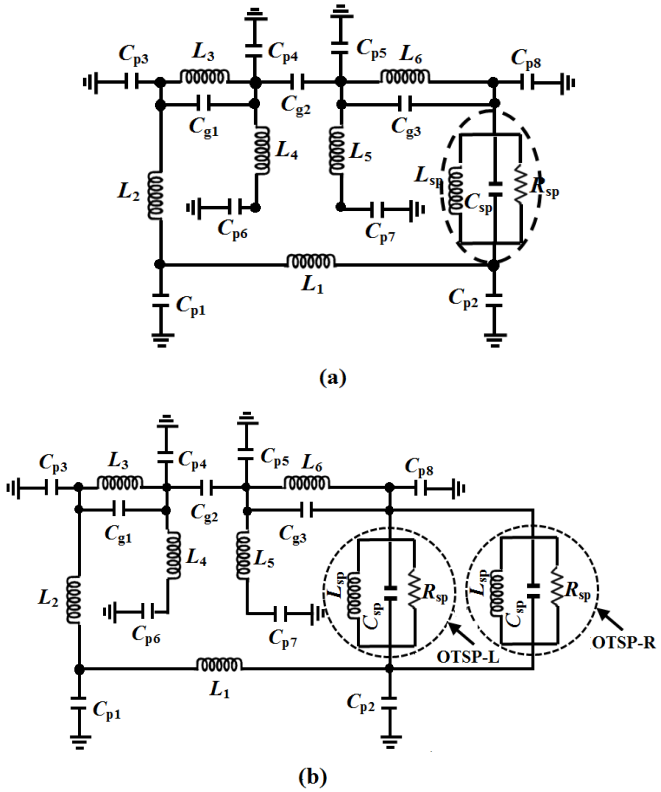

Fig. 4.78. Equivalent lumped elements circuit of a unit FHL cell with T-shaped spurline: (a) OTSP based, (b) DTSP based line.

Table 4.6. Values of the equivalent lumped elements of the unit FHL cell with T-spurline.

Inductors (nH)		**Capacitors (pF)**	
L_1	2.426	$C_{p1} = C_{p2}$	0.167
L_2	3.011	$C_{p3} = C_{p8}$	0.287
$L_3 = L_6$	1.169	$C_{p4} = C_{p5}$	0.083
$L_4 = L_5$	3.685	$C_{p6} = C_{p7}$	0.275
L_{sp}	2.305	$C_{g1} = C_{g2} = C_{g3}$	0.015
		C_{sp}	1.738

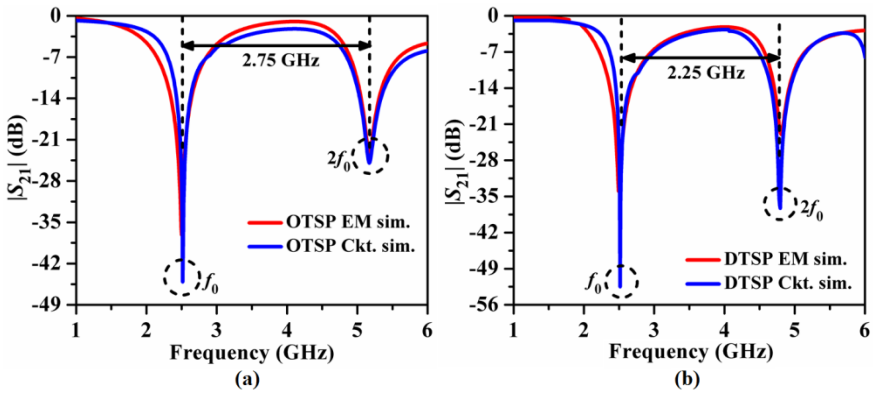

Fig. 4.79. Comparison of EM simulated vs. circuit simulated $|S_{21}|$ (dB) plots of a unit FHL cell with (a) OTSP based and (b) DTSP spurline.

It has been observed that the stopband attenuation level has been degraded more for DTSP based spur-line than OTSP based line. However, the FHL cell with DTSP based spur-line has been exhibited narrow 3 dB bandwidth along with steeper skirt selectivity of the bandstop response. Moreover, the attenuation level at $2f_0$ has been increased due to the additional inductive and capacitive effects of the DTSP based FHL cell. The distributions of surface current vectors for the unit FHL cell with OTSP and DTSP based spurline have been explored in Figs. 4.80(a)-(b). It has been revealed that the surface current vectors are highly concentrated in the thin and narrow strip of the spurline.

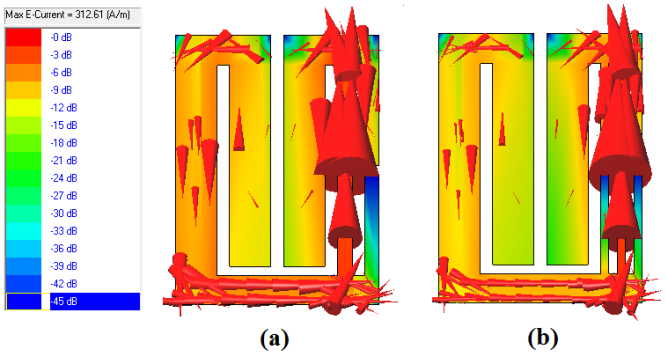

Fig. 4.80. Distribution of surface current for a unit FHL cell with (a) OTSP based spurline, (b) DTSP based spurline at f_0 = 2.5 GHz.

However, the strength of the current vectors become minimum at the open ends of the spurline as desired rom this study of FHL cell with T-shaped spurline, it has been concluded that both DTSP and OTSP spurline can suppress the higher-order harmonics of the hairpin-line due to its bandstop behavior.

4.4.3. Resonance Characteristics of Pair of FHL Cells with T-Spurline

The study has been extended further for the pair of FHL cells with two types of spurline OTSP and DTSP. The layouts of the OTSP and DTSP based pair of FHL cells are highlighted in Fig. 4.81(a) and Fig. 4.82(a) respectively. The dimensions of the pair of the FHL cells are the same as those for the unit FHL cell. For the dimensions of the spurline, the value of the open-end gap and the slot gap has been chosen uniformly as 0.3 mm. Accordingly, the length of the spurline has been incremented to study the effects of spurline's slow-wave nature and bandstop properties on the wideband resonant characteristics of the pair FHL cells as illustrated in Fig. 4.81(b) and Fig. 4.82(b) respectively.

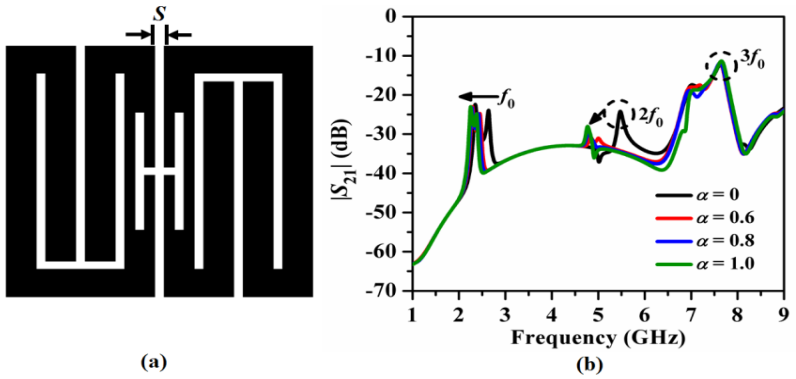

Fig. 4.81. (a) Layout and (b) resonant characteristics of the simulated $|S_{21}|$ (dB) plots for a pair of FHL cells with OTSP based spurline.

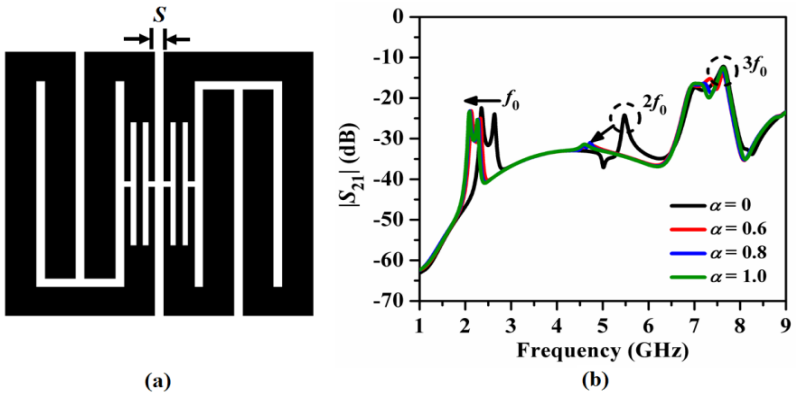

Fig. 4.82. (a) Layout and (b) resonant characteristics of the simulated $|S_{21}|$ (dB) plots for a pair of FHL cells with DTSP based spurline.

It has been observed that maximum suppression of the second harmonic's attenuation level has been achieved at α = 0.6 for OTSP case and at α = 0.8 for DTSP case. However, for both the cases there are negligible effects on $3f_0$. Accordingly, Fig. 4.83(a) illustrates the effects of different T-spurline combinations on the even- and odd-mode resonant frequencies f_e and f_o for a pair of FHL cells in the passband. It has been observed that the bandwidth δf greatly reduces with spurline due to the phase velocity compensation between the even- and odd-mode. Accordingly, the variation of f_e and f_o with incremental values of α has been explored in Fig. 4.83(b). It has been observed clearly that the gap between f_o and f_e i.e. Δf_s has been reduced as the value of α increases, justifying the modal phase velocity compensation. For more justification, the vector surface current density distribution profile for the pair of FHL cells at f_e = 2.28 GHz and f_o = 2.46 GHz for OTSP case with α = 0.6 has been demonstrated in Figs. 4.84(a)-(b). It has been observed that the current vectors are propagating unidirectional for even-mode and in reverse direction for odd-mode as expected.

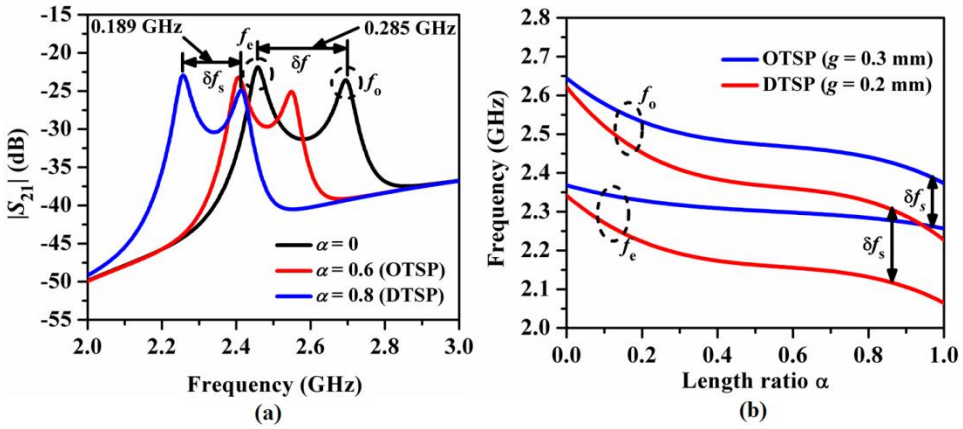

Fig. 4.83. (a) Comparison of passband resonant frequencies f_e and f_o of the simulated $|S_{21}|$ (dB) and (b) variation of f_e and f_o with incremental values of α for a pair of FHL cells without spurline and T-spurline.

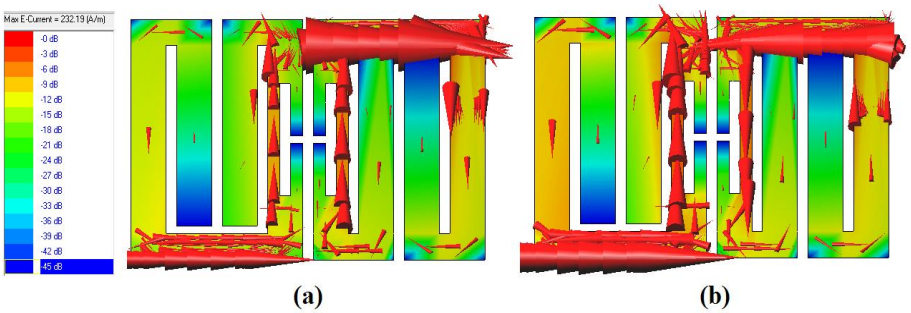

Fig. 4.84. Distribution of surface current for a pair FHL cell with (a) OTSP based spurline, (b) DTSP based spurline at f_0 = 2.5 GHz.

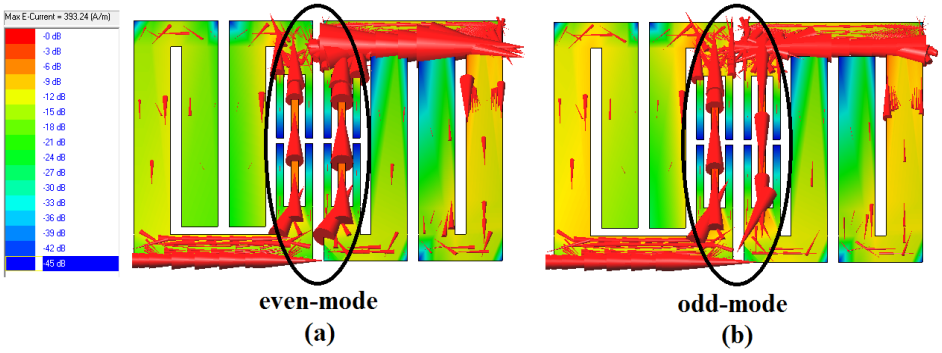

Fig. 4.85. Distribution of surface current for a pair FHL cell with (a) OTSP based spurline, (b) DTSP base spurline at f_0 = 2.5 GHz.

Accordingly, Figs. 4.85(a)-(b) elaborate the distribution of surface current vectors for the pair of FHL cells with DTSP based spurline at f_e = 2.11 GHz and f_o = 2.3 GHz. The same phenomenon as the OTSP case has been happened for the even- and odd-mode respectively. It can be concluded from this section that the T-spurline with optimum dimensions has suppressed the attenuation level at the second harmonic effectively and has a little effect on the third harmonic. Accordingly, two fourth-order folded hairpin-line bandpass filters have been designed with OTSP and DTSP type spurline having optimum dimensions in the next section.

4.4.4. Fourth-Order Folded Hairpin-Line Bandpass Filters with T-Spurline

The optimum values of length ratio $\alpha = L_{sp}/L$ for maximum second harmonic suppression have been chosen as 0.6 for outer and 0.8 for double T-shaped spur-lines from the parametric study. Accordingly, initial values of the coupling gap between the adjacent FHL cells have been obtained from the design graphs of the coupling coefficient (M) as shown in Fig. 4.86 marked by A, B for M = 0.0541 and C, D for M = 0.0397.

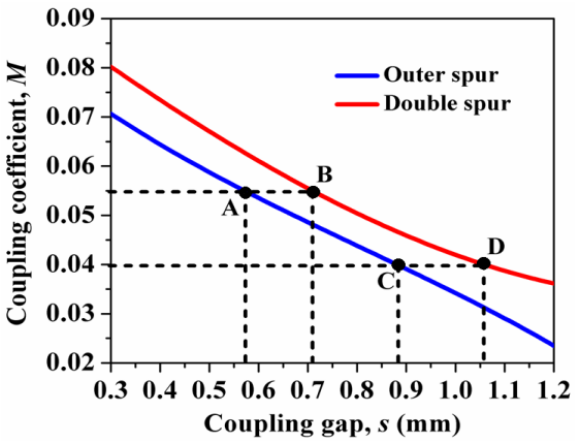

Fig. 4.86. Design curves for coupling coefficient vs. coupling gap for a pair of FHL cells with T-spurline.

The layouts of the fourth-order folded filters with OTSP and DTSP are shown in Figs. 4.87(a)-(b) respectively. The sizes of the designed filters are $0.49\lambda_g \times 0.12\lambda_g$ and $0.49\lambda_g \times 0.11\lambda_g$ respectively. Size reductions of 46% have been achieved for both the filters. The equivalent lumped elements circuits of the filters have been modeled by cascading the circuits of Fig. 4.88(a) for OTSP based and Fig. 4.88(b) for DTSP in hybrid configuration based just like Fig. 4.66 for L-spurline. The values of the derived lumped elements for the circuits are listed in Table 4.7 with i = 1, 2, 3, 4.

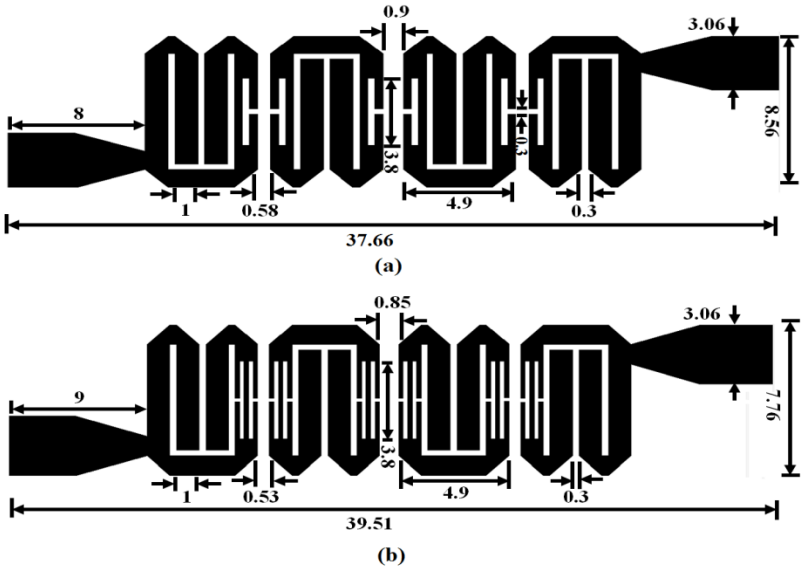

Fig. 4.87. Layouts of fourth-order folded hairpin-line filters with spur-lines: (a) OTSP based and (b) DTSP based. All dimensions are in mm.

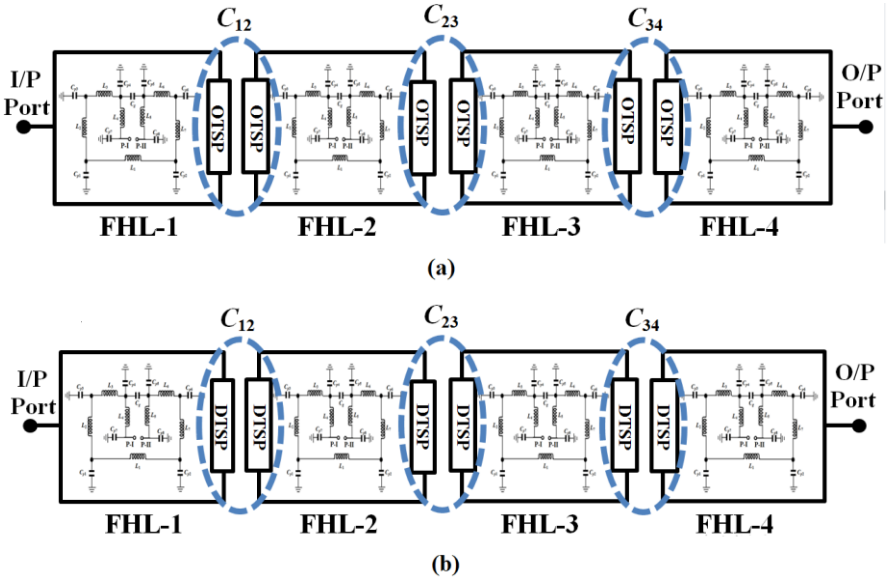

Fig. 4.88. Block diagram of the equivalent lumped elements model of the fourth-order folded hairpin-line filters with spurlines: (a) OTSP based and (b) DTSP based.

Table 4.7. Values of the equivalent lumped elements of the unit FHL cell with T-spurline for fourth-order filter.

Inductors (nH)		**Capacitors (pF)**	
L_{i1}	1.849	$C_{pi1} = C_{pi2}$	0.44
$L_{i2} = L_{i7}$	1.916	$C_{pi3} = C_{pi8}$	0.324
$L_{i3} = L_{i6}$	1.318	$C_{pi4} = C_{pi5}$	0.101
$L_{i4} = L_{i5}$	1.481	$C_{pi6} = C_{pi7}$	0.187
L_{sp} (OTSP)	2.305	$C_{gi1} = C_{gi2} = C_{gi3}$	0.033
L_{sp} (DTSP)	1.452	$C_{12}=C_{34}$	0.183
R_{sp} = 3.448 kΩ (for both)		C_{23}	0.163
		C_{sp} (OTSP)	1.738
		C_{sp} (DTSP)	1.562

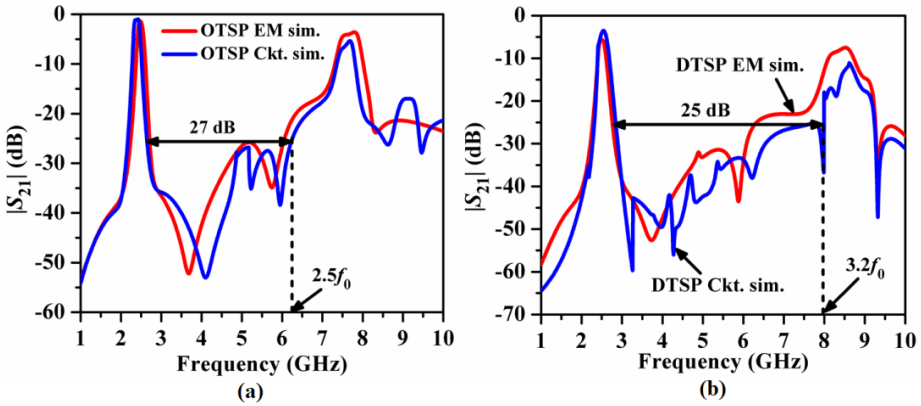

Fig. 4.89. Comparison of $|S_{21}|$ (dB) plots between EM simulation and circuit simulation for a fourth-order folded filters with (a) OTSP and (b) DTSP based spurline.

Subsequently, the $|S_{21}|$ (dB) plots have been compared between the EM-simulation and the circuit-simulation in IE3D solver with excellent agreement as highlighted in Figs. 4.89(a)-(b) respectively. It has been observed that the plots are in good agreement to each other, reflecting the superiority of DTSP based filter over OTSP based filter regarding the stopband rejection bandwidth.

4.4.4.1. Fabricated Prototypes

Accordingly, two prototypes of the proposed filters have been fabricated on FR4 laminate as shown in Figs. 4.90(a)-(b).

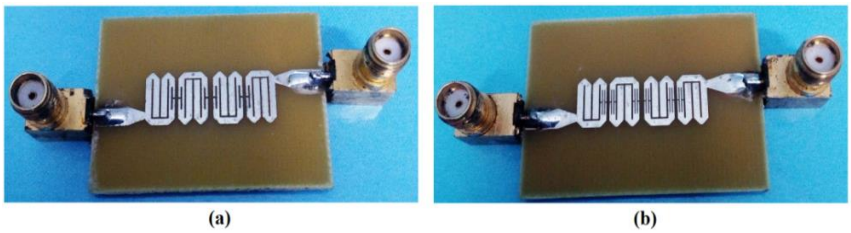

Fig. 4.90. Fabricated prototypes of the fourth-order filters: (a) OTSP based and (b) DTSP based [14].

4.4.4.2. Comparison of EM simulation vs. Measurement Results

The experiment has been carried out in the Agilent N9928A vector network analyzer in the similar way of 3.14.4.1 and the measured vs. simulation $|S_{21}|$ (dB) plots have been highlighted in Figs. 4.91(a)-(b).

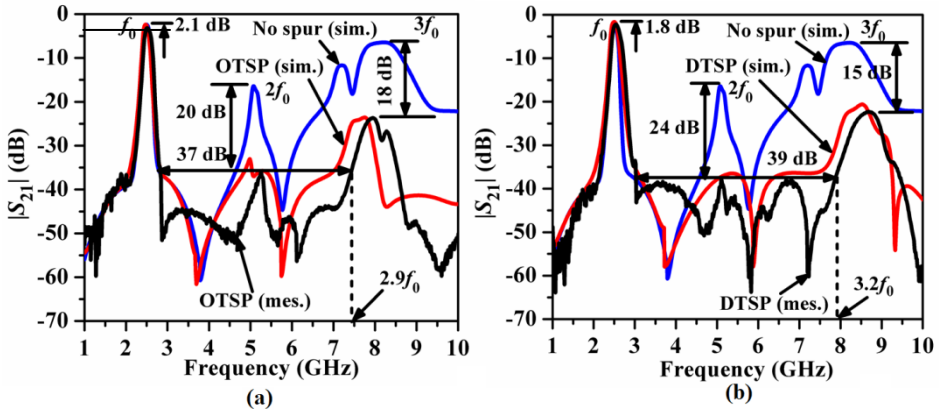

Fig. 4.91. Comparison between simulated vs. measurements results of $|S_{21}|$ (dB) for fourth-order folded filters with (a) DTSP based and (b) OTSP based spurlines.

An extended stopband of rejection levels of 37 dB from 2.87 GHz to 7.4 GHz i.e., up to $2.9f_0$ and 39 dB from 3.0 GHz to 7.8 GHz i.e., up to $3.2f_0$ have been obtained for the OTSP and DTSP based fitter respectively. The second harmonic's attenuation levels have been suppressed by 20 dB and 24 dB for OTSP and DTSP based filter respectively over the folded filter without spurline. Moreover, the third harmonic's attenuation levels have been suppressed by 18 dB and 15 dB for OTSP and DTSP based filter respectively compared to the folded filter without spurline. The measured insertion loss becomes 2.1 dB for OTSP based filter and 1.8 dB for DTSP based filter. The measured insertion loss for the filters becomes quite large (< 2.2 dB) due to the lossy FR4 substrate material and tolerances incurred near the SMA connectors and spectrum analyzer during measurement. The comparison between measured and simulated $|S_{11}|$ (dB) pots has been illustrated in Figs. 4.92(a)-(b). The return losses become more than 30 dB and 18 dB for OTSP and DTSP based filters. Fig. 4.93 compares the measured group delay plots of $|S_{21}|$ in ns for the fabricated filters, exhibiting symmetry at the narrow passband edges as an improvement over conventional folded filters without spurline. The distribution of surface current has been explored in Figs. 4.94(a)-(b) and Figs. 4.95(a)-(b) for the OTSP and DTSP based filters at f_0 = 2.5 GHz and $2f_0$ = 5.0 GHz respectively.

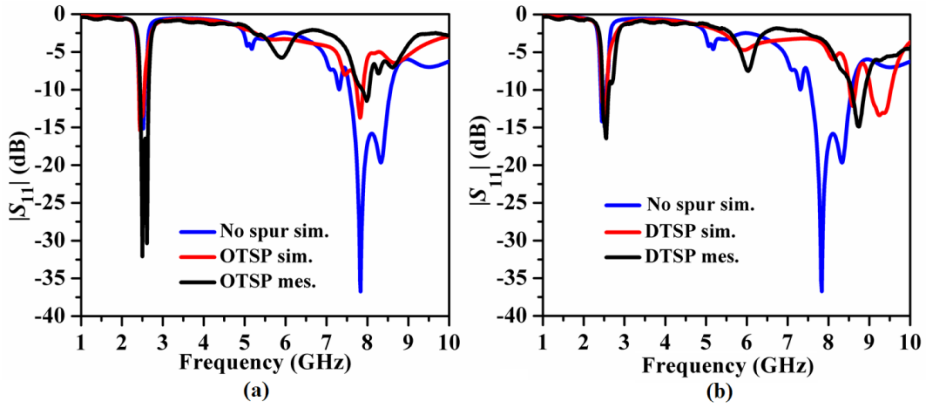

Fig. 4.92. Comparison between simulated vs. measurements results of $|S_{11}|$ (dB) for fourth-order folded filters with (a) DTSP based and (b) OTSP based spurlines.

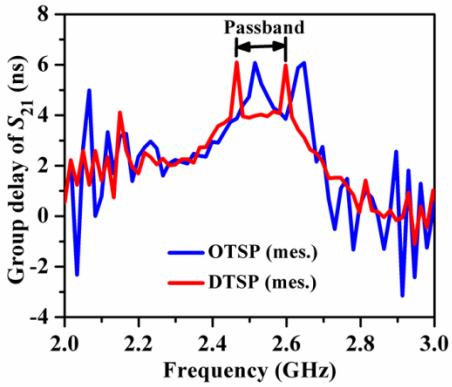

Fig. 4.93. Comparison between measured group delay (ns) of $|S_{21}|$ for fourth-order folded filters with T-spurline.

It has been observed from the plots that the strength of the surface current becomes strong at f_0 due to the passband and very week at $2f_0$ due to the suppression of the attenuation level by spurline. From this section it can be concluded that the T-spurline has the ability to suppress the harmonics significantly up to $3f_0$. However, for WLAN systems an extended stopband greater than $4f_0$ with suppression level better than 35 dB are utmost requirements.

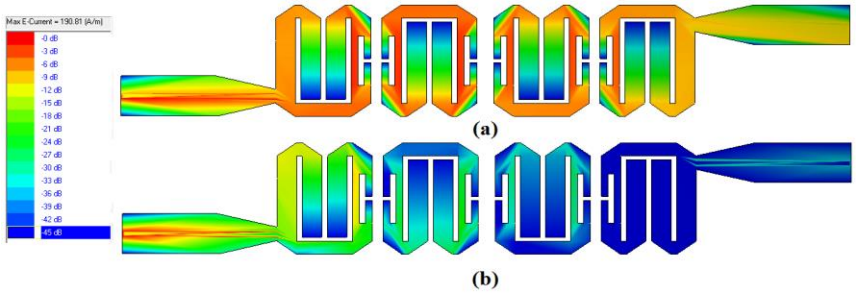

Fig. 4.94. Distribution of surface current for the fourth-order folded filter with OTSP based spurline: (a) at f_0 = 2.5 GHz and (b) $2f_0$ = 5.0 GHz.

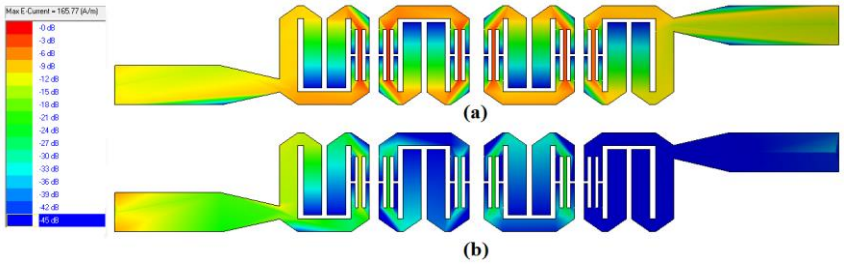

Fig. 4.95. Distribution of surface current for the fourth-order folded filter with DTSP based spurline: (a) at f_0 = 2.5 GHz and (b) $2f_0$ = 5.0 GHz.

Thus, the study of spurline has been extended further in the next section by replacing the conventional L-spurline or T-spurline by meander spurline.

4.5. Fourth-Order Folded Hairpin-Line Bandpass Filters with Meander Spurline

4.5.1. Resonance Characteristics of Meander Spurline

In order to provide more slow-wave resonance behavior, the L-shaped conventional spurline has been modified to meander spurline as shown in Fig. 4.96(a). The meander spurline is constructed by cascading periodic alternate corrugations along the line and it is characterized by slot length l_T, slot width w_T, slot gap g, periodicity p, and overall spur-line length l_{sp}. Fig. 4.96(b) shows the equivalent lumped elements circuit diagram of the meander spurline.

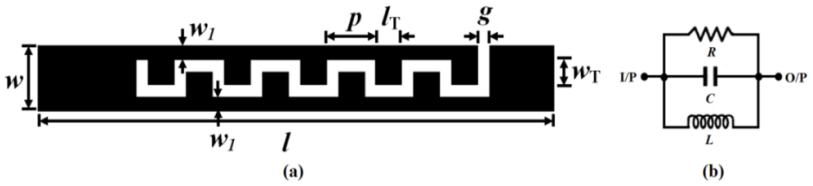

Fig. 4.96. Meander spurline: (a) layout diagram and (b) equivalent lumped elements circuit.

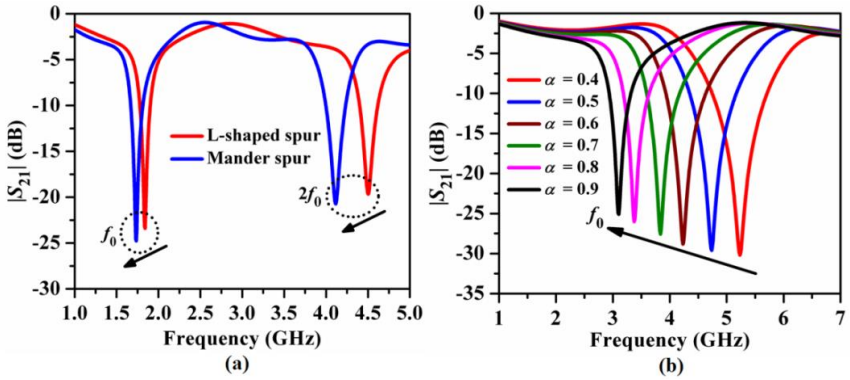

Fig. 4.97. (a) Comparison of simulated $|S_{21}|$ (dB) plots between L-shaped and meander spurline and (b) variation of f_0 of simulated $|S_{21}|$ (dB) plots with different slot number N of the meander spurline.

The comparison of $|S_{21}|$ plots between the L-shaped and the meander spurlines has been highlighted in Fig. 4.97(a). It has been observed that the meander spurline has exhibited a more sharp and narrow stopband with the resonance frequency of f_0 = 1.75 GHz (attenuation level of 25 dB) and $2f_0$ = 4.15 GHz (attenuation level of 22 dB) due to its increased slow-wave property over L-spurline. Moreover, f_0 and $2f_0$ have been shifted to lower frequencies due to the increment of the effective electrical length of the line. Accordingly, the overall length of the line is to be reduced to tune the resonant frequency at f_0 = 2.5 GHz. Hence, the overall size of the final filter based on the meander spurline will be reduced compared to the filter based on the L-spurline. This justifies the effectiveness of the meander spurline over the L-spurline to design narrowband, compact and wide stopband filters. The variation of f_0 for the transmission characteristics of the meander spurline for different values of spurline length ratio, $\alpha = l_{sp}/l$ has been highlighted in Fig. 4.97(b). It has been observed that the resonant frequency f_0 has been shifted towards a lower frequency along with a decrement in the rejection level. This is due to the fact that the velocity of the EM wave gradually decreases as the wave propagates through the zigzag meander spur-line structure. Accordingly, the effect of the variation of slot gap's dimension on the bandwidth of the transmission characteristics, $|S_{21}|$ (dB) has been compared in Fig. 4.98(a). It can be concluded that the bandwidth of the stopband has been reduced as the slot gap's dimension decreases due to the increase of the signal coupling in the slot. This justifies the effectiveness of the meander spurline over the L-spurline for the improvement in the filter stopband characteristics. Subsequently, the equivalent circuit for the resonant characteristics of the meander spurline has been exhibited by a parallel *RLC* resonant circuit (Fig. 4.96(b)).

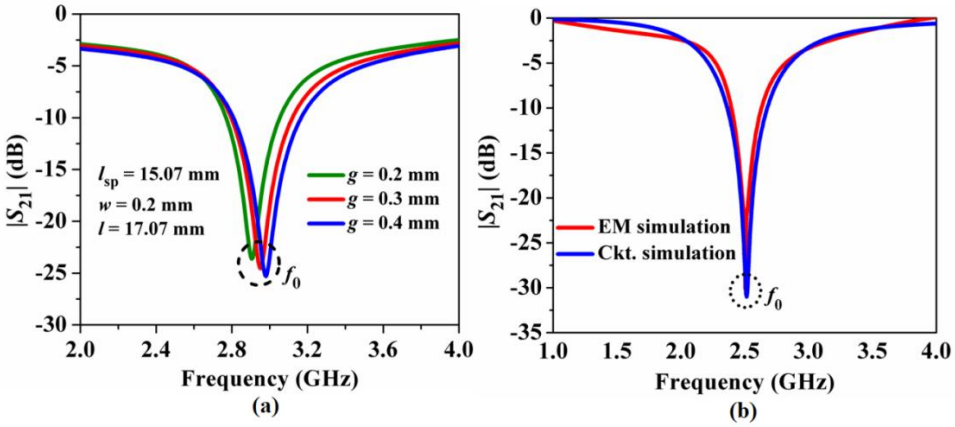

Fig. 4.98. (a) Variation of stopband bandwidth with different slot gap g (mm) for the simulated $|S_{21}|$ (dB) plots, and (b) comparison between EM simulation and circuit simulation of meander spurline.

In the equivalent circuit R has been included for the radiation effect and conductor loss, the slot is characterized by the inductance and the coupling gap due to the slot is modelled by the capacitance. The transmission line theory and the spectral domain approach have been employed to calculate the equivalent circuit parameters. The maximum value of attenuation, $|S_{21}|$ (dB) at the resonant frequency of 2.5 GHz corresponding to the meander spurline has been obtained as 32 dB from the EM simulation plot in IE3D EM solver as shown in Fig. 4.98(b). Accordingly, by following the Equation 33-35 [11] the circuit parameters are calculated as L = 2.3049 nH, C = 1.738 pF, and R = 3.448 kΩ. An admirable amount of agreement between the circuit simulation and the EM simulation has been achieved in Fig. 4.98(b). It has been clearly observed that a sharp transmission zero has been obtained at f_0 = 2.5 GHz as required. The expression of the transmission zero frequency f_{z1} and f_{z2} for the equivalent *RLC* circuit has been formulated in (36) - (38) by following the method as mentioned in [15].

$$\frac{v_o}{v_o} = \frac{r(LCRs^2 + Ls + R)}{LCRrs^2 + L(r+R)s + Rr} \tag{36}$$

$$f_{z1} = \frac{1}{2\pi}\left(\frac{L - \sqrt{L^2 - 4LCR^2}}{2LCR}\right) \tag{37}$$

$$f_{z2} = \frac{1}{2\pi}\left(\frac{L + \sqrt{L^2 - 4LCR^2}}{2LCR}\right) \tag{38}$$

In (4) r refers to the matching resistance, f_{z1} and f_{z2} are the corresponding transmission zeros. The value of f_{z1} has been calculated as 2.515 GHz by putting the values of R, L and C, which matches perfectly with the EM simulated result. The calculation of $f_{z2} = 2f_0$ has not been considered for the study. Fig. 4.99(a) illustrates the variation of f_{z1} (GHz) with the variation of L (nH) for constant values of R and C. It has been observed that the resonant frequency decreases exponentially for incremental L. Moreover, the value of L has been obtained as 2.32 nH corresponding to f_0 = 2.5 GHz (marked as A), which has an error of 0.66% compared to the optimized value of L (2.3049 nH) obtained in the EM simulation. Similarly, the variation of f_{z1} (GHz) with the variation of C (pF) for constant values of R and L has been highlighted in Fig. 4.99(b). It has been noticed that f_{z1} decreases exponentially for incremental C. The value of C has been obtained as 1.72 pF corresponding to f_0 = 2.5 GHz (marked as B), which has an error of 1.04% compared to the optimized value of C i.e., 1.738 nH obtained in

the EM simulation. In this context, the interdependence of the lumped elements of the meander spurline has been studied in Figs. 4.100(a)-(d). It has been revealed from Fig. 4.100(a) that the equivalent resistance R (KΩ) varies asymmetrically with incremental values of the spurline length ratio α due to the decrease of the effective surface area of the conductor.

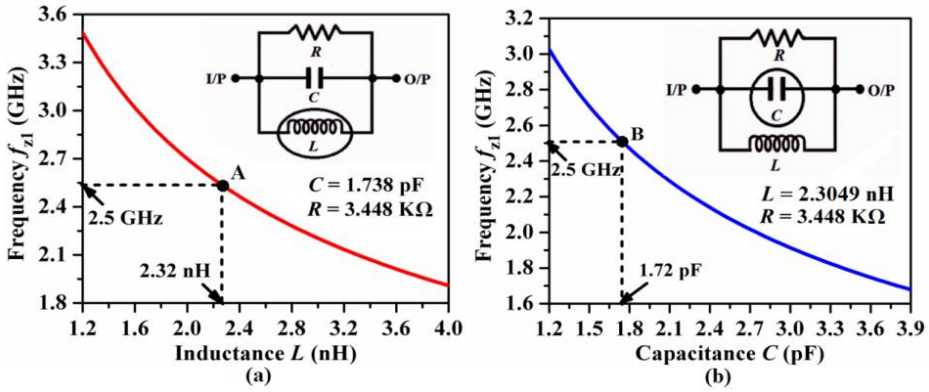

Fig. 4.99. Variation of resonant frequency f_{z1} (GHz) with (a) inductance L (nH) and (b) capacitance C (pF) for the equivalent meander spurline circuit.

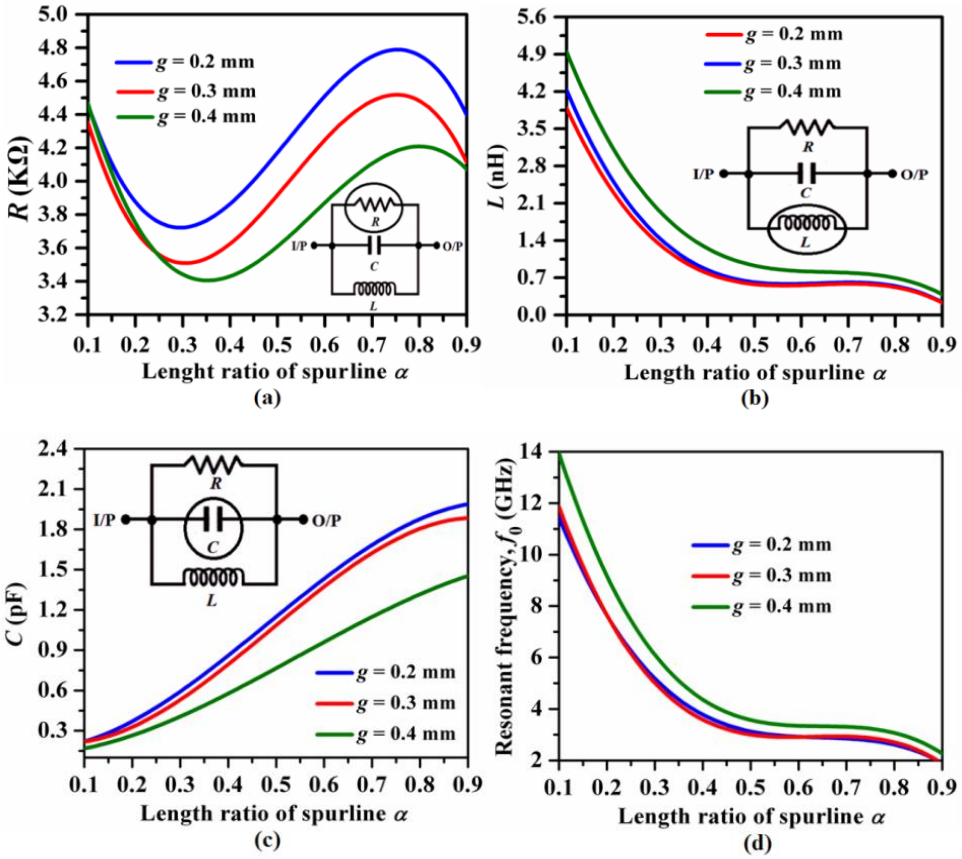

Fig. 4.100. (a) Variation of R (KΩ), (b) variation of L (nH), (c) variation of C (pF), and (d) variation of f_0 (GHz) with incremental value of α, l = 17.07 mm, w = 1 mm, w_1 = 0.2 mm, p = 0.05l.

Accordingly, the values of the equivalent inductance L (nH) have been decreased exponentially with the incremental values of α as shown in Fig. 4.100(b) due to the reduction of the width of the microstrip line and the increment of the effective electrical length. Likewise, the values of the equivalent capacitance, C (pF) have been increased exponentially with the incremental values of α as elaborated in Fig. 4.100(c) due to the additional cross-coupling between the two arms of the spurline. Moreover, the resonant frequency f_0 has been decreased exponentially with the incremental value of α in Fig. 4.100(d). This is because the electrical length of the spurline has been increased due to the increment of the slot length. The slow-wave property of the L-spurline and the meander spurline has been justified further by the surface current distribution at f_0 = 2.5 GHz as shown in Figs. 4.101(a)-(b). The surface current vectors are in opposite direction and are concentrated more in the narrow line segments (marked by *a* and *b*) of the meander spurline compared to the less number of vectors propagated for L-spurline. It justifies the improved slow-wave property of meander spurline over L-spurline. Accordingly, such improved bandstop behavior and the circuit size reduction feature of the meander spurline have been utilized for a unit folded hairpin-line bandpass filter to obtain a wide stopband by suppressing the spurious harmonics as discussed in the next section.

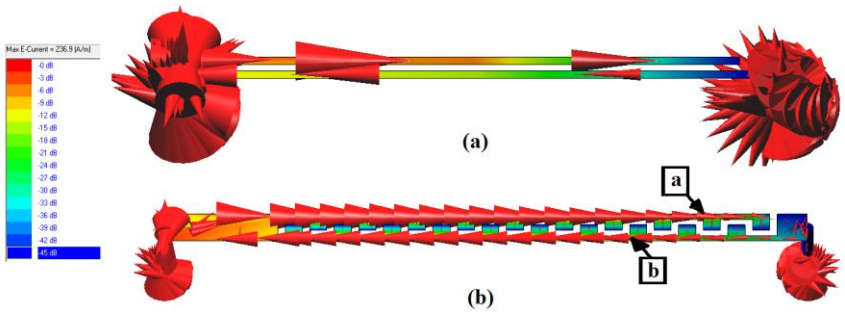

Fig. 4.101. Surface current distribution of spur-line: (a) Conventional L-shaped spurline, and (b) meander spurline.

4.5.2. Resonance Characteristics of Unit Folded Hairpin-Line Cell with Meander Spurline

The layouts of the folded hairpin-line (FHL) cell with the conventional L-shaped spurline and the meander spurline introduced in the right-side coupling arm are shown in Figs. 4.102(a) and (b) respectively. Accordingly, the effects of the L-spurline and the meander spurline on the resonant characteristics of the unit FHL cell have been studied in

Fig. 4.102(c). The dimensions of the unit FHL cell with L spurline tuned at f_0 = 2.5 GHz have been determined as l_1 = 8.51 mm, l_2 = 2.3 mm, d = 0.3 mm, w_1 = 1.0 mm, g = 0.2 mm, w = 0.4 mm, l_{sp} = 6.31 mm, α = 0.74. The overall size of the unit FHL cell with the L-spurline is 8.51 mm × 4.9 mm i.e., 0.124λ_g × 0.072λ_g and accordingly, size reduction of 6.97% has been achieved compared to unit FHL cell without any spurline (8.51 mm × 4.9 mm i.e., 0.134λ_g × 0.072λ_g). The dimensions for the meander spurline based unit FHL cell have been tuned to f_0 = 2.5 GHz optimally and determined as l_1 = 7.11 mm, l_2 = 2.3 mm, d = 0.3 mm, w_1 = 1.0 mm, g = 0.2 mm, l_{sp} = 4.91 mm, p = 0.6 mm, l_T = 0.2 mm, and w_T = 0.4 mm, number of corrugations, N = 13, α = 0.69. The overall size of the unit FHL cell with meander spurline is 7.11 mm × 4.9 mm i.e., 0.119λ_g × 0.072λ_g and accordingly size reductions of 22.28% and 16.45% have been achieved compared to unit FHL cell without any spurline and with L- spurline respectively.

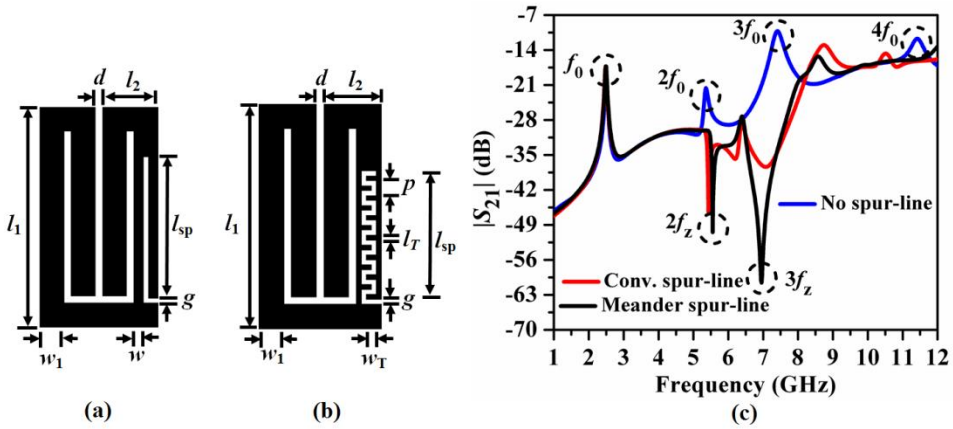

Fig. 4.102. (a) Layout of unit FHL cell with L spurline, (b) meander spurline, and (c) comparison of simulated $|S_{21}|$ (dB) plots of a unit FHL cell with L- and meander spurline.

From Fig. 4.102(c) it has been revealed that two sharp transmission zeros $2f_z$ and $3f_z$ have been with the attenuation levels of 53 dB and 60 dB at 5.5 GHz and 7 GHz compared to FHL cell with the L- spurline. The transmission zeros have been occurred in the stopband due to the bandstop characteristics of the meander spurline, exhibiting more slow-wave properly as discussed in the previous section. However, for the L-spurline, the wave propagation has not been affected much due to the straight microstrip slot. Hence, it has been concluded that the meander spurline has the following advantages over the conventional spurline such as it provides (1) narrow bandwidth, (2) more slow-wave property, (3) more attenuation levels at the transmission zeros in the stopband, and (3) exhibits more compact size. Such properties of

the meander spurline make it a very attractive element to design a compact, narrowband and wide stopband bandpass filter suitable for modern wireless and satellite communication. Accordingly, different parametric studies for meander spurline-based unit FHL cells have been performed as follows. The comparison of $|S_{21}|$ (dB) for a unit FHL cell with a different number of periodic corrugations N of the meander spurline has been illustrated in Fig. 4.103(a). The attenuation levels at $2f_0$ and $3f_0$ have been degraded gradually as N increases due to the zigzag slow-wave structure of the meander spurline. Accordingly, maximum harmonic suppression has been obtained for N = 13 chosen as the optimum value. However, the attenuation levels have been increased for N = 14 due to the additional cross-coupling between the adjacent corrugations of the meander spurline after a certain length.

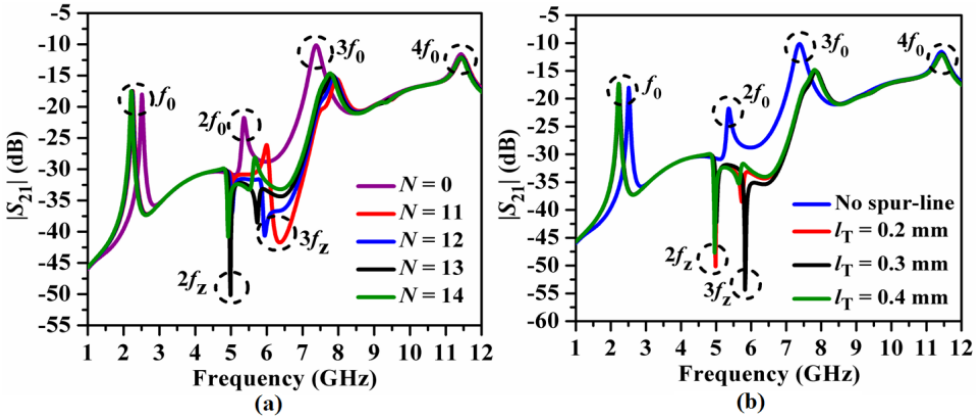

Fig. 4.103. Comparison of simulated $|S_{21}|$ (dB) plots of a unit FHL cell with meander spurline for (a) different number of corrugations N and (b) different values of l_T.

Subsequently, the optimum value of l_T has been chosen as 0.3 mm from Fig. 4.103(b) as two sharp transmission zeros peaks ($2f_z$ and $3f_z$) along with the stopband rejection level of 30 dB up to 7 GHz have been obtained for this case. The equivalent lumped elements circuit of a unit FHL cell with meander spurline has been depicted in Fig. 4.104(a) by following the conventional transmission line theory as mentioned in [1-2]. The right arm of the FHL cell (as highlighted by dotted circle in Fig. 4.104(a)) has been modified by the equivalent *RLC* parallel resonant circuit of the meander spurline and the corresponding lumped elements values are listed in Table 4.8. The comparisons of the EM simulated and the circuit simulated plots of $|S_{21}|$ (dB) for the unit FHL cell with and without the meander spurline have been explored in Fig. 4.104(b). The results are in excellent agreement with each other with an attenuation level of 45 dB at f_0 = 2.5 GHz.

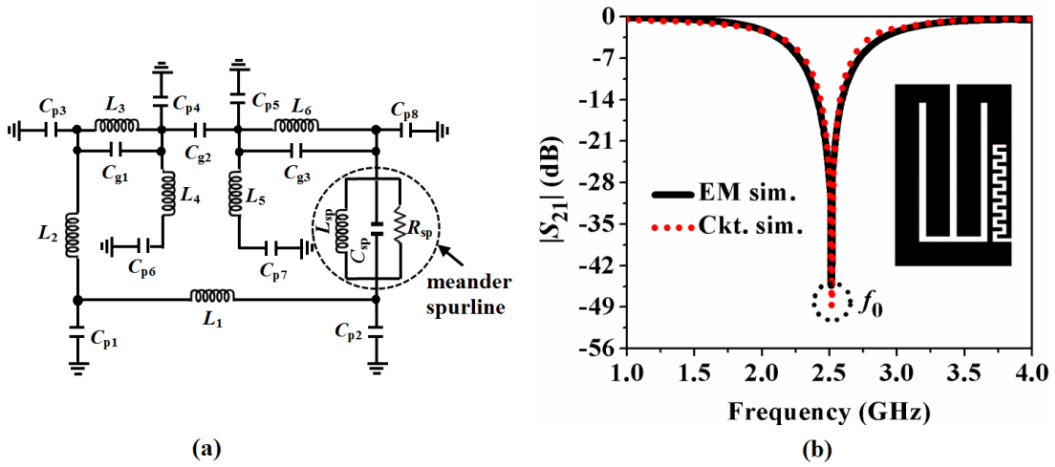

Fig. 4.104. (a) Equivalent lumped elements circuit of a unit FHL cell with meander spurline, (b) comparison between EM simulation vs. circuit simulation plots without spurline, and (c) with meander spurline.

Table 4.8. Values of the equivalent lumped elements of the unit FHL cell with meander-spurline.

Inductors (nH)		**Capacitors (pF)**	
L_1	2.426	$C_{p1} = C_{p2}$	0.167
L_2	3.011	$C_{p3} = C_{p8}$	0.287
$L_3 = L_6$	1.169	$C_{p4} = C_{p5}$	0.083
$L_4 = L_5$	3.685	$C_{p6} = C_{p7}$	0.275
$L_{sp} = 2.305$		$C_{g1} = C_{g2} = C_{g3}$	0.015
$R_{sp} = 3.448$ kΩ		C_{sp}	1.738

Moreover, the FHL cell with meander spurline exhibits narrow 3 dB bandwidth along with a steeper skirt selectivity of the bandstop response. This phenomenon has been observed due to the generation of an additional coupling region between the two arms of the meander spurline resulting in an interdigital capacitance effect. The effects of the meander spurline in the FHL cell have been further explored by the surface current vector distribution at f_0 = 2.5 GHz as highlighted in Figs. 4.105(a)-(b) by gap-coupled feeding technique [3]. It has been explored that current vectors with higher degree of strength have been concentrated through the left side thin segment (marked as *b*) of the meander spurline, representing the filter's passband. However, very small of amount of current vectors have been propagated through the right side thin segment (marked as *c*). Accordingly, Figs. 4.106(a)-(c) highlight the surface current distribution for unit FHL cells at f_0, $2f_0$ and $3f_0$. It has been shown that strong current has been flown at f_0 = 2.5 GHz (passband), very weak current has been travelled at $2f_0$ = 5.0 GHz and $3f_0$ = 7.5 GHz, representing the wide stopband and suppression of harmonics by the meander spurline.

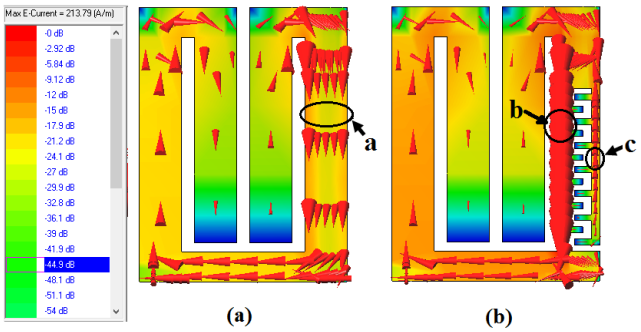

Fig. 4.105. Surface current vector distribution of a unit FHL cell at f_0 = 2.5 GHz: (a) without spurline and (b) with meander spurline.

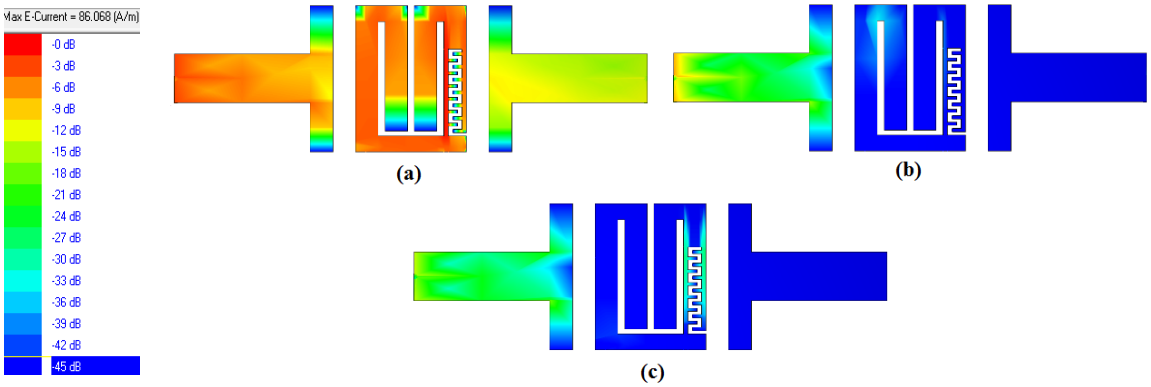

Fig. 4.106. Surface current distribution of a unit FHL cell with meander spurline at (a) f_0 = 2.5 GHz, (b) $2f_0$ = 5.0 GHz, and (c) $3f_0$ = 7.5 GHz.

This justifies the fact that the stopband suppression performance of the FHL cell has been greatly influenced by this unequal distribution of surface current. Accordingly, such unit FHL cells have been cascaded in hybrid configuration and meander spurlines have been incorporated in the coupled arms of the adjacent cells as discussed in the next section.

4.5.3. Resonance Characteristics of Pair of Folded Hairpin-Line Cells with Meander Spurline

Fig. 4.107(a) shows the layout of the pair of FHL cells with meander spurline and Fig. 4.107(b) illustrates its wideband resonance characteristics. It has been observed that the harmonics' attenuation levels have been decreased drastically by the generation of multiple transmission zeros in the stopband as the number of corrugations of the meander spurline have been increased. For further understanding the effects of spurline on the even- and odd-mode resonant frequencies f_e and f_o, a comparison of the passbands has been carried out in Fig. 4.108(a) and the variation of passband bandwidth Δf has been explored in Fig. 4.108(b)

accordingly. It has been observed from the plots that the difference between the even- and odd-mode resonant peaks i.e., $\Delta f = f_o - f_e$ has been decreased gradually with the incremental value of N. As well as the entire passband has been shifted to the lower frequency region due to the slow-wave property of the meander spurline. Moreover, the odd-mode resonant frequency peak f_o has been shifted more towards the lower frequency region compared to that of the even-mode resonant frequency peak f_{oe}. This justifies that the meander spurline has the ability to achieve modal phase velocity compensation which is the primary objective of harmonics suppression.

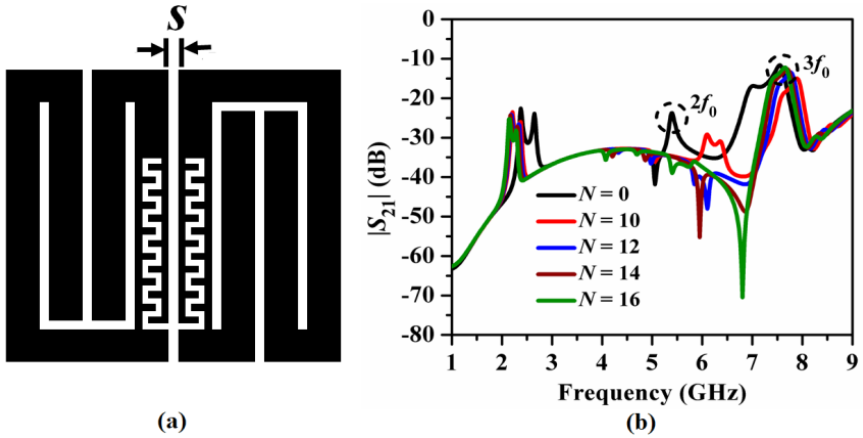

Fig. 4.107. Pair of FHL cells with meander spurline: (a) structure and (b) wideband resonance characteristics of simulated $|S_{21}|$ (dB) plots.

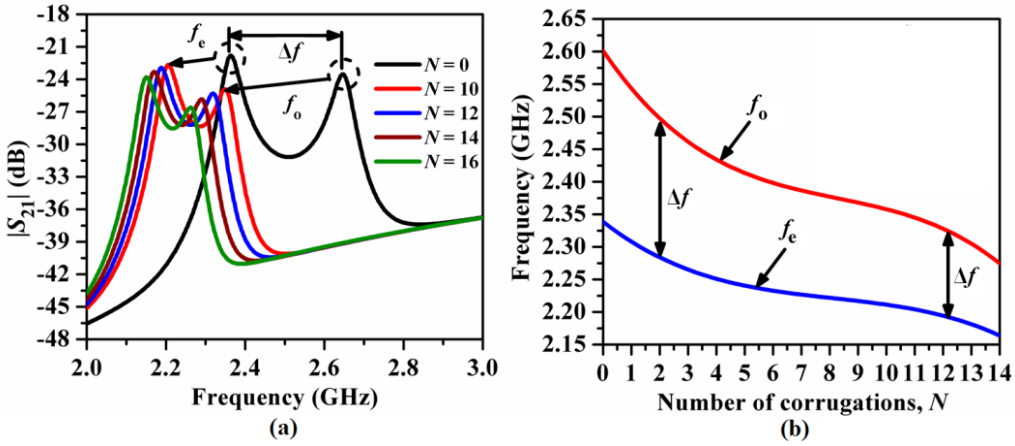

Fig. 4.108. (a) Even- and odd-mode resonance analysis of simulated $|S_{21}|$ (dB) plots for a pair of FHL cells with meander spurline and (b) variation of modal resonant frequencies with different number of corrugations N.

Subsequently, the distribution of the surface current vectors has been elaborated in Figs. 4.109(a)-(b) to illustrate the even-mode and odd-mode.

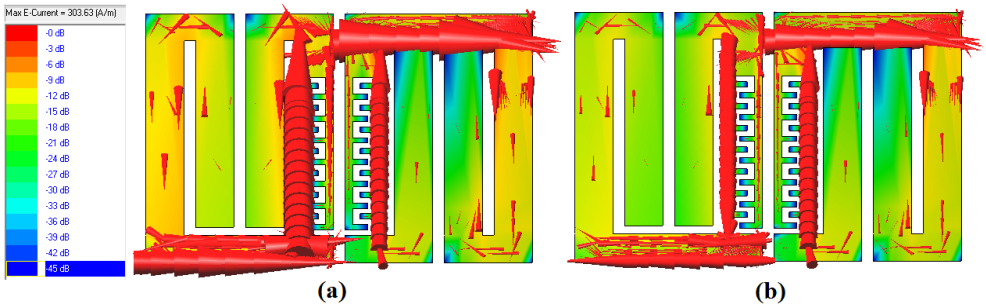

Fig. 4.109. Distribution of surface current vectors for the pair of FHL cells with meander spurline with N =14: (a) at f_e = 2.17 GHz and (b) f_o = 2.29 GHz.

It has been observed clearly that the direction of surface current is same for even-mode and opposite for odd-mode as expected. Subsequently, based on such knowledge gathered from all the studies discussed so far, fourth-order folded hairpin-line bandpass filter has been designed in the subsequent section.

4.5.4. Design of Folded Hairpin-Line Bandpass Filter with Meander Spurline

The general layout of the fourth-order folded filter with meander spur-line has been depicted in Fig. 4.110(a) and the equivalent lumped elements circuit diagram has been obtained by following the same methodology as that for L- and T- spurlines (refer Fig. 4.64 and Fig. 4.104). Accordingly, the comparison of the circuit simulated $|S_{21}|$ (dB) plots for the fourth-order folded filters with and without meander spurline. The coupling regions have been represented by the equivalent capacitances C_{12}, C_{23}, and C_{34} respectively. The values of L and C values are same as that of a unit FHL cell and the equivalent capacitance values for the coupling gaps between the adjacent FHL cells have been extracted accordingly. Fig. 4.110(b) compares the circuit simulated $|S_{21}|$ (dB) plots of fourth-order folded filter with and without meander spurline. It has been observed the second harmonic frequency $2f_0$ has been suppressed completely and three transmission zeros (marked as f_{z1}, f_{z2}, and f_{z3}) have been obtained in the stopband due to three coupling regions in the filter structure. Accordingly, the initial coupling gaps between the two adjacent FHL cells with meander spurline have been determined from the design graph of coupling coefficient vs. coupling gap in Fig. 4.111. The values of coupling gaps are extracted as s_{12} = s_{34} =1.02 mm and s_{23} = 1.57 mm for $M_{1,2} = M_{3,4} = 0.0432$, $M_{2,3} = 0.0318$ (marked as A and B).

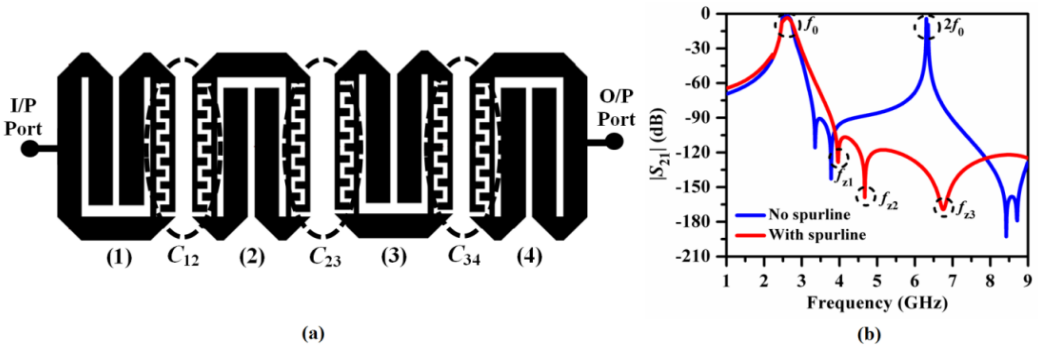

Fig. 4.110. (a) Layout of a fourth-order folded filter with meander spurline and (b) comparison of circuit simulated $|S_{21}|$ (dB) plots between fourth-order folded filters with and without meander spurline.

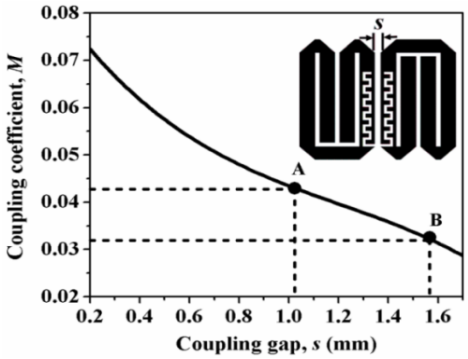

Fig. 4.111. Variation of coupling coefficient *M* vs. coupling gap *s* (mm) for a pair of FHL cells with meander spurline.

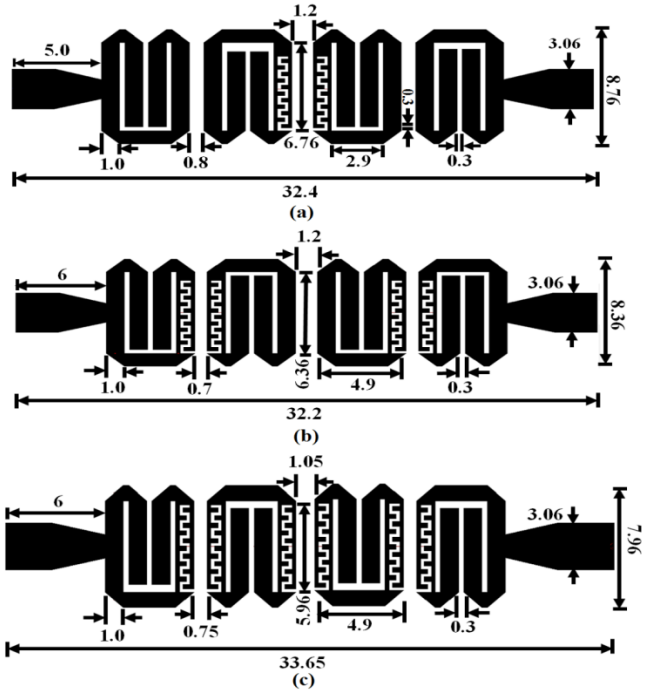

Fig. 4.112. Layouts of fourth-order folded filters with meander spurline: (a) Filter-I (middle pair with spurline, N = 14), (b) Filter-II (end pairs with spurline N = 15), and (c) Filter-III (all pairs with spurline N = 16).

Figs. 4.112(a) - (c) shows the layouts of fourth-order filters with meander spurline employed between the middle-coupled arms (Filter-I), between the end-coupled arms (Filter-II), and between all the coupled arms (Filter-III) respectively. All the dimensions of the designed filters are in mm and have been determined by tuning the filter structure at f_0 = 2.5 GHz optimally in the IE3D EM simulator. The sizes of the filters are 283.82 mm^2, 269.19 mm^2, and 267.85 mm^2 i.e., $0.47\lambda_g \times 0.13\lambda_g$, $0.47\lambda_g \times 0.12\lambda_g$, and $0.49\lambda_g \times 0.17\lambda_g$ respectively. Accordingly, size reductions of 34.61%, 37.98%, and 38.28% have been obtained compared to the conventional hairpin-line filter with the same specifications.

4.5.4.1. Fabricated Prototypes

The fabricated prototypes of the designed filters have been shown in Figs. 4.113(a)-(c).

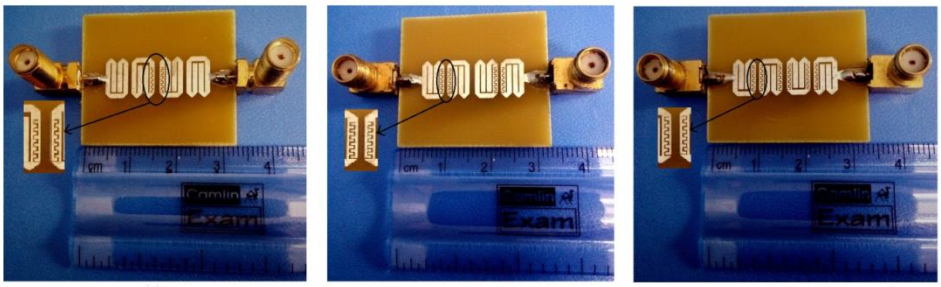

Fig. 4.113. Fabricated prototypes: (a) Filter-I (middle pair with spurline), (b) Filter-II (end pairs with spurline), and (c) Filter-III (all pairs with spurline) [16].

4.5.4.2. Comparison of EM simulation vs. Measurement Results

The measurements have been carried out in the Agilent N9928A vector network analyzer in the similar way of 3.14.4.1 and the comparisons between the simulated vs. measured $|S_{21}|$ (dB) have been illustrated in Figs. 4.114(a)-(c). It has been observed that a wide stopband below rejection levels of 38 dB up to $3.88f_0$ for Filter-I (middle pair with spurline), 38 dB up to $3.84f_0$ for Filter-II (end pairs with spurline), and 40 dB up to $4f_0$ for Filter-III (all pairs with spurline) have been obtained. The attenuation levels at $2f_0$ have been suppressed by 25 dB, 26 dB, and 27 dB and those at $3f_0$ have been suppressed by 34 dB, 35 dB, and 36 dB for the designed filters respectively compared to the folded filter without meander spurline. For all the filters multiple transmission zeros (seven for Filter-I, ten for Filter-II, and eleven for Filter-III) have been obtained in the stopband due to the bandstop nature of the meander spurline. Thus, the stopband behaviour of the designed filters has been improved greatly over

the folded filter without spurline. The insertion losses in the desired passband have been measured near to 1.2 dB, 1.1 dB, and 1.05 dB for the filters respectively. Fig. 4.115(a) shows the comparison between the measured $|S_{11}|$ (dB) plots of the designed filters. It has been explored that for all the filters the return losses in the desired passband become better than 16 dB with a maximum of 25 dB for Filter-I.

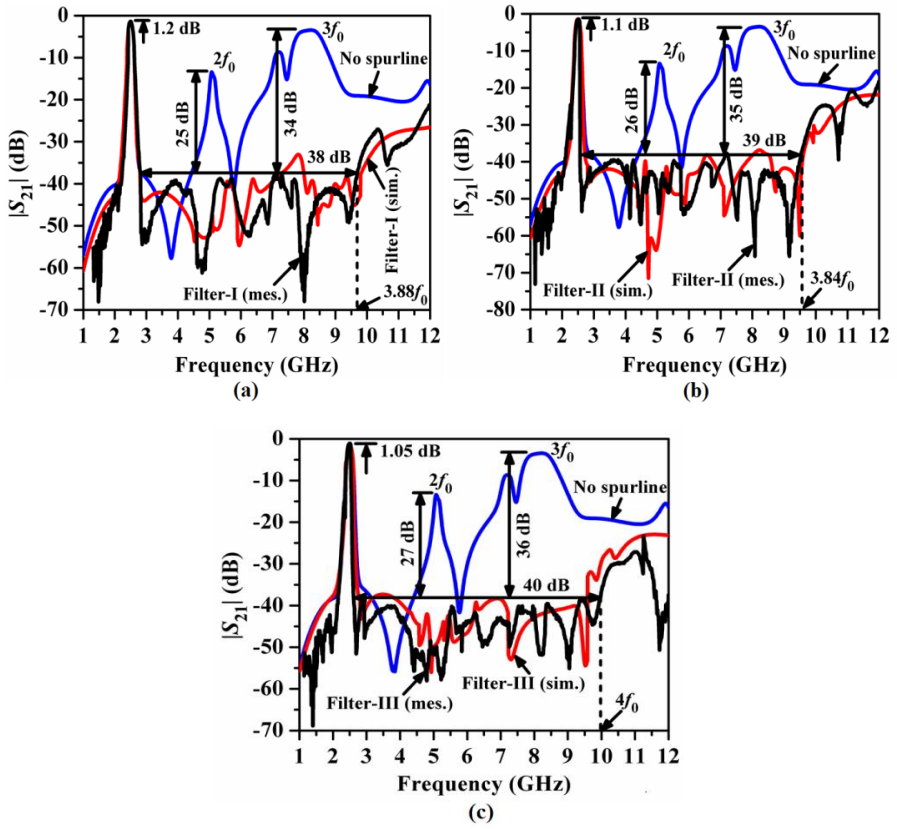

Fig. 4.114. Comparison between simulated vs. measurements results of $|S_{21}|$ (dB) for folded filters: (a) Filter-I (middle pair with spurline), (b) Filter-II (end pairs with spurline), (c) Filter-III (all pairs with spurline).

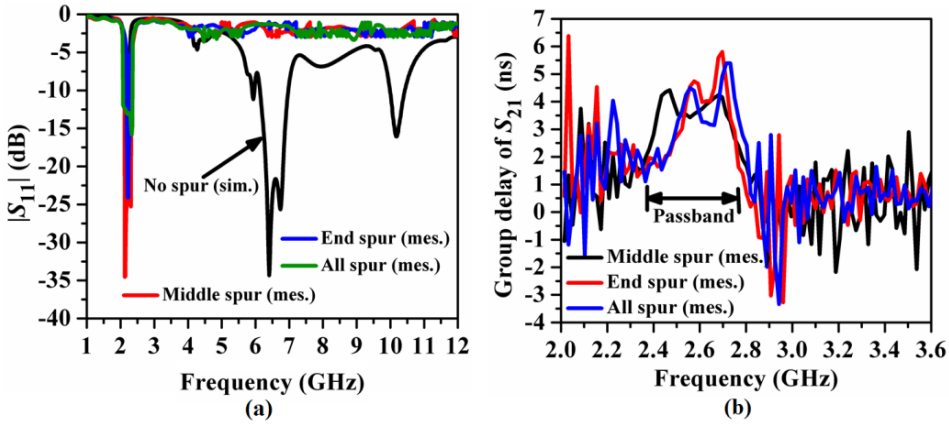

Fig. 4.115. (a) Comparison between measurements results of $|S_{11}|$ (dB) for the folded filters and (b) comparison of measured group delay (ns) of S_{21}.

Moreover, the return losses in the stopband have been measured as less than 3 dB, justifying the wide stopband rejection performance of the filters. Fig. 4.115(b) illustrates the comparison between the measured group delays of S_{21} for the designed filters. Symmetrical group delay variation in the passband with a value of 4.5 ns has been observed for the filter with the middle spurline. However, asymmetrical group delay variations have been noticed for Filter-II and Filter-III due to the fabrication tolerances. Accordingly, the surface current distribution of Filter-III at f_0 = 2.5 GHz, $2f_0$ = 5.0 GHz, $3f_0$ = 7.5 GHz and have been illustrated in Figs. 4.116(a)-(c). It has been revealed from Fig. 4.116(a) that the surface current has been distributed evenly from the input port to the output port with pretty large strength due to the existence of the passband. However, it has been witnessed from Figs. 4.116(b)-(c) that the surface current has been degraded gradually towards the output port from the input port, justifying the suppression of the spurious harmonics and thus, improving the stopband attenuation levels of the filters using spurline. Table 4.9 compares the filter's specifications for all the spurline based fourth-order filters. It has been explored that although the meander spurline based filter provides maximum stopband rejection level, however, OTSP type T-spurline based filter exhibits the highest figure-of-merit (*FOM*).

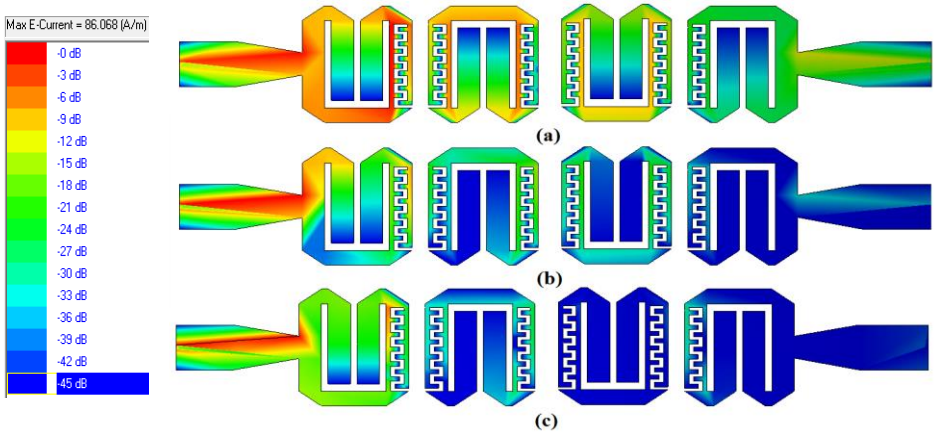

Fig. 4.116. Distribution of the surface current for the Filter-III with meander spurline: (a) at f_0 = 2.5 GHz, (b) at $2f_0$ = 5.0 GHz, and (b) at $3f_0$ = 7.5 GHz.

Table 4.9. Determination of different filters' parameters.

f_o (GHz)	*Type of filter*		ξ (dB/GHz)	*SBRL* (dB)	*SBW* (x f_0)	*RSB*	*SF*	*NCS*	*AF*	*FOM*
2.5 GHz	L-spurline		135	36	4.68	0.615	3.6	0.075	1	3985.2
	T-spurline	OTSP	180	37	2.9	0.691	3.7	0.069		6669.7
		DTSP	130	39	3.2	0.688	3.9	0.066		5285.1
	Rectangular meander spurline		90	40	4	0.632	4.0	0.057		3991.6

It can be concluded from this section that spurline has exhibited enhanced stopband rejection level with extended stopband bandwidth up to $4f_0$. However, for all the folded hairpin-line filters proposed so far the folded arms are unperturbed. Subsequently, the folded arms have been replaced by interdigital microstrip capacitor to improve the skirt characteristics and to achieve better passband symmetry as discussed in the next section.

4.6. Centrally Corrugated Folded Hairpin-Line Bandpass Filter

4.6.1. Unit Folded Hairpin-Line Cell with Corrugations

In general, the folded arms of the folded filters are producing cross-coupling capacitive effects inside the cell. The skirt characteristics of the folded filter have been improved due to such cross-coupling capacitive effects as explored in Fig. 4.30. It has been revealed from the literature [1-3] that interdigital capacitor (IDC) provide high quality factor [17]. Thus, the bandwidth of the filters based on IDC has narrow bandwidth and improved skirt characteristics. Such idea of IDC has been studied in the present work by replacing the unperturbed folded arms of the folded hairpin-line (FHL) cell with the interdigital capacitor based folded arms as exhibited in Fig. 4.117(a). Such FHL cell with IDC occupies small circuit area akin to the unperturbed FHL cell. In general, conventional IDC is constructed by placing periodic rectangular slots (corrugations) alternately as shown in in Fig. 4.117(a). However, in the present work, such conventional IDC has been modified by replacing the rectangular slots with trapezoidal slots. It has been revealed from Chapter 3 (Section 3.19) that trapezoidal corrugations exhibit strong capacitive effects compared to rectangular corrugations.

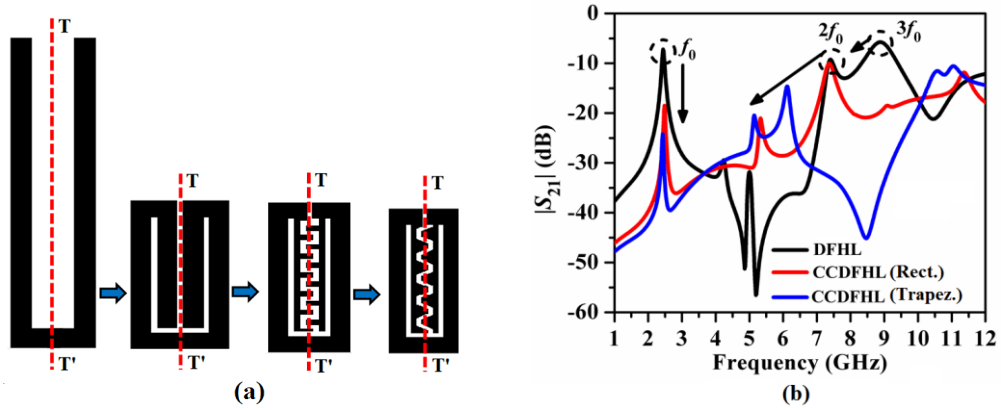

Fig. 4.117. (a) Folding mechanism of the conventional hairpin line (CHL) cell to CCDFHL with corrugations, (b) comparison of wideband resonance characteristics of simulated $|S_{21}|$ (dB).

DFHL cell with corrugations has been named as centrally corrugated double folded hairpin-line (CCDFHL) cell. The circuit area of the CHL cell is 69.48 mm^2, that of the DFHL cell is 44.84 mm^2 and that of CCDFHL is 39.3 mm^2. Thus size reductions of 43.4% and 12.4% have been obtained for CCDFHL cells over CHL and DFHL cells respectively. For simplicity of the DFHL and CCDFHL cells uniform inner coupling gap has been chosen. The effects of trapezoidal shaped IDC and rectangular shaped IDC on the wideband resonant characteristic for a double-folded hairpin-line (DFHL) cell tuned at f_0 = 2.5 GHz has been compared in Fig. 4.117(b). It has been witnessed that the attenuation level at f_0 = 2.5 GHz has been decreased gradually with minimum for CCDFHL cell due to the reduction in the effective conductive area for the two side arms owing to inward folding. Moreover, the locations of $2f_0$ and $3f_0$ for CCDFHL cell have been shifted to lower frequency regions along with the reduction in the corresponding attenuation levels due to the reduction in the overall effective electrical length. An important observation has been further noticed that the passband bandwidth at f_0 has been reduced gradually with narrowest for CCDFHL cell due to the additional capacitive coupling effects in the inner coupling regions between the corrugated folded arms. Fig. 4.118 highlights the distribution of surface current vectors in a CCDFHL cell with tapering bent edges at f_0 = 2.5 GHz. The four corners of the cell have been tapered by 45^o chamfering to reduce the radiation effects at the sharp bent edges. It has been revealed from Fig. 4.118 that the current distribution vectors have been concentrated in large strength in the inner coupling regions between the corrugated folded arms. This clearly justifies the generation of large capacitive effects between the folded arms of the cell due to the slow-wave structure of the corrugations. Accordingly, such CCDFHL cells have been utilized to design the fourth-order bandpass filter as discussed in the next section

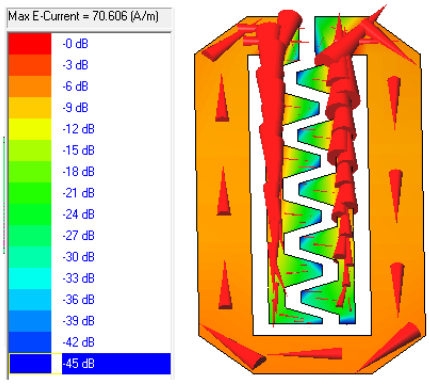

Fig. 4.118. Distribution of surface current vectors in a CCDFHL cell with trapezoidal corrugations.

4.6.2. Fourth-Order Folded Hairpin-Line Filter with Corrugations

The proposed fourth-order folded filter has the same specifications listed in Table 4.3. Accordingly, the initial values of the coupling coefficients for a pair of CCDFHL cells have been determined from the design curve as highlighted in Fig. 4.119(a). Afterward, the dimensions of the CCDFHLBF have been obtained optimally by performing EM simulations in IE3D. The layout of the fourth-order CCDFHLBF is depicted in Fig. 4.119(b). The size of the filter is 268.35 mm^2 i.e., $0.44\lambda_g \times 0.13\lambda_g$.

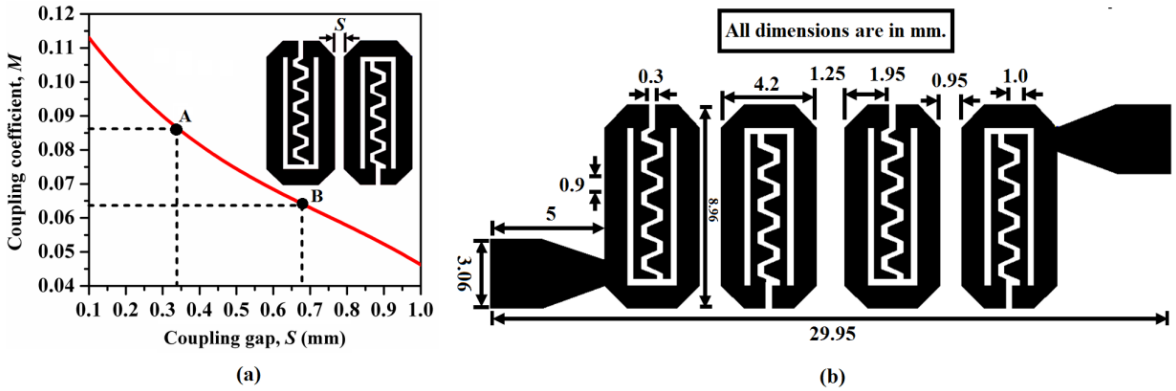

Fig. 4.119. (a) Variation of coupling coefficient vs. coupling gap for a pair of CCDFHL cells, (b) layout of the fourth-order CCDFHL bandpass filter with optimized dimensions in mm [18].

Thus, a size reduction of 18.27% has been achieved further than DFHLBF (Fig. 4.42). Figs. 4.120(a) - (b) compare the simulated *S*-parameters plots between the DFHLBF and CCDFHLBF. It has been observed from Fig. 4.120(a) that the transmission zero f_z at the upper passband edge has been shifted from 4.0 GHz to 4.5 GHz with the increment of the attenuation peak from -60 dB to -49 dB. This happens due to the additional capacitive effects that occurred due to the inner trapezoidal corrugations. For both the filters the passband insertion loss is less than 1.4 dB and return loss greater than 15 dB (Fig. 4.120(b)). It can be concluded from this section that the CCDFHLBF has not only occupied less circuit area than DFHLBF, but also exhibits improved skirt characteristics. However, the attenuation levels at the spurious harmonics are still pretty large (more than 10 dB). Figs. 4.121(a)-(b) explore the surface current distribution for the designed filters at f_0, $2f_0$ and $3f_0$ respectively. It has been revealed that the surface current distributes with higher degree of strength at f_0 and slightly less degree of strength at $2f_0$ and $3f_0$ due to large attenuation levels at the harmonics.

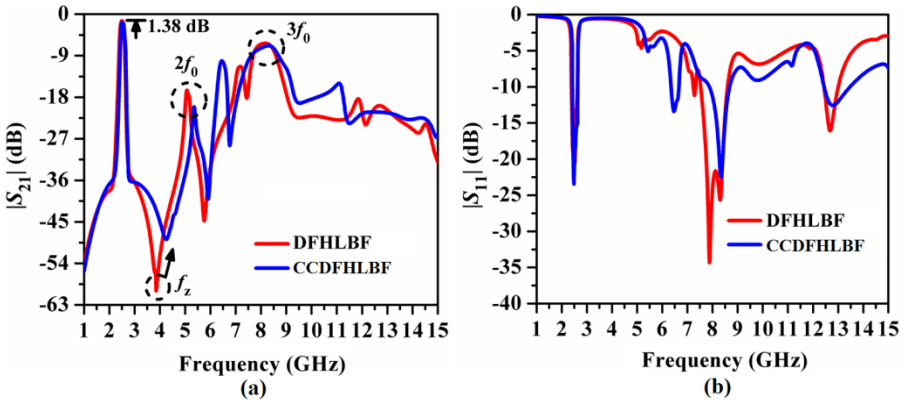

Fig. 4.120. Comparison of simulated *S*-parameters plots between the fourth-order DFHLBF vs. CCDFHLBF: (a) $|S_{21}|$ (dB) and (b) $|S_{11}|$ (dB).

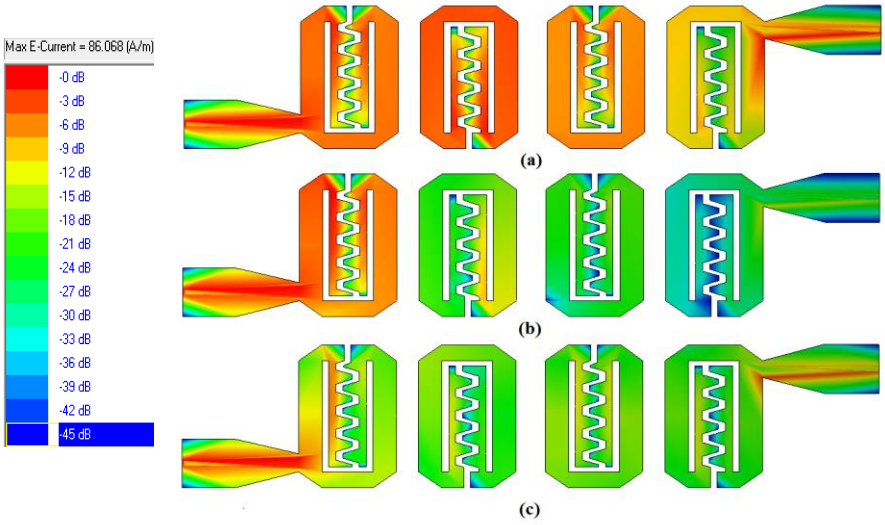

Fig. 4.121. Distribution of the surface current for the CCDFHLBF: (a) at f_0 = 2.5 GHz, (b) at $2f_0$ = 5.0 GHz, and (b) at $3f_0$ = 7.5 GHz.

Accordingly, a trapezoidal-shaped meander spurline has been investigated for the CCDFHLBF in the next section to suppress the harmonics' attenuation levels (more than 30 dB) and improve the stopband bandwidth accordingly.

4.6.3. Harmonics Suppression by Trapezoidal Shaped Meander Spurline

The conventional L-shaped spurline discussed early has been modified to a trapezoidal-shaped meander spurline as shown in Fig. 4.122 to generate a more slow-wave structure for the EM wave. The basic purpose for this meandering of spurline is to utilize its bandstop nature and to produce transmission zeros in the stopband of the filter's response. The trapezoidal-shaped meander spurline has been characterized by the overall spurline length l_{sp}

and open-end discontinuity gap g, corrugation width W_T, corrugation length l_T, and period of corrugation p. Accordingly, such trapezoidal meander spurline has been employed to the coupled arm of the unit CCDFHL cell as shown in Fig. 4.123(a) to generate transmission zeros in the stopband.

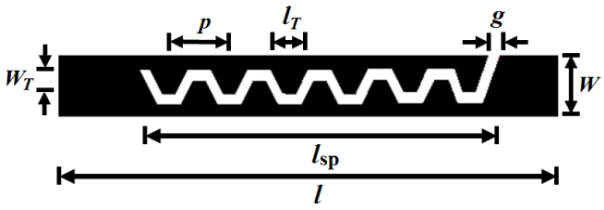

Fig. 4.122. Structure of a trapezoidal shaped meander spurline.

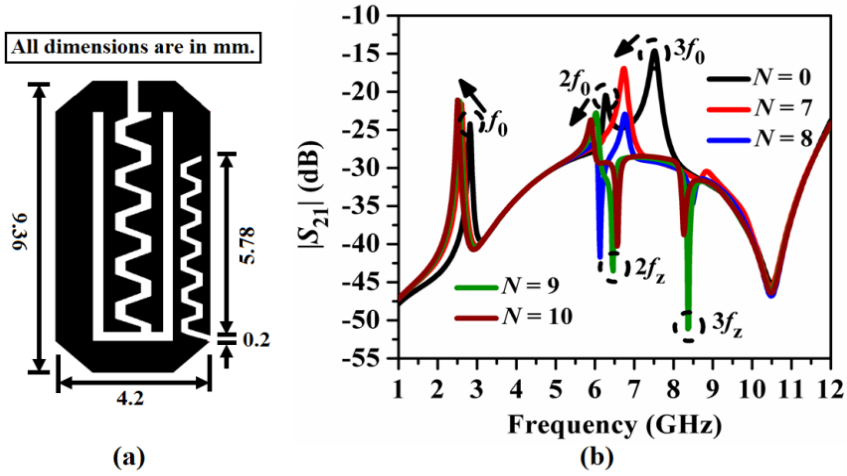

Fig. 4.123. Unit CCDFHL cell with trapezoidal shaped meander spurline: (a) layout (mm), (b) wideband resonant characteristics of simulated $|S_{21}|$ (dB).

The dimensions of the spurline tuned at f_0 = 2.5 GHz have been considered as g = 0.2 mm, W_T = 0.4 mm, l_T = 0.6 mm, W = 1.0 mm, and l_{sp} is increasing with the increase of a number of periodic corrugations N. The comparison of wideband resonance characteristics of $|S_{21}|$ (dB) for different values of N has been highlighted in Fig. 4.123(b). It has been witnessed from Fig. 4.123(b) that as the value of N increases the attenuation levels at $2f_0$ and $3f_0$ have been decremented gradually due to the bandstop nature of the spurline and the generation of multiple transmission zeros accordingly. To understand the effects of spurline for a CCDFHL cell, the distribution of surface current vectors at f_0 and $2f_0$ have been depicted in Figs. 4.124(a)-(b) respectively. It has been explored that the current vectors have been propagated densely through the narrow spurline slot near the inner coupled edge of the folded arm at f_0 due to the passband.

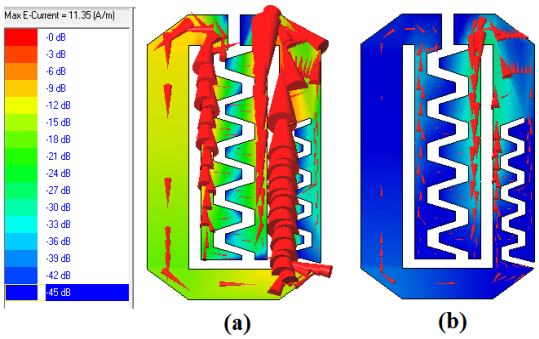

Fig. 4.124. Current distribution for a unit CCDFHL cell at (a) f_0 = 2.5 GHz and (b) $2f_0$ = 5.0 GHz.

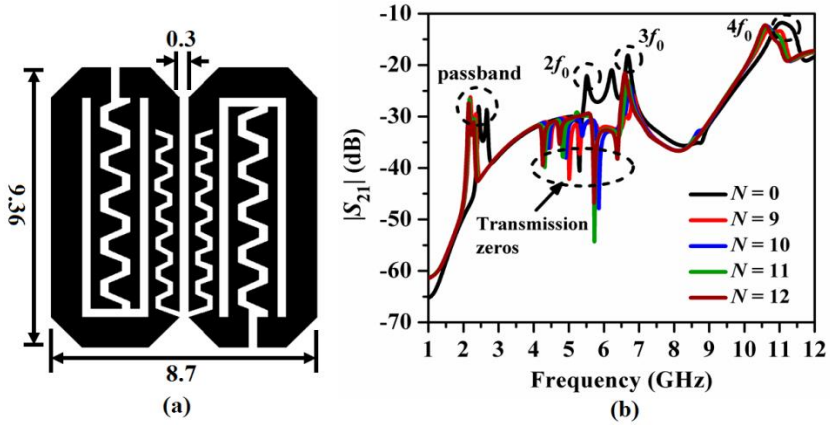

Fig. 4.125. Pair of CCDFHL cells with trapezoidal meander spurline: (a) layout (mm), (b) wideband resonance characteristics of simulated $|S_{21}|$ (dB).

However, the density of the surface current vectors becomes minimum at $2f_0$ through the entire cell due to the generation of multiple transmission zeros in the stopband. With this knowledge of unit CCDFHL cell with spurline, the study has been extended further for a pair of CCDFHL cells as shown in Fig. 4.125(a). The dimensions are tuned at f_0. From the wideband resonant characteristics as shown in Fig. 4.125(b), it has been revealed that the attenuation levels at both $2f_0$ and $3f_0$ have been decreased with incremental values of N just like the unit CCDFHL cell's study. Moreover, multiple transmission zeros have been generated in the stopband with a maximum attenuation peak of 55 dB for N =11. In general, the modal phase velocity compensation is the primary reason for such phenomenon; which is occurred due to the slow-wave structure of the spurline. Fig. 126(a) demonstrates the passband response of the pair of CCDFHL cells and it has been observed that the difference between the odd-mode and even-mode resonant frequency peaks f_{po} and f_{pe} gradually decreases for incremental values of N with more shifting of f_{po} compared to f_{pe} ($\delta f_{ps} < \delta f_p$), justifying the modal phase velocity compensation ability of the spurline based CCDFHL cells

pair. The coupling coefficient vs. coupling gap plot for a pair of CCDFHL cells with spurline having N = 11 is depicted in Fig. 4.126(b). The optimized layout of the fourth-order spurline based filter is depicted in Fig. 4.126. The locations of the feed ports have been decided by performing EM simulation to achieve the desired external quality factor.

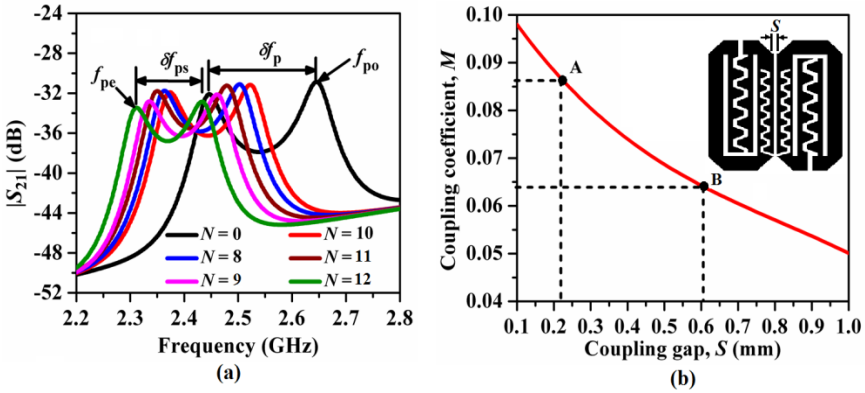

Fig. 4.126. Passband modal resonant characteristics of simulated $|S_{21}|$ (dB) plot, and (b) coupling coefficient vs. coupling gap plot for a pair of CCDFHL cells with spurline having N = 11.

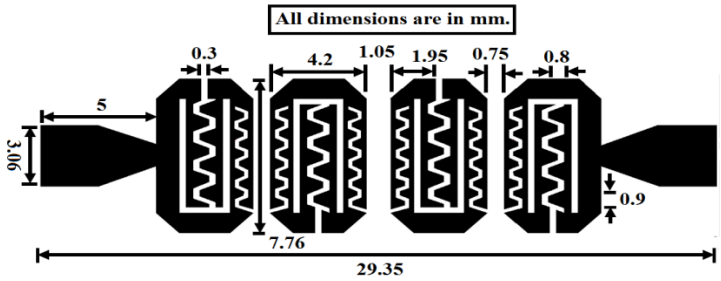

Fig. 4.127. Layout of the fourth-order CCDFHL based filter with trapezoidal shaped meander spurline optimized at f_0 = 2.5 GHz [18].

The size of the designed filter is 228 mm^2 i.e., $0.43\lambda_g \times 0.11\lambda_g$. Accordingly, size reductions of 15% compared to the filter without spurline (Fig. 4.118(b)), 31% compared to the DFHL filter (Fig. 4.42) and 59.6% than conventional filter have been achieved. The comparison of simulated $|S_{21}|$ (dB) plots between the proposed fourth-order CCDFHL filters without spurline and with trapezoidal meander spurline has been highlighted in Fig. 4.128(a). It has been revealed that the spurline based filter has exhibited improved skirt selectivity with the upper passband edge's attenuation level of 45 dB. Moreover, an extended stopband with the rejection level of 25 dB up to $6f_0$ and 35 dB up to $3.88f_0$ has been obtained. Five distinct transmission zeros have been generated in the stopband with attenuation levels more than 45 dB. Fig. 4.128(b) illustrates the simulated $|S_{11}|$ (dB) plots of the proposed filters and it has been observed that the value of $|S_{11}|$ becomes more than 18 dB for the filter with spurline and

becomes less than 3 dB up to 3.88f_0. The closure view of the passband response for the final filter has been highlighted in Fig. 4.128(c). The high value of insertion loss (1.45 dB) has been occurred due to the large value loss tangent (0.02) for the FR4 substrate material.

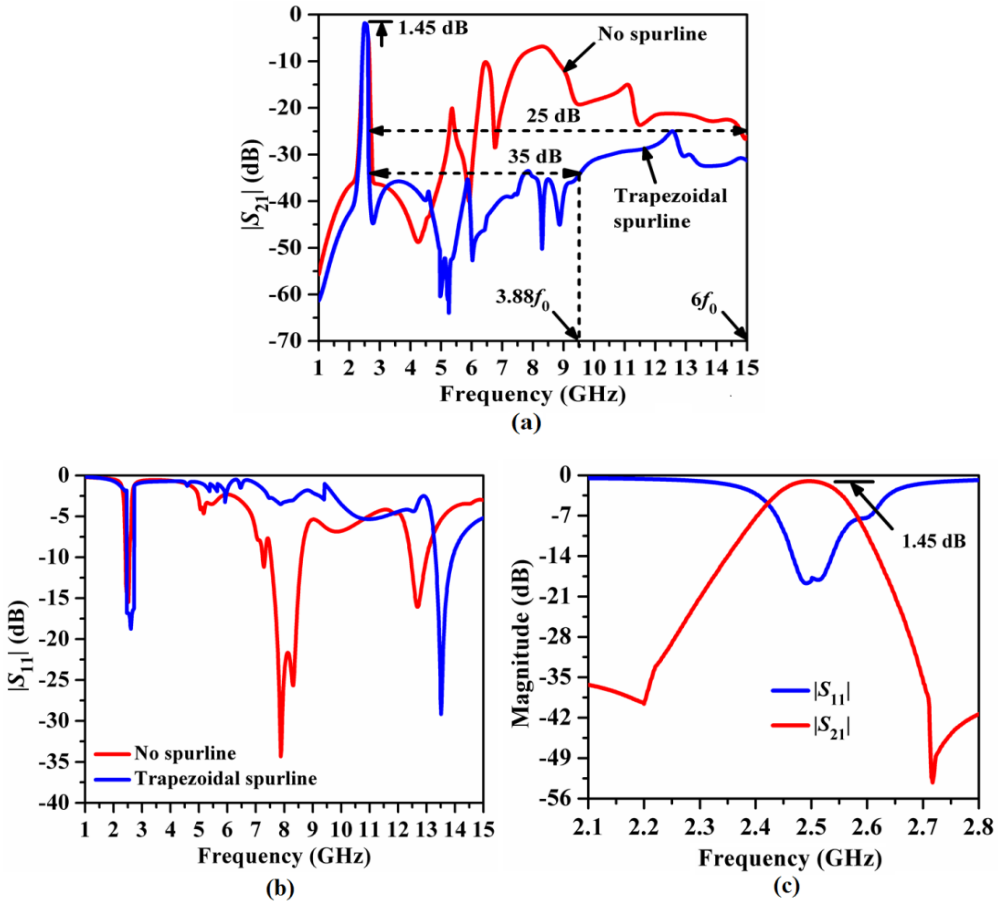

Fig. 4.128. Comparison of simulated (a) $|S_{21}|$ (dB), (b) $|S_{11}|$ (dB) plots between the fourth-order CCDFHL filters with and without spurline, and (c) passband response of the final filter.

Table 4.10. Determination of different filters' parameters.

f_o (GHz)	*Type of filter*	ξ (dB/GHz)	*SBRL* (dB)	*SBW* (x f_0)	*RSB*	*SF*	*NCS*	*AF*	*FOM*
2.5	CCDFHLBF (without spurline)	90	8	6	0.59	0.8	0.058	1	732.4
	CCDFHLBF (with spurline)	135	35 25	3.88 6	0.59	3.5 2.5	0.049		5689.3 4063.8

Table 4.10 compares the filters' specifications for both the centrally corrugated fourth-order filters with and without spurline. It has been explored that trapezoidal shaped meander spurline based filter exhibits large value of *FOM* justifying its effectiveness for harmonics suppression performance and achieving compactness.

Table 4.11. Comparison of all designs.

f_o (GHz)	*Type of perturbation*	ξ (dB/GHz)	*SBRL* (dB)	*SBW* (x f_0)	*RSB*	*SF*	*NCS*	*AF*	*FOM*
2.5	Periodic square grooves (N = 3)	14.59	40	2.2	0.588	4	0.052	1	659.9
	Minkowski fractal	77	33	3.04	0.691	3.3	0.066		2660.4
	L-spurline	135	36	4.68	0.615	3.6	0.075		3985.2
	T-spurline	180	37	2.9	0.691	3.7	0.069		6669.7
	Rectangular meander spurline	90	40	4	0.632	4.0	0.057		3991.6
	Trapezoidal meander spurline	135	35	3.88	0.59	3.5	0.049		5689.3

Accordingly, the performances of all the filters with different types of perturbations have been compared in Table 4.11 and it has been revealed that the folded filter with T-spurline has exhibited the highest *FOM* value. It can be concluded from this chapter that folded hairpin-line filters provide very compact structures with size reduction more than 60% over the conventional hairpin-line filter. However, the presence of spurious harmonics restricts their applications. Accordingly, various harmonics suppression methods have been studied in details for such filters and as an optimum result a wide stopband up to $4.68f_0$ with a rejection level more than 36 dB has been achieved by L-spurline. However, the highest FOM value has been obtained for the filter with T-spurline. Although, folded hairpin-line filters have exhibited satisfactory harmonics suppression performance, but the sizes of such filters are still quite large due to their longitudinal structure. In modern days' wireless communication systems the sizes of different blocks are so compact that fitting of such filter structures might be a problem. Moreover, for hairpin-line filters the skirt characteristics have been improved for the upper passband edge compared to the lower passband edge due to the hybrid configuration of the filter's structure. Thus, cross-coupled filter topology with harmonics suppression performance has been chosen to be studied as the extension of the present work in next chapter.

Reference:

[1] G. Mattaei, L. Young and E. M. T. Jones, "Microwave Filters, Impedance- matching Networks and Coupling Structures," *Artech House, Norwood*, MA, vol. 1, ch.4, 84-94, pp.1980.

[2] D. M. Pozar, "Microwave Engineering," *John Willey and Sons*, Inc., 4th. ed., ch. 2, pp. 48-59, 2011.

[3] J. S. Hong and M. J. Lancaster, "Microstrip Filters for RF/Microwave Applications," *John Willey & Sons, Inc.*, New York, NY, 2001, ISBN 0-471-22161-9, Ch. 3, pp. 29-30, 2001.

[4] S. Sun and L. Zhu, "Periodically nonuniform coupled microstrip-line filters with harmonic suppression using transmission zero reallocation," *IEEE transactions on microwave theory and techniques*, vol. 53, no. 5, pp. 1817-1822, May 2005.

[5] S. Chatterjee and T. K. Das, "Compact Hairpin-Line Bandpass Filter with Harmonic Suppression by Periodic Grooves," *Proceedings of 19th Mediterranean Microwave Symposium (MMS 2019)*, October 2019, Hammamet, Tunisia, 9157328.

[6] T. K. Das and S. Chatterjee, "Compact hairpin line bandpass filter with improved spurious passbands suppression," *International Journal of Electronics*, vol. 108, no. 8, pp. 1309-1325, December 2020.

[7] C. Wang, Z. Zhang, L. Shi, L. Shen, H. Liu and D. Ahn, "Miniaturized Hairpin Filter using Asymmetrical Spur-lines with Multiple Transmission Zeros," *Journal of Electromagnetic Waves and Applications*, vol. 24, no. 2, pp. 341-349, January 2010.

[8] C. W. Tang, C. H. Teng, J. M. Sun, "Design of wide-stopband microstrip bandpass filter with assistance of spur lines," *Electronics Letters*, vol. 49, no. 2, pp. 126-127, January 2013.

[9] T. Huang, Z. H. Shao, and Z. Chen, "Miniaturized wideband bandpass filter with enhanced selectivity and stopband suppression," *Microw Opt Technol Lett.* , vol. 60, no. 3, pp. 769-772, March 2018.

[10] F. Yan, Y. M. Huang, T. Huang, S. Ding, K. Wang, and M. Bozzi, "Transversely Compact Single-Ended and Balanced Bandpass Filters with Source-Load-Coupled Spurlines," *Electronics*, vol. 8, no. 4, pp. 416-429, April 2019.

[11] R. N. Bates, "Design of Microstrip Spur-line Band-stop Filters," *IEE Journal on Microwaves, Optics and Acoustics*, vol. 1, no. 6, pp. 209-214, November 1977.

[12] C. Nguyen, C. Hsieh, and D. W. Ball, "Millimeter wave printed circuit spurline filters," *IEEE MTT-S Int. Microw. Symp. Dig*., 98-100, May 1983.

[13] T. K. Das, and S. Chatterjee, "Spur-Line Embedded Compact Hairpin-Line Bandpass Filter for Wide Harmonic Suppression," *International Journal of Microwave and Wireless Technologies*, June 2021.

[14] T. K. Das, and S. Chatterjee, "Harmonic Suppression by using T-shaped Spur-Line in a Compact Hairpin-Line Bandpass Filter," *Radioengineering*, vol. 30, no. 2, June 2021, DOI: 10.13164/re.2021.0296

[15] G. Karimi, H. Siahkamari, F. K. Hamedani, A. Lalbakhsh, "Design of Modified Z-Shaped and T-Shaped Microstrip Filter Based on Transfer Function Analysis," *Wireless Pers Commun*, 2015.

[16] G. D. Alley, "Interdigital capacitors and their application to lumpedelement microwave integrated circuits," *IEEE Trans. Microwave Theory Tech.*, vol. MTT-18, pp. 1028-1033, Dec. 1970.

[17] I. Bahl, "Lumped Elements for RF and Microwave Circuits," *Artech House*, Boston, ch.7, pp. 229-251, 2003.

[18] T. K. Das and S. Chatterjee, "Wide Stopband Centrally Corrugated Folded Bandpass Filter with Trapezoidal Spurline," *Proceedings of IEEE WAMS 2022*, June, 2022, Rourkela, India.

Design of Cross-Coupled Bandpass Filter

5.1. Introduction

Folded parallel-coupled line and hairpin-line bandpass filters exhibit compact structures and wide stopbands with enhanced rejection levels as discussed in Chapter 3 and Chapter 4 respectively. However, such filters have the limitations of asymmetrical skirt selectivity. In general, hybrid-mode coupling has occurred between two adjacent resonators for parallel-coupled filters, capacitive gap coupling, and hairpin-line filters. Moreover, for such filters, a Chebyshev type transfer function is generally used for the design of lowpass prototype filters, exhibiting infinite attenuation at infinite frequencies. Thus, the group delay variation in the passband of such filters becomes asymmetrical, restricting their performance for modern wireless systems where highly selective filters are in great demand. Besides, for both the parallel-coupled line and hairpin-line filters, the sizes of the filters have been reduced by folding the resonators in the transverse direction. However, the size of the filter along the longitudinal plane is still pretty large. Keeping all such limitations in mind, the objectives of the present work have been decided to study the cross-coupled bandpass filters in two aspects:

- Reduction of the size of the cross-coupled filter by folding
- Suppression of the harmonic's attenuation level

The folded hairpin-line cells have been utilized to achieve the first objective, and spurline has been employed in the cross-coupled filter to achieve the second objective. The spurline has been studied only because it has exhibited the best harmonics suppression performance for the folded hairpin-line filter as discussed in Chapter 4.

5.2. General Theory of Cross-Coupled Filter

In general, coupled resonators are used for designing narrowband microwave filters. The equivalent two-port network of the *n*-coupled resonator filter is depicted in Fig. 5.1, where V_1,

V_2 and I_1, I_2 are the voltage and current variables at the filter ports, and the wave variables are denoted by a_1, a_2, b_1, and b_2.

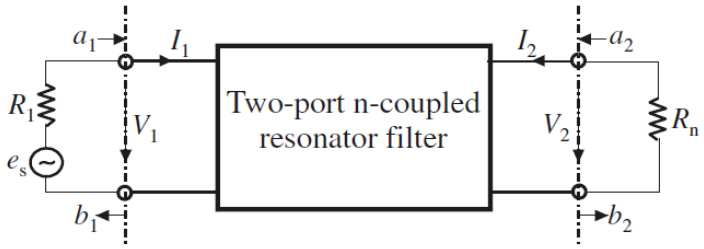

Fig. 5.1. Two-port network representation of *n*-coupled resonator filter [1].

The required coupling matrix for the desired filtering characteristic is determined first, and then the relationship between the coupling coefficient and the physical structure of coupled resonators is established to obtain the physical dimensions of the filter for fabrication. In general, the coupling coefficient k of coupled RF/microwave resonators with the same or different structures and the same or different self-resonant frequencies can be defined on the basis of the ratio of coupled energy to stored energy [1] as

$$k = \frac{\iiint \varepsilon \vec{E}_1 . \vec{E}_2 \, dv}{\sqrt{\iiint \varepsilon |\vec{E}_1|^2 \, dv \times \iiint \varepsilon |\vec{E}_2|^2 \, dv}} + \frac{\iiint \mu \vec{H}_1 . \vec{H}_2 \, dv}{\sqrt{\iiint \varepsilon |\vec{H}_1|^2 \, dv \times \iiint \mu |\vec{H}_2|^2 \, dv}} \tag{1}$$

where and represent the electric and magnetic field vectors, respectively, ε is the permittivity, and μ is the permeability. The first term on the right-hand side indicates the electric coupling and the second term represents the magnetic coupling. The interaction of the coupled resonators is represented by the dot operation of the space vector fields, and accordingly, the coupling may have either a positive or negative sign. For a positive sign means that the stored energy of uncoupled resonators is being enhanced by the coupling, whereas a reduction of energy is indicated by a negative sign. As a result, Fig. 5.2(a) depicts a synchronously tuned coupled resonator circuit with electric coupling, where L and C are the self-inductance and self-capacitance, respectively, so that $(LC)^{-1/2}$ equals the angular resonant frequency of uncoupled resonators and Cm is the mutual capacitance. Fig. 5.2(b) shows the equivalent *J*-inverter based circuit diagram. If the symmetry plane T-T′ in Fig. 5.2(b) is replaced by an electric wall (or a short circuit), the resulting circuit has a lower resonant frequency than an uncoupled single resonator.

$$f_e = \frac{1}{2\pi\sqrt{L(C + C_m)}} \tag{2}$$

In this case, the coupling effect enhances the capability to store charge of the single resonator when the electric wall is inserted into the symmetrical plane of the coupled structure. Similarly, if the symmetry plane T-T′ in Fig. 5.2(b) were surrounded by a magnetic wall (or an open circuit), a single resonant circuit with a resonant frequency of (3) would result.

$$f_m = \frac{1}{2\pi\sqrt{L(C - C_m)}} \tag{3}$$

In this case, the coupling effect reduces the capability to store charge so that the resonant frequency increases. Accordingly, the electric coupling coefficient k_E has been formulated as

$$k_E = \frac{f_m^2 - f_e^2}{f_m^2 + f_e^2} = \frac{C_m}{C} \tag{4}$$

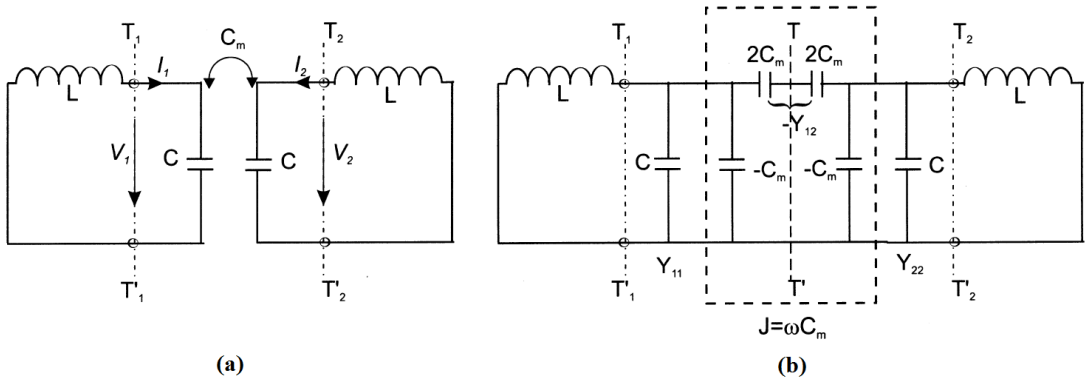

Fig. 5.2. (a) Synchronously tuned coupled resonator circuit with electric coupling, (b) an alternative form of the equivalent circuit with an admittance inverter $J = \omega C_m$ to represent the coupling [1].

Subsequently, an equivalent lumped-element circuit model for magnetically coupled resonator structures is depicted in Fig. 5.3(a), where L and C are the self-inductance and self-capacitance, respectively, and L_m represents the mutual inductance. If the symmetry plane T-T′ in Fig. 5.3(b) is replaced by an electric wall (or a short circuit), the resulting single resonant circuit has the frequency (5).

$$f_e = \frac{1}{2\pi\sqrt{(L - L_m)C}} \tag{5}$$

It can be shown from (5) that the increase in resonant frequency is due to the coupling effect, reducing the stored flux in the single resonator circuit when the electric wall is inserted in the symmetric plane.

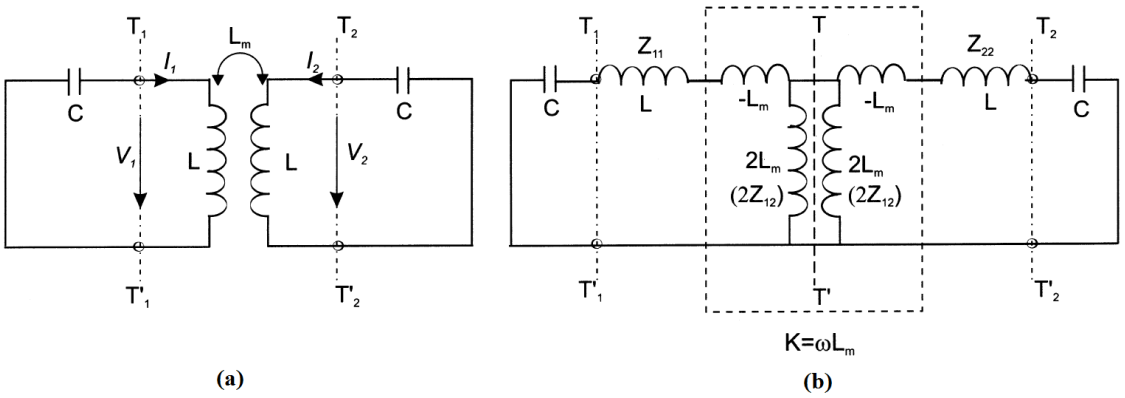

Fig. 5.3. (a) Synchronously tuned coupled resonator circuit with magnetic coupling, and (b) an alternative form of the equivalent circuit with an impedance inverter $K = \omega L_m$ to represent the coupling [1].

Likewise, if the symmetry plane is replaced by a magnetic wall (or an open circuit) in Fig. 5.3(b), then resultant single resonant circuit has a resonant frequency

$$f_m = \frac{1}{2\pi\sqrt{(L+L_m)C}} \tag{6}$$

In this case, the stored flux increases due to the coupling effect, so that the resonant frequency has been shifted down. Accordingly, the magnetic coupling coefficient k_M is defined as

$$k_M = \frac{f_e^2 - f_m^2}{f_e^2 + f_m^2} = \frac{L_m}{L} \tag{7}$$

In this context, Fig. 5.4(a) represents the synchronously tuned coupled resonator circuit with mixed coupling and Fig. 5.4(b) depicts the equivalent circuit with an impedance inverter $K = \omega L'_m$ and an admittance inverter $J = \omega C'_m$ to represent the magnetic coupling and the electric coupling respectively. In Fig. 5.4(b) C, L, C'_m, and L'_m are the self-capacitance, the self-inductance, the mutual capacitance, and the mutual inductance of an associated equivalent lumped-element circuit. By inserting an electric wall and a magnetic wall, respectively, into the symmetry plane T-T′ of the equivalent circuit in Fig. 5.4(b) the resonant frequencies are obtained as (8)-(9) respectively.

$$f_e = \frac{1}{2\pi\sqrt{(L-L'_m)(C-C'_m)}} \tag{8}$$

$$f_m = \frac{1}{2\pi\sqrt{(L+L'_m)(C+C'_m)}} \tag{9}$$

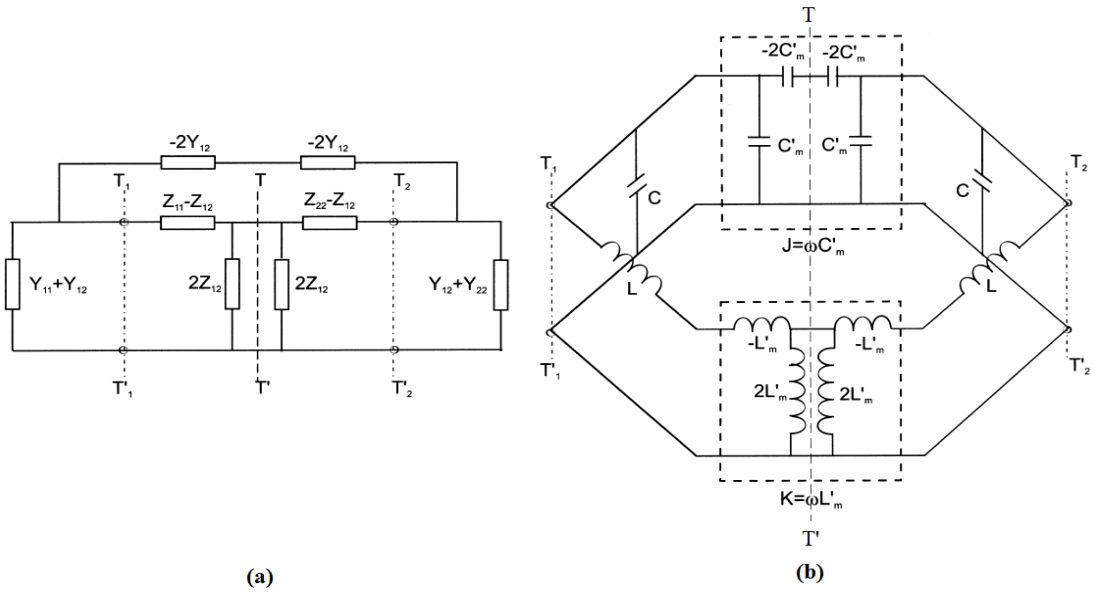

Fig. 5.4. (*a*) Network representation of synchronously tuned coupled resonator circuit with mixed coupling, (*b*) An associated equivalent circuit with an impedance inverter $K = \omega L'_m$ and an admittance inverter $J = \omega C'_m$ to represent the magnetic coupling and electric coupling respectively [1].

Accordingly, the mixed coupling coefficient k_X can be computed as (10).

$$k_X = \frac{f_e^2 - f_m^2}{f_e^2 + f_m^2} = \frac{CL'_m + LC'_m}{LC + L'C'_m} \tag{10}$$

By assuming that $L'_m C'_m << LC$, (10) becomes

$$k_X \approx \frac{L'_m}{L} + \frac{C'_m}{C} = k'_M + k'_E \tag{11}$$

It can be clearly seen that the mixed coupling results from the superposition of the magnetic and electric couplings.

5.3. Design of a Cross-Coupled Bandpass Filter

In general, a cross-coupled bandpass filter utilizes a quasi-elliptic transfer function to generate one pair of transmission zeros at the edges of the passband (i.e., at finite frequencies), increasing the skirt selectivity of the filter to a high degree, akin to the Chebyshev type filters [1]. The transfer function of such a quasi-elliptic type filter is as (12).

$$\left|S_{21}(\Omega)\right|^2 = \frac{1}{1+\varepsilon^2 F_n{}^2(\Omega)} \tag{12}$$

where

$$\varepsilon = \frac{1}{\sqrt{10^{-\frac{L_R}{10}} - 1}} \tag{13}$$

$$F_n(\Omega)=\cosh\left\{(n-2)\cosh^{-1}(\Omega)+\cosh^{-1}\left(\frac{\Omega_a\Omega-1}{\Omega_a-\Omega}\right)+\cosh^{-1}\left(\frac{\Omega_a\Omega+1}{\Omega_a+\Omega}\right)\right\} \qquad (14)$$

where Ω is the frequency variable, normalized to the passband cut-off frequency of the lowpass prototype filter, ε is a ripple constant corresponding to a given return loss $L_R = 20\log|S_{11}|$ in dB, and n is the degree of the filter. The frequency locations of a pair of attenuation poles are determined by $\Omega = \pm\Omega_a$ ($\Omega_a > 1$). The lowpass prototype filter for the filter synthesis is depicted in Fig. 5.5 where the rectangular boxes represent ideal admittance inverters with characteristic admittance J.

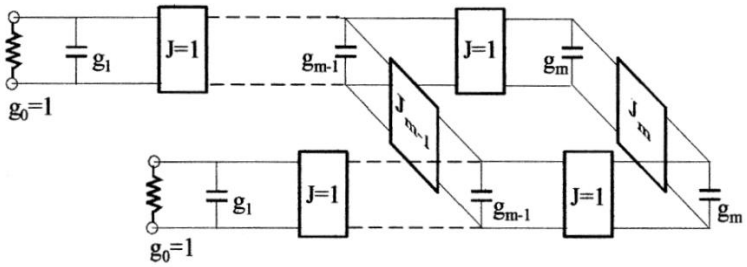

Fig. 5.5. Lowpass prototype filter for the quasi-elliptic cross-coupled filter synthesis [1].

A general coupling structure for a fourth-order cross-coupled filter is shown in Fig. 5.6. There are three different types of coupling that occur in the whole structure: electric coupling (1-4), magnetic coupling (2-3) and hybrid coupling (1-2 and 3-4). The specifications of the proposed quasi-elliptic type cross-coupled bandpass filter applicable for WLAN (IEEE 802.b) systems are listed in Table 5.1.

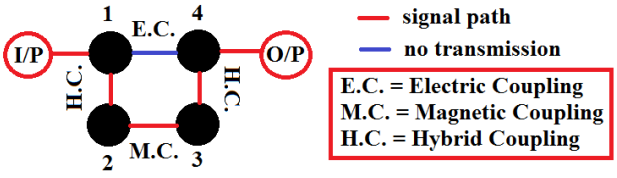

Fig. 5.6. General coupling structure of the fourth-order cross-coupled bandpass filter.

Table 5.1. Specifications of the cross-coupled bandpass filter.

Parameters	Specifications
Cut-off frequency, f_0 (GHz)	2.5
Transfer function type	quasi-elliptic
Fractional bandwidth, Δ (%)	4
Bandwidth, BW (MHz)	100
Passband ripple, L_{Ar} (dB)	0.1
Insertion loss, IL (dB)	<2
Return loss, RL (dB)	>15
30 dB Rejection bandwidth (MHz)	125

The synthesis procedures to design the cross-coupled bandpass filter is described as follows:

Step 1: Determination of the order of the filter

The order of the filter has been chosen as n = 4 to keep the continuity of the fourth-order folded hairpin-line bandpass filter as discussed in Chapter 4. However, the skirt characteristics of the cross-coupled filter would be greatly increased with the increment of the order [1]. But, the size of the overall filter structure will be increased accordingly. Thus, the order of the proposed filter has been fixed to four.

Step 2: Determination of the elements of the lowpass prototype

The pair of attenuation poles are placed at Ω_a = ±1.80 in order to meet the rejection specification. The elements of the prototype low-pass filter with a passband ripple of 0.1 dB have been obtained from [3] as g_1=0.95974, g_2=1.42192, J_1 = -0.21083 and J_2 = 1.11769.

Step 3: Determination of the coupling coefficients and external quality factors

The coupling coefficients and external quality factors as referring to the general coupling tructure of Fig. 5.6, have been determined by the formulas

$$M_{i,i+1} = M_{n-i,n-i+1} = \frac{FBW}{\sqrt{g_i g_{i+1}}} \tag{15}$$

$$M_{m,m+1} = \frac{FBW.J_m}{g_m} \tag{16}$$

$$M_{m-1,m+2} = \frac{FBW.J_{m-1}}{g_{m-1}} \tag{17}$$

$$Q_{ei} = Q_{eo} = \frac{g_1}{FBW} \tag{18}$$

The coupling coefficients have been calculated as $M_{1,2}$ = $M_{3,4}$ = 0.0428, $M_{2,3}$ = 0.0393, $M_{1,4}$ = -0.0277 and the external quality factors have been computed as Q_{e1} = Q_{e4} = 19.1948. The general layout diagram of the fourth-order folded cross-coupled bandpass filter is shown in Fig. 5.7.

Step 4: Determination of the coupling gaps

From the design curve shown in Fig. 5.7 the initial values of the coupling gaps for the pair of adjacent folded hairpin-line cells have been determined as S_{12} = S_{34} = 0.56 mm, S_{23} = 0.28 mm, and S_{14} = 0.8 mm.

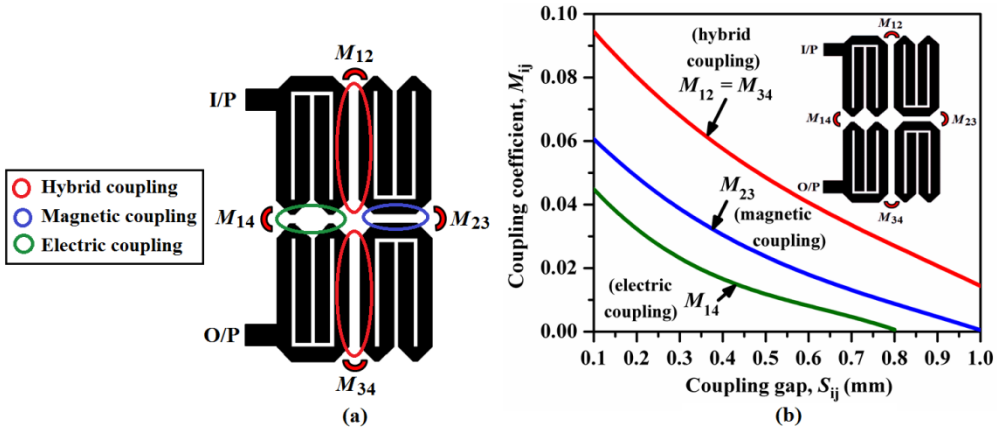

Fig. 5.7. (a) General layout of the fourth-order folded cross-coupled bandpass filter, (b) variation of the coupling-coefficient vs. coupling gap for a pair of folded hairpin-line cells in different coupling configurations.

Step 5: Determination of the optimum dimensions of the final filter

The optimum dimensions of the final folded cross-coupled filter have been obtained by performing multiple simulations in the IE3D EM simulator to satisfy the specifications mentioned in Table 5.1, and it is depicted in Fig. 5.8(a). The size of the filter is 291.04 mm^2 i.e., $0.22\lambda_g \times 0.28\lambda_g$, where λ_g is the guided wavelength at the center frequency f_0 = 2.5 GHz. Accordingly, the simulated *S*-parameters plots of the folded cross-coupled bandpass filter have been illustrated in Fig. 5.8(b). It has been witnessed that two sharp transmission zeros have been generated at 2.33 GHz (f_{z1}) and 2.74 GHz (f_{z2}) having attenuation levels of 47 dB and 51 dB. The combinations of electric, magnetic, and mixed coupling in the cross-coupled structure are the primary reasons for the generation of such transmission zeros. The passband insertion loss and the return loss have been observed as 0.95 dB and 25 dB, respectively. The skirt characteristics of the cross-coupled filter have been governed by the following parameters: shape factor (*SF*) (dimensionless), roll-off slope factors (*ROSFs*) (dB/GHz), and transmission zero selectivity factor (*TZSF*) (dimensionless). Such parameters are defined with respect to Fig. 5.9 as *SF* = ratio of the 30 dB rejection bandwidth (f_{r2}-f_{r1}) to the 3 dB bandwidth (f_{p2}-f_{p1}) [1], *ROSFs* = slope θ_1 for the lower passband (27 dB/(f_{r2}-f_{p2}) GHz) and θ_2 for the upper passband (27 dB/(f_{p1}-f_{r1}) GHz), *TZSF* = ratio of the center frequency f_0 to the difference between the transmission zero frequencies at the passband edges i.e., *TZSF* = f_0/(f_{z2}-f_{z1}). Such values have been computed from Fig. 5.9 as *SF* = 2.5, *ROSF* = 245.45 dB/GHz (for both lower and upper passband edges), and *TZSF* = 6.1.

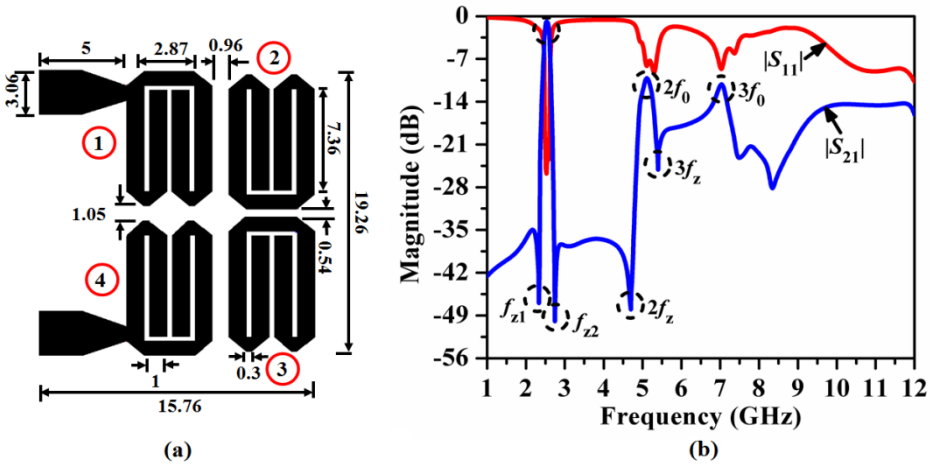

Fig. 5.8. Layout of the fourth-order quasi-elliptic folded cross-coupled bandpass filter with optimum dimensions in mm, (b) simulated *S*-parameters plots of fourth-order cross-coupled bandpass filter.

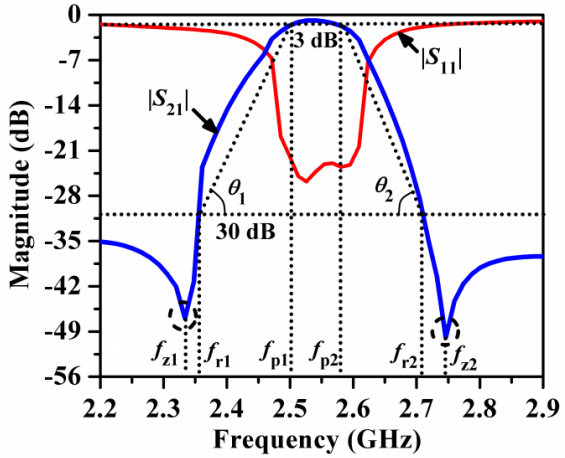

Fig. 5.9. Calculation of shape factor and selectivity factor from the simulated *S*-parameters plot.

Accordingly, the performance of the filter has been characterized by a slightly higher value of *SF* (greater than the ideal value of unity), symmetrical passband response due to the equal values of *ROSF*, and narrow bandwidth due to the higher value of *TZSF*. Although the passband response of the designed filter is quite satisfactory, however, the presence of two harmonic peaks at $2f_0$ and $3f_0$ with attenuation levels near 10 dB restricts the filter's applications in the WLAN system. The equivalent lumped elements circuit diagram of the fourth-order folded cross-coupled bandpass filter has been depicted in Fig. 5.10. The values of the lumped elements have been obtained in Table 5.2 by following the same conversion procedures demonstrated in Chapter 4.

Table 5.2. Values of the equivalent lumped elements of the unit FHL cell of the cross-coupled filter.

Inductors (nH)		Capacitors (pF)	
L_1	2.426	$C_{p1} = C_{p2}$	0.167
L_2	3.011	$C_{p3} = C_{p8}$	0.287
$L_3 = L_6$	1.169	$C_{p4} = C_{p5}$	0.083
$L_4 = L_5$	3.685	$C_{p6} = C_{p7}$	0.275
		$C_{g1} = C_{g2} = C_{g3}$	0.015
		C_{14}	0.015
		$C_{12} = C_{34}$	0.035
		C_{23}	0.238

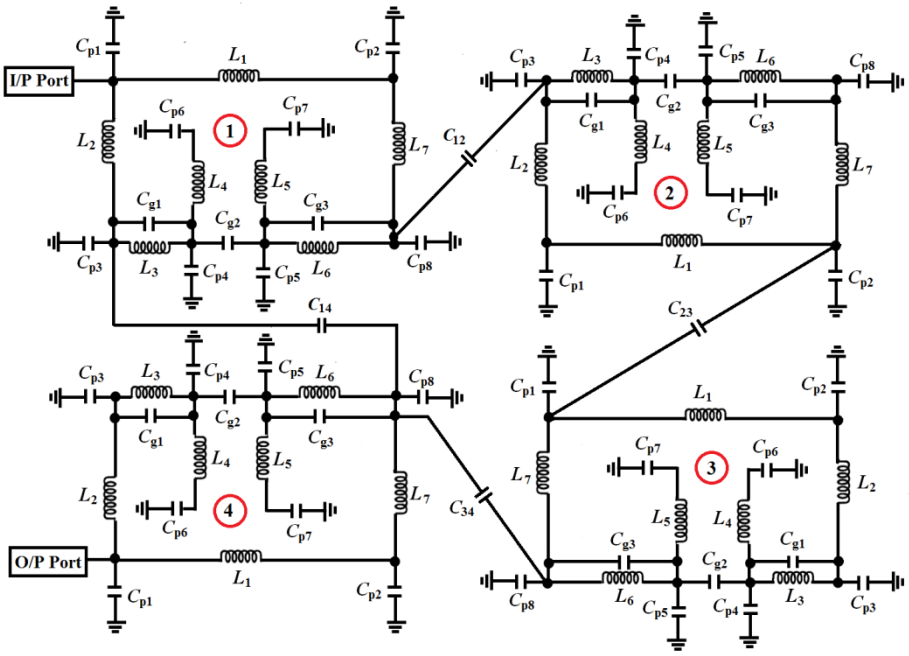

Fig. 5.10. Equivalent lumped elements circuit diagram of the fourth-order folded cross-coupled bandpass filter.

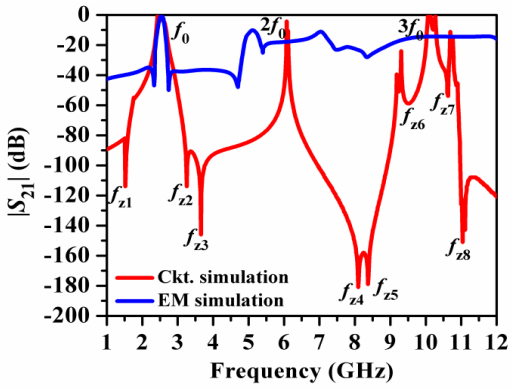

Fig. 5.11. Comparison between the EM and the circuit simulated $|S_{21}|$ (dB) plot of the fourth-order folded cross-coupled bandpass filter.

As a result, Fig. 5.11 compares the EM and circuit simulated $|S_{21}|$ (dB) plots, and a close agreement in the passband has been observed, as well as mismatches at the harmonics due to

the reasons discussed earlier in Chapter 4. Moreover, eight transmission zeros have been generated up to 12 GHz in the circuit simulation. Figs. 5.12(a)-(b) show the distribution of surface current vectors for the cross-coupled filter. A high degree of strength for the density vectors has been observed at f_0 = 2.5 GHz due to the passband and a slightly lower degree of strength at $2f_0$ = 5.0 GHz due to the second harmonic.

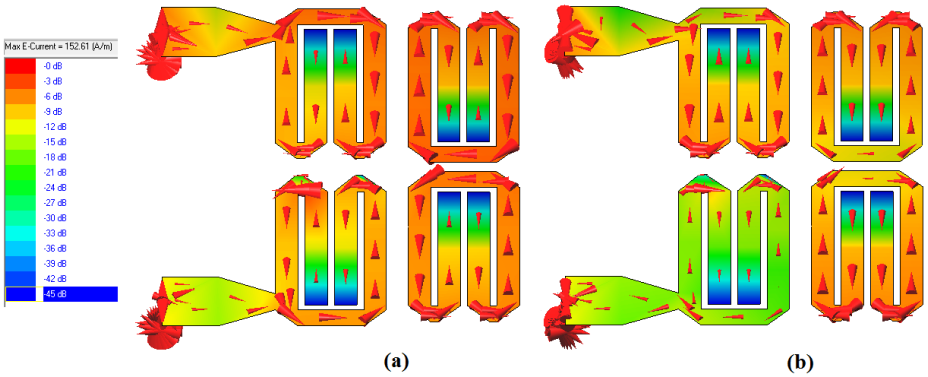

Fig. 5.12. Distribution of surface current vectors for the fourth-order cross-coupled filter at (a) f_0 = 2.5 GHz, and (b) $2f_0$ = 5.0 GHz.

It has been witnessed from Chapter 4 that spurline exhibits the maximum suppression of harmonics along with a wide stopband bandwidth for folded hairpin-line filters. Thus, the employment of spurline for folded cross-coupled filters has been extended in the next section for harmonics suppression. The study has been divided into two sections:

- Incorporation of the conventional L-spurline
- Modification of the L-spurline by a meander spurline

5.4. Harmonics Suppression by L-spurline for Cross-Coupled Filter-Simulation Study

The general layout of the fourth-order folded cross-coupled filter with conventional *L*-spurline is shown in Fig. 5.13(a). It has been revealed from the study of the folded hairpin-line filter that the harmonics are generated due to the imbalance between the even-and odd-mode phase velocities for a pair of coupled arms placed in a hybrid configuration. Thus, for the folded cross-coupled filter, spurlines have only been incorporated into the hybrid coupling region, as shown by the red dashed lines in Fig. 5.13(a). The spurline length ratio α has been defined as $\alpha = l_{sp}/l$, where l is the length of the coupled line and l_{sp} is the length of the spurline (Refer. Chapter 4, Fig. 4.46(a)).

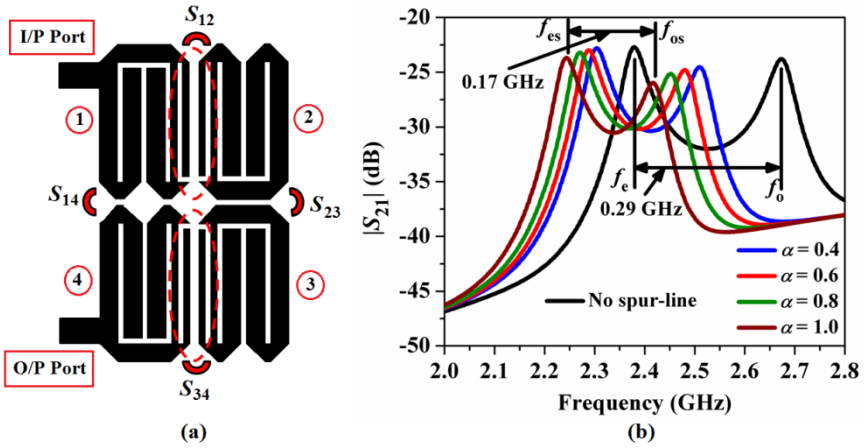

Fig. 5.13. (a) General layout of the fourth-order folded cross-coupled bandpass filter with L-shaped spurline, (b) passband characteristics of simulated $|S_{21}|$ (dB) for a pair of folded cells in hybrid coupling with L-spurline.

As a result, Fig. 5.13(b) shows how different values of affect the even- and odd-mode resonant frequencies f_e and f_o for a pair of folded hairpin-line (FHL) cells in hybrid coupling with the same dimension as shown in Fig. 5.8(a). As the value of increases, it can be seen in Fig. 5.13(b) that f_o shifts more to the lower frequency region than f_e. This indicates that spurline has the ability to attain modal phase velocity compensation and, accordingly, can suppress the harmonics. Different parametric studies for the cross-coupled filter are shown in Figs. 5.14(a)-(c) by varying the coupling gaps S_{12} (hybrid coupling), S_{23} (magnetic coupling), and S_{14} (electric coupling). It has been observed from Fig. 5.14(a) that as the values of S_{12} increase, the attenuation levels at f_{z1} and f_{z2} have been increased; the insertion loss at f_0 has been increased; and the passband bandwidth becomes constricted. Thus, the value of S_{12} should be kept moderate for better response. Similar events have been noticed in Fig. 5.14(b) for the incremental values of S_{23}. However, the insertion loss at f_0 increases rapidly in the case of S_{23} compared to that of S_{12} due to the magnetic coupling. Thus, the value of S_{23} has been kept lower for a better response. However, in Fig. 5.14(c), a completely reverse phenomenon has been noticed as the value of S_{14} increases due to the electric coupling akin to the other two cases. Thus, the value of S_{23} has been kept large for a better response. Accordingly, the initial values of the coupling gaps have been obtained from the design curve of the coupling coefficient vs. coupling gap in Fig. 5.15(a). After multiple EM simulations, the optimized layout of the folded cross-coupled filter with L-spurline has been obtained in Fig. 5.15(b).

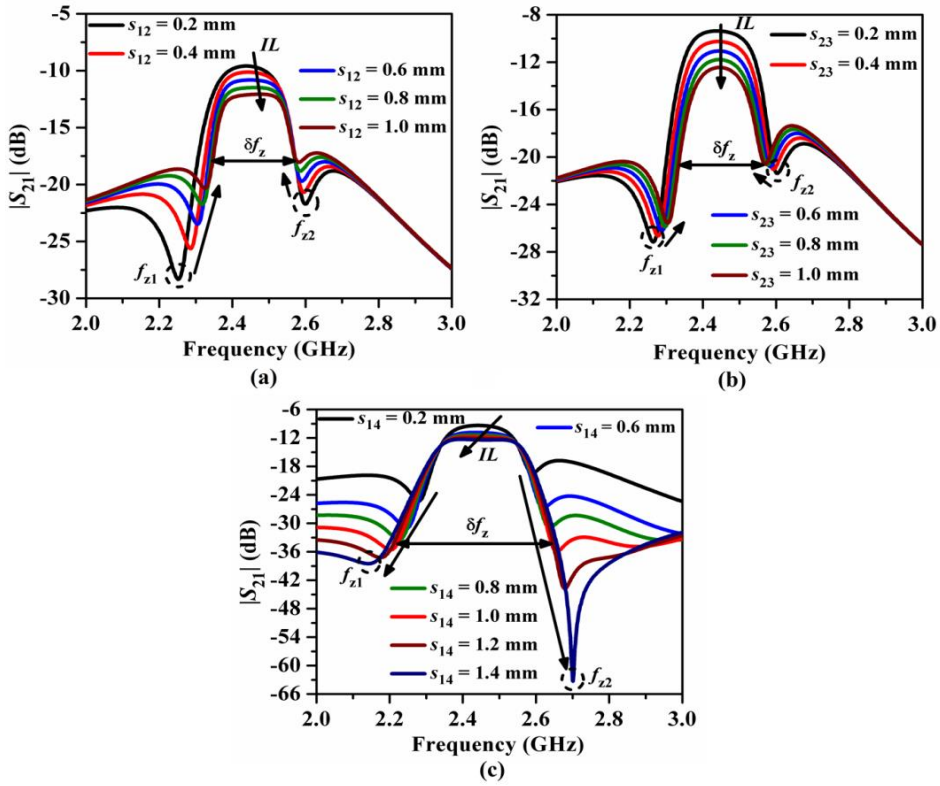

Fig. 5.14. Passband variations of the simulated $|S_{21}|$ (dB) plot for the folded cross-coupled filter with L-spurline for different coupling gaps variations: (a) $S_{12} = S_{34}$, (b) S_{23}, and (c) S_{14}.

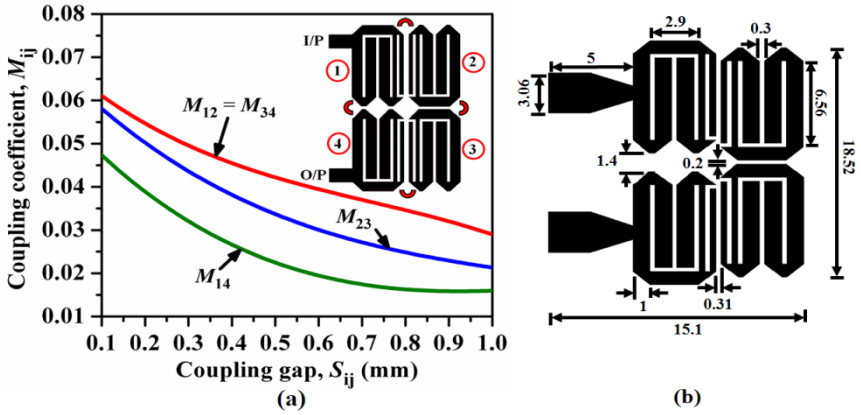

Fig. 5.15. (a) Coupling coefficients vs. coupling gaps plots, (b) layout of the fourth-order folded cross-coupled bandpass filter with L-shaped spurline. All dimensions are in mm.

The filter occupies a circuit area of 279.65 mm^2, i.e., $0.22\lambda_g \times 0.27\lambda_g$. The wideband frequency responses of $|S_{21}|$ and $|S_{11}|$ are shown in Fig. 5.16(a)-(b). The $|S_{21}|$ (dB) plot in Fig. 5.16(a) shows that two sharp transmission zeros were generated at 2.12 GHz and 2.72 GHz, with attenuation levels of 47 dB and 53 dB, respectively. Moreover, the stopband has been extended up to 3.16 f_0 with a rejection level of 35 dB.

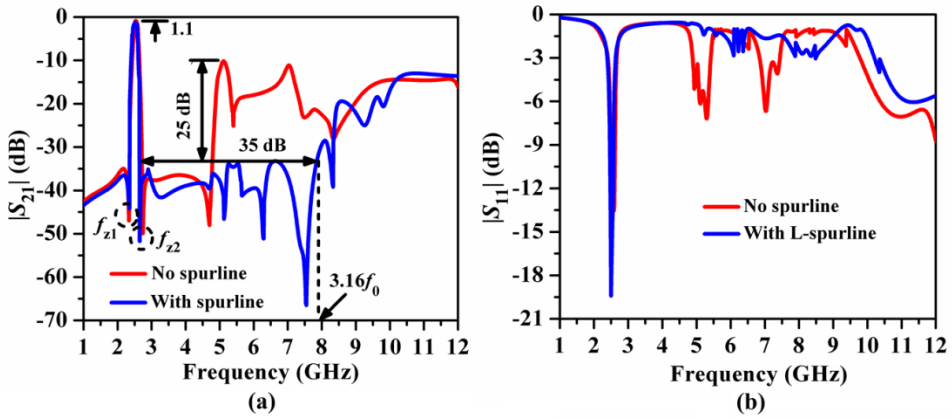

Fig. 5.16. Simulated *S*-parameters plots of a fourth-order cross-coupled filter with L-spurline: (a) $|S_{21}|$ (dB), and (b) $|S_{11}|$ (dB) plots.

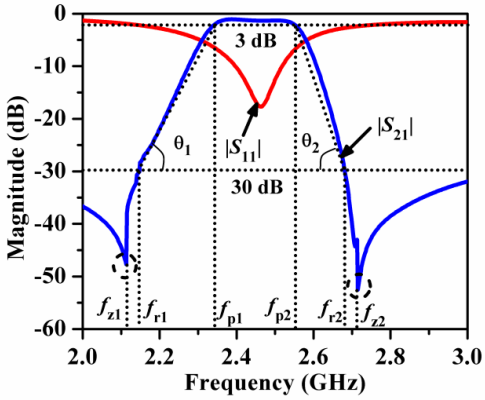

Fig. 5.17. Calculation of shape factor and skirt selectivity factor from the simulated *S*-parameters plot for the cross-coupled filter with L-spurline.

Accordingly, the attenuation levels of the spurious harmonics for the filter without spurline have been suppressed by 25 dB. The passband insertion loss has been obtained as 1.1 dB, and the return loss is more than 18 dB. Fig. 5.17 explores the magnified view of the passband response of the filter. The values of *SF*, *ROSF*, and *TZSF* have been computed as *SF* = 2.57, *ROSF* = 135 dB/GHz for the lower passband edge, 225 dB/GHz for the upper passband edge, and *TZSF* = 4.17. An improvement has been obtained with L-spurline compared to the filter without spurline (Refer Fig. 5.9). The equivalent lumped element circuit diagram of the folded cross-coupled filter with L-spurline has been obtained in Fig. 5.18. The equivalent lumped elements circuit of the L-spurline (Refer to Chapter 4, Fig. 4.48(a)) has been used in Fig. 5.18, with the lumped element values remaining unchanged. The values of the other lumped elements are listed in Table 5.3. Accordingly, Fig. 5.19 compares the EM and the circuit simulated $|S_{21}|$ (dB) plots.

Table 5.3. Values of the equivalent lumped elements of the unit FHL cell of the cross-coupled filter with L-spurline.

Inductors (nH)		Capacitors (pF)	
L_1	2.226	$C_{p1} = C_{p2}$	0.142
L_2	2.871	$C_{p3} = C_{p8}$	0.287
$L_3 = L_6$	1.145	$C_{p4} = C_{p5}$	0.062
$L_4 = L_5$	3.265	$C_{p6} = C_{p7}$	0.255
		$C_{g1} = C_{g2} = C_{g3}$	0.012
		C_{14}	0.012
		$C_{12} = C_{34}$	0.031
		C_{23}	0.218

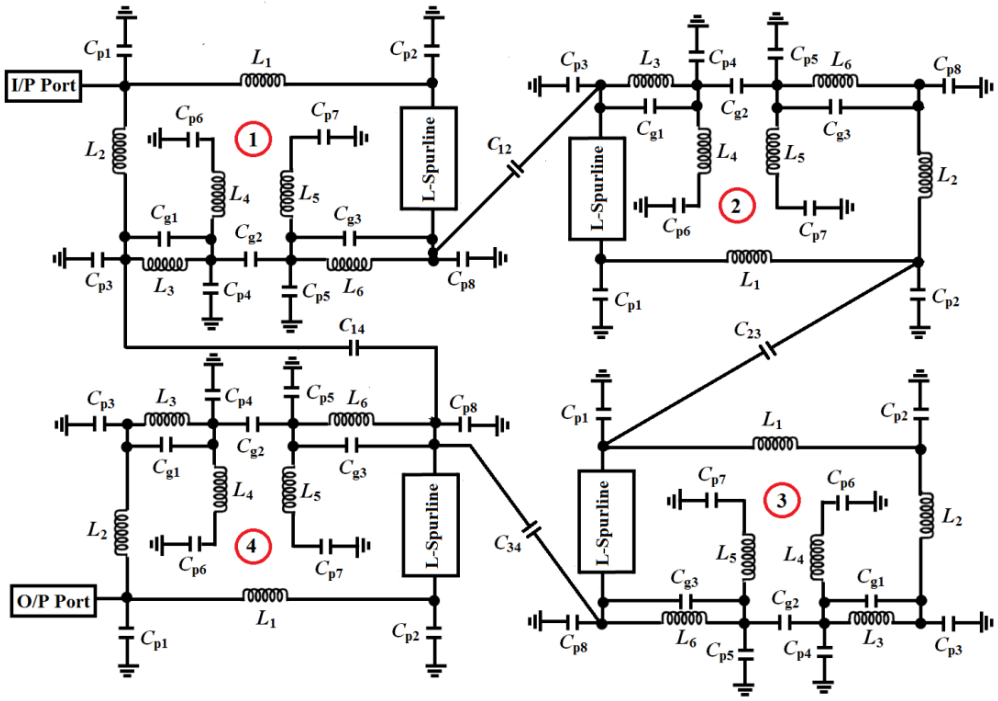

Fig. 5.18. Equivalent lumped elements circuit diagram of the fourth-order folded cross-coupled bandpass filter with L-spurline.

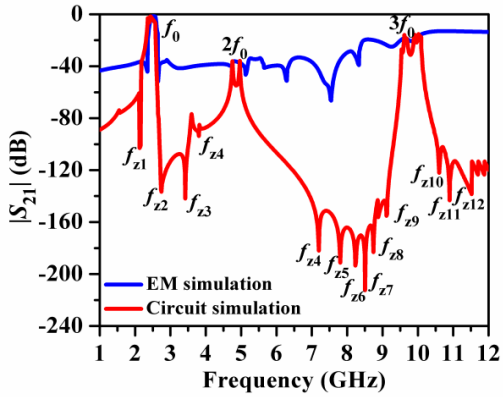

Fig. 5.19. Comparison between the EM and the circuit simulated $|S_{21}|$ (dB) plot of the fourth-order folded cross-coupled bandpass filter with L-spurline.

A close agreement between the passband responses has been obtained, and twelve transmission zeros have been generated up to 12 GHz for the circuit simulated plot.

5.4.1. Fabricated Prototype

The fabricated prototype of the fourth-order folded cross-coupled bandpass filter with L-spurline is shown in Fig. 5.20(a) and the experimental set up is shown in Fig. 5.20(b)-(c).

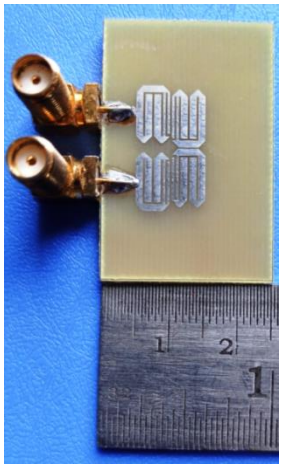

Fig. 5.20. Fabricated prototype of the fourth-order folded cross-coupled bandpass filter with L-spurline.

5.4.1. Comparison of Simulation vs. Measurement Results

The experiment has been carried out with the N9928A vector network analyzer by Keysight Technologies in the similar way of 3.14.4.1. As a result, Fig. 5.21(a)-(b) compare the measured and simulated *S*-parameter plots. It has been observed from Fig. 5.21(a) that the stopband has been extended up to $3.76f_0$ with a rejection level of 35 dB.

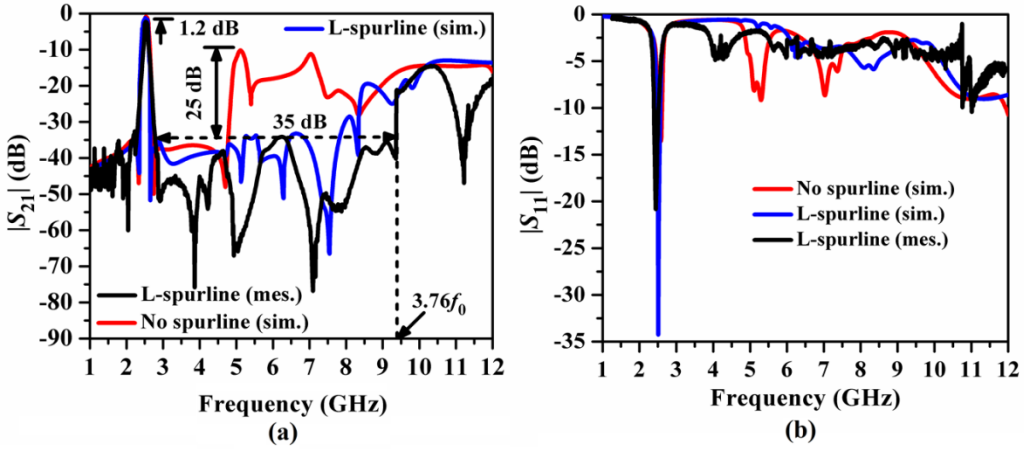

Fig. 5.21. Comparison between the simulated and measured *S*-parameters plots for the fourth-order folded cross-coupled filter with L-spurline: (a) $|S_{21}|$ (dB) and (b) $|S_{11}|$ (dB).

The harmonics' attenuation levels have been suppressed by 25 dB compared to the filter without spurline. The measured insertion loss has been recorded as 1.2 dB. Moreover, eight sharp transmission zeros have been generated in the stopband, improving its rejection performance. The measured return loss has been recorded as 20 dB from Fig. 5.21(b). The distribution of the surface current vectors at f_0 = 2.5 GHz and $2f_0$ = 5.0 GHz is then elaborated in Figs. 5.22(a)-(b). It has been observed that the density of the surface current vectors becomes large at 2.5 GHz throughout the entire structure due to the passband response and very little at the output port for 5.0 GHz due to the suppression of the attenuation level. In the next section, the L-shaped spurline has been modified by a meander spurline to provide additional slow wave effects for the odd-mode of the EM wave and to achieve more suppression of the harmonics along with the extension of the stopband.

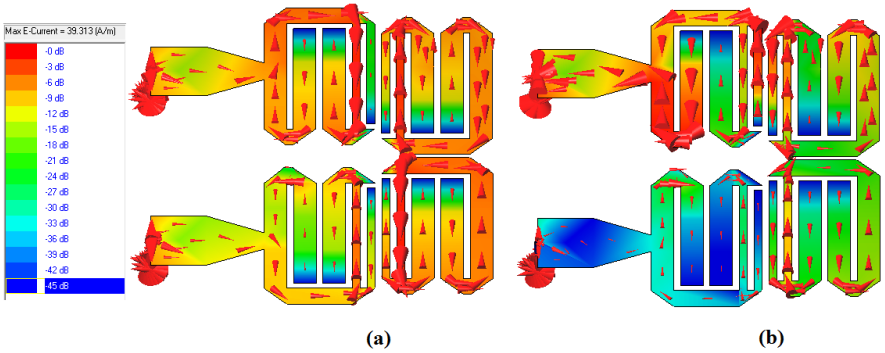

Fig. 5.22. Distribution of surface current vectors for the fourth-order cross-coupled filter with L-spurline at (a) f_0 = 2.5 GHz, and (b) $2f_0$ = 5.0 GHz.

5.5. Harmonics Suppression by Meander Spurline for Cross-Coupled Filter-Simulation Study

From the previous section, it has been revealed that the stopband rejection level for the final filter has been restricted to 35 dB and the rejection bandwidth has been extended only up to 3.16 f_0. As the attenuation level increases gradually beyond $3.16f_0$, the next objective has been decided to suppress such an attenuation level by replacing the L-spurline with a meander spurline. Fig. 5.23(a) depicts the general layout of the fourth-order folded cross-coupled filter with meander spurline. Accordingly, Fig. 5.23(b) explores the passband characteristics for a pair of folded hairpin-line cells placed in a hybrid coupling configuration. The incremental values of N have been observed to reduce the bandwidth between the even- and odd-mode resonant frequencies ($f = f_o$-f_e) at a faster rate than L-spurline (Refer to Fig. 5.13(b)). This

indicates the increase of slow-wave effects due to the zigzag structure of the meander spurline. Following that, parametric studies for the fourth-order cross-coupled filter with meander spurline are shown in Figs. 5.24(a)-(c) by varying the values of different coupling gaps S_{12} (hybrid coupling), S_{23} (magnetic coupling), and S_{14} (electric coupling).

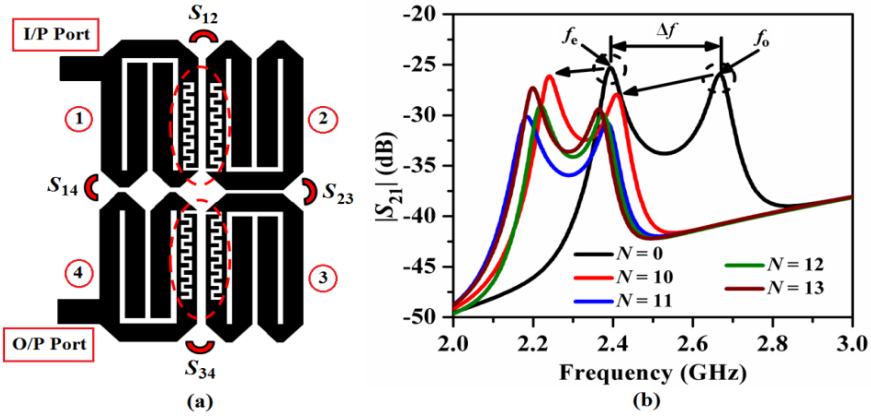

Fig. 5.23. (a) General layout of the fourth-order folded cross-coupled bandpass filter with meander spurline, (b) passband characteristics of the simulated $|S_{21}|$ (dB) for a pair of folded cells in hybrid coupling with meander-spurline.

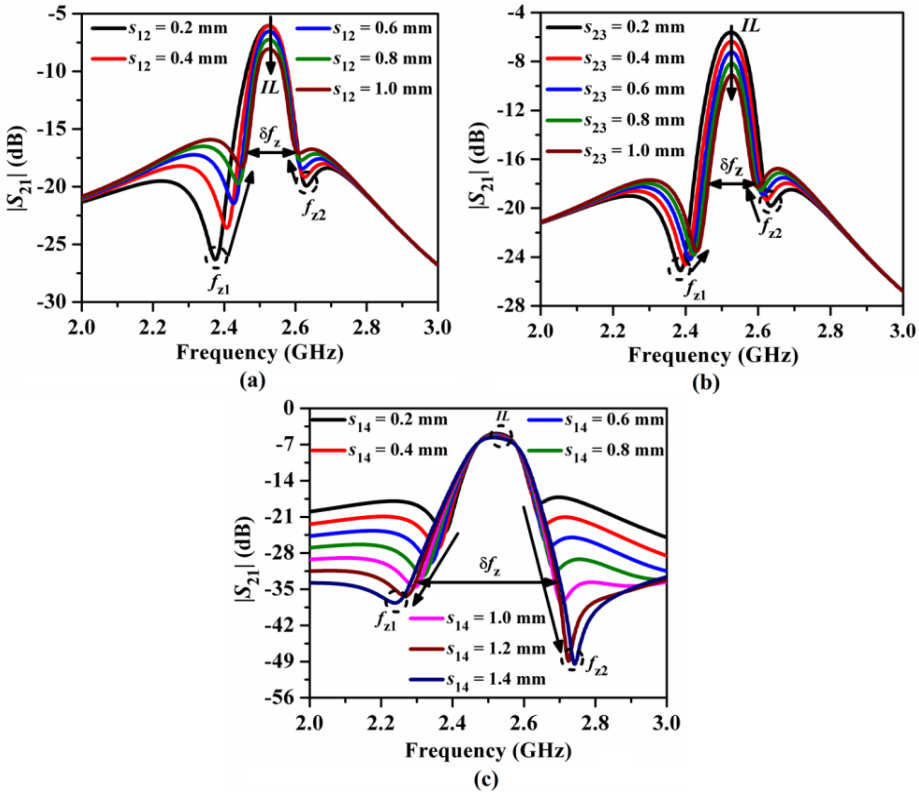

Fig. 5.24. Passband variations for the folded cross-coupled filter with meander-spurline for different coupling gaps variations: (a) $S_{12} = S_{34}$, (b) S_{23}, and (c) S_{14}.

The insertion loss has been gradually increased and the attenuation levels at f_{z1} and f_{z2} have been enhanced with a decrease in the passband bandwidth as the values of S_{12} and S_{23} have been increased, as shown in Fig. 5.24(a)-(b). However, a completely reverse phenomenon has been observed for the incremental values of S_{12} (mm). Thus, the values of S_{12} and S_{23} have been considered small, whereas the value of S_{14} has been considered large enough to achieve better passband response. Accordingly, the initial values of S_{12}, S_{23}, and S_{14} have been obtained from the design curves of coupling coefficients vs. coupling gaps as shown in Fig. 5.25(a). The final optimized layout of the folded cross-coupled filter with meander spurline has been shown in Fig. 5.25(b).

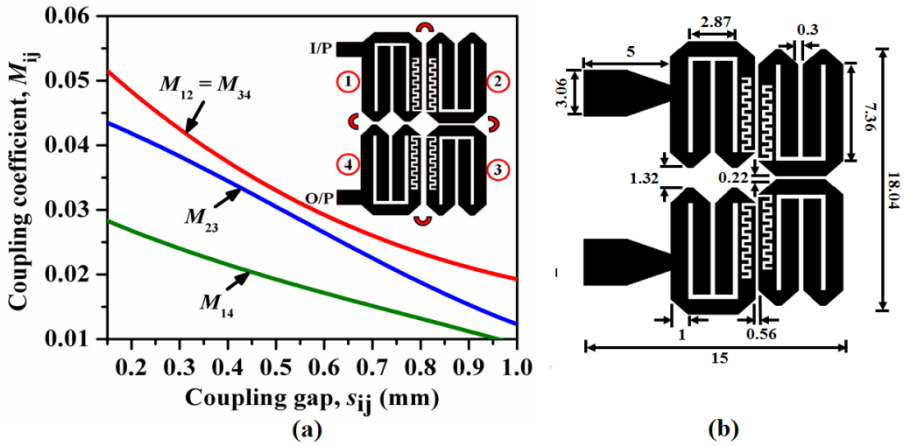

Fig. 5.25. (a) Coupling coefficients vs. coupling gaps plots, (b) layout of the fourth-order folded cross-coupled bandpass filter with meander spurline. All dimensions are in mm.

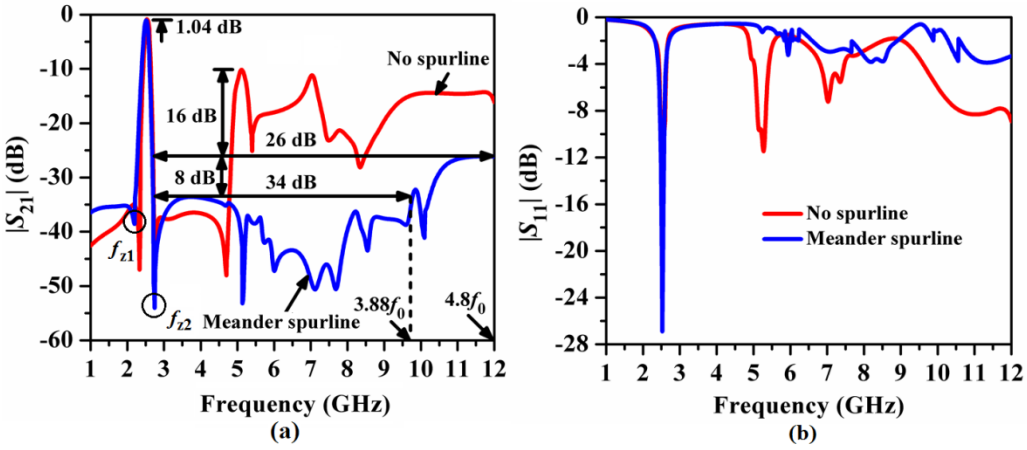

Fig. 5.26. Simulated *S*-parameters plots of a fourth-order folded cross-coupled filter with meander spurline: (a) $|S_{21}|$ (dB), and (b) $|S_{11}|$ (dB) plots.

The overall size of the filter is 270.6 mm^2 i.e., $0.22\lambda_g \times 0.26\lambda_g$. As a result, Figs. 5.26 (a)-(b) compare the simulated *S*-parameter plots for fourth-order folded cross-coupled filters without and with meander spurline. In Fig. 5.26(a), two sharp transmission zeros, f_{z1} and f_{z2}, were observed at 2.3 GHz and 2.7 GHz with attenuation levels of 38 dB and 55 dB, respectively. The passband insertion loss was measured to be 1.04 dB. Moreover, the stopband has been extended up to $3.88f_0$ with a rejection level of 34 dB and up to $4.8f_0$ with a rejection level of 26 dB. Hence, the harmonics' attenuation levels have been suppressed by 24 dB with the meander spurline over the filter without spurline. Accordingly, a steeper passband with a return loss better than 25 dB has been observed in Fig. 5.26(b). The magnified passband response has been explored in Fig. 5.27 for calculating the skirt selectivity and shape factor for the filter. From the plot, the values of *SF*, *ROSF*, and *TZSF* have been computed as *SF* = 5.5, *ROSF* =122.73 dB/GHz for the lower passband edge, 192.86 dB/GHz for the upper passband edge, and *TZSF* = 4.8. It has been concluded that the skirt selectivity of the filter has been improved compared to the L-spurline-based filter.

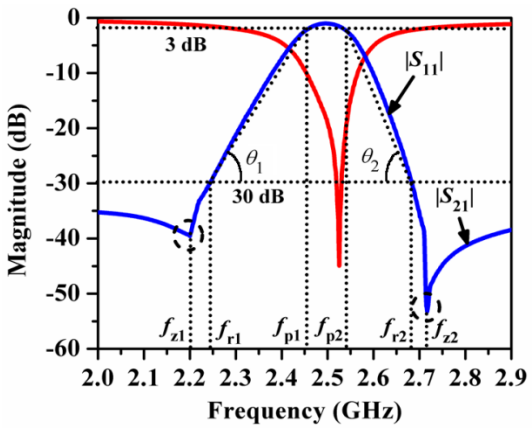

Fig. 5.27. Calculation of shape factor and skirt selectivity factor from the simulated *S*-parameters plot for the folded cross-coupled filter with meander spurline.

The equivalent lumped element circuit of the folded cross-coupled filter with the meander spurline has been obtained in Fig. 5.28 by following the same procedure as L-spurline. The lumped elements circuit of the meander spurline (Refer Chapter 4, Fig. 4.93(b)) has been incorporated into the lumped elements circuit of the cross-coupled filter for the coupled arms as shown in Fig. 5.29. The values of the lumped elements have been computed by following the conventional transmission line theory [1] and are listed in Table 5.4, where L_s, C_s and R_s are the equivalent inductance, capacitance, and resistance for the meander spurline circuit.

The circuit simulated $|S_{21}|$ (dB) plot has been compared with that of the EM simulated plot in Fig. 5.29. It has been witnessed that passbands are in close agreement and fourteen transmission zeros have been generated up to 12 GHz for the circuit simulation plot.

Table 5.4. Values of the equivalent lumped elements of the unit FHL cell of the cross-coupled filter with meander spurline.

Inductors (nH)		**Capacitors (pF)**	
L_1	2.115	$C_{p1} = C_{p2}$	0.121
L_2	2.325	$C_{p3} = C_{p8}$	0.262
$L_3 = L_6$	1.101	$C_{p4} = C_{p5}$	0.048
$L_4 = L_5$	2.965	$C_{p6} = C_{p7}$	0.185
L_s = 2.319 nH C_s = 1.738 pF R_s = 3.448 kΩ		$C_{g1} = C_{g2} = C_{g3}$	0.01
		C_{14}	0.008
		$C_{12} = C_{34}$	0.025
		C_{23}	0.201

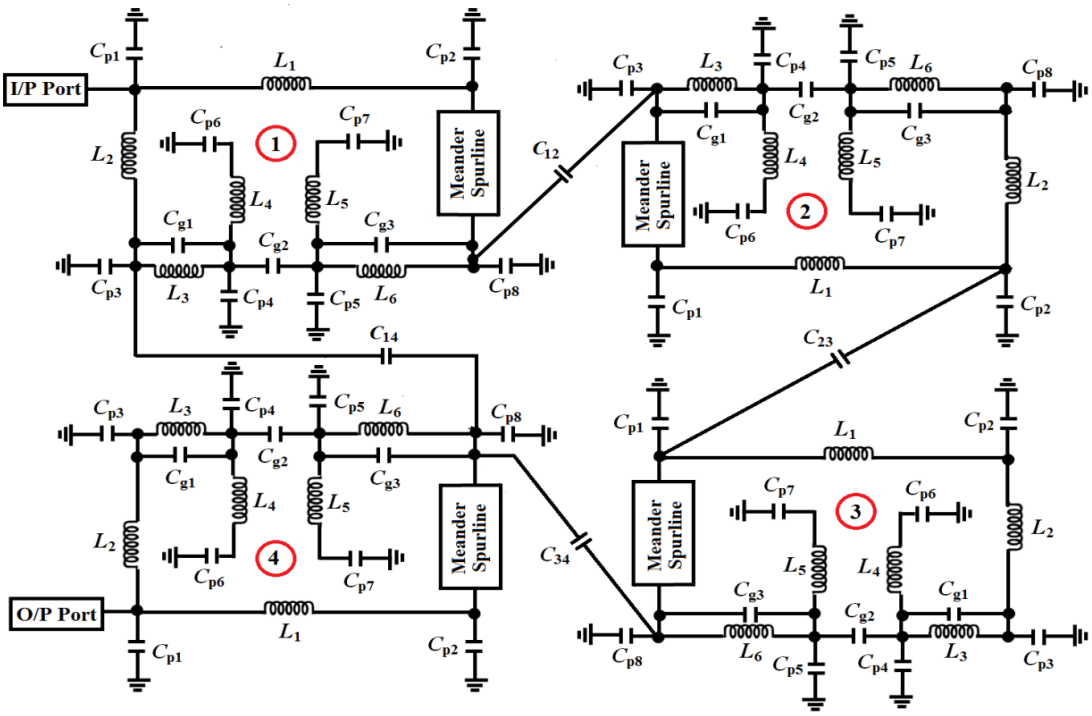

Fig. 5.28. Equivalent lumped elements circuit diagram of the fourth-order folded cross-coupled bandpass filter with meander spurline.

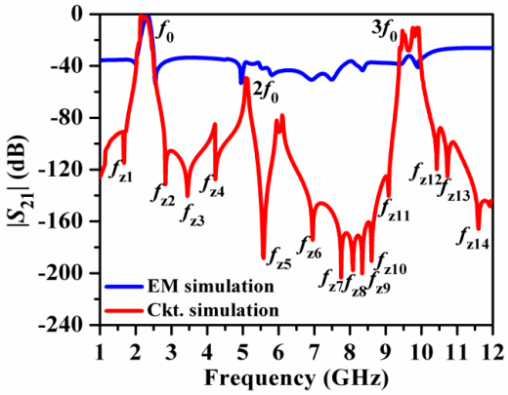

Fig. 5.29. Comparison between the EM and the circuit simulated $|S_{21}|$ (dB) plot of the fourth-order folded cross-coupled bandpass filter with meander spurline.

Moreover, it has been revealed that the attenuation level at $2f_0$ and $3f_0$ has been suppressed greatly due to the spurline.

5.5.1. Fabricated Prototype

The fabricated prototype of the fourth-order folded cross-coupled bandpass filter with meander spurline is shown in Fig. 5.30(a) and the experimental set up is shown in Fig. 5.30(b)-(c).

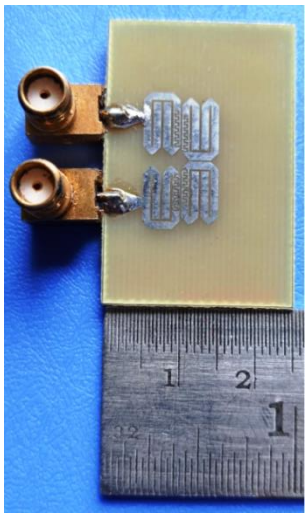

Fig. 5.30. Fabricated prototype of the fourth-order folded cross-coupled bandpass filter with the meander-spurline [4].

5.5.2. Comparison of Simulation vs. Measurement Results

Figs. 5.31(a)-(b) compare the measured and simulated *S*-parameter plots. The experimental procedure has been carried out in the similar way of 3.14.4.1. The generation of transmission zeros at the passband edges with attenuation levels greater than 45 dB has greatly improved the

skirt selectivity of the passband for the cross-coupled filter with a meander spurline, as shown in Fig. 5.31(a). Moreover, the stopband has been extended up to $4f_0$ with a rejection level of 38 dB and up to $4.8f_0$ with a rejection level of 34 dB in measurement. Moreover, multiple transmission zeros have been generated in the stopband with an attenuation level greater than 50 dB. Such a generation of transmission zeros confirms the ability of the meander spurline for enhanced harmonics suppression performance over the L-spurline based filter. Following that, at f_0 = 2.5 GHz and $2f_0$ = 5.0 GHz, the distribution of the surface current vectors for the cross-coupled filter with meander spurline is shown in Fig. 5.32(a)-(b). The surface current vectors have been distributed strongly through the central meander wiggle and have reached the output port with a large strength at 2.5 GHz due to the passband response. However, the distributions of surface current vectors become very small at 5.0 GHz (Fig. 5.31(b)) due to the suppression of the harmonics by the spurline.

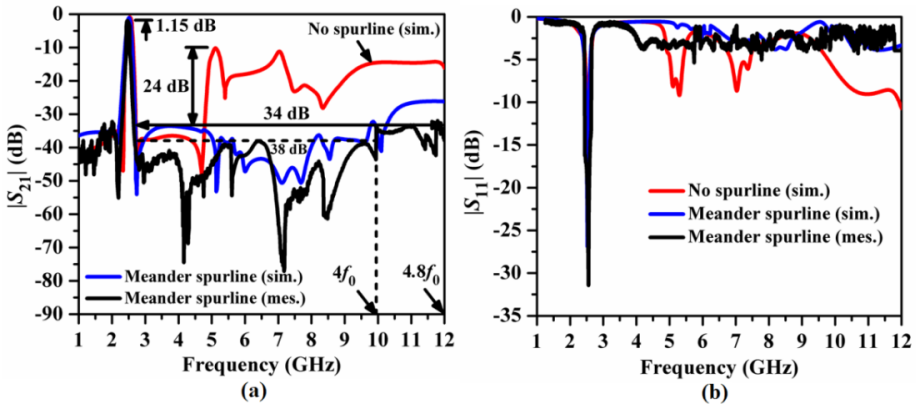

Fig. 5.31. Comparison between the simulated and measured *S*-parameters plots for the fourth-order folded cross-coupled filter with meander spurline: (a) $|S_{21}|$ (dB) and (b) $|S_{11}|$ (dB).

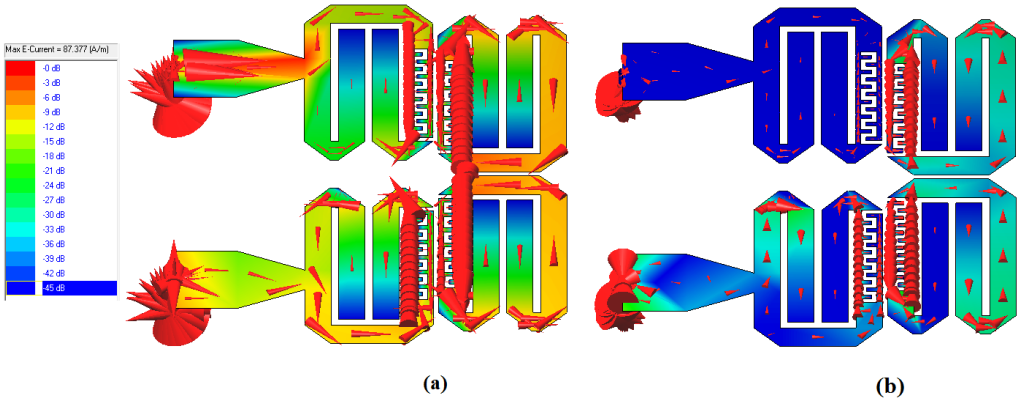

Fig. 5.32. Distribution of surface current vectors for the fourth-order cross-coupled filter with meander spurline at (a) f_0 = 2.5 GHz, and (b) $2f_0$ = 5.0 GHz.

Table 5.5. Determination of different filters' parameters.

f_o (GHz)	*Type of filter*	ξ (dB/GHz)	*SBRL* (dB)	*SBW* (x f_0)	*RSB*	*SF*	*NCS*	*AF*	*FOM*
2.5 GHz	Folded	100	10	4.8	0.608	1.0	0.062	1	980.65
	Folded, L-spurline	135	35	3.76	0.649	3.5	0.061		5027.1
	Folded, meander spurline	270	34 38	4.8 4.0	0.608 0.633	3.4 3.8	0.058		9623.2 11197.6

Table 5.5 tabulates different filters' parameters designed so far as already defined in Chapter 3. It has been revealed from Table 5.5 that a fourth-order folded cross-coupled filter with meander spurline exhibits the maximum Figure-of-Merit (*FOM*) of 11197.6. This value is the maximum of all the filters designed so far in Chapter 3 (parallel-coupled line filters) and Chapter 4 (hairpin-line filters). However, for all cross-coupled filters designed so far in this chapter, the folded hairpin-line cells have been utilized. As it has been discussed in Section 4.6, Chapter 4, centrally corrugated folded hairpin-line cells have the ability to not only decrease the filter size, but also enhance the skirt characteristics of the folded hairpin-line filter. Thus, such centrally corrugated hairpin-line cells with trapezoidal corrugations have been utilized in the next section to design a more compact cross-coupled bandpass filter. Subsequently, trapezoidal-shaped meander spurlines have been incorporated to suppress the harmonics.

5.6. Design of Centrally-Corrugated Cross-Coupled Bandpass Filter

The general structure of the fourth-order centrally corrugated folded cross-coupled bandpass filter (CCFCCBF) with trapezoidal corrugation is shown in Fig. 5.33(a). The centrally-corrugated folded hairpin-line cells have been arranged in hybrid coupling, magnetic coupling, and electric coupling as highlighted in the structure.

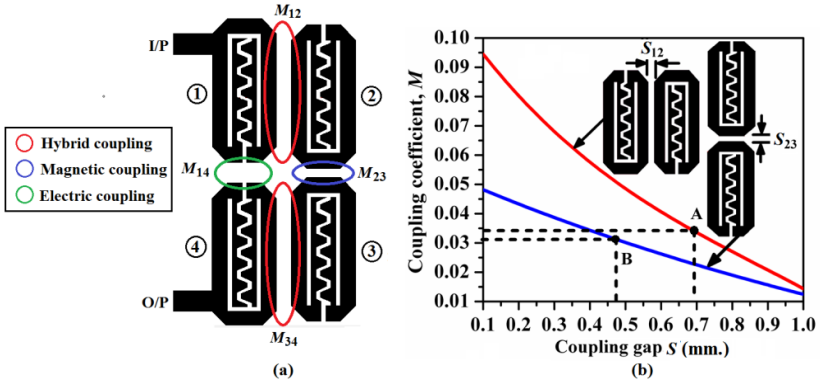

Fig. 5.33. (a) General layout of the fourth-order centrally-corrugated folded cross-coupled bandpass filter, (b) variation of the coupling-coefficient vs. coupling gap between the folded cells.

Accordingly, the initial values of the coupling gaps between the folded cells have been obtained from Fig. 5.33(b). Fig. 5.34 depicts the final optimized layout with dimensions in mm. The filter has occupied a circuit area of 288.75 mm^2 i.e., $0.21\lambda_g \times 0.29\lambda_g$. In Fig. 5.35(a)-(b), the simulated *S*-parameter plots of folded cross-coupled filters with and without central corrugations are compared. It has been observed that two sharp transmission zeros, f_{z1} and f_{z2} have occurred at 2.4 GHz and at 2.6 GHz with attenuation levels of 33 dB and 37 dB. Thus, the skirt characteristics have been improved greatly over the filter without corrugations. Although the attenuation levels at both $2f_0$ and $3f_0$ have been reduced, the stopband rejection level becomes quite large (nearly 6 dB), restricting its applications.

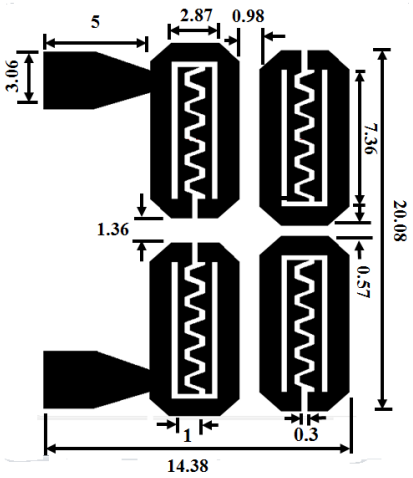

Fig. 5.34. Layout of the fourth-order quasi-elliptic centrally corrugated folded cross-coupled bandpass filter. All dimensions are in mm.

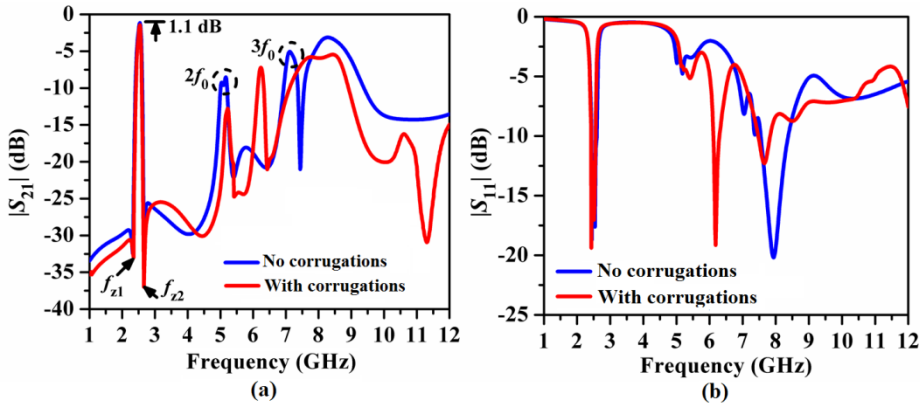

Fig. 5.35. Comparison of the simulated *S*-parameters plots between the fourth-order folded cross-coupled filters with and without corrugations: (a) $|S_{21}|$ (dB) and (a) $|S_{11}|$ (dB).

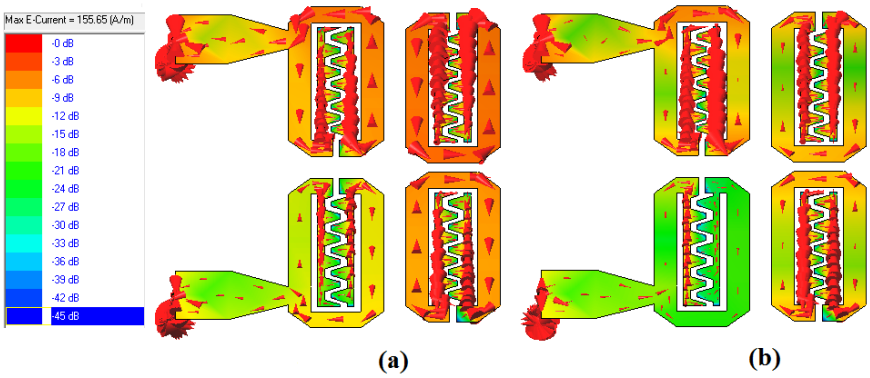

Fig. 5.36. Distribution of surface current vectors for the fourth-order folded cross-coupled filter with trapezoidal corrugations at (a) 2.5 GHz, and (b) 6.27 GHz.

Following that, at 2.5 GHz (f_0) and 6.27 GHz (f_0), the distribution of the surface current vectors for the folded cross-coupled filter with trapezoidal corrugations was investigated in Fig. 5.36(a)-(b). The surface current vectors have been concentrated strongly through the central corrugations at 2.5 GHz due to the passband response. Moreover, the distribution of the surface current vectors becomes less strong at 6.27 GHz due to the presence of $3f_0$. Hence, in the next section, suppression of the harmonics' attenuation level below 35 dB has been achieved by introducing trapezoidal-shaped meander spurline in the coupled regions of the folded cells.

5.7. Suppression of Harmonics for the Centrally-Corrugated Cross-Coupled Bandpass Filter by Trapezoidal Meander Spurline

It has been revealed from Section 4.6.3 of Chapter 4 that trapezoidal shaped meander spurline has the ability to suppress the harmonics up to $3.88f_0$ with a rejection level of 35 dB for the fourth-order folded hairpin-line bandpass filter. As a result, as shown in Fig. 5.37(a), a trapezoidal-shaped meander spurline was used for the fourth-order folded cross-coupled filter. The meander spurline is highlighted by red ink. As a result, the values of the coupling gaps between adjacent cells for the meander spurline, with a number of alternate slots N = 8, were determined from the design curve, as shown in Fig. 5.37(b). The layout of the final filter with spurline is shown in Fig. 5.38(a). All dimensions are in mm. The final filter occupies a circuit area of 241.57 mm^2 i.e., $0.2\lambda_g \times 0.26\lambda_g$.

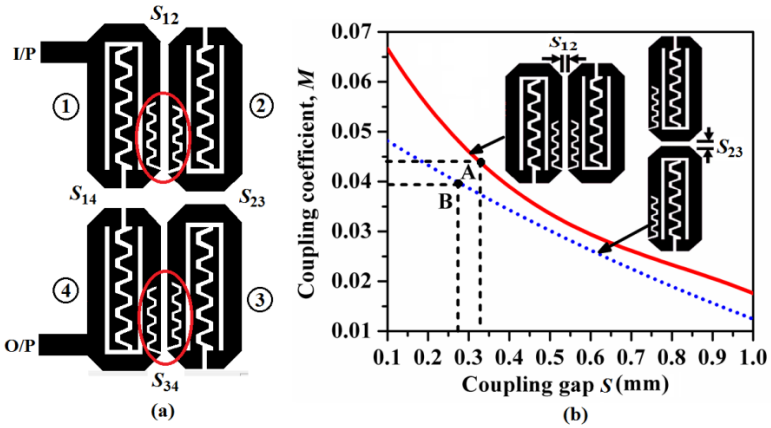

Fig. 5.37. (a) Layout of the fourth-order folded centrally corrugated cross-coupled bandpass filter with spurline, (b) variation of coupling-coefficient vs. coupling gap for a pair of meander spurline based corrugated cells.

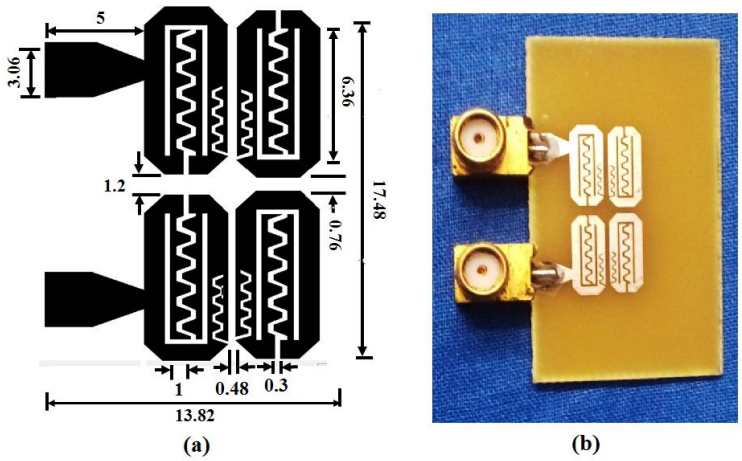

Fig. 5.38. Layout of the fourth-order cross-coupled CCDFHL based bandpass filter with spurline.

Accordingly, size reductions of 9.56% compared to the filter without spurline (Fig. 5.34), and 20.42% compared to the DFHL filter (Fig. 5.9). Fig. 5.38(b) shows the fabricated prototype.

5.7.1. Comparison of Simulation vs. Measurement Results

The simulated vs. measured *S*-parameter plots for the proposed filters without and with spurline are shown in Figs. 5.39(a)-(b). It has been revealed that the measured passband response is quite satisfactory with the simulated plot. The passband insertion loss becomes 1.05 dB. The stopband has been extended up to $2.88f_0$ with a rejection level of 29 dB and a rejection level of 16 dB up to $4.8f_0$. Multiple transmission zeros have been generated in the stopband from 2.6 GHz to 12 GHz.

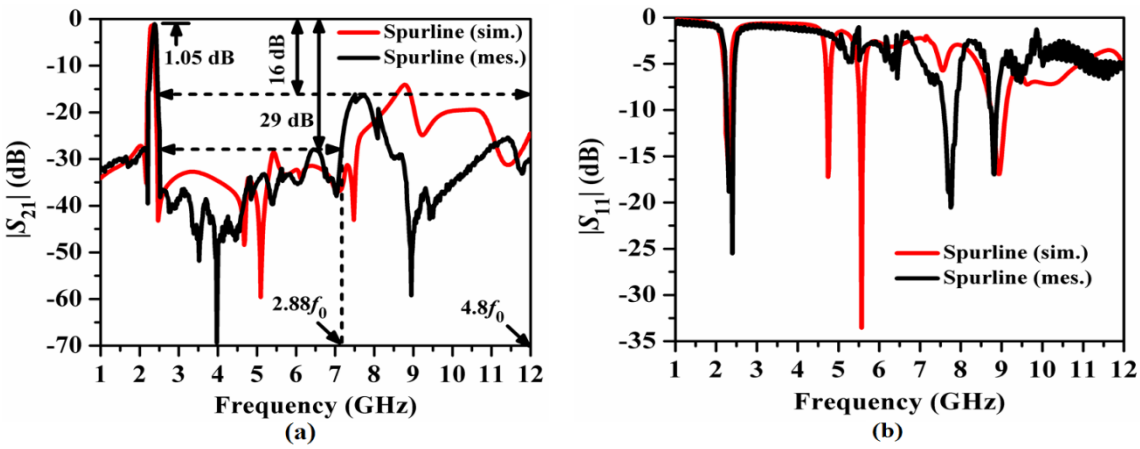

Fig. 5.39. Comparison between the simulated vs. measured (a) $|S_{21}|$ (dB) and (b) $|S_{11}|$ (dB) plots.

Moreover, the value of the passband return loss has been obtained to be more than 20 dB for the filter with spurline. Following that, at 2.5 GHz (f_0) and 5.0 GHz ($2f_0$), the distribution of the surface current vectors for the folded centrally-corrugated cross-coupled filter with trapezoidal corrugations was investigated in Figs. 5.40(a)-(b). The surface current vectors have been concentrated strongly through the trapezoidal meander spurline at 2.5 GHz due to the passband response.

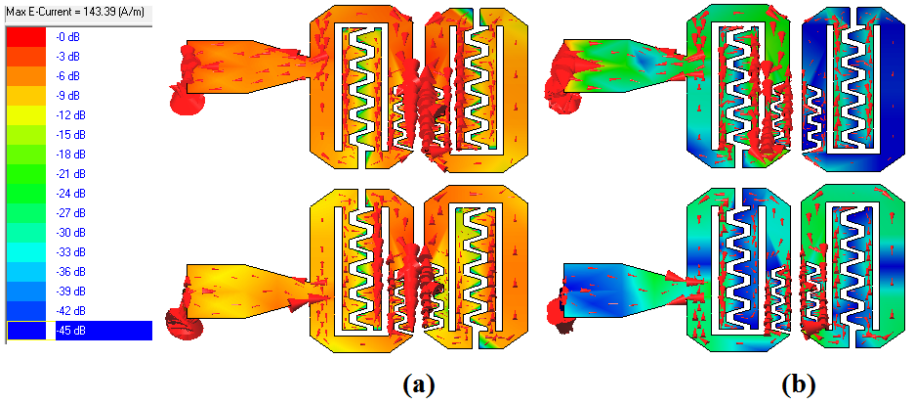

Fig. 5.40. Distribution of surface current vectors for the fourth-order folded cross-coupled filter with trapezoidal corrugations at (a) 2.5 GHz, and (b) 6.27 GHz.

Table 5.6. Determination of different filters' parameters.

f_o (GHz)	*Type of filter*	ξ (dB/GHz)	*SBRL* (dB)	*SBW* (x f_0)	*RSB*	*SF*	*NCS*	*AF*	*FOM*
2.5 GHz	without spurline	135	7	4.8	0.608	0.7	0.062	1	926.7
	with spurline	108	29 16	2.88 4.8	0.674 0.604	2.9 1.6	0.052		4059.6

Moreover, the distribution of the surface current vectors becomes less strong at 5.0 GHz due to the presence of $2f_0$. Table 5.6 tabulates corrugated filters' parameters with and without spurline. It has been revealed from Table 5.6 that a fourth-order folded centrally-corrugated cross-coupled filter with trapezoidal-shaped meander spurline has achieved the Figure-of-Merit (*FOM*) of 4059.6, which is 77.2% more than the filter without spurline. Thus, the effectiveness of the trapezoidal-shaped meander spurline based cross-coupled filter on harmonic suppression along with compactness has been justified. It can be concluded from this chapter that the folded cross-coupled bandpass filter has improved skirt selectivity, narrow passband, low insertion loss, high return loss, wide stopband up to $4.88f_0$, improved rejection level of 40 dB, enhanced Figure-of-Merit value (more than 10000), and occupies a compact structure to be fitted in modern WLAN systems.

References:

[1] J. S. Hong and M. J. Lancaster, "Microstrip Filters for RF/Microwave Applications," *John Willey & Sons, Inc.*, New York, NY, 2001, ISBN 0-471-22161-9, Ch. 8, pp. 235-258, 2001.

[2] T. K. Das, S. Chatterjee, S. K. A. Rahim, and T. K. Geok, "Compact High-Selectivity Wide Stopband Microstrip Cross-Coupled Bandpass Filter With Spurline,' *IEEE Access*, vol. 10, pp. 69866-69882, June 2022, doi: 10.1109/ACCESS.2022.3187408.

[3] T. K. Das, A. Chakraborty, S. Chatterjee, B. Gupta, "Centrally Corrugated Cross-Coupled Wide Stopband Folded Bandpass Filter with Spurline," *Proceedings of 2022 Microwave Mediterranean Symposium (MMS)*, pp. 1-6, May 2022.

Conclusions and Future Scope

6.1. Conclusions

In the present thesis, design of compact microstrip bandpass filters with multispurious harmonics suppression has been reported. With the advancements of modern-days wireless communication systems the demands for compact bandpass filters are increasing day-by-day. Moreover, for faithful reproduction of the received signal, the filters must have the capability to reject the unwanted spurious signals either completely (ideal situation) or suppress their attenuation levels to an acceptable limits. In this context, the proposed filters have been designed based on two primary objectives: (1) reduction of size by folding (2) suppression of the harmonics due to folding. From the literature review it has been revealed that researches have been carried out primarily in two ways: (1) size reduction of filters by different folding mechanism where the improvement of the passband responses have been mainly focussed and (2) employment of different nonuniform perturbations to suppress the harmonics. However, very few works have been performed where both the above features have been integrated in a single filter.

Subsequently, in the first phase of our work, two conventional parallel-coupled line filters with center frequency, f_0 = 2.5 GHz and 5.25 GHz with fractional bandwidth of 20% applicable for WLAN have been proposed in chapter 3. The sizes of the filters have been reduced by folding the structure symmetrically in the transverse plane and accordingly more than 60% of size reduction has been achieved. All the filters have been designed on FR4 substrate materials with ε_r = 4.4, thickness, h =1.6 mm, loss tangent, tanδ = 0.02. In addition, the skirt characteristics of the passband have been improved significantly due to additional cross-coupling between two inline resonators at the symmetry plane. However, the attenuation level of the harmonics has not been degraded much by the folding mechanism. Accordingly different types of perturbations with optimum dimensions such as periodic rectangular, saw-toothed and quarter-elliptical grooves, Koch rectangular fractals, periodic rectangular corrugations, periodic triangular corrugations, asymmetric perturbations, quasi

Minkowski fractals have been investigated. As an optimum result, a stopband up to $2.4f_0$ with a rejection level of 35 dB has been achieved with quarter-elliptical grooves and a stopband up to $2.4f_0$ with a rejection level of 39 dB has been recorded with the triangular corrugations. Thus, periodic corrugations have enhanced the rejection level over periodic grooves.

As an alternative approach asymmetric rectangular perturbations have been studied for folded and inline parallel-coupled line filters for both S- and C- band and a stopband upto $2.4f_0$ with a rejection level of 33 dB has been achieved as an optimum result. Subsequently, fractal geometries like Koch and Minkowski fractal have been incorporated to utilize their space filling and self-similarity properties. As the best result a stopband upto $2.3f_0$ with a rejection level of 36 dB has been recorded for Minkowski fractal based S-band inline filter. For all the designs mentioned so far the stopband width has been limited to only $2.4f_0$, although the rejection level becomes quite satisfactory. Thus, the study has been extended further in chapter 3 by incorporating periodic trapezoidal corrugations for higher order harmonics suppression. By properly adjusting the coupling periods of the trapezoidal corrugations between the parallel-coupled lines, a stopband upto $4.8f_0$ with a rejection level of 36 dB has been achieved for the S-band inline filter.

However, the sizes of both the folded and inline parallel-coupled line filters are still quite large, restricting their applications in modern wireless systems. Moreover, it is lest possible to design narrowband filters by this topology as the coupling gaps will be increased, degrading the passband response. Accordingly, folded hairpin-line filter has been proposed as the second work in chapter 4 in which narrowband filter (less than 5%) have been designed by keeping the center frequency unaltered. In this work, the open-end arms of the conventional hairpin-line filters have been folded twice symmetrically toward the inward direction forming a folded hairpin-line cell. Accordingly, the skirt characteristics have been improved and the harmonics have been shifted to higher frequencies. However, the attenuation levels at the harmonics have not been affected much by this folding mechanism. Accordingly, periodic grooves with optimum dimensions and Minkowski fractals have been incorporated to the coupled edges of the adjacent folded hairpin-line cells. As an optimum result an extended stopband up to $3f_0$ with a rejection level of 33 dB along with a size reduction of 30% compared to the size of the folded parallel-coupled line filter has been achieved. The stopband has been extended further by employing spurline to the coupled arms. Three

different types of spurline such as L-shaped, T-shaped and meander shaped have been studied in detail. The equivalent lumped elements circuits have been obtained for all the filters. As an optimum result compactness of 46%, a stopband up to $4.48f_0$ with a rejection level of 40 dB have been recorded. As a modification, the folded arms of the hairpin-line cells have been modified with trapezoidal shaped corrugated arms. As a result, the size of the filter has been reduced more by 10% and a stopband up to $3.88f_0$ with a rejection level of 35 dB have been achieved with trapezoidal meander spurline.

Subsequently, the folded hairpin-line cells have been rearranged in cross-coupled configuration in chapter 5. Thus, the skirt selectivity of the proposed cross-coupled filters have been enhanced greatly. Subsequently, L-spurline and rectangular meander spurline have been investigated for the cross-coupled filters for harmonics suppression. As an optimum result, a stopband up to $4f_0$ with a rejection level of 38 dB have been achieved with rectangular meander spurline. The study has been finished with trapezoidal corrugated folded arms along with trapezoidal meander spurline. This time, although the size of the cross-coupled filter has been reduced by 70% which is the minimum size, but the stopband bandwidth has been reduced to only $2.88f_0$ with the rejection level of 29 dB. For all the filters the passband insertion loss has been recorded as less than 2 dB and return loss has been recorded better than 15 dB.

6.2. Future Scope

Though an extensive study of multispurous harmonics suppression for compact bandpass filters has been carried out in the thesis there are still a lot of possibilities to be explored for achieving better performance. Some such possibilities are briefly mentioned bellow.

1. The size of the proposed cross-coupled filters is still quite large which can be further reduced by performing multiple folding.
2. The bandwidth of the proposed filters is restricted to 4% which can be further reduced for narrowband filters. However, the coupling would be reduced then, resulting increase of the insertion loss and decrease of the return loss. This in turn will degrade the filter's passband. Thus, detailed analysis will be required for such narrowband filter design.
3. In the present thesis parallel-coupled line, hairpin-line and cross-coupled filters' topologies have been studied in detail. However, dual-mode filter topology has not

been studied. It has been revealed from the literature study that dual-mode filter has the capability to exhibit not only compact structure but also narrow bandwidth. Very few works have been carried out on the harmonics suppression for dual-mode filters.

4. In the present thesis only L-shaped, T-shaped and meander spurline of rectangular and trapezoidal shapes have been investigated in detail. However, there are other spurline structures available in literatures which could be studied for the proposed filters.
5. Finally, in the present thesis, all the filters designed have a single passband. However, the demands for dual-band filters with harmonics suppression feature are increasing greatly for the modern day's wireless systems. Therefore, the knowledge gathered so far from this research work could be applied for dual-band filters applicable for WLAN.

PUBLISHED PAPER

Journals:

1) Improved second harmonic suppression in a compact coupled-line bandpass filter with triangular corrugations

Tarun Kumar Das and Sayan Chatterjee

Microsystem Technologies, vol. 25, no. 5, pp. 1945-1956, May 2018, doi: 10.1007/s005420183940-0

Abstract

This paper presents the design of a miniaturized coupled-line bandpass filter centered at 5.25 GHz with a fractional bandwidth of 20% for wireless local area network applications. Size reduction has been achieved by incorporating two different approaches in which symmetrical folding techniques have been employed. Periodic triangular corrugations have been introduced in the coupled edges of line for compensating the asymmetry in even- and odd-mode phase velocities. Accordingly, two different filter structures have been designed and optimized: folded V-shaped with five corrugations and in-line W-shaped with four corrugations. Second harmonic suppression of 62 dB and 30 dB and size reduction of 62% and 74% are achieved for folded and in-line filter respectively.

2) Spurious harmonic suppression in compact coupled-line bandpass filter with asymmetric perturbations

Tarun Kumar Das and Sayan Chatterjeee

International Journal of Electronics, vol. 107, no. 4, pp. 576-595, 2020,
doi:10.1080/00207217.2019.1672801

Abstract

Present article exhibits the design of a third-order compact parallel-coupled line bandpass filter at 5.25 GHz having asymmetric perturbations to suppress the second harmonic. Initially, the effects of compactness on filter characteristics have been studied by synthesizing the distributed filter network into its equivalent circuit model. The design has been initiated by computing the unit cell model, which leads to the first-order and third-order design instances with an improvement in compactness over the traditional parallel-coupled line filter. In contrary, compactness in the filter characteristics degrades the second harmonic level subject to enhanced imbalances among the odd- and even-mode velocities at the coupled lines. Subsequently, the improvement in the harmonic suppression of 53 dB and 58 dB has been achieved by incorporating different non-uniform perturbations to the outer and

coupled edges of the compact filters. Accordingly, compactness of 58% and 71% have been obtained subject to the folded and in-line designs over the conventional layout.

3) Compact hairpin line bandpass filter with improved spurious passbands suppression

Tarun Kumar Das and Sayan Chatterjee

International Journal of Electronics, vol. 108, no. 8, pp. 1309-1325, August 2021

doi: 10.1080/00207217.2020.1859142

Abstract

The present paper describes the design of a folded hairpin-line bandpass filter centered at 2.5 GHz applicable for Wireless Local Area Network (WLAN) with improved spurious suppression. The size of the conventional filter has been reduced by 30% by folding the open-end arms towards the inward direction. Thus, improvements over the skirt characteristics and shifting of the second harmonic to higher frequency region have been obtained. However, the attenuation level at the harmonic frequency remains

almost unaffected. Subsequently, the inner and outer edges of the coupled-lines have been modified with Minkowski fractals to compensate for the modal phase velocities. As a result, more than 36 dB of harmonic suppression up to three times the center frequency along with size reduction of 30% has been achieved.

4) Multi-Spurious Harmonics Suppression in Folded Hairpin Line Bandpass Filter by Meander Spur-Line

Tarun Kumar Das and Sayan Chatterjee

International Journal of RF and Microwave Computer-Aided Engineering, vol. 31, no. 11, pp. e22858, May 2021, doi:10.1002/mmce.22858

Abstract

The current paper describes the design of a fourth-order compact narrow-band hairpin-line bandpass filter centered at 2.5 GHz and enhanced stopband suppression ∼38 dB required for wireless local area network (IEEE802.11b). The size reduction of 24% has been achieved for a conventional hairpin-line filter with a second-order inward folding of the open-end arms with an improvement in the skirt characteristics. However, the folding mechanism has been overshadowed by the presence of spurious harmonics with an attenuation level of <10 dB. Subsequently, L-shaped spurlines with optimum dimensions have been incorporated in the coupled arms of the folded hairpin-line cells. Three fourth-order filters have been designed with the incorporation of spurlines in different coupling regions, fabricated, and tested experimentally. Accordingly, an extended stopband with a rejection level of 38

dB up to 4.48f_0 and a size reduction of 18% over the conventional hairpin-line filter has been achieved.

5) Harmonic Suppression by using T-shaped Spur-Line in a Compact Hairpin-Line Bandpass Filter

Tarun Kumar Das and Sayan Chatterjee

Radioengineering, vol. 30, no. 2, June 2021, doi: 10.13164/re.2021.0296

Abstract

This article exhibits the design of a fourth-order compact hairpin-line bandpass filter centered at 2.5 GHz and with a 3 dB fractional bandwidth of 5% along with a sharp roll-off factor and wide stopband characteristics required for Wireless Local Area Network (WLAN). Miniaturization of the conventional hairpin-line filter has been achieved by folding the open end arms twice towards the inward direction and accordingly, a size reduction of 42% has been obtained. Subsequently, T-shaped spur-lines with optimum dimensions have been incorporated at both the inner and outer edges of the coupled arms of the folded hairpin-line cell. Accordingly, two fourth-order folded fitters with outer T-shaped and double T-shaped spur-lines have been designed and verified experimentally. An extended stopband with a rejection level of 39 dB up to 3.2f_0 along with a size reduction of 46% has been achieved.

6) Spur-Line Embedded Compact Hairpin-Line Bandpass Filter for Wide Harmonic Suppression

Tarun Kumar Das and Sayan Chatterjee

International Journal of Microwave and Wireless Technologies, pp. 1-13, June 2021,

doi: 10.1017/S1759078721001197

Abstract

The present article exhibits the improvement in wide stopband harmonic suppression techniques of fourth-order compact hairpin-line Chebyshev type narrowband (4%) bandpass filter centered at 2.5 GHz by meander spur-line. Initially, the compactness of 42% over the conventional hairpin-line cell has been achieved by folding the open-end arms of the hairpin line to folded hairpin-line cell. Accordingly, the improvement of the skirt characteristics and the shifting of the harmonics to higher frequencies have been observed with the cost of harmonics attenuation levels' degradation. Subsequently, an improvement in the stopband rejection level of 40 dB up to 4f_0 has been achieved by incorporating meander spur-line to all the coupled edges of the adjacent folded cells of the compact filters along with compactness of 38%.

7) Compact High-Selectivity Wide Stopband Microstrip Cross-Coupled Bandpass Filter With Spurline

Tarun Kumar Das, Sayan Chatterjee, Sharul Kamal Abdul Rahim and Tan Kim Geok

IEEE Access, vol. 10, pp. 69866-69882, June 2022, doi: 10.1109/ACCESS.2022.3187408

Abstract

The article presents the design of a compact narrowband microstrip cross-coupled bandpass filter with improved selectivity and a wide stopband. The proposed fourth-order quasi-elliptic filter is designed at 2.5 GHz with a fractional bandwidth of 4% suitable for WLAN applications. At first, doubly- folded half-wavelength hairpin lines have been arranged symmetrically in a cross-coupled configuration combining the electric, magnetic, and mixed-coupling. Accordingly, a size reduction of 17% over the folded inline hairpin-line filter with the same specifications has been achieved. Moreover, the selectivity has been improved greatly by the introduction of two deep transmission zeros with an attenuation level of 48 dB at the edges of the passband. However, the presence of the spurious harmonics with an attenuation level of 10 dB limits the performance of the filter related to the stopband rejection. As a remedy, conventional and meander spurlines have been incorporated in each hybrid coupled section of adjacent cross-coupled cells for achieving the modal phase velocity compensation. Accordingly, an extended stopband with a rejection level of 38 dB up to $4f_0$ has been recorded by using a meander spurline and an overall size reduction of 33% has been achieved.

Conference proceedings:

1) Design of a finite attenuation pole miniaturized S-band lowpass filter using elliptic function

Tarun Kumar Das and Sayan Chatterjee

Proceedings of International Conference on Microwave, Optical and Communication Engineering (ICMOCE 2015), Bhubaneswar, India, pp. 404-407, 18-20 December, 2015, doi: 10.1109/ICMOCE.2015.7489778

Abstract

A miniaturized microstrip lowpass filter design using elliptic function is presented in this paper. The proposed filter has a cut-off frequency of 2.5 GHz with passband ripple 0.1 dB and stopband insertion loss greater than 20 dB at 2.85 GHz. It provides two finite attenuation poles at 2.945 GHz and 4.015 GHz in the stopband having attenuation of the order of 35 dB and 50 dB respectively. Different types of design characterization have been investigated of the proposed filter and a comparative study based on design parameters and dimensions has been provided.

2) Design of a compact symmetrical C-Band Microstrip Bandpass Filter with periodic Sawtooth Grooves

Tarun Kumar Das and Sayan Chatterjee

Proceedings of 2nd International Conference on Innovative Advancements in Engineering & Technology (IAET 2016), Jaipur, India, vol. 5, no. 1, pp. 254-259, 1-2 April, 2016.

Abstract

Design of a miniaturized symmetrical bandpass filter (BPF) using parallel-coupled half-wavelength microstrip resonators with improved stopband characteristics and 2nd harmonic suppression is presented. The proposed filter is designed at a center frequency of 5.25 GHz with a stopband insertion loss greater than -10 dB at 5.15 GHz and fractional bandwidth of 20% (4.74 - 5.80 GHz). The conventional parallel-coupled line bandpass filter structure has been folded symmetrically about the horizontal plane and consecutive sawtooth periodic grooves are introduced to the parallel lines. Thus there has been a significant improvement in 2nd harmonic suppression to almost -34.51 dB. Size reduction of 46.73% is accomplished with respect to the conventional filter

3) Performance of periodic grooves on harmonic rejection in C band folded edge coupled microstrip bandpass filters

Tarun Kumar Das and Sayan Chatterjee

Proceedings of International Conference on Computational Science and Engineering (ICCSE 2016), Kolkata, India, pp. 205-209, 4-6 October, 2016, doi: 10.1201/9781315375021-40.

Abstract

Design of a miniaturized and compact V-shaped half-wavelength edge-coupled microstrip bandpass filter with improved harmonic suppression is presented. The proposed filter is designed at a center frequency of 5.25 GHz with 20% fractional bandwidth (4.75-5.80 GHz) applicable in WLAN. The conventional parallel-coupled bandpass filter structure has been folded symmetrically about horizontal plane and consecutive square and rectangular shaped periodic grooves are inserted to the parallel lines. Thus, the 2nd harmonic is suppressed significantly to -44.38 dB and -43.71 dB and a size reduction of 59.05% and 59.67% is achieved for square and rectangular grooves respectively with respect to the conventional filter.

4) 2nd Harmonic Suppression in Parallel-Coupled Microstrip Bandpass Filter by using Koch Fractals

Tarun Kumar Das and Sayan Chatterjee

Proceedings of IEEE Annual India Conference (INDICON 2016), Bengaluru, India, pp. 1-6, 16-18 December, 2016, doi: 10.1109/INDICON.2016.7838919

Abstract

Design of a folded miniaturized band pass filter using parallel-coupled half-wavelength microstrip resonators with improved stopband skirt characteristics and harmonic suppression is presented in this paper. The proposed filter has fractional bandwidth of 20% subject to design frequency of 5.25 GHz. Koch fractal geometry has been employed in each section of coupled lines for improvement in bandwidth and harmonic suppression. Accordingly, 2nd harmonic suppression of -36 dB and size reduction of 58.4% is achieved compared to the conventional parallel-coupled bandpass filter. The folded structure is modified further to an in-line parallel-coupled filter structure in which 2nd harmonic suppression of -34dB and size reduction of 72.1% has been achieved by using Fractals.

5) Spurious Harmonic Suppression in a Folded Parallel-Coupled Microstrip Bandpass Filter by using Triangular Corrugations

Tarun Kumar Das and Sayan Chatterjee

Proceedings of Devices for Integrated Circuit (DevIC 2017), Kalyani, India, pp. 391–395, 23-24 March, 2017, doi: 10.1109/DEVIC.2017.8073977

Abstract

Design of a compact band pass filter using parallel-coupled half-wavelength microstrip resonators with improved stopband skirt characteristics and harmonic suppression is presented in this paper. The proposed filter has fractional bandwidth of 20% subject to design frequency of 5.25 GHz for WLAN applications. Periodic triangular corrugations have been employed in each coupled section of parallel lines for suppression of 2nd harmonic. Accordingly, 2nd harmonic suppression of 62.45 dB and size reduction of 63% is achieved compared to the conventional parallel-coupled bandpass filter.

6) Harmonic Suppression in In-line Parallel-Coupled Microstrip Bandpass Filter by Minkowski Fractals

Sayan Chatterjee, Tarun Kumar Das, and Bhaskar Gupta

Proceedings of 17th Mediterranean Microwave Symposium (MMS 2017), Marseille, France, pp. 1-4, 28-30 November, 2017, doi: 10.1109/MMS.2017.8497142

Abstract

Present paper highlights an in-line third order parallel-coupled microstrip line Chebyshev bandpass filter at 2.5 GHz with Minkowski fractals. An in-line configuration provides more than 62% of size reduction compared to conventional coupled-line filter, with a degradation of second harmonic passband. By employing fractals at the edges of each section of the coupled-lines, modal characteristic impedances are modulated to achieve phase velocity compensation, resulting around 42 dB suppression of the unwanted second harmonic in the modified in-line structure having 65% of size reduction. Present design with a fractional bandwidth of 15% has been utilized for WLAN application.

7) Harmonic Suppression in an In-line Chebyshev Bandpass Filter by Asymmetrical Perturbations

Tarun Kumar Das and Sayan Chatterjee

Proceedings of IEEE MTT-S International Microwave and RF Conference (IMaRC 2017), Ahmedabad, India, pp. 1-5, 11-13 December, 2017, doi: 10.1109/IMaRC.2017.8449689.

Abstract

Present article provides the design of an in-line parallel-coupled Chebyshev bandpass filter centered at 5.25 GHz with a fractional bandwidth of 20% for WLAN applications. The coupled-lines are modified by asymmetric rectangular perturbations subject to strong and weak coupling. The proposed filter structure exhibits second harmonic suppression of 51dB with a size reduction of 71% and 31% compared to conventional and folded parallel–coupled lines filters respectively.

8) Phase Velocity Compensation in Compact Coupled-Line Bandpass Filter with Square Corrugations

Tarun Kumar Das and Sayan Chatterjee

Chapter of Social Transformation – Digital Way, Communications in Computer and Information Science Book Series (CCIS) Springer, Singapore, Annual Convention of the Computer Society of India, (CSI 2018), Kolkata, India, vol. 836, pp. 29–41, 19-21 January, 2018, doi:10.1007/978-981-13-1343-1_4.

Abstract

Present paper highlights the design of a compact coupled-line bandpass filter with extended stopband and improved second harmonic suppression. The proposed filter is designed at a center frequency of 2.5 GHz with 20% fractional bandwidth applicable in WLAN. The size of the ladder-type parallel-coupled line bandpass filter has been reduced to 44% and 62% by modifying it to folded and in-line structure. Accordingly, periodic square shaped corrugations are inserted to the coupled edges of the parallel lines. The second harmonic suppression of 60dB with stopband rejection level of 62 dB and a

size reduction of 52% have been achieved for folded filter with 6 periodic square corrugations. The in-line filter with four square corrugations gives the second harmonic suppression of 55 dB with a stopband rejection level of 58dB and a size reduction of 70%.

9) Multispurious Harmonic Suppression in Compact Coupled-Line Bandpass Filters by Trapezoidal Corrugations

Sayan Chatterjee and Tarun Kumar Das

Proceedings of IEEE 18th Mediterranean Microwave Symposium (MMS 2018), Istanbul, Turkey, 31 October- 2 November, 2018, pp. 149–152, doi: 10.1109/MMS.2018.8611809.

Abstract

Present paper highlights the design of compact third-order coupled-line Chebyshev bandpass filters centered at 2.5 GHz with multispurious harmonics suppression. The conventional filter has been folded symmetrically about the horizontal plane miniaturized to folding and in-line configurations with compactness of more than 50% and 60%. However, degradations of harmonic levels have been occurred for the proposed folding configurations due to additional open-end couplings. Accordingly, trapezoidal corrugations with optimum dimensions and periodicity have been employed in both $\lambda/4$ length coupled end sections and $\lambda/6$ length coupled middle sections to suppress spurious harmonics at $2f_0$, $3f_0$ and $4f_0$. As a result, an extended stopband with suppression level around 28dB upto $4.8f_0$ along with a compactness of 67% has been obtained.

10) Compact Hairpin-Line Bandpass Filter with Harmonic Suppression by Periodic Grooves

Sayan Chatterjee and Tarun Kumar Das

Proceedings of IEEE 19th Mediterranean Microwave Symposium (MMS 2019), Hammamet, Tunisia, pp. 1-4, 31 October-2 November, 2019, doi: 10.1109/MMS48040.2019.9157328

Abstract

The present paper highlights the design of a third-order double-folded hairpin line Chebyshev bandpass filter centered at 2.5 GHz with improved second harmonic suppression performance applicable for Wireless Local Area Network (WLAN). The conventional hairpin-line filter has been folded twice at the open end arms and accordingly, a size reduction of 19% has been obtained. The skirt characteristics have been improved and the second harmonic has been shifted to higher frequency due to the folding mechanism. However, the harmonic attenuation level remains almost unaffected. Subsequently, square grooves with optimum dimensions and periodicity have been employed at the outer edges of the coupled resonators to achieve phase velocity compensation between even- and odd-

modes. As a result, more than 40 dB of harmonic suppression along with size reduction of 25% has been achieved with three periodic square grooves.

11) Compact coupled-line microstrip bandpass filter with spurious passband suppression using Minkowski fractal

Tarun Kumar Das and Sayan Chatterjee

Proceedings of URSI Regional Conference on Radio Science (URSI-RCRS 2020), Varanasi, India, pp. 1-4, 12-14 February, 2020, doi: 10.23919/URSIRCRS49211.2020.9113422

Abstract

The present article exhibits the improvement in harmonic suppression of the compact third-order coupled-line Chebyshev bandpass filter centered at 2.5 GHz by Minkowski fractals. The harmonic suppression performance has been investigated for the symmetrically folded coupled-line filter by incorporating Minkowski fractals with proper indentation to the outer and coupled edges. Accordingly, the modal phase velocity compensation has been achieved by the space filling property of the fractals. More than 46 dB and 48 dB of stopband rejection levels along with a size reduction of more than 50% have been obtained experimentally for the filters with first and second order iteration of the fractals.

12) Improved Stopband Rejection in Compact Microstrip Filters by Transmission Zero Reallocation

Tarun Kumar Das and Sayan Chatterjee

Proceedings of IEEE Calcutta Conference (CALCON2020), Kolkata, India, pp. 10-14, 28-29 February, 2020, doi: 10.1109/CALCON49167.2020.9106476

Abstract

The design of compact microstrip bandpass filters with a center frequency of 5.25 GHz applicable for WLAN with the standard of IEEE 802.11a is presented in this article. The conventional coupled-line filter has been folded at the symmetry plane, which results in the improvement of upper stopband skirt characteristics. However, the harmonic rejection level remains almost unaffected due to the phase velocity imbalance. Subsequently, the coupled-lines have been modified by inserting quarter-elliptical grooves and the transmission zero reallocation has been employed. Fabrication of the optimized third-order folded filters has been carried out to justify the effectiveness of periodic grooves in the improvement of harmonic suppression. A wide stopband below 35 dB of attenuation level up to $2.4f_0$ has been obtained experimentally. Moreover, the filter size has been reduced to 58% compared to the conventional filter.

13) Harmonic Suppression in a Folded Hairpin-Line Cross-Coupled Bandpass Filter by using Spur-Line

Tarun Kumar Das and Sayan Chatterjee

Proceedings of IEEE Devices for Integrated Circuit (DevIC 2021), Kalyani, India, pp. 474-478, 19-20 May, 2021 doi: 10.1109/DevIC50843.2021.9455915

Abstract

The design of a compact bandpass filter using cross-coupled half-wavelength open-loop microstrip hairpin resonators with improved stopband skirt characteristics and spurious harmonic suppression is presented in this article. The proposed filter has a fractional bandwidth of 5% subject to the design frequency of 2.5 GHz for WLAN applications. At first, a fourth-order compact hairpin-line bandpass filter has been designed by arranging the doubly folded hairpin-line cells symmetrically in a cross-coupled configuration. Accordingly, a size reduction of 11.36% over folded hairpin-line filter has been achieved with an improvement in the skirt characteristics by placing two deep transmission zeros at the edges of the passband. However, the benefits of cross-coupled configuration have been overshadowed by the presence of spurious harmonics with an attenuation level of 10 dB. Subsequently, spur-line has been employed in each coupled section of adjacent folded hairpin-line cells for achieving modal phase velocity compensation. As a result, an extended stopband with a rejection level of 35 dB up to $3.16f_0$ and overall size reduction of 20.46% has been achieved.

14) Multi-Folded Bandpass Filter with Harmonic Suppression by Meander Spurline

Tarun Kumar Das, Pritam Paul, Suprava Das, and Sayan Chatterjee

Proceedings of IEEE INDICON 2022, Guwahati, India, pp. 1-6, 19-21 December, 2021, doi: 10.1109/INDICON52576.2021.9691654

Abstract

The design of a fourth-order compact bandpass filter using multi-folded hairpin resonators with an improvement in the skirt characteristics and an extended stopband is presented in this article. At first, the compactness of 40% has been achieved for a fourth-order bandpass filter centered at 2.5 GHz and fractional bandwidth of 5% over the conventional hairpin-line filter by cascading the multi-folded hairpin line (MFHL) cells in a hybrid configuration. Accordingly, the skirt characteristics have been improved by the introduction of a deep transmission zero of attenuation level of 56 dB at the upper edge of the passband. However, the presence of the spurious harmonics with the attenuation level of 10 dB has overshadowed the benefits of the multi-folding of the hairpin lines. In this context, a meander spur line with optimum dimensions was incorporated symmetrically in each coupled section of adjacent MFHL cells to achieve modal phase velocity compensation. As a result, an extended

stopband with a rejection level of 25 dB up to $4.8f_0$ and 33 dB up to $4.16f_0$ has been obtained. Besides, an overall size reduction of 49% has been achieved accordingly.

15) Wide Stopband Centrally Corrugated Folded Bandpass Filter with Trapezoidal Spurline

Tarun Kumar Das and Sayan Chatterjee

Proceedings of IEEE WAMS 2022, Rourkela, India, 5-8 June, 2022, pp. 1-5,
doi: 10.1109/WAMS54719.2022.9848230

Abstract

The present article describes the design of a compact fourth-order centrally corrugated hairpin line bandpass filter with an improved skirt characteristic and an extended stopband. At first, the compactness of 52% has been achieved for a fourth-order bandpass filter centered at 2.5 GHz and fractional bandwidth of 5% over the conventional hairpin-line filter by cascading the centrally corrugated double folded hairpin line (CCDFHL) cells in a hybrid configuration. Accordingly, a symmetrical passband with attenuation levels of more than 40 dB at the edges and sharp skirt characteristics have been occurred due to the strong capacitive coupling between the corrugated folded arms of each double folded hairpin-line (DFHL) cell. However, the harmonics with the attenuation level of 10 dB have limited the applications of such filter for mixers and frequency synthesizers in WLAN. Subsequently, the coupled arms of two adjacent DFHL cells have been perturbed by a trapezoidal-shaped meander spurline with optimum dimensions to achieve modal phase velocity compensation. As a result, an extended stopband with a rejection level of 35 dB up to $3.88f_0$ and 25 dB up to $6f_0$ has been obtained. Besides, an overall size reduction of 59.6% compared to the conventional filter has been achieved accordingly.

16) Centrally Corrugated Cross-Coupled Wide Stopband Folded Bandpass Filter with Spurline

Tarun Kumar Das, Ayona Chakraborty, Sayan Chatterjee, Bhaskar Gupta

Proceedings of 2022 Microwave Mediterranean Symposium (MMS), Pizzo Calabro, Itally, pp. 1-6, 9-13 May, 2022, doi:10.1109/MMS55062.2022.9825567

Abstract

The present article describes the performance of a fourth-order cross-coupled bandpass filter using double-folded microstrip hairpin resonators for the improvement of skirt characteristics and harmonics suppression. The proposed filter is centered at 2.5 GHz with a fractional bandwidth of 4%. At first, the central folded pair of resonators of the unit hairpin-line cell has been modified with periodic trapezoidal corrugations to achieve improved skirt characteristics with the attenuation level of 40 dB

and a compact circuit area with a size reduction of 11.36% over the conventional cross-coupled filter with the same specifications. However, the harmonics have not been suppressed significantly by this compact structure. Subsequently, trapezoidal- shaped meander spurlines have been incorporated in each coupled section of the adjacent folded hairpin-line cells for achieving modal phase velocity compensation. As a result, an extended stopband with a rejection level of 34 dB up to $3.04f_0$ and an overall size reduction of 20.42% has been achieved.

Tarun Kumar Das
03/11/22

Sayan Chatterjee
03/11/22

Dr. Sayan Chatterjee
Professor
Electronics & Telecomm. Engg. Dept.,
Jadavpur University, Kolkata - 700032.